

Replicating Nature's Design in Steel Structures to Enhance Structural Performance under Transverse Load

Yap Kian Lim (MEng)

A thesis submitted to the University of Nottingham for the degree of Doctor of Philosophy

September 2020

Abstract

Many structural buildings are conceptualised and designed with a key emphasis on vertical imposed loadings and lesser on lateral loadings (other than wind loading consideration). However, in landslide-prone areas, strong coastal waves or earthquake-prone areas, engineers counteract these lateral forces of nature with new and innovative design structures like retaining walls, breakwaters and mechanical dampers. The problem often gets complicated when the effects of earthquake come into the equations, particularly in tall building structures. The solution to the problem lies in nature, where they are suited to surviving the harshest environment. The research aims to enhance the efficiency of steel structures under lateral loading by replicating the design found in nature (trees). Since there is no study on utilising nature's notch shape profile and integrating nature's design in civil engineering structures, three separate linear studies were conducted. The first study compares the traditional cantilever beam designs against the cantilever beam with the projection according to the Method of Tensile Triangles (MTT) across the various loading conditions and beam depths. The second study investigates the various cantilever beam geometries' load paths to understand better their behaviour and structural performance through the topology optimisation technique. The third study investigates the feasibility of introducing columns with the Method of Tensile Triangles (MTT) projection in the connections or joints in steel multistorey moment-resisting frame structures under earthquake loadings. The studies found that the MTT cantilever beams perform best when the projection considered is small. The load path obtained through the topology optimisation study shows better utilisation of the projection in smaller

MTT cantilevers beam projections. In addition, the multistorey achieves better lateral resistance by introducing a better connections/joints system in both analysis under the equivalent lateral force method and the response spectrum. Hence, utilising the MTT shape profile or replicating nature's shape profile in steel structures can lead to better structural design. Thus, the size and shape of a structure play a pivotal role in the performance of a structure. However, it should be noted that further in-depth studies are still required to validate the numerical model and to expand the research further into other civil engineering structures, e.g., gravity walls, water dams and counterfort.

List of Publications

Published:

KIAN LIM YAP, MOHAMMED PARVEZ ANWAR, JAYAPRAKASH JAGANATHANA, WAEL ELLEITHY and TECK LEONG LAU, 2018. Feasibility Study on Replicating Tree Design Structure in Trusses Subjected to Lateral Loading International Journal of Engineering and Technology. 7(3.36), 84-89

YAP KIAN LIM, ANWAR MOHAMMED PARVEZ, JAYAPRAKASH JAGANATHAN, WAEL ELLEITHY and LAU TECK LEONG, 2019. Nature's Design Shapes in Civil Engineering Structures to Enhance Performance and Efficiency: A review International Journal of Innovative Technology and Exploring Engineering (IJITEE). 8(6S3), 79-86

KIAN LIM YAP, ANWAR MOHAMMED PARVEZ, JAYAPRAKASH JAGANATHAN, WAEL ELLEITHY, TECK LEONG LAU and JING YING WONG, 2019. Biomimicry in Civil Engineering Structures under Transverse Loading In: International Conference on Recent Trends in Construction Materials and Structures (ICON2019), VIT, Vellore, India (In Press.)

Others:

AW JIA HAO, MOHAMMED PARVEZ ANWAR, WAEL ELLEITHY, JAYAPRAKASH JAGANATHAN, YEONG TUCK WAI and YAP KIAN LIM, 2019. A Review of Seismic Vulnerability and Rehabilitation of Reinforced Concrete Structures In: International Conference on Recent Trends in Construction Materials and Structures (ICON2019), VIT, Vellore, India. (In Press.)

SHADY ADEL FAHIM REZKALLA, MOHAMMED PARVEZ ANWAR, JAYAPRAKASH JAGANATHANA, WAEL ELLEITHY, TECK LEONG LAU and KIAN LIM YAP, 2018. Parametric Study on Seismic Response of RCS Structures International Journal of Engineering and Technology. 7(3.36), 90-95

Acknowledgements

A significant amount of time was invested in completing this thesis, and I would like to thank those involved. Firstly, I would like to thank my principal supervisor, Dr. Abdullahi Ali Mohamed, for his supervision, guidance and support throughout the final years of completing the thesis.

Secondly, a personal thank you to my initial principal supervisor Dr. Anwar Mohammed Parvez, for his supervision, guidance and support throughout the entire duration.

Thirdly, I have my co-supervisors to thank for their valuable input towards finishing my thesis, namely Dr. Jaganathan Jayaprakash, Dr. Wael Elleithy and Dr. Anwar Mohammed Parvez.

Finally, I want to thank the University of Nottingham Malaysia Campus for providing me with a platform and the opportunity to conduct research. Finally, I am grateful to my friends and family for all their support during this period. My family also share their burden by providing me with financial support to support my research development interest.

Table of Contents

Abstract ii

List of Publications iv

Acknowledgements vi

Table of Contents vii

List of Figures xv

List of Tables xxx

List of Abbreviations xxxiv

Chapter 1 Introduction 1

1.1 Background of the Research 1

1.2 Problem Statement 2

1.3 Aim & Objectives 4

1.3.1 Aim 4

1.3.2 Objectives 4

1.4 Scope of the Research 4

1.5 Significance of Research 5

1.6 Limitations of the Study 6

1.7 Outline of the Thesis 8

Chapter 2 Literature Review 10

2.1 Introduction 10

2.2 Studying and Learning from Nature (Replicating from Nature) 10

2.3 Principle of Biological Growth 12

2.3.1 Tree's Adaptation to External Forces 15

2.3.2 Development of Buttresses in Trees 16

2.4 Secrets of Trees 17

2.4.1 The Anatomy of Trees 17

2.4.2 Correlation between the Development of Trees and its Environmental Condition 18

2.4.3 Buttresses in Trees 19

2.5 Notch Profile and Stress Concentration in Structural Components 27

2.5.1 Understanding Notch Stresses 28

2.5.2 Optimisation of Notch Profile with Different Optimisation Methods 29

2.5.3 Effects of Mechanical Performance with Different Notch Profiles Lengths 30

2.5.4 Application of Computational Aided Optimisation (CAO) and Soft Kill Optimisation (SKO) Method in Manufacturing 33

2.6 Graphical Optimisation Method 35

2.6.1 Background 35

2.6.2 Nature Inspired Contours 36

2.6.3 Method of Tensile Triangles 41

2.6.4 Effectiveness of Method of Triangles in Comparison with Other Notch Profile 46

2.6.5 Applications and Success of using the "Method of Tensile Triangles" 60

2.7 Biomimicry in Civil Engineering 65
2.7.1 Trees and Civil Engineering Structures 66
2.7.2 Safety Factor of Trees 66
2.7.3 Resolving Stress Singularities in Dissimilar Material Joints with A Biologically Inspired Design 69
2.8 Loading Patterns of Structural Members 84
2.8.1 Strut and Tie Models (STM) 85
2.8.2 Topology Optimisation Methods in Reinforced Concrete structures 87
2.8.3 Optimisation of a Cantilever Beam 93
2.8.4 Optimisation of a Bracing System for Multistorey Steel Building Framework 95
2.8.5 Topology Optimisation of Building Structures under Dynamic Loads ... 102
2.9 Earthquake Resistance Designs 106
2.9.1 Steel Structures 106
2.9.2 Beam to Column Connections 111
2.9.3 Column-Tree Moment Connections 112
2.10 Summary 117
Chapter 3 Methodology 121
3.1 Introduction 121
3.2 MATLAB Script Structure 125
3.2.1 Finite Element Modelling and Topology optimisation 125
3.2.2 Dynamic Behaviour in Structural Analysis 130

3.3 Validation of the Numerical Model 136

3.3.1 ANSYS (Finite Element Method and Topology Optimisation) 137

3.3.2 GSA OASYS (Trusses) 141

3.3.3 SAP2000 (Seismic Analysis of Multistorey) 143

Chapter 4 Comparison of Various Cantilever Beam Geometries under Transverse Loading 148

4.1 Details of the Finite Element Model 148

4.1.1 The Geometry of the Model Specimens 150

4.1.2 Loading Conditions of Models 152

4.2 Deflection Performance of the Various Cantilever Beams 154

4.2.2 Improvement and Limitation of the Cantilever Beams 156

4.2.3 Suggested Optimum Values through the 3 Axes Graph Method 163

4.2.4 Workable/Acceptable Range of Cantilever Design Parameter 180

4.3 Stress profile 202

4.4 Discussion 208

4.5 Summary 211

Chapter 5 Investigation on the Effects of Load Faces and Aspect Ratios on the Various Cantilever Beam Geometries 212

5.1 Details of the Finite Element Model 212

5.2 Comparison of the 4 Single Point Load Conditions 214

5.3 Deflection Resistance of the Various Cantilever Beam Geometries and its Loading Condition 221

5.3.1 Deflection limit 221
5.3.2 The Combined Result of Each Cantilever Geometry 224
5.3.3 Variation in Cantilever Beam Depth 226
5.3.4 Deflection Performance for the Volume of Up to 50% 228
5.4 Discussion 230
5.5 Summary 234
Chapter 6 Topology Optimisation of Various Cantilever Beam Geometries 235
6.1 Retained Volume Ratio and its Compliance 235
6.2 Load Path of the Various Cantilever Beam Geometries 238
6.2.1 Topology Plots 240
6.3 Replicating the Topology Optimised Models 243
6.4 Replicating the Topology Plots as Trusses 255
6.4.1 Pin and Roller Support 256
6.4.2 Pin and Pin Support 262
6.5 Discussion 270
6.6 Summary 273
Chapter 7 Replicating Nature's Design in Multistorey Structures 274
7.1 Detail of the Finite Element Model 274
7.2 Replicating MTT Design Profile in the Columns 276
7.2.1 Modal Analysis 280
7.2.2 MTT Column Design using Industry Sections versus Custom Sections 281
7.2.3 The Effect of Reduction in Beam Section 289

7.2.4 Minimising the Capacity in both Beam and Column Sections 291
7.3 Discussion 296
7.4 Summary 298
Chapter 8 Conclusion and Recommendations for Future Works 299
8.1 Conclusions 299
8.2 Recommendations for Future Works 301
References 302
Appendix A. MATLAB Script 314
A.a. Finite Element Modelling and Topology Optimisation 314
A.a.a The Main Script 314
A.a.b Finite Element Subscript 314
A.b. Trusses 314
A.b.a The Main Script 314
A.b.b Parameters and Details of the Model 314
A.b.c Results Output 314
Appendix B. Effects of Load Face on the Various Cantilever Beam Geometries 316
B.a. Displacement 316
B.a.a Plots 316
B.a.b Charts 318
B.b. Stress Profile 331
B.b.a Plots 331

B.b.b Charts 333

Appendix C. Topology Optimisation of a Cantilever Beam 347

C.a. Topology Plots 347

C.a.a Depth of 20mm 347

C.a.b Depth of 30mm 347

C.a.c Depth of 40mm 348

C.a.d Increased Depth (20mm to 67mm) 348

C.b. Topology Optimised Models 349

C.b.a Method of Tensile Triangles (MTT) 349

C.b.b Method of Tensile Triangles Rule of Thumb (MTTR) 352

C.b.c Standard Triangle (ST) 355

C.b.d Increased Depth (ID) 358

C.c. Comparison plot between the Replicated Truss versus Topology Optimised versus Original 362

C.c.a Method of Tensile Triangles (MTT) 362

C.c.b Method of Tensile Triangles Rule of Thumb (MTTR) 363

C.c.c Standard Triangle (ST) 364

C.c.d Increased Depth (ID) 365

Appendix D. Multistorey 367

D.a. SAP2000 Verification 367

D.a.a Eurocode 8 Worked Example 367

D.b. Multistorey Structure 368

D.b.a Assumptions 368

D.b.b Base Model 369

D.b.c MTT Model 369

List of Figures

Figure 1-1: Historical Structures around the world: (a) Parthenon, Acropolis of Athens (Swayne, 1978) (b) Great Pyramids of Giza, Giza Pyramid Complex, Egypt (Liberato, 2006) (c) Colosseum Rome, Italy (Hakim, 2015) 2

Figure 2-1: Inspired by gecko's climbing ability. A man hanging himself above ground using a reusable suction or sticker plate made from synthetic gecko's feet, behind him are his research team (*Van der Waals and the Gecko*, 2014) 11

Figure 2-2: A simplified process of bone tissue regeneration (Guillemin *et al.*, 1987; Petite *et al.*, 2000) 11

Figure 2-3: An illustration of a simplified process of a viral construction for denser material (Lee *et al.*, 2002; Lee, Lee and Belcher, 2003) 12

Figure 2-4: Stress concentration experienced along the tree branch towards its stem (Mattheck, 1990a) 13

Figure 2-5: Antler of a red deer optimised in nature (Mattheck, 1990a) 14

Figure 2-6: CAO method used to prove the growth pattern of a vertebral arch (Mattheck, 1990a) 14

Figure 2-7: Graphical display of stresses in the vertebral arch. (Mattheck, 1990a) .. 15

Figure 2-8: Increased in the contact area to reduce contact stresses (Mattheck, 1990) 16

Figure 2-9: Cross-section of tree stem affected by stakes on trees (Mattheck, 1990) 16

Figure 2-10: The cross-section of the tree trunk has thicker rings formed at notch stress (Mattheck, 2006) 17

Figure 2-11: (a) Basic Anatomy of trees (Mattheck, Bethge and Schäfer, 1993). (b) Tree stem thickness varying along with its height according to wind loading. (Mattheck, 1990b) 18

Figure 2-12: An illustration of a tree stump experiencing wind loading. (Crook, Ennos and Banks, 1997) 19

Figure 2-13: A graph showing the number of species against the percentage with buttresses at the Lawachara National Park covering 238 trees of 12 different species (Mehedi, Kundu and Chowdhury, 2012). 21

Figure 2-14: An illustration of how trees with buttresses fail (1) Buttresses without sinkers (2) Buttresses with sinkers (Crook, Ennos and Banks, 1997) 23

Figure 2-15: An illustration of how trees without buttresses fail. (Crook, Ennos and Banks, 1997) 23

Figure 2-16: Graphs showing the relationship between the tree height, the tree stem diameter, and the buttressed height at the Lawachara National park, Bangladesh. (**: $p < 0.01$) (Mehedi, Kundu and Chowdhury, 2012)..... 26

Figure 2-17: Graphs showing the relationship between the buttressed height and the tree stem diameter at the O'ahu, Hawaii. (Woodcock, Santos and Taylor, 2000)..... 27

Figure 2-18: Graphs showing the relationship between tree height and tree stem diameter at the O'ahu, Hawaii. (Woodcock, Santos and Taylor, 2000) 27

Figure 2-19: (a) An illustration of the overall stresses near the notch (b) Correlation between lateral forces and bending stresses of notch stresses (Mattheck, 2006)..... 29

Figure 2-20: Notch shape and stresses along the contour (Mattheck, 2006) 30

Figure 2-21: Specimens plotted using finite element modelling for different notch sizing (de Albuquerque Simões, de Castro and Meggiolaro, 2012). 30

Figure 2-22: Stress concentration of each specimen along the fillet (de Albuquerque Simões, de Castro and Meggiolaro, 2012). 31

Figure 2-23: Stress concentration factor for non-optimised specimen II (de Albuquerque Simões, de Castro and Meggiolaro, 2012). 31

Figure 2-24: Stress concentration factor for optimised specimen II (de Albuquerque Simões, de Castro and Meggiolaro, 2012). 32

Figure 2-25: Stress concentration vs R/W ratio vs required length for specimen II (de Albuquerque Simões, de Castro and Meggiolaro, 2012). 32

Figure 2-26: The engine supporting structures in Opel cars (Bar-cohen, 2012)..... 33

Figure 2-27: A mechanical shaft optimised through the CAO method (Bar-cohen, 2012). 34

Figure 2-28: Chain link optimised through the CAO method (Mattheck, 1990)..... 34

Figure 2-29: Optimisation result of a crane hook (Mattheck, 1990)..... 35

Figure 2-30: An illustration of the original Baud curve for bending and tensile (Mattheck, 1990a) 37

Figure 2-31: Baud curve in relation to a human tibia (the leg bone below the knee) (Mattheck, 1990a) 37

Figure 2-32: (a) Claw of a bear (b) A Set of 10 cat claws (Bone Clones Inc., 2016) 38

Figure 2-33: An illustration of a sample variation of the logarithmic spiral. (Mattheck and Reuss, 1991) 38

Figure 2-34: The graph shows a dimensionless Mises equivalent stress vs Contour coordinate s (Mattheck and Reuss, 1991). 39

Figure 2-35: The illustrations above show the distribution of Mises stress iso-lines with (a) circular contours designed by most engineers and (b) optimised logarithmic spiral design (Mattheck and Reuss, 1991) 40

Figure 2-36: An illustration of how a tree optimises notch stresses through a simple graphical procedure. This method is known as the “Method of Tensile Triangle”. (Mattheck, 2007) 42

Figure 2-37: An illustration of how a tree grows to reduce notch stresses. (Mattheck, Kappel and Sauer, 2007) 43

Figure 2-38: The difference of stress concentration along the notch contour between the engineer’s notch and the tree’s notch (Mattheck, Kappel and Sauer, 2007)..... 44

Figure 2-39: Shape optimisation of a (1) symmetrical and (2) unsymmetrical tree fork. (Mattheck, 2006) 45

Figure 2-40: Claws do follow the shapes similar to the “Method of Tensile Triangles”. (Mattheck, 2006) 45

Figure 2-41: Comparison between different notch shapes in relation to stress concentration factor (de Albuquerque Simões, de Castro and Meggiolaro, 2012).... 46

Figure 2-42: Geometrical profiles of different notches (de Albuquerque Simões, de Castro and Meggiolaro, 2011)..... 47

Figure 2-43: Flat bar subjected to (a) pure tension (b) pure bending (de Albuquerque Simões, de Castro and Meggiolaro, 2011) 48

Figure 2-44: Cut out window steel plate subjected to pure tension pulling (de Albuquerque Simões, de Castro and Meggiolaro, 2011) 49

Figure 2-45: SCF of notch under tension load for a flat bar (de Albuquerque Simões, de Castro and Meggiolaro, 2011). 49

Figure 2-46: SCF of notch under bending load for a flat bar. (de Albuquerque Simões, de Castro and Meggiolaro, 2011) 50

Figure 2-47: Peterson’s charts for a flat bar with shoulder fillet under (a) tension load (b) bending load (Pilkey *et al.*, 2007; de Albuquerque Simões, de Castro and Meggiolaro, 2011) 50

Figure 2-48: Smoothing of corner within the cut-out window of steel plate with different notch profile (de Albuquerque Simões, de Castro and Meggiolaro, 2011). 51

Figure 2-49: Von Mises stress along the nodal position around the inspection window under tension load (de Albuquerque Simões, de Castro and Meggiolaro, 2011). 52

Figure 2-50: An illustration of the model tested (Ciomber and Jakel, 2014). 53

Figure 2-51: A graph showing a point where the height of the model is no longer influenced by the changes in stress concentration in the testing sample (Ciomber and Jakel, 2014). 54

Figure 2-52: A graph showing a point where the diameter of the model no longer influenced by the changes in stress concentration in the testing sample (Ciomber and Jakel, 2014). 54

Figure 2-53: An illustration showing the following condition that models can undergo (Ciomber and Jakel, 2014). 55

Figure 2-54: A graphical comparison of different notch shape to their overall size (Ciomber and Jakel, 2014). 57

Figure 2-55: Optimisation of shoulder fillet through Mattheck's method of tensile triangles (Komarla, 2011). 60

Figure 2-56: The stress distribution diagram "Method of Tensile Triangle" (Komarla, 2011). 60

Figure 2-57: A picture of a Cat 6*A* module (Eichenberger *et al.*, 2011). 61

Figure 2-58: Stress concentration of a screw optimised using the "Method of Tensile Triangles" (Bar-cohen, 2012)..... 61

Figure 2-59: Drilling away slot ends did not stop crack formation and propagation of large industrial drum (Carpi and Brebbia, 2010). 62

Figure 2-60: Drilling of crack tip reduces the stress experienced (Carpi and Brebbia, 2010). 62

Figure 2-61: Notch stresses (A) Orientation of notch shape along the same direction of force (B) Theory of notch stress (Mattheck, 2004)..... 63

Figure 2-62: (A) Application of tensile triangles at slot ends; (B)Theoretical notch stresses; (C) Tension pulling uniformly of a theoretical sample; (D, E) FEM analysis showing stresses experienced; (F) Tension pulling of the sample. (Carpi and Brebbia, 2010) 64

Figure 2-63: Steel plate samples with different shaped slot ending. (A) A slot without modification; (B, C) slots drilled at endings (r=1mm, 2mm); (D) slot cut with straight traverse ending (E, F) Ends of Slot cut with tensile triangle shape (h=2mm, 5mm) (Carpi and Brebbia, 2010)..... 65

Figure 2-64: The graph shows the factor of safety against the cross-section of the tree stem, where R is the stem radius and H is the removed material. (Mattheck, Bethge and Schäfer, 1993) 67

Figure 2-65: Trees near the Mississippi river damaged by beavers (a) Stress magnification of 4; (b) Stress magnification greater than 5 (Mattheck, Bethge and Schäfer, 1993). 68

Figure 2-66: A tree with a window frame of a 2/3 stem diameter (Mattheck, Bethge and Schäfer, 1993). 68

Figure 2-67: Normal stress distribution of a typical tensile specimen (a) same material (b) dissimilar material(Xu and Sengupta, 2004) 70

Figure 2-68: (a) Fringe pattern from a CGS photograph showing the stress concentration at the free edges between the two materials under tensile load. (b) An illustration of a joint angle between material 1 and 2. (Xu and Sengupta, 2004)..... 70

Figure 2-69: A graphical illustration of the various aluminium–polycarbonate joint specimens (a) straight edge (baseline), (b) shaped edge with least stress singularities, (c) axisymmetric straight-edge specimen, and (d) axisymmetric shaped edge specimen (Xu, 2004) 71

Figure 2-70: A set of two different types of joint angles in the aluminium-polycarbonate joint specimen. (a) Straight edge (90°-90°) (b) convex-shaped (45°-65°)(Xu and Sengupta, 2004)..... 72

Figure 2-71: (a) A proposed convex joint of metal and polymer interface. (b) Finite-element mesh and boundary conditions of joint subjected to in-plane tensile load. (Xu, 2004) 74

Figure 2-72: A finite element analysis of a tree to a steel railing interface. 76

Figure 2-73: Stress singularity order λ obtained from finite-element analysis (showing its distribution close to the free edge and its fitted λ value). (a) Interfacial normal stress (b) Interfacial shear stress (Xu, 2004)..... 77

Figure 2-74: A comparison between the numerical and the experimental fringe pattern (d) and (f) in aluminium-polycarbonate joints with a straight edge joint. (Xu, 2004) 78

Figure 2-75: (A) and (B) are a comparison between the numerical and the experimental fringe pattern in aluminium-polycarbonate joints with the shape edged joint. (Xu, 2004; Xu and Sengupta, 2004)..... 79

Figure 2-76: (a) Interfacial normal stress and (b) Interfacial shear stress, with different extension distances (joint angles polycarbonate $\theta 1 = 45°$; aluminium $\theta 2 = 65°$ and it is a straight edge specimen when t = 0)(Xu, 2004) 80

Figure 2-77: Normalized interfacial normal stress with various aluminium joint angle $\theta 2$ while fixing the polycarbonate joint angle at $\theta 1 = 45°$ and t = 3 mm (Xu, 2004) 80

Figure 2-78: Interfacial cracks originated from initial defects before the final tensile failure in (a) shaped edge specimen (b) straight edge specimen(Xu and Sengupta, 2004) 81

Figure 2-79: 3D finite element model (a) Interfacial normal stress and shear stress along its width. (b) Interfacial normal stress along with its thickness (t = 3 mm)(Xu, 2004) 82

Figure 2-80: Interfacial normal stress and shear stress of the finite element model (a) unshaped axisymmetric (b) shaped axisymmetric (t = 3 mm)(Xu, 2004) 82

Figure 2-81: The laboratory results of specimens are summarized as a bar chart (a) PMMA & Aluminium (b) Polycarbonate and Aluminium (Xu and Sengupta, 2004)84

Figure 2-82: A deep simply supported beam with two concentrated loads (Liang, Xie and Steven, 2000; 2000b)..... 90

Figure 2-83: A deep simply supported beam with 2 openings is loaded by 2 concentrated loads. (Kong and Sharp, 1977) 90

Figure 2-84: A deep beam simply supported with a large hole and factored by a top-loading (Schlaich, Schafer and Jennewein, 1987b). 91

Figure 2-85: A simply supported beam loaded with a top mid-span concentrated load (Liang, Xie and Steven, 2000; 2000b) 91

Figure 2-86: iteration process of an optimum topology for a simply supported beam loaded with a top mid-span concentrated load (Liang, Xie and Steven, 2000; 2000b) 91

Figure 2-87: A corbel and column connection loaded by a concentrated load (Schlaich, Schafer and Jennewein, 1987b)..... 92

Figure 2-88: iteration process of an optimum topology for a corbel and column connection loaded by a concentrated load (Liang, Xie and Steven, 2000; 2000b).... 92

Figure 2-89: A cantilever beam with a point load at the centre of the free end (Liang, Xie and Steven, 1999). 94

Figure 2-90: Topology result by (1) (Liang, Xie and Steven, 1999). (2) (Chu *et al.*, 1996) (3) (Suzuki and Kikuchi, 1991) 94

Figure 2-91: Stress concentration for a cantilever beam with a point load at the bottom end (Mattheck, Kappel and Sauer, 2007). 95

Figure 2-92: The performance index of the full-width bracing system (Liang, 2007). 99

Figure 2-93: A 4 bays 12-story steel frame optimal topology of the bracing system (Liang, 2007)..... 99

Figure 2-94: The performance index of the two bays or a half bracing system (Liang, 2007). 100

Figure 2-95: A 2 bays 12-story steel frame optimal topology of the bracing system (Liang, 2007)..... 100

Figure 2-96 Comparison of topology optimisation techniques with the same total volume of material: (a) continuum approach; (b) topology obtained using quadrilateral

elements; (c) combined approach; (d) topology obtained through quadrilateral and discrete column elements. (Stromberg *et al.*, 2012)..... 102

Figure 2-97: Final topology for trial (a) 1; (b) 2; (c) 3; (d) 4. (Suksuwan and Spence, 2018) 103

Figure 2-98: Finite Element Analysis model of a beam to column frame connection and its stress concentration (Lee, Yang and Starossek, 2012) 104

Figure 2-99: Optimal topology layout for the two structural models of a beam to column frame connection (Lee, Yang and Starossek, 2012) 105

Figure 2-100: Eccentric bracing damping under lateral loading (G. MacRae, 2013; BRANZ's Seismic Resilience, 2020)..... 107

Figure 2-101: A single post-tensioned steel tendon (G. MacRae, 2013; BRANZ's Seismic Resilience, 2020) 108

Figure 2-102: Buckling restrained braces in steel frames (BRANZ's Seismic Resilience, 2020)..... 108

Figure 2-103: Mechanism of a symmetrical friction damper (G. MacRae, 2013; BRANZ's Seismic Resilience, 2020)..... 109

Figure 2-104: Various friction brace configurations (G. MacRae, 2013; BRANZ's Seismic Resilience, 2020) 109

Figure 2-105: Sliding hinge joint in steel moment-resisting frames (Sidwell G., 2010) 110

Figure 2-106: Joint Spring system (G. MacRae, 2013; BRANZ's Seismic Resilience, 2020) 111

Figure 2-107: Various types of column tree moment connections (Astaneh-Asl, 1997) 113

Figure 2-108: Traditional moment frame vs column tree frame (Astaneh-Asl, 1997) 114

Figure 2-109: Model detail and FEM result of the study of tree column connection design by (Chen, Lin and Lin, 2006; Chen and Lin, 2013) 116

Figure 3-1: Methodology Flow Chart 122

Figure 3-2: Finite Element Procedure (also applies to MATLAB)..... 124

Figure 3-3: Topology Optimisation Procedure 125

Figure 3-4: Stress-strain curve for the cantilever beam base model (200,40,1)mm 138

Figure 3-5: (a) Mesh (b) Comparison between MATLAB FEM and Euler Bernoulli 139

Figure 3-6: MATLAB FEM plots (a) Displacement (mm) (b) Stress (MPa) 140

Figure 3-7: ANSYS Workbench plots (a) Displacement (mm) (b) Stress (MPa).... 140

Figure 3-8: Cantilever beam 160mm x 100mm x 1mm 141

Figure 3-9: Topology plots (a) MATLAB (b) ANSYS (c) results by (Chu *et al.*, 1996) 141

Figure 3-10: Pratt truss-like structure 2m x 4m 142

Figure 3-11: Truss displacement plots (a) MATLAB (b) GSA 143

Figure 3-12: Reference model EC8 plan layout and column orientation (Philippe *et al.*, 2012) 144

Figure 3-13:Reference model EC8 bending moment diagram (a) Eqx (b) RS (Philippe *et al.*, 2012) 146

Figure 3-14: SAP2000 bending moment diagram (a)&(b) Eqx ;(c)&(d) RS 146

Figure 4-1: Simple Cantilever Beam (Base Model)..... 150

Figure 4-2: Cantilever Beam with Increased Depth (Traditional Model)..... 150

Figure 4-3: Cantilever Beam with a Tapering Triangle at the Bottom Face (Traditional Method)..... 151

Figure 4-4: Cantilever Beam with a Triangle Projection following the Method of Tensile Triangles' Shape Profile (Tree Buttress)..... 151

Figure 4-5: Cantilever Beam with a Triangle Projection using the Method of Tensile Triangles' Rule of Thumb..... 152

Figure 4-6: One Point Load (Downwards, Free-End, Top Face, 1000N)..... 153

Figure 4-7: Triangular Pressure Load (5MPa, Downwards, Top Face, Max at Free-End)..... 153

Figure 4-8: Various Cantilever Beams under the Deflection Limit of L/180; One Point Load (Downwards, Free-End, Top Face, 1000N)..... 157

Figure 4-9: Various Cantilever Beams under the deflection limit of L/180; (1) Black: "Increased Depth", (2) Blue: "Tapering Triangle", (3) Red: "Method of Tensile Triangle's Rule of Thumb", (4) Green: "Method of Tensile Triangle's Shape Profile"; One Point Load (Downwards, Free-End, Top Face, 1000N)..... 158

Figure 4-10: Various Cantilever Beams under the Deflection Limit of L/240; One Point Load (Downwards, Free-End, Top Face, 1000N)..... 158

Figure 4-11: Various Cantilever Beams under the deflection limit of L/240; (1) Black: "Increased Depth", (2) Blue: "Tapering Triangle", (3) Red: "Method of Tensile

Triangle's Rule of Thumb", (4) Green: "Method of Tensile Triangle's Shape Profile"; One Point Load (Downwards, Free-End, Top Face, 1000N)..... 159

Figure 4-12: Bending Moment Diagram for a cantilever beam (single point load at free-end)..... 160

Figure 4-13: Various Cantilever Beams at Maximum Additional Cantilever Depth; One Point Load (Downwards, Free-End, Top Face, 1000N)..... 161

Figure 4-14: Various Cantilever Beams at Maximum Additional Cantilever Depth; Triangular Pressure Load (5MPa, Downwards, Top Face, Max at Free-End) 162

Figure 4-15: Various Cantilever Geometry at Maximum Additional Cantilever Depth; (1) Black: "Increased Depth", (2) Blue: "Tapering Triangle", (3) Red: "Method of Tensile Triangle's Rule of Thumb", (4) Green: "Method of Tensile Triangle's Shape Profile"..... 163

Figure 4-16: Method of Tensile Triangles Deflection vs Total Length of Triangle vs Required Area for Various Cantilever Beams; One Point Load (Downwards, Free-End, Top Face, 1000N)..... 164

Figure 4-17: Method of Tensile Triangles Deflection vs Total Length of Triangle vs Required Area for Various Cantilever Beams; Triangular Pressure Load (5MPa, Downwards, Top Face, Max at Free-End)..... 165

Figure 4-18: Individual graph for Cantilever with Method of Tensile Triangles' Shape Profile; One Point Load (Downwards, Free-End, Top Face, 1000N)..... 166

Figure 4-19: Individual graph for Cantilever with Increased Depth; One Point Load (Downwards, Free-End, Top Face, 1000N)..... 167

Figure 4-20: Individual graph for Cantilever with Method of Tensile Triangles' Rule of Thumb; One Point Load (Downwards, Free-End, Top Face, 1000N)..... 167

Figure 4-21: Individual graph for Cantilever with Tapering Triangle; One Point Load (Downwards, Free-End, Top Face, 1000N)..... 168

Figure 4-22: Individual graph for Various Cantilever Beams; (1) Black: "Increased Depth", (2) Blue: "Tapering Triangle", (3) Red: "Method of Tensile Triangle's Rule of Thumb", (4) Green: "Method of Tensile Triangle's Shape Profile"; One Point Load (Downwards, Free-End, Top Face, 1000N)..... 169

Figure 4-23: Individual graph for Cantilever with Method of Tensile Triangles' Shape Profile; Triangular Pressure Load (5MPa, Downwards, Top Face, Max at Free-End) 169

Figure 4-24: Individual graph for Cantilever with Increased Depth; Triangular Pressure Load (5MPa, Downwards, Top Face, Max at Free-End) 170

Figure 4-25: Individual graph for Cantilever with Tapering Triangle; Triangular Pressure Load (5MPa, Downwards, Top Face, Max at Free-End) 170

Figure 4-26: Individual graph for Cantilever with Method of Tensile Triangle's Rule of Thumb; Triangular Pressure Load (5MPa, Downwards, Top Face, Max at Free-End) 171

Figure 4-27: Individual graph for Various Cantilever Beams; (1) Black: "Increased Depth", (2) Blue: "Tapering Triangle", (3) Red: "Method of Tensile Triangle's Rule of Thumb", (4) Green: "Method of Tensile Triangle's Shape Profile"; Triangular Pressure Load (5MPa, Downwards, Top Face, Max at Free-End) 172

Figure 4-28: Global graph for Various Cantilever Beams; One Point Load (Downwards, Free-End, Top Face, 1000N) 174

Figure 4-29: Global graph for Various Cantilever Beams; (1) Black: "Increased Depth", (2) Blue: "Tapering Triangle", (3) Red: "Method of Tensile Triangle's Rule of Thumb", (4) Green: "Method of Tensile Triangle's Shape Profile"; One Point Load (Downwards, Free-End, Top Face, 1000N) 175

Figure 4-30: Global graph for Various Cantilever Beams; Triangular Pressure Load (5MPa, Downwards, Top Face, Max at Free-End) 176

Figure 4-31: Global graph for Various Cantilever Beams; (1) Black: "Increased Depth", (2) Blue: "Tapering Triangle", (3) Red: "Method of Tensile Triangle's Rule of Thumb", (4) Green: "Method of Tensile Triangle's Shape Profile"; Triangular Pressure Load (5MPa, Downwards, Top Face, Max at Free-End) 177

Figure 4-32: Multiple geometries with normalised scale; One Point Load (Downwards, Free-End, Top Face, 1000N) 178

Figure 4-33: Multiple geometries with normalised scale; (1) Black: "Increased Depth", (2) Blue: "Tapering Triangle", (3) Red: "Method of Tensile Triangle's Rule of Thumb", (4) Green: "Method of Tensile Triangle's Shape Profile"; One Point Load (Downwards, Free-End, Top Face, 1000N) 179

Figure 4-34: Multiple geometries with normalised scale; Triangular Pressure Load (5MPa, Downwards, Top Face, Max at Free-End) 179

Figure 4-35: Multiple geometries with normalised scale; (1) Black: "Increased Depth", (2) Blue: "Tapering Triangle", (3) Red: "Method of Tensile Triangle's Rule of Thumb", (4) Green: "Method of Tensile Triangle's Shape Profile"; Triangular Pressure Load (5MPa, Downwards, Top Face, Max at Free-End) 180

Figure 4-36: Area vs Deflection for Various Cantilever Beams; One Point Load (Downwards, Free-End, Top Face, 1000N) 182

Figure 4-37: Area vs Deflection for Various Cantilever Beams subjected to Triangular Pressure Load (5MPa, Downwards, Top Face, Max at Free-End) 182

Figure 4-38: Area vs Deflection for the area around $8300mm2$; (1) Black: "Increased Depth", (2) Red: "Method of Tensile Triangle's Rule of Thumb", (3) Green: "Method of Tensile Triangle's Shape Profile"; One Point Load (Downwards, Free-End, Top Face, 1000N) 183

Figure 4-39: Area vs Deflection for the area around 8900$mm2$-9200$mm2$; (1) Black: “Increased Depth”, (2) Blue: “Tapering Triangle”, (3) Red: “Method of Tensile Triangle’s Rule of Thumb”, (4) Green: “Method of Tensile Triangle’s Shape Profile”; One Point Load (Downwards, Free-End, Top Face, 1000N)..... 183

Figure 4-40: Area vs Deflection for the Bisected Value; (1) Black: “Increased Depth”, (2) Red: “Method of Tensile Triangle’s Rule of Thumb”, (3) Green: “Method of Tensile Triangle’s Shape Profile”; Triangular Pressure Load (5MPa, Downwards, Top Face, Max at Free-End)..... 186

Figure 4-41: Depth vs Deflections for Various Cantilever Beams; One Point Load (Downwards, Free-End, Top Face, 1000N)..... 188

Figure 4-42: Depth vs Deflections for Various Cantilever Beams; Triangular Pressure Load (5MPa, Downwards, Top Face, Max at Free-End)..... 188

Figure 4-43: Depth vs Deflections for Various Cantilever Beams; (1) Black: “Increased Depth”, (2) Blue: “Tapering Triangle”, (3) Red: “Method of Tensile Triangle’s Rule of Thumb”, (4) Green: “Method of Tensile Triangle’s Shape Profile”; One Point Load (Downwards, Free-End, Top Face, 1000N)..... 189

Figure 4-44: Depth vs Deflections for Various Cantilever Beams; (1) Black: “Increased Depth”, (2) Blue: “Tapering Triangle”, (3) Red: “Method of Tensile Triangle’s Rule of Thumb”, (4) Green: “Method of Tensile Triangle’s Shape Profile”; Triangular Pressure Load (5MPa, Downwards, Top Face, Max at Free-End) 190

Figure 4-45: Clear Optimum Comparison Value for the Cantilever with Method of Tensile Triangles’ Shape Profile; (1) Black: “Increased Depth”, (2) Blue: “Tapering Triangle”, (3) Red: “Method of Tensile Triangle’s Rule of Thumb”, (4) Green: “Method of Tensile Triangle’s Shape Profile”; One Point Load (Downwards, Free-End, Top Face, 1000N)..... 192

Figure 4-46: Efficiency (area/deflection vs area) for Various Cantilever Beams (up to 20000$mm2$); One Point Load (Downwards, Free-End, Top Face, 1000N) 196

Figure 4-47: Efficiency (area/deflection vs area) for Various Cantilever Beams (up to 13500$mm2$); One Point Load (Downwards, Free-End, Top Face, 1000N) 196

Figure 4-48: Efficiency (area/deflection vs area) for Various Cantilever Beams (up to 20000$mm2$); Triangular Pressure Load (5MPa, Downwards, Top Face, Max at Free-End)..... 197

Figure 4-49: Efficiency (area/deflection vs area) for Various Cantilever Beams (up to 13500$mm2$); Triangular Pressure Load (5MPa, Downwards, Top Face, Max at Free-End)..... 198

Figure 4-50: Efficiency (area/deflection vs area) for Various Cantilever Beams (up to 9400$mm2$); One Point Load (Downwards, Free-End, Top Face, 1000N)..... 199

Figure 4-51: Efficiency (area/deflection vs area) for Various Cantilever Beams (up to 10000$mm2$); Triangular Pressure Load (5MPa, Downwards, Top Face, Max at Free-End)..... 200

Figure 4-52: Performance of Cantilever (Deflection vs Area "%") for Various Cantilever Beams; One Point Load (Downwards, Free-End, Top Face, 1000N).... 201

Figure 4-53: Performance of Cantilever (Deflection vs Area "%") for Various Cantilever Beams; Triangular Pressure Load (5MPa, Downwards, Top Face, Max at Free-End)..... 201

Figure 4-54: Equivalent stress for 40mm cantilever beam under STD load..... 204

Figure 4-55: Equivalent stress vs volume for 40mm cantilever beam under TTD load 205

Figure 4-56: Stresses experience across the various 40mm cantilever beam geometries. (a) STD 300MPa, (b) STD 600MPa, (c) TTD 100MPa, (d) TTD 200MPa..... 207

Figure 5-1: Separate loading conditions on the cantilever beam. (a) 1000N single point load top face downwards (STD); (b) 1000N single point load bottom face downwards (SBD); (c) 1000N single point load top face upwards (STU); (d) 1000N single point load bottom face upwards (SBU); (e) 5MPa triangular pressure top face downwards with the maximum at its free end (TTD). 213

Figure 5-2: Various cantilever beam geometries. (a) standard (base model), (b) cantilever beam with increased depth (CID), (c) cantilever beam with a tapering triangle (ST), (d) cantilever beam with a triangular projection following the Method of Tensile Triangles Rule of Thumb (MTTR), (e) cantilever beam with a triangular projection following the Method of Tensile Triangles (MTT). 214

Figure 5-3: Deflection comparison across the various cantilever beam geometries 217

Figure 5-4: Deflection comparison over the various cantilever beam geometries (continued) 218

Figure 5-5: Stress profile (a) 12mm ST (b) 24mm ST (c) 75mm MTTR (d) 175mm MTT 220

Figure 5-6: Relative cantilever beam dimension (a) 20mm STD, (b) 30mm STD, (c) 40mm STD (d) 20mm TTD (e) 30mm TTD..... 224

Figure 5-7: Combined results on each of the cantilever beam geometries under STD loading condition..... 225

Figure 5-8: Combined results on each of the various cantilever beam geometries under TTD loading condition..... 226

Figure 5-9: Deflection vs volume plot of the different cantilever beam depths 228

Figure 5-10: Deflection performance for the volumes of up to 50%..... 230

Figure 6-1: Cantilever beam of 200mm x 40mm x 1mm subjected to a point load 236

Figure 6-2: Compliance vs Retained Volume Ratio 236

Figure 6-3: Topology plot of a (200mm x 40mm x 1mm) cantilever beam showing the various retained volume ranging from 0.3 to 0.9. 237

Figure 6-4: Topology plots for 75mm MTT cantilever beam (a) retained density plot (b) density plot 239

Figure 6-5:Underutilisation of the triangular projection in the MTT beam (200mm x 20mm x 1mm) with a 30mm projection. 240

Figure 6-6: Less structured topology at the end of the MTT beam (200mm x 20mm x 1mm) with a 100mm triangular projection 241

Figure 6-7: Triangle-shaped topology in MTTR beam (200mm x 20mm x 1mm) with a 200mm projection. 241

Figure 6-8: Increased Depth Topology (a) 25mm (b) 55mm 242

Figure 6-9: Method of Tensile Triangles cantilever beam (200mm x30mm x 1mm) with a 180mm triangle projection (a) Topology generated (b) Post-processed topology (c) Deflection plot (mm) (d) Stress plot (MPa) 244

Figure 6-10:Average Deflection Difference Between The Optimised and the Original Cantilever Beam 247

Figure 6-11: Average Stress Difference Between The Optimised and the Original Cantilever Beam 247

Figure 6-12: Comparison of the deflection vs volume between the original cantilever and the topology optimised model. (a) 20mm MTT (b) 20mm MTTR (c) 20mm ST (d) 30mm MTT (e) 30mm MTTR (f) 30mm ST (g) 40mm MTT (h) 40mm MTTR (i) 40mm ST (j) 20mm–40mm ID 249

Figure 6-13: Comparison of the stress vs volume between the original cantilever and the topology optimised model. (a) 20mm MTT (b) 20mm MTTR (c) 20mm ST (d) 30mm MTT (e) 30mm MTTR (f) 30mm ST (g) 40mm MTT (h) 40mm MTTR (i) 40mm ST (j) 20mm–40mm ID 251

Figure 6-14: Triangular projection of a 20mm MTT cantilever beam (a) 25mm length (b) 200mm length 252

Figure 6-15: Triangular projection in a 20mm St cantilever beam (a) 1mm depth (b) 24mm depth 253

Figure 6-16: Deflection vs volume and Stress vs Volume Plot for the various cantilever beam geometries, (1st row) 20mm, (2nd row) 30mm, (3rd row) 40mm 254

Figure 6-17: Topology of the truss design (a) according to the generated topology (b) modified topology 255

Figure 6-18: Deflection plot for MTT 180mm truss on a pin and roller support 257

Figure 6-19: Deflection plot for MTTR 200mm truss on a pin and roller support 258

Figure 6-20: Deflection plot for ST 24mm truss on a pin and roller support 259

Figure 6-21: Deflection plot for ID 45mm truss on a pin and roller support..... 261

Figure 6-22: Deflection plot for MTT 180mm truss on a pin and pin support..... 263

Figure 6-23: Deflection plot for MTTR 200mm truss on a pin and pin support 264

Figure 6-24: Deflection plot for ST 24mm truss on a pin and pin support..... 266

Figure 6-25: Deflection plot for ID 45mm truss on a pin and pin support 267

Figure 6-26: Difference in Mass and Deflection Between The Truss and The Original Cantilever Beam..... 270

Figure 7-1: Plan and elevation layout of a three-storey building structure..... 275

Figure 7-2: 1st Mode of the various floors model (a) 3 floors (b) 9 floors (c) 15 floors (d) 21 floors (e) 27 floors..... 280

Figure 7-3: 3 storey multistorey building MTT (110mm) custom column design extruded view (a) Overview (b) Magnified view..... 282

Figure 7-4: Non-continuous section of the MTT column (a) solid view (b) wireframe 282

Figure 7-5: Eqx Displacement of MTT Column Design By Floor..... 283

Figure 7-6: RS Displacement of MTT Column Design By Floor..... 284

Figure 7-7: Self-Weight of MTT Column Design By Floor..... 285

Figure 7-8: Eqx Displacement of MTT Column Industry vs Custom Section across Storey Height 287

Figure 7-9: RS Displacement of MTT Column Industry vs Custom Section across Storey Height 288

Figure 7-10: Self-Weight of MTT Column Industry vs Custom Section across Storey Height..... 288

Figure 7-11: Eqx Displacement of MTT Column Reduced Beam Section across Storey Height..... 290

Figure 7-12: RS Displacement of MTT Column Reduced Beam Section across Storey Height..... 290

Figure 7-13: Self-Weight of MTT Column Reduced Beam Section across Storey Height..... 290

Figure 7-14: Eqx Displacement of MTT Column Min Capacity in Beam and Column By Floor 292

Figure 7-15: RS Displacement of MTT Column Min Capacity in Beam and Column By Floor 293

Figure 7-16: Self-Weight of MTT Column Min Capacity in Beam and Column By Floor 294

Figure 7-17: Eqx Displacement of MTT Column Min Capacity in Beam and Column across Storey Height 295

Figure 7-18: RS Displacement of MTT Column Min Capacity in Beam and Column across Storey Height 296

Figure 7-19: Self-Weight of MTT Column Min Capacity in Beam and Column across Storey Height 296

List of Tables

Table 2-1: Result summary of stress concentration for different notch profile. (de Albuquerque Simões, de Castro and Meggiolaro, 2011) 51

Table 2-2: An illustration of the different notch shapes (Ciomber and Jakel, 2014). 56

Table 2-3: Result summary of the different notch shapes in their optimum size and contour in relation to their stress concentration (Ciomber and Jakel, 2014). 58

Table 2-4: Result summary of fatigue life with different ends of slots (Carpi and Brebbia, 2010). 64

Table 2-5: PMMA–Aluminium Joints tensile test (laboratory results) (Xu and Sengupta, 2004) 83

Table 2-6 Polycarbonate–aluminium joint tensile test (laboratory results) (Xu and Sengupta, 2004) 83

Table 2-7: Hazard information for all 4 trials. (Suksuwan and Spence, 2018)..... 103

Table 3-1: Summary of the number of models conducted in the thesis for each chapter 123

Table 3-2: Comparison of nodal displacements between MATLAB and GSA..... 143

Table 3-3: Reference model EC8 applied load 145

Table 3-4: Reference model EC8 frame section details..... 145

Table 3-5: Results of the EC8 reference model and SAP2000 147

Table 4-1: Various Cantilever Beams under the Deflection Limit of L/180; One Point Load (Downwards, Free-End, Top Face, 1000N)..... 157

Table 4-2: Various Cantilever Beams under the Deflection Limit of L/240; One Point Load (Downwards, Free-End, Top Face, 1000N)..... 159

Table 4-3: Various Cantilever Beams at Maximum Additional Cantilever Depth; One Point Load (Downwards, Free-End, Top Face, 1000N) 161

Table 4-4: Various Cantilever Beams at Maximum Additional Cantilever Depth; Triangular Pressure Load (5MPa, Downwards, Top Face, Max at Free-End) 162

Table 4-5: Individual graph for Various Cantilever Beams; One Point Load (Downwards, Free-End, Top Face, 1000N)..... 168

Table 4-6: Individual graph for Various Cantilever Beams; Triangular Pressure Load (5MPa, Downwards, Top Face, Max at Free-End)..... 172

Table 4-7: Global graph for Various Cantilever Beams; One Point Load (Downwards, Free-End, Top Face, 1000N)..... 174

Table 4-8: Global graph for Various Cantilever Beams; Triangular Pressure Load (5MPa, Downwards, Top Face, Max at Free-End)..... 176

Table 4-9: Multiple geometries with normalised scale; One Point Load (Downwards, Free-End, Top Face, 1000N)..... 178

Table 4-10: Multiple geometries with normalised scale; Triangular Pressure Load (5MPa, Downwards, Top Face, Max at Free-End)..... 180

Table 4-11: Area vs Deflection for Various Cantilever Beams; One Point Load (Downwards, Free-End, Top Face, 1000N)..... 183

Table 4-12: Area vs Deflection for Various Cantilever Beams; Triangular Pressure Load (5MPa, Downwards, Top Face, Max at Free-End)..... 185

Table 4-13: Area vs Deflection for Various Cantilever Beams (Bisected Value); Triangular Pressure Load (5MPa, Downwards, Top Face, Max at Free-End) 185

Table 4-14: Depth vs Deflections for Various Cantilever Beams; One Point Load (Downwards, Free-End, Top Face, 1000N)..... 189

Table 4-15: Depth vs Deflections for Various Cantilever Beams; Triangular Pressure Load (5MPa, Downwards, Top Face, Max at Free-End)..... 190

Table 4-16:Suggested Recommended Design Range of Various Cantilever Beams; One Point Load (Downwards, Free-End, Top Face, 1000N)..... 191

Table 4-17: Clear Optimum Comparison Value for the Cantilever with Method of Tensile Triangles' Shape Profile; One Point Load (Downwards, Free-End, Top Face, 1000N) 192

Table 4-18: Suggested Recommended Design Range of Various Cantilever Beams; Triangular Pressure Load (5MPa, Downwards, Top Face, Max at Free-End) 194

Table 4-19: Clear Optimum Comparison Value for the Cantilever with Method of Tensile Triangles' Shape Profile; Triangular Pressure Load (5MPa, Downwards, Top Face, Max at Free-End)..... 195

Table 4-20: Equivalent stress for 300MPa & 600MPa under One Point Load..... 206

Table 4-21: Equivalent Stress for 200MPa & 100MPa under Triangular Pressure Load 206

Table 5-1: Average difference between the maximum and the minimum values of the various geometries 216

Table 5-2: Deflection performance comparison of the cantilever beam geometries under STD, STU and SBD. 216

Table 5-3: Results and design details for STD loading condition under the deflection limit. 222

Table. 5-4. Results and design details for TTD loading condition under the deflection limit. 223

Table 6-1: Average deflection and stress between the processed topology and the original cantilever beam. 246

Table 6-2: Results for the MTT truss (pin and roller support) 257

Table 6-3: Results for the MTTR truss (pin and roller support) 259

Table 6-4: Results for the ST truss (pin and roller support) 260

Table 6-5: Results for the ID truss (pin and support) 261

Table 6-6: Comparison of pin and roller support trusses through their deflection per mass output 262

Table 6-7: Results for the MTT truss (pin and pin support) 264

Table 6-8: Results for the MTTR truss (pin and pin support) 265

Table 6-9: Results for the ST truss (pin and pin support) 267

Table 6-10: Results for the ID truss (pin and pin support) 268

Table 6-11: Comparison of pin and pin support trusses through their deflection per mass output 269

Table 6-12:Comparison of the mass and deflection between the truss and the original cantilever beam 270

Table 7-1: Base frame section 278

Table 7-2: Results for the MTT Column Design using Industry Section vs Custom Section 278

Table 7-3: Results for the Minimising Capacity in both Beam and Column 279

Table 7-4: Minimum frame section for both beam and column 291

Table C.c.a-0-1: Node coordinate for the MTT truss 362

Table C.c.a -0-2: Element details for the MTT truss 363

Table C.c.b -0-3: Node coordinate for the MTTR truss 363

Table C.c.b -0-4:Element details for the MTTR truss 364

Table C.c.c -0-5: Node coordinate for the ST truss 364

Table C.c.c-0-6: Element details for the ST truss 365

Table C.c.d -0-7: Node coordinate for ID truss 365

Table C.c.a -0-8: Element details for the ID truss..... 366

List of Abbreviations

ID – Increased Depth

MTT – Method of Tensile Triangles

MTTR – Method of Tensile Triangles Rule of Thumb

SBD – Single Point Load Bottom Face Downwards

SBU – Single Point Load Bottom Face Upwards

ST – Standard Triangle

STD - Single Point Load Top Face Downwards

STU – Single Point Load Top Face Upwards

TTD – Triangle Pressure Top Face Downwards (maximum at its free end)

Chapter 1 Introduction

1.1 Background of the Research

Many historical structures worldwide do not possess any lateral load resisting system, as shown in Figure 1-1. However, they provide a large self-weight to compensate for a certain degree of lateral loading due to their large and heavy design. Historical buildings like the Dionysus temple in Athens applies the same physics as a building with rocking walls. The earthquake resisting solutions applied in the ancient Greek and Roman temples are through the segmental construction of the marble blocks, allowing rocking under lateral loads. The self-weight of the blocks and the massive roof beams provide the required clamping and recentering vertical force. Shear keys made of cast lead allows the shear force to be transferred between the elements, preventing the eventuality of sliding (Buchanan *et al.*, 2011).

Generally, structures built before the 1960s used the old building practice code and are different from the current practice. In the old practice, the structural analysis's primary focus was more on vertical loading than lateral loading. Thus, it was inadequate with the change in time where buildings are taller, slender and lighter. Because of the changes in geometry and weight, new structures became more vulnerable to lateral loads. With the addition of earthquakes and/or wind loads on structures, lateral loading has become a more crucial element in the analysis and design of structures than before. Therefore, the old practice was replaced with a new one to cope with the changes.

(a)  (b)  (c) 

Figure 1-1: Historical Structures around the world: (a) Parthenon, Acropolis of Athens (Swayne, 1978) (b) Great Pyramids of Giza, Giza Pyramid Complex, Egypt (Liberato, 2006) (c) Colosseum Rome, Italy (Hakim, 2015)

To overcome some of these challenges, engineers look into nature, where it is filled with inspiration and knowledge about survival and blending with its environment while utilising limited resources. Nature has indeed inspired and influenced some of the well known architectural building design. More of these examples are mentioned in Chapter 2.7. One of the design consideration that is not often considered is the exterior shape of the structure or structural element. Geometrical shape plays a vital role in the stability of a structure, and its physics can be explained through the state of equilibrium. Shapes can also play a key role in relation to fluid dynamics. It can easily be used to smoothen, disrupt or redirect airflow in engineering designs (e.g. buildings, cars and computers). Chapter 2 demonstrates how nature grows along with its environment, how engineers capitalise on nature's design in their products, and how civil engineers approach building design challenges.

1.2 Problem Statement

Dealing with various types of lateral loading remains a challenge for structural engineers, especially when an economical and efficient structure is required. Hence, innovative designs are required to meet the current demand for a safe and yet sustainable building design. Often, civil engineers find ways to improve building designs through topology optimisation methods, material strength, mechanical system and many more. Civil engineers have not considered the area of stress distribution and energy absorption effects using this concept. In design practice, diagonal braces are

often used in reducing lateral displacement. However, in the analysis/design of large multistorey buildings, introducing a new design shape/profile in reducing the lateral stress at its connection between the column and the beam is often not considered. Similarities have been found in the stress profile between small (micro) mechanical components and structural beam sections or multistorey frame structure.

Since nature has its way of evolving and coping with various lateral loading (e.g. wind and earthquake), replicating nature's design to enhance structural performance through optimisation may result in a sustainable and efficient structure. Mechanical engineers were the pioneers in capitalising on this advantage by optimising mechanical components through changing the profile to achieve minimum stress peak level within the component. Researchers like Baud (1934) and Mattheck (1990a), and many more have found that by replicating certain natural profiles or topography, they were able to dissipate and transfer stress levels smoothly, hence reducing failure rates and increasing durability.

Considering the above matter, replicating nature's design in civil engineering structures seems like a natural pathway in a better design. If possible, it aims to find a common surface profile and capitalise on its usefulness in civil engineering. In addition, there is no study on utilising nature's notch shape profile and integrating nature's design in civil engineering structures, and many structures remain in a standard design of shapes that may not follow the internal force flow under lateral loading conditions. Therefore, a research study in this area is needed, and the aims of this research are outlined in section 1.3.

1.3 Aim & Objectives

1.3.1 Aim

This study aims to improve and optimise the structural system by replicating nature's design to enhance structures performance under lateral loading. The research focuses on identifying and investigating the suitability, efficiency and limitations of replicating nature's design in steel structures or components.

1.3.2 Objectives

The specific objectives of this study are

1. To determine the optimal configuration of cantilever steel structural elements under transverse loading replicating nature's design.
2. To optimise the replicated shape of cantilever structural elements and investigate its applicability under transverse loading.
3. To investigate the static and dynamic lateral responses of multistorey structures with optimised replicated joints/connections shapes.

1.4 Scope of the Research

With the ever-growing population, while the earth's resources are becoming more limited, the way that many buildings are designed are still relatively crude. There are no structures in nature that are straight nor have sharp corners. Nature has been a great source of inspiration and knowledge in modern-day sciences, and it is known for its effective use of resources. Current studies show that stress concentration in the joints or connection can lead to early failure, and these stresses can often be reduced or eliminated through a better notch profile. Since there are no studies on utilising nature's notch shape profile and the integration of nature's design in civil engineering structures, this study identifies and investigates the suitability, efficiency, and

limitation of replicating nature's design in steel structures or components. The aim is to improve and optimise the structural system by replicating nature's design to enhance structures performance under lateral loading.

The scope of the study on nature's notch shape profile is limited to the notch design profile found in tree buttresses. Four different studies were conducted to meet the objectives set out in this study, two cantilever beam studies with various geometrical projections (including the topology optimisation study), replicating the optimised shapes as trusses and a multistorey moment-resisting frame structure study with columns connections/joints with nature's notch shape profile.

The models in the studies are simplified to understand better the behaviour of nature's notch shape profile projection. The study compares to a typical method of engineering design. Numerical studies are performed instead of experimental studies due to cost and time constraints. Hence, a numerical validation study is performed prior to each of the studies conducted.

1.5 Significance of Research

The design of tall and slender buildings is a challenge for many structural engineers when lateral loadings are considered. In the situation of earthquakes generated lateral loadings, for example, it is often resolved by introducing a separate mechanical system (e.g. damping system) and/or through bracing systems. The use of stronger material (e.g. new composites) can enhance the structure's durability, strength, and stability. However, introducing these new materials or bracing systems into a structure often does not resolve the underlying stress concentration within the structure. Topology optimisation is often used to reduce material wastage through the removal of low strain energy elements in a structure, and it also does not alleviate stress concentrations. The

crucial question for optimised structures is how one determines whether the theoretical well optimised structured shape/profile gets constructed accurately? Imperfection in construction may include human errors, material quality or defects, impairing an optimised system. Safety is another concern when optimising structures or structural systems designed to a specific loading direction or scenario as it would not be able to resist the unforeseeable events or unaccounted loadings imposed due to the lack of redundant elements. Some older trees are known to have survived countless environmental challenges and exposure to natural forces. Hence, trees may be a viable solution and suitable teacher to civil engineers towards a better structure as both building structures and trees share similar mechanics in their environment. The findings of this study will assist in enhancing steel structures under lateral loading through the replication of shapes found in nature. The proposed design may create a more efficient steel design structure while maintaining its design functions. The research study looks into improving the design in cantilever beams and moment-resisting frame structures. Therefore, this research looks into enhancing steel structures by replicating the design found in nature (mainly trees) to improve structural performance and push traditional building norms.

1.6 Limitations of the Study

This is a fundamental study of applying nature's design in civil engineering to provide greater insight into the limitation and suitability of replicating nature's design in steel structures. Therefore, the parameters of this study were simple to eliminate other factors that may influence the results. The following listed are the known limitations in this study:

1. Results obtained may not reflect or translate to the actual structural behaviour and performance in a real-life scenario or practice as the study is a feasibility study and does not include other factors. Hence, it is purely an academic exercise.
2. The study only considers the standard structural steel as the sole material for all the analysis conducted.
3. The study is limited to the defined geometry (dimension, cross-sections and size) and does not consider other load distributions.
4. The analyses conducted in this study considers only the linear elastic zone.
5. The cantilever beam study analysis does not consider the effects of dynamics and other forms for beam structures/supports.
6. The sections considered in the multistorey study are all the European IPE and HE steel sections available in SAP2000.
7. The dynamic analysis only accounts for the x-direction of the plan layout in the multistorey study.
8. It is assumed that the orientation for both the beams and columns are in a single direction, and no additional assumption was applied at the joints/connections of the building structure.
9. The analysis of the multistorey frame section is assumed to be at the centreline of the section. Hence, the triangular projections are projected on both faces of the column steel sections.
10. No laboratory testing was conducted for these studies to verify and validate the said computer simulations. Hence, it is limited to the parameter restraints and limitation of the software.

1.7 Outline of the Thesis

The thesis consists of eight chapters, with the first three chapters being the Introduction, Literature Review and the General Methodology. The main body of the thesis is from Chapter 4 to Chapter 7. The final chapter presents an overall summary and future research recommendation.

An outline of each chapter is as follows:

Chapter 1 provides an overall view of lateral loadings on civil engineering structures. It emphasises the importance and challenges of lateral loadings. A brief statement on how civil engineers may compensate for the effects of lateral loading is mentioned. It also introduces the application of nature in civil engineering to be a grey area for further research. The aims, objectives and scope of research are stated.

Chapter 2 presents a comprehensive review of research in the various field that demonstrates the advancement in technology with the help of nature. Enclosed in this chapter are the various optimisation techniques used in mechanical and civil engineering to enhance structural performance while improving efficiency and reducing material usage. Research relating to the relationship of graphical optimisation and nature coupled with optimisation techniques are mentioned. The development of trees in nature and their lateral load resisting system is also reviewed.

Chapter 3 presents the methodology and validates the numerical model conducted in chapters 4, 5, 6 and 7.

Chapter 4 presents a parametric study on the various cantilever beam geometry using Finite Element Software to identify its optimal projection sizing.

Chapter 5 is a continuation to the previous chapter that seeks to expand the knowledge on the cantilever beam performance under various loading condition, face and aspect ratio.

Chapter 6 presents a parametric study on the various cantilever beam geometry to identify the load path or pattern of the structure to validate the projection's effectiveness as conducted in chapters 4 and 5.

Chapter 7 investigates the effectiveness of using the naturally occurring shape (obtained from chapter 4, 5 and 6) as a projection for moment-resisting framed structure columns.

Chapter 8 presents the conclusion and finding alongside its future research direction.

Chapter 2 Literature Review

2.1 Introduction

This chapter presents how nature may provide some practical solutions to the analysis and design of civil engineering structures through a comprehensive overview of the application of replicating nature's design in various fields and its optimisation processes. Section 2.2 briefly introduces an overview of replicating nature-inspired designs in the various fields of work. Section 2.3 presents an overview of how nature overcomes daily challenges by the growth method and its features that assist many living and non-living objects in reducing localised stresses. Section 2.4 demonstrates the factors behind the formation of tree buttresses and their relation to notch stresses. Section 2.5 shows how notch stresses can affect stress concentration in mechanical components. The literature then highlights some of the common nature's design used in improving the performance of mechanical components and a study on the efficiency of using them in section 2.6. Trees are the main subject of this research as it is closely related to civil engineering structures. Section 2.7 to 2.9 describes the nature and the current research in civil engineering to improving structural performance.

2.2 Studying and Learning from Nature (Replicating from Nature)

The topic of nature in recent years has become the main highlight of today's research. Many researchers find the structures of many biological organisms are both complex and fascinating. Their structure has unique properties well ordered from macroscopic level down to its molecules. The word "Bionics" is a popular word that proves the feasibility and success of biologically inspired designs over recent years. Recent advancement allows researchers to mimic biological structures with absolute precision

and accuracy in non-living objects. Examples of this success include gecko tape, bone tissue regeneration using coral and marine sponges in Figure 2-2, densification of material through viral in Figure 2-3 and many others. It provides science with a step forward in copying or incorporating more living designs in building structures. Most biological structures are generally adaptive. They can add or remove material throughout their structure to reduce stresses as well as increased fatigue life without any superfluous material. A biological structure can be in many ways described as a mechanical load-carrier as it is optimised for mechanical strength and weight to withstand the daily challenges in nature. Biological structures can grow into shape with no or minimal notch stresses to better survive in the environment it grows in.



Figure 2-1: Inspired by gecko's climbing ability. A man hanging himself above ground using a reusable suction or sticker plate made from synthetic gecko's feet, behind him are his research team (*Van der Waals and the Gecko*, 2014)

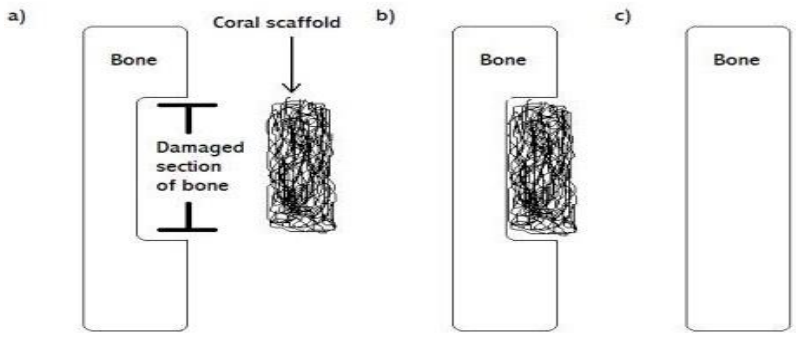


Figure 2-2: A simplified process of bone tissue regeneration (Guillemin *et al.*, 1987; Petite *et al.*, 2000)

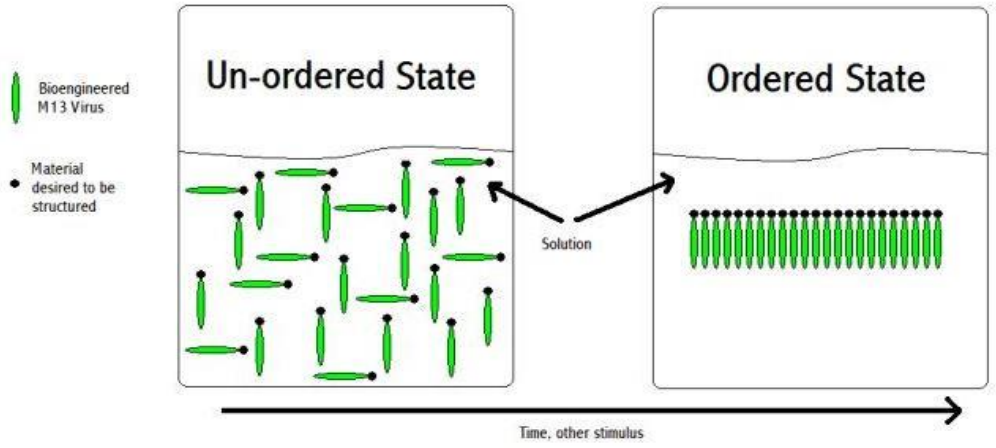


Figure 2-3: An illustration of a simplified process of a viral construction for denser material (Lee *et al.*, 2002; Lee, Lee and Belcher, 2003)

2.3 Principle of Biological Growth

The stress concentration factor (SCF) is a dimensionless factor that quantifies stress localisation. Failure of component usually initiates at its surface when it comes to bending stresses or small defects. Mattheck (1990a) believed that a good mechanical design should have a homogeneous stress distribution along its surface and a constant Mises-stress along its surface; it must be mechanically optimised. However, one must consider the limitations of mechanically optimised designs as they cannot satisfy all possible loading conditions. This section demonstrates the function or benefits of optimisation in lowering stress concentrations and the adaptation of biological structures to different loading conditions in nature to maintain a homogenous stress state. Figure 2-4 shows the stress concentration and behaviour of a joint between the branch and its stem. The stress concentration factor can be determined using Equation (2-1) (Pilkey *et al.*, 2007). It can be calculated analytically through the elastic theory method, finite element method or experimental (e.g. through strain gauges).

$$K_t = \frac{\sigma_{max\ (peak\ stress)}}{\sigma_{0\ (reference\ stress)}}\ or\ K_s = \frac{\tau_{max}}{\tau_0} \tag{2-1}$$

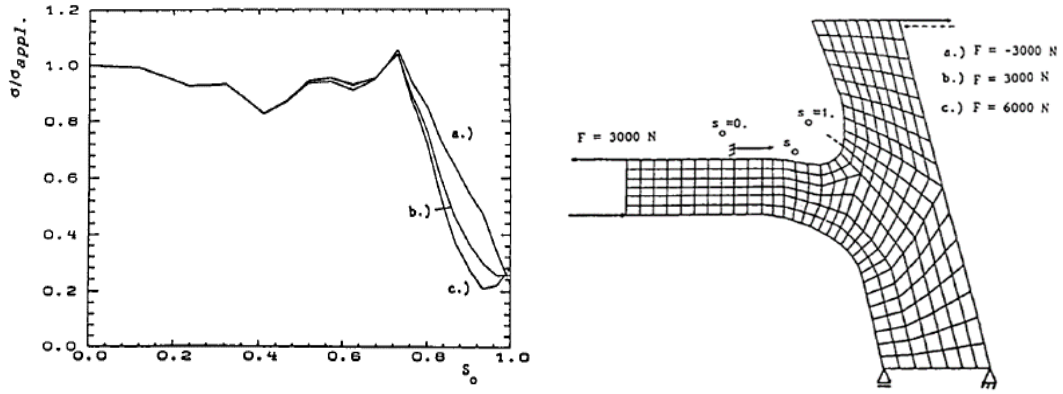


Figure 2-4: Stress concentration experienced along the tree branch towards its stem (Mattheck, 1990a)

Mattheck (1990a) studied finite element analysis on the upper side of the tree branch, as illustrated in Figure 2-4, as it is exposed to a higher risk of failure. The load applied involves a downward bending of a tree branch and the stem with dissimilar bending moment. The joint between the branch and the stem does not suffer any localised stress in all the experimental load cases, and interestingly the stress distribution was hardly affected by the bending of the stem. A localised redirection of force flow creates notch stresses between the branch and the stem, and the tree avoided this by a well-optimised thickening of the branch and stem.

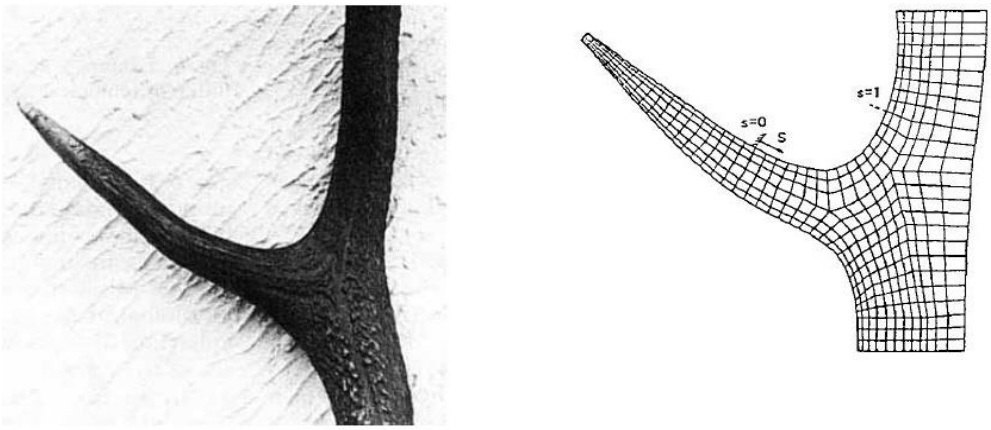


Figure 2-5: Antler of a red deer optimised in nature (Mattheck, 1990a)

Similarly to the branch as illustrated in Figure 2-4, a similar biological optimisation effect was demonstrated when tensile stress is applied along its upper contour on the antler of a red deer as in Figure 2-5. Although the antler is good in bending like in branches, the antler's spike is poor in axial tension. Nevertheless, the anther's spike is best suited for a single lateral load applied at the spike's tip than a distributed load applied along with the spike.

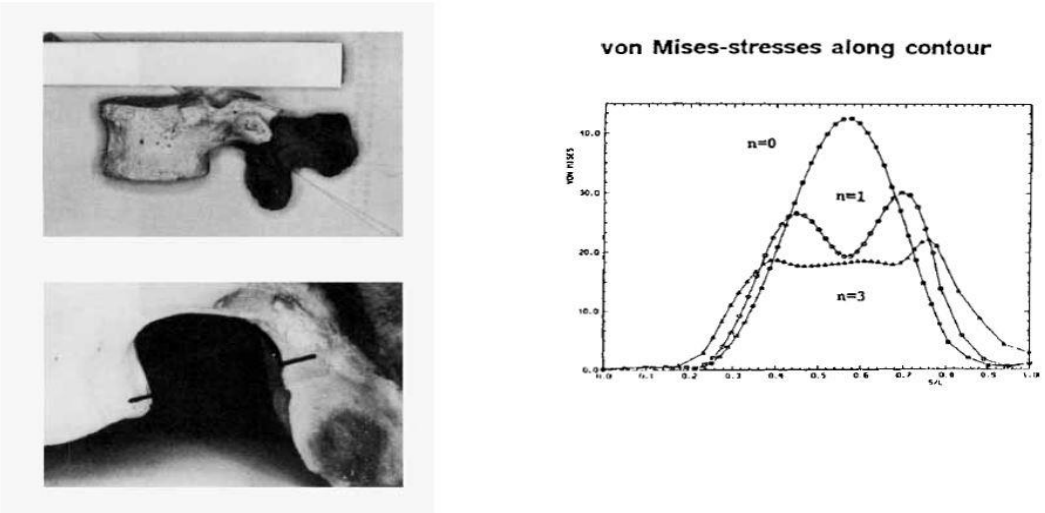


Figure 2-6: CAO method used to prove the growth pattern of a vertebral arch (Mattheck, 1990a)

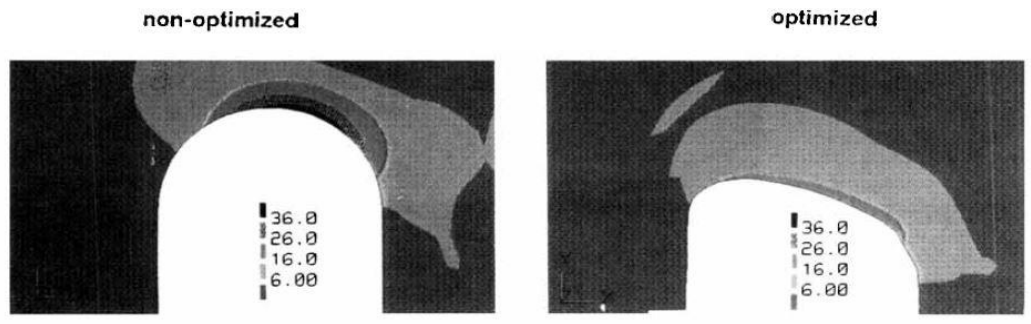


Figure 2-7: Graphical display of stresses in the vertebral arch. (Mattheck, 1990a)

Other examples include a vertebral arch, as in Figure 2-6. It is a section of a human spine with a small opening for nerves to leave the spine. The irregular shape structure was no mere coincidence, and its phenomenon was demonstrated through the Computer-Aided Optimisation (CAO) method, as shown in Figure 2-7. A nearly constant normalised stress was demonstrated in all the three examples mentioned without any localised stresses, which indicate a perfectly shaped optimisation of the biological structures. The examples demonstrated also indicate that shape optimisation does not cater for all loading conditions, and the resulting shape emphasises the most crucial load case. (Mattheck, 1990a). Therefore, growth optimisation is not limited to tree structures. (Mattheck, 1990a)

2.3.1 Tree's Adaptation to External Forces

Applying a mechanical load on a tree with a heavy stone, as shown in Figure 2-8, can create high-localised contact stress. The tree overcomes this through an "overgrowth" method. The additional growth increases the contact area, which reduces contact stress (Mattheck, 1990a, 1990b). Likewise, stakes attached to trees are meant to restrict movement from wind loads. However, as mentioned earlier, biological structures live in a homogeneous stress state. Therefore, the tree's stability has changed from a stake-

tree composite back to stem only, as shown in Figure 2-9, eliminating the need for a thicker cross-section below the stake. The stem's increased in cross-section above the stake support was to maintain homogeneity. If the stake were removed, the tree's cross-section would thicken and restore to its normal/natural shape. This is again to maintain a constant stress state along its stem (Mattheck, 1990a, 1990b)

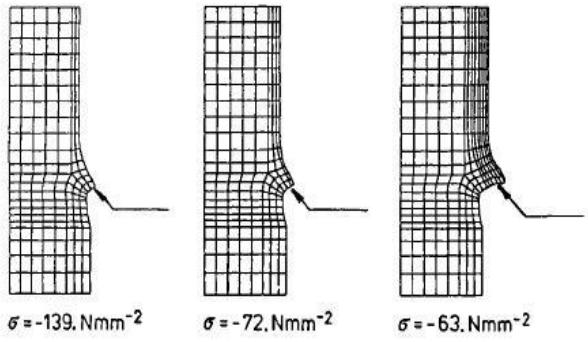


Figure 2-8: Increased in the contact area to reduce contact stresses (Mattheck, 1990)

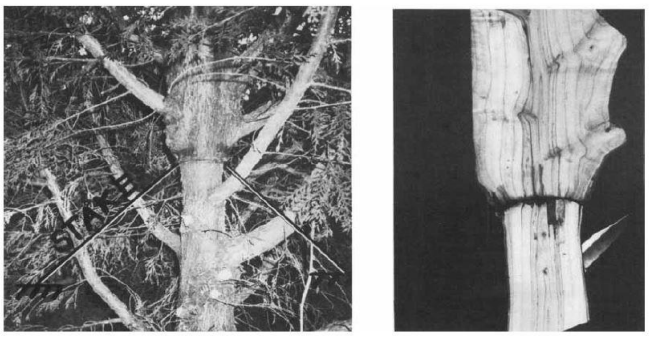


Figure 2-9: Cross-section of tree stem affected by stakes on trees (Mattheck, 1990)

2.3.2 Development of Buttresses in Trees

The formation of buttresses along the tree trunk's outer ring, as shown in Figure 2-10, is due to the increased stresses along its trunk and roots (mainly notch stresses). Throughout its lifetime, stresses experienced by the tree are recorded in the cross-

section of the tree trunk (growth rings). The tree compensates for this effect by forming buttresses for an increased cross-section. Ultimately, the biological growth follows the requirement of a constant Mises stress surface without stress peaks or concentration. (Mattheck, 2006)

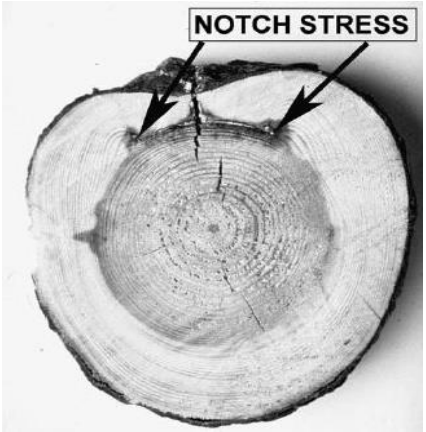


Figure 2-10: The cross-section of the tree trunk has thicker rings formed at notch stress (Mattheck, 2006)

2.4 Secrets of Trees

From the previous section, trees developed buttresses to reduce notch stresses, but to why trees develop buttresses, a good understanding of a tree's anatomy and its environment can shed some light on the matter.

2.4.1 The Anatomy of Trees

A tree can be subdivided into three sections, crown sail, stem and root anchorage, as shown in Figure 2-11a (Mattheck, Bethge and Schäfer, 1993). These individual sections work together as a single continuous unit with an equally strong chain link to resist wind loads and prevent breaking in vulnerable sections. Trees grow in a slender form for the competition of light sources, but they must also be able to withstand breakage from wind loads. Figure 2-11b illustrates its tree diameter with relation to its height may be a function described as $h \approx D^3$ for trees with localized crown as it was

discovered experimentally in some cases (Alexander, 1971; Wilson and Archer, 1979; Mattheck, 1990b). However, trees like Sitka, spruce-like trees have their crown distributed along their tree stem. Therefore, its function relating to its tree height and diameter can be different.

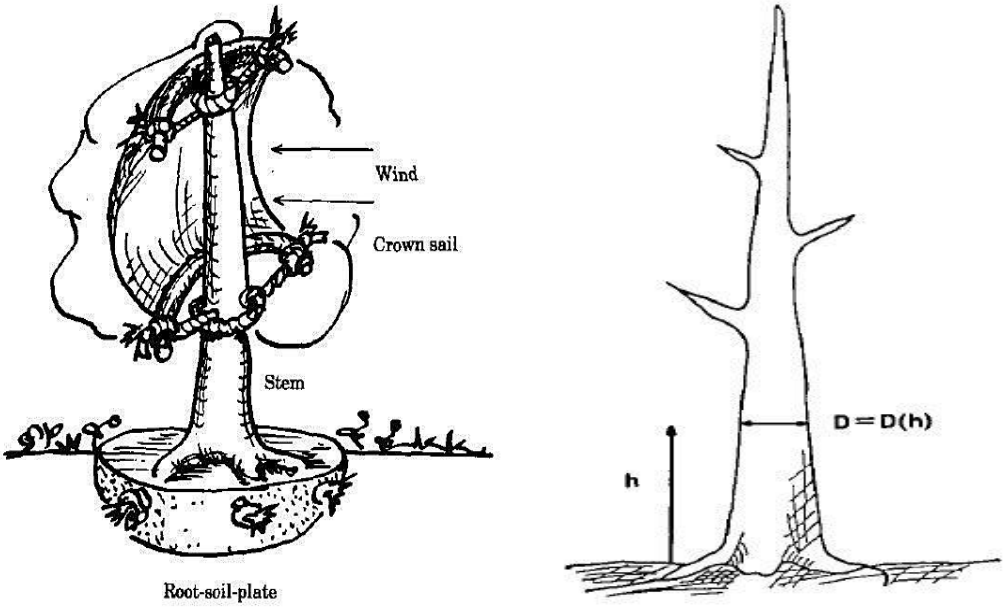


Figure 2-11: (a) Basic Anatomy of trees (Mattheck, Bethge and Schäfer, 1993). (b) Tree stem thickness varying along with its height according to wind loading. (Mattheck, 1990b)

2.4.2 Correlation between the Development of Trees and its Environmental Condition

Traditionally many researchers thought that buttress tree roots grow randomly. However, this is not entirely true, which leads to further research determined to find a relationship in the trees growth pattern to predict the development of trees better and reduce tree growth hazard in urban development. The relationship between its crown asymmetry and its buttress formation may be less correlated. However, many researchers have confirmed that wind effects on the buttresses are indeed valid. The wind is an essential factor to stimulate wood production for the development of

buttress in trees. Quararibea asterolepis has its buttress height increased rapidly with its tree height (Richter, 1984). Figure 2-12 illustrates a tree stump's mechanics in relation to its buttress root system. There is a higher frequency of buttressed formation in canopy trees, particularly in emergent (Chapman, Kaufman and Chapman, 1998). Buttresses are believed to help prevent roots from splitting or snapping between their roots and the trunk as they can smoothly transmit, transfer and distribute internal forces between them.

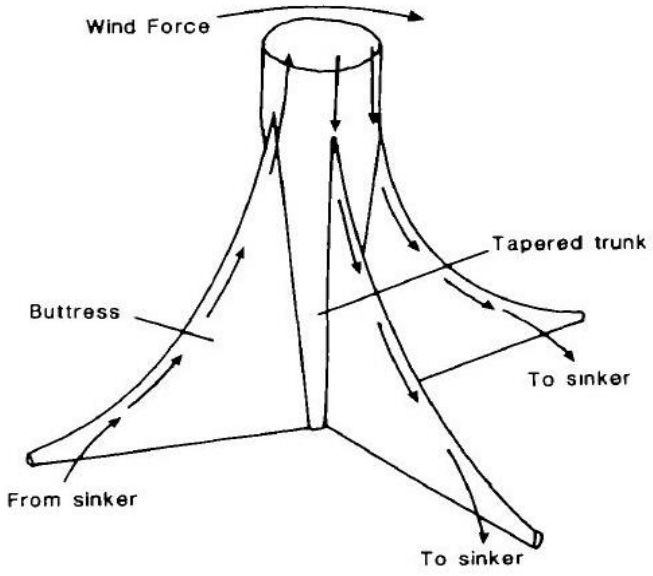


Figure 2-12: An illustration of a tree stump experiencing wind loading. (Crook, Ennos and Banks, 1997)

2.4.3 Buttresses in Trees

Not all trees share a common necessity of buttress root for stability. The formation of buttress roots depends on both the species and the location that it is grown. The extension of buttresses in trees may be correlated to their soil texture, depth and wind direction. The tree buttress tends to be larger, longer and more pronounced in the area of the prevailing wind, wet, weak silty soils, shallow humus layer overlying rock and shallow waterlogged soils (Navez, 1930; Petch, 1930; Richards, 1952). The difference

in climate area also affects its formation of buttresses. Trees in the tropical rain forest have a larger size, number, and more pronounced buttress roots than temperate forest (Richards *et al.*, 1996).

Researchers believed that large tree buttress is formed in tall or shallow-rooted trees to increase stability and nutrients acquiring (Young and Perkocha, 1994; Crook, Ennos and Banks, 1997; Newbery *et al.*, 2009). Some species do not have buttress roots, for example, the Alstonia scholaris. Although buttress roots provide stability to trees with this feature, they do not necessarily imply that trees without buttress roots are less stable. Ceiba pentandra is one species that has a buttress in a forest environment and lacks buttress in savanna areas (Mehedi, Kundu and Chowdhury, 2012).

Abu Hanifa Mehedi, Kundu and Qumruzzaman Chowdhury (2012) conducted a study on the buttress characteristics of trees (buttress height, mean buttress length, total buttress length and length of secondaries) and tree architectural parameters (diameter at breast height and tree height) at the Lawachara National park, Bangladesh. A total of 238 trees were analysed. Out of the 12 different species, only “Alstonia scholaris” did not have any buttress. “Artocarpus chaplasha Roxb” has the highest number of trees that developed buttresses, with a total of 27/31 trees investigated. The percentage of buttress formation against the number of species is shown in Figure 2-13.

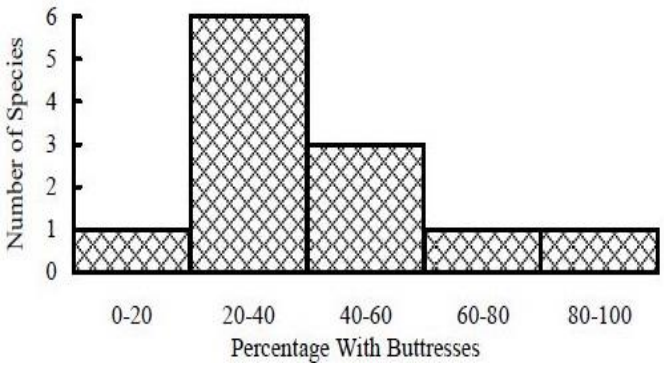


Figure 2-13: A graph showing the number of species against the percentage with buttresses at the Lawachara National Park covering 238 trees of 12 different species (Mehedi, Kundu and Chowdhury, 2012).

2.4.3.1 Root Morphology

As the tree gets older, the roots developed are more towards fine-absorbing roots than larger structural roots. The tree's buttress is believed to have two kinds of buttresses: leeward for compression and windward for tension. Non-buttressed trees have more lateral roots than buttressed trees. The lateral roots of non-buttressed trees tend to grow horizontally instead of growing further into the soil like buttressed trees. The roots cross-sections for buttressed trees are more rectangular, while non-buttressed trees' roots are more circular. The buttressed roots have a height to width ratio of 8, while the non-buttressed roots have a height to width ratio of around 1 as it is circular. Larger trees are believed to have a higher number of sinker roots accompanied to their buttresses. There is a trend, but there is no statistical support yet. Sinker roots appear in 10 out of 15 buttressed trees analysed in Crook's report (Crook, Ennos and Banks, 1997). The tree rooting system's failure mechanism, buttressed and non-buttressed trees, are shown and explained in Figure 2-14 and Figure 2-15. Trees root morphology can be broken down into:

1. Buttressed
    a. Sinker roots

b. Non-sinker roots

2. Non-buttressed

2.4.3.2 Sinker Roots

The majority of buttressed trees roots do not have sinker roots that assist in root anchorage. There is no extensive research on the rooting structure, but the sinker roots that appeared in buttresses were similar to Crook, Ennos and Banks (1997) description for Nephelium ramboutan. Sinker roots are found to be most effective in windward buttress roots. The presence of sinker roots in leeward buttresses shows no difference in its anchorage performance. Sinker roots increase the tree's uprooting resistant strength by anchoring its roots firmly into the soil. Buttress with sinker roots are better in tension, and buttress without sinker roots are better in compression. In the study, the buttressed tree with sinkers tends to delaminate instead of uprooting.

2.4.3.3 Failure in Buttressed and Non-Buttressed Trees

Crook, Ennos and Banks (1997) found that trees' anchorage strength (Aglaia and Nephelium; 10.6kNm) with buttress is almost twice the anchorage strength of trees (Mallotus wrayi; 4.9kNm) without buttress. Both buttressed and non-buttressed tree failed in their root system instead of trunk breaking. Non-buttressed trees tend to have an evenly distributed root system.

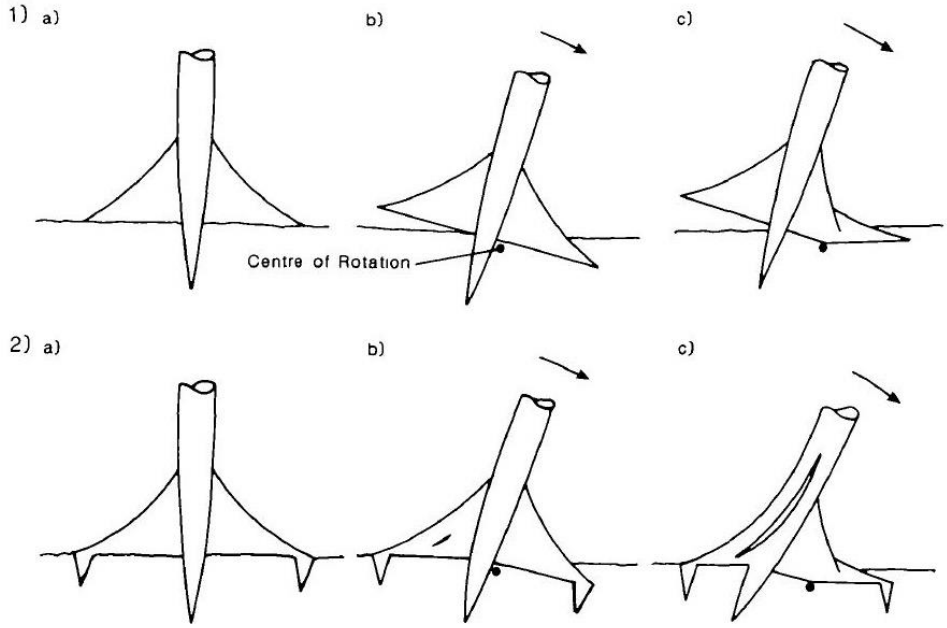


Figure 2-14: An illustration of how trees with buttresses fail (1) Buttresses without sinkers (2) Buttresses with sinkers (Crook, Ennos and Banks, 1997)

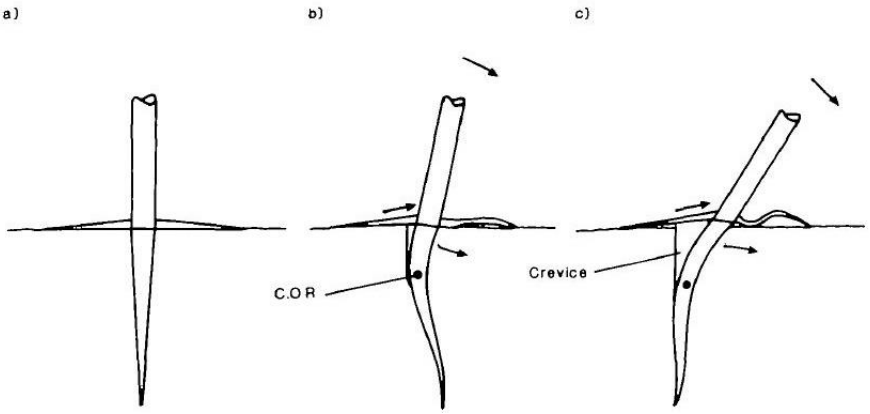


Figure 2-15: An illustration of how trees without buttresses fail. (Crook, Ennos and Banks, 1997)

2.4.3.4 Buttressed Trees (Aglaia and Nephelium)

Significant movement is seen in both with or without sinker-buttressed tree when the trunk is displaced by 20° from vertical. Both buttressed initially rotate about a point at the trunk's leeward side. The leeward laterals bent and pushed into the soil. The centre of rotation moves away from the trunk towards the leeward side for both buttressed tree as it is continually pulled. Both buttressed tree has their leeward broken at the end,

but their windward fails in a dissimilar manner. Buttressed that possess sinker roots to delaminate along its trunk from the middle of the buttress roots at $20°$ from vertical and snapping of fine roots at around $30°$ from vertical while buttressed without sinkers roots will uproot between $30 - 35°$.

2.4.3.5 Non-Buttressed Tree (M. wrayi)

Non-buttressed trees fail in a dissimilar manner to buttressed trees. Significant movement is seen when the non-buttressed trunk is displaced by $10°$ from vertical and rotates about a point near the trunk's leeward side. Due to its low bending rigidity, the leeward laterals bend and buckles instead of being pushed into the ground. The windward laterals can either snap at its base or uprooted together with its trunk. The taproots can be pushed sideways into soil towards the leeward side, leaving a cavity.

Taproots play a more vital role in the anchorage strength of non-buttressed trees than in buttressed trees. The buttressed trees' force flow was concentrated along their buttresses instead of their trunk, while non-buttressed trees' force flow was concentrated in their taproot instead of their laterals. The buttress roots correlate with its anchorage of $r^2 = 0.46$, while the area of taproots and windward lateral strongly correlated to its anchorage strength of $r^2 = 0.82$.

For buttressed trees, 60 % of the total resistance to uprooting goes to its buttress, while the remaining 40% goes to its taproots. For non-buttressed trees, the anchorage moment of resistance in taproots is similar to the buttress trees, but the thin lateral roots provide only 1/6 of the buttress resistant strength. The buttress higher second-moment area provides a bending rigidity of almost 20 times greater than non-buttressed trees, assuming both tree wood's material stiffness is the same. Buttressed

trees are most likely to overturn before anchorage failure occurs, while non-buttressed trees fail in anchorage first, reducing its effectiveness.

Gordon (1978) believe that the lateral roots of non-buttressed in the windward are thin and strong in tension while the leeward is thicker and strong in bending. However, because of their thin roots and poor orientation for uprooting resistance in non-buttressed trees M. Wrayi, only restores a small moment force, making uprooting easy (Coutts, 1983, 1986; Crook, Ennos and Banks, 1997). The formation of non-buttressed trees may be due to the reduced mechanical stresses during growth development. Roots may be used as historical data for the tree growth pattern and stresses experienced by the tree over its lifetime.

2.4.3.6 Buttress Characteristics and Tree Architectural Parameters

2.4.3.6.1 Wood Density

Wood density is another factor to be considered. Buttressed trees often occur in wood with a higher density than those of non-buttressed. Some dense wood trees have thin trunks and weaker taproot that makes buttresses more critical for stability. The tree's rooting pattern may be due to its water and nutrient intake requirements.

2.4.3.6.2 Relationship between the Tree Height, the Diameter of Tree Stem and the Buttressed Height

Graphs have been plotted and extrapolated against its tree height to understand the buttress's formation in buttressed trees, as shown in Figure 2-16 is the diameter of the tree stem and the buttressed height. Abu Hanifa Mehedi, Kundu and Qumruzzaman Chowdhury (2012) found that the relationship between them is significant, but the buttressed height has a better or stronger relationship with the tree height than its diameter at breast height with ($R^2 = 0.39\ vs\ R^2 = 0.47$). Its relationship is

approximately a linear curve. The buttressing pattern in trees changes accordingly to its mechanical stability. Results obtained show a moderate effect of buttress height on the ability to resist bending or compression.

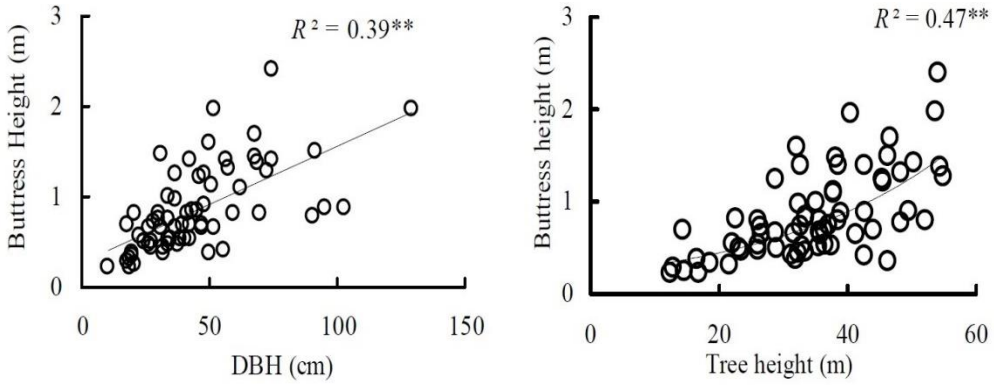


Figure 2-16: Graphs showing the relationship between the tree height, the tree stem diameter, and the buttressed height at the Lawachara National park, Bangladesh. (**: $p < 0.01$) (Mehedi, Kundu and Chowdhury, 2012)

The stem's diameter governs flexural stiffness in the tree stem. Abu Hanifa Mehedi, Kundu and Qumruzzaman Chowdhury (2012) also found that the slope of land has little to no effects on the buttress characteristics similar to Wahala, Huang and Dibor (2005). The buttress characteristic has a strong correlation with the canopy category. However, the under-storey and mid-canopy trees have lesser developed buttresses than emergent.

Woodcock, Santos and Taylor (2000) conducted a study in O'ahu on Elaeocarpus angustifolius's buttressing growth pattern in trees. Elaeocarpus angustifolius was originated in Australia and was planted in Hawaii in the 1930s. The relationship between its diameter and buttress height is shown in Figure 2-17.

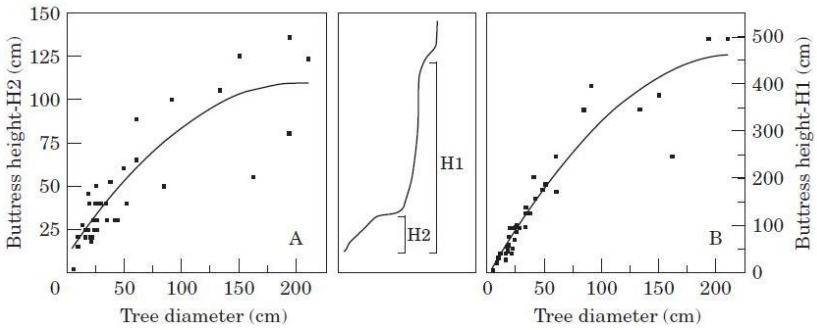


Figure 2-17: Graphs showing the relationship between the buttressed height and the tree stem diameter at the O'ahu, Hawaii. (Woodcock, Santos and Taylor, 2000)

H1 is the distance where the buttress emerges from the tree to the ground. H2 is the distance where the buttress becomes horizontally aligned to the ground. Woodcock, Santos and Taylor (2000) found that the buttressed height is strongly correlated with its tree diameter "Elaeocarpus angustifolius", as shown in Figure 2-18 and is in agreement with Chapman, Kaufman and Chapman (1998) findings.

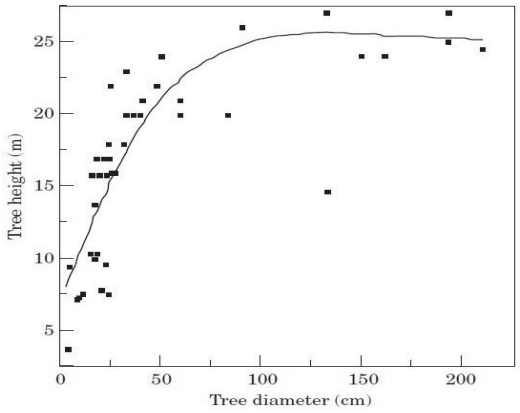


Figure 2-18: Graphs showing the relationship between tree height and tree stem diameter at the O'ahu, Hawaii. (Woodcock, Santos and Taylor, 2000)

2.5 Notch Profile and Stress Concentration in Structural Components

As seen in tree buttresses, notches are merely geometric details that can be found inevitably in any structural components. Stress concentration often develops between the joints or connections of the structural component, and to reduce the stress

concentration between them, notches are often introduced. The efficiency and effects on the failure mechanism of the notch's functionality depend on its geometrical transition along the shoulder fillet. The tip curvature of notches can be optimised numerically.

Similarly, organic material tends to grow accordingly to sections of high-localised stress concentration. An abrupt change in geometry at the shoulder can affect its stress concentration along its surface. This section demonstrates the importance of a good notch profile in components to obtain a homogeneous stress state.

2.5.1 Understanding Notch Stresses

"Ropes" can be idealised as a lateral force acting on a circular notch in a tension plate when the ropes in the plate are being straightened, as shown in Figure 2-19. Ropes are best represented in this case as they do not have bending stiffness. The deformation in the notch contour creates bending stresses, and these are known as notch stresses. Overall stress can be divided into two components, nominal stress and bending stress. One can try to shape the profile of the notch stress in a way so that the sum of both components leads to homogeneous stress along with the notch profile. This can be done by increasing bending stress along its notch surface that equals a decrease in nominal stresses and vice versa. Therefore, the summation of both stress components,

in this case, will be constant (Mattheck, 2006). This method is called “pocket calculator” (Mattheck, 2006).

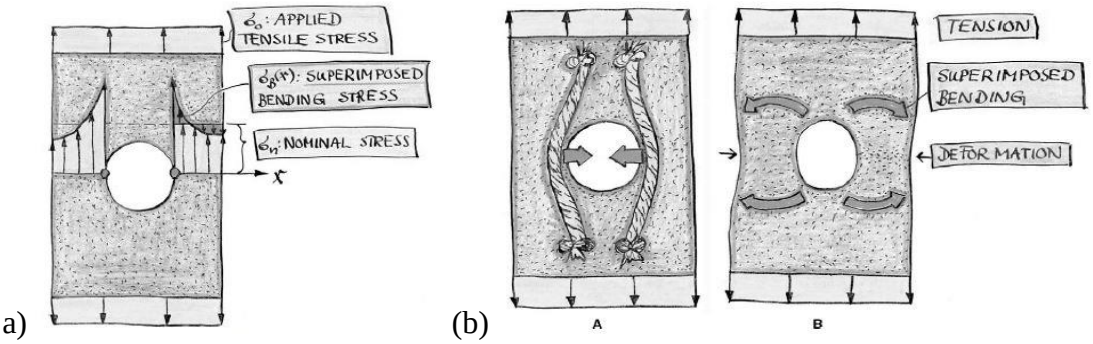


Figure 2-19: (a) An illustration of the overall stresses near the notch (b) Correlation between lateral forces and bending stresses of notch stresses (Mattheck, 2006)

2.5.2 Optimisation of Notch Profile with Different Optimisation Methods

Many mathematical optimisation methods are available, but its effectiveness/efficiency in reducing notch stresses differ slightly between different optimisation methods. Nevertheless, the notch profiles obtained through different optimisation methods are similar. The following shows the importance of a good notch profile.

Notch stresses were traditionally reduced using the pocket calculator method (Mattheck, 2004) or the circular method (Mattheck, 2006). They were subsequently replaced with better optimisation methods (e.g. Computational Aided Optimisation (CAO) method), and its application is shown in section 2.5.4. Figure 2-20 shows how the simplest optimisation method can reduce notch stress effectively, demonstrating the importance of a good notch profile (Mattheck, 2006). CAO method was the best compared to the other optimisation methods in the study.

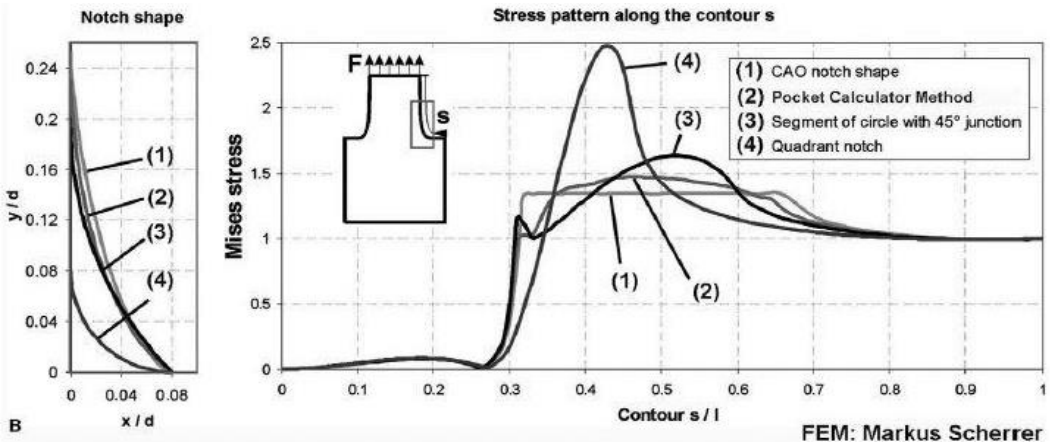


Figure 2-20: Notch shape and stresses along the contour (Mattheck, 2006)

2.5.3 Effects of Mechanical Performance with Different Notch Profiles Lengths

As shown in Figure 2-21, de Albuquerque Simões, de Castro and Meggiolaro (2012) analysed a set of test specimens using ANSYS APDL v12 under plane stresses with 12 degrees of freedom. As expected, the optimised notch shape for each specimen, as shown in Figure 2-22, experienced lower stress concentration than the original or non-optimised contour. Therefore, the application of traditional notch design as a transitioning geometry is far from optimum and can be improved further.

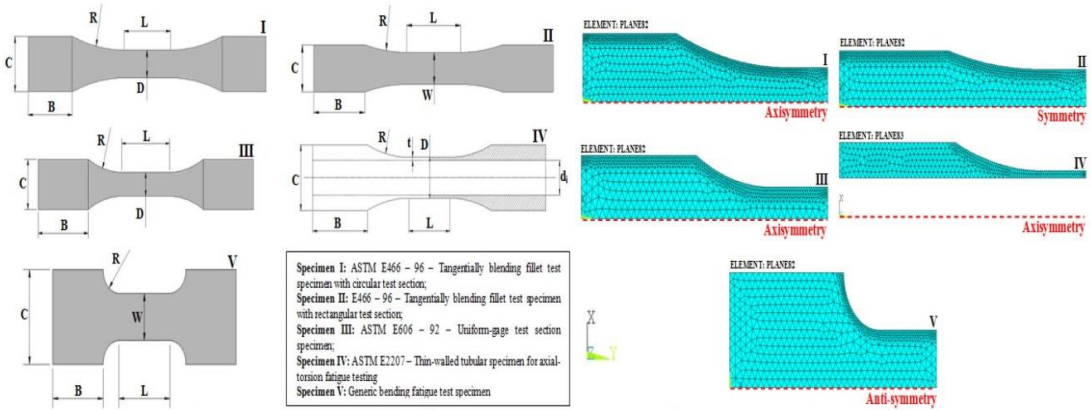


Figure 2-21: Specimens plotted using finite element modelling for different notch sizing (de Albuquerque Simões, de Castro and Meggiolaro, 2012).

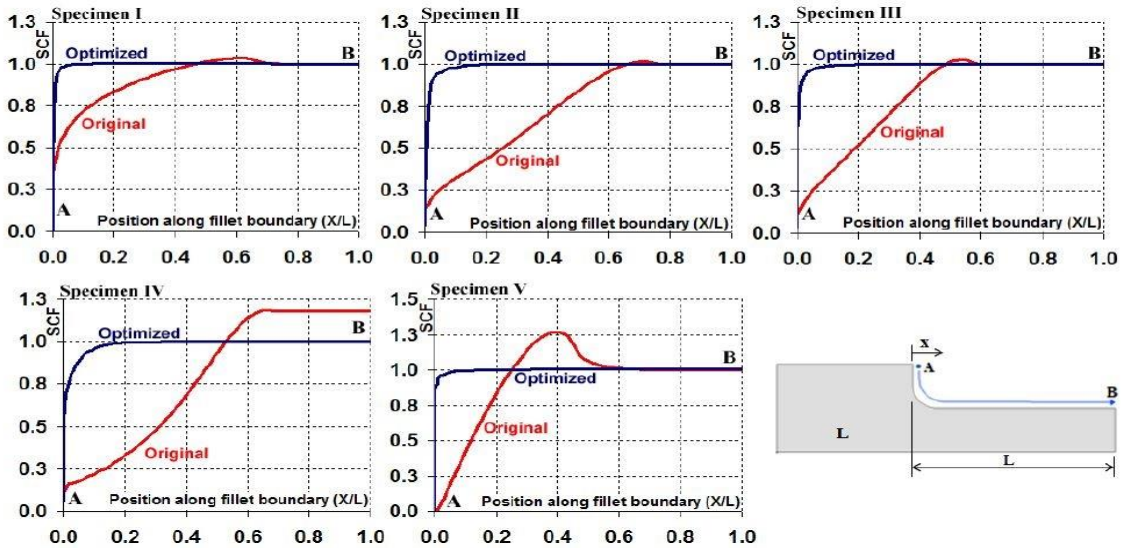


Figure 2-22: Stress concentration of each specimen along the fillet (de Albuquerque Simões, de Castro and Meggiolaro, 2012).

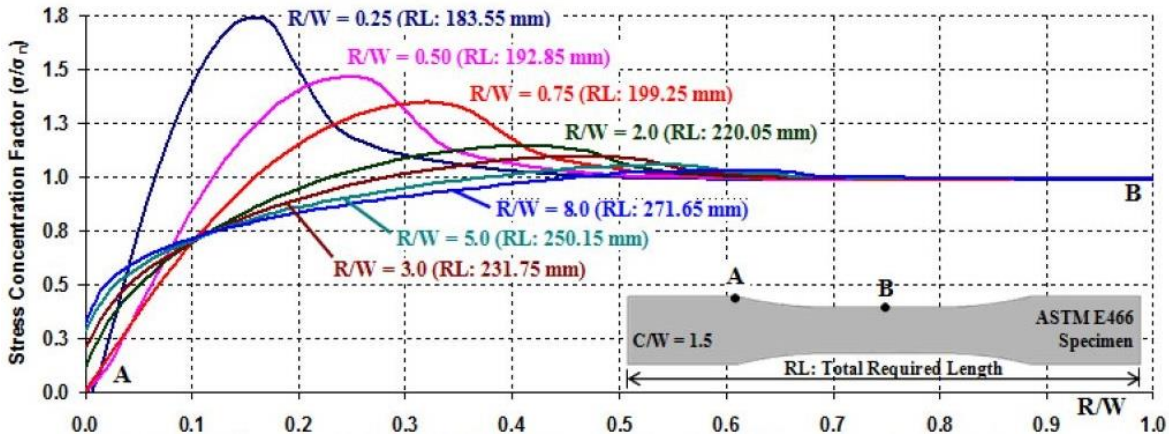
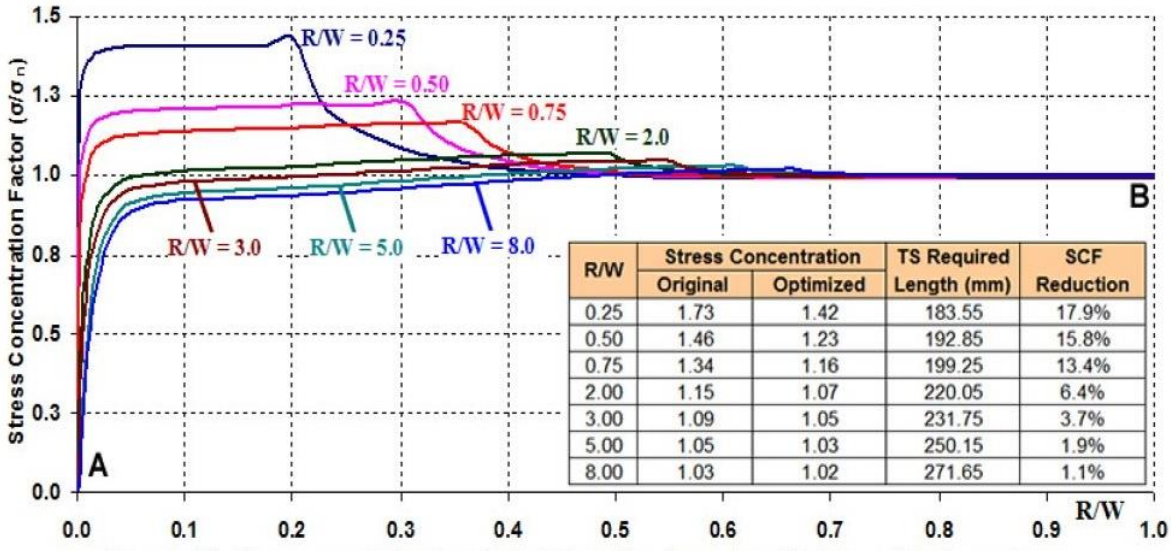


Figure 2-23: Stress concentration factor for non-optimised specimen II (de Albuquerque Simões, de Castro and Meggiolaro, 2012).

Figure 2-23 shows the influence of the R/W ratio with regards to the stress concentration. Specimen II was analysed in this example due to its low C/W ratio. The ratios defined are shown in Figure 2-21. A low C/W ratio specimen requires a larger radius arc to reduce stress concentration. The overall specimen length increases when the R/W ratio increases. An increase in the total overall length does not only increase the material required, but it also increases the risk of buckling due to its additional length (de Albuquerque Simões, de Castro and Meggiolaro, 2012).



R/W	Stress Concentration		TS Required	SCF
	Original	Optimized	Length (mm)	Reduction
0.25	1.73	1.42	183.55	17.9%
0.50	1.46	1.23	192.85	15.8%
0.75	1.34	1.16	199.25	13.4%
2.00	1.15	1.07	220.05	6.4%
3.00	1.09	1.05	231.75	3.7%
5.00	1.05	1.03	250.15	1.9%
8.00	1.03	1.02	271.65	1.1%

Figure 2-24: Stress concentration factor for optimised specimen II (de Albuquerque Simões, de Castro and Meggiolaro, 2012).

Figure 2-24 shows similar results in terms of the R/W ratio. The R/W ratio ranges from 0.25 – 8. The R/W ratio shows an SCF reduction of up to 18% when the ratio reaches towards an R/W value of 8 from 0.25, but the space required for a smooth transition curve is almost 1.5 times its original length. The optimisation of the specimen in reducing stress concentration is more effective for geometrics with a low R/W ratio. As the R/W ratio increases, its effectiveness diminishes (de Albuquerque Simões, de Castro and Meggiolaro, 2012).

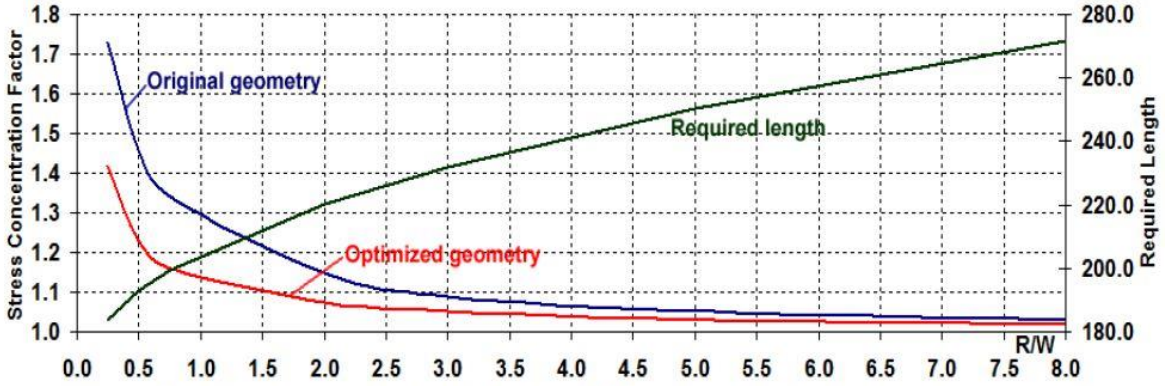


Figure 15. Stress concentration factor along the boundary fillet for optimized specimen II.

Figure 2-25: Stress concentration vs R/W ratio vs required length for specimen II (de Albuquerque Simões, de Castro and Meggiolaro, 2012).

As shown in Figure 2-25, a graph is plotted to obtain the best R/W ratio with the lowest stress concentration. The best R/W ratio in practice depends on its feasibility. The feasibility depends on its usage, space limitation and economic standpoint. The material-saving and buckling resistance of specimen II (Figure 2-21) for both optimised and non-optimised increases with a diminishing R/W ratios (de Albuquerque Simões, de Castro and Meggiolaro, 2012).

2.5.4 Application of Computational Aided Optimisation (CAO) and Soft Kill Optimisation (SKO) Method in Manufacturing

Figure 2-26 shows how car manufacturers like Opel manufacture their engine mount supporting structures using CAO and SKO methods (Bar-cohen, 2012). It achieved 25% weight reduction, and 60% increased stability than the previous engine mount (using the conventional design process). CAO method was also used to prevent the development of high-localized stresses at the rectangular aperture shaft, as shown in Figure 2-27. Replacing the existing rectangular aperture shaft with a more optimised notch profile increases the fatigue life by 40 times greater than a non-optimised shaft aperture (Bar-cohen, 2012). Other examples include a chain and a hook, as shown in Figure 2-28 and Figure 2-29, that experienced greater material efficiency with enhanced performance (Mattheck, 1990).



Figure 2-26: The engine supporting structures in Opel cars (Bar-cohen, 2012).

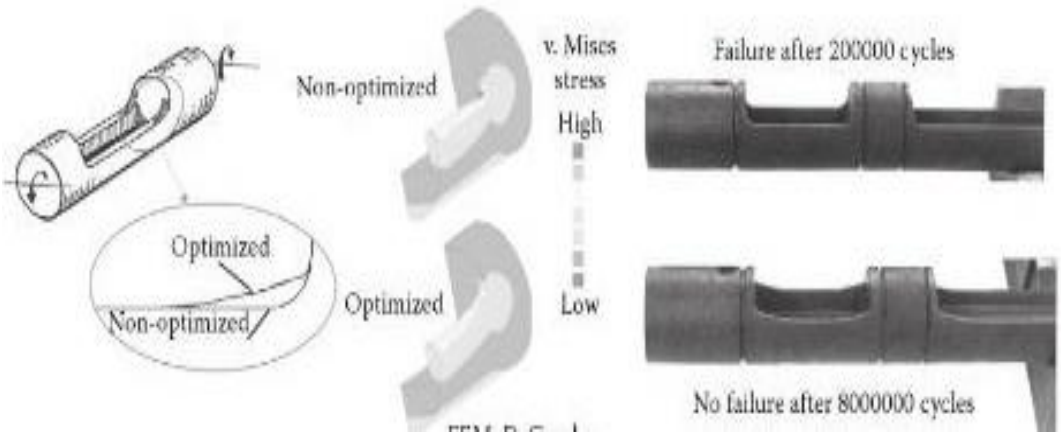


Figure 2-27: A mechanical shaft optimised through the CAO method (Bar-cohen, 2012).

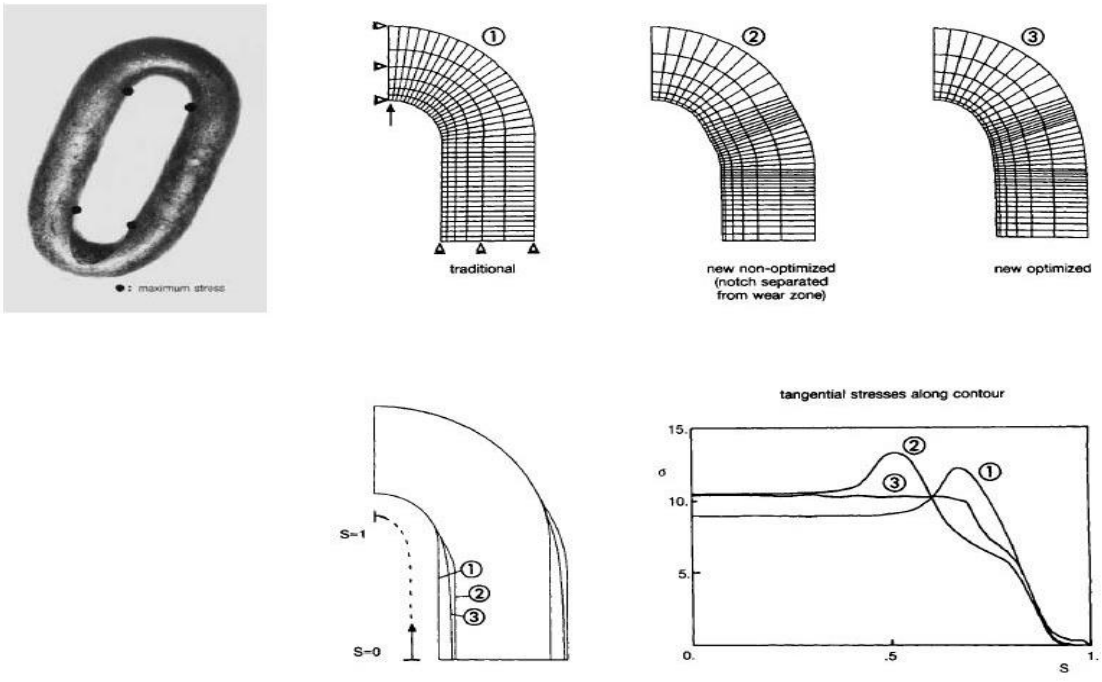


Figure 2-28: Chain link optimised through the CAO method (Mattheck, 1990)

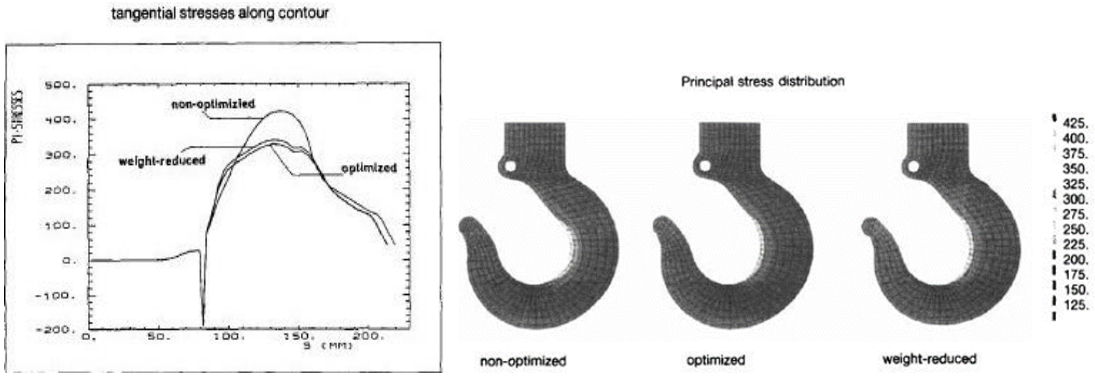


Figure 2-29: Optimisation result of a crane hook (Mattheck, 1990)

2.6 Graphical Optimisation Method

2.6.1 Background

Shape optimisation through biological has long been used and widely accepted by many German industries for many years. The Forschungsaentrum Karlsruhe GmbH (Research Centre Karlsruhehas) has been conducting shape optimisation methods in mechanical components since the late 1980s. They have been investigating trees, bones of animals and human beings to find the best or optimum design shape to enhance optimisation methods.

The finite element method used stress calculation and stress-controlled thermal expansion to mimic growth and reduce notch stress. The solution of this method is attained when notch stresses are reduced to a bare minimum or stopped by functional limitations. The Computer-Aided Optimisation (CAO) method was significantly simplified in 2003 as the understanding of notch stresses in nature is better understood. Notch shape optimisation can now be done through a graphical method, avoiding the

need for complicated FEM codes or models (Mattheck, 2007; Mattheck, Kappel and Sauer, 2007).

The graphical notch shape optimisation method became possible as the understanding of notch stresses in nature is better understood, avoiding the need for complicated FEM codes or models. Graphical optimisation methods allow reworking and reshaping of geometry easier for application and optimisation of components with less or no calculation while meeting the geometrical limitations. Geometrical limitations or constraints are not limited to interference with other components and spacing limits (e.g. extension of the curve along its shoulder) and vary according to its application.

2.6.2 Nature Inspired Contours

2.6.2.1 Baud Curve

Baud curve is a type of empirical shape optimisation that has a transition contour line with a narrowing cross-section of a beam suitable for bending and tensile loads. As shown in Figure 2-30, two different contour lines were found for bending and tensile loads. Large varieties of biological specimens (e.g. branches, antler joints, and human tibia shown in Figure 2-31) follow a similar pattern of a modified Baud's curve design. Although Baud's curve may seem to be a shared design rule for many biological beams with tapering cross-section, it should be carefully understood and not be applied in a general way for all types of structures (Mattheck, 1990a).

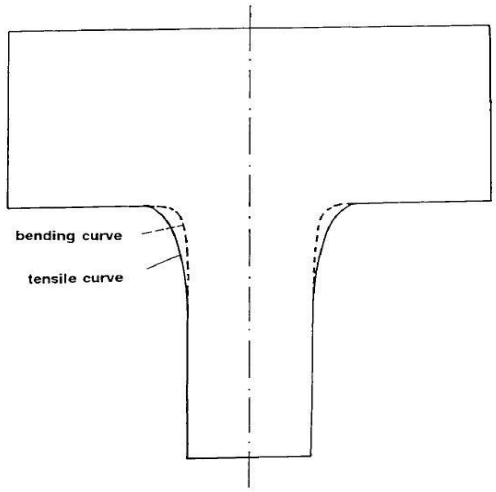


Figure 2-30: An illustration of the original Baud curve for bending and tensile (Mattheck, 1990a)

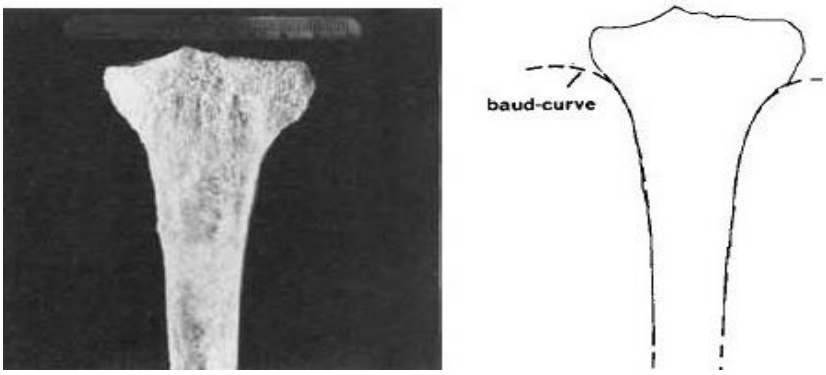


Figure 2-31: Baud curve in relation to a human tibia (the leg bone below the knee) (Mattheck, 1990a)

2.6.2.2 Logarithmic Spiral

For short beam, the modified Baud's curve may not be suitable in the case of pure bending. Short beams applied under pure bending and fixed at its opposite end are subjected to a steep gradient of bending moment (e.g. single lateral force loaded on its free end). This gradient of bending moment experienced in short beams is the reason why a logarithmic spiral is more suitable than Baud's curve. As shown in Figure 2-32 and Figure 2-40, the claw's concave contour follows a logarithmic spiral because of high loads subjected to the claws in the daily lives of these animals (Mattheck, 1990a).

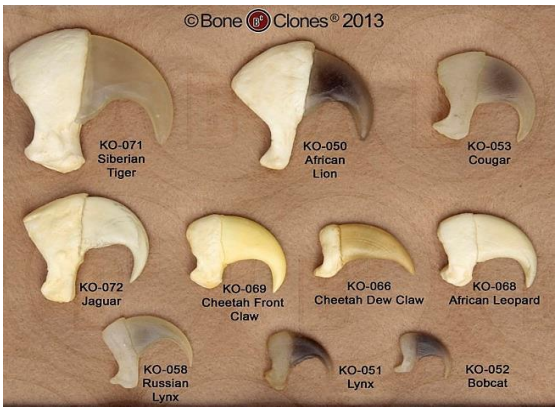
(a)  (b) 

Figure 2-32: (a) Claw of a bear (b) A Set of 10 cat claws (Bone Clones Inc., 2016)

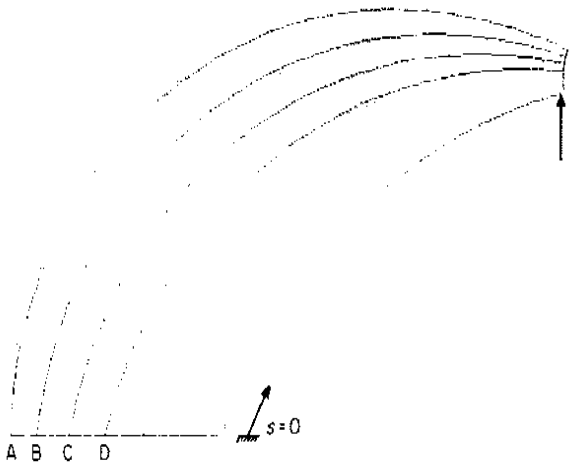


Figure 2-33: An illustration of a sample variation of the logarithmic spiral. (Mattheck and Reuss, 1991)

The experiment was conducted by clamping the opposite end of the short beam and loading the free end with a single lateral load to induce a steep gradient of bending moment. The concave contour line was fixed while the convex contour line was varied with a different “a” value, as illustrated in Figure 2-33, to create a variation of the logarithmic spiral hook. The samples were secured at the base (Mattheck and Reuss, 1991).

The logarithmic spiral is simplified, as shown in Equation (2-2):

$$r = a^{\theta} \tag{2-2}$$

Where "r" is the radius, "a" is the initial radius, and "θ" is the constant angle between "r" and the tangent of the spiral. The parameter for estimating biological growth from Mattheck (1990a) earlier studies can be well defined by Mises equivalent stress. Living creatures are self-optimising, and they often tend to optimise their structures to an almost uniaxial force flow. The uniaxial force flow in tree stems is directed axially, while in animal claws, they are parallel to the curved contour. The logarithmical spiral was variated with curves A, B, C and D. All the curves exhibit an almost constant stress distribution except for the circular approach, as shown in Figure 2-34. The logarithmical spiral exhibits no localised peak stresses (Mattheck and Reuss, 1991).

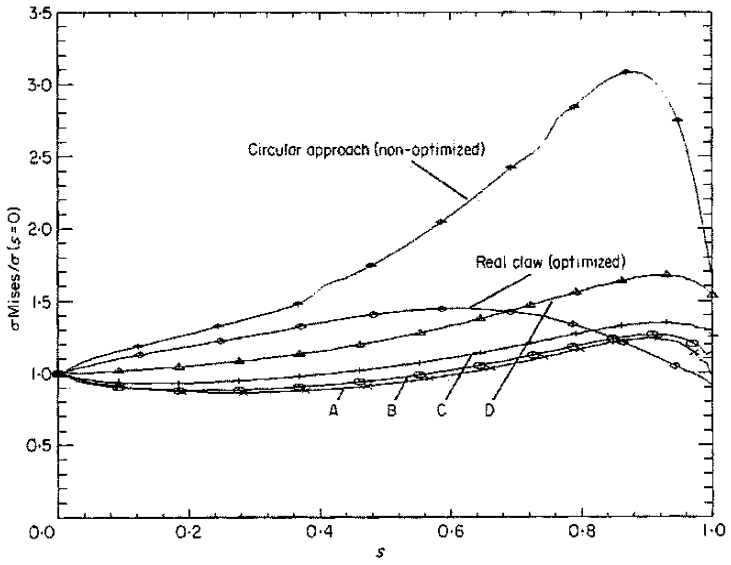


Figure 2-34: The graph shows a dimensionless Mises equivalent stress vs Contour coordinate s (Mattheck and Reuss, 1991).

((2-3 is applicable to 2D plane stresses)

$$\sigma_{Mises} = \sqrt{{\sigma_1}^2 + \sigma_1\sigma_2} \tag{2-3}$$

An optimum design should have constant stress distributed throughout its surface, and in this particular case, the load was fairly distributed. As shown in Figure 2-35, the concave contour line analysed shows the disadvantages of circular design compared to the other logarithmic spirals. The Mises stress iso-lines in the optimised design are almost parallel to the concave contour, as shown in Figure 2-35. The shape of the design was optimised through computer-simulated growth (Mattheck and Reuss, 1991).

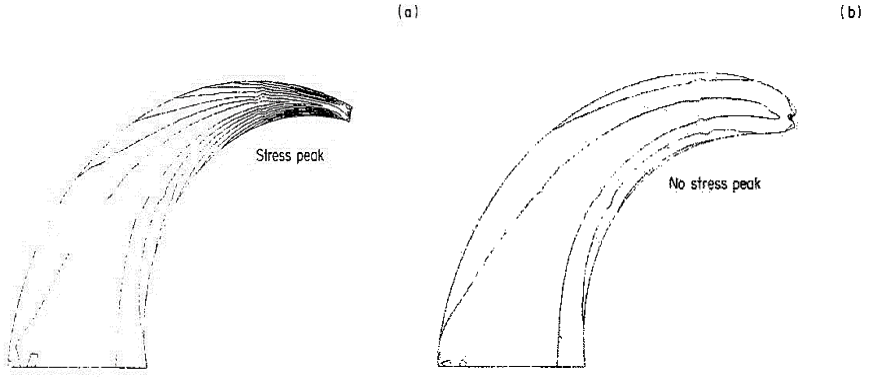


Figure 2-35: The illustrations above show the distribution of Mises stress iso-lines with (a) circular contours designed by most engineers and (b) optimised logarithmic spiral design (Mattheck and Reuss, 1991)

As first mentioned by Thompson (1942), the logarithmic spiral shape structure is a highly optimised design for short hooks, and it may be well said to have the best claw design for the task at hand. Carnivores like bears and tigers require the best tools to claw and shred their prey. The logarithmic spiral design has a near steady stress state, and it performs better than a circular arch design. The logarithmic spiral is a general sub-design rule for biological load carriers. Different logarithmic spiral configuration leads to slightly different stress profile. Therefore, an ideal combination of a concave

and convex curve may be created from these different logarithmic spirals configuration (Mattheck and Reuss, 1991). The finite element modelling was done under a 2D analysis, and the horny segment of the claw was considered. Other authors believe the fibre orientation in the horny segment of the claw carries most of the work. However, a more uniform stress state may be achieved if a 3D analysis model was conducted (Mattheck and Reuss, 1991).

2.6.3 Method of Tensile Triangles

Mattheck, 2007; Mattheck, Kappel and Sauer (2007) begins with studying how small changes in notches can make a big difference in stress imposed on a structure. He then investigates how ready grown biological designs, "mainly trees," can be used to improve engineering applications. Mattheck (2007) found trees to be a more straightforward method to explain the function of its load adaptive growth. Trees can distribute stresses efficiently along their surface to prevent localised peak stresses and avoid potential failure points (Mattheck, Kappel and Sauer, 2007). He made replicating design rules found in nature for engineering components understandable and straightforward.

"Method of Tensile Triangles" is a purely graphical method that was derived by Mattheck, Kappel and Sauer (2007) in late 2005. Nature's shape design can both ease the analysis of computer optimisation in mechanical structures and prevent/reduce component damage. Countless application of this graphical method in optimising component structures has been demonstrated. Its limitations are still not known yet, but a variation of this method has been used and tested (Mattheck, Kappel and Sauer, 2007).

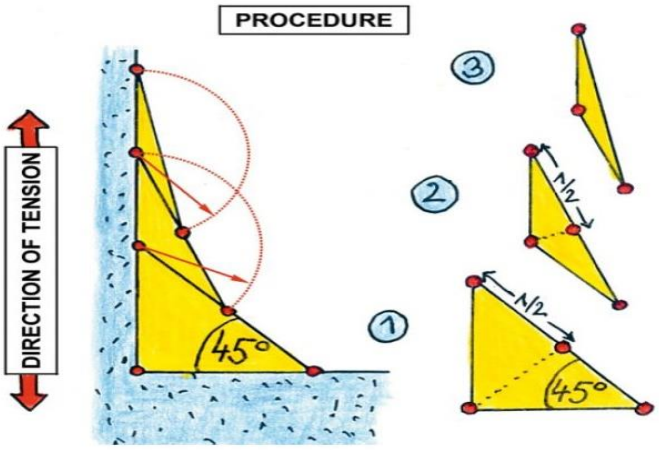


Figure 2-36: An illustration of how a tree optimises notch stresses through a simple graphical procedure. This method is known as the "Method of Tensile Triangle". (Mattheck, 2007)

Mattheck (2007) idealised concepts found in nature applicable to actual mechanical components, continued his research on nature and developed additional optimisation tools. The following is a list of optimisation tools developed by Mattheck modelled from nature, but only the latter is discussed.

1) Shear quadrangles
2) Force cones
3) Method of Tensile Triangles (Universal shape in nature)

Optimisation methods developed in the early years requires several hours or even days to optimise a component. "Soft Kill Option" was one of the previous methods used to optimise components before being replaced by the Force Cone method. Understanding the underlying structure of nature can help identify key mechanical failure or leading cause of damage in components to create a more reliable design (Refractories World Forum, 2011).

2.6.3.1 The Contour in Nature

The contour found in nature resembles the tension triangle developed by Mattheck, Kappel and Sauer (2007). This universal shape can be found in animate or inanimate objects, and an example of this contour can be seen in trees, as shown in Figure 2-37. Wind trimmed tree or water smoothed stones are among nature's optimisation methods of structures resulting from flow resistance. Erosion gradually smoothen compression bearing components or structures into ideal shapes (e.g. cliff lines or earth pyramids). Lighter and more durable components are created through the addition and removal of material to eliminate redundancy, e.g. the function of Osteoblast cells (formation) and Osteoclast/Scavenger cells (degeneration) in bones (Refractories World Forum, 2011). The "Method of Triangles" contour can be easily drawn, as shown in Figure 2-36. (Refractories World Forum, 2011).

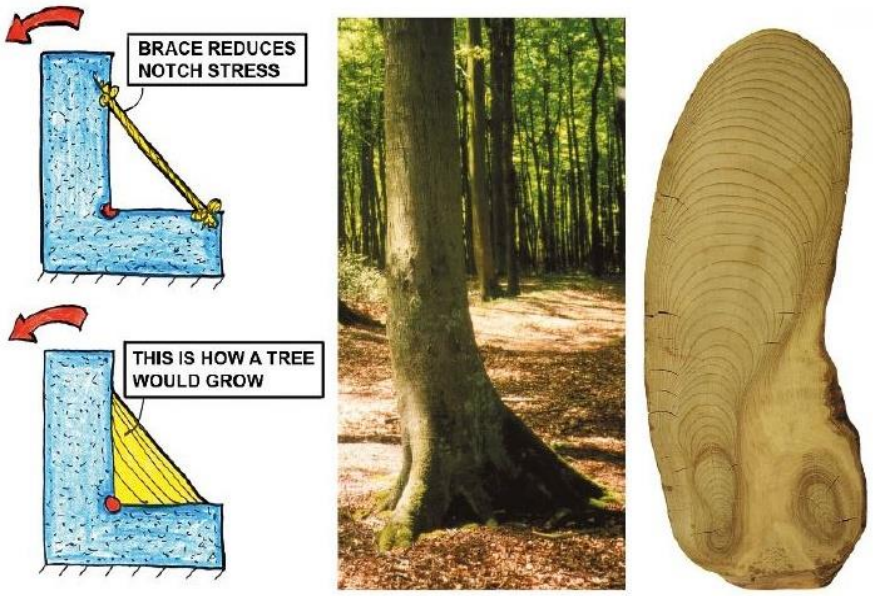


Figure 2-37: An illustration of how a tree grows to reduce notch stresses. (Mattheck, Kappel and Sauer, 2007)

2.6.3.2 Tree's Notch versus Engineer's Notch

The fundamental concept of forces and reactions must be well understood first to grasp the concept and better understand how nature adapts to its environment. Figure 2-38 shows the effectiveness of the tree's notch against the engineer's notch. Changing the notches' geometry, the results conducted by Mattheck, Kappel and Sauer (2007) shows that the tree notch could sustain higher stress when compared to the engineer's notch. Circular notches give rise to sharp corners or edges, usually lead to fatigue crack initiation and propagation, resulting in failure from high-localised stresses. Uniform stresses along its surface are achieved when the buttress root of a tree smoothen its sharp edges by creating a less dangerous notch shape with large angles to reduce notch stresses. The size of this shape varies accordingly to its dimension limitation and availability of space.

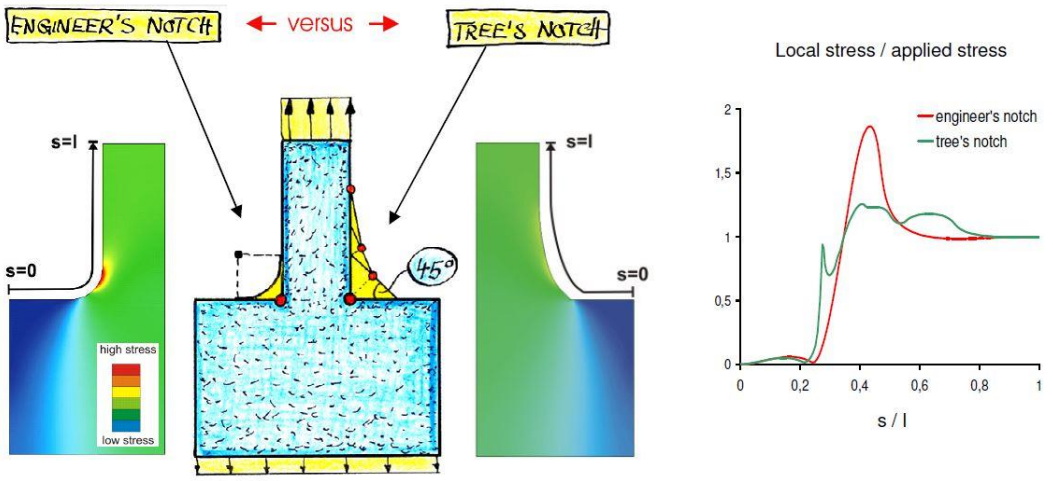


Figure 2-38: The difference of stress concentration along the notch contour between the engineer's notch and the tree's notch (Mattheck, Kappel and Sauer, 2007).

Through the evolution of biological shape optimisation, as shown in Figure 2-39 and Figure 2-40, notches in nature have changed the current engineering methods and views on optimising notch shape from a complex solution to a purely graphical method. The Method of Tensile Triangles, also known as a universal notch shape, has

survived countless merciless trials throughout its evolution, but every design has its limitations. Although not perfect, the implementation of this method in CAD systems or design component, at the very least, helps improves its fatigue, service life and sustainability. Trees can be a teacher to new optimisation method as it teaches engineers that adding and/or removing elements according to its environmental loading conditions can reduce weight without the potential risk of failure (Mattheck, 2006).

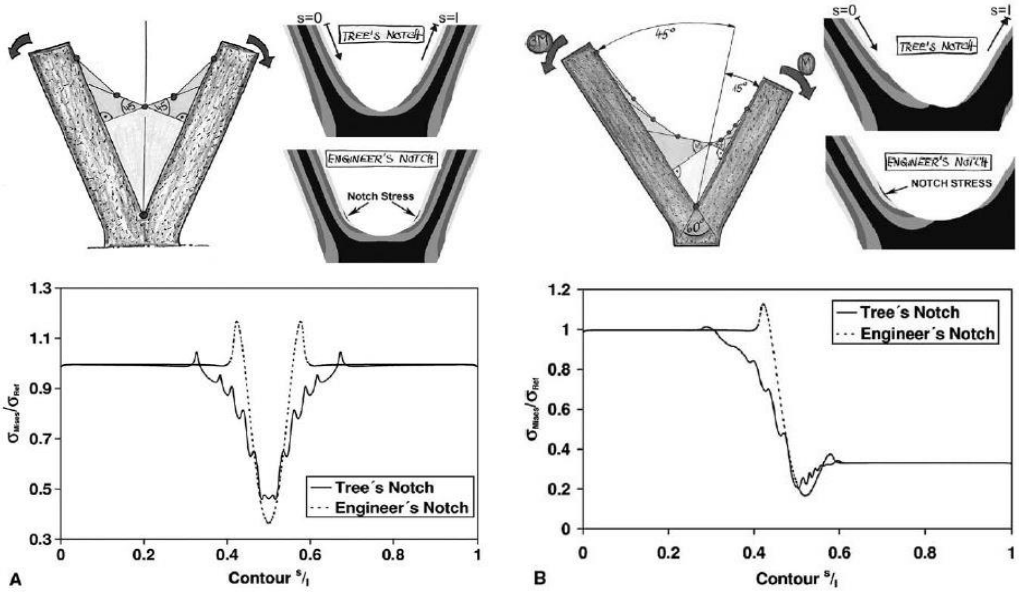


Figure 2-39: Shape optimisation of a (1) symmetrical and (2) unsymmetrical tree fork. (Mattheck, 2006)

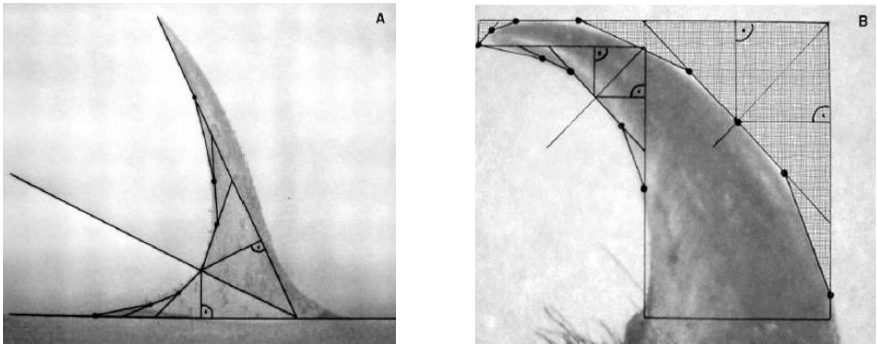


Figure 2-40: Claws do follow the shapes similar to the "Method of Tensile Triangles". (Mattheck, 2006)

2.6.4 Effectiveness of Method of Triangles in Comparison with Other Notch Profile

2.6.4.1 Fatigue Testing of Specimens with Notches

Finite element analysis was conducted according to the American Standard for Testing and Material (ASTM) to quantify stress concentration and the achievable improvement by optimising the various notch radiuses for a common push-pull, rotatory bending and bending fatigue testing. The improved notch design should have an increased fatigue life without affecting its global dimension and weight (de Albuquerque Simões, de Castro and Meggiolaro, 2012).

With the help of a computer numerical control (CNC) machine, various notch shapes can be manufactured economically with precision and accuracy. The testing specimen (TS) often fails at the section's ends of the straight gauge where the notches' curvature starts (de Albuquerque Simões, de Castro and Meggiolaro, 2012).

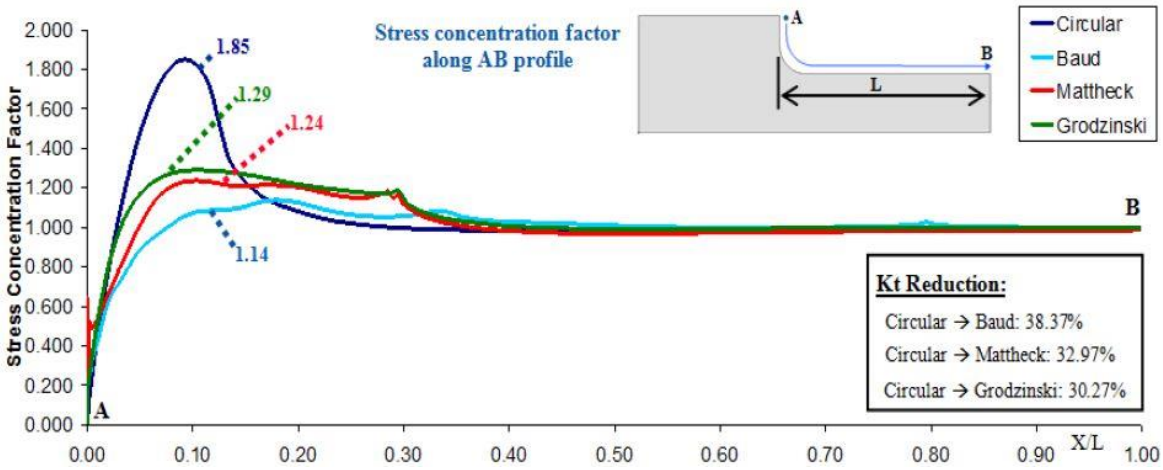


Figure 2-41: Comparison between different notch shapes in relation to stress concentration factor (de Albuquerque Simões, de Castro and Meggiolaro, 2012).

Figure 2-41 shows a stress concentration comparison chart between Baud, Mattheck, Grodzinski and Circular. The analysed specimen was loaded by a centred tensile load, and it was found that the notch shape for Baud, Mattheck and Grodzinski (Pilkey *et al.*, 2007) have higher efficiency at lowering stress concentration when compared to the circular notch shape (de Albuquerque Simões, de Castro and Meggiolaro, 2012). However, Baud's notch profile performs better than the notch profile proposed by Mattheck and Grodzinski. If the notch profile is correctly applied, they all can at the very least improve fatigue life with the lowering of Stress Concentration Factor (SCF) that evidently will also reduce the overall costing (de Albuquerque Simões, de Castro and Meggiolaro, 2012).

2.6.4.2 Performance of Notch Profile (Grodzinski versus Mattheck)

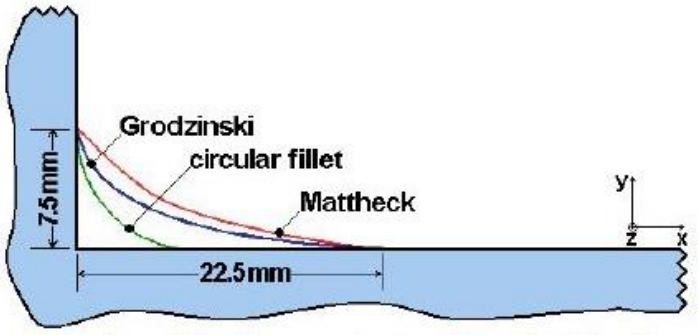


Figure 2-42: Geometrical profiles of different notches (de Albuquerque Simões, de Castro and Meggiolaro, 2011)

Notch profile found in nature does not have a constant radii notch as they vary accordingly to the loading condition. The two graphical methods proposed by Mattheck and Grodzinkis are systematically compared, as shown in Figure 2-42, to identify its notch shape performance. The two proposed notch shapes are differed by their geometrical size along the x and y direction. Graphical methods allow easier application and optimisation of components with little to no calculation while meeting

the geometrical limitations. Geometrical limitation or constraints are not limited to the interference with other components and spacing limits (e.g. extension of the curve along its shoulder) and varied accordingly to its application (de Albuquerque Simões, de Castro and Meggiolaro, 2011). The notches are tested under two different conditions through the finite element method, as shown in Figure 2-43 and Figure 2-44.

1. Flat bar
    a. bending
    b. tension
2. Cut-out window steel plate
    a. tension

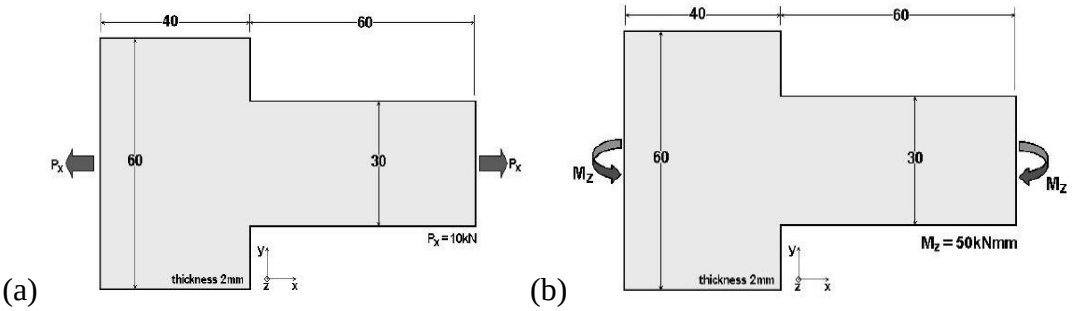


Figure 2-43: Flat bar subjected to (a) pure tension (b) pure bending (de Albuquerque Simões, de Castro and Meggiolaro, 2011)

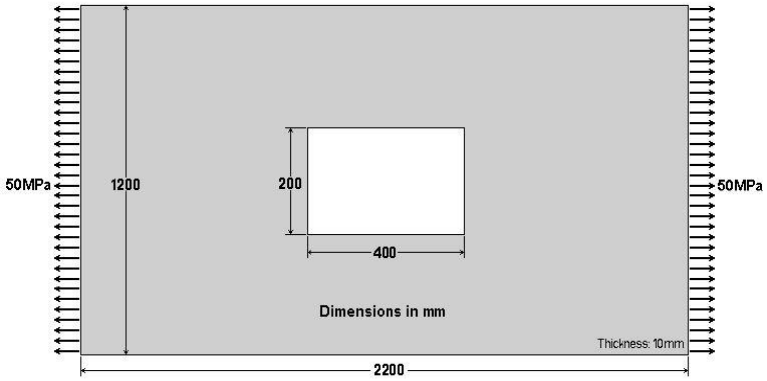


Fig. 16: Example of an inspection window cutout subject to pure tension loading

Figure 2-44: Cut out window steel plate subjected to pure tension pulling (de Albuquerque Simões, de Castro and Meggiolaro, 2011)

Organic material tends to grow accordingly to sections of high-localised stress concentration. An abrupt change in geometry at the shoulder can affect its stress concentration along its surface. Figure 2-45 and Figure 2-46 show the stress concentration factor of different notches along its surface under tension and bending (de Albuquerque Simões, de Castro and Meggiolaro, 2011). The values obtained in the finite element for circular notch profile was verified with two different Peterson's charts, as shown in Figure 2-47. One is for a flat bar with shoulder fillet under tension load and the other for bending load.

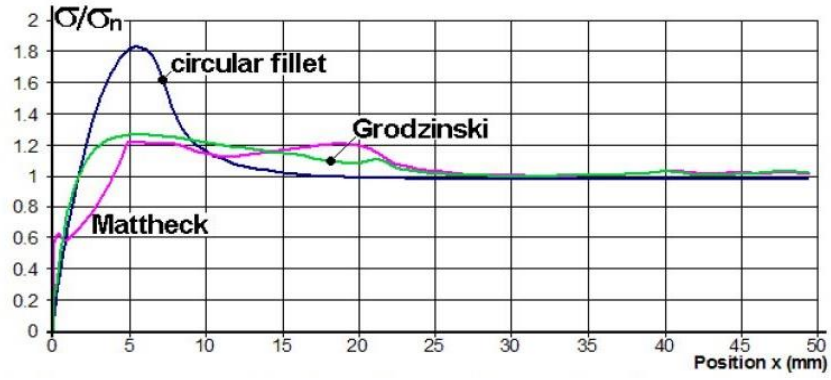


Figure 2-45: SCF of notch under tension load for a flat bar (de Albuquerque Simões, de Castro and Meggiolaro, 2011).

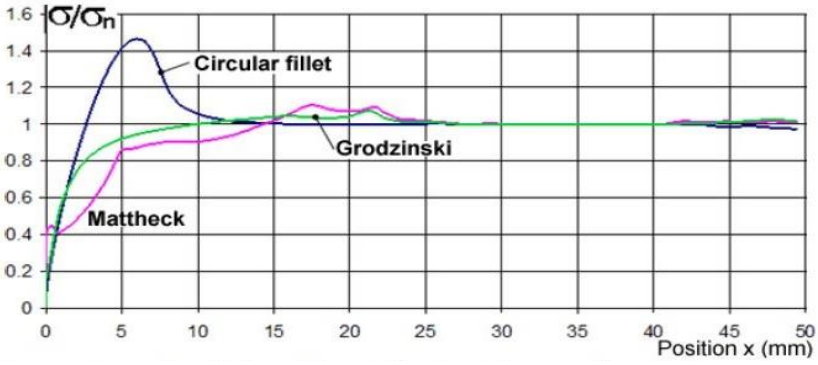


Figure 2-46: SCF of notch under bending load for a flat bar. (de Albuquerque Simões, de Castro and Meggiolaro, 2011)

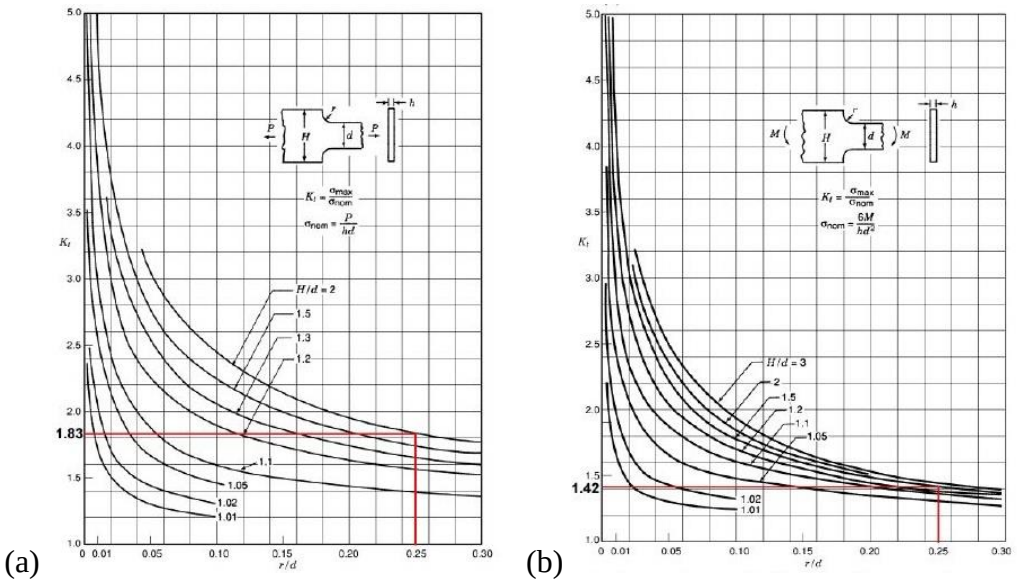


Figure 2-47: Peterson's charts for a flat bar with shoulder fillet under (a) tension load (b) bending load (Pilkey *et al.*, 2007; de Albuquerque Simões, de Castro and Meggiolaro, 2011)

Table 2-1 shows a summary result of the stress concentration factors in the different notch shapes tested. Both graphical methods proposed by Mattheck and Grodzinski have lower SCF than the circular profile. Mattheck's notch profile is better than Grodzinski's notch profile under tension load but suffers under bending load. Offshore structures (e.g. semisubmersible platforms) have numerous steel plate-like elements with an opening for reinforcing girders and other structural components. Therefore, a

practical application example of a centre cut out steel plate, as shown in Figure 2-44, was tested by de Albuquerque Simões, de Castro and Meggiolaro (2011) under tension load to determine the concentration of stresses around the corners of the hole (de Albuquerque Simões, de Castro and Meggiolaro, 2011).

Table 2-1: Result summary of stress concentration for different notch profile. (de Albuquerque Simões, de Castro and Meggiolaro, 2011)

Fillet profile	**Stress Concentration Factor (SCF)**	
	Pure tension	Pure bending
Circular	1.83	1.46
Mattheck	1.22	1.10
Grodzinski	1.26	1.07

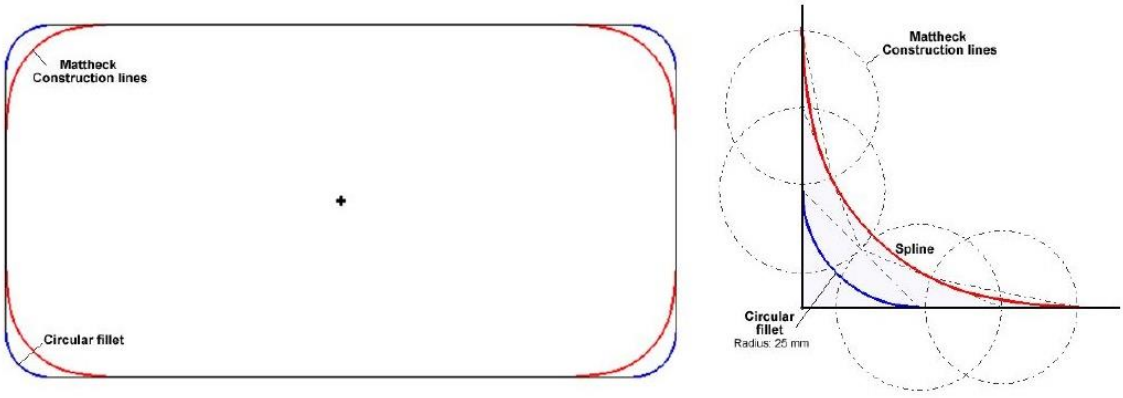


Figure 2-48: Smoothing of corner within the cut-out window of steel plate with different notch profile (de Albuquerque Simões, de Castro and Meggiolaro, 2011)

As shown in Figure 2-49, Mattheck's graphical method reduced stress concentration by approximately 19% compared to the circular fillet profile (de Albuquerque Simões, de Castro and Meggiolaro, 2011). However, the result in Figure 2-49 also shows no optimum solution, and it is more towards an improved solution grounded on heuristic geometrical models (de Albuquerque Simões, de Castro and Meggiolaro, 2011).

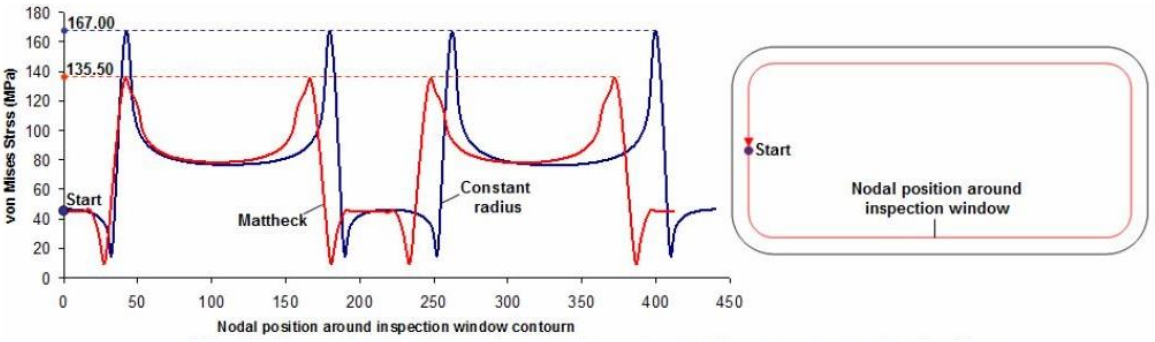


Figure 2-49: Von Mises stress along the nodal position around the inspection window under tension load (de Albuquerque Simões, de Castro and Meggiolaro, 2011).

Both methods proposed by Mattheck and Grodzinski improve the notch fillet profile in terms of reducing stress concentration compared to the circular fillet profile, but it does not neglect the fact that both graphical methods still require further optimisation. Graphical methods allow reworking and reshaping of geometry easy for optimisation. The reduction of stress concentration in both graphical methods shows substantial improvement in notch stress, and therefore its ability to plausibly increase fatigue life should not be ignored (de Albuquerque Simões, de Castro and Meggiolaro, 2011).

2.6.4.3 The comparison of Popular Notch Profiles with Method of Tensile Triangles

A company known as ALTRAN conducted an analysis and made a comparison of minimising notch stress with different popular notch profiles. A more detailed stress concentration analyses on different notch profiles can be referred in their paper (Ciomber and Jakel, 2014).

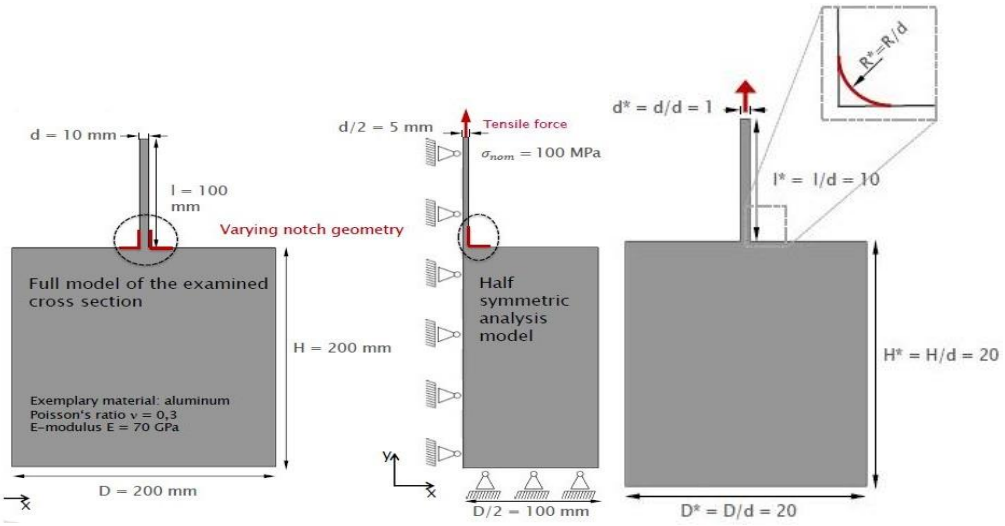


Figure 2-50: An illustration of the model tested (Ciomber and Jakel, 2014).

As shown in Figure 2-50, the model was made dimensionless to obtain an accurate and unbiased result without the influence of other factors. The l* was randomly set as 100mm to ensure that the load-induced point is far and long enough from the notch. The web thickness was maintained at d=10 mm. Since the assumption was based on the two halves that are symmetrical to each other and the notch's influence is also half of the column's diameter, only one-half was considered in the analysis, as shown in Figure 2-50. The worst-case scenario of notch stresses is obtained by ensuring that D* and H* are adequately large. The D* and H* values are obtained, as shown in Figure 2-51 and Figure 2-52. Smaller D* often leads to smaller notch stress. The non-circular notches have their normalised notch height referred to as h*=h/d and width as b*=b/d.

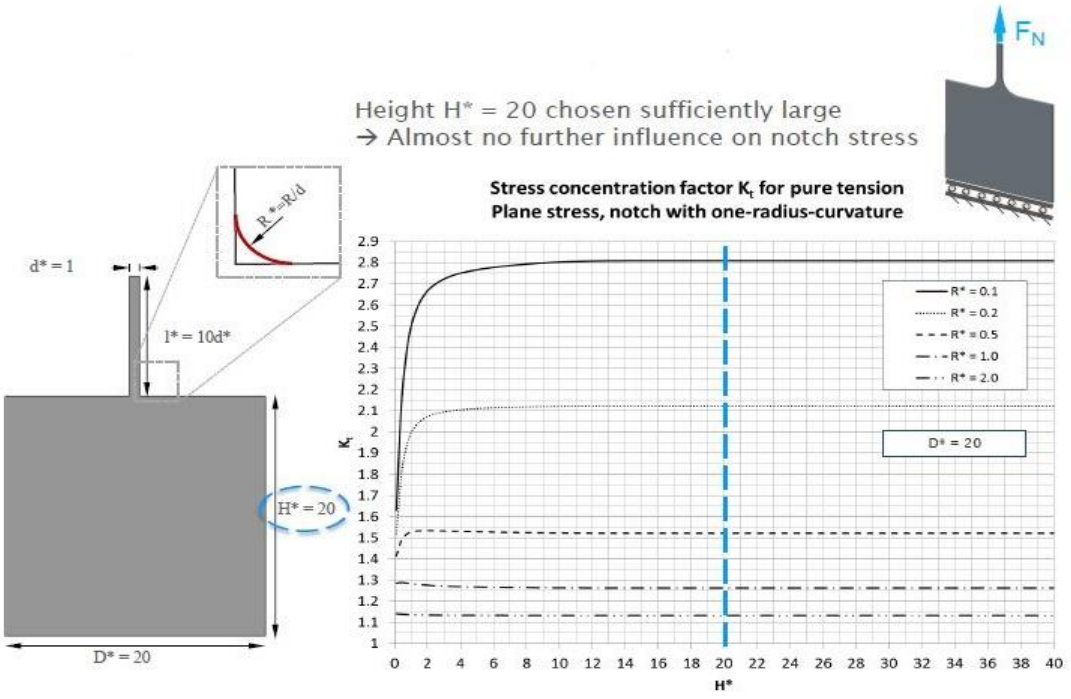


Figure 2-51: A graph showing a point where the height of the model is no longer influenced by the changes in stress concentration in the testing sample (Ciomber and Jakel, 2014).

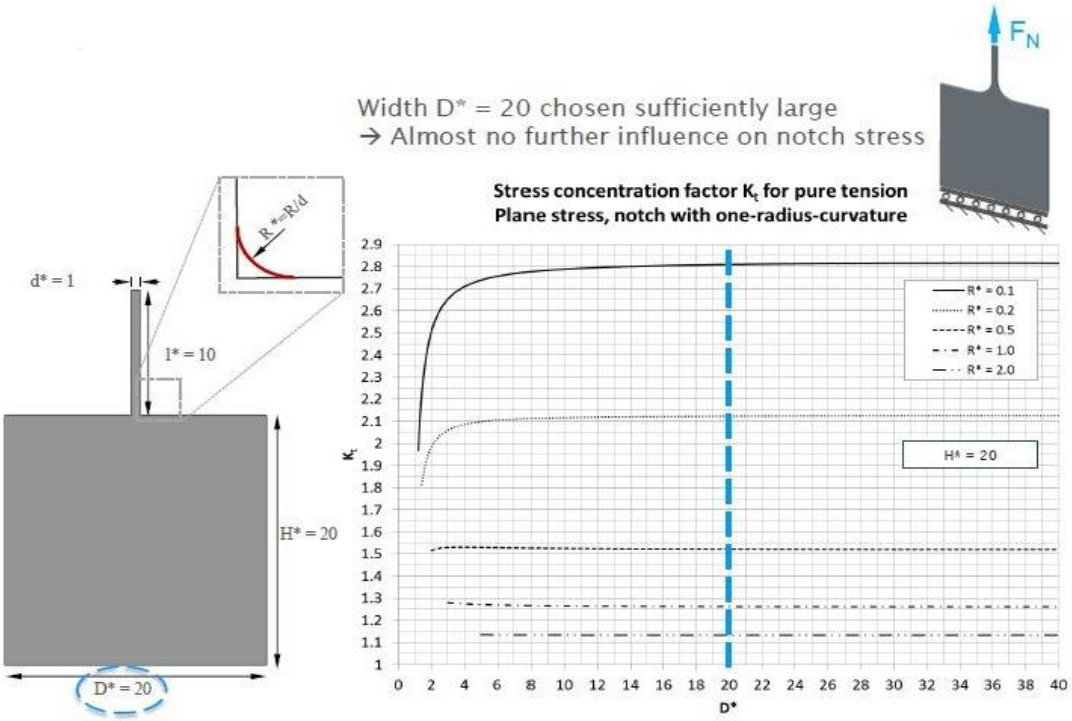


Figure 2-52: A graph showing a point where the diameter of the model no longer influenced by the changes in stress concentration in the testing sample (Ciomber and Jakel, 2014).

The notches are analysed under the worst-case loading, as shown in Figure 2-53, to determine the best-notch design. Bending creates lesser notch stress than tension; thus, tension is more critical. 2D plane stress incurs the highest notch stress when compared to 2D plain strain and rotational symmetry. Therefore, the notches were analysed only in tension and under 2D plane stress condition.

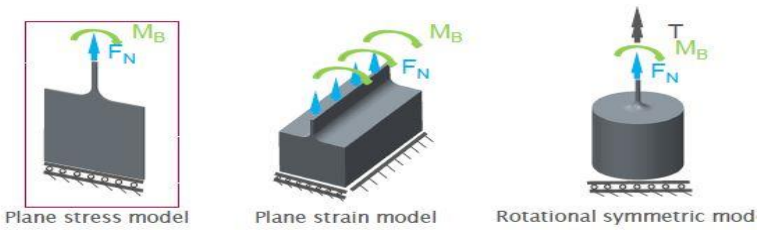
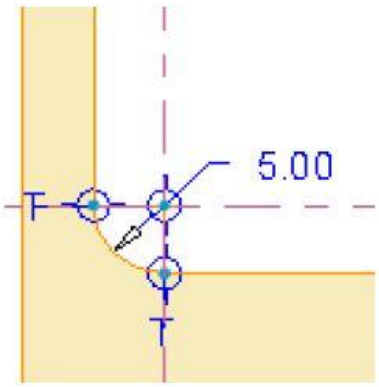
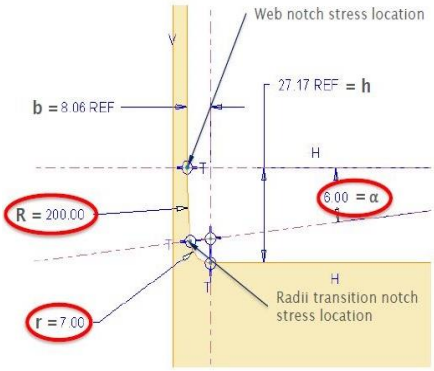
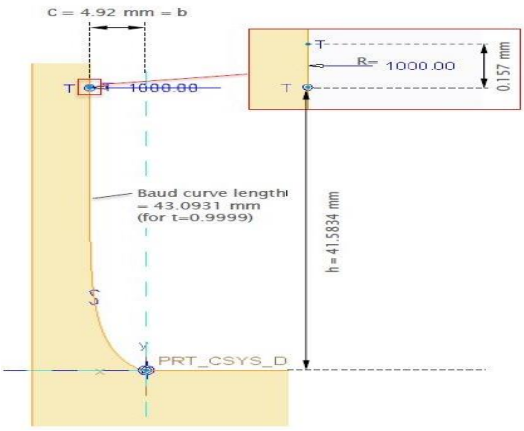
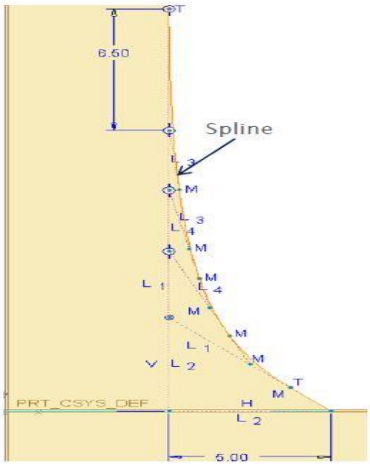
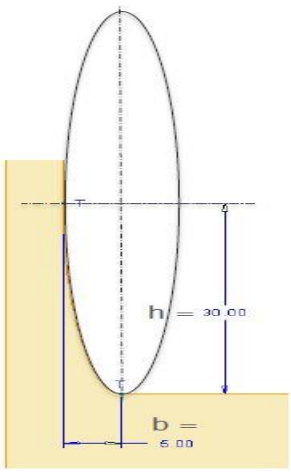
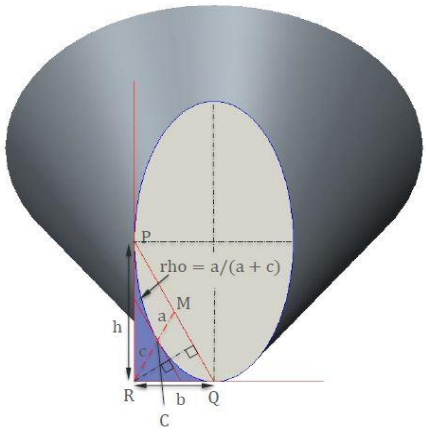


Figure 2-53: An illustration showing the following condition that models can undergo (Ciomber and Jakel, 2014).

There are six different approaches of notch shapes, as shown in Table 2-2 (Ciomber and Jakel, 2014):

1) One radius fillet
2) Two radii fillet
3) Baud fillet
4) Method of tensile triangles
5) Standard elliptical fillet
6) Conical round “generalised elliptical fillet”

Table 2-2: An illustration of the different notch shapes (Ciomber and Jakel, 2014)

One radius fillet	Two radii fillet
	 Radii R, r and angle α are varied (height h and width b of the notch geometry only as reference dimension!)
Baud fillet	**Method of Tensile Triangles**
	
Standard elliptical fillet	**Conical round "generalised elliptical fillet"**
	

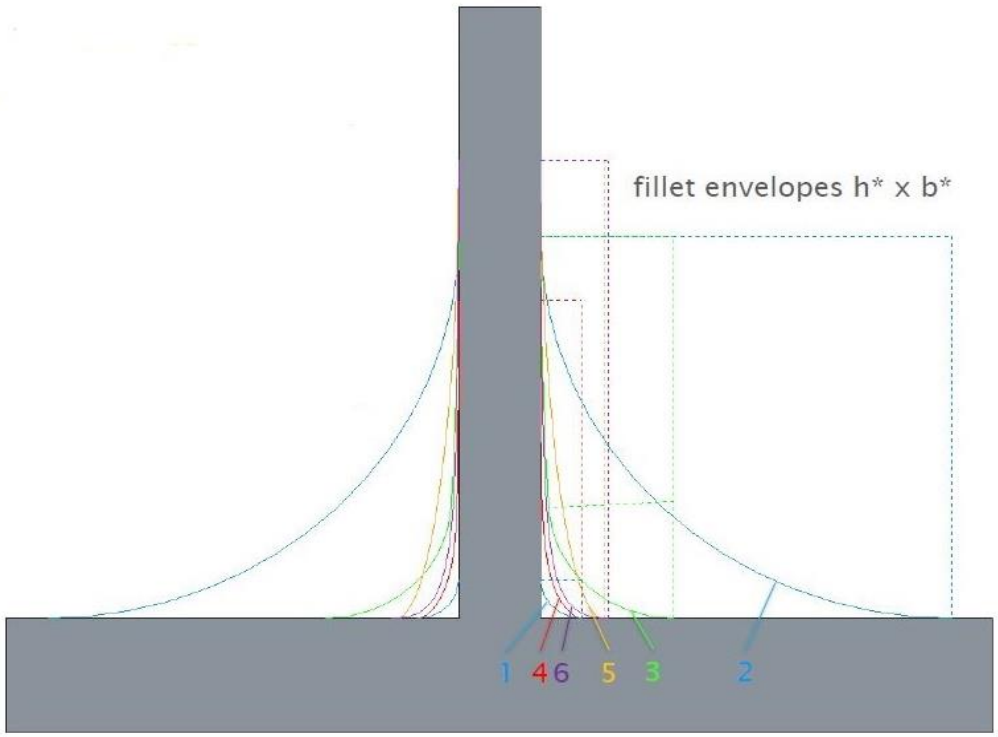


Figure 2-54: A graphical comparison of different notch shape to their overall size (Ciomber and Jakel, 2014).

All the best-optimised notch shapes are shown in a single figure to illustrate the notch sizes, except for the "method of tensile triangles", which is not included in Figure 2-54.

The numbering of notch shapes in Figure 2-54 is as follows:

1) One radius fillet (R*=0.5)
2) One radius fillet (R*=5)
3) Two radii fillet
4) Baud fillet
5) Standard elliptical fillet
6) Conical round "generalised elliptical fillet"

Table 2-3: Result summary of the different notch shapes in their optimum size and contour in relation to their stress concentration (Ciomber and Jakel, 2014).

Notch type	No	height*	breath*	Radius*	Angle α [$*$]	Conical bow segment PQ (rho)	Stress concentration K_t	Remarks
One radius fillet	1	-	-	0.5	-	-	1.5257	Notch stresses experienced is too high. Not a recommended shape in practice.
		-	-	5	-	-	1.0544	In practice, the size of the notch is too large. Therefore, not efficient.
Two radii fillet	2	5	1.62	-	3	-	1.0042	
Baud fillet	3	-	0.492	-	-	-	1.00046	1) Baud's recommendation is b*= $\frac{1}{\pi} = 0.3183$, but the better value found is 0.492. 2) Initially, its shape follows a conical round with $rho > \sqrt{2} - 1$ and then a standard elliptical fillet 3) Baud's curve is too difficult for replication in practice. Its ends were "cut" after $\theta =$ 89,991°, and it has to be rounded to prevent the formation of a singular location ($edge <$ 180°).
Method of tensile triangles	4	-	0.5	-	-	-	≈1.1	A one radius fillet of 1mm is applied at the base of the triangle.
Standard elliptical fillet	5	6	0.76	-	-	-	1.00608	
Conical round	6	6	0.825	-	-	0.7	1.00064	(Rho=a/ (a+c)) but due to high stress level, the rho was modified at a trial and error basis until a value of 0.7 is obtained.

Baud fillet was indeed the best among the other notch designs. The notch shape becomes very sensitive as $K_t \approx 1$. However, this shows how small curvature changes can lead to higher stresses or lower stresses. Such tedious work in practice is difficult in the civil engineering world. The testing of notches described above does not reflect the actual seismic effect of actual bending and torsion. The testing sample result was more suited for small mechanical equipment subjected to this specific type of tension, bending and torsion. Even though the differences in stress concentration between Baud's and Mattheck's notch profile may be large, a stress concentration of 1.02 can be achieved in Mattheck's notch profile.

Research conducted by Komarla (2011) proves that a stress concentration of 1.02 in Mattheck's design shape, as shown in Figure 2-55, is obtainable. With careful iteration and trial and errors, they managed to minimise the maximum stress to a near nominal stress concentration, as shown in Figure 2-56. The maximum stress experienced in the component is approximately 10.2MPa, with the nominal stress at 10MPa; thus, having a stress concentration of 1.02. However, stress minimisation is at the expense of a larger fillet. Therefore, there is a lack of evidence to deny the idea of infusing Mattheck's notch design in civil engineering structure. More research is required in this area, and Mattheck's notch design is a good direction to start with, as it is practical and straightforward.

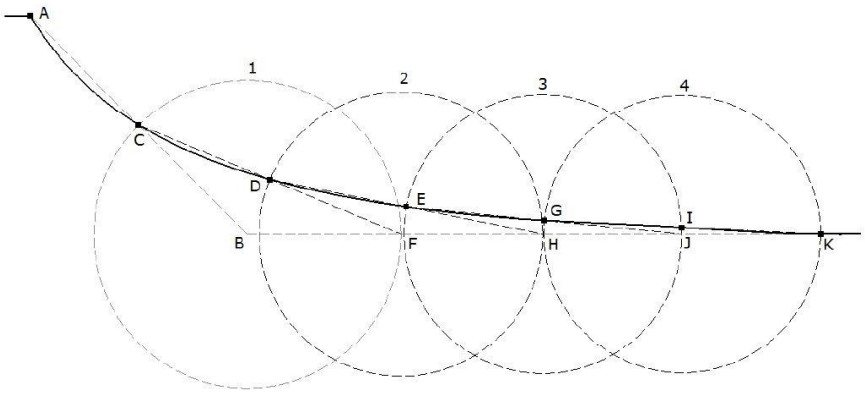


Figure 2-55: Optimisation of shoulder fillet through Mattheck's method of tensile triangles (Komarla, 2011).

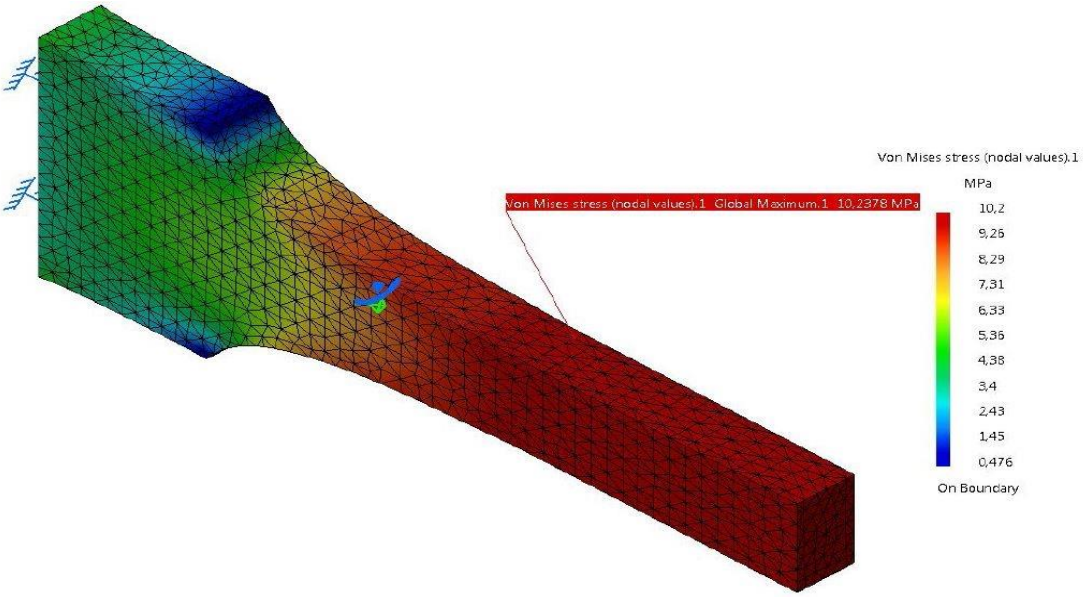


Figure 2-56: The stress distribution diagram "Method of Tensile Triangle" (Komarla, 2011).

2.6.5 Applications and Success of using the "Method of Tensile Triangles"

Engineers of Reichle & De-Massari managed to take advantage of Mattheck design in their $Cat\ 6_A\ Module$ as shown in Figure 2-57, and they were able to produce a product that is hard, stable, resilient and torsion-resistant. Their product was neither over rigid nor over weak, and it was the perfect size at a minimal cost (Eichenberger *et al.*, 2011).

Screws threads optimised with Mattheck's Method of triangles, as shown in Figure 2-58, also helped reduce stresses at the screw threads by 34%. This reduces failure on the screw threads. The finite element method was used to confirm the said results (Bar-cohen, 2012). Screw thread infused with this design for orthopaedic bone surgery has a greater defect-free service life (Refractories World Forum, 2011)



Figure 2-57: A picture of a Cat 6_A module (Eichenberger *et al.*, 2011).

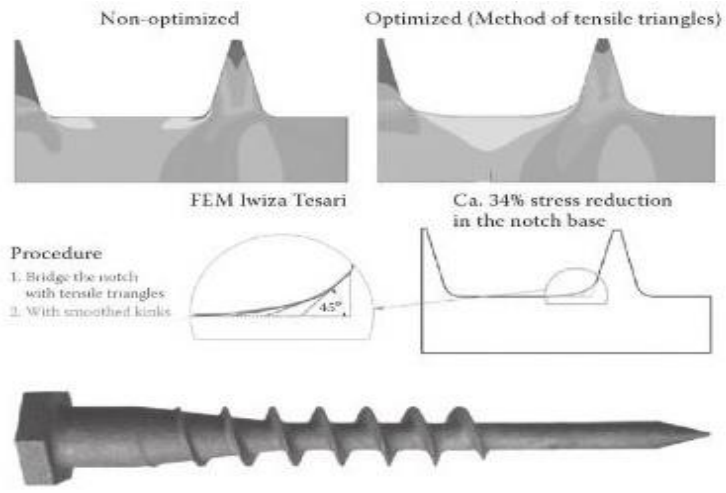


Figure 2-58: Stress concentration of a screw optimised using the "Method of Tensile Triangles" (Bar-cohen, 2012).

2.6.5.1 Crack Control of Components or Structures

Mattheck *et al.* (2010) investigated the traditional crack control method to drill a circular hole into the intended surface crack at its crack tip, as shown in Figure 2-59. This is to enlarge the notch radius to reduce stresses, as shown in Figure 2-60, but this does not stop the underlying problem. Therefore, it continues to crack after drilling. If

the crack's ends were cut according to the tensile triangle contour, stresses could be reduced. This is because as the tension crack propagation is converted into a compression that prevented further tearing, this eliminates crack initiation risk. Therefore, fatigue life is increased.



Figure 2-59: Drilling away slot ends did not stop crack formation and propagation of large industrial drum (Carpi and Brebbia, 2010).

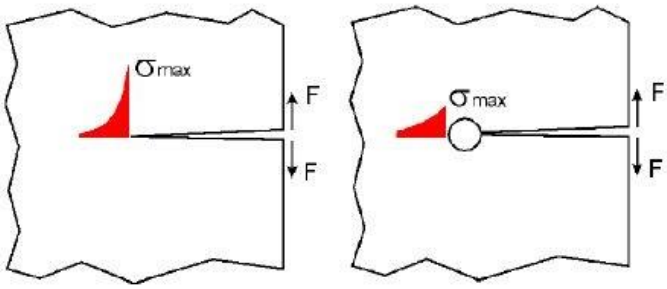


Figure 2-60: Drilling of crack tip reduces the stress experienced (Carpi and Brebbia, 2010).

Applying tension similar to Figure 2-61, the concentration of notch stresses increases with the diminishing notch radii. It is because the tearing effects are parallel to its tension zone and sharp corners often experience higher stress concentration. Figure

2-61 shows the stress concentration from a circular notch to a flat elliptical notch. The far-right corner of the figure shows a theoretical notch with zero radiuses, and it should, in theory, have infinite notch stress (Mattheck *et al.*, 2010).

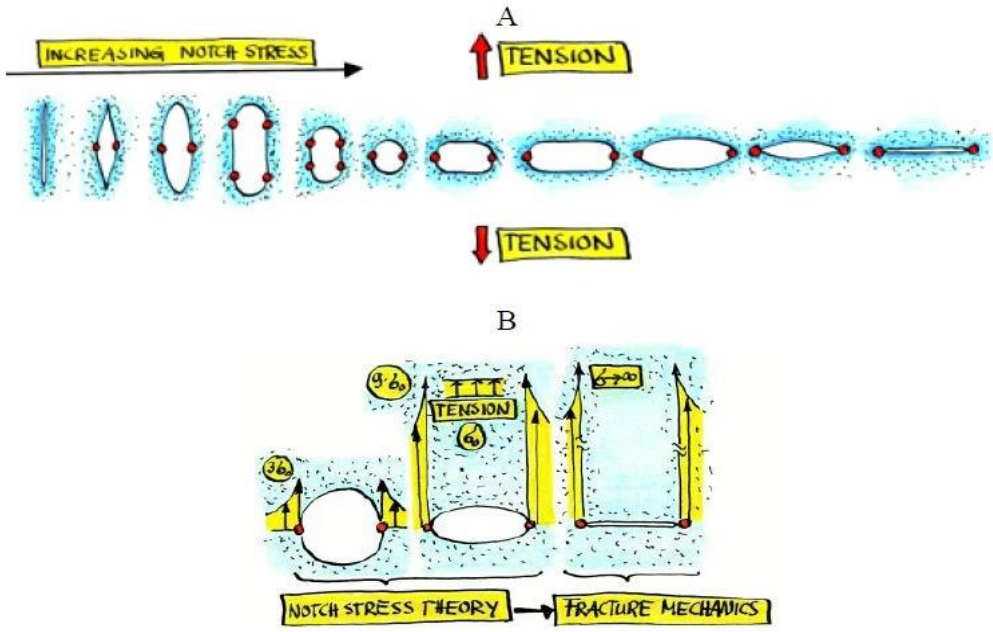


Figure 2-61: Notch stresses (A) Orientation of notch shape along the same direction of force (B) Theory of notch stress (Mattheck, 2004)

Steel samples with different shaped slot ending, as shown in Figure 2-62 and Figure 2-63, were tested under cyclic loading to determine their fatigue lifecycle. The results shown in Table 2-4 shows that the method of tensile triangles is a better solution in reducing crack propagation than the traditional method of drilling the slot away with a circular notch. The leading cause of failure in any component is the disturbance of its force flow due to local stress concentration. This stress raising effect reduces its fatigue resistance over its lifespan. Good mechanical components are lightweight and able to maintain their reliability and usability during their estimated service lifetime. The tensile triangle contour was discovered to be a useful tool for different technical problem (mainly mechanical) (Mattheck et al., 2010).

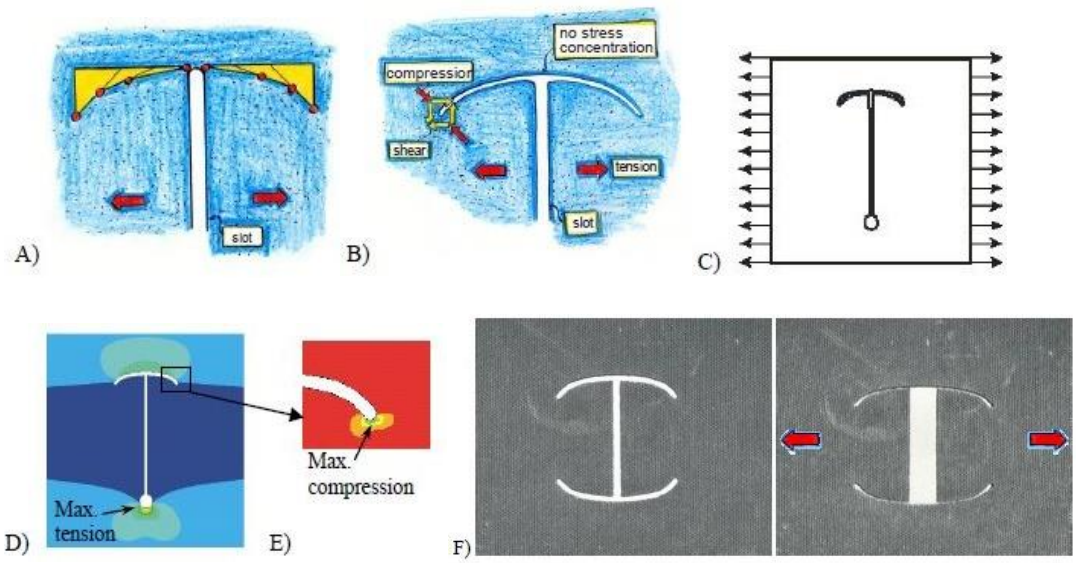


Figure 2-62: (A) Application of tensile triangles at slot ends; (B)Theoretical notch stresses; (C) Tension pulling uniformly of a theoretical sample; (D, E) FEM analysis showing stresses experienced; (F) Tension pulling of the sample. (Carpi and Brebbia, 2010)

Table 2-4: Result summary of fatigue life with different ends of slots (Carpi and Brebbia, 2010).

Sample	Ends of slot	Fatigue life cycles
A	no modification	26,445
B	circular ends (r=1mm)	44,973
C	circular ends (r=2mm)	91,686
D	Straight traverse ends	64,750
E	tensile triangle shaped ends (h=2mm)	219,235
F	tensile triangle shaped ends (h=5mm)	1,591,414

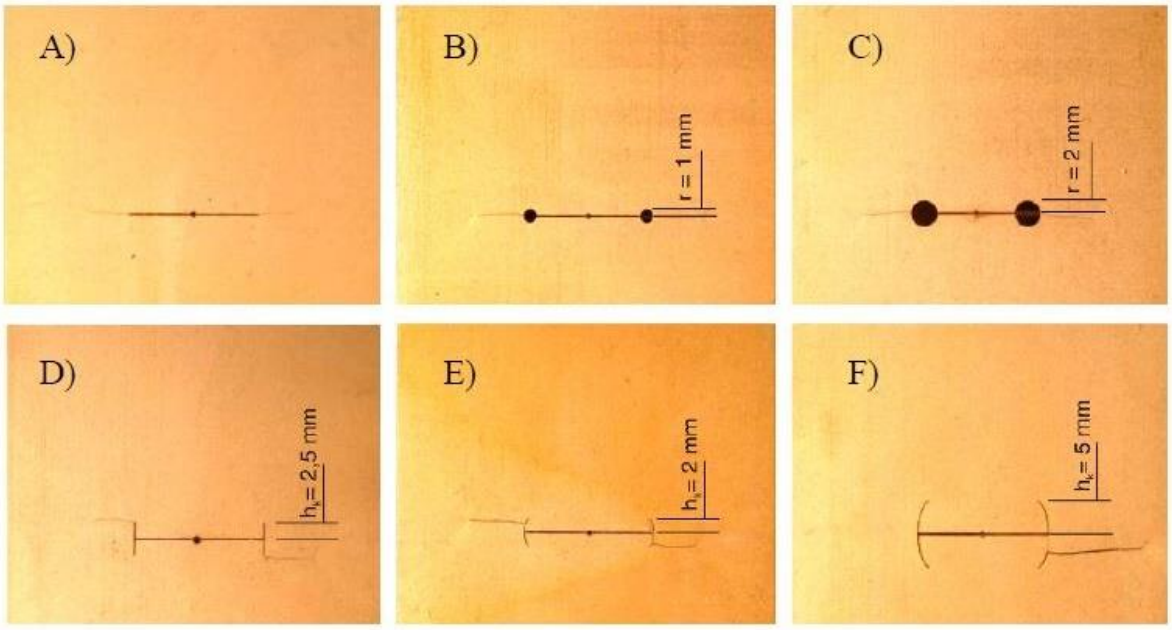


Figure 2-63: Steel plate samples with different shaped slot ending. (A) A slot without modification; (B, C) slots drilled at endings (r=1mm, 2mm); (D) slot cut with straight traverse ending (E, F) Ends of Slot cut with tensile triangle shape (h=2mm, 5mm) (Carpi and Brebbia, 2010)

2.7 Biomimicry in Civil Engineering

Biomimicry has been widely used to inspire architecture designs and to solve many engineering problems alike. Antoni gaudí once said "*There are no straight lines or sharp corners in nature. Therefore, buildings must have no straight lines or sharp corners*." (Gaudi, 2014). Some notable nature-inspired architectural designs are like "The Crystal Palace" by Sir Joseph Paxton that has a roof design similar to a leaf of a water lily, the "Armadillo Concert Hall (Clyde Auditorium)" that follows the shape of an armadillo, the "Bahai House of Worship" and the "Beijing National Stadium" inspired by a lotus flower and a birds nest respectively and the "Lisbon Orient Train Station" that utilises a tree branch design (Tavsan, Tavsan and Sonmez, 2015; Radwan and Osama, 2016). These designs are mainly for architectural purpose but there some like the "Eastgate Centre" of Zimbabwe that follows the design of an ant's nest that can reduce energy consumption through better heat transfer mechanism (Tavsan,

Tavsan and Sonmez, 2015; ElDin, Abdou and ElGawad, 2016). The building is able to maintain a good internal thermal comfort without suffering the effects of the daily temperature fluctuation in the external surroundings (Beghini *et al.*, 2014; ElDin, Abdou and ElGawad, 2016). Hence, structural optimisation is the natural solution in creating a "biomimetic like architecture" that is innovative in design with higher material efficiency. The introduction or adoption of any new design in civil engineering structures has to be coherent as they are primarily associated with higher risk. Some factors associated are constructability (that includes manufacturability), performance, stability, efficiency, design space dimensionality, safety, total embodied energy and aesthetic.

2.7.1 Trees and Civil Engineering Structures

As seen in Section 2.4.1, the tree's anatomy shares similarities with building structures in terms of its mechanics. It is a fixed upright cantilever structure that requires a firm base to overcome whatever nature throws at it. Therefore, research in trees may be a suitable path for civil engineers to learn its ways of overcoming the challenges faced in its environment. The following section demonstrates the benefits of trees if one should replicate a structure similar to that.

2.7.2 Safety Factor of Trees

The current building codes for British Standards and Eurocode suggest that the safety factor of structures within 2.5 – 3 is considered sufficient. However, in trees, this is not the case. Trees were believed and assumed to have a safety factor of 1.5 before Mattheck (1991) discovering their real strength. However, trees have a safety factor of at least 4.5 (Graham, 2007). Similarly, mammal bones have a safety factor of 3 – 4, and for manufactured structure, a safety factor of 10 is considered normal (Mattheck,

Bethge and Schäfer, 1993). That leaves the British standard and Eurocodes having far less safety factor than trees in comparison.

Civil Engineers rarely design a building for the extreme possible earthquake scenario as the design would require an additional safety factor of 2-3 because this often results in a costly, limited working space and a massive structure. Buildings with this design feature will look similar to a military shelter or a nuclear power plant. Trees have a higher safety factor than mammal bones due to their difference in locomotion. Trees are static and can resist violent storms and wind, as it does not possess any locomotion while animals have the locomotion to move around to find food and seek shelter. Trees need to grow tall and slender to reduce competition for light reception from neighbouring trees, thus requiring a higher safety factor (Mattheck, Bethge and Schäfer, 1993).

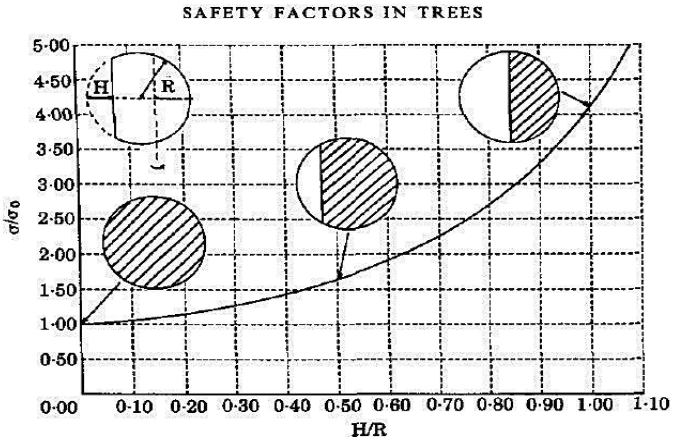


Figure 2-64: The graph shows the factor of safety against the cross-section of the tree stem, where R is the stem radius and H is the removed material. (Mattheck, Bethge and Schäfer, 1993)

The safety factor of a tree is determined by creating a window frame with varying sizes in the tree stem. Figure 2-64 shows that the window frame reduces the wood's stiffness laterally, resulting in a higher lateral contraction followed by the bending of the stem. The bending of the tree stem at the window frame increases notch stresses. The smoothness on the corners of the window frame affects the amount of notch stresses

experienced. Hence, a window frame with smoother corners experiences lesser notch stresses. Therefore, the radius of the corners in the window frames was maintained. The upper safety limit is determined by gradually increasing the window frame's size over several years until breakage (Mattheck, Bethge and Schäfer, 1993).

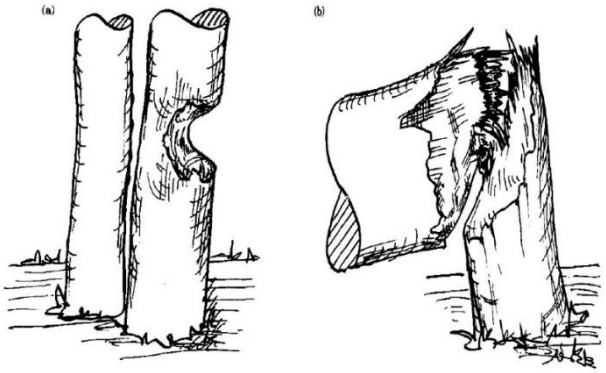


Figure 2-65: Trees near the Mississippi river damaged by beavers (a) Stress magnification of 4; (b) Stress magnification greater than 5 (Mattheck, Bethge and Schäfer, 1993).



Figure 2-66: A tree with a window frame of a 2/3 stem diameter (Mattheck, Bethge and Schäfer, 1993).

Window frames can occur naturally through means of decaying, disintegration by termites or chewed off by beavers, as shown in Figure 2-65. The breakage of the tree stem generally occurs when the window size is about 2/3 diameter of the stem, as shown in Figure 2-66, and no breakage was found when the window size is 1/3 diameter of the stem. Wood is an orthotropic material, but the safety factor of a tree is

based on the assumption that wood is an isotropic material. This is because different trees or plants experience different stress magnification due to their material composition. If the wood is calculated based on orthotropic material, a tree's safety factor can reach above 5.4 (Mattheck, Bethge and Schäfer, 1993). Generally, one would favour the safety factor with a lower limit for a reasonable assumption. Therefore, in general, trees have a safety factor of more than 4.5 (Graham, 2007). The evolution success of trees allows them to survive even in the harshest environment.

2.7.3 Resolving Stress Singularities in Dissimilar Material Joints with A Biologically Inspired Design

There have been many studies conducted on the interfaces or joints of dissimilar material, and it is found that failure often occurs at its interface or joint in between the two material types, especially with high property mismatch (Hutchinson and Suo, 1992; Needleman and Rosakis, 1999; Xu, Huang and Rosakis, 2003). As shown in Figure 2-67, the interface strength between two similar materials has a uniform stress distribution. This is, however, not true for dissimilar material joints, leading to stress singularities at the corner of its joints. Therefore, a new specimen design is needed to remove stress singularities to provide a reasonable interfacial strength and suppress edge debonding on the joints of dissimilar material (Xu and Sengupta, 2004).

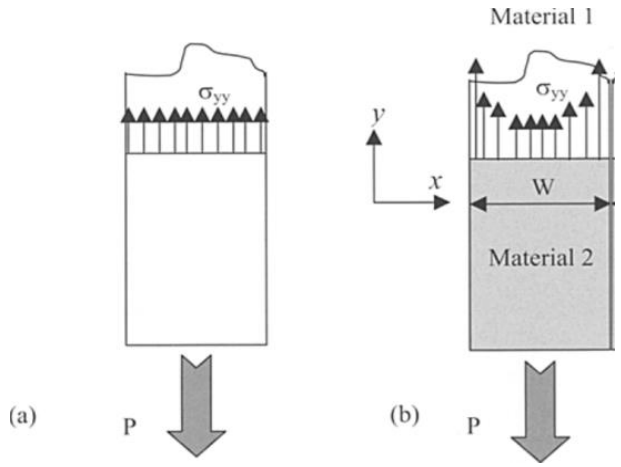


Figure 2-67: Normal stress distribution of a typical tensile specimen (a) same material (b) dissimilar material(Xu and Sengupta, 2004)

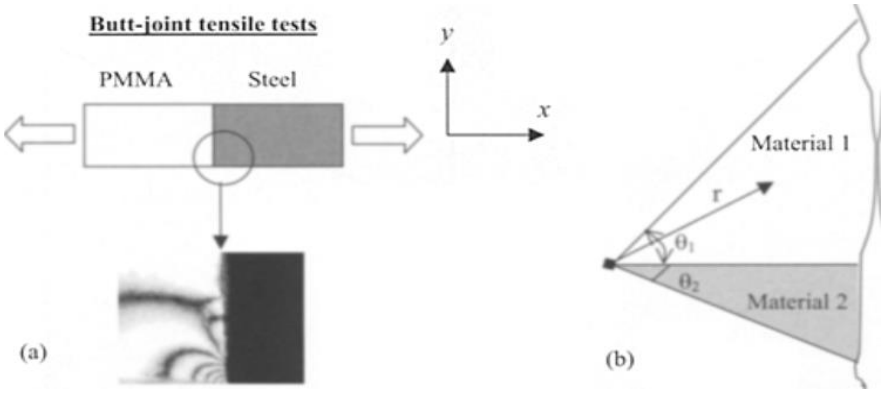


Figure 2-68: (a) Fringe pattern from a CGS photograph showing the stress concentration at the free edges between the two materials under tensile load. (b) An illustration of a joint angle between material 1 and 2. (Xu and Sengupta, 2004)

A nature-inspired design using the shape and mechanics of a tree may be a feasible solution to the problem of dissimilar material joints. Thus, experimental and numerical research was conducted to understand the behaviour on the joints of dissimilar material and validate its suitability to resolve the free-edge stress singularities problem. The creation of a uniform interfacial stress state in joints eliminates stress singularities that are very important for joints subjected to fatigue and dynamic loading (Xu, 2004; Xu and Sengupta, 2004).

Stress singularities often occur due to boundary conditions (e.g. geometric parameters, material interaction). Coherent gradient sensing (CGS) was used to view the fringe patterns in the specimen to identify the location of stress concentrations. Figure 2-68 shows the accumulation of localised stresses at the corners of the bi-material specimen. The fringe patterns obtained from CGS resemble the gradients in $\sigma_{xx} + \sigma_{yy}$ (Xu and Sengupta, 2004).

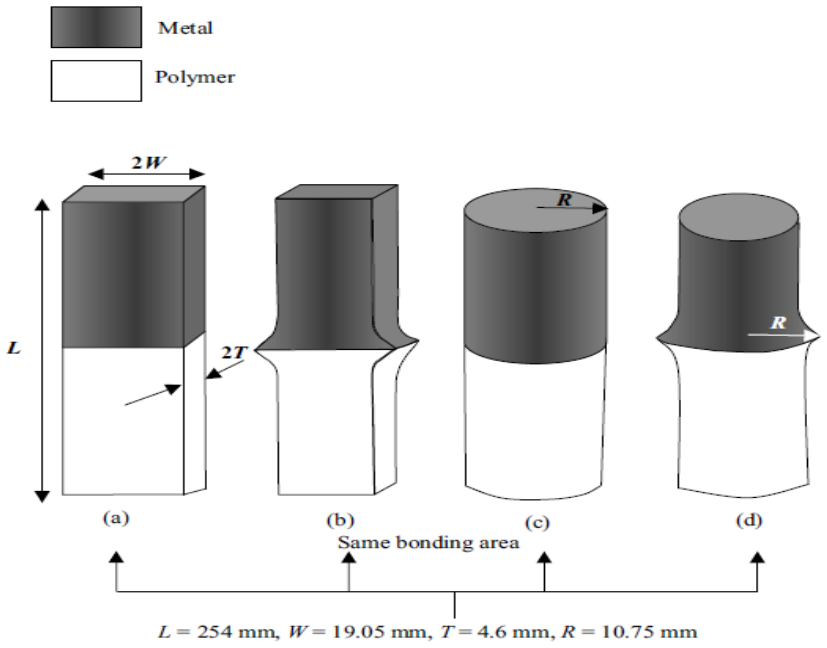


Figure 2-69: A graphical illustration of the various aluminium–polycarbonate joint specimens (a) straight edge (baseline), (b) shaped edge with least stress singularities, (c) axisymmetric straight-edge specimen, and (d) axisymmetric shaped edge specimen (Xu, 2004)

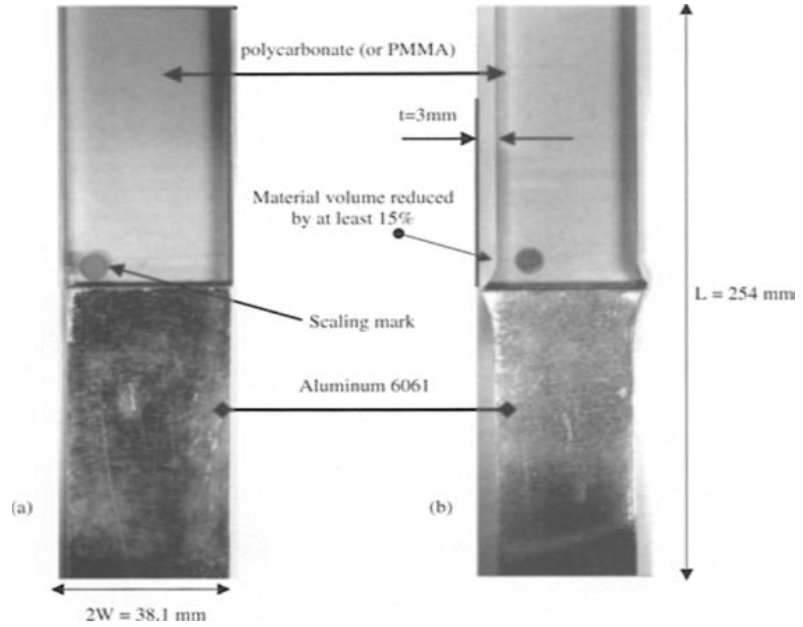


Figure 2-70: A set of two different types of joint angles in the aluminium- polycarbonate joint specimen. (a) Straight edge (90°-90°) (b) convex-shaped (45°- 65°)(Xu and Sengupta, 2004)

Four specimen designs were analysed using ANSYS, as shown in Figure 2-69. In addition, laboratory testing was conducted on two types of specimens that were designed and prepared for validation purposes, as shown in Figure 2-70. Joining angles and other parameters of the convex specimens were varied in the simulation (e.g. convex extension distance, joint angles). The tested materials were Polymethylmethacrylate (PMMA), polycarbonate and aluminium and they are grouped into groups: (a) PMMA and aluminium (laboratory test only) ;(b) polycarbonate and aluminium. The nominal thickness of the specimen was 6.35mm, and thicker specimens (9.35mm) of the polycarbonate and aluminium were used to obtain more fringes in the photoelasticity experiment. To prevent third material involvement in a bi-material experiment, the commercial epoxy chosen as the bonding agent has similar properties as those in PMMA or polycarbonate. Sandblasting and

acetone were used to clean the surface before applying the adhesive to the bonding areas (Xu, 2004; Xu and Sengupta, 2004).

For the finite analysis model, as illustrated in Figure 2-71, the straight edge specimens were L = 254mm; half-width W = 19.05mm; thickness 2T = 6.35mm for thin specimens and 9.2mm for thick specimens. For the shaped specimens, the transitional curve between its straight edge to its curved edge of the interface corner is defined by a circular arc radius of $= \left\{\frac{t}{[1-sin(\theta)]}\right\}$, where θ is the joining angle and t is the convex extension distance. Roller boundary conditions were used along the midplane section of the specimen (e.g. x=W). The finite element mesh type applied is PLANE 42 elements for 2D models and iso-parametric quadrilateral 20 node SOLID95 elements for 3D models. The stiffness properties for aluminium chosen were $E = 71GPa, \nu = 0.33$ and for polycarbonate $E = 2.4GPa, \nu = 0.34$ (Xu, 2004). The singularity order is λ instead of the other form λ-1 for the ease of the readers, and its value may be real or complex. This Equation (2-4) can define the asymptotic stress field of a bi-material corner

$$\sigma_{ij}(r,\theta) = \sum_{k=0}^{N} r^{-\lambda_k} K_k f_{ijk}(\theta); \quad (i,j = 1,2,3) \tag{2-4}$$

$$f_{ijk}(\theta) = angular\ function$$
$$K_k = stress\ intensity\ factor$$
$$\lambda = stress\ singularity\ order$$

The material property mismatch can be defined in terms of Dundurs' parameter $\alpha\ and\ \beta$ that are two non-dimensional parameters calculated from the two-bonded material's elastic constants

$$\alpha = \frac{\mu_1 m_2 - \mu_2 m_1}{\mu_1 m_2 + \mu_2 m_1} \tag{2-5}$$

$$\beta = \frac{\mu_1 (m_2 - 2) - \mu_2 (m_1 - 2)}{\mu_1 m_2 + \mu_2 m_1}$$

where

$\mu_1 = shear\ modulus\ of\ material\ 1$

$\mu_2 = shear\ modulus\ of\ material\ 2$

$m = 4(1 - \upsilon)\ for\ plane\ strain$

$m = \frac{4}{(1 + \upsilon)}\ for\ generalised\ plane\ stress$

$\upsilon = Poisson\ ratio$

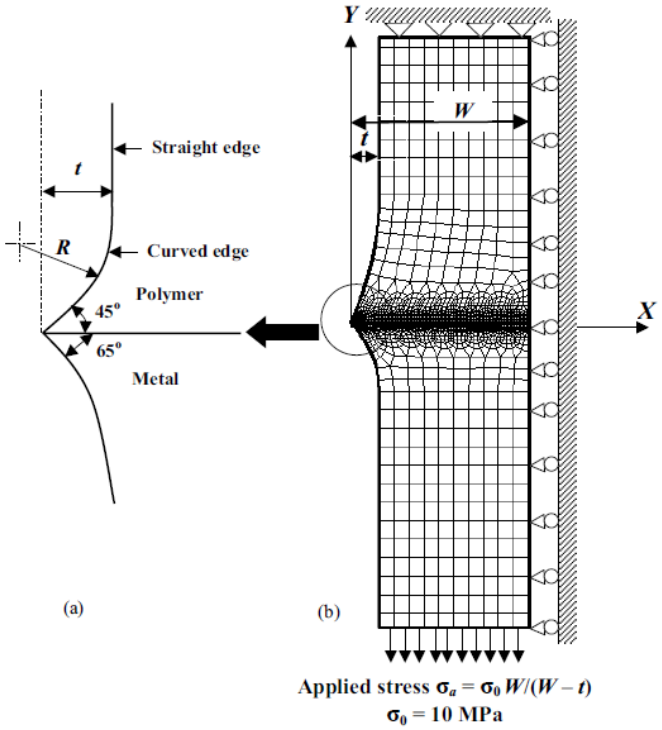


Figure 2-71: (a) A proposed convex joint of metal and polymer interface. (b) Finite-element mesh and boundary conditions of joint subjected to in-plane tensile load. (Xu, 2004)

Mattheck (1998) demonstrates an interesting problem between the tree and steel railing interface as shown in Figure 2-72; the tree grows around the steel railing in a convex

manner to reduce the intrusion by the railing that gives rise to higher stresses in the tree trunk. Mattheck showed that if the total joining angle $\theta_1 + \theta_2 = 270^{\circ}$ as illustrated in Figure 2-68, the Mises stress experienced higher stress concentration at its joint corner. It was proposed that choosing the appropriate angular combination accordingly to the different material combinations will result in a lower degree of stress singularity and to obtain a negative/non-positive or zero $Re[\lambda]$ (Xu and Sengupta, 2004).

An appropriate joining angle is required at the edge of the bi-material to reduce its stress singularities, and from numerous mathematical case studies, the two-joining angle at its interface appropriate for this experiment is narrowed down to $\theta_1 = 65°$ for hard material and $\theta_2 = 45°$ for soft material. The stress singularity order is related to its material and geometric parameters and is determined by a set of coefficient A (θ_1, θ_2, p) to F (θ_1, θ_2, p) and can be expressed by

$$f(\theta_1, \theta_2, \alpha, \beta, p) = A\beta^2 + 2B\alpha\beta + C\alpha^2 + 2D\beta + 2E\alpha + F = 0 \quad (2\text{-}6)$$

where

$p = 1 - \lambda$

$A, B, C, D, E \text{ and } F \text{ are constants defined by Bogy}$

$(\theta_1, \theta_2, \alpha, \beta) \text{ are independent parameters}$

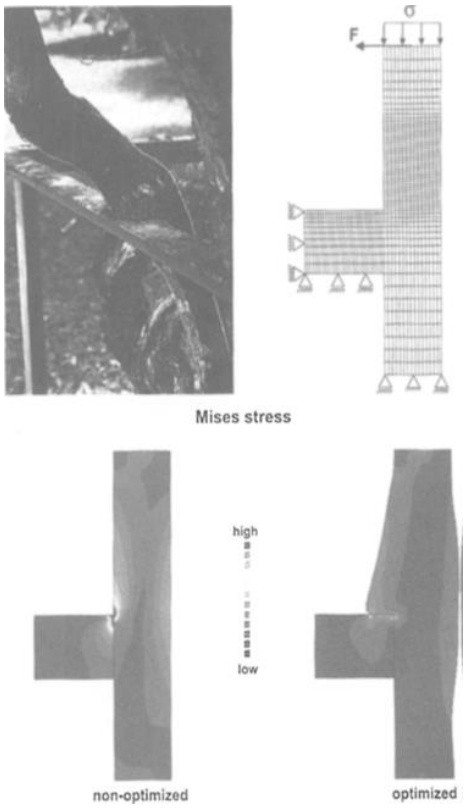


Figure 2-72: A finite element analysis of a tree to a steel railing interface.

From the finite element analysis, the stress singularity order λ ranges from 0.216 - 0.223, and the obtained value, as shown in Figure 2-73, is similar to the λ value obtained (0.225) through Equation (2-6). The fringe order N was computed at every node and plotted as shown in Figure 2-74. Clear fringe concentrations are seen originating at its interface corner of the straight edge specimen, and the bi-material interfacial cracks cause these. The stress singularity order λ for Aluminium/polycarbonate joints is about -0.2, which can be removed, and the interfacial cracks $(-0.5 + i\varepsilon)$ is intrinsic (Xu, 2004; Xu and Sengupta, 2004). The isochromatic fringes observed are contours of the maximum in-plane shear stress, and this can be expressed as

$$\tau_{max} = \frac{(\sigma_1 - \sigma_2)}{2} = \frac{N f_\sigma}{2} \tag{2-7}$$

where

σ_1 *and* σ_2 *are in* $-$ *plane priciple stresses*

$N = fringe\ order$

$f_\sigma = stress\ fringe\ constant$ (e.g. 7kN/m for polycarbonate)

$h = specimen\ thickness$

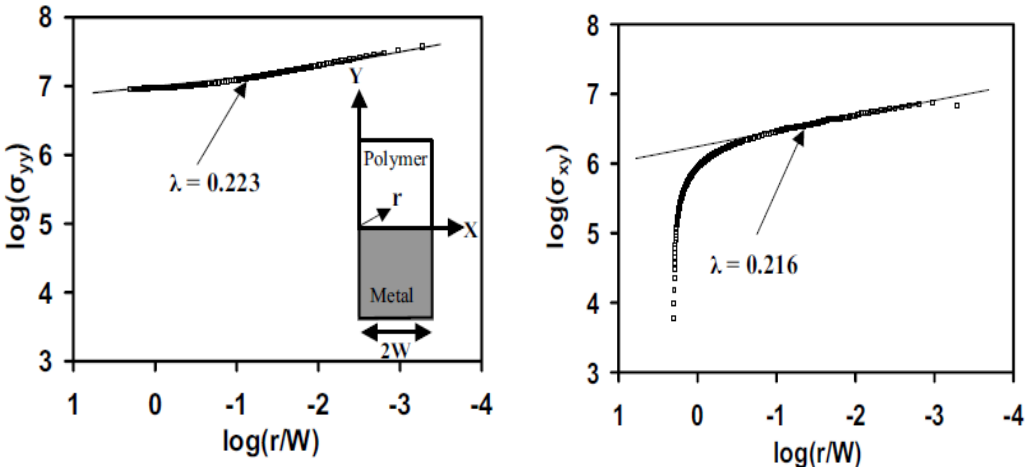


Figure 2-73: Stress singularity order λ obtained from finite-element analysis (showing its distribution close to the free edge and its fitted λ value). (a) Interfacial normal stress (b) Interfacial shear stress (Xu, 2004)

The accumulation of fringes in the straight specimen shown in Figure 2-74 at the bi-material interfacial corner has completely disappeared for the convex specimen as shown in Figure 2-75 because of the smoother stress distribution (due to redistribution stresses). For the same applied load of 500N, the highest fringe order in the shaped specimen was 6.5, whereas the straight edge specimen was 23.5. The number of fringes shown in Figure 2-74 and Figure 2-75 in (d) and (f) do not match precisely to each other as the finite element model assumes ideal conditions, whereas in actual experimental does not, although the general stress pattern may be similar (Xu, 2004; Xu and Sengupta, 2004).

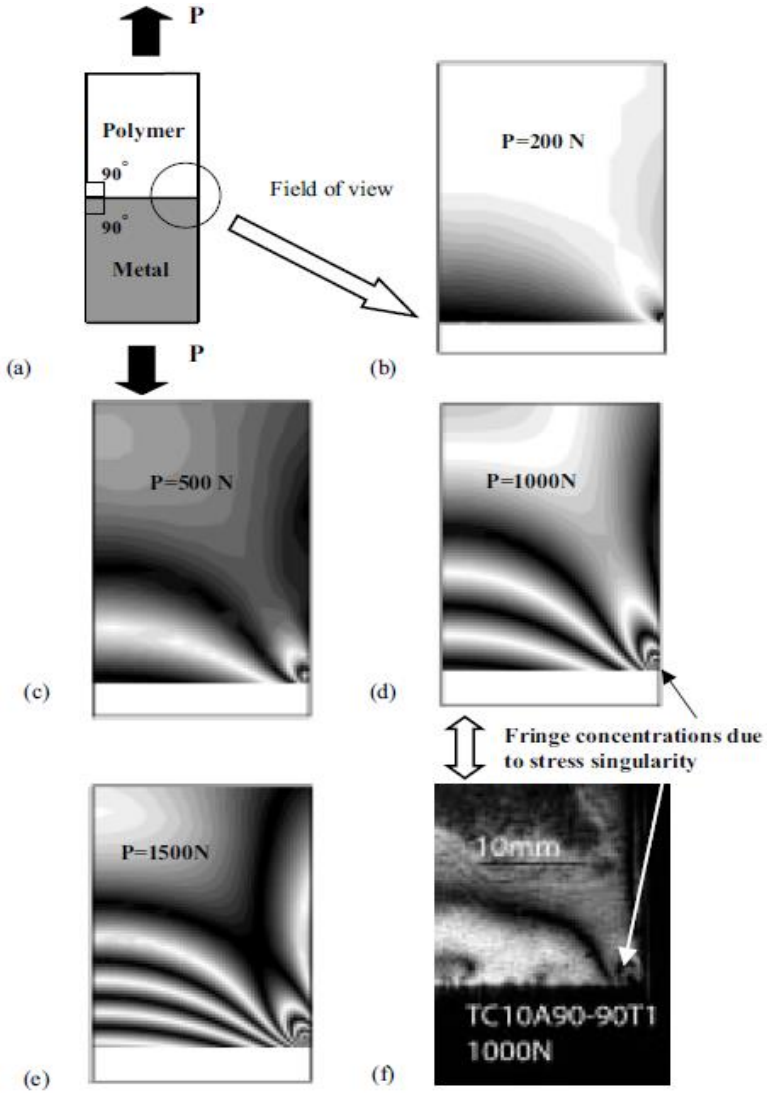


Figure 2-74: A comparison between the numerical and the experimental fringe pattern (d) and (f) in aluminium-polycarbonate joints with a straight edge joint. (Xu, 2004)

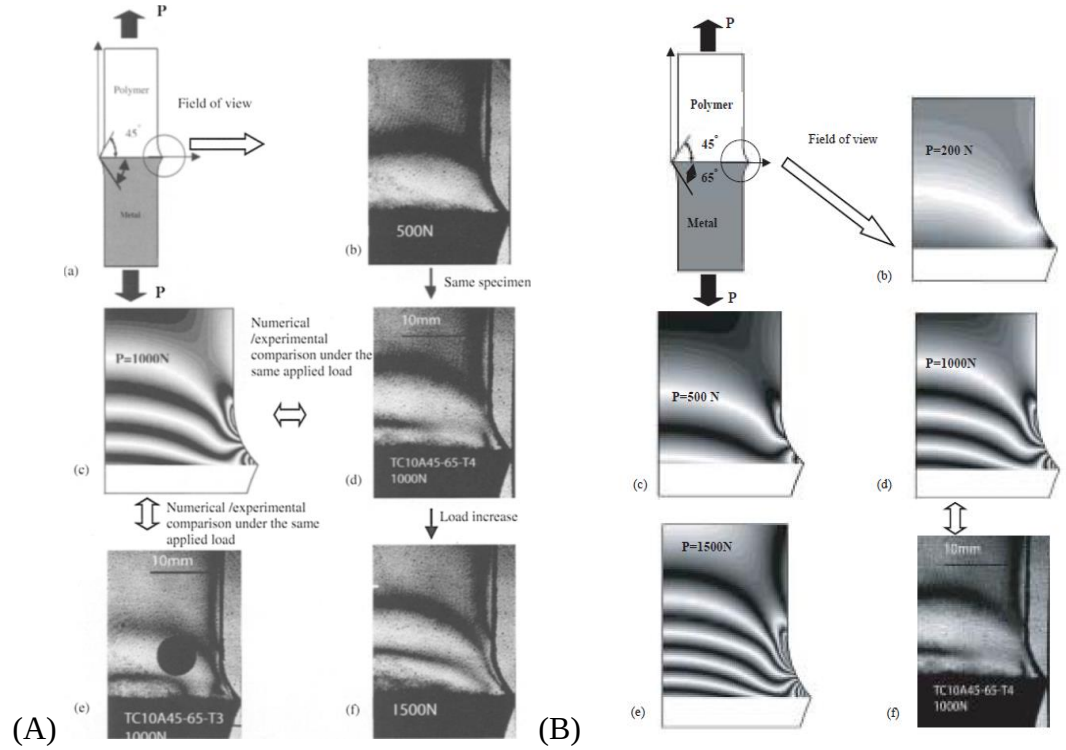


Figure 2-75: (A) and (B) are a comparison between the numerical and the experimental fringe pattern in aluminium-polycarbonate joints with the shape edged joint. (Xu, 2004; Xu and Sengupta, 2004)

The parameter of the convex extension distance t, as shown in Figure 2-76, was evaluated and varied with four different distance t, t = 0 (for straight-edged specimens); t = 0.5; 1.0 and 3.0 (for shaped specimens). The increment of distance t provides a more uniform stress distribution at its interface. Different thickness of specimens was also tested and found that the thicker specimens (9mm for FEM; 9.35mm for experimental) show lesser tensile strength increment than the thinner specimens (6mm for FEM; 6.35mm for experimental). Convex interface design does not show significant improvement in performance due to the size effect. The other reason was the existence of free-edge stress singularity in the thickness direction of the convex plane joint (Convex interface design), and this can be resolved with an axisymmetric design (Xu, 2004; Xu and Sengupta, 2004).

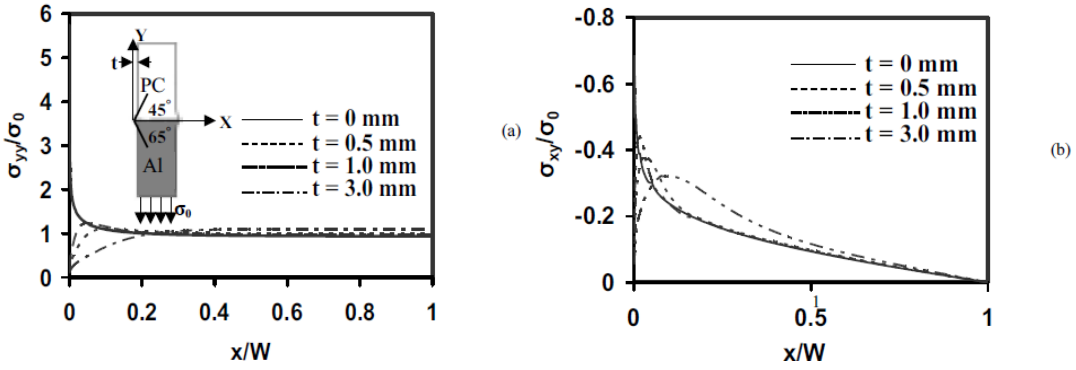


Figure 2-76: (a) Interfacial normal stress and (b) Interfacial shear stress, with different extension distances (joint angles polycarbonate $\theta_1 = 45°$; aluminium $\theta_2 = 65°$ and it is a straight edge specimen when t = 0)(Xu, 2004)

Figure 2-77 shows the results of retaining the joint angle of polycarbonate (45°)while varying the joint angle of aluminium between $45° - 90°$. Between the varied joint angles $(45° - 90°)$, the stress singularities were still successfully removed. It shows that if the total joint angle is less than 180°, and each joint angle is less than 90°, it can reduce stress singularities (Xu, 2004).

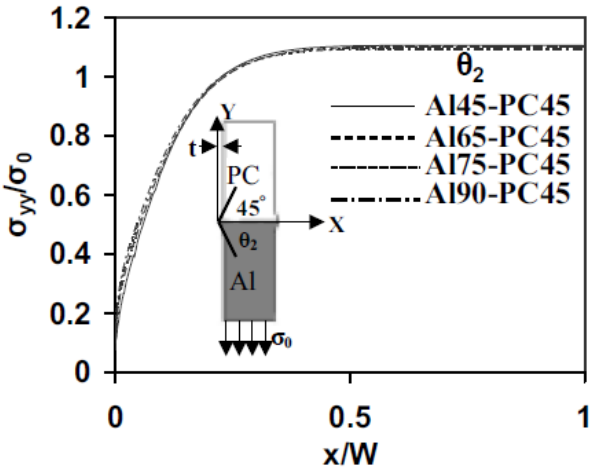


Figure 2-77: Normalized interfacial normal stress with various aluminium joint angle θ_2 while fixing the polycarbonate joint angle at $\theta_1 = 45°$ and t = 3 mm (Xu, 2004)

The final failure of manufactured components is often limited to its initial defect presence. Thus, specimens with different sizes will yield different strength. This is also known as the “size effect”. Therefore, a perfect uniform stress state at its interface is not achievable. Hence, the experiment is directed at resolving free edge stress concentration as they are the leading cause of initial failure. The analysis conducted assumes a perfect bonded interface, but the laboratory experiment conducted, as shown in Figure 2-78, shows the macroscale interfacial cracks from the effects of initial defects before final failure in both straight edge and shaped specimens. Therefore, the assumptions of perfect/ideal conditions in finite element analysis do not reflect actual practice (Xu and Sengupta, 2004).

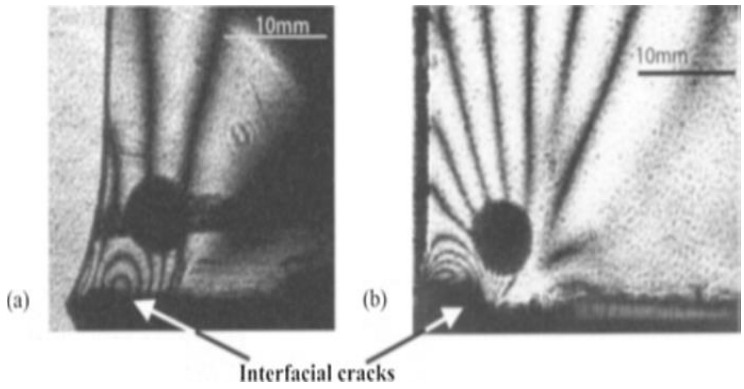


Figure 2-78: Interfacial cracks originated from initial defects before the final tensile failure in (a) shaped edge specimen (b) straight edge specimen(Xu and Sengupta, 2004)

The experiment shows that the failure load values with the same interface of different edge shape were different, as shown in Figure 2-74 and Figure 2-75. The 3D finite element analysis shows the existence of stress singularities along the thickness direction, as illustrated in Figure 2-79; thus, a convex axisymmetric joint was proposed to provide better interfacial strength. An axisymmetric design eliminates the existence of stress singularity in the thickness direction (Y-Z plane) due to the existence of straight edges. The results are shown in Figure 2-80 (Xu, 2004).

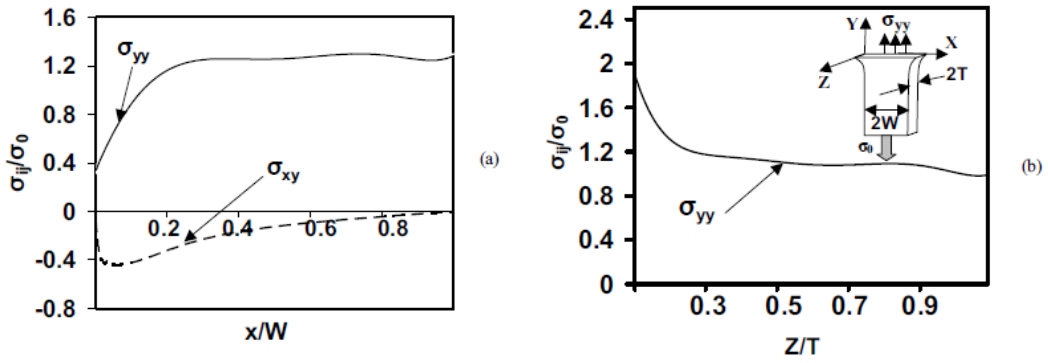


Figure 2-79: 3D finite element model (a) Interfacial normal stress and shear stress along its width. (b) Interfacial normal stress along with its thickness (t = 3 mm)(Xu, 2004)

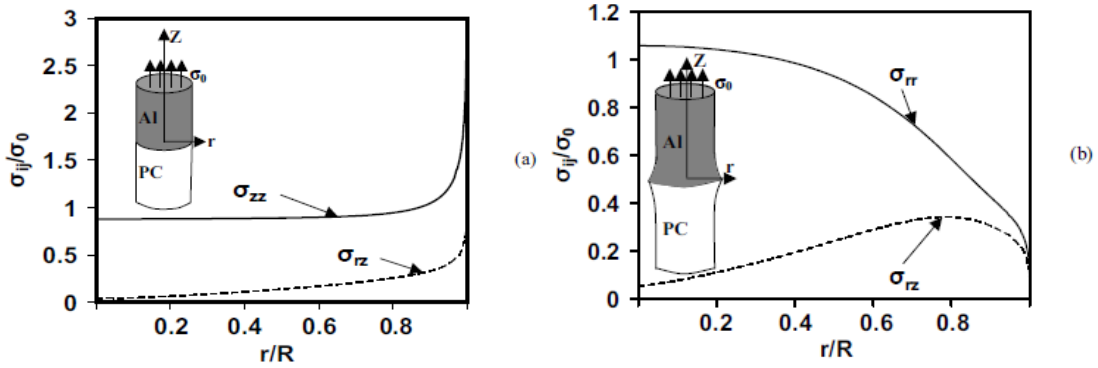


Figure 2-80: Interfacial normal stress and shear stress of the finite element model (a) unshaped axisymmetric (b) shaped axisymmetric (t = 3 mm)(Xu, 2004)

The new convex joints managed to reduce/remove free edge stress singularities effectively in different material and structure. It can improve the tensile load capacity of hybrid joints. The convex joint has better tensile load capacity and increased material volume reduction than the traditional butt joint for all specimens. The convex interface design has reduced the material volume by 15% while increasing the ultimate tensile load capacity by 81% compared to traditional butt joints (Xu, 2004; Xu and Sengupta, 2004). A higher total material volume reduction may be achievable if the area away from the interface is considered. Therefore, nature can provide an efficient

and effective solution to current technological difficulties. The laboratory results are summarised in Figure 2-81, Table 2-5 and Table 2-6.

Table 2-5: PMMA–Aluminium Joints tensile test (laboratory results) (Xu and Sengupta, 2004)

Specimen	Joint Angles (Material 1 - Material 2)	Tensile Strength (MPa)	Change of Strength	Standard Deviation (MPa)	Specimen Thickness (mm)
TP10A90-90	90° - 90°	5.9	0%	1.2	6
TP10A45-65	45° - 65°	10.1	71%	1.4	6

Table 2-6 Polycarbonate–aluminium joint tensile test (laboratory results) (Xu and Sengupta, 2004)

Specimen	Joint Angles	Tensile Strength (MPa)	Change of Strength	Standard Deviation (MPa)	Specimen Thickness (mm)
TC10A90-90	90° - 90°	2.6	0	0.7	6
TC10A45-65	45° - 65°	4.7	81%	2.0	6
TC10A90-90T	90° - 90°	5.3	0	1.4	9
TC10A45-65T	45° - 65°	5.6	6%	1.5	9

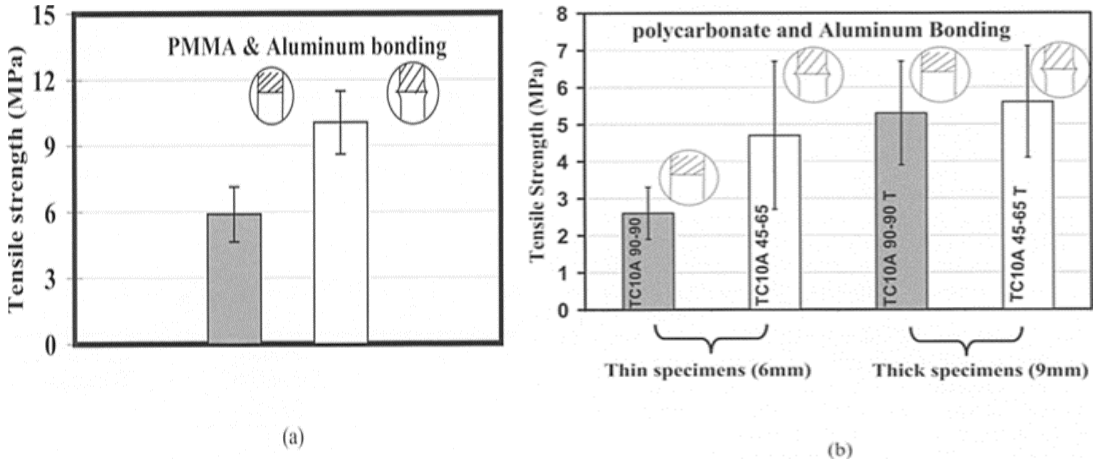


Figure 2-81: The laboratory results of specimens are summarized as a bar chart (a) PMMA & Aluminium (b) Polycarbonate and Aluminium (Xu and Sengupta, 2004)

2.8 Loading Patterns of Structural Members

Besides the benefits of trees as a research interest for civil engineers, understanding how forces are distributed in a structure is just as important as merely replicating nature itself. Topology in any structural member is affected by the applied shearing force, bending moment and torque. Different load conditions will produce a different diagram of shear, bending moment and torque. Any equal or similar load case with a different load magnitude will produce the same diagram for bending moment, shear and torque but with a different amplitude. With the basic understanding of nature's method of stress distribution, as discussed earlier, the same can be said for isolated civil engineering structural components. The study of topology shows similar triangular force flow and concentration as experienced in plants and animals. The path to least resistance and efficient load transfer follows the shape profile found in nature. Capitalising the topography and using these results may reveal new ways of designing and constructing engineering structural components or buildings that may yield higher safety factor with dynamic load resistance capabilities.

2.8.1 Strut and Tie Models (STM)

Strut and tie models are often used to idealise the load transfer mechanism in structural concrete for a safer/better transfer of the applied load to its supports. It was initially developed by Ritter (1899), and its methods were later furthered by Schlaich, Schafer and Jennewein (1987a). Schlaich, Schafer and Jennewein (1987a) proposed an STM evaluation criterion that the least and shortest ties are the best designs (Schlaich, Schafer and Jennewein, 1987a; Zhong *et al.*, 2017). Topology optimisation is an approach to determine an optimum material distribution while maximizing structural performance under a given set of constraints. There are two methodologies in the topology analysis, the macro and the micro approach. Readers are referred to Bendsøe and Sigmund (2004) on the theory, method and applications of topology optimisation, Tsavdaridis, Kingman and Toropov (2015) for a brief history towards the progress and the development of the various topology optimisation methods and (Almeida, Simonetti and Neto, 2013; Tsavdaridis, Kingman and Toropov 2015) for a detailed explanation and comparison of the two approaches.

Structural optimisation techniques have been successfully implemented in many fields to improve its performance without increasing the total embodied energy cost through better topology and shapes (e.g. aerospace engineering (Sigmund and Bendsøe, 2004), mechanical industries and many more). They can be subdivided into 3 categories; topology, shape and size and any overlapping that consists of 2 or more categories are be deemed a 4th category (Christensen and Klarbring, 2009; Tsavdaridis, Kingman and Toropov, 2015). One of the earliest solutions to a topology optimisation problem was developed by Michell (William Prager, 1978), which provided an optimal truss-like structure. Currently, there are numerous numerical topology optimisation methods been proposed or developed to find the optimal load path (Bruggi, 2016) with an

objective to increase design robustness and reduce overall cost and time (Zhong *et al.*, 2017) (e.g. Evolutionary Structural Optimisation (ESO) (Xie and Steven, 1993), Simple Isotropic Material with Penalisation (SIMP) (Bendsøe and Sigmund, 2004), Sequential Quadratic Programming (SQP) (Rong *et al.*, 2013), Method of Moving Asymptotes (MMA) (Svanberg, 1987), Moving Iso-Surface Threshold method (MIST) (Chen, Tong and Liu, 2017), Parametric Level Set Method (PLSM) (Li *et al.*, 2018), Robust topology optimisation (RTO) (Wu *et al.*, 2016), Genetic Algorithms (GA) (Perera and Vique, 2009)). While many numerical methods are currently available, these techniques remain an academic exercise for civil engineering structures (or commercial application) due to their challenges (Tsavdaridis, Kingman and Toropov, 2015).

Nevertheless, the possible benefits of using strut and tie models (STM) and topology optimisation in the application of civil engineering structures have led to more in-depth research studies. Current studies have since been well extended into studying the effects on, shear failure (Kim, Lee and Lee, 2014; Lim and Hwang, 2016; Hanoon *et al.*, 2017; Chen, Yi and Hwang, 2018), nonlinear response (Bogomolny and Amir, 2012; Nakshatrala, Tortorelli and Nakshatrala, 2013; Nakshatrala and Tortorelli, 2016), dynamic/seismic excitation (Allahdadian, Boroomand and Barekatein, 2012; Zhang, Liu and Gao, 2015; Allahdadian and Boroomand, 2016; Yang *et al.*, 2017; Zhu *et al.*, 2017; Zhao, Yoon and Youn, 2019), fibre reinforcement/fibre reinforced polymer (Bruggi and Taliercio, 2013; Kim, Lee and Lee, 2014; Hanoon *et al.*, 2017; Moradi and Esfahani, 2017), distribution/placement of reinforcement (Amir and Sigmund, 2013) , shrinkage and strength failure (Luo *et al.*, 2015), beam to column connection (Desnerck, Lees and Morley, 2018), beams (Kim, Lee and Lee, 2014; Hardjasaputra, 2015; Tsavdaridis, Kingman and Toropov, 2015; Hanoon *et al.*, 2017;

Moradi and Esfahani, 2017; Chen, Yi and Hwang, 2018), layout/conceptual design (Stromberg *et al.*, 2011), rehabilitation (deterioration aspect) (Desnerck, Lees and Morley, 2018), fire safety (Madsen *et al.*, 2016) and 3D structures (DOMBERNOWSKY and SØNDERGAARD, 2009; Kazakis *et al.*, 2017). Aside from that, there are also studies presented that utilise both shape and topology optimisation techniques to create an optimum 3D structure (Christiansen *et al.*, 2015; Lian *et al.*, 2017).

2.8.2 Topology Optimisation Methods in Reinforced Concrete structures

Many extensive research works have been conducted on reinforced concrete structures (Amir, 2013), and efforts have been made to evaluate and enable better reinforcement design in reinforced concrete design through topology optimisation. However, the shear behaviour of the reinforced concrete member remains less understood. The load transfer mechanism through reinforced concrete members cannot be defined as a function of a single variable as it depends on its geometry, loading and support conditions. Therefore, an analogous truss model is used to idealise internal forces within a reinforced concrete member into compressive struts and tensile ties. This is to investigate the equilibrium relationship between the loads, reaction and internal forces (Liang, Xie and Steven, 2000; 2000b).

A good understanding of the failure mechanism on reinforced concrete member will assist concrete designers in designing and detailing of new concrete members. The ACI Committee 445 (1998) recommends using a truss model approach for the shear designing of concrete structures. This provides a clear understanding of concrete behaviour under multiple and combined load effects. Besides, the shrinkage effect on concrete should not be neglected as it can result in an unsafe design (Luo *et al.*, 2015). The topology optimisation method in reinforcement concrete can provide an

alternative load-carrying structure when compared to its original domain, but it should be noted that it does not assure a close relation to its original stress field. Hence, attention is required if the actual stress path of the detailed structural element is not close to the truss-like layout (Bruggi, 2009). Nevertheless, there have been studies that show a positive correlation between the strut and tie model and its failure that may provide better failure prediction (Almeida, Simonetti and Neto, 2013; Kim, Lee and Lee, 2014; Lim and Hwang, 2016; Hanoon *et al.*, 2017; Moradi and Esfahani, 2017; Chen, Yi and Hwang, 2018).

2.8.2.1 Topology Optimisation of the Various Structural Component

The following case examples from Figure 2-82 to Figure 2-88 show a typical topology plot generated using the Evolutionary Structural Optimisation (ESO) method. It demonstrates the effects of the different load pattern, aspect ratio, size and type of structure and further details on the models can be found through their corresponding papers (Liang, Xie and Steven, 2000; 2000b). The strut and tie model shows the solid line in tension and the dotted line in compression.

The strut and tie model obtained in the concrete member, as shown in Figure 2-82, are in tension except for the compressive arch. The topology shows the location where steel reinforcement can be placed along the vertical and inclined lines to transfer loads to the compression arch efficiently (Liang, Xie and Steven, 2000; 2000b). Besides, the topology also shows that the internal forces of the concrete member track the shortest load path between the loading and reaction point. The loading path was being rerouted around the opening of the concrete member (Kong and Sharp, 1977). The load path in a simply supported deep beam with a large hole, factored by a top load as shown in Figure 2-84, was also rerouted around the opening similarly as shown in Figure 2-83 regardless on the location of the opening.

The effects of the span to depth ratio of beams were also investigated through a simply supported beam loaded with a top mid-span concentrated load as shown in Figure 2-85, and the depth to span ratios tested are shown in Figure 2-86. From deep to slender beams, the optimal topology obtained move towards a continuum structure where tie and strut models become more complex (Liang, Xie and Steven, 2000b). The angles indicated in the optimal tie and strut model shows angles between the compression struts and the longitudinal ties to be equal or larger than 45 degrees. Bottom bars may be required to be bent upwards to resist tensile or shear stresses in the span.

Figure 2-88 shows the iteration process of the topology optimisation conducted on a corbel and column. The corbel and column analysed by Schlaich, Schafer and Jennewein (1987b) have the column fixed on both ends and assumed as a whole structure designed to support a concentrated load at the corbel, as shown in Figure 2-87. The obtained topology provides insight into the strategic placement of steel reinforcement to transfer loads and distribute in the beam efficiently (Liang, Xie and Steven, 2000b). Hence, it can control crack propagation to maintain the ultimate load capacity.

Case 1: Deep simply supported beam with two concentrated loads

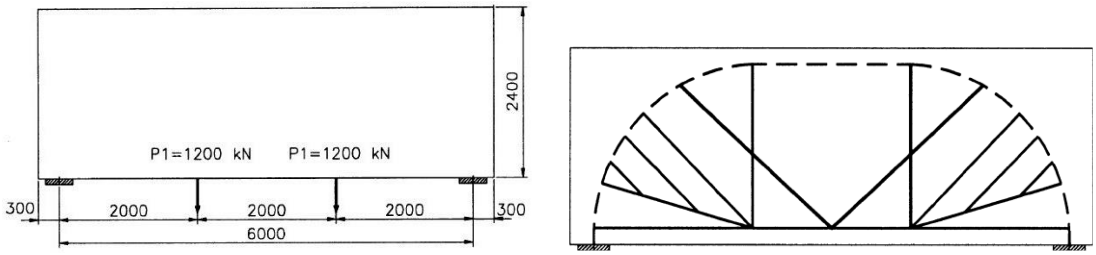


Figure 2-82: A deep simply supported beam with two concentrated loads (Liang, Xie and Steven, 2000; 2000b)

Case 2: Deep simply supported beam with two openings

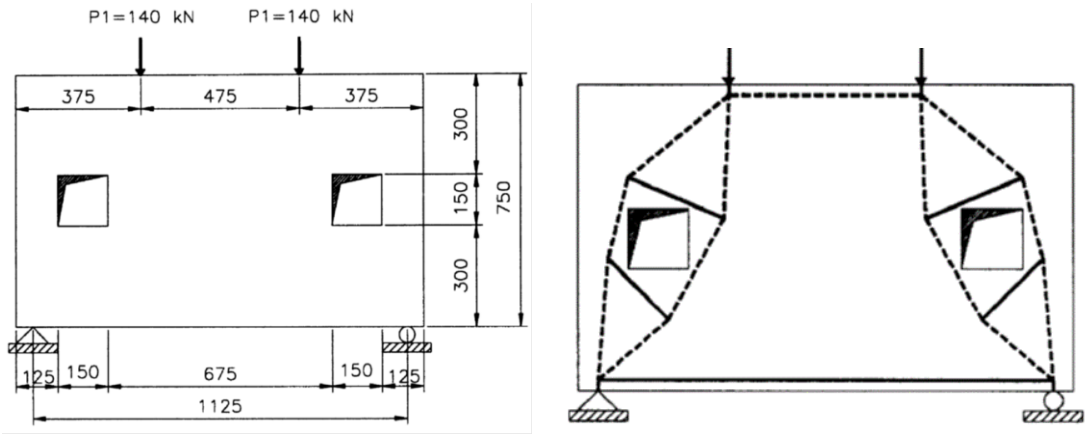


Figure 2-83: A deep simply supported beam with 2 openings is loaded by 2 concentrated loads. (Kong and Sharp, 1977)

Case 3: Simply supported deep beam with a large hole

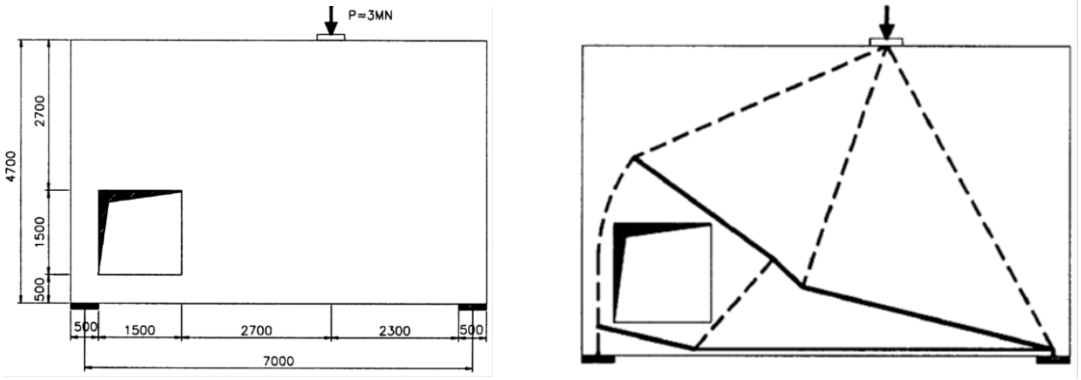


Figure 2-84: A deep beam simply supported with a large hole and factored by a top-loading (Schlaich, Schafer and Jennewein, 1987b).

Case 4: A study on the effects of the span to depth ratio in simply supported beams

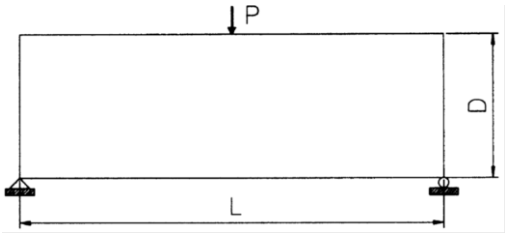


Figure 2-85: A simply supported beam loaded with a top mid-span concentrated load (Liang, Xie and Steven, 2000; 2000b)

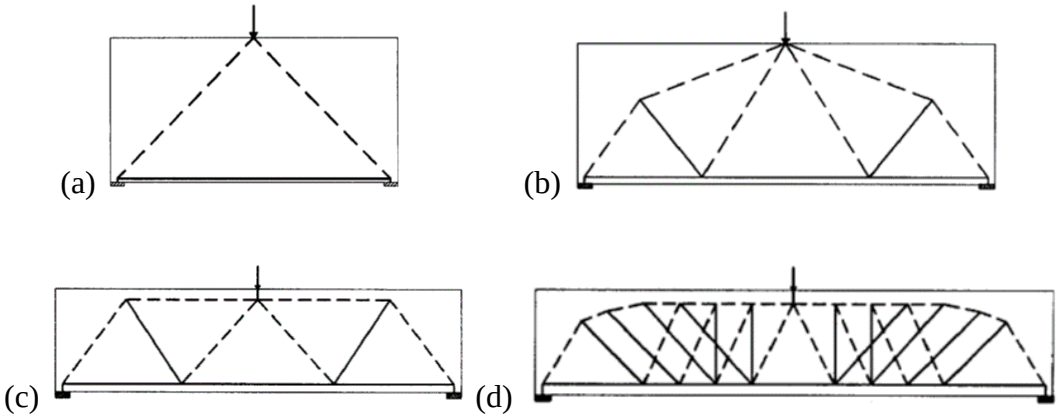


Figure 2-86: iteration process of an optimum topology for a simply supported beam loaded with a top mid-span concentrated load (Liang, Xie and Steven, 2000; 2000b)

Case 5: Corbel and column

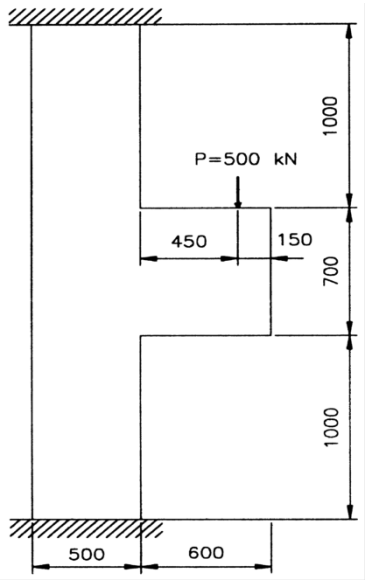


Figure 2-87: A corbel and column connection loaded by a concentrated load (Schlaich, Schafer and Jennewein, 1987b)

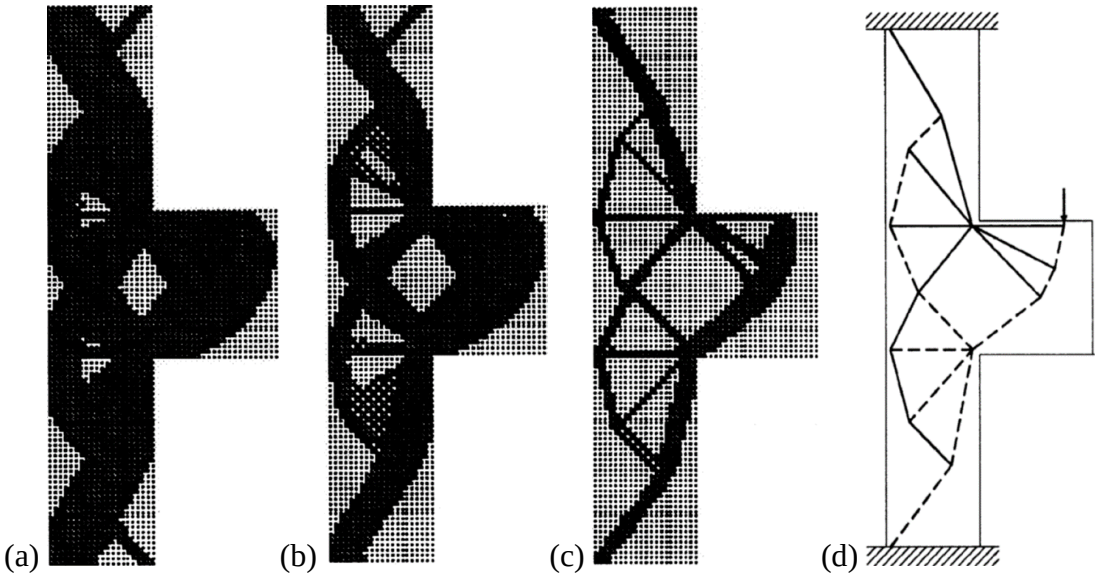


Figure 2-88: iteration process of an optimum topology for a corbel and column connection loaded by a concentrated load (Liang, Xie and Steven, 2000; 2000b)

The load transfer mechanism in reinforced concrete members relies on its geometry, loading type and support conditions. The defined tie and strut model is explicitly designed for that specific concrete member and cannot be replicated in other different members. The strut and tie model is effective in determining its optimal topology in non-flexural concrete members and slender beams with an L/D ratio bigger or equal to 5. Continuum structures like slender beams are hard to be identified using strut and tie models as their topology becomes complicated. The steel reinforcement layout should follow closely to the obtained topology of the strut and tie models for a given loading application (Liang, Xie and Steven, 2000a; 2000b). Different numerical optimisation method applied may lead to very different and complex strut and tie model. However, in terms of structural fire safety, it was found that simple and few thick bars are the ideal strut and tie model for fire safety of a specified time period (Madsen *et al.*, 2016). Nevertheless, the optimised topology obtained for fire resistance is not suitable for the designs against accidental actions (e.g. explosions.) as these are dynamic and often concentrated at a particular section. Redundancy designs are often required to ensure structural stability. Further studies on the subject are required to consider the effects on material property degradation and other possible unintentional loading conditions for a safer structure (Madsen *et al.*, 2016).

2.8.3 Optimisation of a Cantilever Beam

A study conducted by Chu *et al.* (1996) (cited in Liang, Xie and Steven, 1999; 2000), and Suzuki and Kikuchi (1991) demonstrates the similarities in the topology of a cantilever beam with a point load of 3kN loaded at the centre of the free end as illustrated in Figure 2-89 in various loading condition using different optimisation methods. The assumptions are as follows E=200GPa, ν=0.3, t=1mm, Element Removal Ratio (ERR) =2%. Although the generated result as shown in Figure 2-90

proposed by (Liang, Xie and Steven, 1999; 2000) and Chu *et al.* (1996) using the ESO method are somewhat similar to (Suzuki and Kikuchi, 1991) homogenisation method, the Performance Index (PI) value obtained suggest Liang et al. [59,60] have a better and more efficient topology with a PI of 1.20. This is followed by Chu *et al.* (1996) at PI = 1.11 and finally Suzuki and Kikuchi (1991) at PI = 1.04. The topologies produced have a similar design to a Prager truss (Prager, 1977; 1978a; 1978b; Mazurek, Baker and Tort, 2011).

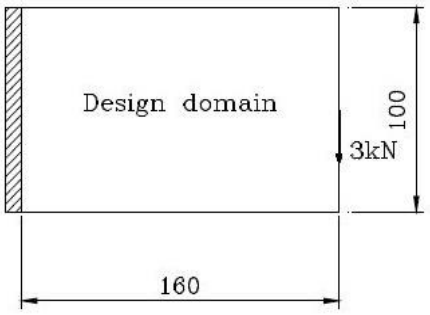


Figure 2-89: A cantilever beam with a point load at the centre of the free end (Liang, Xie and Steven, 1999).

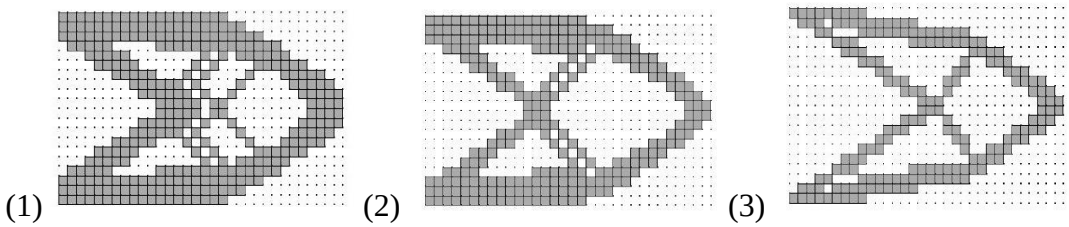


Figure 2-90: Topology result by (1) (Liang, Xie and Steven, 1999). (2) (Chu *et al.*, 1996) (3) (Suzuki and Kikuchi, 1991)

Similarly, Mattheck, Kappel and Sauer (2007) demonstrated a load path of a similar single concentrated load at the bottom end of a cantilever beam, as shown in Figure 2-91, that is similar to the previous work conducted by other researchers as shown in Figure 2-90. The square root shape of a bending bar is defined in many mechanical

textbooks, but this method is less optimised. The graphical method proposed has better or well control of the stress concentration along the beam when compared to the square root method. For a uniform distribution of bending stresses, one can obtain an analytical formula of the height function of a bar length to be $h(x) = k \times \sqrt{x/l}$. (Mattheck, Kappel and Sauer, 2007)

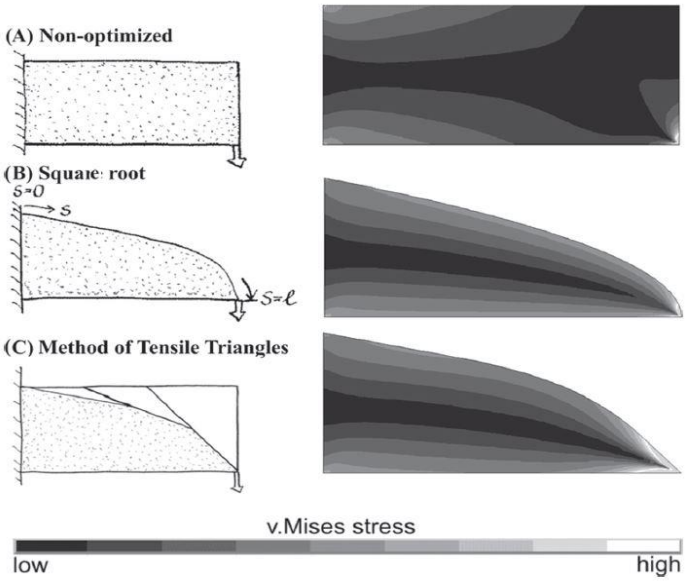


Figure 2-91: Stress concentration for a cantilever beam with a point load at the bottom end (Mattheck, Kappel and Sauer, 2007).

2.8.4 Optimisation of a Bracing System for Multistorey Steel Building Framework

Buildings of different shape and sizes require a different way of supporting/resisting lateral load. Topology optimisation is often utilised to create an ideal lateral supporting system, but optimal topology design can result in several possible arrangements of bracing members. Optimisation of a structure needs to meet the stress and displacements constraints while maintaining minimum weight and satisfying the drift limit. The sizing method is often used to minimise weight design in lateral loading

system, but it is only suitable for horizontal load resisting system with a fixed topology. The motivation to find a better optimisation method has led to developing the continuum topology optimisation method, and it has since gained popularity (Liang, 2007). There are many optimisation methods (e.g. SKO, ESO), but in this sub-chapter, the Performance-based Optimisation (PBO) technique was used to identify the optimal bracing systems in the continuum structure for the multistorey steel building.

2.8.4.1 Resolving Optimisation Problems

A continuum design domain analysed under plane stress condition was used to stiffen the multistorey steel building framework that was initially sized with standard steel sections under-strength restrictions. The optimisation process treats the framework as a non-design domain where beam elements are not eliminated during the process. The result is to determine an optimal topology for the bracing system. In addition, a uniform sizing thickness of the design domain was used to ease the optimisation process (Liang, 2007). The design optimisation problem can be expressed by Equation (2-8):

$$W = \sum_{e=1}^{N} w_e(t) \tag{2-8}$$

$$C_p \leq C^* \ (p = 1,2, \dots, NL)$$

$$t^L \leq t \leq t^U$$

where

$W = total\ weight$

$W_e = weight\ of\ e^{th}\ element$

$t^L = lower\ bound\ element\ thickness$

$t^U = upper\ bound\ element\ thickness$

$N = Total\ number\ of\ elements$

$C_p = absolute\ mean\ compliance\ under\ load\ p$

$C^* = prescribed\ limit of\ C_p$

$NL = total\ number\ of\ load\ cases$

2.8.4.2 Element Elimination Criteria

The element elimination criteria seek to achieve minimum weight and maximum lateral support. An element's contribution to the system performance can be measured through strain energy density. The equation for the element strain energy density is shown in Equation (2-9):

$$\gamma_e = \frac{\frac{1}{2}\{u_e\}^T(k_e)\{u_e\}}{w_e} \tag{2-9}$$

where

$\gamma_e = Strain\ energy\ density$

$u_e = displacement\ vector\ (eth\ element)$

$k_e = Stiffness\ matrix\ (eth\ element)$

Elements of the lowest strain energy densities are removed systematically to obtain an optimal bracing system. Each iteration has an element removal ratio (R), as shown in (2-10):

$$R = \frac{Number\ of\ removed\ elements}{Total\ number\ of\ elements} \tag{2-10}$$

2.8.4.3 Performance-Based Optimality Criteria (PBOC)

Low strained elements are gradually removed during the optimisation process from the braced steel building framework. Performance indices are used to evaluate the performance of the bracing system (Liang, 2007). Performance-based optimality criteria (PBOC) maximise the performance index, as shown in (2-11). Using strain

energy at critical loads, one can calculate the performance index of a structure subjected to multiple load cases. An optimal bracing system is obtained when the strain energy and material usage is minimum.

$$PI = \frac{C_0 W_0}{C_i W_i} \tag{2-11}$$

where

$C_0 = initial\ absolute\ strain\ energy\ under\ loads$

$C_i = current\ absolute\ strain\ energy\ under\ loads\ at\ i^{th}\ iteration$

$W_0 = initial\ weight$

$W_i = current\ weight\ at\ i^{th}\ iteration$

The rigid multistorey steel building analysed was a 4 bay and 12 stories building, as shown in Figure 2-93. It was subjected to two wind load cases, left and right, as shown in Figure 2-93. The structure was optimised with an element removal ratio of 2% (Liang, 2007). Two different methods of bracing are analysed to determine its optimal layout and performance for a tall steel building:

1) Full width
    a. Bracing across the width of the frame structure (Figure 2-93)
2) Centred two bays
    a. Bracing only at the centre with a width of two bays (Figure 2-95)

2.8.4.3.1 Full-width Braced Framework (4 bays)

Full width braced framework structures are the most effective lateral load resisting system as the bracings spans across the whole width of the frame structure. Figure 2-92 shows the number of iterations required to obtain a minimum performance index. The PBO process resulted in a material volume reduction of 76% and an increase in mean compliance compared to the initial.

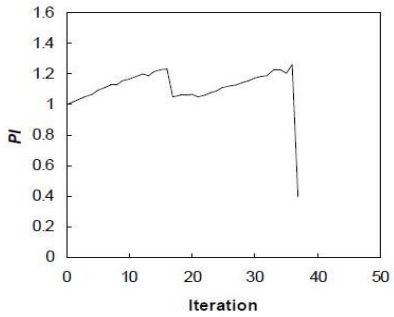


Figure 2-92: The performance index of the full-width bracing system (Liang, 2007).

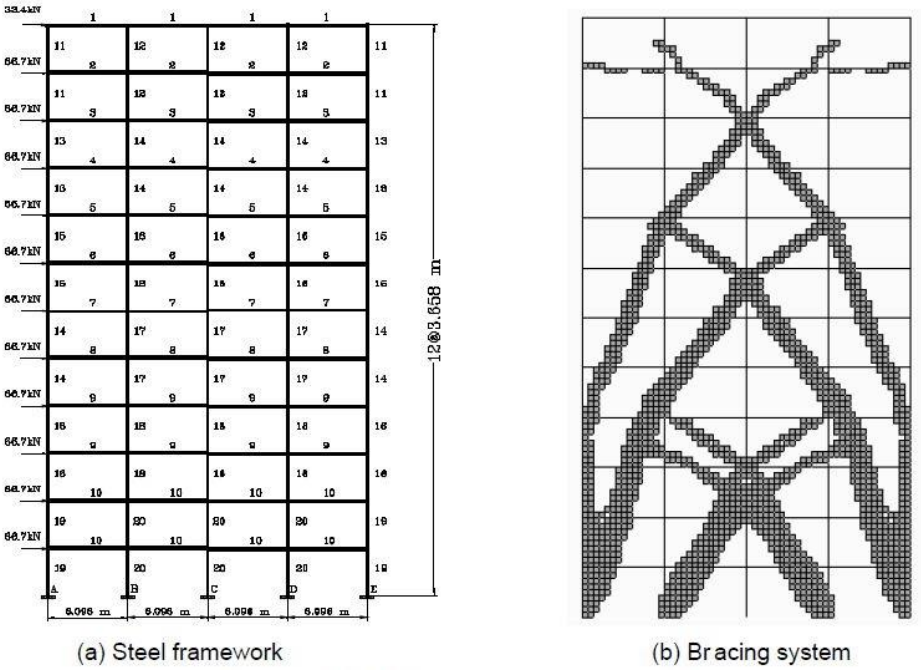


Figure 2-93: A 4 bays 12-story steel frame optimal topology of the bracing system (Liang, 2007)

2.8.4.3.2 Two Bays Braced Framework

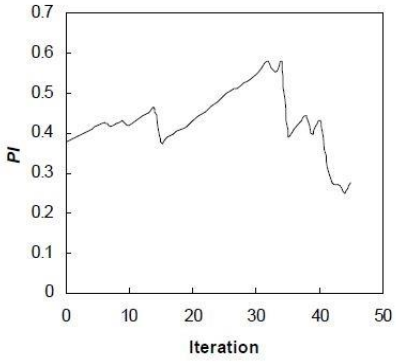


Figure 2-94: The performance index of the two bays or a half bracing system (Liang, 2007).

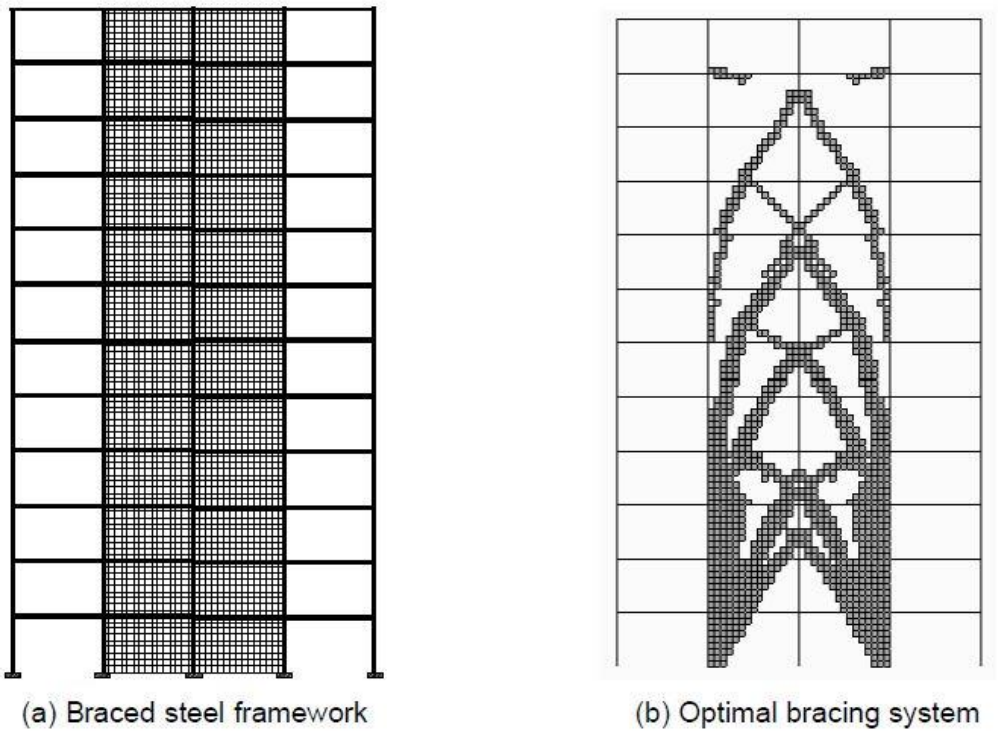


Figure 2-95: A 2 bays 12-story steel frame optimal topology of the bracing system (Liang, 2007)

The bracing system in the two bays braced framework, as illustrated in Figure 2-95, is to determine the effect of regions without bracing on the layout and performance of an ideal bracing system. This building structure represents a practical challenge for tall

building structures that require some free bays or less obstructive outside view. Figure 2-94 shows the number of iterations required to obtain a minimum performance index. The PBO process results in 66% of elements removal and a 92% increase in mean compliance compared to the initial. Columns in the lower storey are needed to be resized for sufficient lateral support (Liang, 2007).

The initial continuum designs of the multistorey steel building set a base to create an optimum bracing system to stiffen the framework. As shown in Figure 2-93, the full-width bracing system is better than the two bays bracing system, as shown in Figure 2-95 in terms of efficiency. An innovative bracing system for multiple lateral loads was produced through the PBO method. The optimal bracing system also indicates the relative dimensions of bracing members, proportional to the forces they sustain (Liang, 2007).

Stromberg *et al.* (2012) proposed a different approach to identifying optimal bracing. The research introduces a new approach that can elevate practical problems in the topology obtained in most research studies, as shown in Figure 2-96 through a combination of discrete members and continuum quadrilateral members (Stromberg *et al.*, 2012). It resulted in a more simplistic design similar to a truss where the braces are clearly defined. A 3D rendering of the topology design of tall building structures is plotted according to the findings is shown in Figure 2-96 (Stromberg *et al.*, 2012).

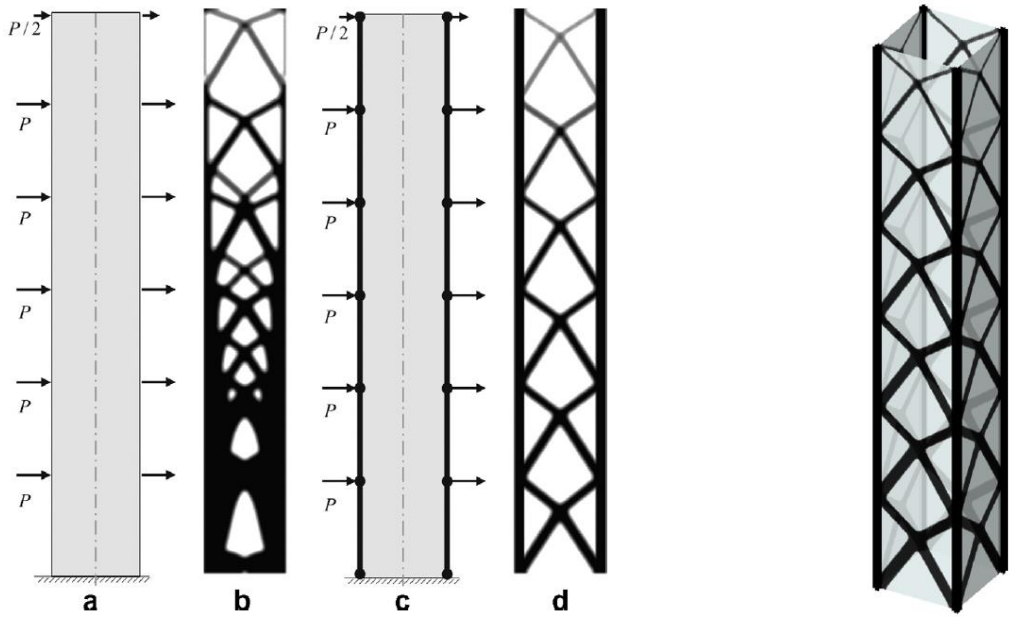


Figure 2-96 Comparison of topology optimisation techniques with the same total volume of material: (a) continuum approach; (b) topology obtained using quadrilateral elements; (c) combined approach; (d) topology obtained through quadrilateral and discrete column elements. (Stromberg *et al.*, 2012)

2.8.5 Topology Optimisation of Building Structures under Dynamic Loads

The topology can vary in design when subjected to different loading conditions. Hence, the topology optimisation of a building structure can become complicated when considering seismic excitation. A study was conducted to identify the optimal bracing system of high rise structures under wind and seismic excitation, and as expected, the topology varies according to the different load imposed. It creates a new problem for designers to design a structural system with a topology that can sustain uncounted loading conditions as the design is for a specific parameter. The topologies obtained are shown in Figure 2-97, and the assumed loading conditions are shown in Table 2-7 (Suksuwan and Spence, 2018). Therefore, no one shape or design is suitable for all loading conditions.

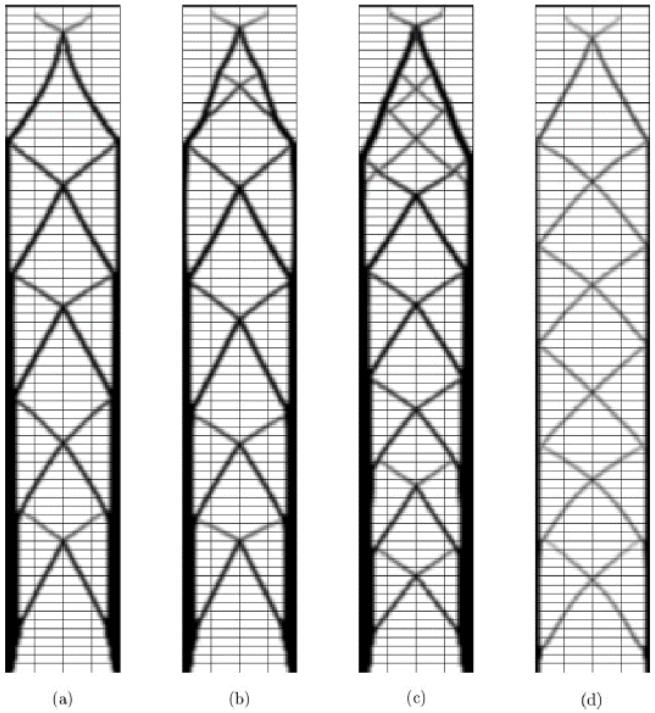


Figure 2-97: Final topology for trial (a) 1; (b) 2; (c) 3; (d) 4. (Suksuwan and Spence, 2018)

Table 2-7: Hazard information for all 4 trials. (Suksuwan and Spence, 2018)

Trial	**Hazard**	η_W	η_E	**Mean of** V_{Hmet}	**C.O.V. of** V_{Hmet}	**Mean of r**
1	Wind	1	N/A	27 m/s	0.35 m/s	N/A
2	Wind & Seismic	0.5	0.5	27 m/s	0.35 m/s	25 km
3	Wind & Seismic	0.5	0.5	27 m/s	0.35 m/s	10 km
4	Wind & Seismic	1	0.5	15 m/s	0.20 m/s	10 km

Failure often occurs at its joints or its discontinuous sections, and in terms of a building structure, refers to the corner of the beam to column sections where are often weak points that lead to structural damage. Localised stress concentrations are observed in the beam to column frame connection, as shown in Figure 2-98. These regions are to

have additional reinforcement by inserting materials like steel or fibre to stop structural cracks. A study conducted by Lee and his research team in the topology of a beam to column frame connection (Lee, Yang and Starossek, 2012) shows that the topology layout obtained for static and dynamic analysis is different. Hence, it was suggested that the combination of the two topology layouts would overcome the problem in both the static and dynamic (Lee, Yang and Starossek, 2012). The topology layout result of both the static and the dynamic analysis are shown in Figure 2-99. Nonetheless, an optimised notch design may provide a better solution to reduce localised stresses.

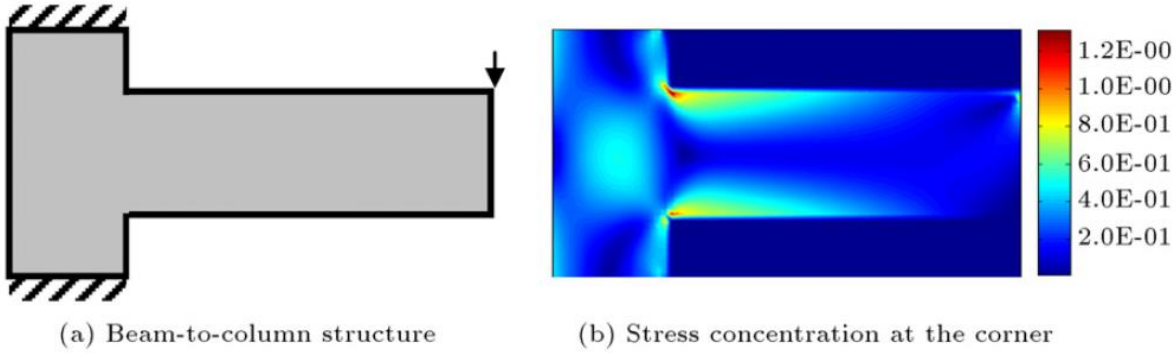


Figure 2-98: Finite Element Analysis model of a beam to column frame connection and its stress concentration (Lee, Yang and Starossek, 2012)

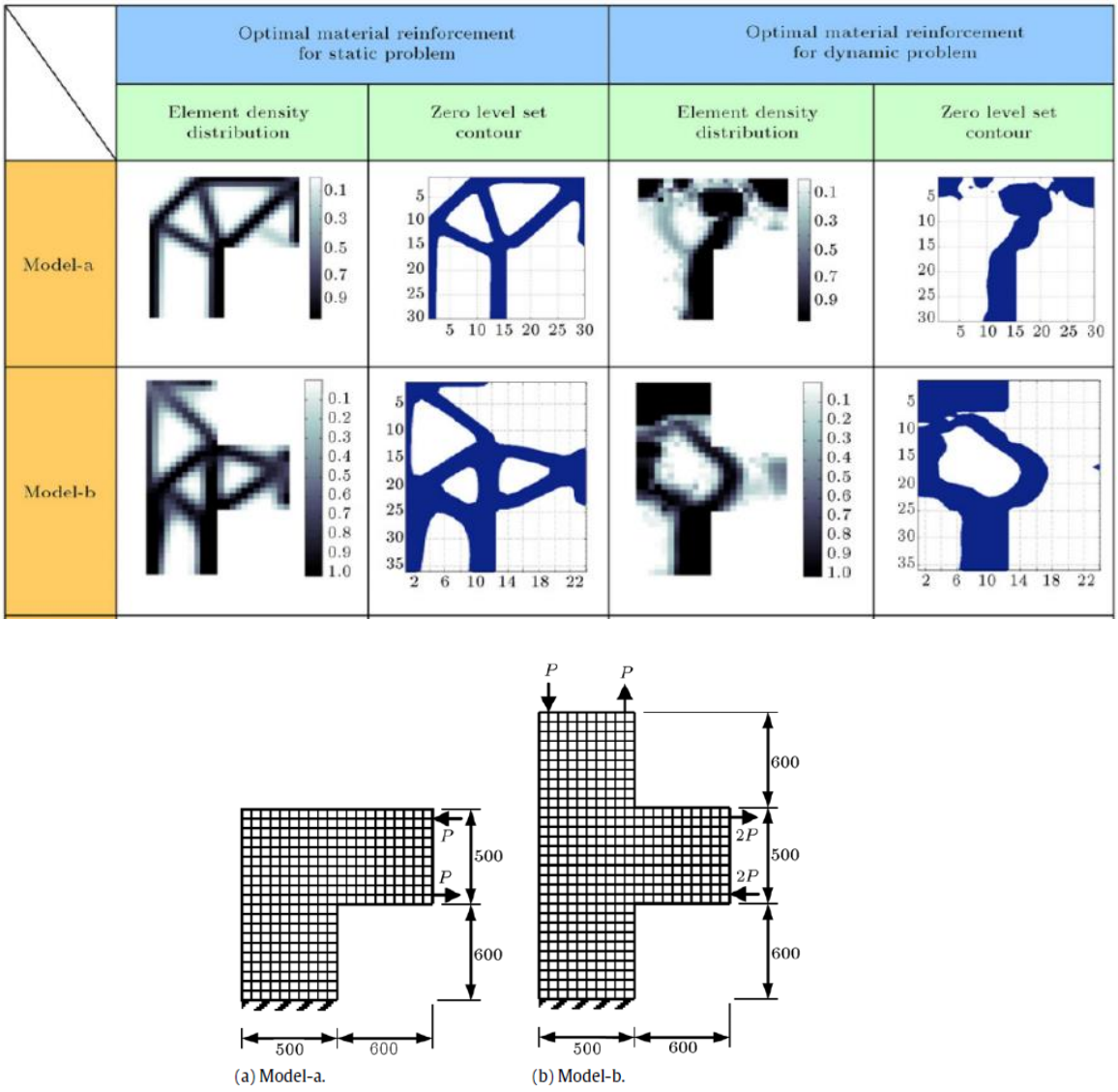


Figure 2-99: Optimal topology layout for the two structural models of a beam to column frame connection (Lee, Yang and Starossek, 2012)

Aside from the current topology optimisation research, Yap *et al.* (2019) proposed an alternative solution that looks into replicating nature's design in structures. An analysis was conducted on replicating nature's design in trusses and found that the tree design shows possible potential benefits in improving structural performance. Trusses with the tree design ratio show an increased displacement resistance of 12% to 35%, with a stress reduction of 19% to 22%. The tree design truss was not the best truss design but showed high flexibility that can plausibly provide better dynamic performance in

structures. Ongoing research is still being conducted to identify the effects of applying nature's contour design in connection designs.

2.9 Earthquake Resistance Designs

There are three basic approaches to limiting damage to a structure during a seismic event. The first and most straightforward approach is for the structure to resist damage through strength and stiffness like those in the ancient structures, where they are over-engineered to a point where the strongest expected seismic wave may not attain or exceed the design limit. Hence, allowing the building to remain within the elastic region undamaged. The second is damage avoidance by isolating the structure from the ground. Lastly, reducing damage through the dissipation of seismic energy with the assistance of isolation or damping devices (*Encyclopedia of Earthquake Engineering*, 2015).

There are a few structural design approaches for a building to resist seismic loads. It can be through moment frames, braced frames (concentric and eccentric), shear panels, or horizontal diaphragms. Moment frames are a set of interconnected members designed to carry vertical and horizontal loads. Frame structures can be designed with bracing, shear panels and horizontal diaphragms. (BRANZ's Seismic Resilience, 2020).

2.9.1 Steel Structures

There are three common methods in mitigating the effects of earthquakes in steel structures, bracing, post-tensioning and damping devices. Additional dissipative components can be added to some braces to enhance the effect of damping (Buchanan *et al.*, 2011). However, eccentric steel braces are particularly vulnerable to buckling if it lacks reinforcement, as shown in Figure 2-100.

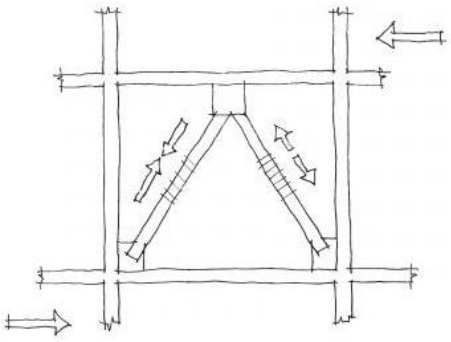


Figure 2-100: Eccentric bracing damping under lateral loading (G. MacRae, 2013; BRANZ's Seismic Resilience, 2020)

A moment frame can be created through a system that utilises a set of jointed steel members connected with post-tensioning tendons. Damping devices may also be utilised together to dissipate energy. A tie-down approach through a single post-tensioned steel tendon from top to bottom, as in Figure 2-101, has also been proposed for steel-framed buildings.

As for steel-framed buildings, there are many damping devices available, such as link beams, buckling restrained braces, friction dampers, friction damped braces, sliding hinge joints, and spring joints. Link beams are an indirectly part of an eccentric brace system designed to dissipate energy through yielding in shear. Hence, they are designed to be unbolted and replaced as required. Buckling restrained braces, also known as tension-compression braces, shown in Figure 2-102, is a type of hysteretic damper. The yielding is to be spread out along the full length of the brace, minimising the chances of fatigue failure. Similar to a link beam, they may require replacement if damaged (Buchanan *et al.*, 2011).

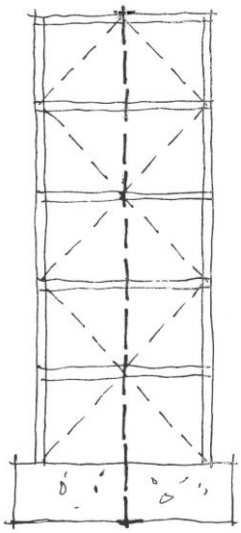


Figure 2-101: A single post-tensioned steel tendon (G. MacRae, 2013; BRANZ's Seismic Resilience, 2020)



Figure 2-102: Buckling restrained braces in steel frames (BRANZ's Seismic Resilience, 2020)

Friction dampers utilised the friction between the metal surfaces to dissipate energy through heat conversion, as shown in Figure 2-103. They are used together with other structural systems like diagonal bracing, adding friction damping. There are several forms of friction dampers, but they can be defined into two primary varieties, symmetrical and asymmetrical. They are chosen according to the bracing type that they are to be combined.

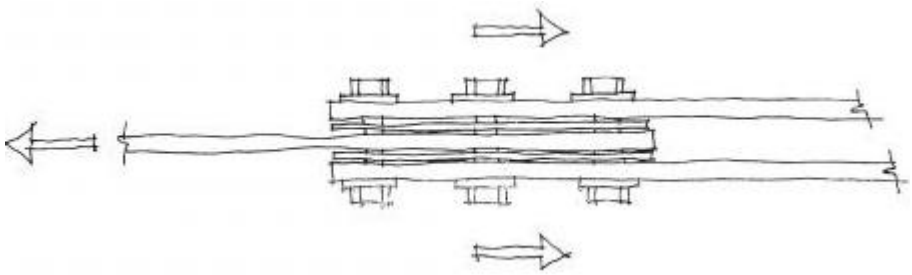


Figure 2-103: Mechanism of a symmetrical friction damper (G. MacRae, 2013; BRANZ's Seismic Resilience, 2020)

Friction braces is a combination of a concentric or eccentric brace with a friction damper. Concentric friction braces may either use a friction damper with a diagonal brace or as part of a gusset plate attached to a beam or slide at the bottom flange of the beam, as shown in Figure 2-104. Eccentric friction braces may be utilised as a part of a gusset plate attachment, a sacrificial link below the beam or an in-line device that forms an asymmetrical pair. The friction braces offer a similar damping level under compression and tension loads, but careful design is necessary to ensure that they do not buckle out of plane during compression. The braces offer no self-centring action, and it is essential to be paired with other systems as required by the building design (Buchanan *et al.*, 2011).

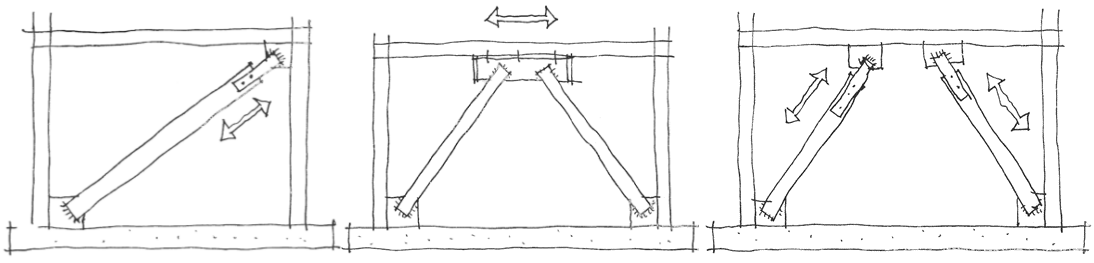


Figure 2-104: Various friction brace configurations (G. MacRae, 2013; BRANZ's Seismic Resilience, 2020)

Sliding hinge joints are a specialised type of friction damper that adds friction damping to a steel moment frame at the beam and column connection, as shown in Figure 2-105. The joint movement is dampened with this system, reducing yielding in the main structural elements. This method is also not fully self-centring, as there is extra friction in the system (Buchanan *et al.*, 2011).



Figure 2-105: Sliding hinge joint in steel moment-resisting frames (Sidwell G., 2010)

Spring joints are another type of rocking structure, as shown in Figure 2-106. It consists of a set of a self-centring cable attached to high strength springs at the bottom of the legs that provides restorative and damping forces to a building structure during an earthquake. The system also protects the foundation and the column foot from impact damage while rocking.

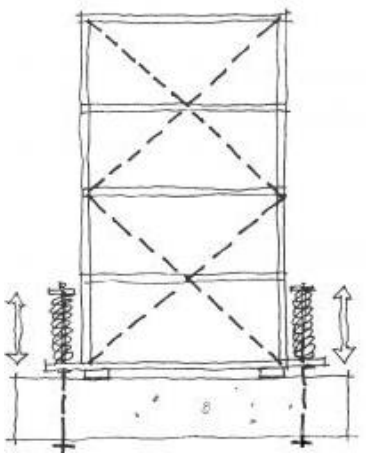


Figure 2-106: Joint Spring system (G. MacRae, 2013; BRANZ's Seismic Resilience, 2020)

2.9.2 Beam to Column Connections

The steel moment frames are conventionally designed with a rigid full strength connection and are often utilised in high seismic regions. The design provision ensures that the connections are sufficiently overstrength to create dissipative zones in the beams. The reliability of these full-strength beams to column connection came into question when buildings were seen to perform poorly during the significant events in the mid-1990s. The extended repetitive nature of the damage observed in various types of welded and hybrid connection has led a research effort to new restoration methods of existing structures and an alternative connection configuration to be included in new building designs (Elghazouli, 2009).

The observed damage was associated with several factors, including defects in the weld and steel materials, stress concentration, high rotational demands, and scale effects. Since then, numerous suggestions have been forwarded to upgrade existing connections (Elghazouli, 2009). Other alternative connections have been proposed, such as strengthening connections through haunches, cover or side plates, or by weakening the beams by trimming the flanges(Elghazouli, 2015). The trimming

method of the flanges, known as the “RBS” reduced beam section, or ‘dog-bone’ connection, was one of the proposed improved joint details in the aftermath of the Northridge earthquake. It moves the formation of plastic hinges away from the column face. This mechanism fulfils the design requirement by trimming the beam flanges (Jones, Fry and Engelhardt, 2002; Ohsaki, Tagawa and Pan, 2009; Pachoumis *et al.*, 2009). This is to create a weak beam strong column connection allowing the beams to fail before the columns.

2.9.3 Column-Tree Moment Connections

The moment connections are designed to join the beam flange to the column through a complete joint penetration groove weld in the field (Chen, Lin and Lin, 2006). During the Northridge earthquake, many connections failed under a local brittle failure. Other factors include stress concentration in the weld of access hole regions, weld defects and crack initiation from the back-up bars at the beam bottom flanges (Mahin, 1998; Miller, 1998; Chen and Lin, 2013). Brittle failure at the weld of the beam to column connection can have dire consequences. If the plastic deformation in the main component is not fully developed, the overall structure loses its bearing capacity from brittle failure, preventing seismic energy from dissipating and eventually leading to a less satisfactory seismic performance in steel structures. Brittle fracture is very high in the column tree moment connections because of the utilisation of the welded flange-welded web connections. Many fractures were observed in these connections during the 1995 Kobe earthquake (Nakashima, Inoue and Tada, 1998).

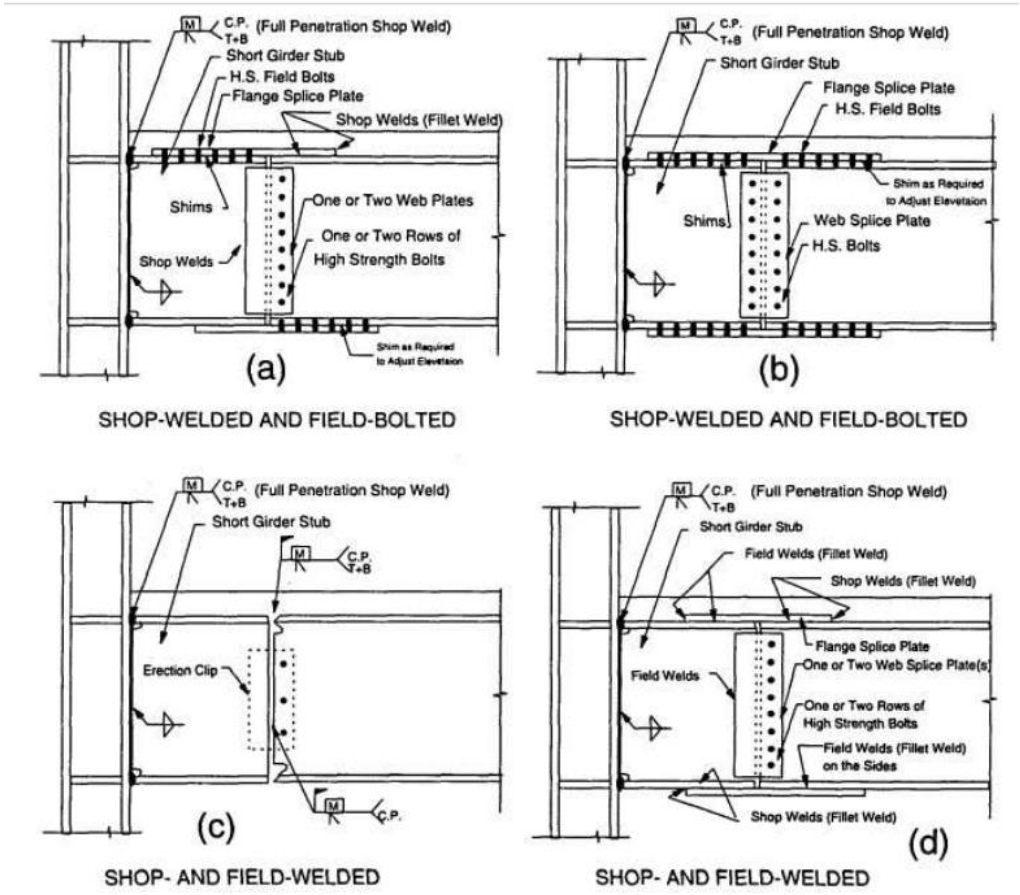


Figure 2-107: Various types of column tree moment connections (Astaneh-Asl, 1997)

Figure 2-107 shows a set of various types of tree moment connections. They are one of the often used beam to column connections utilised in the moment-resisting frames in Japan and Korea (Oh *et al.*, 2014). There are 3 types of column tree MRF based stiffness, namely rigid, semi-rigid and flexible. Stiffness, strength, ductility and energy dissipation capacity can be effortlessly manipulated through the utilisation of semi-rigid connections to lessen seismic forces and displacements to satisfactory levels to improve seismic performance. McMullin et al. (1993) conducted a study that shows that the semi-rigid column tree system can result in a potentially reliable and economic seismic resisting system (Astaneh-Asl, 1999). One of the key advantages of a semi-rigid column tree system over the traditional rigid system (as in Figure 2-108) is that

the bolted connection situated at the girder splice acts as a fuse and protect the welded connections at the column face from large moments (Astaneh-Asl, 1997). Furthermore, semi-rigid connections can lengthen the damping period of vibration, reducing stiffness to a favourable level, reducing seismic forces and displacements.

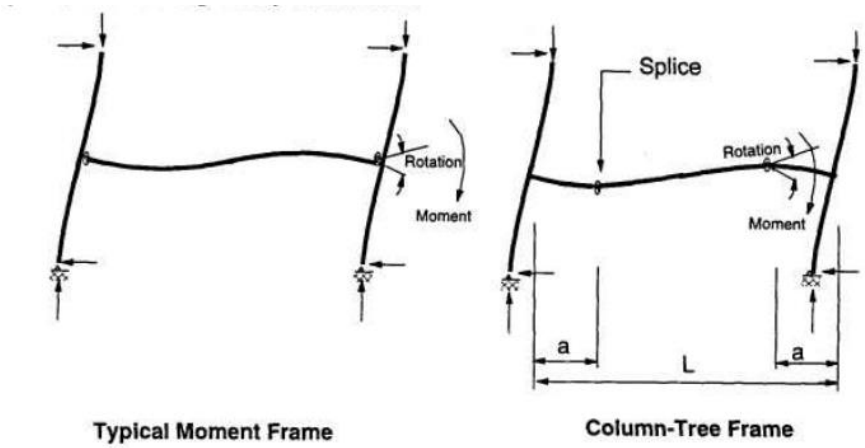


Figure 2-108: Traditional moment frame vs column tree frame (Astaneh-Asl, 1997)

The following are some studies conducted on tree column frames. Astaneh-Asl (1997) looked into the weld damage by earthquake and conducted studies on the slippage of the bolt during earthquakes. Lee and Park (1998) studied the effects of the panel zones strength on the column tree's seismic performance and found that the mode of failure in their specimens was due to the fracture in the beam flange. Chen, Lin and Lin (2006) presented a widened flange column-tree connections with 2 methods of connection detail enhancements, the removal of the weld access hole caused by localised plastic strain and the widening of the stub beam flanges to improve ductility and strength. Chen and Lin (2013) later performed 6 column tree connection with the proposed widening and tapering on the ends of the beam flanges. All proposed tapered beam flanges received satisfactory ductile behaviour by forming plastic hinges away from the column face. These methods assist in reducing the occurrence of brittle failure.

Numerous experimental studies were carried out to determine the splice slip behaviour in column tree connections (Lee and Park, 1998; Schneider and Teeraparbwong, 2002; McMullin and Astaneh-Asl, 2003; Lee *et al.*, 2014; Oh *et al.*, 2014, 2015, 2016; Kim and Yu, 2019). It showed that the slip at the splice region occurred at approximately 1/2 of the beam moment capacity even when the beam splice was designed to transfer the full strength of the connecting beams (Lee *et al.*, 2014; Oh *et al.*, 2014, 2016). Kim and Yu (2019) found that the column tree type construction is a worthwhile option for steel moment framed buildings in areas with low to moderate seismicity.

The proposed work studied by (Chen, Lin and Lin, 2006; Chen and Lin, 2013) on column tree connections is particularly interesting. It shows a similar usage pattern of shape profile on the widening and tapering of the ends of the beam flanges. Their work capitalised on the technique or idea of using a tapering shape profile to shift stress localisation away from the support. Although their work has not resulted in a clear seismic resistance system, their work holds merits towards a better structural system. The following figures shown in Figure 2-109 are the work studied.

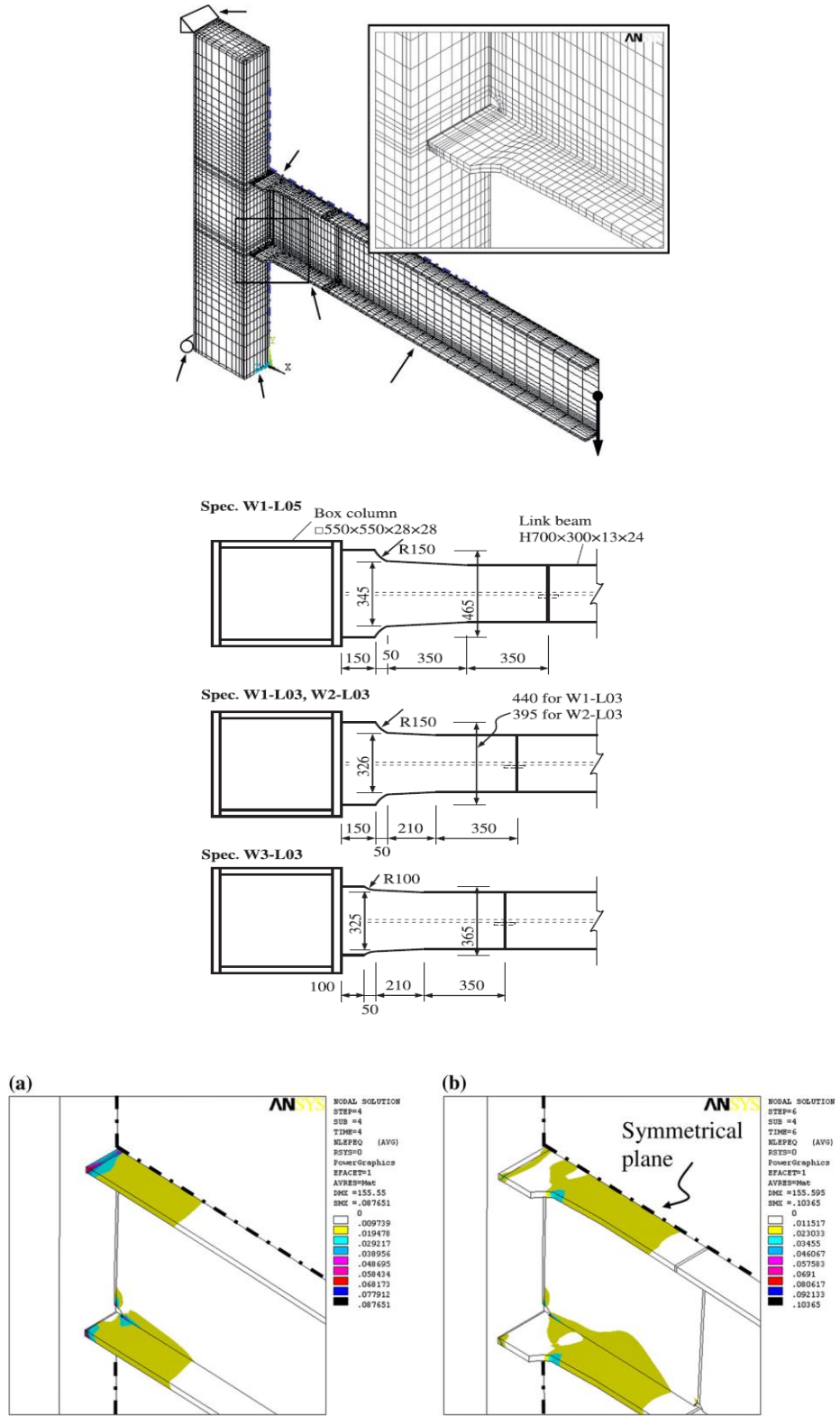


Figure 2-109: Model detail and FEM result of the study of tree column connection design by (Chen, Lin and Lin, 2006; Chen and Lin, 2013)

2.10 Summary

The study of nature's development and evolution in relation to their shape and sizes in trees and animal bone structures has given engineers plenty of insight and ideas on micro designing of mechanical components. The literature review in this chapter demonstrates how small changes in the topography of a mechanical element can change its mechanical performance and function when a biological or natural occurring shape profile is introduced. Trees are part of this literature review as they are both unique biological structures and have significant similarity with civil engineering structures. The idea here is to create a better structural system through a nature-inspired design that can resist lateral loading.

Part of the success in biomimicry is optimisation. The optimisation technique provides solutions to reducing resources without affecting its core function or purpose (e.g. performance). There are many ways one can optimise a design. One of the many different types of algorithms that can be applied is either using gradient-based mathematical programming techniques (e.g. Optimality Criteria algorithm (OC), the Method of Moving Asymptotes (MMA), Sequential Linear Programming(SLP)) or non-gradient based algorithms (e.g. Genetic algorithms (GA), Particle Swarm Optimisation (PSO)).

Mechanical researchers are at the forefront of these studies using optimisation techniques on simple biological profile. Their focus has so far dealt with the micro behaviour in relation to the subject of interest (mechanical components). This particular area of research attracts much attention because of the high-localised stresses developing along its surface. Hence, finding ways of dissipating and removing peak stress along the surface became the final objective.

On the macro level, a multistorey building frame analysis usually focuses on bracing the structure against lateral loading and not on the connection between the column and the beam. The study gives a very good detailed assessment of its function, behaviour and development pattern that resulted from imposed external forces. From the mechanical component to the large-scale analysis in section 2.8.4 (improving bracing systems in steel multistorey structures), a similar internal force pattern can be seen both in micro and macrostructures. However, it should be noted that the structure's internal forces change according to how the loads are applied. Thus, no single shape or structure is suitable for all loading conditions. Furthermore, some of the analysis shown in the literature does not reflect on how building structures function, transfer or dissipate loads (if a different set of external loads is applied).

The limitation to applying topology optimisation structures in a real-world application is that it will reduce its overall capacity to resist and/or absorb excessive energy dissipation of unaccounted loading conditions. The literature presented in Chapter 2.8.5 shows the difference in topology obtained in both static and dynamic conditions, and it may be best to combine the two topologies for a better structure. Other consideration includes fire safety. Thicker members are more fire-resistant than thinner members due to their surface area to volume ratio.

It shows how different shaped joints and material can provide better strength between members. The study shows the plausibility of applying a similar technique in civil engineering to improve the connection in joint members. Bamboos are one of nature's design that is known for resilience in nature. One of its success is in the design of its joint. However, one should not apply nature's design into any structure without understanding its original purpose and behaviour in its natural environment, as shown

in section 2.4. In addition, the dynamic behaviour over time and its sustainability from micro to macro has yet to be investigated.

Based on the results obtained by the research papers presented, the natural conclusion is that the Baud curve is superior over the other profiles. The caveat to applying this is the difficulty in achieving an accurate profile that reflects the Baud curve during the actual assembly and construction of civil engineering structures. Having a close profile to Baud or any suggested ones (as described in section 2.6.4) must consider its practicality, constructability, cost, and benefit. Although mechanical and civil engineering may be similar in mathematical approach (e.g. solid mechanics), the profile in structural members may perform differently when it is analysed as a continuum or discrete structure.

Therefore, it may be possible to create a building connection using a biological profile that is responsive and with the ability to dissipate or absorb the lateral loads. The approach here is to engage the support of computer software to test, simulate and eliminate profiles that are not functional or practical.

Similarities in the topology of a cantilever beam and a steel multistorey structure presented in this paper demonstrate the possibility of finding a common pattern that may be used to improve current structures incorporating nature's design method of survivability. The challenges presented shows that no single design may be suitable for all loading conditions. Optimisation techniques accompanied by nature's design for verification purposes may help new designs through a deeper understanding of the subject. Therefore, replicating the design nature should be applied after understanding the nature of the problem. The topology identification is crucial for both steel and

concrete structures to understand and determine its force flow within the structure as it can affect its structural integrity as a whole.

Through the literature, it was found that there is no study on utilising nature's notch shape profile and integrating nature's design in civil engineering structures. Hence, the research aims to enhance the efficiency of steel structures under lateral loading by replicating the design found in nature (trees).

Chapter 3 Methodology

3.1 Introduction

A multi-phase research methodology was applied to achieve the defined aim and objectives. A comprehensive literature review was conducted to determine a suitable design shape found in nature (e.g. living plants, animal bones, shell structures) to be replicated in steel structures. The contour profile selection was based on the merits of its feasibility and practically of applying the design in steel structures. The ”Method of Tensile Triangles” shape profile was deemed research worthy for further studies in the literature study. The selected designs are then evaluated through Finite Element Packages to identify the feasibility and behaviour of introducing nature’s design in simple structural components (e.g. cantilever beam). A parametric study was also conducted to determine the optimal sizing range of the various cantilever geometries. Subsequently, it is compared with traditional engineering designs (as benchmarks) to determine its suitability, performance and efficiency. The topology optimisation technique is utilised to facilitate further understanding of its load path and possible design improvements. The optimised designs are later evaluated as trusses to investigate the practicality of the design. A refined pool of optimal designs (was obtained through a systematic elimination method) is then introduced into multistorey structures to investigate the behaviour of the design as a single structural system to dissipate or transmit forces experienced at its joints. A summary of the methodology is shown in Figure 3-1.

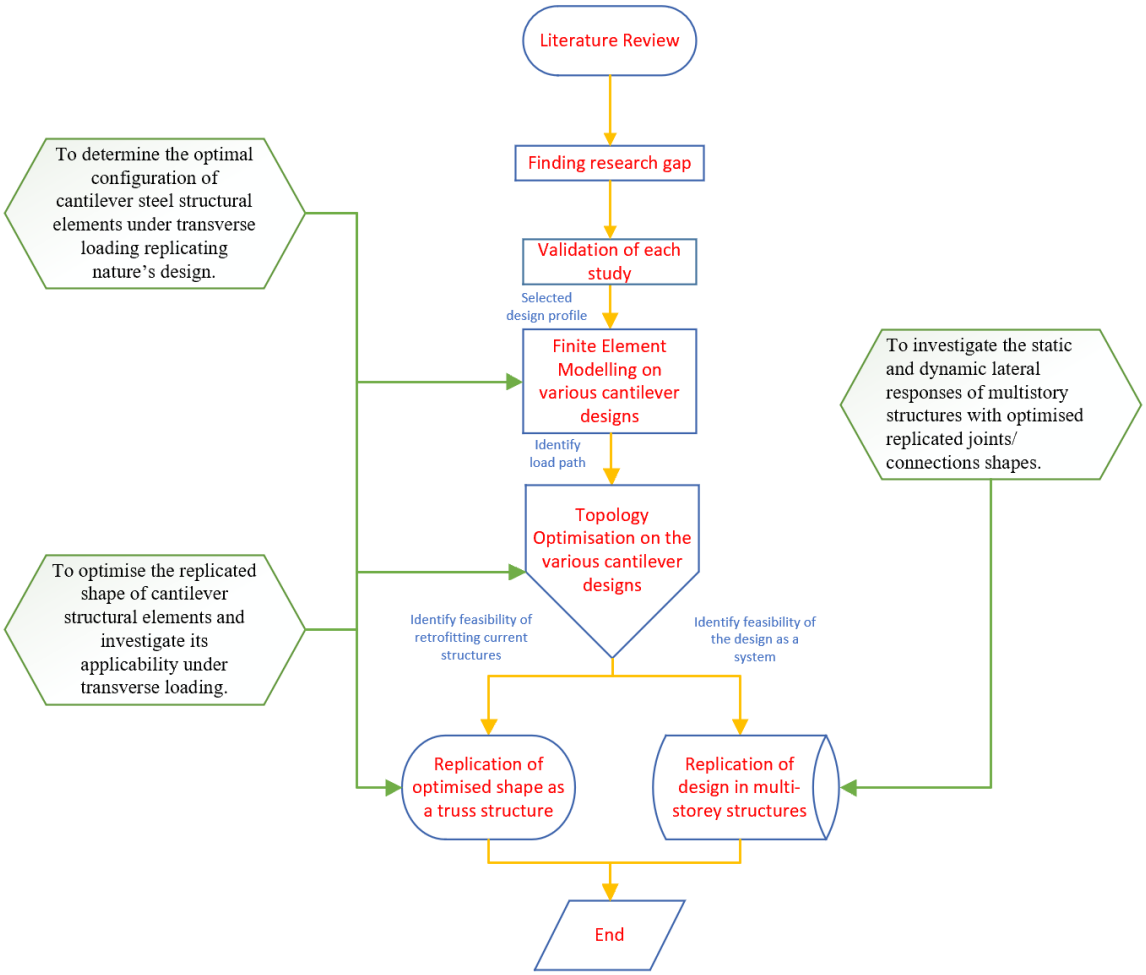


Figure 3-1: Methodology Flow Chart

Outlined earlier are the four analysis conducted to meet the three Objectives set out in the thesis. The FEM modelling, topology optimisation, and the optimised shape replication as truss structure meet the first two Objectives. The replication of the design in a multistorey structure is to meet the third objective of the thesis. Since there is a lack of laboratory validation study due to cost and time constraints, a numerical validation study was conducted prior to the four studies to ensure the results obtained deliver reproducible results using established and accepted methodology. This chapter guides the process for the validation study.

The study was split into two separate studies to cover a wide range of feasibility studies. The first is to determine how the projections under the cantilever are performing, why they are performing better, and the optimised plots feasible in practice. The second is to determine how the projections in the columns will influence the performance of a multistorey structure. Details of the models studied are shown in their respective chapters. Table 3-1 shows a summary of the number of models conducted in the thesis for each chapter.

Table 3-1: Summary of the number of models conducted in the thesis for each chapter

Chapter	**4**	**5**	**6**	**7**
Number of models	276	1890	7+720+8	50
Total		2951		

Presented is the methodology applied for this numerical modelling. Finite element modelling (FEM) is widely used in many industries to improve the performance and efficiency of structural components. It provides valuable insight into structural components on its behaviour and stresses experienced. A list of software utilised to achieve this research aim and objectives are MATLAB, ANSYS, OASYS GSA, and SAP2000. The commercial programming language software MATLAB was utilised to validate the commercially available analysis software as listed above (except for SAP2000). The defined numerical model analysed in the commercial software were also compared against a similar model available in textbooks or research papers. Parameters are maintained to ensure reliable results. A slight numerical deviation is expected as different software may apply slightly different modelling techniques.

The validation of the software is separated into three sections for the respective software used. Parameters and designs used for the numerical modelling are in

accordance with its respective model utilised for the validation process. The utilisation of each software mentioned above is further elaborated in subchapter 3.3. The procedure for the Finite Element Modelling and the Topology Optimisation are shown in Figure 3-2 and Figure 3-3, respectively.

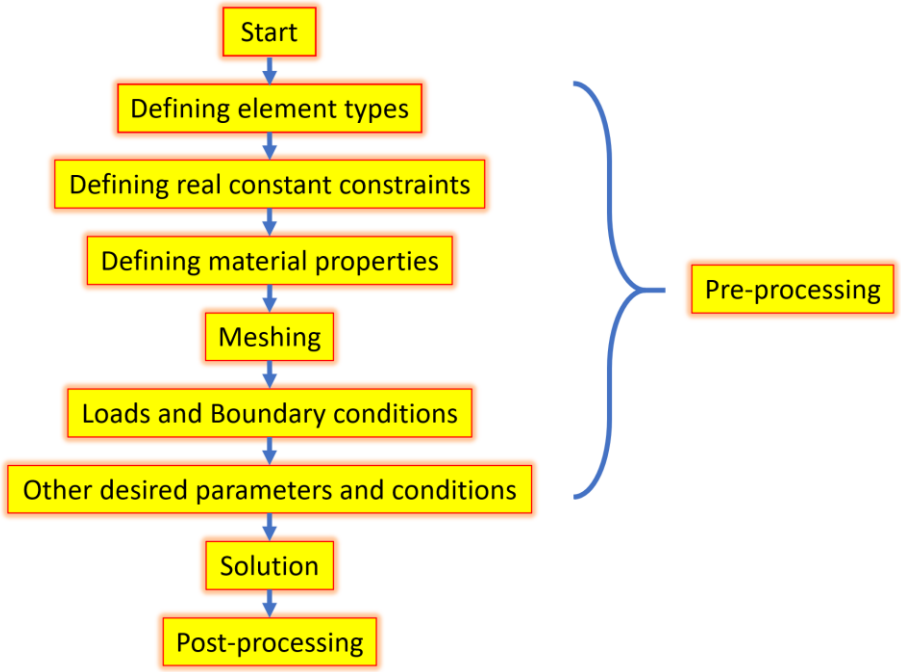


Figure 3-2: Finite Element Procedure (also applies to MATLAB)

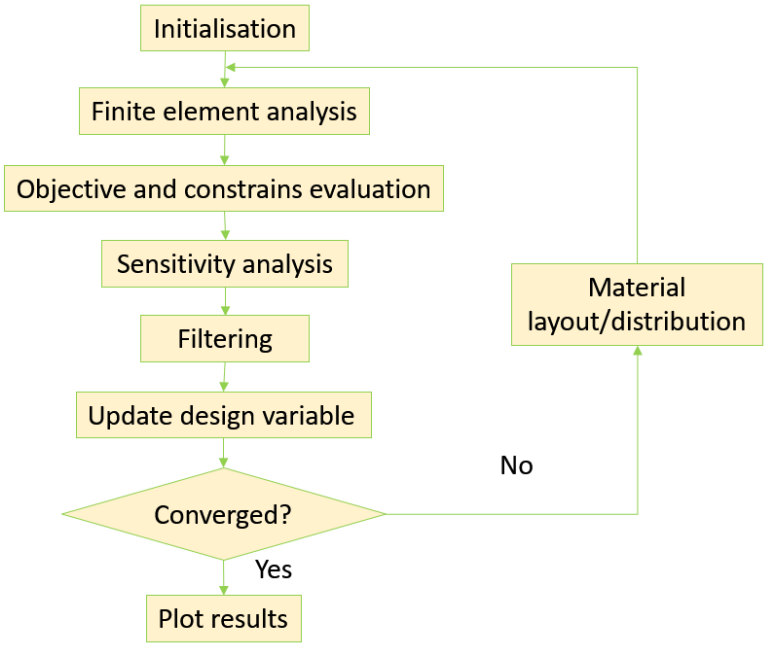


Figure 3-3: Topology Optimisation Procedure

3.2 MATLAB Script Structure

Presented here in this subchapter are the Matlab scripts used to validate the commercially available analysis software. The MATLAB script is separated into the main script and its subscripts in each subsection. Some modifications were applied for the application of the desired model.

3.2.1 Finite Element Modelling and Topology optimisation

The MATLAB script is based on two separate MATLAB coding. The finite element MATLAB code is based on a textbook by Khennane (2013), and for the topology optimisation, the MATLAB code is based on a published paper by Sigmund (2001) using the Solid Isotropic Material with Penalisation (SIMP) method. The MATLAB code can be found in Appendix A.a.

For the design validation purpose, the design domain is assumed as a solid isotropic rectangular plate with square/quadrilateral finite element discretisation. The numbering of elements and nodes follows an orderly fashion of column to column from left to right. The number and ratio of finite element in terms of its horizontal (n_x) and vertical (n_y) direction used in the model must reflect the structure's aspect ratio. The following topology optimisation problem is based on a power-law approach; the objective is to minimise compliance $c(x)$ as defined in Equation (3-1). Compliance can be described or expressed as the strain energy of the structure and is considered a reciprocal measure of stiffness. The lower the strain energy, the higher the stiffness of a structure. Thus, maximising stiffness will minimise compliance.

$$\min_{x}: c(x) = \boldsymbol{U}^T \boldsymbol{K} \boldsymbol{U} = \sum_{e=1}^{N} (x_e)^p \boldsymbol{u}_e{}^T \boldsymbol{k}_0 \boldsymbol{u}_e \tag{3-1}$$

subjected to:

$$\frac{V(x)}{V_0} = f$$

$$\boldsymbol{K}\boldsymbol{U} = \boldsymbol{F}$$

$$0 < x_{min} \leq x \leq 1$$

$U, F, K, u_e \; and \; k_e$ are the global displacement, force vectors, global stiffness matrix, element displacement vector and element stiffness matrix. K can be formed from local element stiffness matrices k_e that is in the form of $k_e(x_e) = E(x_e)k_0$ in Equation (3-2), where

$$E(x_e) = x_e{}^p E_0, \qquad x_e \in [0,1] \tag{3-2}$$

$E, E_0 \; and \; x_e$ are the Young's modulus, the solid material's elastic modulus and the relative element density. x is the design variable vector and x_{min} is a non zero vector

of minimum relative densities to prevent stress singularity (e.g. 10^{-9}). Hence, the stiffness is not completely removed from the model. If x_e corresponds to a value 0, it would be a void, and if it corresponds to a value 1, it would be a solid. Thus, a density parameter is applied as such $10^{-9} \leq {x_e}^p \leq 1$. N $(n_x \times n_y)$ is the number of elements used in the discretisation of the design domain. p is the penalisation power to avoid intermediate densities, and its value is often 3 and above. The SIMP penalisation forces x_e of the solid material towards either of its boundary. A sharper solution can be obtained by increasing the value of p. Intermediate densities provide stiffness smaller than the cost in weight or volume of the material. $V(x), V_0 \; and \; f$ are the material volume, the volume of the design domain and the defined volume fraction.

The optimisation problem was solved using the Optimality Criteria method (OC) according to Bendsoe (1995) heuristic updating scheme for the design variables. The formulation is as follows:

$${x_e}^{new} = \begin{cases} max(x_{min}, x_e - m) \\ \quad if \; x_e {B_e}^{\eta} \leq max(x_{min}, x_e - m) \\ x_e {B_e}^{\eta} \\ \quad if \; max(x_{min}, x_e - m) < x_e {B_e}^{\eta} < min\,(1, x_e + m) \\ min(1, x_e + m) \\ \quad if \; mi\,n(1, x_e + m) \leq x_e {B_e}^{\eta} \end{cases} \tag{3-3}$$

$m \; and \; \eta$ are the move-limit (positive) and the numerical damping ratio. The defined values are 0.2 and 0.5, respectively. B_e is defined in Equation (3-4)

$$B_e = \frac{-\delta c / \delta x_e}{\lambda \, \delta V / \delta x_e} \tag{3-4}$$

The Lagrangian multiplier (λ) can be found using a bi-sectioning algorithm. The objective function's sensitivity or gradient is formulated as

$$\frac{\delta c}{\delta x_e} = -p(x_e)^{p-1} {u_e}^T k_0 u_e \tag{3-5}$$

Mesh dependency relates to the problem of not finding the same solution when using different mesh density to discretise the domain. Therefore, a mesh independency filter technique is introduced to ensure a solution exists and overcome the checkboard problem. The mesh independency filter modifies the element sensitivity as such

$$\frac{\widehat{\delta c}}{\delta x_e} = \frac{1}{x_e \sum_{f=1}^{N} \widehat{Hf}} \sum_{f=1}^{N} \widehat{H_f} x_f \frac{\delta c}{\delta x_f} \tag{3-6}$$

The convolution operator $\widehat{H_f}$(weight factor) is formulated as:

$$\widehat{H_f} = r_{min} - dist(e,f) \tag{3-7}$$

$$\{f \in N | dist(e,f) \leq r_{min}\}, \quad e = 1, \dots, N$$

N is the total number of elements, and the operator distance (e, f) is the distance of the element from the centre to centre (e and f). The convolution operator $\widehat{H_f}$ outside the filter area is zero, and it decays linearly with the distance from element f. The modified sensitivity is used instead of the original sensitivity in the Optimality Criteria update. r_{min} is a limitation criterion on the neighbouring element included in the filtering scheme. All sensitivities are equal when r_{min} approaches infinity; however, r_{min} approaches 0 when the sensitivity converges to the original sensitivity values.

3.2.1.1 Brief Description of the Main MATLAB Script

The main script connects to the subscripts to complete the mathematical problem. The definition of the model (e.g. dimension of the beam, applied load) are defined in the main script. The finite element subscript is to solve the finite element problem. The subscript will be called upon into the main script to complete its function. The subscript under this includes the mesh generation, material matrix, formation of the node and element connectivity, boundary conditions and imposed load. The global stiffness matrix, global force vector and unknown displacement are solved and assembled. The optimality criteria (OC) subscript is utilised to update the design variable. The design update is based on the objective function defined. The mesh independency filtering is applied to ensure a solution exists. The subscript will continue to run in a loop until convergence is met. The displacement, stress and topology are plotted as graphical plots.

3.2.1.2 Modifications

There are some modifications applied to the MATLAB script to suit the desired model of analysis (e.g. model type, size and boundary conditions) for the validation process. Some terms, name functions, method of execution were changed to ensure consistency throughout the other MATLAB scripts and provide better readability.

The MATLAB script is based on a textbook by Khennane (2013). It is an analysis of a Pratt truss-like truss structure, and some modifications were made for the application of the desired model. The MATLAB script can be found in Appendix A.b.

3.2.1.3 Brief Description of the Main MATLAB Script

The main script connects to the subscripts to complete the mathematical problem. The subscripts hold the variables related to solving the mathematical problem—variables

like its parameter and details of the model. The model's parameters and details include the definition for the number of nodes and elements, degrees of freedom, line connectivity (to shape and size of the model), material properties, boundary conditions, imposed load, and graphical plots. These input values are inserted into the main script, where the script will form and solve for the global stiffness matrix, the global force vector and the unknown displacement. These data value outputs are then converted into graphical plots.

3.2.1.4 Modifications

The two primary modifications made in the MATLAB codes are in the parameters and details of the truss model and the truss plots.

3.2.2 Dynamic Behaviour in Structural Analysis

This subchapter provides some equations and explanation on the seismic design fundamental (Elghazouli, 2009). Dynamic analysis is often a 2 stage process where the dynamic properties of the structure are first estimated by analysing the structure in the absence of external loads followed by the determination of the earthquake response using the properties obtained earlier. The dynamic properties of the structure are referred to as the natural frequencies and the mode shape. Although earthquakes usually induce a non-linear response to the structure, most seismic designs remain based on linear analysis.

A structure may be defined by these three critical properties, stiffness (k), mass (m) and damping for linear dynamic analysis. Equation (3-8) is the damping ratio ξ, where c is the damping coefficient. The value of ξ is generally within the value of 0.01 - 0.1 but often assumed as a value of 0.05.

$$\xi = \frac{c}{2\sqrt{km}} \tag{3-8}$$

A single degree of freedom (SDOF) system is of those displacements that can be defined by a single displacement. The system is subjected to a time-varying external force F(t) that cause a displacement x. Through Newton's second law of motion, F=ma, the motion equation of the system can be defined as in Equation (3-9) where $\dot{x}$is the velocity and $\ddot{x}$ is the acceleration.

$$m\ddot{x} + c\dot{x} + kx = F(t) \tag{3-9}$$

The lack of external forces in Newton's second law of motion can be written as Equation (2-9).

$$m\ddot{x} + c\dot{x} + kx = 0 \tag{3-10}$$

Since the stiffness and damping forces are proportional to the relative motion between the mass and the ground and the inertia force is proportional to the absolute acceleration of the mass, the relative displacement between the mass and the ground can be assumed as $y = x - x_g$. Hence, it can be rewritten as in Equation (3-11).

$$m\ddot{y} + c\dot{y} + ky = -m\ddot{x}_g \tag{3-11}$$

As defined in EC8, the elastic response spectra specify 2 groups of spectra with each category to have 5 different soil types. Type 1 spectra are for high seismicity areas ($M_s > 5.5$), and type 2 spectra are for moderate seismicity areas ($M_s < 5.5$). The soil types range from rock to cohesive soil (e.g. A -E). In the plot, the spectral acceleration S_e is normalised by the design peak ground acceleration a_g on the selected ground type. The spectra are assumed with a structural damping ratio of 5%. For the region of the spectra between T_B and T_c, the spectral acceleration is constant with the period.

Whereas between T_C and T_D, the spectral velocity is constant. Beyond T_D, the spectral displacement is constant. Equation (3-12) can be used to determine the force on the structure of an SDOF system.

$$F = mS_e \tag{3-12}$$

However, if the spectral displacement S_D is defined as the peak absolute displacement that corresponds to the spectral acceleration S_e, then $kS_D = mS_e$, using this relationship, it can be written as in Equation (3-13).

$$S_D = \frac{F}{k} = mS_e.\frac{{T_n}^2}{4\pi^2 m} = \frac{S_e {T_n}^2}{4\pi^2} \tag{3-13}$$

Not all structures can be modelled as an SDOF system; thus, a multi-degree of freedom (MDOF) system is required to analysed structures with distributed mass and stiffness as they may undergo significant deformation under several modes of vibrations. Analogous to Equation (3-11), the equation of motion can be rewritten in a matrix form for a system with N degrees of freedom as in Equation (3-14).

$$m\ddot{y} + c\dot{y} + ky = -m\iota\ddot{x}_g \tag{3-14}$$

Values of m, c and k are now in the form of matrices with a dimension of N × N. y is the relative displacement vector, and ι is an N × 1 influence vector containing a set of ones corresponding to the DOFs in the earthquake load direction and zeros elsewhere. Solving the free vibration problem is always helpful before solving Equation (3-14), and with damping omitted, Equation (3-15) is obtained.

$$m\ddot{y} + ky = 0 \tag{3-15}$$

The solution to the above equation has the form of Equation (3-16), where φ is the mode shape. Differentiating and substituting into Equation (3-15) leads to the equation (3-17).

$$y = \varphi sint\omega t \tag{3-16}$$

$$(k - \omega^2 m)\varphi = 0 \tag{3-17}$$

It can be solved to provide N circular natural frequencies ω_N with each associated to a mode shape φ_i. The vibration modes are system properties that are independent of the external loadings. An approximate formula like equation is often used in estimating the fundamental natural period of a multistorey frame building, where T_1 is measured in seconds, H is the building height and C_t is a constant. C_t is taken as a value of 0.085 for steel moment-resisting frames.

$$T_1 = C_t H^{0.75} \tag{3-18}$$

Equation (3-14) is a set of N coupled equations that can be solved using the principle of modal superposition. It states that for any displacements set can be defined as a linear combination of the shapes, as shown in Equation (3-19). The coefficients Y_i are the generalised/modal displacements, where the modal displacements are a function of time, and the mode shape is a function of position.

$$y = Y_1\varphi_1 + Y_2\varphi_2 + Y_3\varphi_3 + \cdots + Y_N\varphi_N = \sum_i Y_i\varphi_i \tag{3-19}$$

Equation (3-19) permits transformation on the equations of motion as modal displacements instead of its original degrees of freedom, as shown in Equation (3-20), where Y is the vector of modal displacements.

$$M\ddot{Y} + C\dot{Y} + KY = \varphi^T m\iota\ddot{x}_g \tag{3-20}$$

Since M, C and K are diagonal matrices due to their orthogonality properties of the modes, the N equations in Equation (3-20) are uncoupled. Hence, it has the form of an equation or Equation (3-21) analogous to Equation (3-22) for an SDOF system.

$$M_i\ddot{Y}_i + C_i\dot{Y}_i + K_iY_i = L_i\ddot{x}_g \tag{3-21}$$

$$\ddot{Y}_i + 2\xi\omega_i\dot{Y}_i + {\omega_i}^2Y = \frac{L_i}{M_i}\ddot{x_g} \tag{3-22}$$

where

$$L_i = \sum_j m_j\varphi_{ij}$$

$$M_i = \sum_j m_j{\varphi_{ij}}^2$$

$i = mode\ shape$

$j = degrees\ of\ freedom\ of\ a\ structure$

$\varphi_{ij} = value\ of\ mode\ shape\ i\ at\ DOF\ j$

$L_i = earthquake\ excitation\ factor$

$M_i = modal\ mass$

$\frac{L_i}{M_i}$ is a dimensionless factor ratio of the MDOF structural response in a specific mode similar to an SDOF system with the same mass and period. Since the system is linear and the ground acceleration is being scaled by a factor of $\frac{L_i}{M_i}$, the structural response will be scaled of a similar amount. Hence, the acceleration amplitude in mode i is $\frac{{L_i}^2}{M_i}S_{ei}$ and the maximum acceleration of DOF j in mode i is as in Equation (3-23).

$$\ddot{x}_{ij}(\max) = \frac{{L_i}^2}{M_i}S_{ei}\varphi_{ij} \tag{3-23}$$

Analogous to Equation (3-13), the displacement can be obtained as in Equation (3-24).

$$y_{ij}(\max) = \frac{{L_i}^2}{M_i} S_{ei} \varphi_{ij} . \frac{{T_i}^2}{4\pi^2} \tag{3-24}$$

Simply multiplying the acceleration by its mass, Equation (3-25) is obtained to find the horizontal forces on mass j in mode i.

$$F_{ij}(\max) = \frac{{L_i}^2}{M_i} S_{ei} \varphi_{ij} m_j \tag{3-25}$$

The total horizontal force on the structure in mode i (also known as base shear) can be obtained by summing all the storey forces that give rise to Equation (3-26).

$$F_{bi}(\max) = \frac{{L_i}^2}{M_i} S_{ei} \tag{3-26}$$

The ratio of $\frac{{L_i}^2}{M_i}$ is the effective modal mass. It is thought of as the amount of mass participating in the structural response of a specific mode. The sum of this amount of all vibration modes will equate to the structure's total mass. The overall response of the structure can be obtained by combining Equation (3-23) to Equation (3-26) with each vibration mode. The effective modal masses should be at least 90% of the total structural mass.

In the equivalent static analysis of the MDOF system, it may be possible to estimate the dynamic behaviour through a single mode. For a single mode of vibration, as in Equation (3-25), the force at level j is proportional to the product of mass and mode shape of level j. In other terms, the modal parameter does not vary with position. Estimating the fundamental mode period T_1 is often done through a simplified approximation method rather than a detailed dynamic analysis as in Equation (3-18). The equivalent static analysis is permitted if $T_1 < 4T_c$ where T_c is the period at the end of the constant acceleration part of the design response spectrum. If these 2

conditions are not satisfied, the multi-modal response spectrum method outlined above must be utilised. For the calculated structural period, the spectral acceleration S_e can be acquired from the design response spectrum. The base shear can now be assumed as Equation (3-27).

$$F_b = \lambda m S_e \tag{3-27}$$

Analogous to Equation (3-26), the ratio ${L_i}^2/M_i$ is replaced with λm. λ is assumed as a value of 0.85 for buildings of more than 2 storeys with $T_1 < 2T_c$ or a value of 1 is otherwise. The total horizontal load is distributed across the building height in proportion to the (mass × mode shape). EC8 assumes the first mode shape to be a straight line where the displacement is proportional to its height for simple regular buildings. The storey force at level k can be defined as in Equation (3-28), where z represents the storey height. The member forces and deformation can be calculated through static analysis.

$$F_k = F_b \frac{z_k m_k}{\sum_j z_j m_j} \tag{3-28}$$

3.3 Validation of the Numerical Model

This subchapter is to validate the numerical model analysed in commercial software like ASNYS, GSA OASYS and SAP2000. Due to time and cost constraints, they were verified against MATLAB code and similar model available in textbooks or research papers. Parameters are maintained to ensure reliable results. A slight numerical deviation is expected as different software may apply slightly different modelling techniques. Since there is a lack of experimental laboratory studies, numerical model validation is necessary to ensure that the results obtained consistently deliver reproducible results using established and accepted methodology.

3.3.1 ANSYS (Finite Element Method and Topology Optimisation)

ANSYS was utilised in the study for its multiphysics software. It provides the flexibility of analysing various engineering problems/systems through a multiphysics environment seamlessly under one integrated software environment, ensuring the modelling workflow remains the same throughout the modelling process. ANSYS Workbench was utilised for the FEM analysis and the topology optimisation analysis instead of the newer platform ANSYS Discovery AIM because Ansys Workbench remains the choice for many research institutions at the time of writing.

3.3.1.1 Finite Element Model

The model to be validated is a cantilever beam of 200mm x 40mm x 1mm (length x depth x thickness) with a single point load at its free end of the cantilever beam model. The beam is assumed to be a single isotropic linear-elastic solid steel section. It has a span to depth ratio of 1/5. The material assumed is structural steel with Young's modulus of 200GPa or 200000N/mm^2 and a Poisson's ratio of 0.3. The meshing was set to program-controlled. The stress-strain curve for the base cantilever beam model is shown in Figure 3-4. The free end of the beam is loaded with a single point load of 1000N. This section is separated into two sections, validating the MATLAB finite element model with Euler-Bernoulli's beam deflection theory, and the other is the validation of MATLAB finite element with other commercial analysis software.

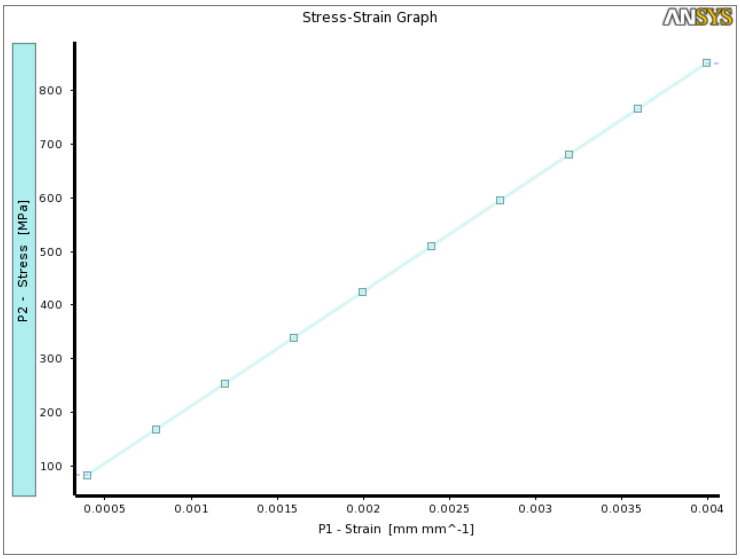


Figure 3-4: Stress-strain curve for the cantilever beam base model (200,40,1)mm

Part 1: Validation of MATLAB FEM against Euler Bernoulli's beam deflection theory

This section presents the validation between the MATLAB FEM and Euler Bernoulli's beam deflection theory. The number of elements used in the x and y direction is 30 units and 10 units, respectively, as shown in Figure 3-5(a). Figure 3-5(b) shows the deflection accuracy of the MATLAB FEM against Euler Bernoulli's beam deflection theory. A degree of truncation error is expected as 2D elements are linearly interpolated in between nodes. The theoretical maximum deflection is 2.5mm, and the deflection for MATLAB FE is 2.5556mm. The percentage error is about 2% which is marginal. The theoretical maximum bending stress is 750MPa, and the equivalent stress for MATLAB FE is 682.274MPa. The percentage error is about 9% which is acceptable.

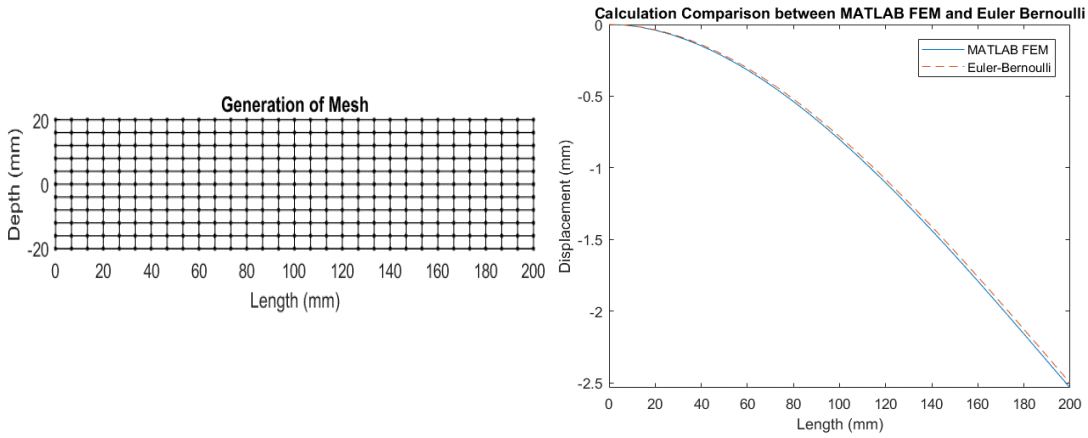


Figure 3-5: (a) Mesh (b) Comparison between MATLAB FEM and Euler Bernoulli

Part 2: Validation of MATLAB FEM against ANSYS Workbench

This section presents the validation between the MATLAB FEM and ANSYS Workbench. The number of elements used in MATLAB in the x and y direction is 30 units and 10 units, respectively. Figure 3-6 and Figure 3-7 show the deflection plot and the stress plot of the MATLAB and ANSYS. A degree of truncation error is expected when comparing the 2D element modelling in MATLAB against the 3D element modelling in ANSYS. The deflection value for the MATLAB is 2.5556mm, while the deflection value for ANSYS Mechanical is 2.5937mm. The percentage error is about 1.5% which is marginal. The equivalent stress for MATLAB is 682.274MPa, while the equivalent stress for ANSYS is 754.32MPa. The percentage error is about 9.5% which is acceptable. In this case of the ANSYS, compared to the theoretical value, the deflection value and the stress value are 2.5mm and 750MPa, respectively. The percentage error between the two is about 4% and 0.5%, respectively. In this example, ANSYS is much closer to the theoretical stress value than MATLAB.

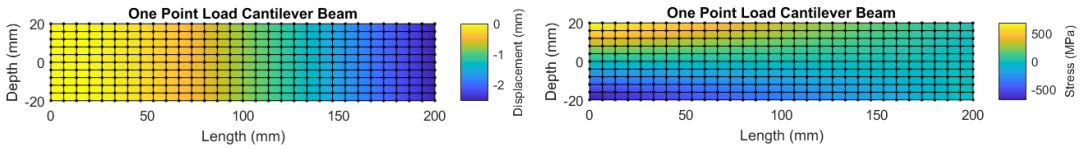


Figure 3-6: MATLAB FEM plots (a) Displacement (mm) (b) Stress (MPa)

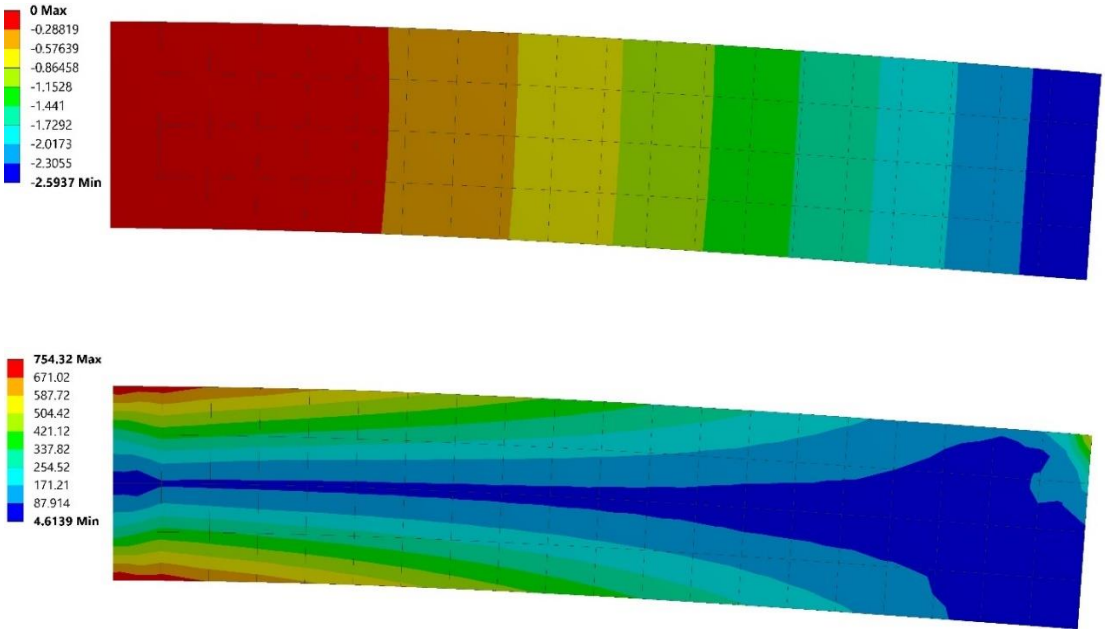


Figure 3-7: ANSYS Workbench plots (a) Displacement (mm) (b) Stress (MPa)

3.3.1.2 Topology Optimisation

Topology optimisation is used to identify the best material distribution within a specified design space, set of loads, boundary conditions, optimisation goal (e.g. mass, compliance) and constraints (e.g. stress, displacement) through a process of removing non-essential material from a solid block of the defined shape. The model validated in this example is a 160mm x 100mm x 1mm cantilever beam with a 3kN single point load at the centre of the free end of the cantilever beam, as shown in Figure 3-8. The beam is assumed to be a linear-elastic isotropic solid steel section. The material

assumed is to be structural steel with a Poisson's ratio of 0.3. The retained volume ratio is set to 0.5 of the domain area. The topologies obtained are shown in Figure 3-9.

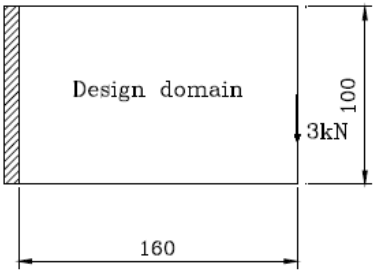


Figure 3-8: Cantilever beam 160mm x 100mm x 1mm

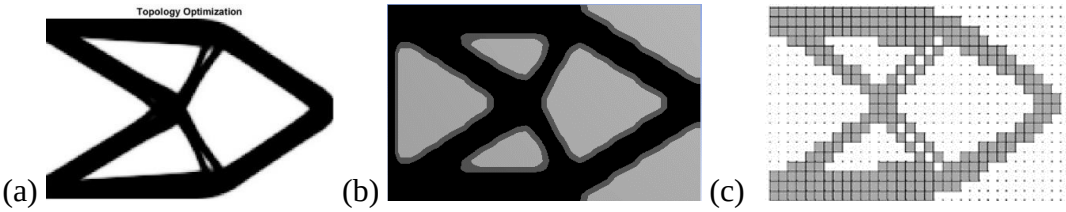


Figure 3-9: Topology plots (a) MATLAB (b) ANSYS (c) results by (Chu *et al.*, 1996)

MATLAB requires 106 iterations to reach its final solution, while ANSYS requires 151 iterations. The topology obtained in MATLAB and ANSYS shows a similar pattern as obtained by Chu *et al.* (1996). The final volume obtained in both the MATLAB and COMSOL is about 50% of the initial volume. Hence, the numerical model in ANSYS is reliable and well correlated with other published work as well as the MATLAB script.

3.3.2 GSA OASYS (Trusses)

GSA Oasys was utilised in the study because of its interface to create and sculpt models with ease while providing quick and accurate results. The parameters and the details of the truss problem analysed in GSA are the same as the truss model in Chapter 6.4.

The truss model analysed to validate the GSA software is based on a Pratt truss-like structure, as shown in Figure 3-10. It is a 2m x 4m structural steel truss with a conventional pin and roller support and a solid cross-sectional area of approximately 3.142cm^2 (diameter of 20mm). The modelled truss is stable and internally determinate. The structural steel has a Young's Modulus of 200GPa. The analysis is set to "bar element". The imposed load applied in this analysis are 15000kN downwards and 10000kN to the right, as shown in Figure 3-10.

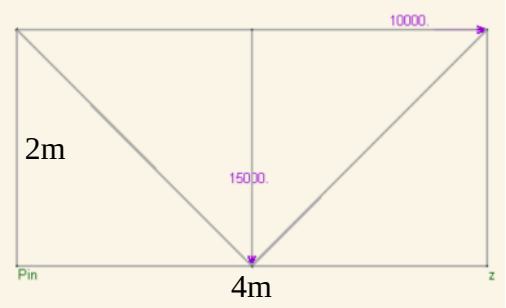


Figure 3-10: Pratt truss-like structure 2m x 4m

Figure 3-11 shows the deflection comparison of the truss model between the two analysis conducted under MATLAB and GSA. The deflection results are shown in Table 3-2. Both GSA and MATLAB show similar stress results, and that the maximum stress experienced in the truss is 56270 N/mm^2 in element 6. The difference between the results of the two software is marginal. The full results output is shown in Appendix A.b.c. Therefore, the model is validated.

Table 3-2: Comparison of nodal displacements between MATLAB and GSA

Displacement (mm)	**MATLAB**		**GSA**	
Node	x	Y	x	y
1	0	0	0	0
2	1.0072	-0.07958	0.9826	0.07764
3	0.31831	-0.99355	0.3105	0.9693
4	0.92762	-0.99355	0.9050	0.9693
5	0.31831	0	0.3105	0
6	0.84805	0.39789	0.8274	0.3882

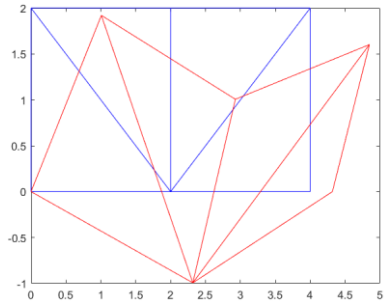
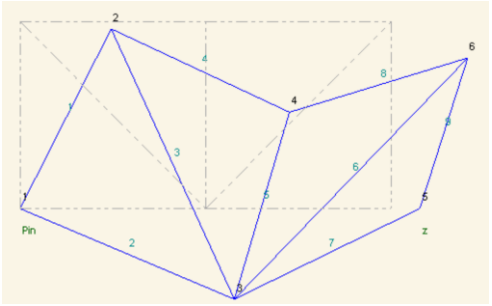
(a)  (b) 

Figure 3-11: Truss displacement plots (a) MATLAB (b) GSA

3.3.3 SAP2000 (Seismic Analysis of Multistorey)

For validation purposes, an example from the Eurocode 8 worked example report was used to verify the assumptions applied in the analysis through SAP2000. The complete details of the worked example can be found in Philippe *et al.* (2012). Slabs of grade C30/37 were applied for both models with a thickness of 150mm. The joints of the beam to column connection are assumed rigid where the beam meets the centre of the column. A diaphragm constraint is applied on all floors to create a link between joints located within a plane to ensure they move together as a planar diaphragm. The seismic mass utilised in the analysis is associated with a load combination of G + $\Psi_{E,i}$Q where

$\Psi_{E,i}$ is taken as 0.3. The moment frame steel structure analysis considers both the Equivalent Lateral Force Method and Response Spectrum Analysis in both studies. For the auto lateral load, Eurocode 8 2004 was applied. The seismic evaluation considered is in the X-direction of the plan. The correction factor, lambda, eccentricity ratio, modal damping and C_t defined are 0.85, 0.05, 0.05 and 0.085 respectively. For the response spectrum analysis, the modal and directional combination/type utilised are CQC and SRSS. A 90% mass participation criteria are used as per code to ensure the modal analysis sufficiently captures the response of all modes of vibration contributing to the global response of the structure.

The reference model is based on the publication in the Joint Research Centre (European Commission) Scientific and Technical Research Report (Philippe *et al.*, 2012). The building is a 30m x 24m, 6 story steel moment frame. The plan and column orientation are shown in Figure 3-12. The structural steel strength used is S355. The slab defined has no stiffness, mass or weight and only carry load directly to the frames. The design response spectrum utilised are as follows: Type 1 spectrum, soil type B, reference peak acceleration of 2.6m/s^2, importance factor of the building is 1 and a behaviour factor of 4.

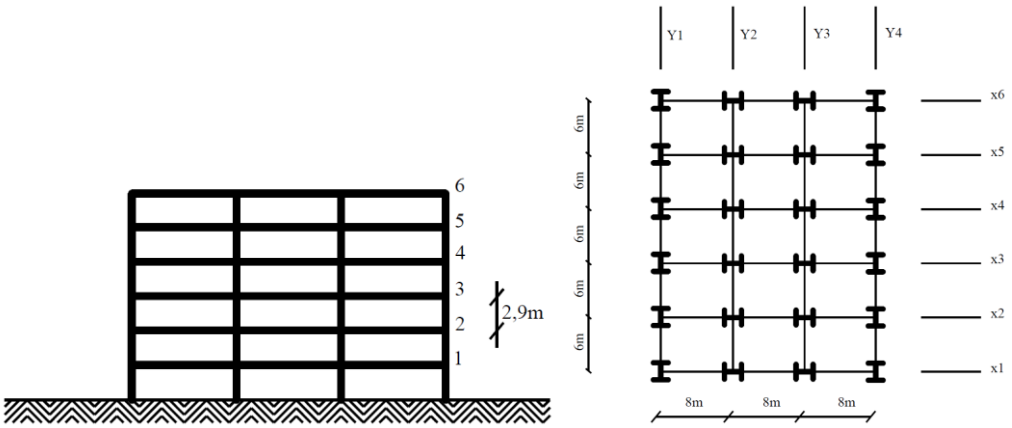


Figure 3-12: Reference model EC8 plan layout and column orientation (Philippe *et al.*, 2012)

Table 3-3 and Table 3-4 show the loads and frame sections applied in the reference study. IPE450A frame section is not available in the default library. Thus, the manual input of the frame section is required. However, a software bug in the SAP2000 prevented accurate calculated value of the second moment of area (I) and plastic section modulus (Wpl) in the IPE450A beam, as shown in Appendix D.a.a. The calculated I and Wpl are 28160 x10^4 mm^4 and 1416 x10^3 mm^3. Hence, it is reasonable to find a small difference in the results between the SAP2000 and the reference model. The analysis includes the self-weight of the structure.

Table 3-3: Reference model EC8 applied load

Loading Type	**Load**
Floor	5kN/m^2
Wall	3kN/m
Service	3kN/m^2

Table 3-4: Reference model EC8 frame section details

Frame section		**I**	**Wpl**
Beam in the x-direction	IPE500	48200x10^4 mm^4	2194x10^3 mm^3
Beam in the y-direction	IPE450A	29760x10^4 mm^4	1494x10^3 mm^3
Column	HE340M	Strong axis: 76370x10^4 mm^4 Weak axis: 19710x10^4 mm^4	Strong axis: 4718x10^3 mm^3 Weak axis: 1953x10^3 mm^3

The moments generated from the equivalent lateral load (Eqx) and response spectrum (RS) analysis through SAP2000 are shown in Figure 3-14, while the reference model is shown in Figure 3-12. The moment results are shown in separate figures due to the orientation of the column as the local axis is different between the outer and inner

columns, as shown in Figure 3-12. The enlarged figures can be found in Appendix D.a.a.

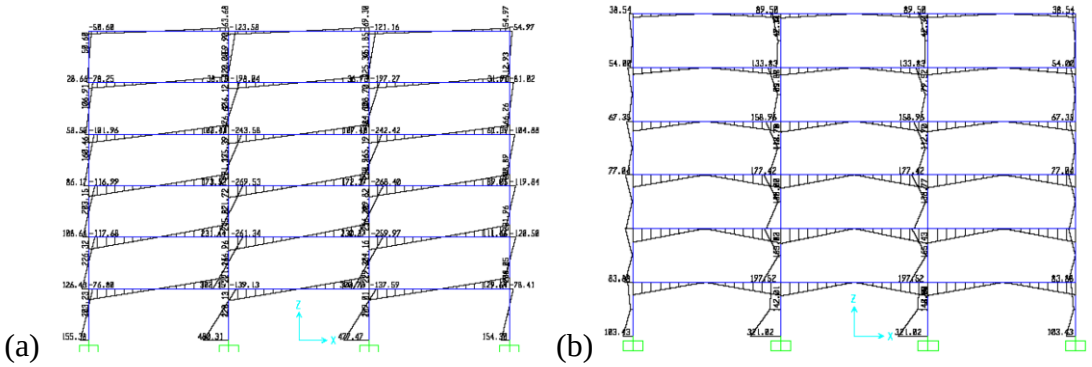


Figure 3-13:Reference model EC8 bending moment diagram (a) Eqx (b) RS (Philippe *et al.*, 2012)

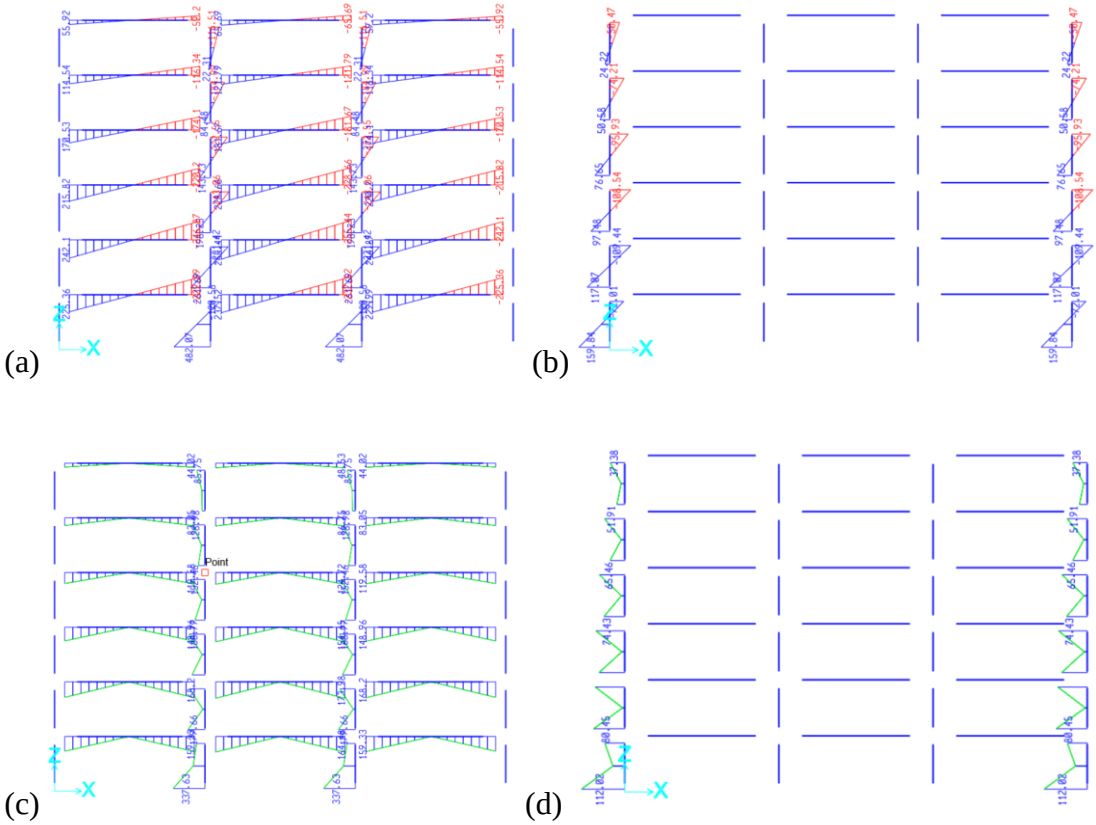


Figure 3-14: SAP2000 bending moment diagram (a)&(b) Eqx ;(c)&(d) RS

For comparison purposes, Table 3-5 shows a selected set of moment obtained from the equivalent lateral method and the response spectrum analysis. The corresponding building weight and base shear in the reference model are 30600kN and 2705kN, whereas in SAP2000, the seismic weights and response spectrum base shear are 32480.82kN and 2668.9kN. The difference between the two results is less than 10%.

Table 3-5: Results of the EC8 reference model and SAP2000

	Equivalent Lateral Load		**Difference (%)**	**Response Spectrum**		**Difference (%)**
	Reference	SAP2000		Reference	SAP2000	
Bottom	480.31	482.07	0.37	321.02	337.63	5.17
Middle	-269.53	-243.06	9.82	177.42	168.77	4.88
Top	-123.58	-116.51	5.72	89.50	85.75	4.19

The difference between the obtained results and the reference model for both studied models is due to the software's calculated assumption and the lack of detailed information to create an accurate model of the studied structure. Since the difference between the obtained value and the reference model is small, the assumptions applied in the SAP2000 can be assumed to be sound.

Chapter 4 Comparison of Various Cantilever Beam Geometries under Transverse Loading

From the literature, it was found that there is a lack of research information in the usage of the tree buttress shape profile in mechanical and structural components. Hence, further study in this subject is required. Geometry plays a pivotal role in the stability of any structures, and for solid mechanics, it is often related to its shape and size. Hence, the structure's geometrical design is often associated with the amplification effects of a loading condition on the structure. In this chapter, a study was conducted on the effects of various cantilever beam geometries to improve structural performance. ANSYS workbench was used for the analysis.

A parametric study was conducted using ANSYS to identify and capture the behaviour of adding a triangle projection support on the bottom face of the cantilever beam that follows the Method of Tensile Triangles-MTT shape profile. It is then compared with the typical/traditional cantilever geometry method to determine whether engineers can modify the commonly used cantilever for better deflection resistance against the amount of material required (cross-sectional area required and additional depth of cantilever).

4.1 Details of the Finite Element Model

The following finite element analysis describes mainly the deflection aspect of each model. For simplicity, the chosen model of analysis is a purely fixed cantilever structure under a linear-elastic isotropic condition to capture and identify the behaviour of adding a triangle projection support on the bottom face of the cantilever beam that follows the Method of Tensile Triangles–MTT shape profile. This is then compared to

the common/traditional cantilever geometry methods to determine whether engineers can improve the commonly used cantilever. The basis of comparison is the deflection resistance against the amount of material required (cross-sectional area/volume and depth of cantilever).

A total of 276 specimens were modelled using Ansys Workbench Mechanical APDL version 17.2 student edition under settings of 3D solid analysis, isotropic, linear-elastic and program-controlled meshing. The deflection value used in the analysis is the total deflection that includes deflection in the x, y and z direction. The deflection value in the x and z direction are minimal and negligible. The base model defined in this analysis is a solid steel cantilever section with a dimension of 200mm x 40mm x 1mm. The models were analysed as a single solid steel section to eliminate any geometrical or discontinuity effect on the structure. The material modelled is an ANSYS default library of structural steel with Young's modulus of 200GPa and a Poisson's ratio of 0.3.

The base cantilever structure/model analysed as illustrated in Figure 4-1 has a depth to span ratio of 1/5 with a deflection of nearly twice the allowable deflection limit set by EC3 (for a single point free-end loading of 1000N). The purpose is to understand and determine the optimal sizing and shape of the projection beneath the cantilever beam. The specimens were tested under the following separate loading condition (described in section 4.1.2), one point downwards (Free-End, Top Face, 1000N) loading and a triangular pressure load (5MPa, Downwards, Top Face) with the maximum load at its free end. The base model was then compared between the different cantilever beam geometry to determine the effectiveness of reducing deflection.

4.1.1 The Geometry of the Model Specimens

A total of five specimens are tested in this analysis as follows:

1. Simple Cantilever Beam (Base Model) as shown in Figure 4-1.

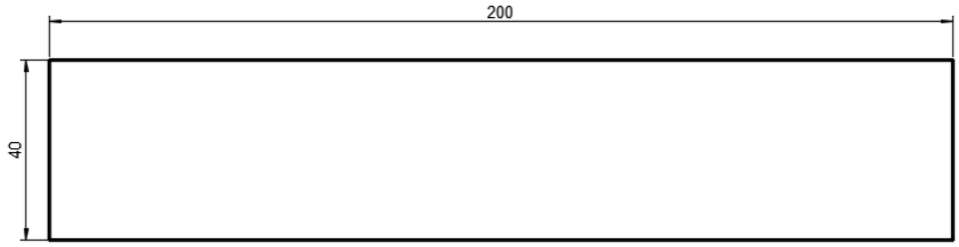


Figure 4-1: Simple Cantilever Beam (Base Model)

2. Cantilever Beam with Increased Depth (Traditional Method) as shown in Figure 4-2.

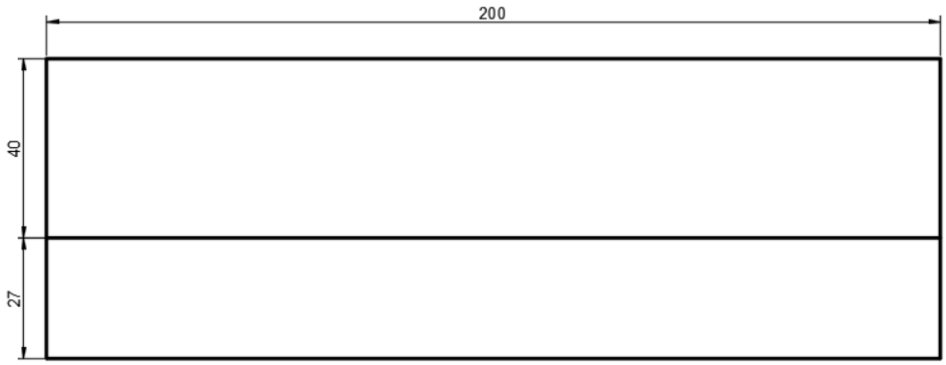


Figure 4-2: Cantilever Beam with Increased Depth (Traditional Model)

3. Cantilever Beam with a Tapering Triangle at the Bottom Face (Traditional Method) as shown in Figure 4-3.

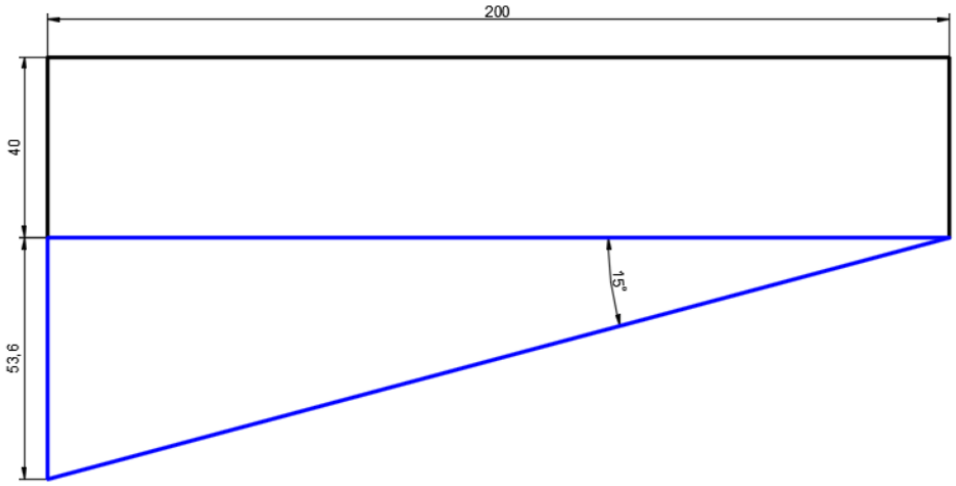


Figure 4-3: Cantilever Beam with a Tapering Triangle at the Bottom Face (Traditional Method)

4. Cantilever beam with a triangle projection following the Method of Tensile Triangles' shape profile (Tree Buttress) as shown in Figure 4-4.

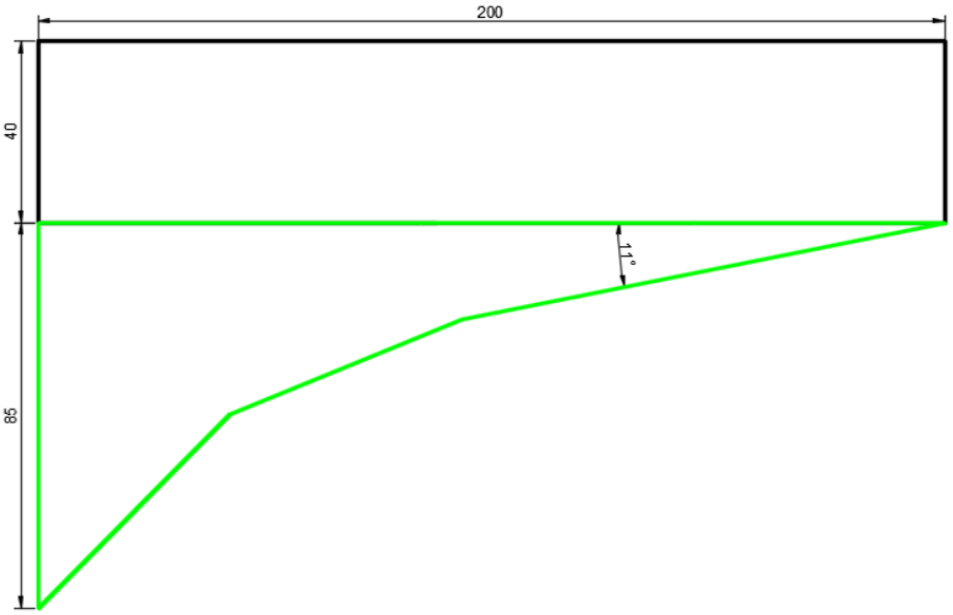


Figure 4-4: Cantilever Beam with a Triangle Projection following the Method of Tensile Triangles' Shape Profile (Tree Buttress)

5. Cantilever Beam with a Triangle Projection using the Method of Tensile Triangles' Rule of Thumb, as shown in Figure 4-5.

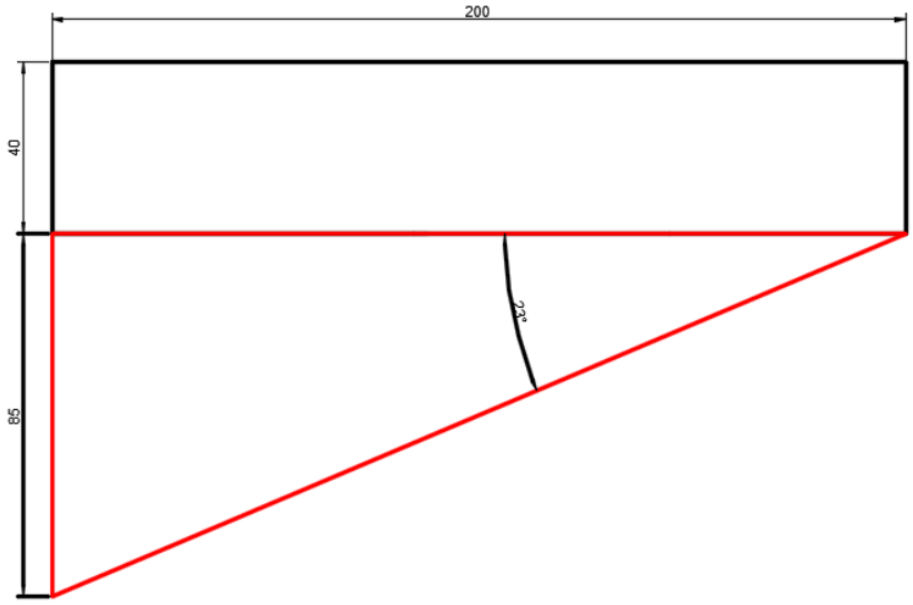


Figure 4-5: Cantilever Beam with a Triangle Projection using the Method of Tensile Triangles' Rule of Thumb

Figure 4-2 through Figure 4-5 show the maximum allowable dimension of each cantilever projection design at its bottom face, the dimensions of the projection are varied. Various highlighted dimensions and sizing of each cantilever design are shown alongside its results in section 4.2.

4.1.2 Loading Conditions of Models

The load case analysed are as follows:

1. One Point Load (Downwards, Free-End, Top Face, 1000N)

   The load case is a single point load acting on the top surface at the edge of the free-end, as shown in Figure 4-6. The load case simulated in this analysis is to create a maximum deflection on a cantilever beam.

However, the result obtained may not be realistic (in actual practice) because any point load (realistically) consists of a pressure loading on a small/finite area.

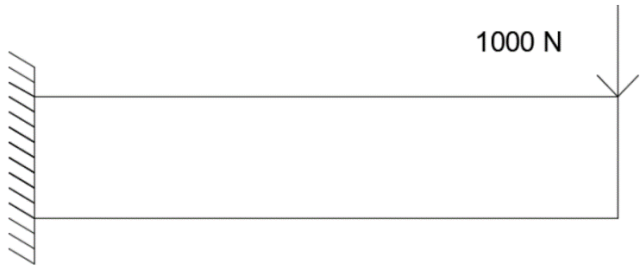


Figure 4-6: One Point Load (Downwards, Free-End, Top Face, 1000N)

2. Triangular Pressure Load (5MPa, Downwards, Top Face, Max at Free-End)

The load case closely simulates an actual working condition or a simplified wind loading condition on a tree structure. The simulated analysis model does not take into consideration of different crown size and distribution of the tree. Therefore, for simplicity, the load case defined is a varying pressure load (triangular) of 5MPa acting downwards on the top surface of the cantilever beam with a maximum loading at its free-end, as shown in Figure 4-7.

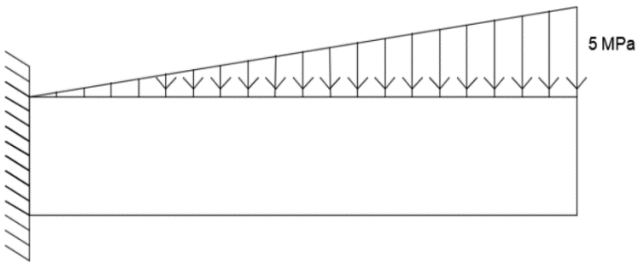


Figure 4-7: Triangular Pressure Load (5MPa, Downwards, Top Face, Max at Free-End)

4.2 Deflection Performance of the Various Cantilever Beams

The current study is to determine how one can improve the performance of current structures by introducing nature's design in structures. The analysis starts by determining whether the shape of projection under a simple cantilever beam used by many civil engineers around the world effectively reduces deflections and stress. The analysis further determines whether nature's design is the answer or solution to enhancing structural performance.

The analysis was broken down into two major sections and accompanied by multiple subsections:

1. Deflection
    a. Cantilever beams within the designed limit defined by the National Annex 2.23 Clause 7.2.1(1) B.
2. Stress

The analysis was divided down into three sections:

1. Improvement and Limitation of the Cantilever Beams
2. Suggested Optimum Values through the 3 Axes Graph Method
3. Workable/Acceptable Range of Cantilever Design Parameter

To determine its improvement and limitation of the cantilever design, section 1 covers the following items:

1. Additional Depth of Cantilever within Allowable Deflection Limit
2. Maximum Additional Cantilever Depth

The 3 axes graph method to find the suggested optimum value can be subjective; thus, this is complemented by the third section. The graph method in section 2 includes the following items:

1) Individual Geometry 1
2) Individual Geometry 2
3) Multiple Geometries
4) Multiple Geometries with Normalised Scale

Each loading condition is compared through multiple graphs directing from a different point of view and angles of the triangle to determine the range of workable/acceptable design value. Certain graph analysis methods used may not follow the standard norm of interpreting the results. The graphs evaluated in section 3 are as follows:

1) Area versus Deflection
2) Depth versus Deflections
3) Various Graphs
4) Efficiency (area/deflection versus area)
5) Performance of Cantilever (Deflection versus Area “%”)

Graphical images of each cantilever geometry are provided for comparison alongside the results to better visualise the cantilever structure itself. The results evaluation is done through the visualisation of the graph, and the values are taken on the next closest analysed value. (4) and (5) are used to provide analysis validation of the graphs.

4.2.2 Improvement and Limitation of the Cantilever Beams

4.2.2.1 Additional Depth of Cantilever within Allowable Deflection Limit

A cantilever beam with a dimension of 200mm x 40mm x 1mm (Figure 4-1) under a One Point Load (Downwards, Free-End, Top Face, 1000N) has a deflection value of 2.6436mm. Under the allowable deflection limit by EC3, the deflection limit is 1.1111mm (L/180) which is already above the allowable deflection limit by 1.5325mm or 238% higher. Therefore, the base cantilever model has failed under the required set of design limit.

The Triangular Pressure Load (5MPa, Downwards, Top Face, Max at Free-End) is not discussed in this subsection as the cantilever beam has a deflection value (0.71766mm) that is well below the allowable deflection limit defined by EC3 (1.1111mm). The results of the cantilever geometries of interest that were increased in size to meet the allowable deflection limits of L/180 as shown in Figure 4-8; Figure 4-9; Table 4-1 and L/240 as shown in Figure 4-10; Figure 4-11; Table 4-2 to have a visual idea on its geometry sizing and the efficiency of these cantilever geometries in reducing deflection.

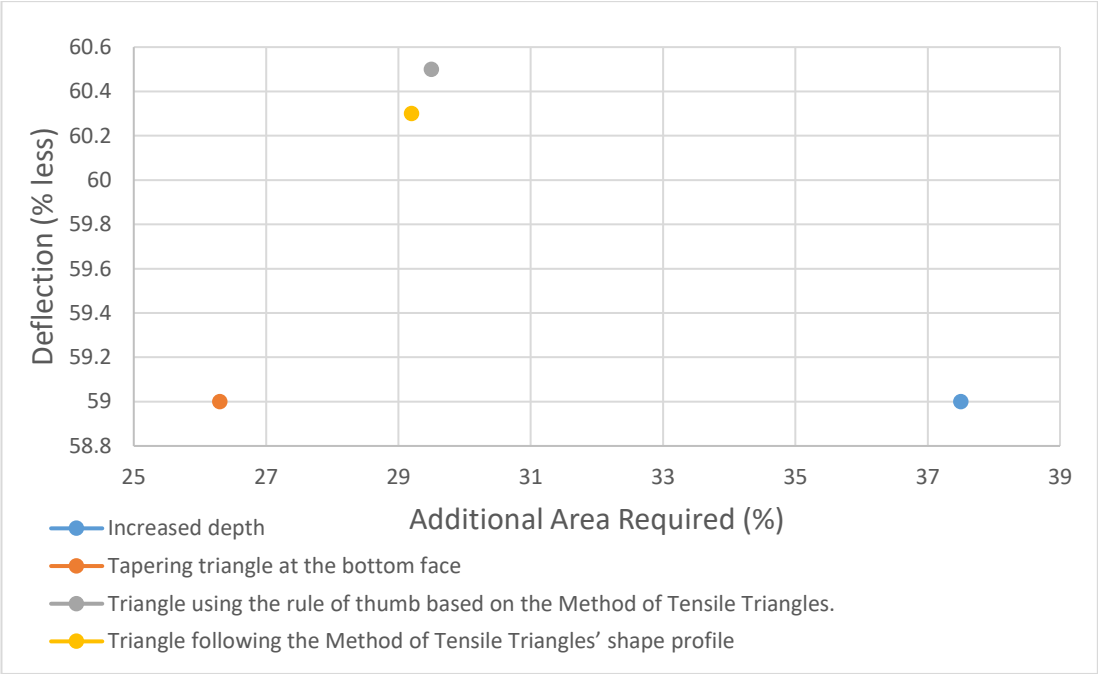


Figure 4-8: Various Cantilever Beams under the Deflection Limit of L/180; One Point Load (Downwards, Free-End, Top Face, 1000N)

Table 4-1: Various Cantilever Beams under the Deflection Limit of L/180; One Point Load (Downwards, Free-End, Top Face, 1000N)

Cantilever Beam Deflection limit (L/180)	**Additional Depth (mm)**		**Deflection (mm)**		**Required Area (mm^2)**	
Cantilever beam	0		2.6399		8000	
Increased depth	15	+37.5%	1.0828	-59%	11000	+37.5%
Tapering triangle at the bottom face	21	+52.5%	1.0818	-59%	10100	+26.3%
Triangle using the rule of thumb based on the Method of Tensile Triangles.	45	+112.5%	1.0438	-60.5%	10362.5	+29.5%
Triangle following the Method of Tensile Triangles' shape profile	55	+137.5%	1.0486	-60.3%	10338	+29.2%

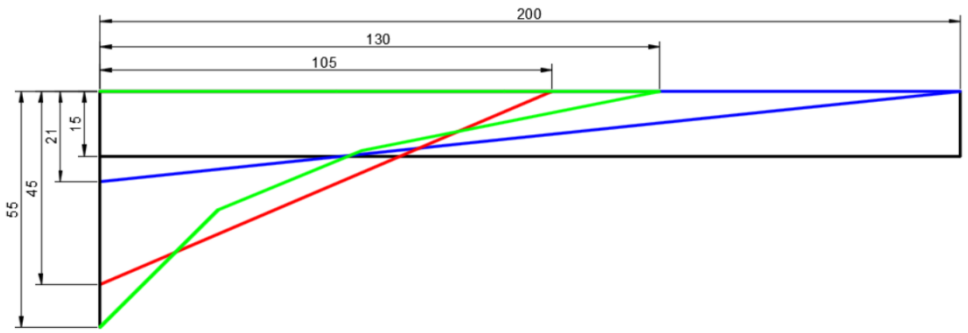


Figure 4-9: Various Cantilever Beams under the deflection limit of L/180; (1) Black: “Increased Depth”, (2) Blue: “Tapering Triangle”, (3) Red: “Method of Tensile Triangle’s Rule of Thumb”, (4) Green: “Method of Tensile Triangle’s Shape Profile”; One Point Load (Downwards, Free-End, Top Face, 1000N)

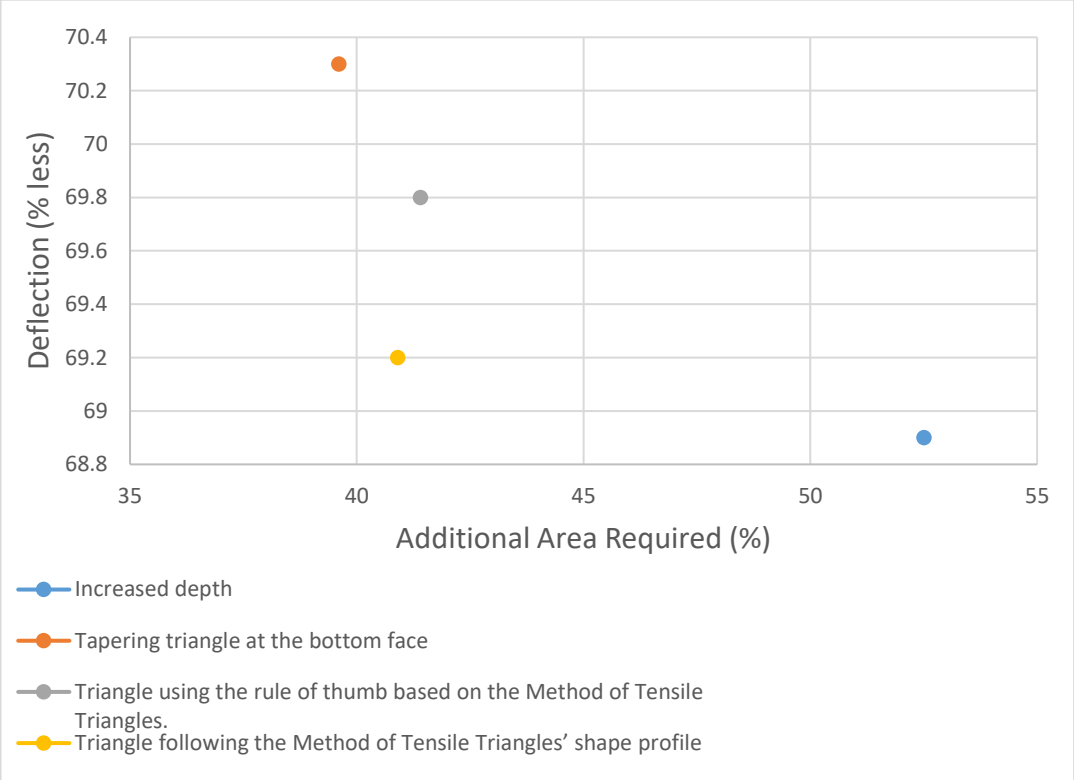


Figure 4-10: Various Cantilever Beams under the Deflection Limit of L/240; One Point Load (Downwards, Free-End, Top Face, 1000N)

Table 4-2: Various Cantilever Beams under the Deflection Limit of L/240; One Point Load (Downwards, Free-End, Top Face, 1000N)

Cantilever Beam Deflection limit (L/240)	**Additional Depth (mm)**		**Deflection (mm)**		**Required Area (mm^2)**	
Cantilever beam	0		2.6399		8000	
Increased depth	21	+52.5%	0.8229	-68.9%	12200	+52.5%
Tapering triangle at the bottom face	31.7	+79.3%	0.7832	-70.3%	11170	+39.6%
Triangle using the rule of thumb based on the Method of Tensile Triangles.	53	+132.5%	0.7967	-69.8%	11312.5	+41.4%
Triangle following the Method of Tensile Triangles' shape profile	66	+165%	0.8143	-69.2%	11269	+40.9%

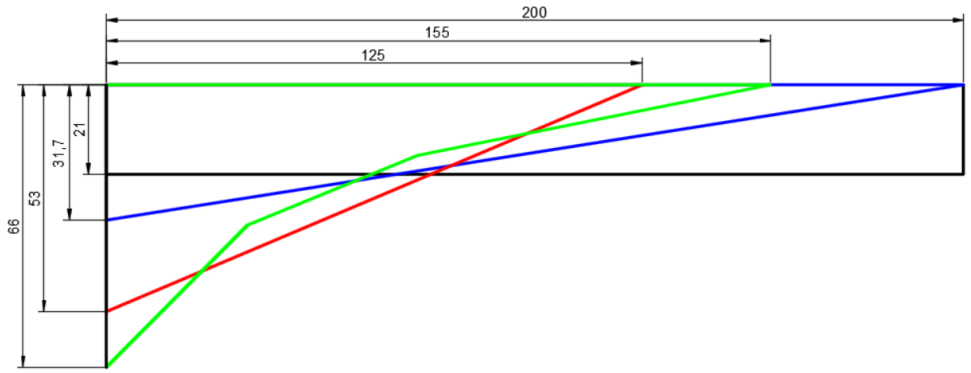


Figure 4-11: Various Cantilever Beams under the deflection limit of L/240; (1) Black: "Increased Depth", (2) Blue: "Tapering Triangle", (3) Red: "Method of Tensile Triangle's Rule of Thumb", (4) Green: "Method of Tensile Triangle's Shape Profile"; One Point Load (Downwards, Free-End, Top Face, 1000N)

The results shown in Table 4-1 and Table 4-2 shows the amount of area and additional depth required for the various cantilever beam geometries to meet the allowable deflection limit by EC3. Under this condition, the cantilever beam with the tapering triangle shows a more optimal design than the other cantilever beam geometries. This is followed by the cantilever beam with the Method of Tensile Triangles' rule of thumb as it provides better overall performance and size. The worst, as expected, is the

cantilever beam with increased depth, which can be proven through a simple bending moment diagram as illustrated in Figure 4-12. Nevertheless, cantilever beams with geometry other than the cantilever beam with increased depth have better deflection resistance and a lower amount of area required.

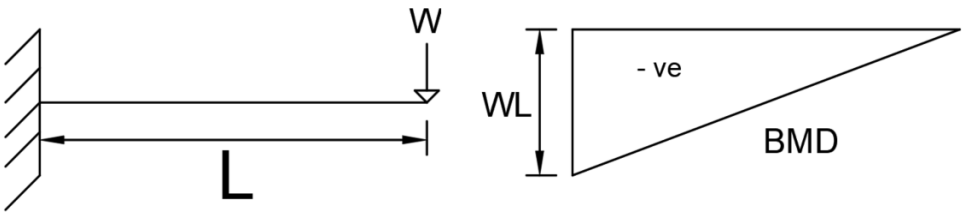


Figure 4-12: Bending Moment Diagram for a cantilever beam (single point load at free-end)

4.2.2.2 Maximum Additional Cantilever Depth

The sizing of the various cantilever beam geometries at their maximum allowable depth associated with their respective geometries are shown in Figure 4-15. They are limited by the maximum comparable area required of (+/– 13400mm^2) between cantilever geometries. The result is tabulated in Table 4-3 and shown in Figure 4-13 for a One Point Load (Downwards, Free-End, Top Face, 1000N) resulted in a similar conclusion as in the earlier subchapter 4.2.2.1. The cantilever beam with the tapering triangle still outperforms the other cantilever beam geometries, while the cantilever beam with the Method of Tensile Triangles' rule of thumb still lacks behind. However, this changes when the cantilever beams are subjected to a Triangular Pressure Load (5MPa, Downwards, Top Face, Max at Free-End), as shown in Table 4-4 and Figure 4-14. The cantilever with the Method of Tensile Triangle's rule of thumb performed better than the cantilever beam with a tapering triangle by a slight margin.

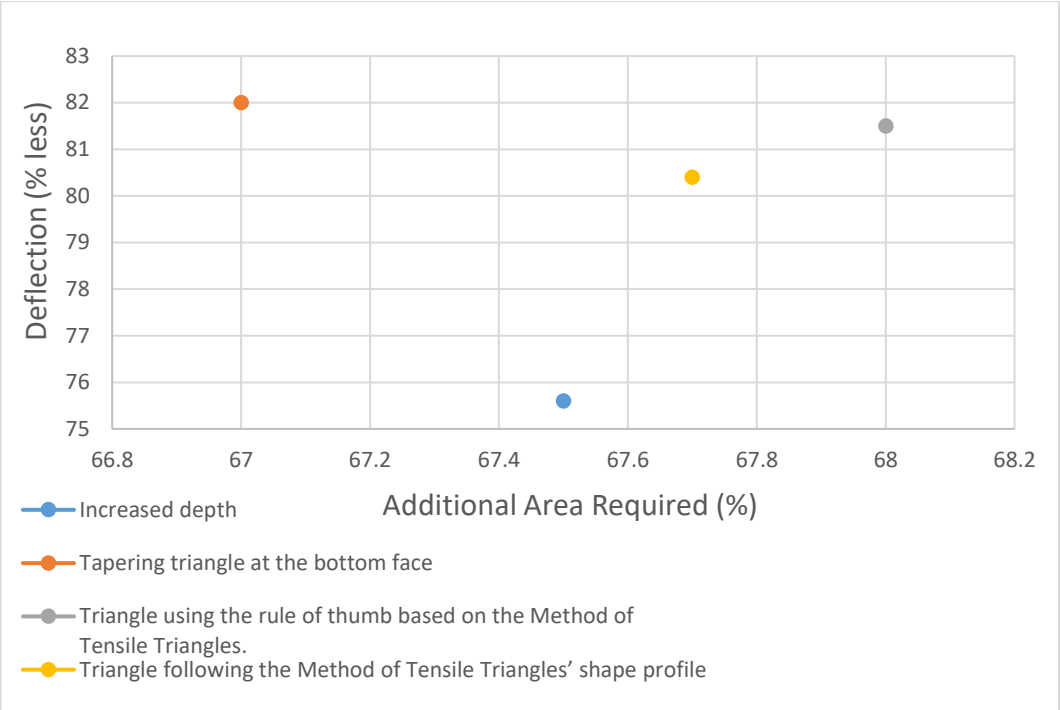


Figure 4-13: Various Cantilever Beams at Maximum Additional Cantilever Depth; One Point Load (Downwards, Free-End, Top Face, 1000N)

Table 4-3: Various Cantilever Beams at Maximum Additional Cantilever Depth; One Point Load (Downwards, Free-End, Top Face, 1000N)

Maximum Additional Cantilever Depth	**Additional Depth (mm)**		**Deflection (mm)**		**Required Area (mm^2)**	
Cantilever beam	0		2.6399		8000	
Increased depth	27	+67.5%	0.64355	-75.6%	13400	+67.5%
Tapering triangle at the bottom face	53.6	+134%	0.47454	-82%	13360	+67%
Triangle using the rule of thumb based on the Method of Tensile Triangles.	68	+170%	0.48733	-81.5%	13440	+68%
Triangle following the Method of Tensile Triangles' shape profile	85	+212.5%	0.51664	-80.4%	13418	+67.7%

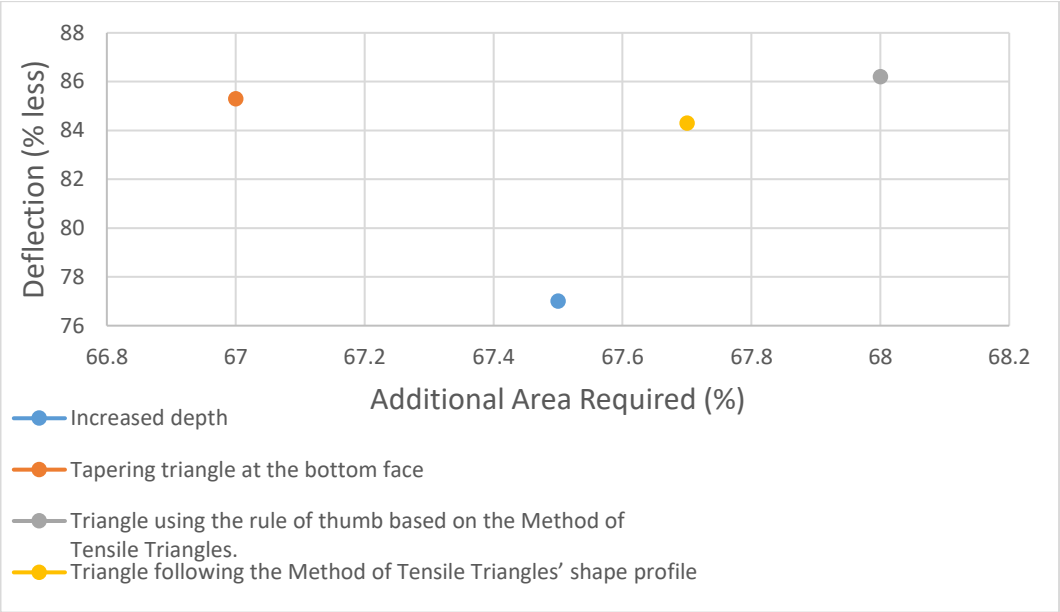


Figure 4-14: Various Cantilever Beams at Maximum Additional Cantilever Depth; Triangular Pressure Load (5MPa, Downwards, Top Face, Max at Free-End)

Table 4-4: Various Cantilever Beams at Maximum Additional Cantilever Depth; Triangular Pressure Load (5MPa, Downwards, Top Face, Max at Free-End)

Maximum Additional Cantilever Depth	**Additional Depth (mm)**		**Deflection (mm)**		**Required Area (mm^2)**	
Cantilever beam	0		0.71766		8000	
Increased depth	27	+67.5%	0.1654	-77%	13400	+67.5%
Tapering triangle at the bottom face	53.6	+134%	0.10541	-85.3%	13360	+67%
Triangle using the rule of thumb based on the Method of Tensile Triangles.	68	+170%	0.098771	-86.2%	13440	+68%
Triangle following the Method of Tensile Triangles' shape profile	85	+212.5%	0.11243	-84.3%	13418	+67.7%

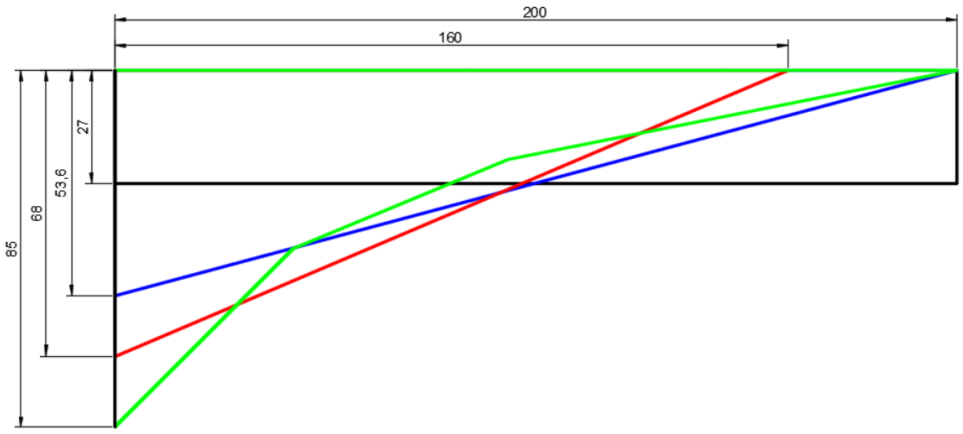


Figure 4-15: Various Cantilever Geometry at Maximum Additional Cantilever Depth; (1) Black: "Increased Depth", (2) Blue: "Tapering Triangle", (3) Red: "Method of Tensile Triangle's Rule of Thumb", (4) Green: "Method of Tensile Triangle's Shape Profile"

4.2.3 Suggested Optimum Values through the 3 Axes Graph Method

In general, the utilisation of the 3-axes graph method to find or obtain the optimum value of a certain analytical or experimental value only provides an indicative optimum value (usually for comparison purposes). It should not be used as a definitive solution as different graph axes scaling may vary its suggested optimum value.

4.2.3.1 Individual Geometry 1

The deflection versus total length of triangle versus area required graph for the Cantilever Beam with the Method of Tensile Triangles' Shape Profile are shown in Figure 4-16 and Figure 4-17. There will be no comparison for the triangle's total length as this does not apply to all the cantilever beams analysed. For the One Point Load, as shown in Figure 4-16, the required area for the cantilever with the Method of Tensile Triangles' Shape Profile is between 8887mm^2-8985.5mm^2 that intersects between 80mm-85mm of the total 200mm cantilever length at a deflection of 1.7049mm-1.6426mm. For the Triangular Pressure Load, as shown in Figure 4-17, the Method of Tensile Triangles' Shape Profile is at its most optimum deflection resistance at an area

around 8772mm^2-8887mm^2 that intersects between 75mm-80mm of the total 200mm cantilever length at a deflection of 0.44898mm-0.42362mm. The differences in the suggested optimum are due to the load reduction in the load case. For comparison between different geometries, the cantilevers can only be compared with their area, deflection and additional depth on the cantilever beam.

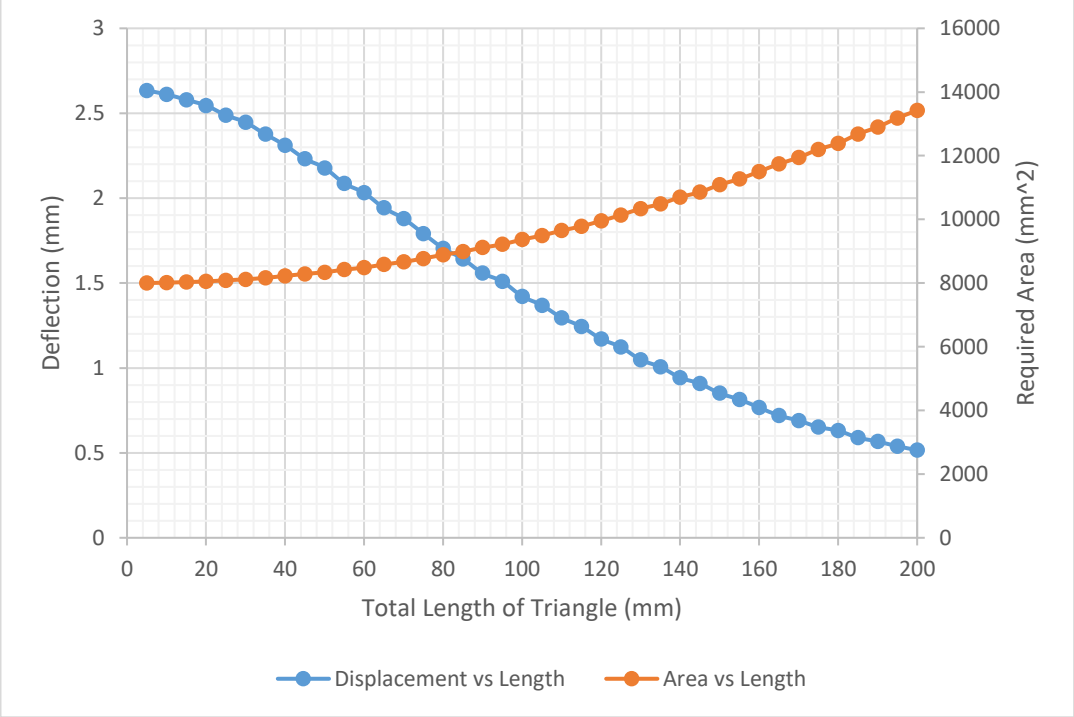


Figure 4-16: Method of Tensile Triangles Deflection vs Total Length of Triangle vs Required Area for Various Cantilever Beams; One Point Load (Downwards, Free-End, Top Face, 1000N)

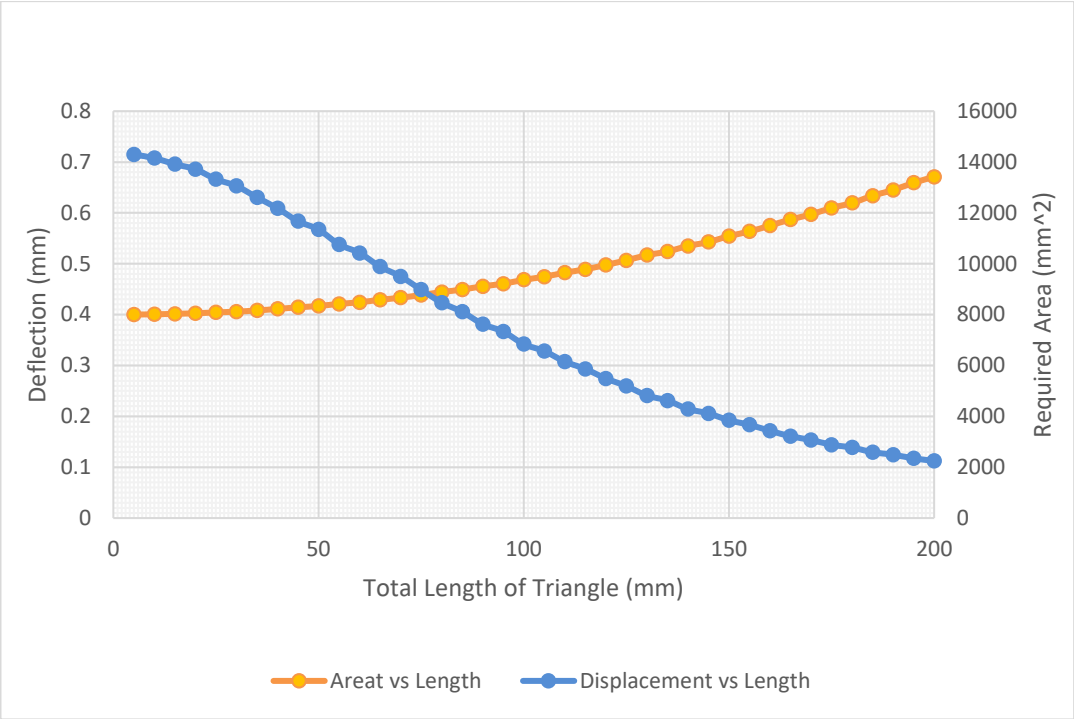


Figure 4-17: Method of Tensile Triangles Deflection vs Total Length of Triangle vs Required Area for Various Cantilever Beams; Triangular Pressure Load (5MPa, Downwards, Top Face, Max at Free-End)

4.2.3.2 Individual Geometry 2

The graphs below show the intersection for an ideal projection size in reference to its required area, deflection and its additional depth for the One Point Load in Figure 4-18, Figure 4-19, Figure 4-20 and Figure 4-21 and for the Triangular Pressure Load in Figure 4-23, Figure 4-24, Figure 4-25 and Figure 4-26. The required area defined here is the total surface area of the cantilever beam. The result obtained for the "Individual Geometry" cannot be compared directly with one another as the area required, and the axis scaling of the various model analysed are different. Hence, other graph methods are applied to assist the determination of the best effective results between the different cantilever geometries in reducing deflections.

The result summary of the data obtained for the One Point Load is shown in Table 4-5, and for the Triangular Pressure Load is shown in Table 4-6. The figures of the

respective cantilever geometry sizing are shown in Figure 4-22 and Figure 4-27, respectively. The beam with increased depth has the highest deflection compared to the other cantilever models of similar or comparable area size. The effective area required against its deflection varies between the different geometries. The additional depth required by the different cantilever geometries for One Point Load is in linear order, as shown in Table 4-5.

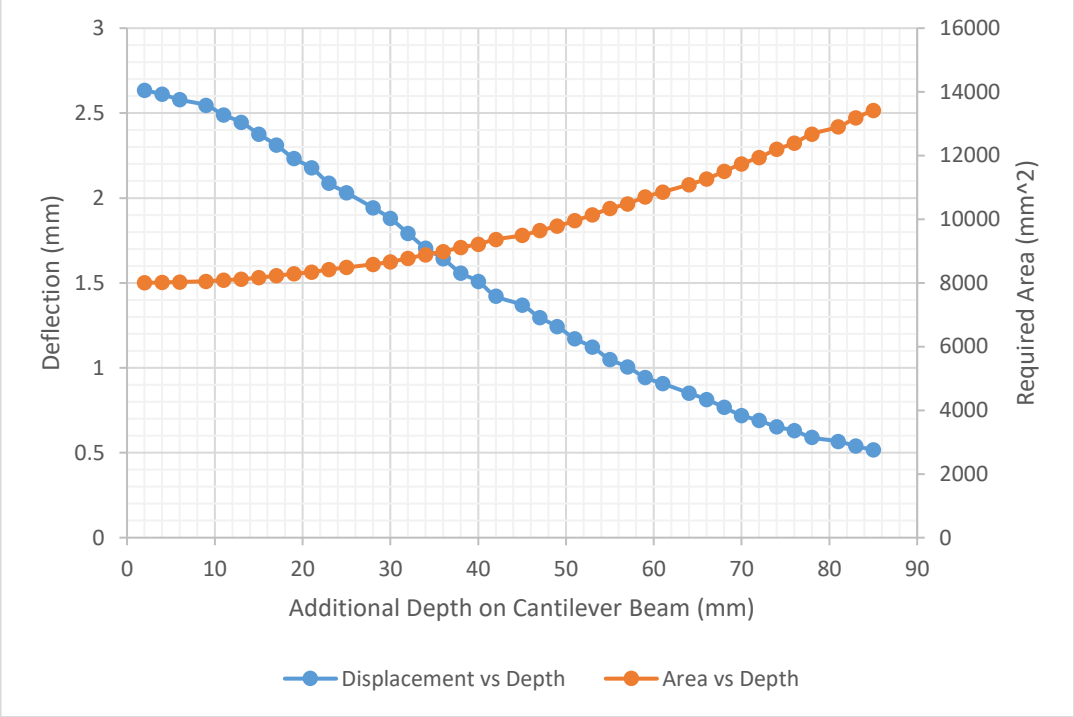


Figure 4-18: Individual graph for Cantilever with Method of Tensile Triangles' Shape Profile; One Point Load (Downwards, Free-End, Top Face, 1000N)

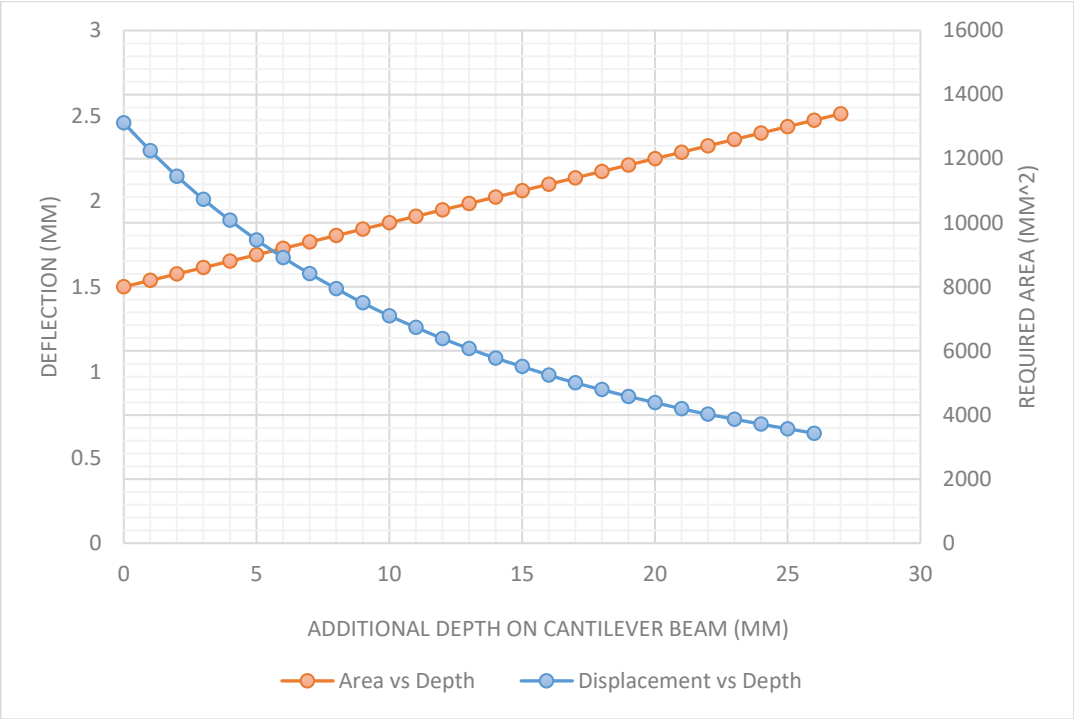


Figure 4-19: Individual graph for Cantilever with Increased Depth; One Point Load (Downwards, Free-End, Top Face, 1000N)

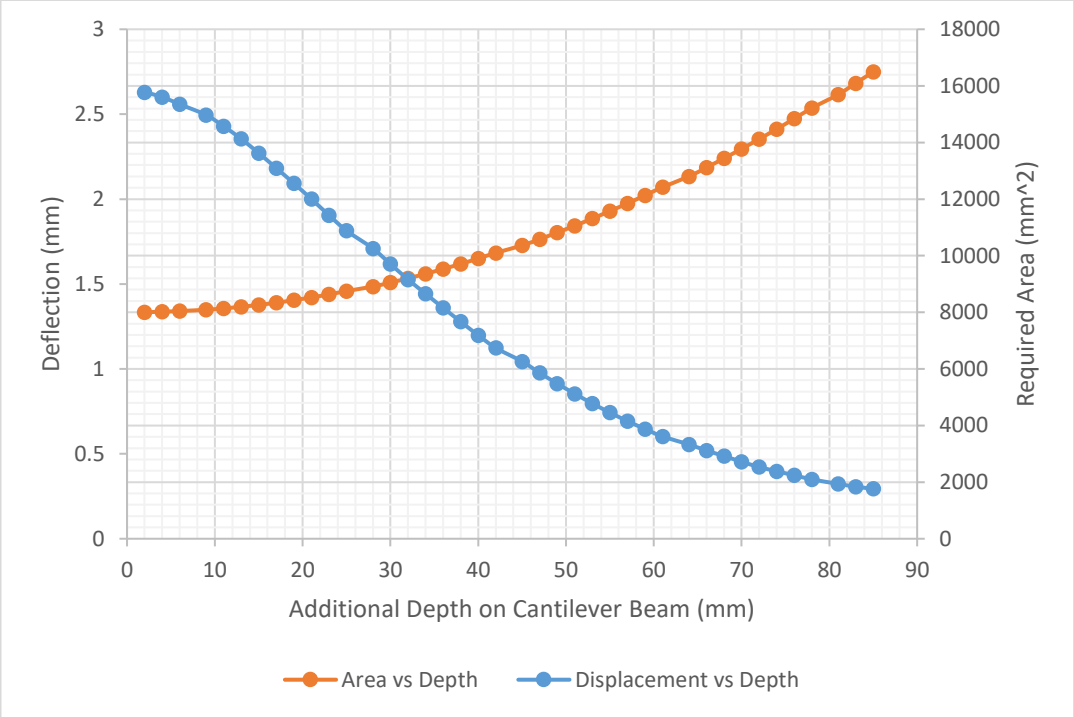


Figure 4-20: Individual graph for Cantilever with Method of Tensile Triangles' Rule of Thumb; One Point Load (Downwards, Free-End, Top Face, 1000N)

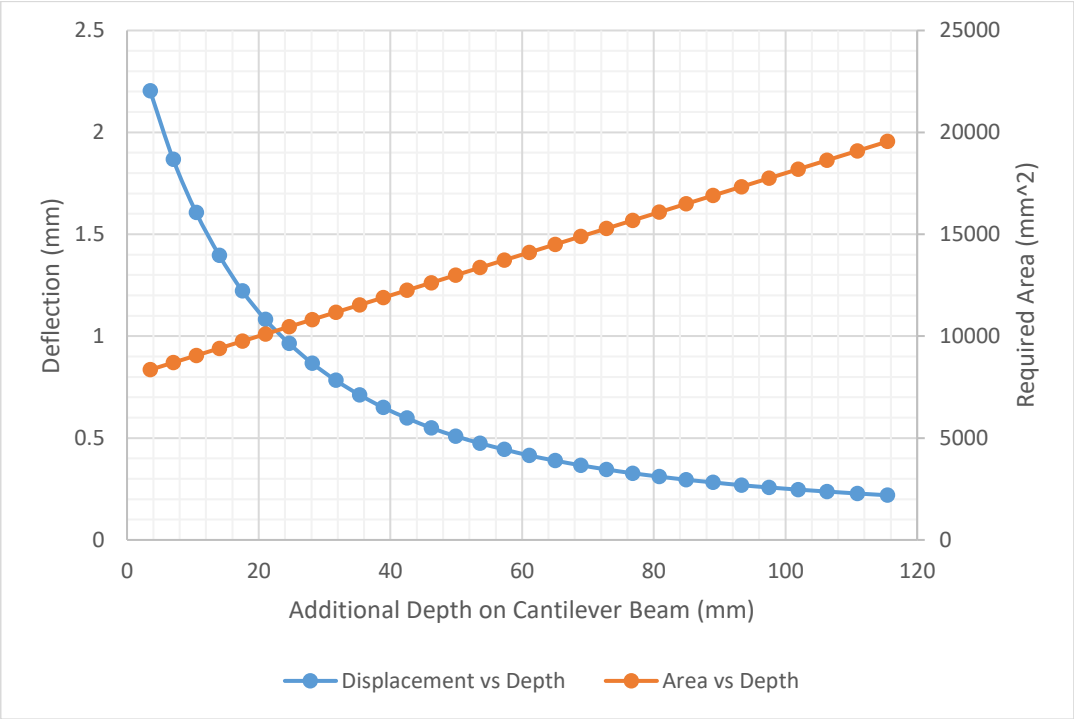


Figure 4-21: Individual graph for Cantilever with Tapering Triangle; One Point Load (Downwards, Free-End, Top Face, 1000N)

Table 4-5: Individual graph for Various Cantilever Beams; One Point Load (Downwards, Free-End, Top Face, 1000N)

Cantilever Beam	**Additional Depth (mm)**		**Deflection (mm)**		**Required Area (mm^2)**	
Cantilever beam	0		2.6399		8000	
Increased depth	5-6 (approx. 5.6)	+15%	1.7745-1.6711	-36.7%	9000-9200	+15%
Tapering triangle at the bottom face	21-24.6 (approx. 22.5)	+52.5%	1.0818-0.96483	-59%	10100-10460	+26.3%
Triangle using the rule of thumb based on the Method of Tensile Triangles.	32	+80%	1.5266	-42.2%	9200	+15%
Triangle following the Method of Tensile Triangles' shape profile	34-36 (approx. 35)	+90%	1.7049-1.6426	-37.8%	8887-8985.5	+12.3%

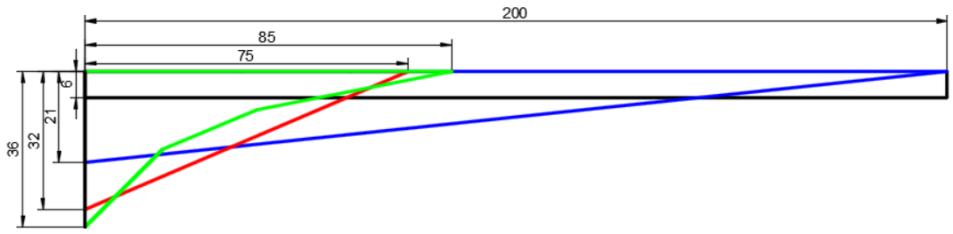


Figure 4-22: Individual graph for Various Cantilever Beams; (1) Black: “Increased Depth”, (2) Blue: “Tapering Triangle”, (3) Red: “Method of Tensile Triangle’s Rule of Thumb”, (4) Green: “Method of Tensile Triangle’s Shape Profile”; One Point Load (Downwards, Free-End, Top Face, 1000N)

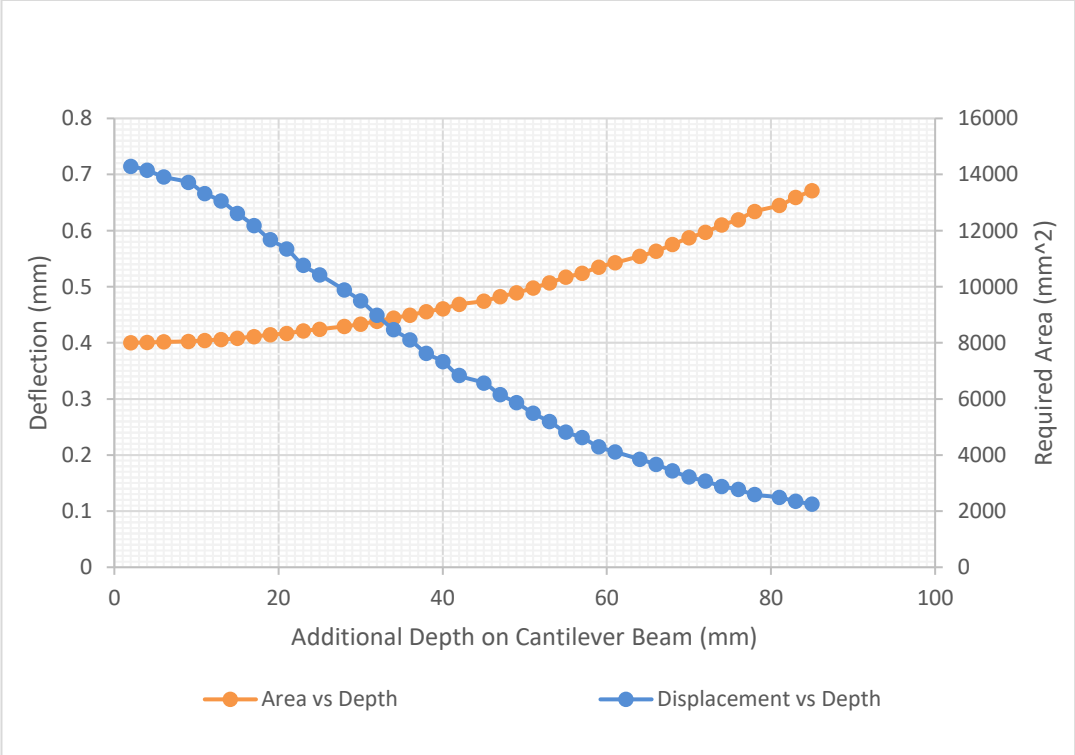


Figure 4-23: Individual graph for Cantilever with Method of Tensile Triangles’ Shape Profile; Triangular Pressure Load (5MPa, Downwards, Top Face, Max at Free-End)

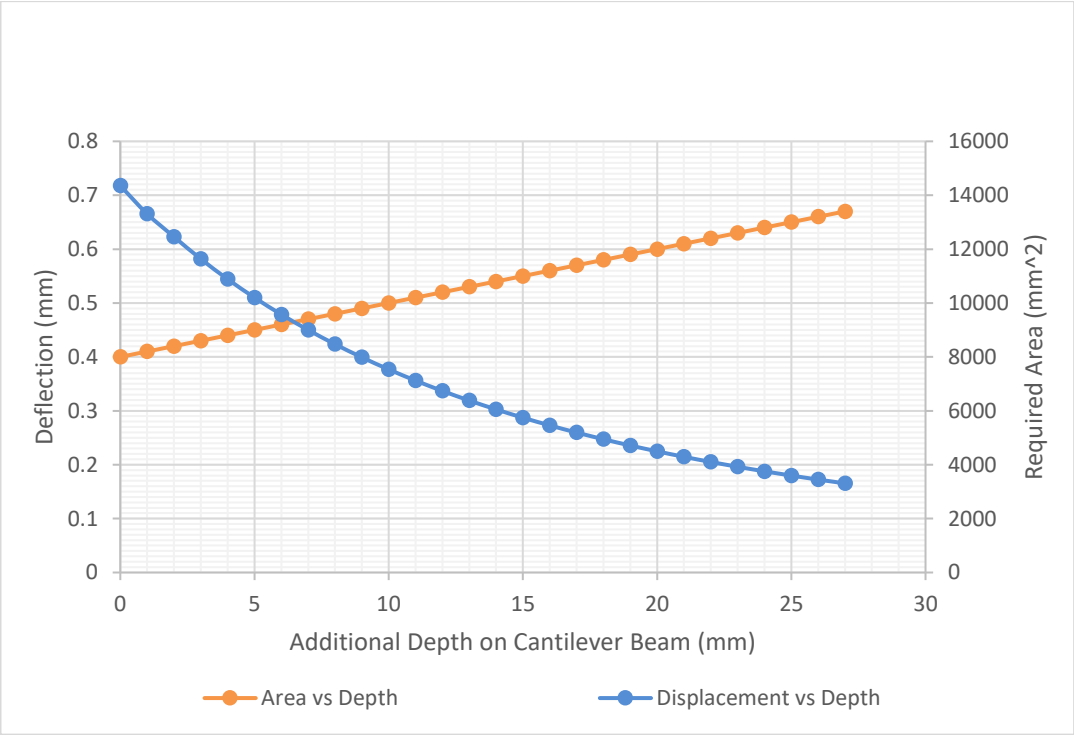


Figure 4-24: Individual graph for Cantilever with Increased Depth; Triangular Pressure Load (5MPa, Downwards, Top Face, Max at Free-End)

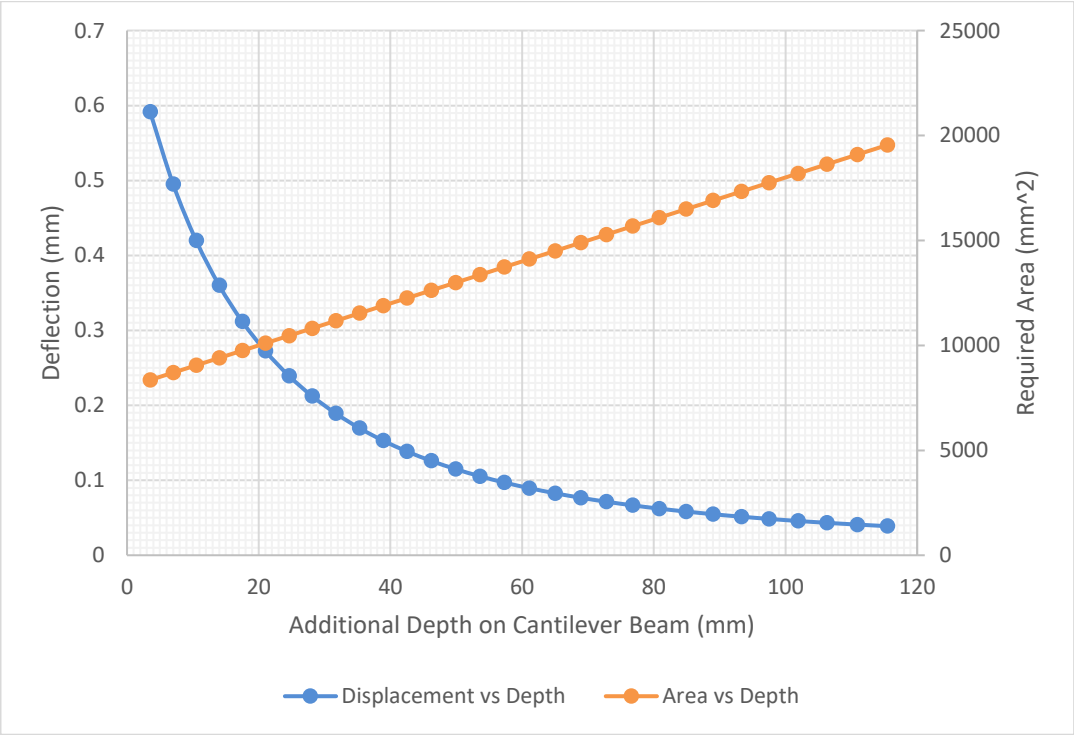


Figure 4-25: Individual graph for Cantilever with Tapering Triangle; Triangular Pressure Load (5MPa, Downwards, Top Face, Max at Free-End)

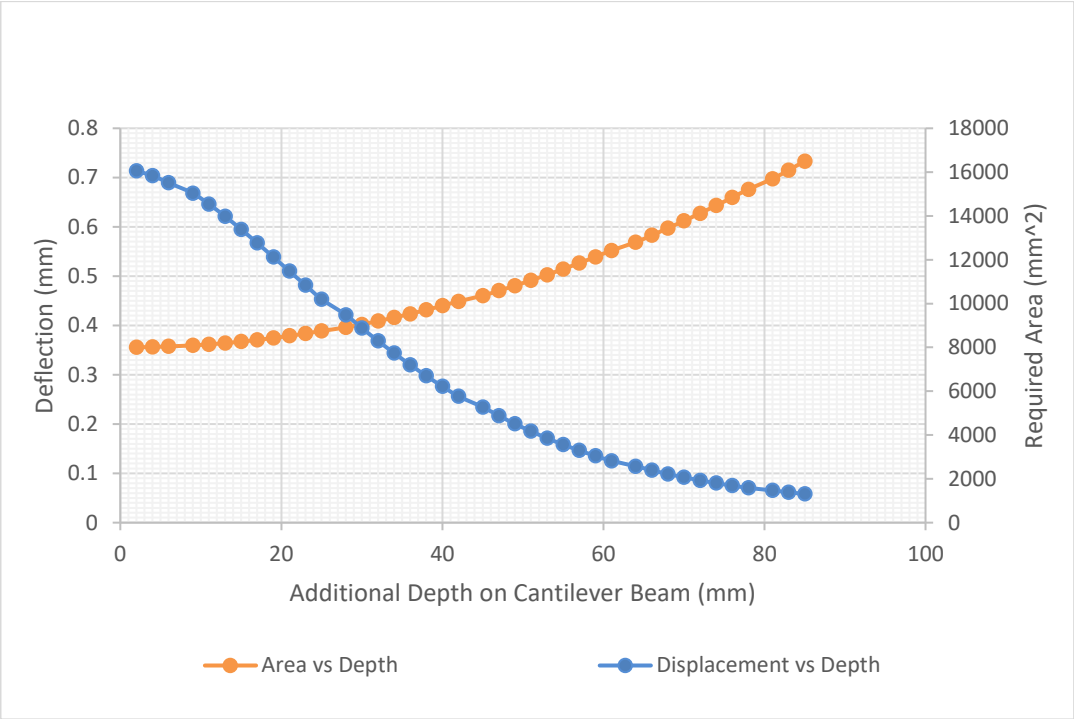


Figure 4-26: Individual graph for Cantilever with Method of Tensile Triangle's Rule of Thumb; Triangular Pressure Load (5MPa, Downwards, Top Face, Max at Free-End)

As expected for the Triangular Pressure Load, as shown in Table 4-6, the effective area required, deflection, and additional depth required are lower due to its loading condition (lighter load). The cantilever beam with a tapering triangle in this case, however, performed worse than the one presented in the load case for the One Point Load. It requires about 2.7x the required area for a deflection reduction of about 1.66x compared to the Method of Tensile Triangles. This cantilever geometry also lacks behind the two Method of Tensile Triangles geometries analysed. The difference in loading condition has a significant effect on this cantilever geometry. The results shown in Table 4-5 and Table 4-6 show that a higher cantilever depth does not always reflect a higher amount of required area due to the difference in surface area distribution. Both cantilevers with the Method of Tensile Triangles method performed equally well, apart from the cantilever with the Method of Tensile Triangles' shape

profile performing slighter better when it comes to its deflection, the area required and additional depth. The comparison between the cantilever geometries may not be ideal to conclude the cantilever's performance as the area and deflections compared are not at a level field from the graph's axis scaling. Therefore, the cantilever models are be fitted into one graph as a single global scale for a fairer comparison.

Table 4-6: Individual graph for Various Cantilever Beams; Triangular Pressure Load (5MPa, Downwards, Top Face, Max at Free-End)

Cantilever Beam	**Additional Depth (mm)**		**Deflection (mm)**		**Required Area (mm^2)**	
Cantilever beam	0		0.71766		8000	
Increased depth	6-7 (approx. 6.5)	+17.5%	0.47873-0.45001	-37%	9200-9400	+17.5%
Tapering triangle at the bottom face	17.5-21 (approx. 20.5)	+52.5%	0.31183-0.27254	-62%	9750-10100	+26.3%
Triangle using the rule of thumb based on the Method of Tensile Triangles.	28-30 (approx. 29.5)	+75%	0.42146-0.39466	-45%	8910-9050	+13.1%
Triangle following the Method of Tensile Triangles' shape profile	32-34 (approx. 32.5)	+80%	0.44898-0.42362	-37.4%	8772-8887	+9.7%

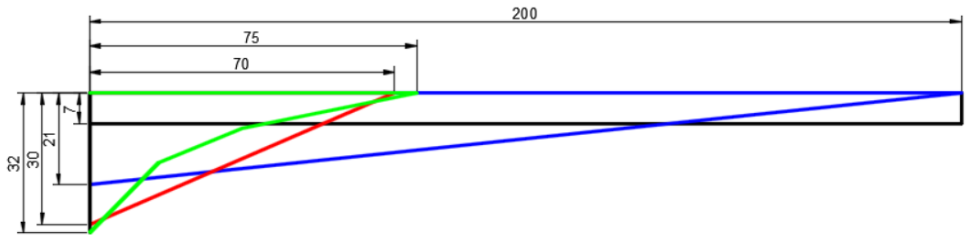


Figure 4-27: Individual graph for Various Cantilever Beams; (1) Black: "Increased Depth", (2) Blue: "Tapering Triangle", (3) Red: "Method of Tensile Triangle's Rule of Thumb", (4) Green: "Method of Tensile Triangle's Shape Profile"; Triangular Pressure Load (5MPa, Downwards, Top Face, Max at Free-End)

4.2.3.3 Multiple Geometries

The graphs shown in Figure 4-28 and Figure 4-30 are a combination of all cantilever geometry types with respect to their area, deflection and additional depth required fitted into one graph. The figures of the respective cantilever geometry sizings are shown in Figure 4-29 and Figure 4-31. One would expect a scaling issue may occur when comparing with 3 axes; thus, the intersection between the effective area and the deflection resistance is now different from the earlier graphs (as demonstrated in the "Individual Geometry). The differences between the individual and the global are the scale of the graph. Hence, there is a scaling issue.

The cantilever beam with increased depth performed the worst compared to the other geometries, but it uses the least amount of depth. For the One Point Load in Table 4-7 and Figure 4-28, the cantilever beam with the tapering triangle performed the best as the required area was minimal as well as its deflection. In terms of practical constructability, the cantilever beam with the triangle projection based on the Method of Tensile Triangles' rule of thumb performed second best as the amount of area required to deflection resistance and the depth required is more economical when compared to the cantilever beam with a triangle projection based on the Method of Tensile Triangles' shape profile that requires more depth, although it displays a better deflection resistance to the area required. Both geometries have less headroom towards its support, but it provides better headroom towards the free end of the cantilever beam.

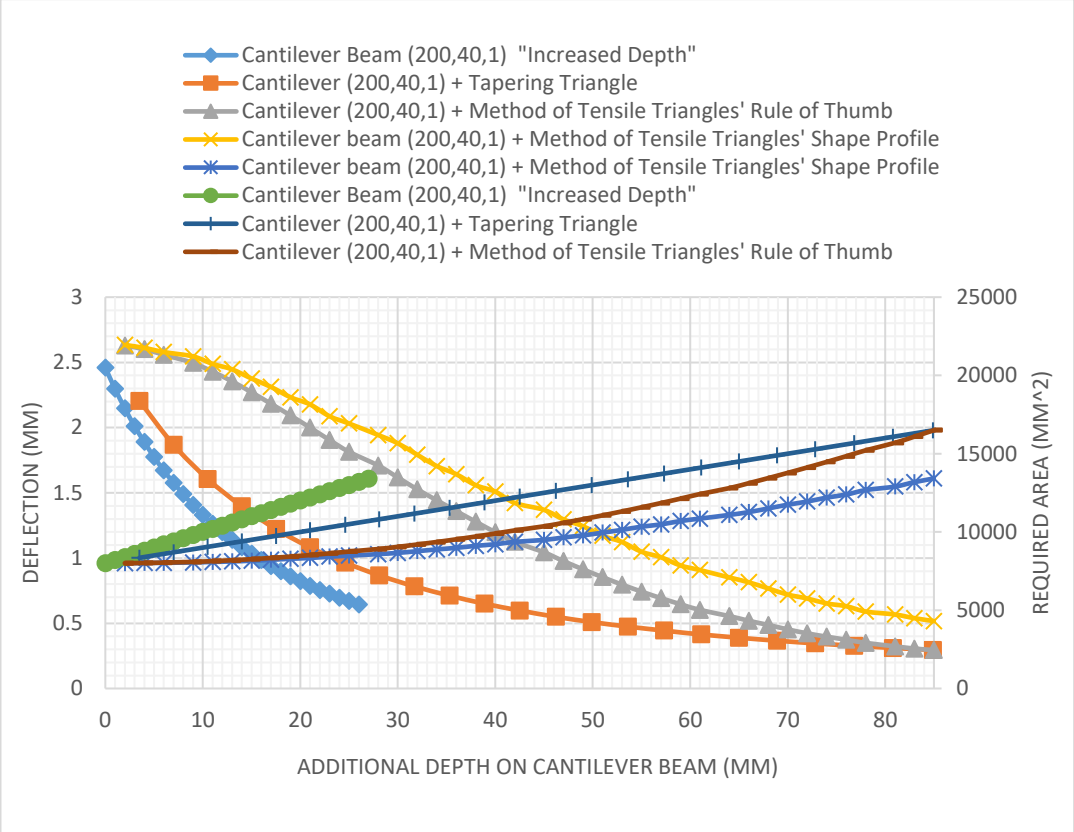


Figure 4-28: Global graph for Various Cantilever Beams; One Point Load (Downwards, Free-End, Top Face, 1000N)

Table 4-7: Global graph for Various Cantilever Beams; One Point Load (Downwards, Free-End, Top Face, 1000N)

Cantilever Beam	**Additional Depth (mm)**		**Deflection (mm)**		**Required Area (mm^2)**	
Cantilever beam	0		2.6399		8000	
Increased depth	11-12 (approx. 11.5)	+27.5%	1.2629-1.1977	-52.2%	10200-10400	+27.5%
Tapering triangle at the bottom face	17.5-21 (approx. 18.5)	+43.8%	1.222-1.0818	-53.7%	9750-10100	+21.9%
Triangle using the rule of thumb based on the Method of Tensile Triangles.	40	+100%	1.1981	-54.6%	9900	+23.8%
Triangle following the Method of Tensile Triangles' shape profile	49-51 (approx. 50.5)	+127.5%	1.2439-1.1711	-55.6%	9782-9955	+24.4%

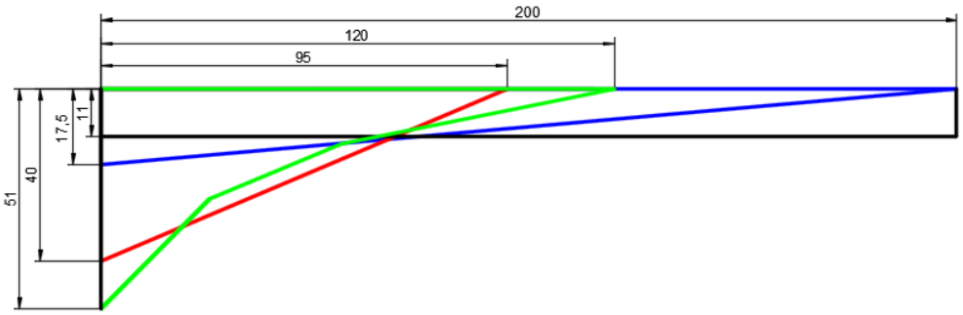


Figure 4-29: Global graph for Various Cantilever Beams; (1) Black: “Increased Depth”, (2) Blue: “Tapering Triangle”, (3) Red: “Method of Tensile Triangle’s Rule of Thumb”, (4) Green: “Method of Tensile Triangle’s Shape Profile”; One Point Load (Downwards, Free-End, Top Face, 1000N)

As shown in Table 4-8 and Figure 4-30 for the Triangular Pressure Load, the cantilever with the Method of Tensile Triangles’ shape profile performed the best in terms of deflection and area required. It also offers the lowest amount of area required and deflection, providing the best available space underneath a cantilever beam. Again, the issue with this method is the high amount of additional depth required at its support, which can be an obstacle to projects requiring specific criteria. Both cantilever beams with the Method of Tensile Triangles offers the best free-end headroom. The case models' performance is in linear order as in Table 4-8, from the worst to the best. The results show the efficiency and effectiveness of trees using this shape profile similar to the shape developed by Mattheck (Method of Tensile Triangles). However, the suggested optimum value of the cantilever geometries is investigated in subchapter 4.2.4 to confirm and validate each cantilever's effectiveness in areas other than the suggested optimum value.

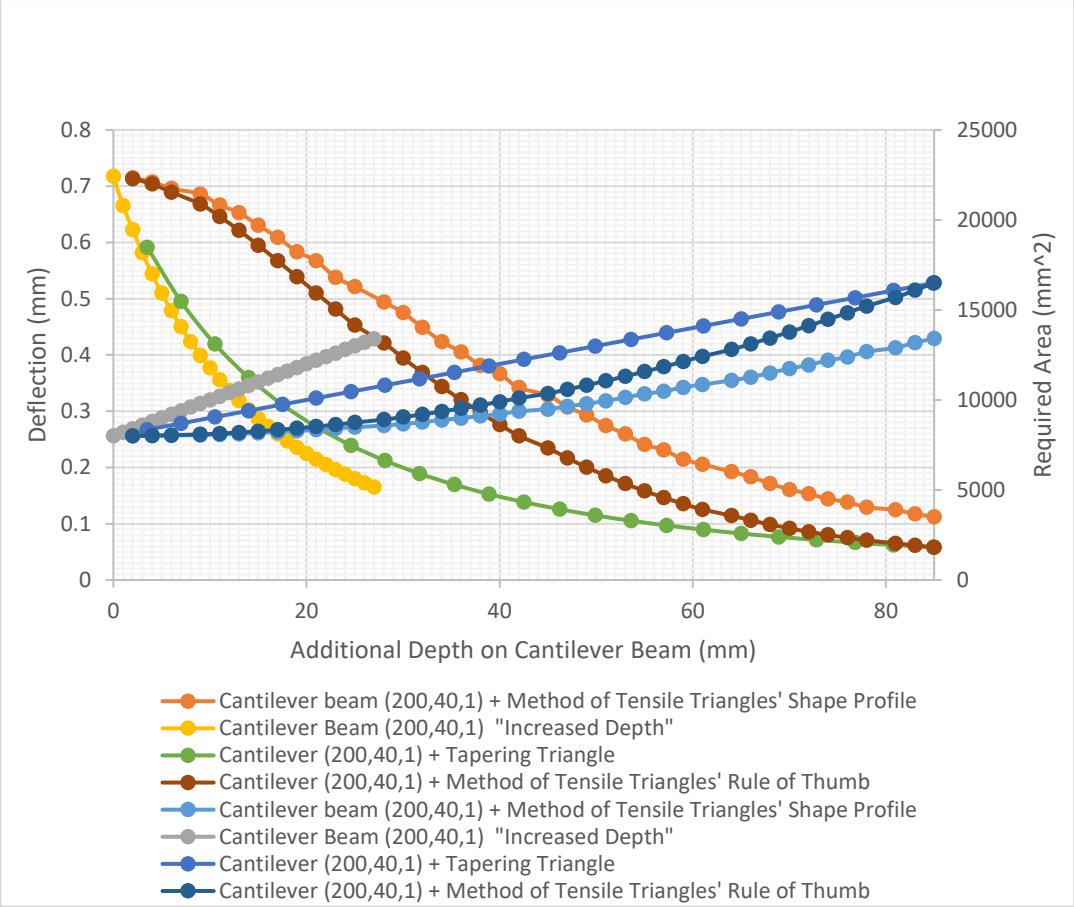


Figure 4-30: Global graph for Various Cantilever Beams; Triangular Pressure Load (5MPa, Downwards, Top Face, Max at Free-End)

Table 4-8: Global graph for Various Cantilever Beams; Triangular Pressure Load (5MPa, Downwards, Top Face, Max at Free-End)

Cantilever Beam	**Additional Depth (mm)**		**Deflection (mm)**		**Required Area (mm^2)**	
Cantilever beam	0		0.71766		8000	
Increased depth	12	+30%e	0.3369	-53.1%	10400	+30%
Tapering triangle at the bottom face	17.5	+43.8%	0.31183	-56.5%	9750	+21.9%
Triangle using the rule of thumb based on the Method of Tensile Triangles.	36-38 (approx. 37)	+95%	0.32029-0.29777	-58.5%	9530-9710	+21.4%
Triangle following the Method of Tensile Triangles' shape profile	47	+117.5%	0.30762	-57.1%	9649	+20.6%

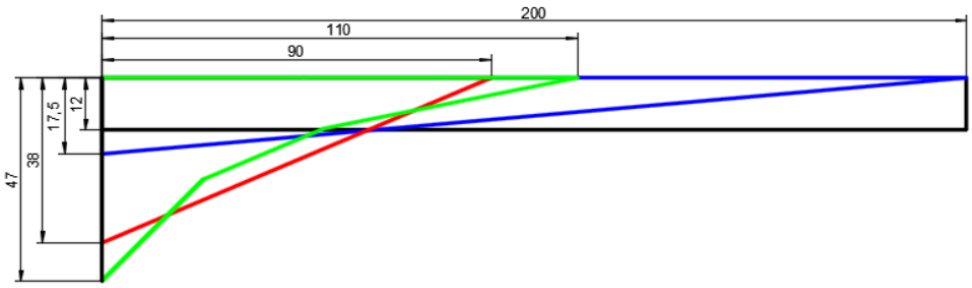


Figure 4-31: Global graph for Various Cantilever Beams; (1) Black: “Increased Depth”, (2) Blue: “Tapering Triangle”, (3) Red: “Method of Tensile Triangle’s Rule of Thumb”, (4) Green: “Method of Tensile Triangle’s Shape Profile”; Triangular Pressure Load (5MPa, Downwards, Top Face, Max at Free-End)

4.2.3.4 Multiple Geometries with Normalised Scale

The scale of the two y-axes is normalised to resolve the scaling issue. The graphs shown in Figure 2-43 and Figure 2-44 are graphs with normalised scales where the two y-axes are normalised as percentages, and their intersections are shown in Table 4-9 and Table 4-10. The figures of the respective cantilever geometry sizings are shown in Figure 4-33 and Figure 4-35. The normalised graphs show the intersections of the various cantilever beam geometries to be less than the deflection limit that is 1.1111mm. It was also found that the surface area of intersections for loading conditions was around a +/- 30% increased in surface area. The suggested optimum sizing for the normalised graphs shows a larger projection than the earlier graphs in subchapter 4.2.3. The ID cantilever beam in both loading conditions displayed the highest surface area required and the lowest deflection resistance. For the one point load, the ST cantilever has the lowest surface area required and the highest amount of deflection resistance. The MTTR cantilever beam performed second while the MTT cantilever beam came in third.

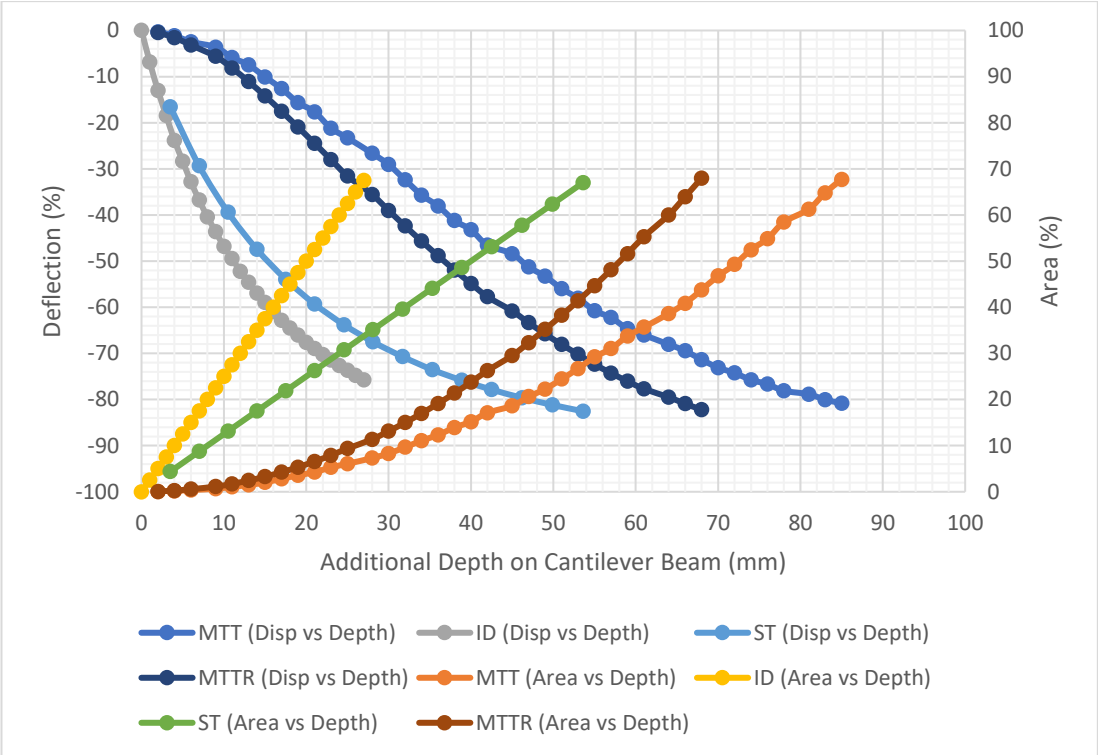


Figure 4-32: Multiple geometries with normalised scale; One Point Load (Downwards, Free-End, Top Face, 1000N)

Table 4-9: Multiple geometries with normalised scale; One Point Load (Downwards, Free-End, Top Face, 1000N)

Cantilever Beam	**Additional Depth (mm)**	**Deflection (mm)**		**Required Area (mm^2)**	
Cantilever beam	0				
Increased depth	15 – 16	1.0852 – 1.0309	(-58.93) – (-60.98)	11000 – 11200	37.5 – 40
Tapering triangle at the bottom face	24.6 – 28.1	0.956 – 0.85854	(-63.82) – (-67.50)	10460 – 10810	30.75 – 35.125
Triangle using the rule of thumb based on the Method of Tensile Triangles.	47 – 49	0.96814 – 0.90416	(-63.36) – (-65.78)	10585 – 10817.5	32.31 – 35.22
Triangle following the Method of Tensile Triangles' shape profile	59 – 61	0.93333 – 0.89773	(-64.67) – (-66.02)	10700 – 10854	33.75 – 35.365

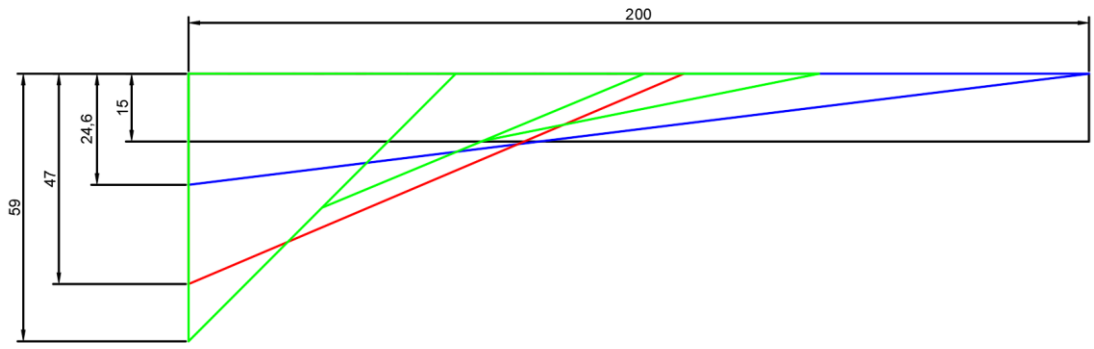


Figure 4-33: Multiple geometries with normalised scale; (1) Black: “Increased Depth”, (2) Blue: “Tapering Triangle”, (3) Red: “Method of Tensile Triangle’s Rule of Thumb”, (4) Green: “Method of Tensile Triangle’s Shape Profile”; One Point Load (Downwards, Free-End, Top Face, 1000N)

In the case of the Triangular pressure, the MTTR cantilever beam has the lowest surface area required and the highest displacement resistance. This is followed by the MTT cantilever beam performing slightly better than the ST cantilever beam.

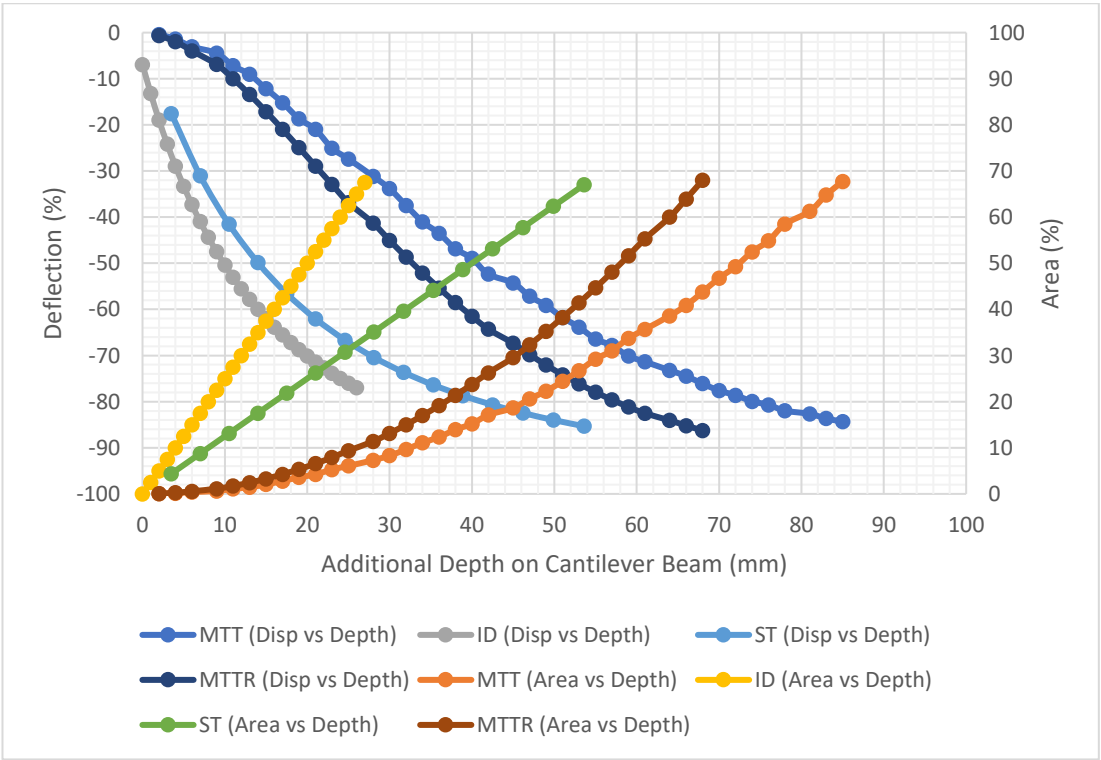


Figure 4-34: Multiple geometries with normalised scale; Triangular Pressure Load (5MPa, Downwards, Top Face, Max at Free-End)

Table 4-10: Multiple geometries with normalised scale; Triangular Pressure Load (5MPa, Downwards, Top Face, Max at Free-End)

Cantilever Beam	**Additional Depth (mm)**	**Deflection (mm)**		**Required Area (mm^2)**	
Cantilever beam	0				
Increased depth	15 – 16	0.28747 – 0.27316	(-59.97) – (-61.96)	11000 – 11200	37.5 – 40
Tapering triangle at the bottom face	24.6 – 28.1	0.23938 – 0.2125	(-66.67) – (-70.41)	10460 – 10810	30.75 – 35.125
Triangle using the rule of thumb based on the Method of Tensile Triangles.	45 – 47	0.23445 – 0.21693	(-67.35) – (-69.79)	10362.5 – 10585	29.53 – 32.31
Triangle following the Method of Tensile Triangles' shape profile	57 – 59	0.23109 – 0.21459	(-67.82) – (-70.12)	10482 – 10700	31.03 – 33.75

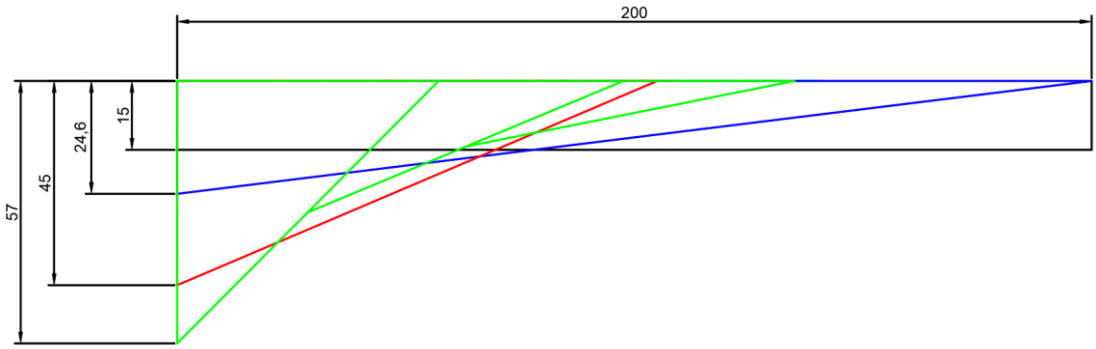


Figure 4-35: Multiple geometries with normalised scale; (1) Black: "Increased Depth", (2) Blue: "Tapering Triangle", (3) Red: "Method of Tensile Triangle's Rule of Thumb", (4) Green: "Method of Tensile Triangle's Shape Profile"; Triangular Pressure Load (5MPa, Downwards, Top Face, Max at Free-End)

4.2.4 Workable/Acceptable Range of Cantilever Design Parameter

4.2.4.1 Area versus Deflection

For the One Point Load, all the cantilever geometries except for the tapering triangle cantilever beam convergence at the area around $8300mm^2$ with a deflection of around +/- 2.2mm, as shown in Figure 4-36. The graph in Figure 4-36 shows the effectiveness

of increasing beam depth with respect to the other two geometries has reached its limits where it will no longer provide effective resistance to deflection along the increasing area. The cantilever geometry sizing is shown in Figure 4-38.

All cantilever geometries except for the cantilever beam with increased depth converged at around 8900mm^2 – 9200mm^2 with a deflection of around 1.5mm-1.7mm. From the graph's interpolation in Figure 4-36, the Method of Tensile Triangles' Shape Profile cantilever beam shows better performance by a minimal margin against the other cantilever geometries. However, again in terms of construction perspective (sizing), the cantilever with the tapering triangle is a preferred choice of most engineers.

Based on a graph in Figure 4-36, the deflection resistance performance for both cantilever beams with Method of Tensile Triangles are almost equal until they have both reached an area of approximately 10800mm^2. From that point onwards, the deflection resistance in the cantilever beam with the Method of Tensile Triangles' rule of thumb performed better than the cantilever beam with the Method of Tensile Triangles' shape profile. As the area increases beyond the area of 9200mm^2 till an area around 16490mm^2-16500mm^2, the cantilever beam with a tapering triangle remains consistently better than the other cantilever geometries. However, at the point of the area around 16490mm^2-16500mm^2, the differences between its deflection for the tapering triangle cantilever beam and the Method of Tensile Triangles' rule of thumb cantilever beam are marginal. The cantilever geometry sizing is shown in Figure 4-39, and the above mentioned are summarised in Table 4-11.

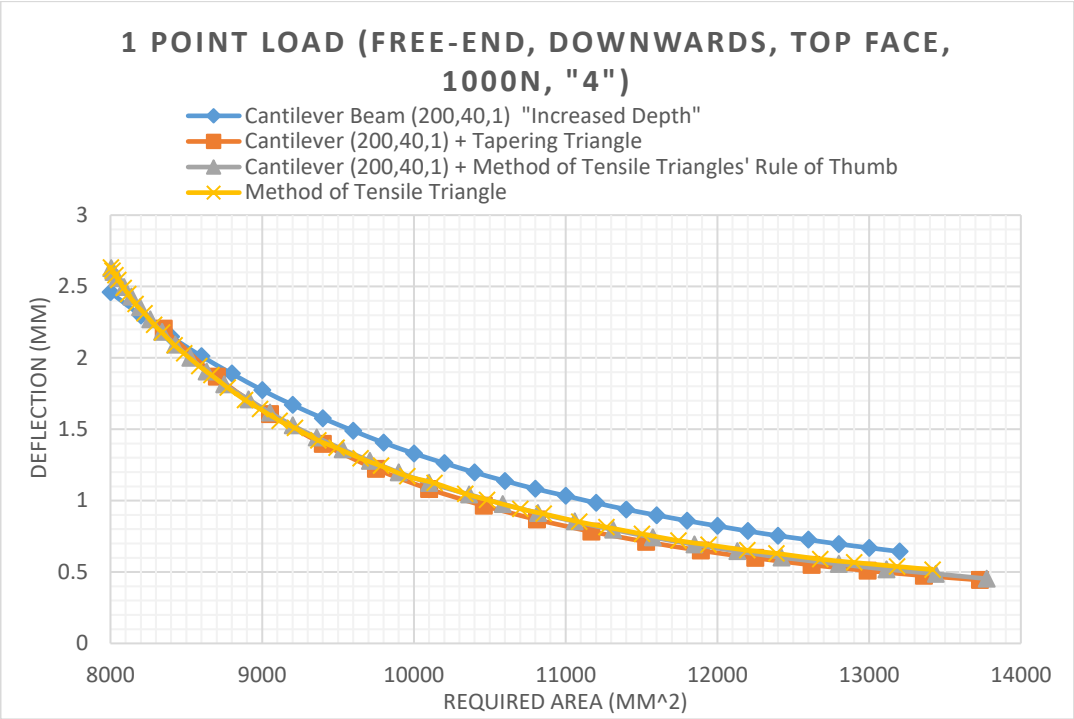


Figure 4-36: Area vs Deflection for Various Cantilever Beams; One Point Load (Downwards, Free-End, Top Face, 1000N)

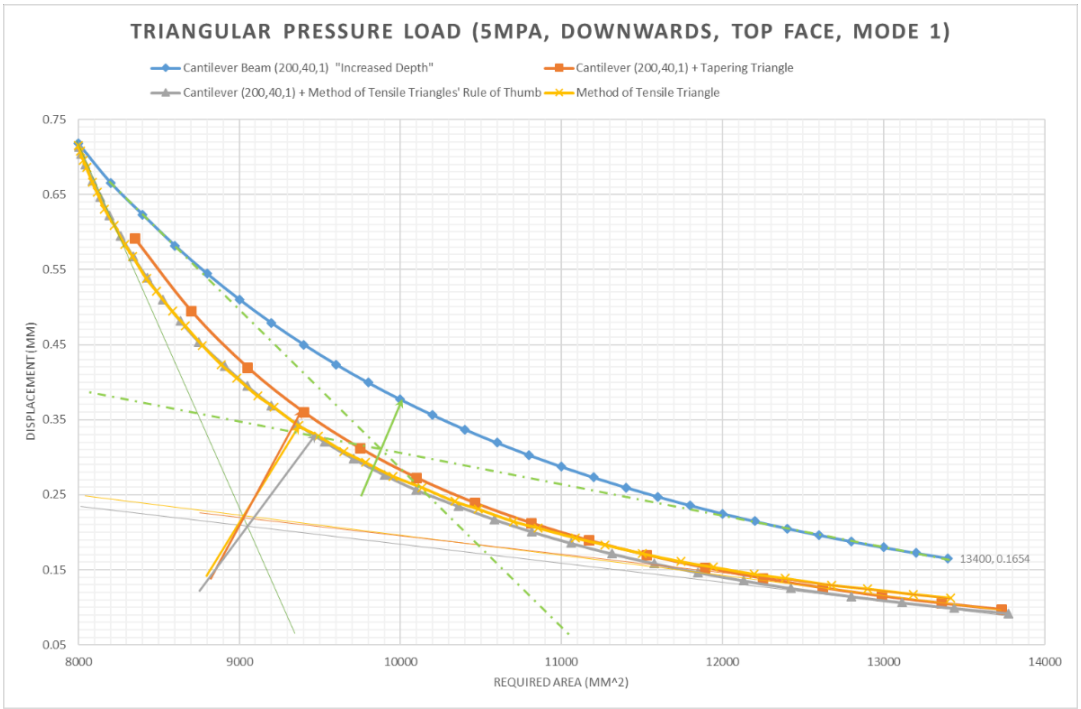


Figure 4-37: Area vs Deflection for Various Cantilever Beams subjected to Triangular Pressure Load (5MPa, Downwards, Top Face, Max at Free-End)

Table 4-11: Area vs Deflection for Various Cantilever Beams; One Point Load (Downwards, Free-End, Top Face, 1000N)

Cantilever Beam	**Additional Depth (mm)**	**Required Area (mm^2)**	**Deflection (mm)**
Cantilever beam	0	8000	2.6399
Increased depth	1-2, 6 (approx. 1-2)	8200-8400, 9200	2.4594-2.2966, 1.7745
Tapering triangle at the bottom face	10.5-14 (approx. 10.5)	9050-9400	1.6065-1.3968
Triangle using the rule of thumb based on the Method of Tensile Triangles.	15-17, 30-32, 34 (approx. 32)	8262.5 – 8340, 9050 – 9200, 9360	2.2705-2.1826, 1.618 - 1.5266, 1.4432
Triangle following the Method of Tensile Triangles' shape profile	19-21, 36-40, 42 (40)	8287.5-8339.5, 8985.5-9215, 9369	2.2325-2.1781, 1.6426-1.5094, 1.4223

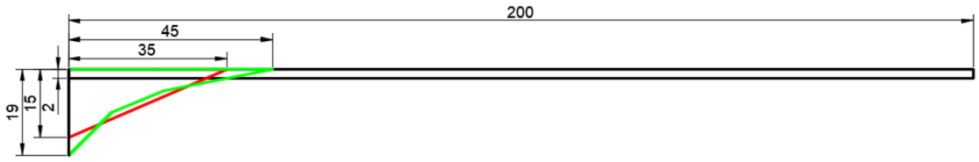


Figure 4-38: Area vs Deflection for the area around 8300mm^2; (1) Black: "Increased Depth", (2) Red: "Method of Tensile Triangle's Rule of Thumb", (3) Green: "Method of Tensile Triangle's Shape Profile"; One Point Load (Downwards, Free-End, Top Face, 1000N)

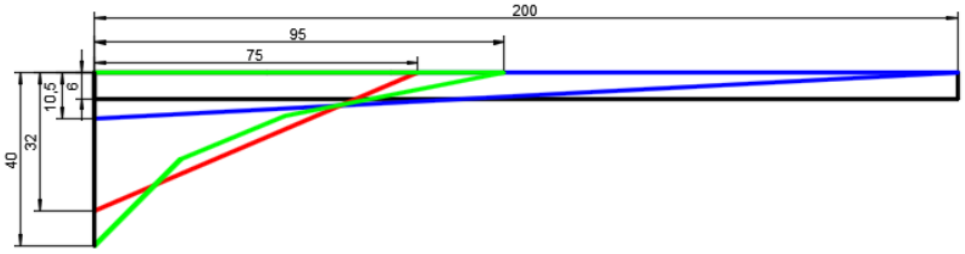


Figure 4-39: Area vs Deflection for the area around 8900mm^2-9200mm^2; (1) Black: "Increased Depth", (2) Blue: "Tapering Triangle", (3) Red: "Method of Tensile Triangle's Rule of Thumb", (4) Green: "Method of Tensile Triangle's Shape Profile"; One Point Load (Downwards, Free-End, Top Face, 1000N)

However, it is different in the case of the Triangular Pressure Load. The graph in Figure 4-37 shows very interesting behaviour on its performance between the three top

cantilever geometries. From an area around 8000mm^2-9400mm^2, both cantilever beams with the Method of Tensile Triangles' performed almost at par with each other. The cantilever beam with the Method of Tensile Triangles' shape profile performing slightly better than the other. Beyond the area of around 9400mm^2, its performance was inverted ,and this may be the reason why tree buttresses only appear as a small feature at its support or base of the tree trunk. As mentioned earlier in this load case, the cantilever with tapering triangles performed worst than the other two geometries. This is, however, true up to an area of around 11200mm^2, where the cantilever with Method of Tensile Triangle's shape profile starts to underperform compared to the tapering triangle cantilever while closing into the performance of the cantilever with the Method of Tensile Triangles rule of thumb. The cantilever with the tapering triangle still underperforms compared to the cantilever with the Method of Tensile Triangles rule of thumb. Figure 4-37 shows the effectiveness of using the Method of Tensile Triangles rule of thumb in a cantilever beam to improve structural performance. The reason behind the shape profile of buttresses is justified in the analysis. The results are summarised in Table 4-12 and for the bisected value in Table 4-13. The sizing of cantilever geometry for the Triangular Pressure Load bisected value is shown in Figure 4-40.

Table 4-12: Area vs Deflection for Various Cantilever Beams; Triangular Pressure Load (5MPa, Downwards, Top Face, Max at Free-End)

Cantilever Beam	**Additional Depth (mm)**	**Deflection (mm)**	**Required Area (mm^2)**
Cantilever beam	0	0.71766	8000
Increased depth	1-27	2.4594-0.6436	8200-13400
Tapering triangle at the bottom face	3.5-31.7, 35.3-53.6	2.204-0.7832, 0.712-0.4745	8350-11170, 11530-13360
Triangle using the rule of thumb based on the MTT.	5-34, 36-68	2.6296-1.4432, 1.3597-0.4873	8005-9360, 9530-13440
Triangle following the Method of Tensile Triangles' shape profile	2-42, 45-64, 66-85	2.6337-1.4223, 1.3695-0.8515, 0.8143-0.5166	8003-9369, 9490.5-11088, 11269-13418

Table 4-13: Area vs Deflection for Various Cantilever Beams (Bisected Value); Triangular Pressure Load (5MPa, Downwards, Top Face, Max at Free-End)

Cantilever Beam	**Additional Depth (mm)**		**Deflection (mm)**		**Required Area (mm^2)**	
Cantilever beam	0		0.71766		8000	
Increased depth	10	+25%	0.37681	-47.5%	10000	+25%
Tapering triangle at the bottom face	14	+35%	0.35998	-49.8%	9400	+17.5%
Triangle using the rule of thumb based on the MTT.	34-36 (36)	+90%	0.34398-0.32029	-55.4%	9360-9530 (approx. 9480)	+19.1%
Triangle following the Method of Tensile Triangles' shape profile	42	+105%	0.34208	-52.3%	9369	+17.1%

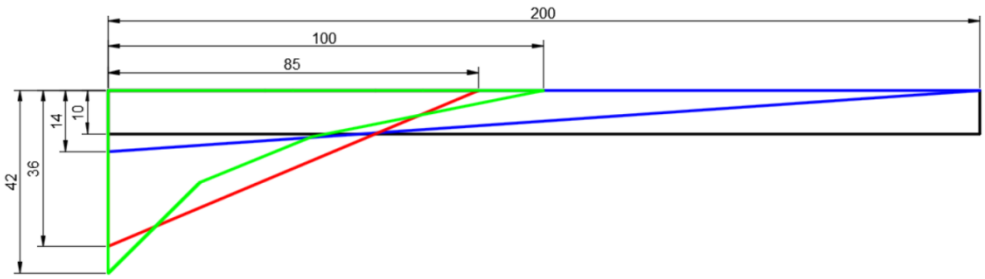


Figure 4-40: Area vs Deflection for the Bisected Value; (1) Black: “Increased Depth”, (2) Red: “Method of Tensile Triangle’s Rule of Thumb”, (3) Green: “Method of Tensile Triangle’s Shape Profile”; Triangular Pressure Load (5MPa, Downwards, Top Face, Max at Free-End)

4.2.4.2 Depth versus Deflections

The following graphs shown in Figure 4-41 and Figure 4-42 show the incremental value of cantilever depth with respect to its deflections. The steepness of the curve in the graphs does not reflect the best interest in reducing depth through the bisector method for lower material consumption. However, it demonstrates a different point of view in identifying its optimum range. A bisector between two gradients of the curve was created to identify the effective depth against its deflection.

For a One Point Load in Figure 4-41, the cantilever beam with increased depth has the steepest gradient, indicating the increase in depth is effective in reducing its deflection. This is followed by the cantilever beam with tapering triangle, the cantilever beam with the Method of Tensile Triangles’ rule of thumb and lastly, the cantilever beam with the Method of Tensile Triangle’s shape profile. As the depth increases, the Method of the Tensile Triangle’s rule of thumb cantilever beam was interestingly able to reduce the amount of deflection difference against the tapering triangle cantilever beam.

Although both cantilevers with the Method of Tensile Triangles’ have a more consistent gradient along with the incremental value of the depth against deflection, it

also shows the lack of efficiency to reduce deflections along with the incremental depth of the cantilever. The results are summarised in Table 4-14, and the various cantilever geometry is shown in Figure 4-43.

For the Triangular Pressure Load in Figure 4-42, the behaviour is similar to the 1 point downwards top face free-end loading with the only exception of slightly different gradient and optimum bisected depth of cantilever beams due to the reduction in load. The results are summarised in Table 4-15, and the various cantilever geometry is shown in Figure 4-44.

The graphs shown for both load cases demonstrate the diminished ability to reduce deflection across the incremental depth of the cantilever beam. The graphs also show both the cantilever beam with the Method Tensile Triangles' design to have a consistent gradient at its middle range depth value. This demonstrates the accurate suggestion of researchers that the Method of Tensile Triangles' may be assumed to be extended at least half of the depth of the cantilever beam. For example, if the beam depth is 40mm, then the Method of Tensile Triangles' should be extended to a depth of at least 20mm, leading to a total depth of 60mm. The shallow gradient of the line curve shows little to no effect of further increasing depth to reduce deflections.

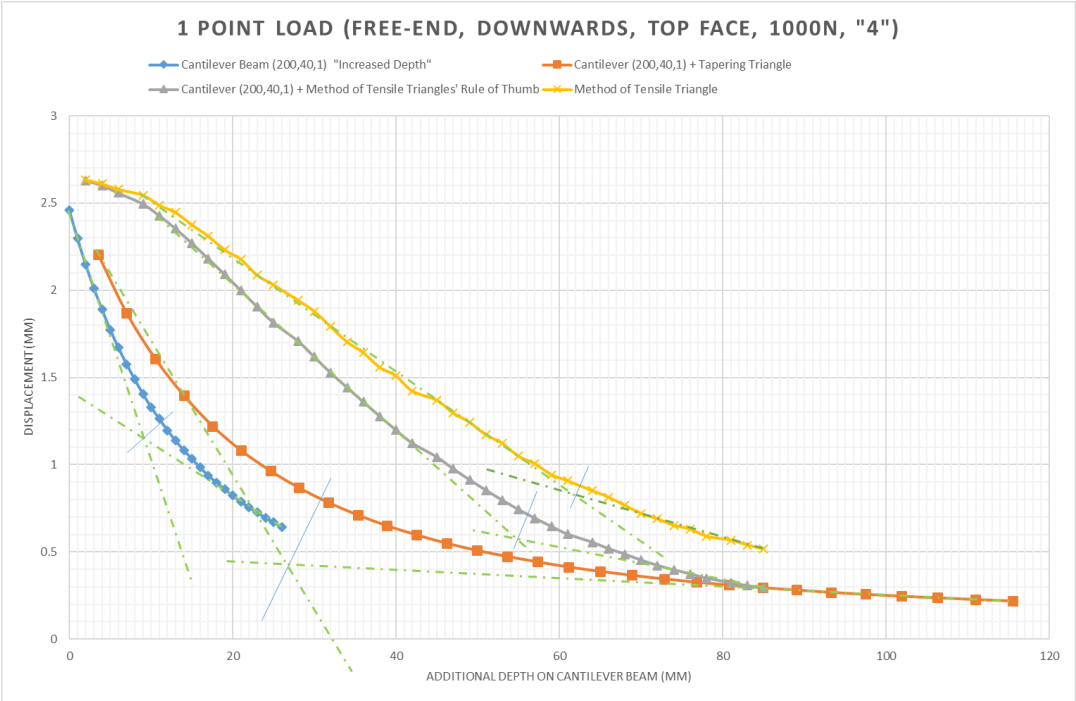


Figure 4-41: Depth vs Deflections for Various Cantilever Beams; One Point Load (Downwards, Free-End, Top Face, 1000N)

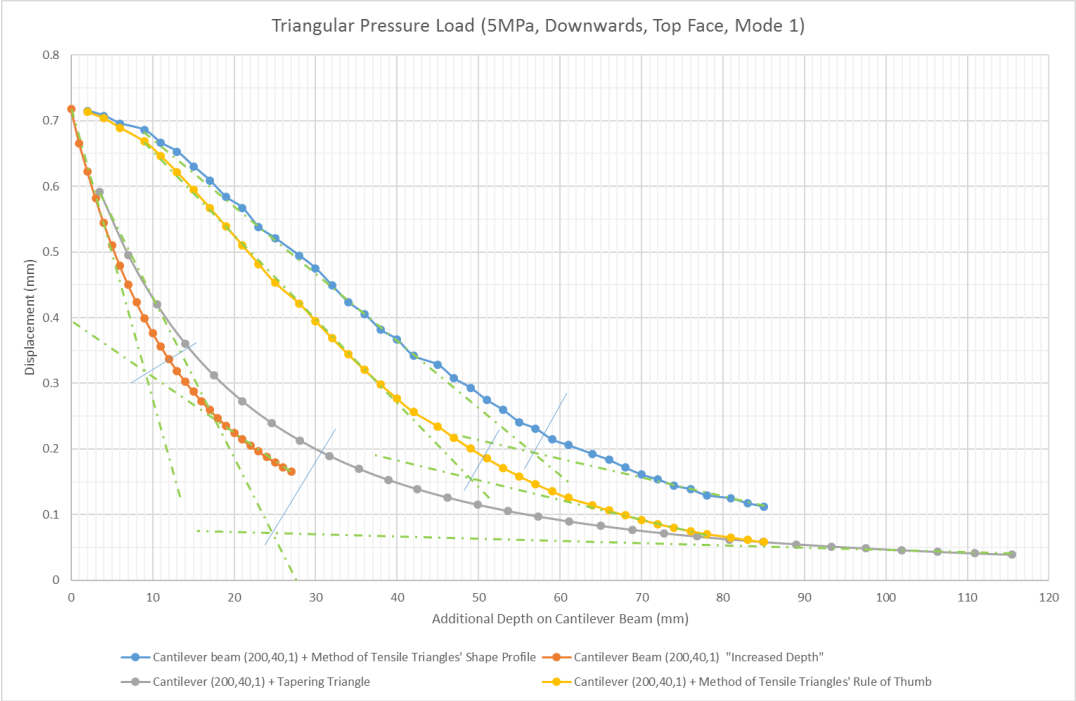


Figure 4-42: Depth vs Deflections for Various Cantilever Beams; Triangular Pressure Load (5MPa, Downwards, Top Face, Max at Free-End)

Table 4-14: Depth vs Deflections for Various Cantilever Beams; One Point Load (Downwards, Free-End, Top Face, 1000N)

Cantilever Beam	**Additional Depth (mm)**		**Deflection (mm)**		**Required Area (mm^2)**	
Cantilever beam	0		2.6399		8000	
Increased depth	15-18 (11)	+27.5%	1.3309	-49.6%	10200	+27.5%
Tapering triangle at the bottom face	14-85 (31) Adjusted - 31.7	+77.5%	0.78319	-70.3%	11170	+39.6%
Triangle using the rule of thumb based on the Method of Tensile Triangles.	40-72 (56) Adjusted - 55	+140%	0.74292	-71.9%	11575	+44.7%
Triangle following the Method of Tensile Triangles' shape profile	53-70 (63) Adjusted - 64	+157.5%	0.85146	-67.8%	11088	+38.6%

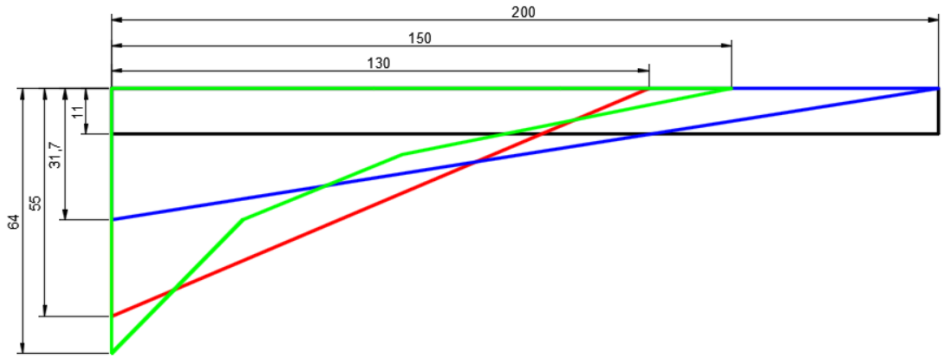


Figure 4-43: Depth vs Deflections for Various Cantilever Beams; (1) Black: "Increased Depth", (2) Blue: "Tapering Triangle", (3) Red: "Method of Tensile Triangle's Rule of Thumb", (4) Green: "Method of Tensile Triangle's Shape Profile"; One Point Load (Downwards, Free-End, Top Face, 1000N)

Table 4-15: Depth vs Deflections for Various Cantilever Beams; Triangular Pressure Load (5MPa, Downwards, Top Face, Max at Free-End)

Cantilever Beam	**Additional Depth (mm)**		**Deflection (mm)**		**Required Area (mm^2)**	
Cantilever beam	0		0.71766		8000	
Increased depth	12	+30%	0.3369	-53.1%	10400	+30%
Tapering triangle at the bottom face	28.1-31.7 (approx. 30.5)	+79.3%	0.2124-0.18919	-73.6%	10810-11170	+39.6%
Triangle using the rule of thumb based on the Method of Tensile Triangles.	49-51 (approx. 50.5)	+127.5%	0.20058-0.18541	-74.2%	10817.5-11060	+38.3%
Triangle following the Method of Tensile Triangles' shape profile	57-59 (approx. 58)	+147.5%	0.23105-0.21454	-70.1%	10482-10700	+33.8%

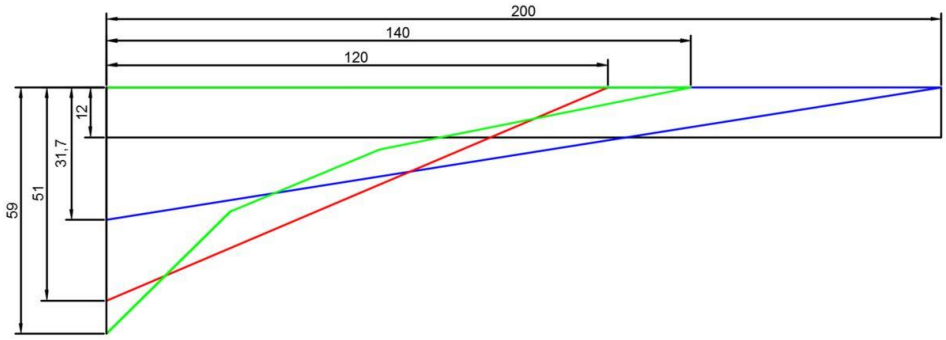


Figure 4-44: Depth vs Deflections for Various Cantilever Beams; (1) Black: "Increased Depth", (2) Blue: "Tapering Triangle", (3) Red: "Method of Tensile Triangle's Rule of Thumb", (4) Green: "Method of Tensile Triangle's Shape Profile"; Triangular Pressure Load (5MPa, Downwards, Top Face, Max at Free-End)

4.2.4.3 Various Graphs

One Point Load

Table 4-16:Suggested Recommended Design Range of Various Cantilever Beams; One Point Load (Downwards, Free-End, Top Face, 1000N)

Additional Depth (mm)	Individual	Combined	Area vs Deflection	Depth vs Deflection	Range (adjusted for compatible model)
Cantilever beam	0	0	0	0	0
Increased depth	5-6 (approx. 5.6)	11-12 (approx. 11.5)	1-2, 6 (approx. 1-2)	15-18 (11)	5-12
Tapering triangle at the bottom face	21-24.6 (approx. 22.5)	17.5-21 (approx. 18.5)	10.5-14 (approx. 10.5)	14-85 (31) Adjusted - 31.7	10.5-31.7
Triangle using the rule of thumb based on the Method of Tensile Triangles.	32	40	15-17, 30-32, 34 (approx. 32)	40-72 (56) Adjusted - 55	32-55
Triangle following the Method of Tensile Triangles' shape profile	34-36 (approx. 35)	49-51 (approx. 50.5)	19-21, 36-40, 42 (40)	53-70 (63) Adjusted - 64	34-64

The range of different effective depth to the area and deflection value across the various graph is summarised in Table 4-16. The difference in the graphs demonstrated earlier in subchapter 4.2 is different due to the scaling and differences in the definition of the plotted graph. Hence, the different range of optimum value presented. The acceptable range defined in the table is based on the minimum optimum value to the estimated bisected value. The acceptable range defined here is the range of values where consideration between depth, required area, and deflection is within sustainable design limits. The acceptable range of the sustainable design model is confined to the model of interest itself.

Within the overall working/acceptable range of the various cantilever models for One Point Load, the cantilever beam with a tapering triangle remains the best, followed by the Method of Tensile Triangles' rule of thumb, then the Method of Tensile Triangles' shape profile and finally the increased depth. However, under a specific area, for example, an area below 9200 mm^2, the Method of Tensile Triangles' Shape Profile is the best. Table 4-17 shows the exact sizing for a cantilever beam with the Method of Tensile Triangles' Shape profile that is clearly better than the other cantilever geometry.

Table 4-17: Clear Optimum Comparison Value for the Cantilever with Method of Tensile Triangles' Shape Profile; One Point Load (Downwards, Free-End, Top Face, 1000N)

Cantilever Beam	**Additional Depth (mm)**		**Deflection (mm)**		**Required Area (mm^2)**	
Cantilever beam	0		2.6399		8000	
Increased depth	2	5% more	2.2966	13% less	8400	5% more
Tapering triangle at the bottom face	3.5	8.8% more	2.204	16.5% less	8350	4.3% more
Triangle using the rule of thumb based on the Method of Tensile Triangles.	17	42.5% more	2.1826	17.3% less	8340	4.25% more
Triangle following the Method of Tensile Triangles' shape profile	21	52.5% more	2.1781	17.5% less	8339.5	4.24% more

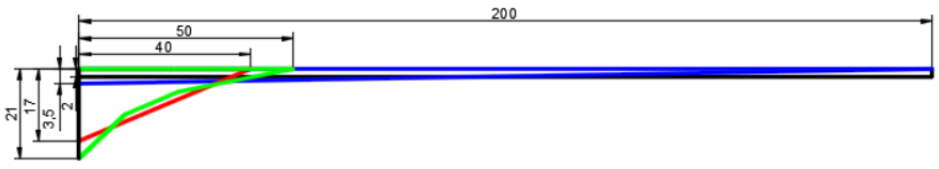


Figure 4-45: Clear Optimum Comparison Value for the Cantilever with Method of Tensile Triangles' Shape Profile; (1) Black: "Increased Depth", (2) Blue: "Tapering Triangle", (3) Red: "Method of Tensile Triangle's Rule of Thumb", (4) Green: "Method of Tensile Triangle's Shape Profile"; One Point Load (Downwards, Free-End, Top Face, 1000N)

The only dimension where the Method of Tensile Triangles' Shape Profile has clearly excelled in terms of exact comparison value (without interpolation or bisecting of the graph) is at an increased depth of 21mm with an area of 8339.5mm^2. The analysis of the case model shows that the Method of Tensile Triangle's shape profile is effective when the loading condition to its support has the force flow passing through its shape extension. The sizing of the cantilever geometries is shown in Figure 4-45.

For the Triangular Pressure Load, the best choice of cantilever beam depends on the work criteria. Within the acceptable/workable range of the various cantilever models, the cantilever beam with a tapering triangle remains the best, followed by the Method of Tensile Triangles' rule of thumb, then the Method of Tensile Triangles' shape profile and finally, the increased depth in terms of both a consistent headroom and deflection resistance. However, in terms of deflection to area efficiency, the Method of Tensile Triangles' rule of thumb is the best, followed by the cantilever beam with a tapering triangle and then the cantilever with the Method of Tensile Triangles' shape profile. This only is true for the required area above 9400mm^2; but for any required area below 9400mm^2, then this is no longer true. For the required area below 9400mm^2, the cantilever with the Method of Tensile Triangles' shape profile is the best, followed by the Method of Tensile Triangles' rule of thumb and then the cantilever beam with a Tapering Triangle.

Although the acceptable/working range of different cantilever geometry presented here may seem complicated, the data summarized in Table 4-16 and Table 4-17 can be reflected accurately in the efficiency graph as well as in the performance graph in the later subchapters 4.2.4.4 and 4.2.4.5. However, it is beyond doubt that increasing the surface area of any structure will increase the deflection resistance, but this may not always translate to higher deflection resistance efficiency, and again this can be

clearly seen in the later subchapters 4.2.4.4 and 4.2.4.5. The analysis performed in this experiment confirms and shows the reason why tree buttress grows only to a certain height at a particular location as it depends on the loading condition. The shape profile of the buttress is also interesting; trees with large buttress often occur at locations with weak soil stability or strong prevalent wind. The tree counter reacts to the issue by emphasising a larger base area while leaving the free-end slender to increase stability. Therefore, the size, shape, amount and location of the increased area should be added at the correct place for a better improved and sustainable structure.

Table 4-18: Suggested Recommended Design Range of Various Cantilever Beams; Triangular Pressure Load (5MPa, Downwards, Top Face, Max at Free-End)

Additional Width/Depth (mm)	**Individual**	**Combined**	**Area vs Deflection (Bisected Value)**	**Depth vs Deflection**	**Range (adjusted for compatible model)**
Cantilever beam	0	0	0	0	0
Increased depth	6-7 (approx. 6.5)	12	10	12	6-12
Tapering triangle at the bottom face	17.5-21 (approx. 20.5)	17.5	14	28.1-31.7 (approx. 30.5)	14-31.7
Triangle using the rule of thumb based on the Method of Tensile Triangles.	28-30 (approx. 29.5)	36-38 (approx. 37)	34-36 (36)	49-51 (approx. 50.5)	28-51
Triangle following the Method of Tensile Triangles' shape profile	32-34 (approx. 32.5)	47	42	57-59 (approx. 58)	32-59

Table 4-19 shows the exact constructible value where the Method of Tensile Triangle's shape profile is ahead in terms of performance and required area for the case of Triangular Pressure Load.

Table 4-19: Clear Optimum Comparison Value for the Cantilever with Method of Tensile Triangles' Shape Profile; Triangular Pressure Load (5MPa, Downwards, Top Face, Max at Free-End)

Cantilever with the Method of Tensile Triangles			
Shape Profile		Rule of Thumb	
Required Area	Deflection	Required Area	Deflection
8087.5	0.66628	8090	0.66824
8339.5	0.56726	8340	0.56733
8423	0.5381	8427.5	0.53891

4.2.4.4 Efficiency (area/deflection versus area)

The following graphs (Figure 4-46, Figure 4-47, Figure 4-50, Figure 4-48, Figure 4-49, Figure 4-51) show the efficiency of different cantilever geometry. The higher the Area/Deflection ratio, the higher the efficiency. The graphs show that the graphs mentioned in the earlier sections to be consistent, and it can be clearly seen that graphs reflect the ranges provided in the summarised table in the earlier sections. Overall, the cantilever with the Tapering Triangle shows the highest efficiency for a One Point Load compared to the other cantilever geometry models in Figure 4-46 and Figure 4-47. The cantilever with the Method of Tensile Triangles' Rule of Thumb has the second-highest efficiency, followed by the cantilever with the Method of Tensile Triangles' Shape Profile. The cantilever with increased depth has the poorest efficiency as expected. This demonstrates the engineer's usage of the cantilever beam with the Tapering Triangle to be effective.

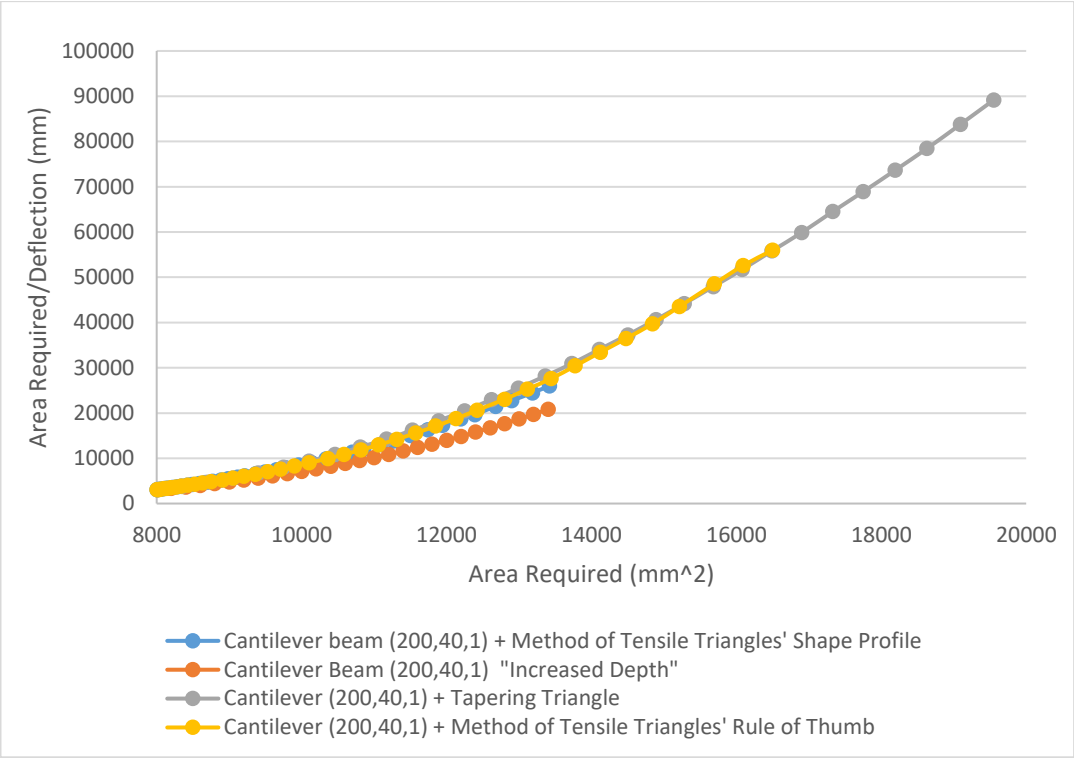


Figure 4-46: Efficiency (area/deflection vs area) for Various Cantilever Beams (up to 20000mm^2); One Point Load (Downwards, Free-End, Top Face, 1000N)

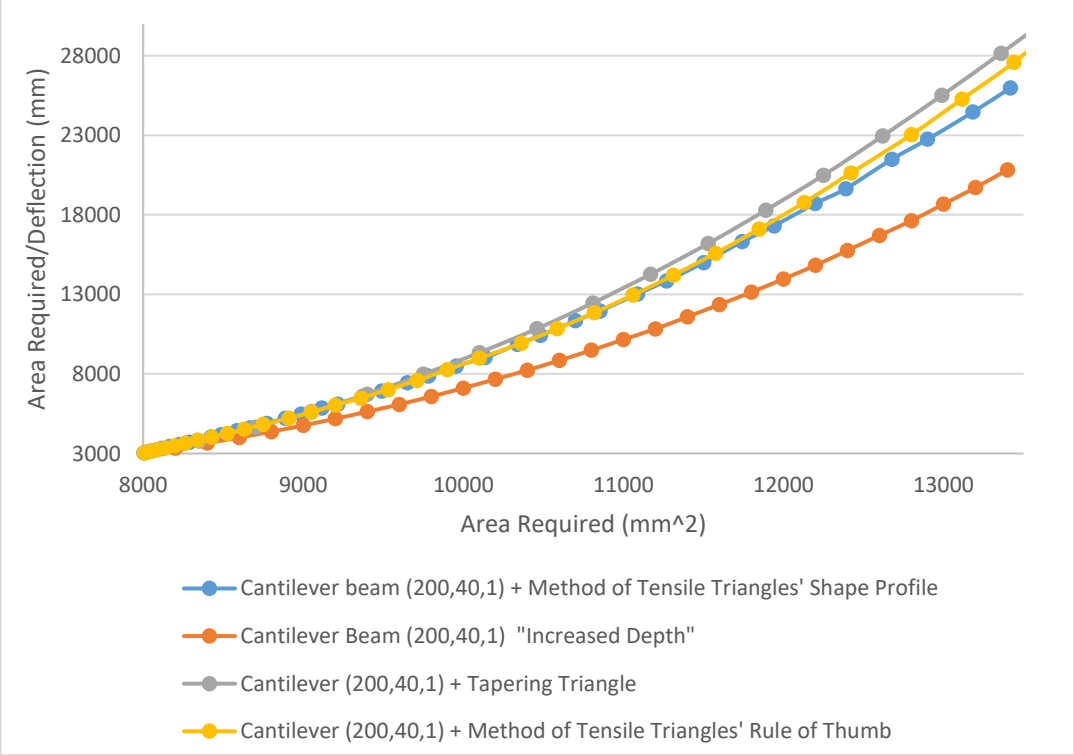


Figure 4-47: Efficiency (area/deflection vs area) for Various Cantilever Beams (up to 13500mm^2); One Point Load (Downwards, Free-End, Top Face, 1000N)

Similarly, the overall performance for a Triangular Pressure Load, the cantilever beam with the Method of Tensile Triangles' Rule of Thumb is the overall best under this loading condition, followed by the cantilever with the Tapering Triangle and lastly, the cantilever beam with the Method of Triangle's Shape Profile. However, the cantilever with increased depth is still the poorest among the three mentioned above. This is also shown in Figure 4-48 and Figure 4-49.

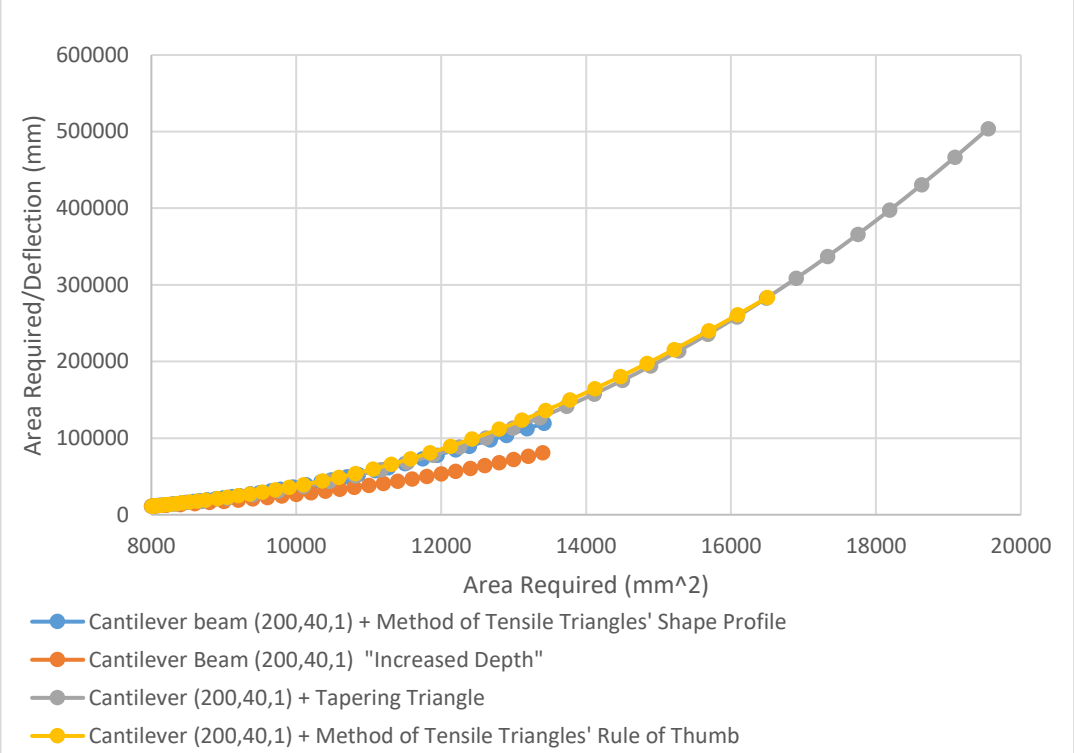


Figure 4-48: Efficiency (area/deflection vs area) for Various Cantilever Beams (up to 20000mm^2); Triangular Pressure Load (5MPa, Downwards, Top Face, Max at Free-End)

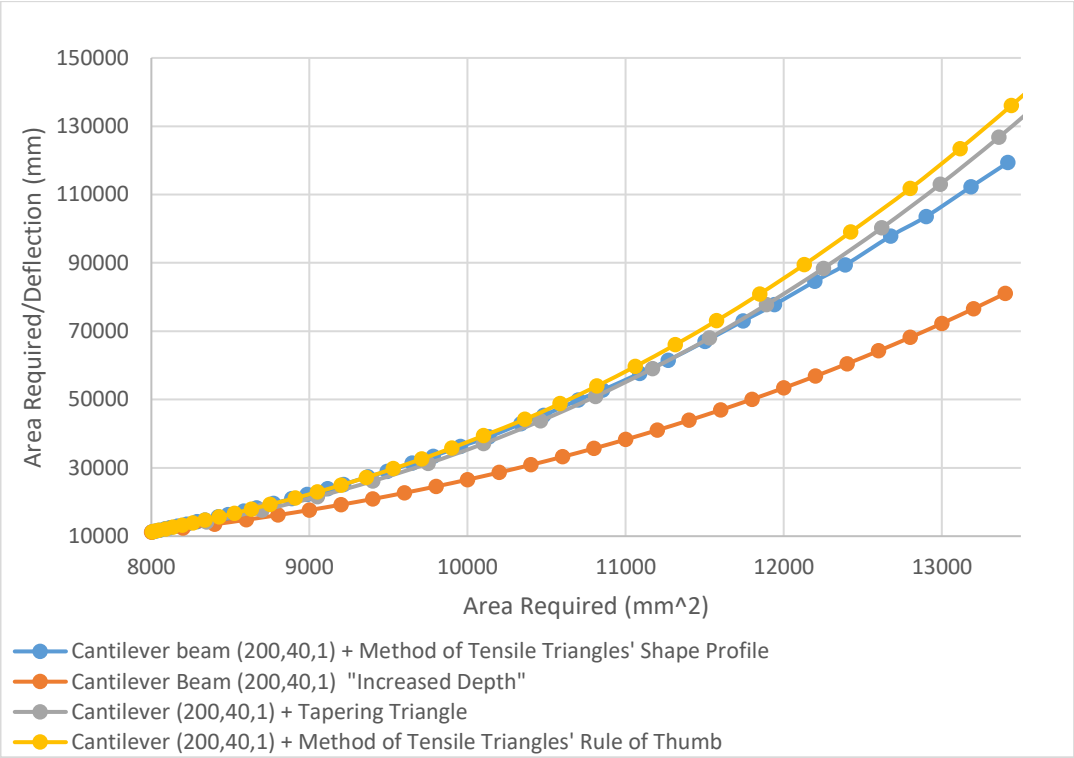


Figure 4-49: Efficiency (area/deflection vs area) for Various Cantilever Beams (up to 13500mm^2); Triangular Pressure Load (5MPa, Downwards, Top Face, Max at Free-End)

However, when the objective changes to improving current structures for both loading condition One Point Load in Figure 4-50 and Triangular Pressure Load in Figure 4-51, the cantilever beam with the tapering triangle and the cantilever beam with the Method of Tensile Triangles' Rule of Thumb are no longer the best in their respective loading cases as mentioned in the earlier sections. Figure 4-47 and Figure 4-49 clearly show that the cantilever beam with the Method of Tensile Triangle's Shape Profile is the best for small improvements (minimal increment of the area required). At the minimal increase of surface area, the Method of Tensile Triangles' Shape Profile has the highest efficiency, followed by the cantilever beam with the Method of Tensile Triangle's rule of thumb and lastly, the cantilever beam with the tapering triangle.

Interpolating from Figure 4-50 for the One Point Load, the suggestive optimum sizing for the cantilever with the Method of Tensile Triangles' Shape Profile in comparison to the Cantilever with the Tapering Triangle is at an area slightly above 8300mm^2 (on the graph a distance of 3mm). The cantilever with the Method of Tensile Triangles' still shows a reasonably consistent efficiency up to an area of 8700mm^2 (on the graph a distance of 2mm).Subsequently, interpolating from Figure 4-51 for the Triangular Pressure Load, the suggestive optimum sizing for the cantilever with the Method of Tensile Triangles' Shape Profile in comparison to the Cantilever with the Tapering Triangle is at an area between 9000mm^2 - 9400mm^2 (on the graph a distance of 8mm). The suggestive optimum sizing mentioned are not definitive, but it can be an excellent initial point for further study.

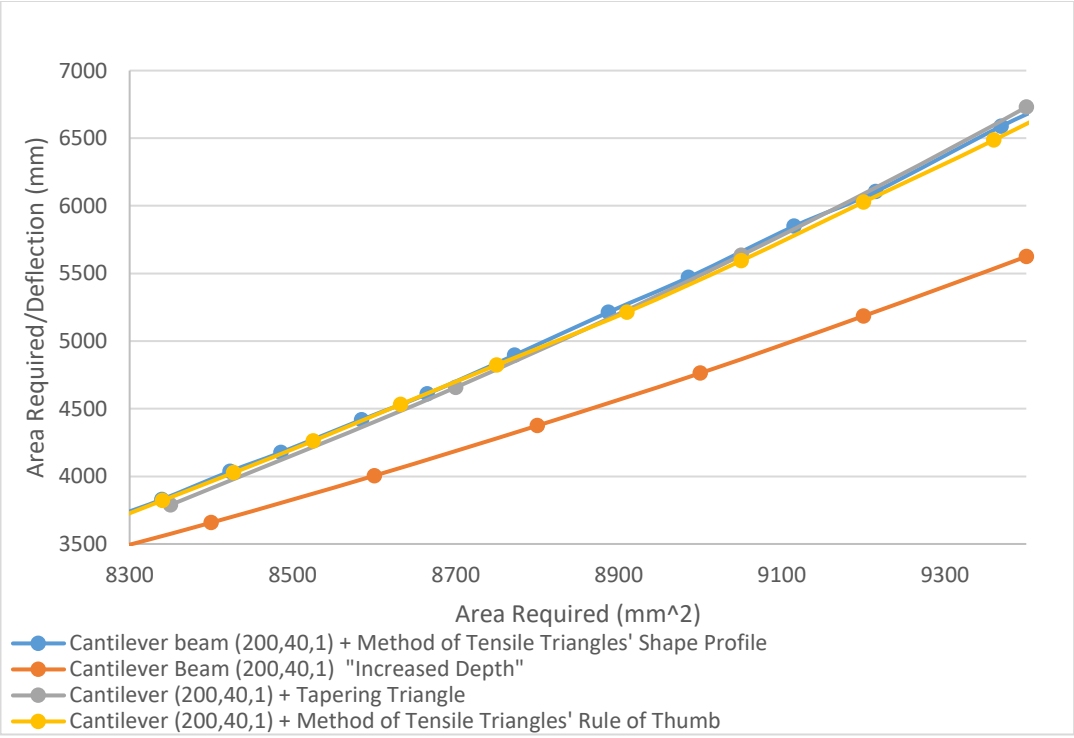


Figure 4-50: Efficiency (area/deflection vs area) for Various Cantilever Beams (up to 9400mm^2); One Point Load (Downwards, Free-End, Top Face, 1000N)

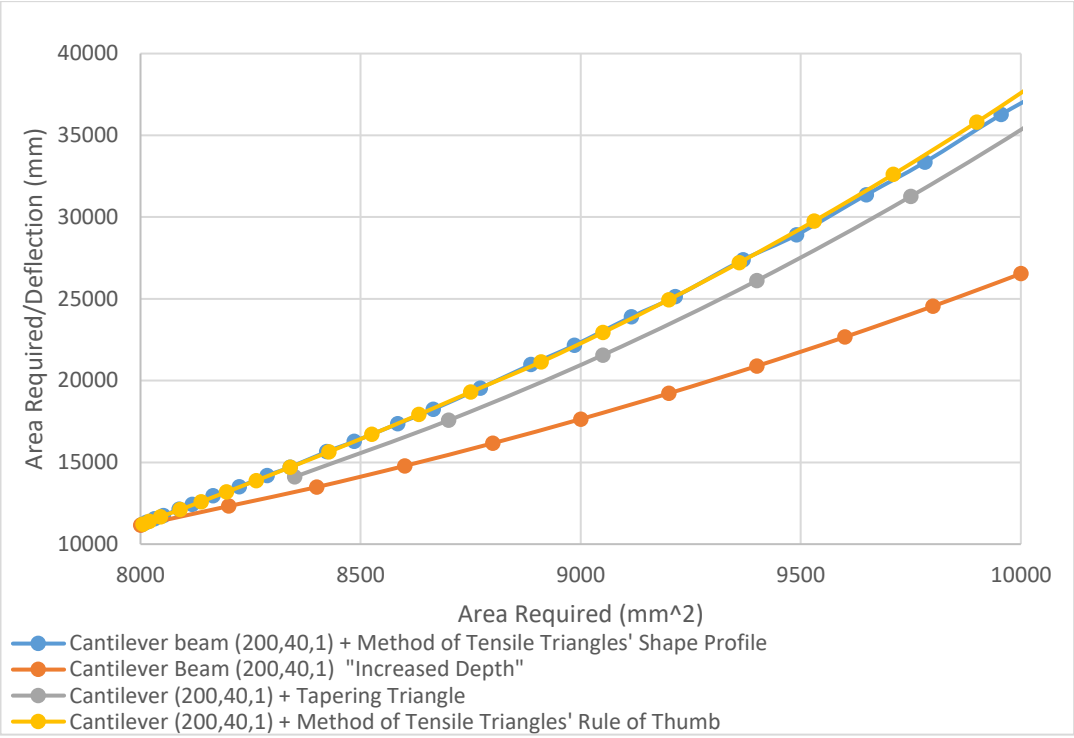


Figure 4-51: Efficiency (area/deflection vs area) for Various Cantilever Beams (up to 10000mm^2); Triangular Pressure Load (5MPa, Downwards, Top Face, Max at Free-End)

4.2.4.5 Performance of Cantilever (Deflection versus Area "%")

The favourable and unfavourable dimension or sizing of each cantilever geometry was highlighted in the previous sections. The cantilevers' performance may be appreciated in terms of percentages wise. At an area of about 13400mm^2, all three cantilever geometries, namely the Tapering Triangle, the Method of Tensile Triangles' Rule of Thumb and the Method of Tensile Triangles' Shape Profile for both loading conditions as shown in Figure 4-52 and Figure 4-53 have a deflection resistance above 80% more than the base model cantilever but requires an additional 65% more material. These cantilever beams are at least 5% better deflection performance than the cantilever beam with increased depth.

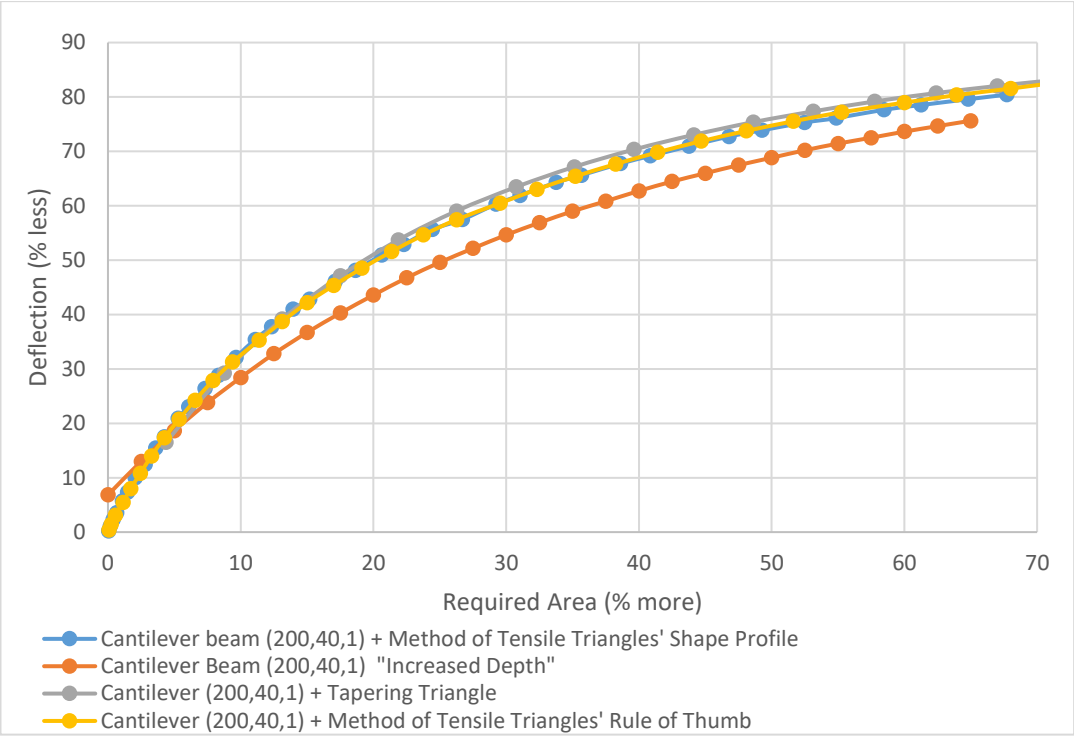


Figure 4-52: Performance of Cantilever (Deflection vs Area "%") for Various Cantilever Beams; One Point Load (Downwards, Free-End, Top Face, 1000N)

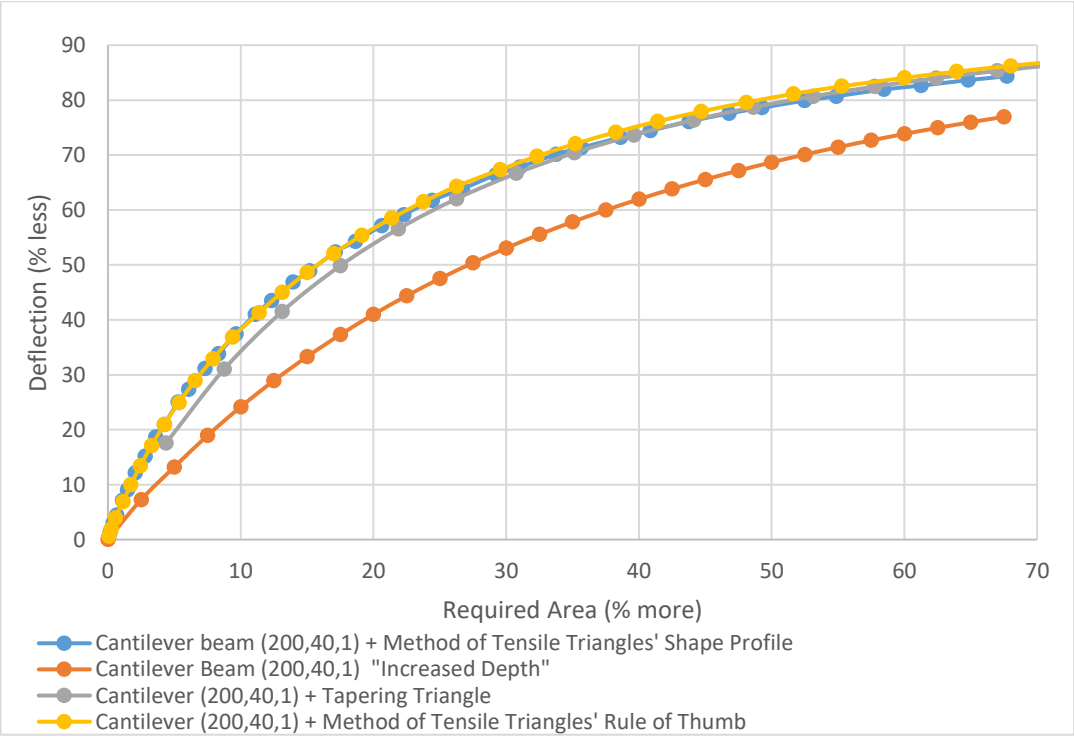


Figure 4-53: Performance of Cantilever (Deflection vs Area "%") for Various Cantilever Beams; Triangular Pressure Load (5MPa, Downwards, Top Face, Max at Free-End)

Introducing a projection beneath a cantilever that follows the Method of Tensile Triangles' Shape Profile can provide an effective deflection resistance up to about 43% with an increase of material of about 14.5% for a One Point Load as shown in Figure 4-52, where the depth is approximately 38mm and the total length of triangle approximately 90mm. However, for a Triangular Pressure Load in Figure 4-53, the effective deflection can go up to around 53% with an increase of material of about 17% (depth ≅ 42mm; total length of triangle ≅100mm).

As seen in the previous graphs in subchapter 4.2, the cantilever beam with the Method of Tensile Triangles' Rule of Thumb has less effective deflection resistance than the Method of Tensile Triangles' at its initial increment of the area, although the area required is more in the Method of Tensile Triangles'' Rule of Thumb. This behaviour also applies to the cantilever beam with Tapering Triangle. This may be due to the force flow between its loading point and its support. All the graphs presented concludes a similar finding through the different method of the graph (axis). Therefore, the finding concluded are accurate.

4.3 Stress profile

In this section, the stress profile of the various geometrical cantilever beams are compared, and the findings show a slightly different beam performance among the cantilever beam geometries. Figure 4-54 and Figure 4-55 show a graph between the equivalent stress experienced (MPa) and the total volume required (mm^3) for One Point Load and Triangular Pressure Load, respectively. Selected group samples on the stress plots of the various cantilever beam geometries are shown in Appendix B.b.a.

The stress profiles are analysed through ANSYS Mechanical as a 2D plane stress due to stress singularity. Both MTT and MTTR cantilever beams suffer this due to sharp corners/edges found between their transition zone. The inclusion of the assumption of sharp corners in the MTT and MTTR cantilever beams is to mimic closely to its design. However, it is unlikely to have a perfectly sharp edge in actual construction as assumed in the analysis because a relatively small radius connection will always exist between the two different line gradient. Thus, the function of "Elemental Mean" was utilised to obtain the stress result.

ANSYS (SimuTechGroup, 2020) defines the "Elemental Mean" von mises stress plot as the elemental average from the averaged component results, whereby it will create a checkboard plot with one value in each element. This technique reduces the effects of stress singularities in pollution the stress profile. However, it should be noted that the presence of stress singularities will generate some discrepancy or fluctuation in the stress result. Consequently, a margin of error is expected (Stress singularities has minimal effect on the deflection results).

In the stress graph in Figure 4-54, the MTT cantilever beam shows the lowest stress value among the other cantilever beam geometries across the smaller volumes. In the deflection graph, the MTT performs the best among the various cantilever beam geometries up to a volume around 9000mm^3. However, in the stress graph, the MTT performs the best up to a volume around 10800mm^3. This suggests that although the deflection was slightly higher than the ST cantilever beam, the MTT cantilever beams experience more uniform stress than the ST cantilever beam. From the stress plots in Appendix B.b.a, the MTT cantilever beams have a longer stress line along with its triangular projection than the ST cantilever that suggests the MTT cantilever has a more distributed stress along with its triangular projection than the ST cantilever beam.

Hence, the triangular projection in the ST cantilever beam can be seen to be slightly underutilised. Similarly, the MTTR cantilever beam also has a better deflection performance but suffers higher stress values across the various volumes. The MTTR cantilever can be seen from the stress plot to experience a higher stress value at the transition zone between the triangular projection and the remaining part of the cantilever beam.

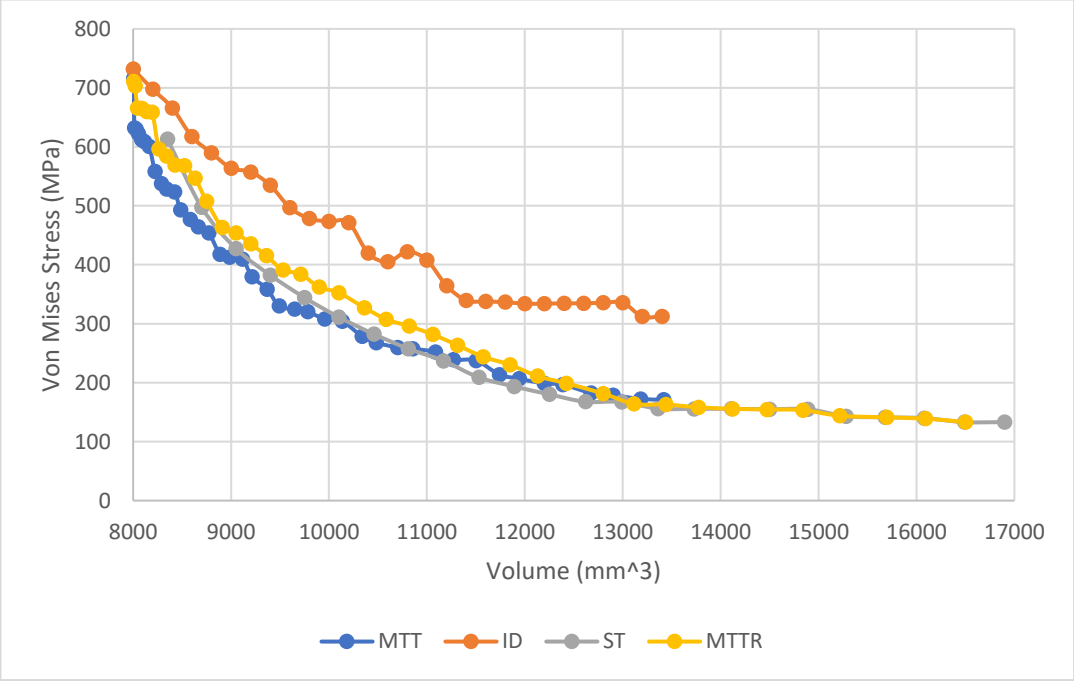


Figure 4-54: Equivalent stress for 40mm cantilever beam under STD load

A similar distribution of stresses in the TTD loading condition is exhibited as in the STD loading across the various cantilever geometries. However, the MTTR cantilever beams experience the lowest stress across the higher volumes as opposed to the ST cantilever beam. The kink in the MTTR cantilever beams is lesser of a problem towards the higher volumes. Both the MTT and MTTR cantilever beams were seen to be more suited to the imposed load than the ST cantilever beam. The stress plots in the MTT and the MTTR cantilever beams show the stress concentration to be further away

from its support and towards the length of the triangular projection. Whereas in the ST cantilever beam, the support was experiencing higher localised stress concentrations. Therefore, the stress results suggest that the triangular profile in the triangular project plays a role in distributing stress along its surface homogenously.

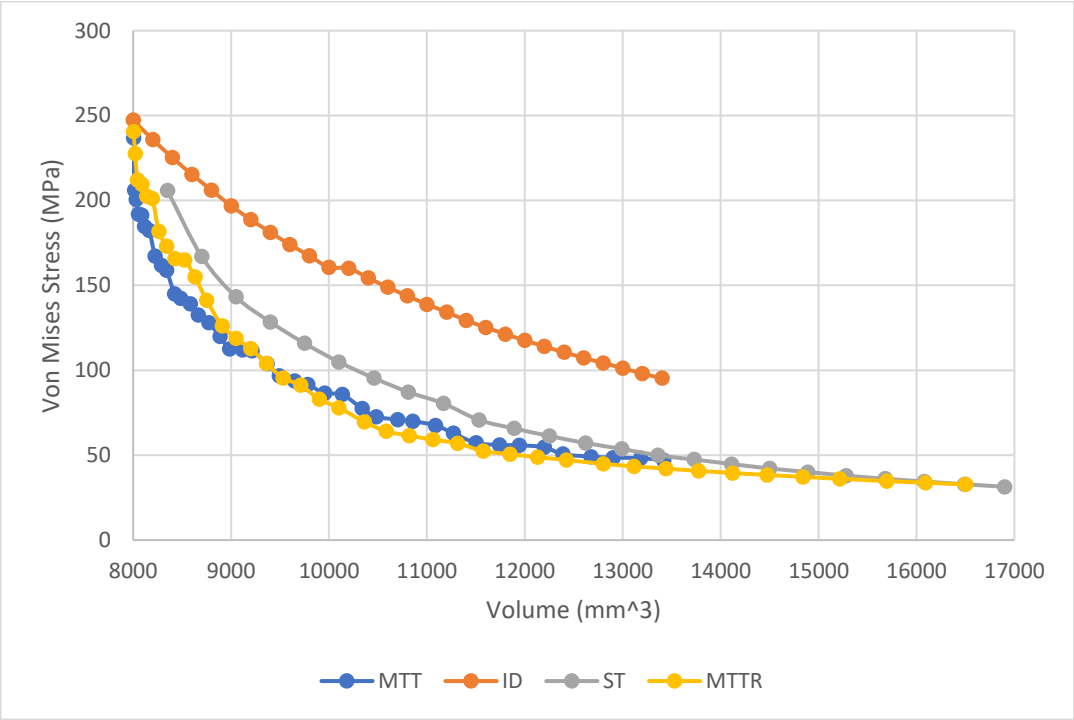


Figure 4-55: Equivalent stress vs volume for 40mm cantilever beam under TTD load

The following sample stress values of 300MPa and 600MPa for the STD load and 100MPa and 200MPa for the TTD load of the various cantilever beam geometries are to determine a general reduction in stresses when compared to the increased cantilever depth. The cantilever beams are chosen by their closest stress value. The performance of the various cantilever beam geometries under STD and TTD are shown in Table 4-20 and Table 4-21, respectively.

Table 4-20: Equivalent stress for 300MPa & 600MPa under One Point Load

Cantilever Beam	**Equivalent Stress (MPa)**	**(%)**	**Required Area (mm^2)**	**(%)**	**Equivalent Stress (MPa)**	**(%)**	**Required Area (mm^2)**	**(%)**
Cantilever beam	731.72		8000				8000	
Increased depth (ID)	617.26	15.643	8600 (43mm depth)	7.5	312.21	57.332	13200 (66mm depth)	65
Tapering triangle (ST)	613.05	16.218	8350 (3.5mm depth)	4.375	311.24	57.465	10100 (21mm depth)	26.25
Method of Tensile Triangles Rule of thumb (MTTR)	596.09	18.536	8262.5 (35mm length)	3.281	295.92	59.558	10817.5 (115mm length)	35.219
Method of Tensile Triangles (MTT)	600.72	17.903	8164.5 (35mm length)	2.056	304.06	58.446	10135 (125mm length)	26.688

Table 4-21: Equivalent Stress for 200MPa & 100MPa under Triangular Pressure Load

Cantilever Beam	**Equivalent Stress (MPa)**	**(%)**	**Required Area (mm^2)**	**(%)**	**Equivalent Stress (MPa)**	**(%)**	**Required Area (mm^2)**	**(%)**
Cantilever beam	247.29		8000				8000	
Increased depth (ID)	196.89	20.381	9000 (45mm depth)	12.5	101.29	59.04	13000 (65mm depth)	62.5
Tapering triangle (ST)	205.87	16.75	8350 (3.5mm)	4.375	95.367	61.435	10460 (24.6mm)	30.75
Method of Tensile Triangles Rule of thumb (MTTR)	201.2	18.638	8195 (30mm length)	2.438	104.11	57.9	9360 (80mm length)	17
Method of Tensile Triangles (MTT)	200.69	18.844	8031.5 (15mm length)	0.394	96.726	60.886	9490.5 (105mm length)	18.63

The graphs shown in Figure 4-56 shows that the MTT cantilever beam has the lowest stress experience and the lowest volume required. The MTTR performed second-best among the other cantilever beam geometries. The ST cantilever beam did not perform well across the higher stress values in both STD and TTD due to geometrical limits. It is primarily due to the underutilisation of the triangular projection that leads to a less uniform force flow. The ID cantilever beam can be seen to perform better across the higher stress value but is most likely due to the larger moment arm around its support due to the increased cantilever beam depth.

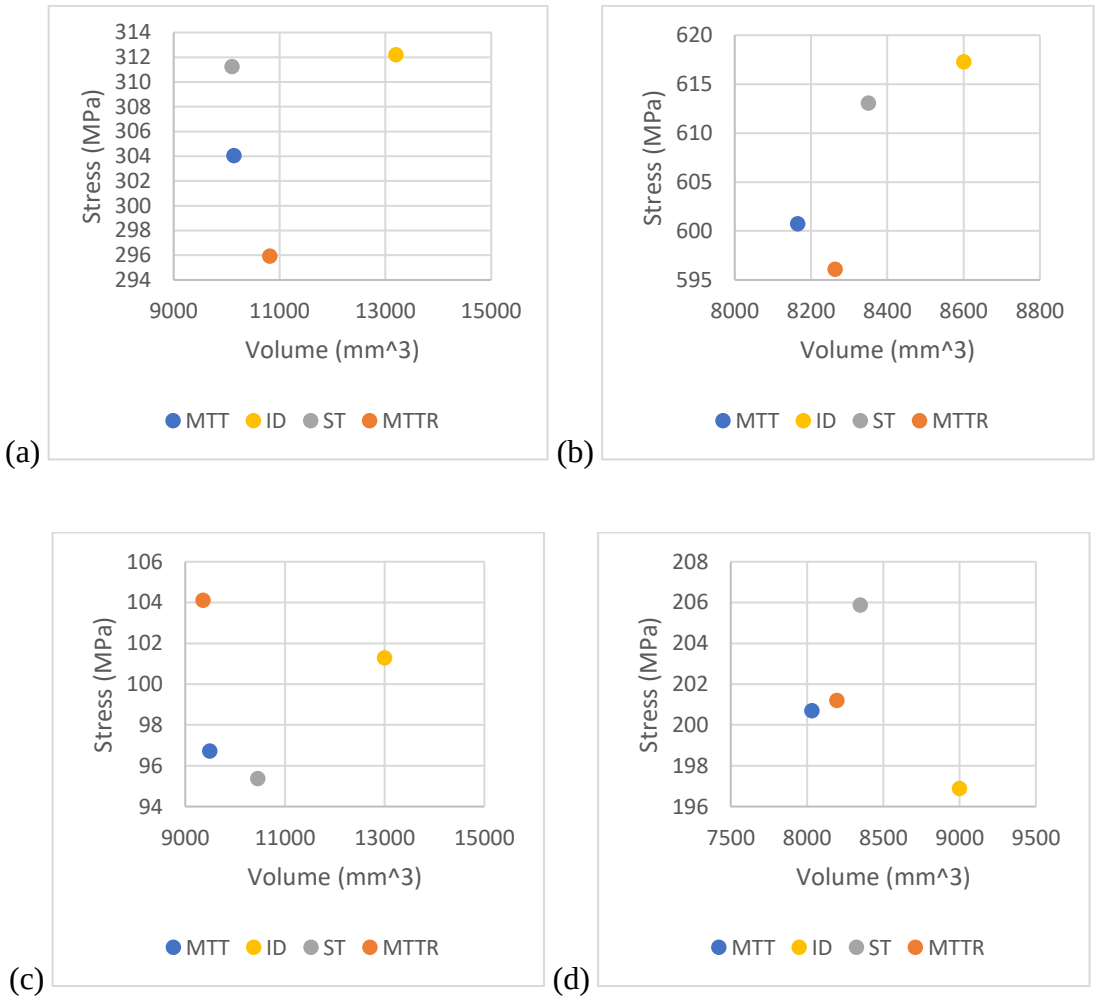


Figure 4-56: Stresses experience across the various 40mm cantilever beam geometries. (a) STD 300MPa, (b) STD 600MPa, (c) TTD 100MPa, (d) TTD 200MPa

Considering only the two cantilever beam geometries, the Method of Tensile Triangles (MTT) and the Standard triangle (ST) for the category of 600MPa, it can be seen that the MTT has 10.39% higher stress reduction and 112.79% material savings than ST. For the 200MPa category, MTT has 12.5% higher stress reduction and 1010.4% material savings than the ST, while the 300MPa category has a 1.71% higher stress reduction but 1.67% lower material savings than the ST. For the 100MPa category, a 0.9% stress increment in MTT leads to a material savings of 65.06% compared to ST. Hence, the MTT cantilever beam has more balanced stresses than the ST cantilever beam.

4.4 Discussion

Multiple graph techniques are applied in this analysis, and all the graphs demonstrate the different approaches used in searching for an optimum design value of each cantilever geometry (mainly for the Cantilever Beam with the Method of Tensile Triangles' Shape Profile). They show a different perspective and point of view on the subject, concluding to an almost similar conclusion. Even though the depth versus deflection graph is a less meaningful graph to study (due to the geometrical differences in relation to its total surface area), it can still provide some practical design limits for each cantilever geometry.

The choice of a cantilever beam model usually depends on the need, requirement or architectural aesthetic. In the case of an isotropic linear-elastic condition, the models analysed do provide some choice to the designer (to either have a higher free-end headroom or a nearly consistent height of headroom). In this situation (overall) for the One Point Load, the Standard Tapering triangle remains the most effective method for deflection resistance. For beams that require minimal depth at their support and a

consistent headroom, the cantilever beam with a tapering triangle is the best choice. However, this does not provide the most headroom at its free-end of the cantilever beam. This is where the cantilever beam with the Method of Tensile Triangle Rule of Thumb can provide (if the additional depth is not a significant concern). The deflection resistance and area required for both cantilever beams mentioned above are comparable as both exhibit similar deflection resistance.

The cantilever beam with the Method of Tensile Triangles' shape profile comes last among the three triangular models (under worst loading case, overall). Although the deflection resistance of the cantilever beam with the Method of Tensile Triangles' shape profile performed the worst among the three cantilever beams, the deflection resistance is still not too far apart when compared to its area required. For a specific range of increased area, for example, the One Point Load; the cantilever beam with the Method of Tensile Triangles' shape profile at an area of 8339.5mm^2, the deflection obtained is the lowest among the various cantilever models analysed. The cantilever with the Method of Tensile Triangles' Shape Profile performed best slightly above 8300mm^2 and between 9000mm^2 - 9400mm^2 range for the separate load cases, One Point Load and the Triangular Pressure Load, respectively. It should be noted that the Method of Tensile Triangles' Shape Profile remains the best in both loading condition below the area of 9200mm^2 but the area limit may be extended to 9400mm^2 for the Triangular Pressure Load. Therefore, this geometry is suitable for deflection improvement. Hence, it is safe to conclude based on the result that the usage of the Tensile Triangles' Shape Profile should be below the depth of 38mm (Total cantilever <78mm).

The stresses among the various cantilever beam geometries also show a similar conclusion, where the cantilever with the Method of Tensile Triangles' Shape Profile

experienced the lowest stress and most effective when the increment in area is minimal for both load cases. For a similar amount of stress, the cantilever with the Method of Tensile Triangles' Shape Profile can have a material savings of up to 1010% and 535% compared to the Standard Triangle and the Increased Depth, respectively. However, taking the lower value for a more realistic stress performance, the material savings should be about up to 65% and a possible stress reduction of about 12.5% compared to the standard triangle.

The results support the reason why tree buttress grow to a certain height and not the entire length or more than 1/2 of the tree height. The cantilever beam with the Method of Tensile Triangle's shape profile benefited the most by showing its performance capabilities under a Triangular Pressure Load with one of the lowest deflection value at its initial buttress area. The uniform force flow within the point of loading to its support may be the reason. The Method of Tensile Triangle's shape profile has shown to be very effective for small improvements with minimal material required with regards to the loading condition (e.g. 1 Point Load and Triangular Pressure load).

The cantilever beam with the Method of Tensile Triangle's rule of thumb overall performed the best under the Triangular Pressure Load, but this may not be the typical type of loading most engineers could appreciate. However, this provides an understanding of how engineers can create a better cantilever structure under this loading case. Overall, both cantilevers with the Method of Tensile Triangles resulted in a higher amount of width, but the deflection resistance by both models are satisfactory. Even though both cantilevers with the Method of Tensile Triangles require a higher depth, the area required, deflection resistance and headroom clearance do provide a substantial amount of consideration into the two models. For small cantilever beam improvement (minimal area increment), the Method of Tensile

Triangles' Shape Profile is the best when it comes to deflection resistance and minimal area required (in both loading conditions). Hence, this geometry comes with no disadvantage in providing the highest deflection resistance performance with the lowest amount of area required. In a general sense, it is worth noting that both cantilever models are very suitable for providing better deflection resistance with minimal material required.

4.5 Summary

The Cantilever with the Method of Tensile Triangles' Shape profile is best suited when the total increased area is small. In general, it will perform better than the other cantilever geometry design with any total increase in the area of less than 9200mm^2. The cantilever with the increased depth performed the worst among the other cantilever geometry designs. The cantilever with the Tapering Triangle and the cantilever with the Method of Tensile Triangles' Rule of Thumb performed better as the area increases but performed differently under different loading conditions. The tapering design performed best under the One Point Load, while the other two performed better under the Triangular Pressure Load. In summary, the cantilever with the Method of Tensile Triangles' Shape Profile projection can achieve a deflection resistance performance between 1.02 – 1.13 times more and material savings between 1.11 – 1.22 times more when comparing between the top three cantilever geometry projection. It is worth studying its behaviour under different types of structures, loading conditions, dynamic loading and in the plastic region. In addition to this analysis, further studies were conducted in the next chapter on the effects on its aspect ratio, loading face, and direction to better understand the triangular projections' behaviour and performance.

Chapter 5 Investigation on the Effects of Load Faces and Aspect Ratios on the Various Cantilever Beam Geometries

In the earlier chapter, the study compares and identifies the best graph method to determine the optimal geometrical range for a set of various cantilever beam geometries. In this chapter, the study compares and evaluates the behaviour of a cantilever beam under different depth, loading direction and loading face. This is to determine better the performance and behaviour related to its triangle projection support in cantilever beams. The preferred graph method identified in the previous chapter is utilised to evaluate the following analysis conducted in this chapter.

5.1 Details of the Finite Element Model

The parameters utilised are similar to Chapter 4 as the study is a continuation of the previous chapter. A total of 378 different sizes of cantilever beam geometries were modelled, generating a total of 1890 specimen variations. With consideration of a larger number of models, the study was analysed under 2D plane stress instead of 3D. Stress singularities are still expected when modelling a purely fixed cantilever beam with a single point load. Therefore, a slight margin of error is expected. The deflection value defined is the total deflection that includes the x and y as the deflection value in the x-direction is small and negligible.

There are three rectangular cantilever base models (a.k.a. standard) with a length of 200mm, and 1mm thick, and they are varied by their depth of 20mm, 30mm, and 40mm with an aspect ratio of 1/10, 3/20 and 1/5, respectively. The cantilever beams were analysed under five separate loading conditions as shown in Figure 5-1, 1000N single point load top face downwards (STD), 1000N single point load bottom face

downwards (SBD), 1000N single point load top face upwards (STU), 1000N single point load bottom face upwards (SBU), 5MPa triangular pressure top face downwards with the maximum at its free end (TTD). The loading condition of a single point load at its free end is used to simulate the behaviour of a cantilever beam with the maximum amount of deflection on, whereas the triangular pressure with its maximum at its free end is to simulate the worst distributed loading condition on a cantilever beam. A total of five cantilever beam geometries were analysed as shown in Figure 5-2, standard (base model), cantilever beam with increased depth (ID), cantilever beam with a tapering triangle (ST), cantilever beam with a triangular projection following the Method of Tensile Triangles Rule of Thumb (MTTR) and cantilever beam with a triangular projection following the Method of Tensile Triangles (MTT). The parameter analysed in this study for length "a" is fixed on all cantilever models, "b" varies between 20mm - 40mm, "c" varies between 0mm - 27mm, "d" varies between 1° - 26°and "e" varies between 5mm - 200mm. Geometrical dimensions are rounded to the next integer in the analysis.

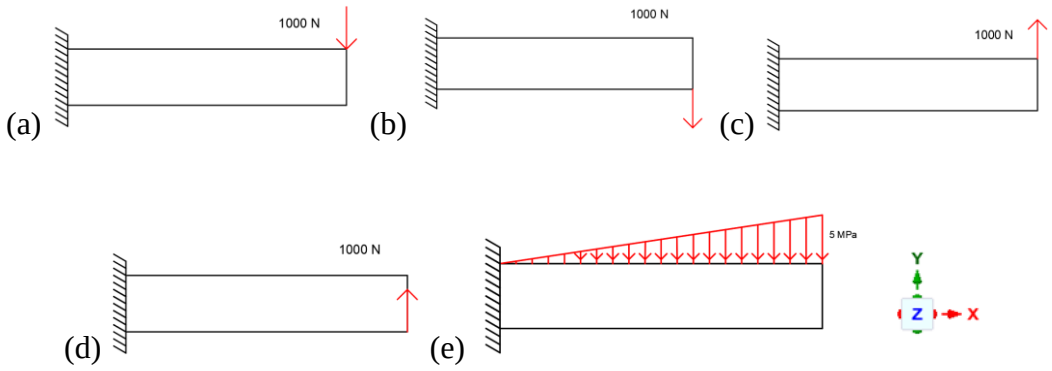


Figure 5-1: Separate loading conditions on the cantilever beam. (a) 1000N single point load top face downwards (STD); (b) 1000N single point load bottom face downwards (SBD); (c) 1000N single point load top face upwards (STU); (d) 1000N single point load bottom face upwards (SBU); (e) 5MPa triangular pressure top face downwards with the maximum at its free end (TTD).

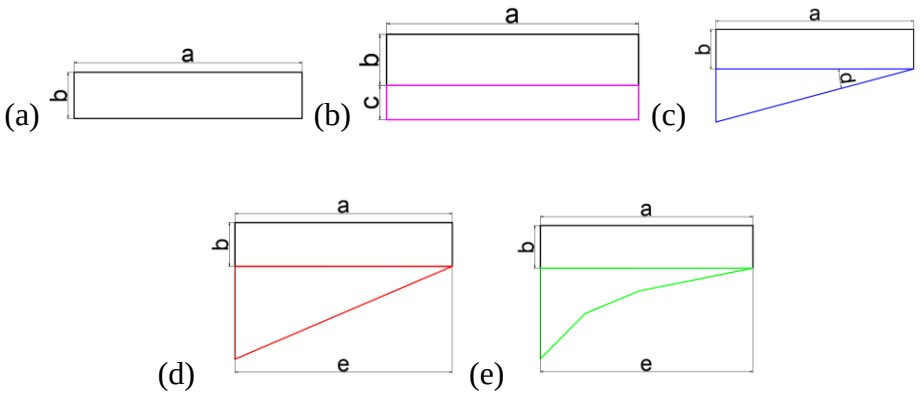


Figure 5-2: Various cantilever beam geometries. (a) standard (base model), (b) cantilever beam with increased depth (CID), (c) cantilever beam with a tapering triangle (ST), (d) cantilever beam with a triangular projection following the Method of Tensile Triangles Rule of Thumb (MTTR), (e) cantilever beam with a triangular projection following the Method of Tensile Triangles (MTT).

5.2 Comparison of the 4 Single Point Load Conditions

In this section, the four different single-point loading conditions are evaluated to determine the worst-case scenario. Among the three cantilever beam depths 20mm, 30mm and 40mm, the 20mm cantilever beam geometries have a higher asymmetry design that emphasises the triangular projection's performance. Furthermore, in all three cantilever beam depths, the “Single Bottom Downward (SBD)” load case is generally experiencing the lowest stress and deflection, while the “Single Top Downward (STD)” load case is generally experiencing the highest stress and deflection. Hence, the results suggest that cantilever beam geometries with a triangular projection, as in these examples, performed better under a downward bottom loading. However, it should be noted that regardless of the loading direction and location, the difference between them is small.

The ID cantilever beams are expected not to differ much with the different loading location and direction as their geometry is symmetrical. However, due to the lack of stiffness in the 20mm cantilever beam, the extreme flexibility can be challenging to

model accurately. Hence, leading to a higher difference between the loading conditions. The higher difference between the different loading conditions in the ST cantilever beams is likely due to the higher dependency of the triangular projection support. The stress localisation slowly shifts towards its support as the inclination of the triangle increases. This should be expected as the inclination moves towards the 45˚degree angle; the force flow would be redirected along the surface of the triangular projection and directed into the support end. Its phenomena can be imagined as a truss. For the MTT and MTTR cantilever beams, the difference between the loading conditions also increases along with the size increment. However, this is due to the magnification of the stress concentration at its transition zones. Similar to the ST cantilever, the increment in the size of the triangle projection increases its function in the cantilever beam to resist deflections.

The remaining 3 cantilever beam geometries for the 20mm cantilever beam depth display better performance under STU loading condition at lower volumes while performing better under SBD loading conditions at higher volumes. Hence, the results support the theory that the triangular projection in the windward side of the tree is better in tension (providing restoring moment). The results are summarised in Table 5-1 and Table 5-2 are the average percentage difference between its maximum and minimum values. Since STD resulted in the worst loading condition (outcome), the STD and TTD loading conditions are further discussed.

Table 5-1: Average difference between the maximum and the minimum values of the various geometries

Cantilever beam	Difference between the Maximum and Minimum (average %)	
	Deflection	Stress
	20mm	
MTT	2.298	2.077
ID	1.087	0.687
ST	3.71	0.506
MTTR	2.819	1.856
	30mm	
MTT	1.759	0.784
ID	0.519	0.315
ST	5.052	2.426
MTTR	2.509	1.925
	40mm	
MTT	1.831	1.423
ID	0.291	0.171
ST	6.333	1.699
MTTR	2.792	1.172

Table 5-2: Deflection performance comparison of the cantilever beam geometries under STD, STU and SBD.

Cantilever beam	DT vs UT (average difference %)	Volume range (mm^3)	DT vs DB (average difference %)	Volume range (mm^3)
MTT	2.69	4003 – 4339.5	2.14	4423 – 9418
ST	1.97	4350 – 4700	3.87	5050 – 12900
MTTR	2.77	4005 – 4427.5	2.88	4525 – 12500

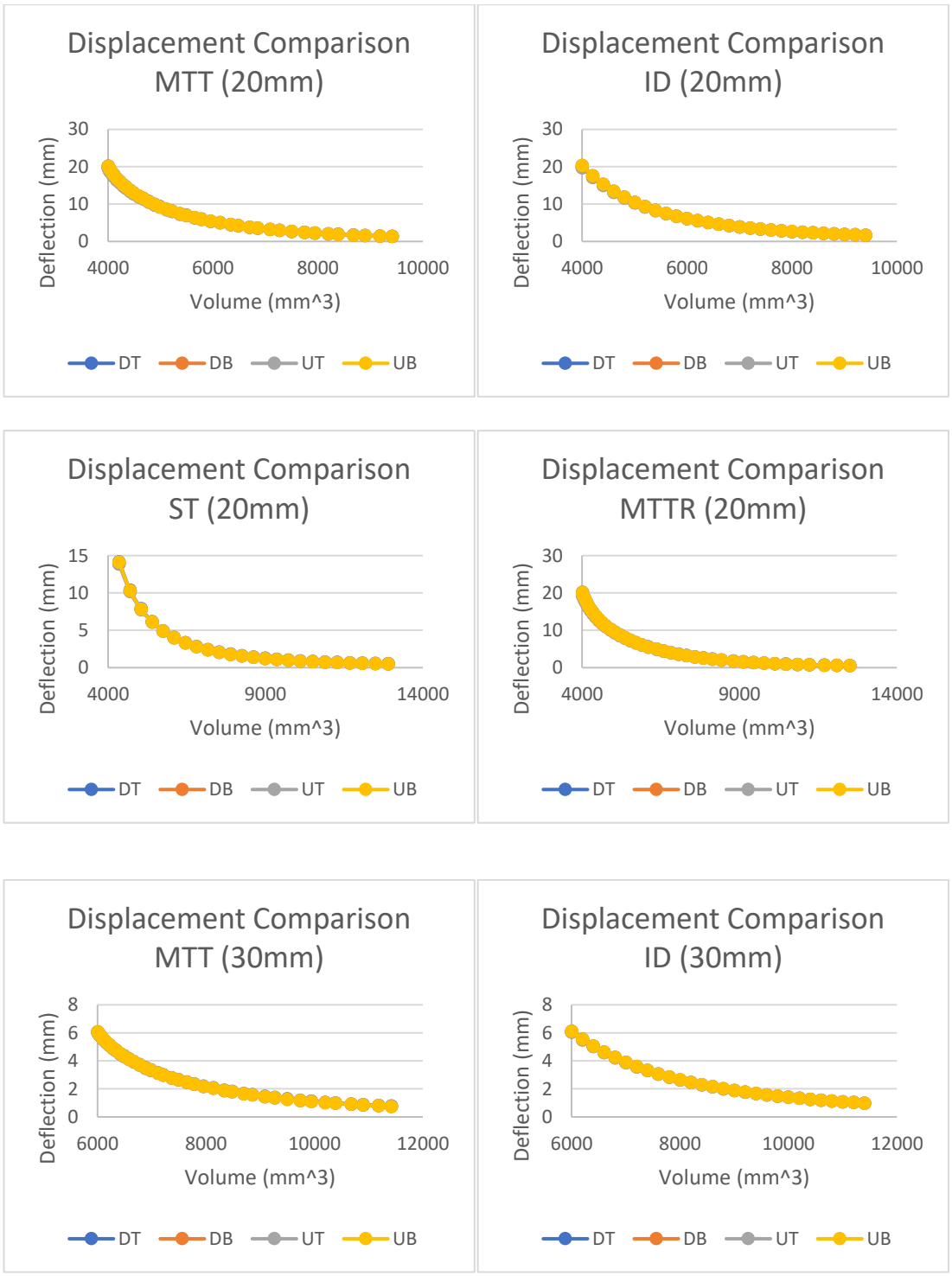


Figure 5-3: Deflection comparison across the various cantilever beam geometries

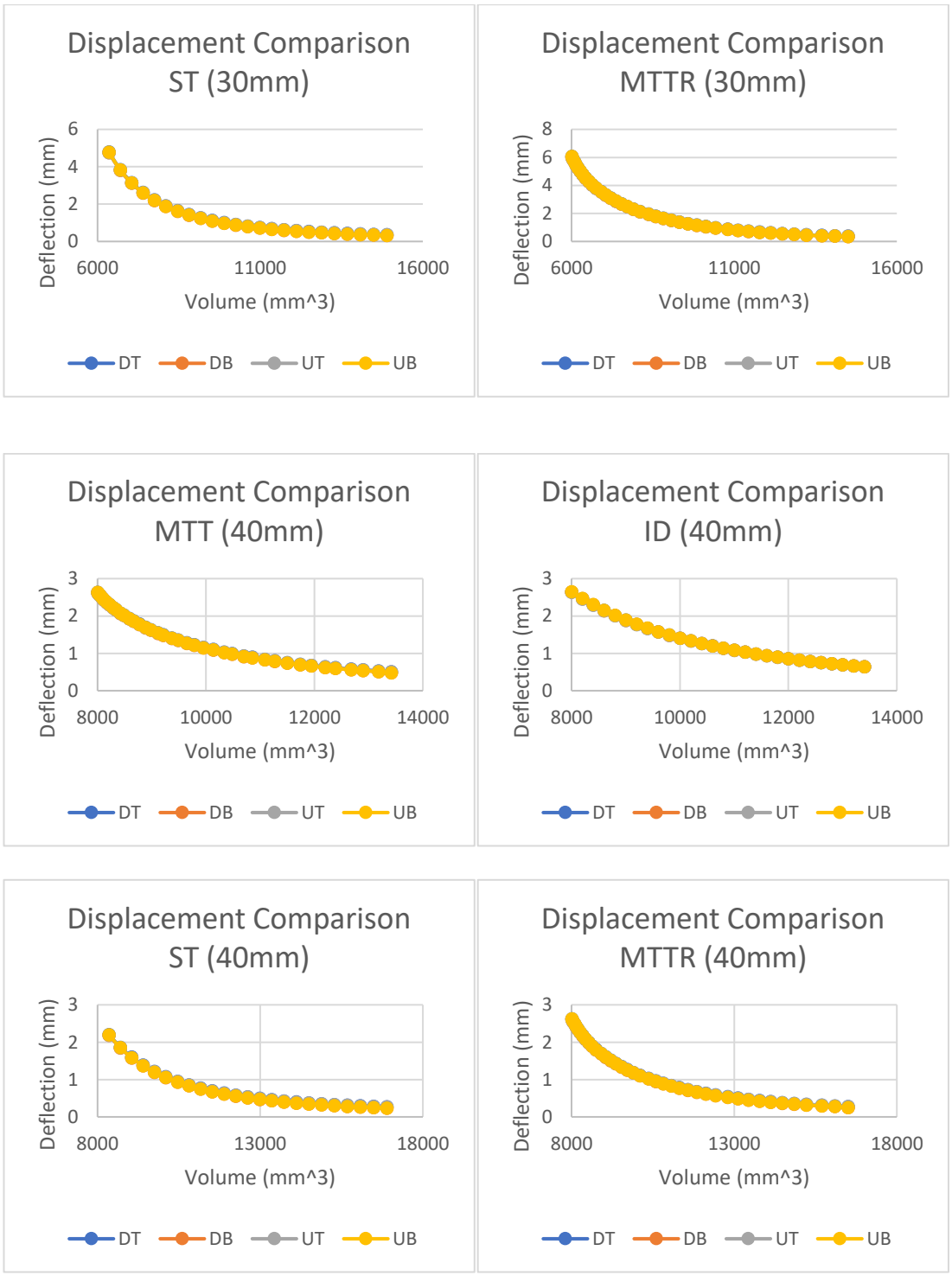


Figure 5-4: Deflection comparison over the various cantilever beam geometries (continued)

In terms of its stress profile, the stress pattern is a mirror image between the “Top” and “Bottom” load faces. The stress concentrations are different between the two-separate

loading location in all the three-cantilever beam except for the cantilever beam with the increased depth, mainly due to the location of the loading point in relation to its centroid body. Therefore, some fluctuation in stress concentrations is expected in the graphs due to stress singularities.

There is no doubt that the stresses experienced in the ID cantilever beams at all depths are the highest among the cantilever beam geometries. However, the MTT cantilever beams on the other end experience the lowest stress across all depth at the lower volumes. From the results, it is generally safe to assume that the first 500mm^3 increment in the volume will provide the lowest stress and deflections. Then, depending on the loading conditions (e.g. 40mm and 30mm depths), that volume increment can be increased to a volume of 1000mm^3 or more.

The ST cantilever beam generally performs better towards the higher volumes, especially in the single point loading conditions of the 30mm and 20mm depths. This is because it experienced the lowest stress and deflection across the higher volumes. The MTTR cantilever beams across the higher volume and particularly in the TTD loading condition seems to perform best among all cantilever beam geometries. It may be due to the sharper transitional zone between the triangular projection and the cantilever beam.

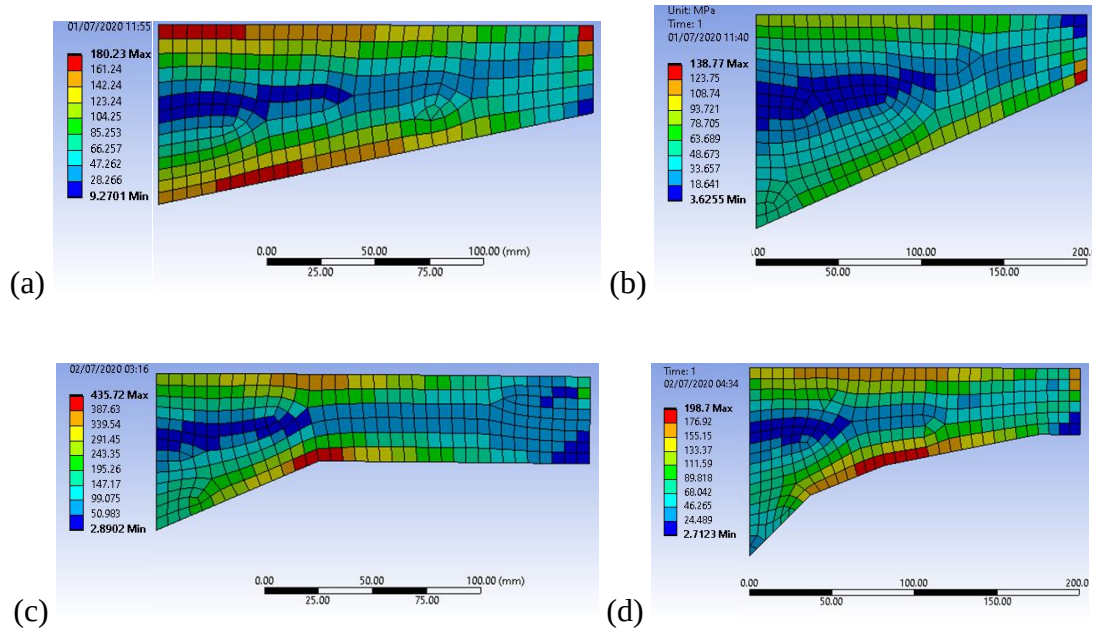


Figure 5-5: Stress profile (a) 12mm ST (b) 24mm ST (c) 75mm MTTR (d) 175mm MTT

Both the MTT and MTTR cantilever beams experienced lower stresses at the corner end of the triangular support, particularly more visible in the MTT cantilever beams. The longer the triangular projection, the lesser stress observed at the corner end of the triangular projection. The results suggest that the load path may no longer flow through along the surface of the triangular projection, which resulted in lower stress. Hence, it may also be another reason why the triangular projection in the MTT performs poorer across the increasing triangular projection length than other cantilever beam geometries of a similar volume. The stress profile between the different load conditions for the various cantilever beam geometrical designs are shown in Appendix B.b.a.

5.3 Deflection Resistance of the Various Cantilever Beam Geometries and its Loading Condition

5.3.1 Deflection limit

In this academic exercise, the base models chosen have a deflection limit greater than L/180 (as defined in the National Annex 2.23 Clause 7.2.1(1) B) to determine the performance of each cantilever beam geometry (British S.I. 2005). For a cantilever beam span of 200mm, the deflection limit is 1.1111mm. Hence, for example, a cantilever beam of 40mm depth under STD loading condition is 136.14% or 1.6238mm higher than the deflection limit, whereas a TTD loading condition of a similar depth is 35.44% or 0.39378mm lower than the deflection limit. Due to the distributed load in TTD, the cantilever beam is only expected to exceed the deflection limit of 1.1111mm with depths less than 35mm. The ST cantilever beam performs the best among all geometries under STD loading condition. MTT and MTTR cantilever beams show a similar performance under STD, but they performed better under TTD condition at 30mm depth. The ID cantilever beam performed the worst under all conditions. The design details and the results for STD and TTD loading conditions are summarised in Table 5-3 and Table. 5-4. Their relative sizing is shown in Figure 5-6.

Table 5-3: Results and design details for STD loading condition under the deflection limit.

Cantilever Beam	Additional depth (mm)	Difference (%)	Deflection (mm)	Difference (%)	Total Volume (mm^3)	Difference (%)
Base (20mm)	0		20.305		4000	
ID	35	175% more	1.0628	94.77% less	11000	175% more
ST	57.3	286.5% more	1.0106	95.02% less	9730	143.25% more
MTTR	72	360% more	1.0779	94.69% less	10120	153% more
Base (30mm)	0		6.0903		6000	
ID	25	83.33% more	1.0628	82.55% less	11000	83.33% more
MTT	74	246.67% more	1.0379	82.96% less	10197	69.95% more
ST	38.9	129.67% more	0.99919	83.59% less	9890	64.83% more
MTTR	59	196.67% more	1.0603	82.59% less	10130	68.83% more
Base (40mm)	0		2.6238		8000	
ID	15	37.5% more	1.0628	59.49% less	11000	37.5% more
MTT	53	132.5% more	1.0946	58.28% less	10135	26.69% more
ST	21	52.5% more	1.0628	59.49% less	10100	26.25% more
MTTR	42	105% more	1.1028	57.97% less	10100	26.25% more

Table. 5-4. Results and design details for TTD loading condition under the deflection limit.

Cantilever Beam	**Additional depth (mm)**	**Difference (%)**	**Deflection (mm)**	**Difference (%)**	**Total Volume (mm^3)**	**Difference (%)**
Base (20mm)	0		5.5437		4000	
ID	15	75% more	1.0594	80.89% less	7000	75% more
MTT	53	265% more	1.097	80.21% less	6135	53.38% more
ST	21	105% more	1.0039	81.89% less	6100	52.5% more
MTTR	45	225% more	1.0272	81.47% less	6362.5	59.06% more
Base (30mm)	0		1.6673		6000	
ID	5	16.67% more	1.0594	36.46% less	7000	16.67% more
MTT	28	93.33% more	1.0476	37.17% less	6584.5	9.74% more
ST	7	23.33% more	1.022	38.7% less	6700	11.67% more
MTTR	21	70% more	1.0923	34.49% less	6525	8.75% more
Base (40mm)	0		0.71732		8000	

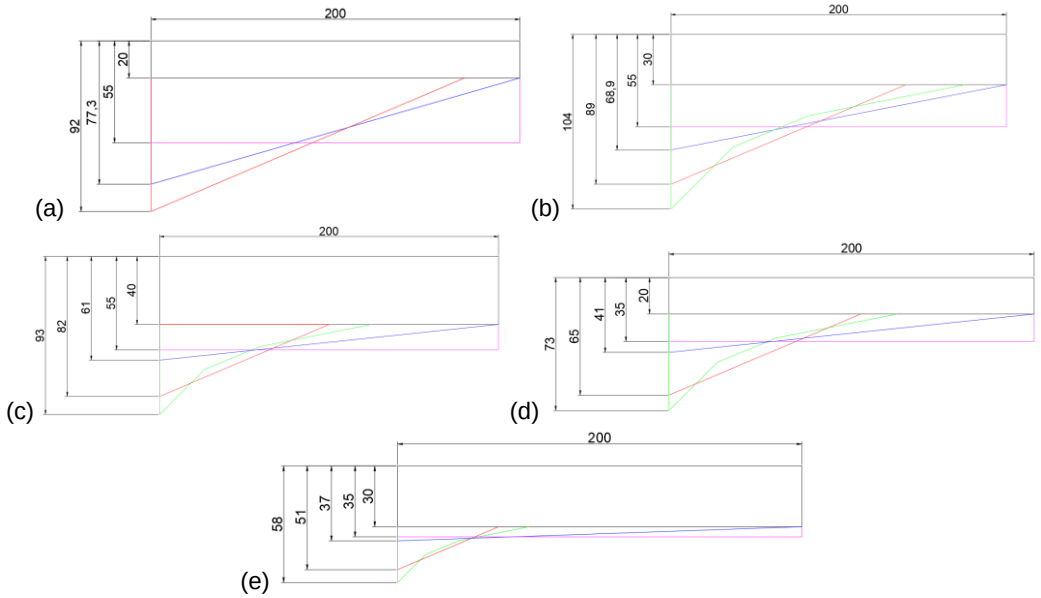


Figure 5-6: Relative cantilever beam dimension (a) 20mm STD, (b) 30mm STD, (c) 40mm STD (d) 20mm TTD (e) 30mm TTD

5.3.2 The Combined Result of Each Cantilever Geometry

As expected, the ID cantilever shows a single continuous curved line as there is no discontinuity between the different depths. For the other three cantilever beam geometries, three separate curves are visible and consistent for each geometry type at different depths. This is due to the irregularity in the shape and size of their respective cantilever beam geometries that affect their load path. Between the three cantilever beam geometries, the ST cantilever beam has the highest effect on the variation of the cantilever beam depth. The graph in Figure 5-7 shows that the ST cantilever beam can perform better through a well-defined triangular projection than a deeper cantilever beam.

Nevertheless, all three cantilever beam geometries show better deflection resistance across higher volumes at the same depth than a deeper beam with lower volume. This is mainly due to the angle of the triangular projection that leads to a different load path. For cantilever beam geometries MTT and MTTR both show lesser geometrical

benefits in reducing the deflection variation between the different depths. Thus, the triangular projection in both MTT and MTTR cantilever beam geometries has a smaller effect on the performance of the cantilever beam. The 30mm depth MTTR cantilever beam under STD loading shows some inconsistency compared to the other models. This may be due to the load transfer between the load and the support.

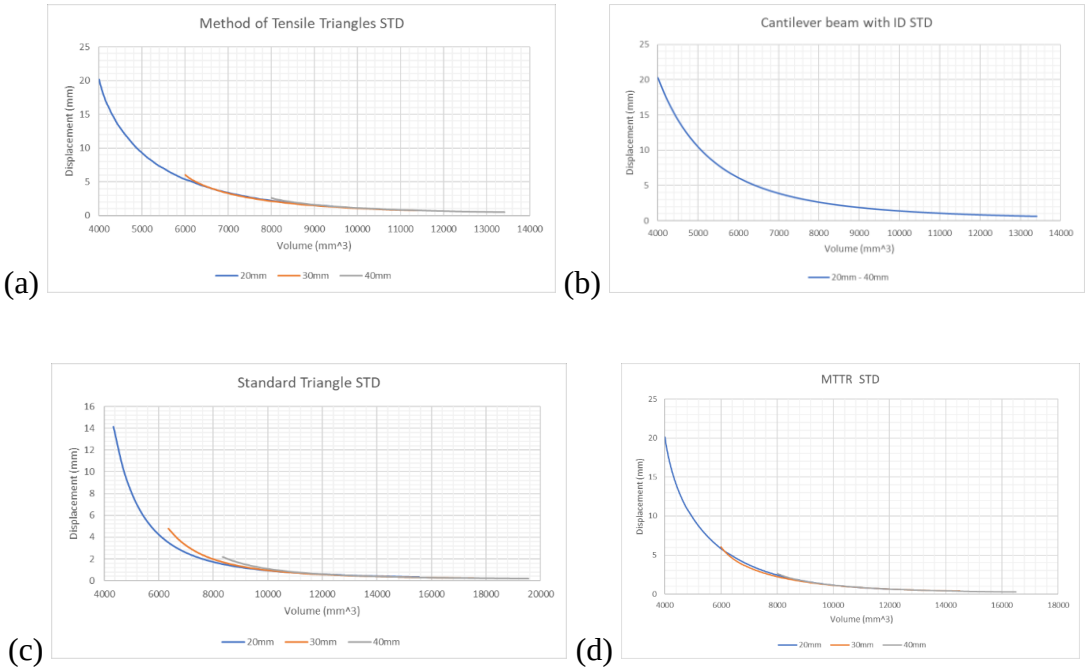


Figure 5-7: Combined results on each of the cantilever beam geometries under STD loading condition.

For the TTD loading condition, all three cantilever beam geometries other than the ID cantilever beam show higher deflection variation between various depths when compared to the STD condition. It suggests that the triangular projection would perform more effectively under the TTD loading condition than the STD loading condition, and this is expected. The combined results are shown in Figure 5-8. It should be noted that the equations provided for both the STD and TTD are merely a general guide instead of absolute value.

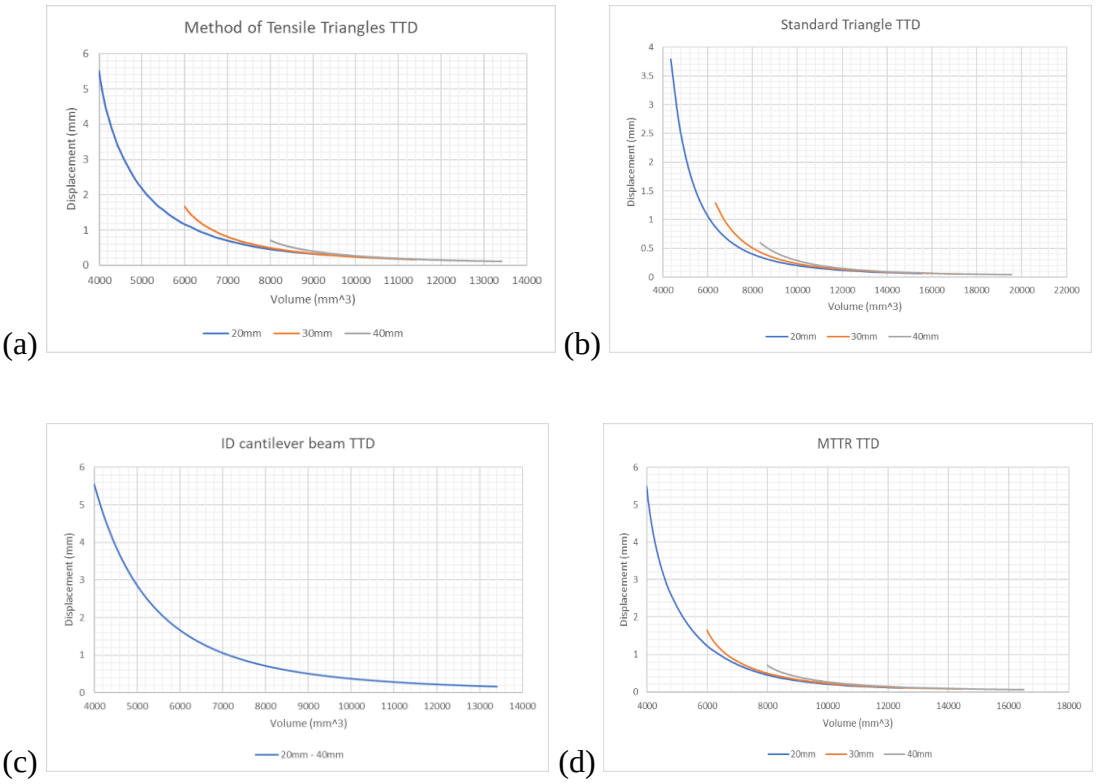


Figure 5-8: Combined results on each of the various cantilever beam geometries under TTD loading condition

5.3.3 Variation in Cantilever Beam Depth

As expected, the ID cantilever beam performed the worst among the other cantilever geometries under all loading conditions, as shown in Figure 5-9. ST cantilever beam is the best overall design under STD loading. Under STD, the ST cantilever beam performed the best across all volumes for the 20mm cantilever beam. The ST cantilever beam performed best at higher volumes for the 30mm and 40mm cantilever beam. In this case, MTT and MTTR cantilever beams are seen to perform better at lower volumes. Under the 30mm and 40mm STD loading condition, MTT performs better than the ST cantilever beam with volumes less than 6485.5mm^3 and 8750mm^{3,} respectively, while for MTTR, volumes less than 6427.5mm^3. MTTR can achieve similar performance as the ST cantilever beam at volumes above 14000mm^3 and 15215mm^{3,} respectively. MTT and MTTR cantilever beams are better supported when

the cantilever beam has sufficient depth, thus, as expected to perform poorer towards shallower cantilever beam depth. The MTT cantilever beam performs better than the MTTR at lower volumes across all cantilever beam depths under STD.

However, under TTD loading condition, the ST cantilever beam performed best at higher volumes for 20mm cantilever beam depth. Both MTT and MTTR cantilever beams performed better at lower volumes as in the STD loading condition for the 20mm cantilever beam depth (with an extended volume range). For depths of 20mm, 30mm and 40mm under TTD loading conditions, MTT perform better than the ST cantilever beam with volumes less than 4584.5mm^3, 8338mm^3, and 11269mm^{3,} respectively. It performs better for MTTR under 20mm TTD loading condition than the ST cantilever beam with volumes less than 4525mm^3. MTTR cantilever beam consistently outperforms the ST cantilever beam across all volume range for beam depth of 30mm and 40mm. MTTR shares similar performance with the ST cantilever beam at volumes above 9600mm3, 8460mm3, and 15215mm3. The MTT cantilever beam performs better than the MTTR at lower volumes across all cantilever beam depths. Towards the higher volume range for both loading conditions, the MTTR cantilever beam performs similarly to the ST cantilever beam. Thus, showing the design to be very comparable.

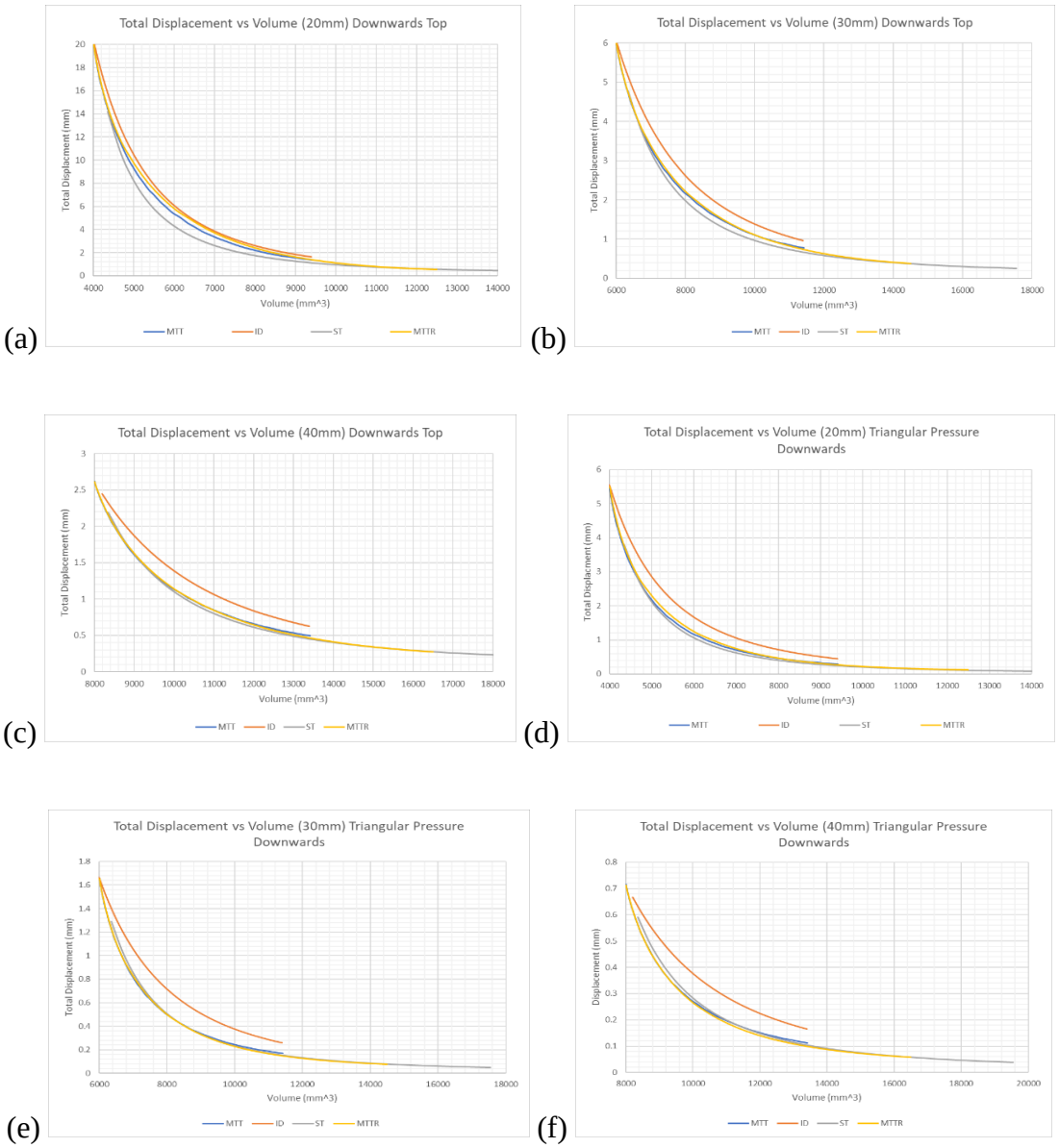


Figure 5-9: Deflection vs volume plot of the different cantilever beam depths

5.3.4 Deflection Performance for the Volume of Up to 50%

The graphs shown in Figure 5-10 is the deflection performance plotted against volume in terms of percentage. The two best cantilever beam geometries cantilever are compared to their respective base cantilever model in each graph set.

For the 20mm STD, the ST cantilever beam has about 7% to 11% better deflection performance than the ID cantilever beam. In contrast, the MTT cantilever beam is 6%

better than the ID cantilever beam. For the 30mm STD deflection performance, the ST cantilever beam has a maximum difference of 11%, while the MTT cantilever beam has a maximum difference of 10% compared to an ID cantilever beam. In the 40mm STD case, the ST cantilever beam and the MTT cantilever beam achieve the 10% deflection resistance at a different volume range, 35% volume, and 27% volume.

While for TTD, the MTT cantilever beam achieves a maximum difference of 10% at 11% volume, while the ST cantilever achieves a maximum difference of 12% at 17.5% volume for the 20mm beam depth. For the 30mm beam depth, the MTT cantilever beam achieves a 14% difference at a volume of around 19%, while the ST cantilever beam achieves a 12% difference at 24% volume. For the 40mm beam depth, the MTT cantilever beam achieves a 15% difference at 34% volume, while the ST cantilever beam achieves only 12% difference at 35% volume. It clearly shows that the MTT cantilever beam generally performs well under the lower volume range.

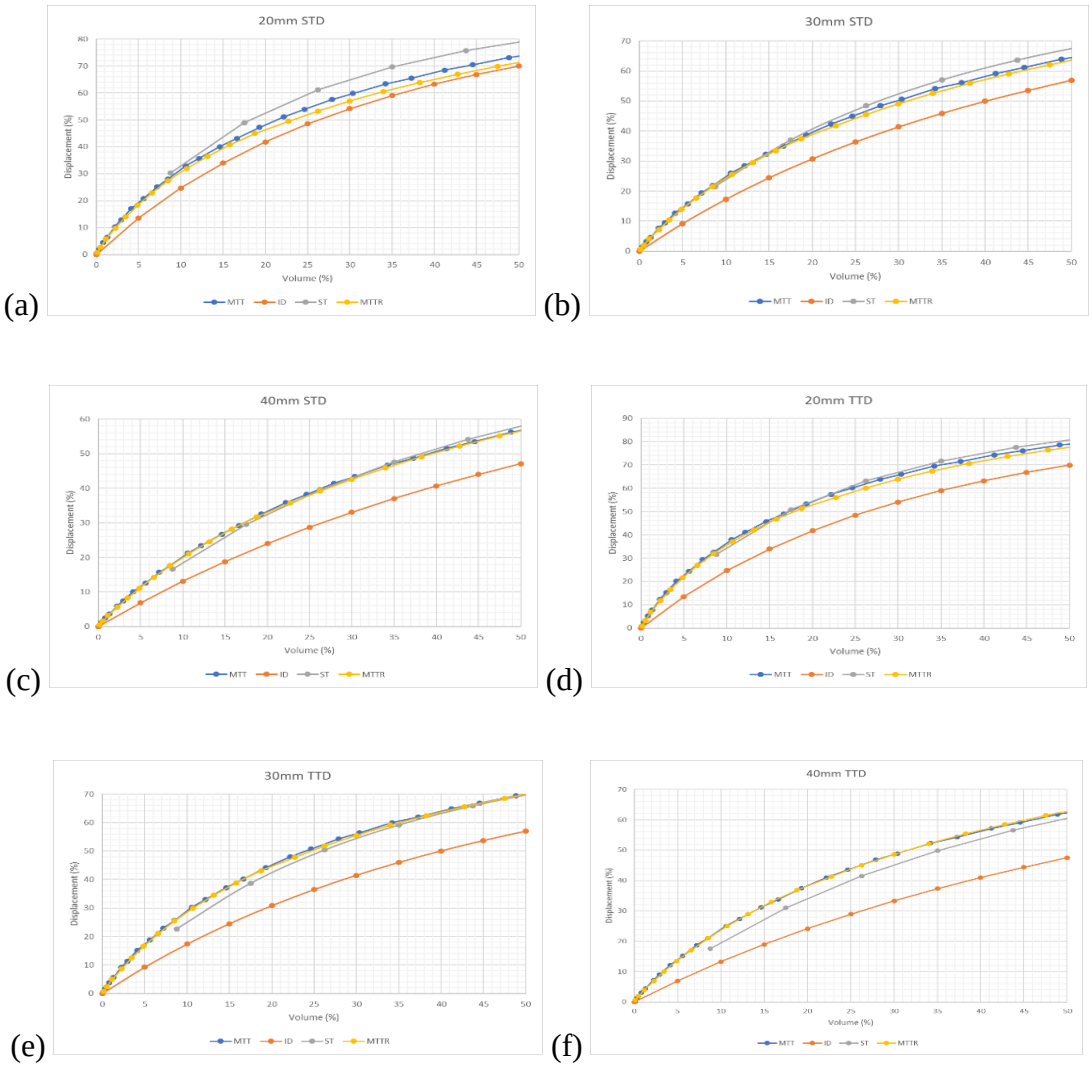


Figure 5-10: Deflection performance for the volumes of up to 50%.

5.4 Discussion

Across all three cantilever beam depths 10mm, 30mm and 40mm, the “Single Bottom Downward (SBD)” load case generally experienced the lowest stress and deflection while the “Single Top Downward (STD)” load case generally experienced the highest stress and deflection. Hence, the cantilever beam geometries with a triangular projection should perform better under a downward bottom loading, further supporting the theory that the windward buttress in trees is suited to be tension. However, since the difference between the different load direction and location is small, it may not be

wise to pursue further into it safe and except if it is reexamined under an anisotropic condition that may bring better results.

The higher difference between the different loading conditions in the ST cantilever beams is likely due to the higher dependency of the triangular projection support. The stress localisation slowly shifts towards its support as the inclination of the triangle increases. One can be imagined as a truss design where the inclination moves towards the 45˚degree angle; the force flow would be redirected along the surface of the triangular projection and directed into the support end. For the MTT and MTTR cantilever beams, the difference between the loading conditions also increases along with the size increment. However, this is due to the magnification of the stress concentration at its transition zones. Similar to the ST cantilever, the increment in the size of the triangle projection increases its function in the cantilever beam to resist deflections.

In terms of its stress profile, the stress pattern is a mirror image between the “Top” and “Bottom” load faces. The location of loading point in reference to the centroid body resulted in the difference of stress concentrations between the two-separate loading location in all the three-cantilever beam except for the ID cantilever beam. The increment of about $500mm^3$ (6.25%) in the MTT cantilever beam is generally beneficial in reducing stresses and deflections. The ST cantilever beam generally performs better towards the higher volumes, especially in the single point loading conditions of the 30mm and 20mm depths. It experienced the lowest stress and deflection across the higher volumes. The MTTR cantilever beams across the higher volume and particularly in the TTD loading condition seems to perform best among the other cantilever beam geometries. It may be due to the sharper transitional zone between the triangular projection and the cantilever beam.

Both the MTT and MTTR cantilever beams experienced lower stresses at the corner end of the triangular support, particularly more visible in the MTT cantilever beams. The longer the triangular projection, the lesser stress observed at the corner end of the triangular projection. The results suggest that the load path may no longer flow through along the surface of the triangular projection, which resulted in lower stress. Hence, it may also be another reason why the triangular projection in the MTT performs poorer across the increasing triangular projection length than other cantilever beam geometries of a similar volume.

The study shows that the ST cantilever beam has the best general overall performance across the higher volume. The ST cantilever performs better through the incremental inclination angle of the triangle projection as opposed to increasing the depth of the beam. As expected, the ID cantilever performed the worst when compared to the other cantilever beam geometries. This is mainly due to the moment induced on the structure. Hence, it can be concluded that a triangular-shaped projection is more suited for a cantilever structure. However, no single solution is appropriate for all cantilever beam designs (aspect ratio) and loading conditions.

The MTT cantilever beam performed better than the ID cantilever but performed poorer than the ST cantilever beam. For cantilever beam depth of 20mm, the MTT cantilever beam was not able to show any benefits across all volume range of the ST cantilever beam under STD. However, the MTT cantilever beam clearly performs better than the ST cantilever beam across the lower volume range under STD and TTD loading conditions when the cantilever beam has sufficient depth (e.g. 40mm). In addition, the MTT cantilever beam performed better than the ST cantilever beam under TTD loading conditions at a lower volume range. Although the MTT cantilever beam

may not display the intended outcome in this numerical example, the deflection resistance was close to the ST cantilever beam.

For cantilever beam depth of 20mm, the MTTR cantilever beam did not display any improvement over the MTT cantilever beam under STD. It shows a poorer deflection resistance than the MTT cantilever beam. As the cantilever beam deepens towards the 30mm and 40mm depth, the MTTR cantilever beam under STD loading condition was found to perform better than the MTT cantilever at the higher volume range. For both STD and TTD at all different cantilever beam depths, the MTT cantilever beam performs slightly better than MTTR cantilever across the lower volume range and, inversely, MTT performing poorer across the higher volume range. MTTR cantilever beam performs better than the ST cantilever beam consistently under TTD loading condition for the 30mm and 40mm cantilever beam depth. The results demonstrated in both MTT and MTTR shows that the triangular projections have reduced efficiency in reducing deflections across the increasing size of the projection. This is likely due to the difference in the distribution of internal forces affected by its geometry. Aside from its deflection performance, the relative sizing of the various cantilever beam geometries plays an important factor.

The ST cantilever beam provides a more consistent ceiling height (e.g. in buildings) but does not provide the benefits of additional height at the free end as in the MTT cantilever beam. The design disadvantage of the MTT cantilever beam is a triangular projection towards its support that requires a large amount of space. The triangular projection support for the ST cantilever beam is much smaller than the support size of the MTT cantilever beam. Therefore, the MTT triangular projection may be better suited in a multistorey design as the MTT cantilever beam performs best when the triangular projection is small. Hence, its design may be appropriate in haunches or

knee braces between joints as they are often small projections. The analysis confirms the study conducted by other researchers in the review paper (Yap et al. 2019).

5.5 Summary

This chapter presents a parametric study on the various cantilever beam geometries to identify the feasibility and performance of introducing nature's design in steel structures. The study demonstrates the standard triangular projection designed by many engineers to be the best overall design. The MTT cantilever beam performed best when the additional volume is small. It may also suggest the reason why tree buttresses appear as small projections instead of their entire length. MTT cantilever beam offers a different design with better height requirement towards the free end but suffers height and space towards its support. MTTR cantilever beam may be an alternative when considering its sizing and performance. Both MTT and MTTR cantilever beam geometrical projections benefited with deeper beam depth, displaying more deflection resistance with a minimal increase in volume. Although the MTT and MTTR geometrical projections do not show significant improvement over the ST cantilever beam, their nature suggests that they might be more suitable for multistorey design. Still, it also does not eliminate the application on other civil engineering structures. Further studies are conducted in Chapter 7 to understand its underlying behaviour and identify the plausibility of replicating nature's design in the support design for the plausible application of retrofitting in existing structures.

Chapter 6 Topology Optimisation of Various Cantilever Beam Geometries

This chapter presents the topology optimisation of the various cantilever beam geometries. Topology optimisation is often applied during the initial phase when identifying the best design structure. Although various topologies can be obtained through this process, it may not always be directly feasible. However, it provides a guideline for future designs. The description of the model is presented in this chapter.

6.1 Retained Volume Ratio and its Compliance

The cantilever beam of a 200mm x 40mm x 1mm, as shown in Figure 6-1, is subjected to a volume constraint value of 0.3, 0.4, 0.5, 0.6, 0.7, 0.8, 0.9 with a single free end downward loading condition of 1kN. A total of 7 models were evaluated. The models were analysed as 3D solid, static, isotropic, linear elastic and fine program-controlled meshing. The material modelled is structural steel with Young's modulus of 200GPa and a Poisson's ratio of 0.3.

The optimisation region is divided into two regions, the design region and the excluded region. The design region is the region allowed to be modified, while the excluded region is the region excluded from any changes, for example, the boundary conditions. The Optimality Criteria was utilised for updating the design variables (e.g. relative densities). The maximum number of iteration and the minimum normalised density was left at the default value of 500 and 0.001, respectively. The convergence accuracy is set to 0.001%. Increasing the penalty value will lead to a sharper solution, creating a more defined strut and tie, but this might not capture the necessary intermediate densities well. Hence, the penalisation power value defined by ANSYS is 3. The criterion for optimality is to minimise its compliance.

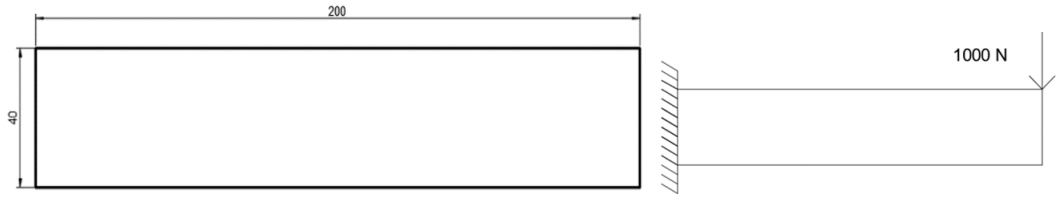


Figure 6-1: Cantilever beam of 200mm x 40mm x 1mm subjected to a point load

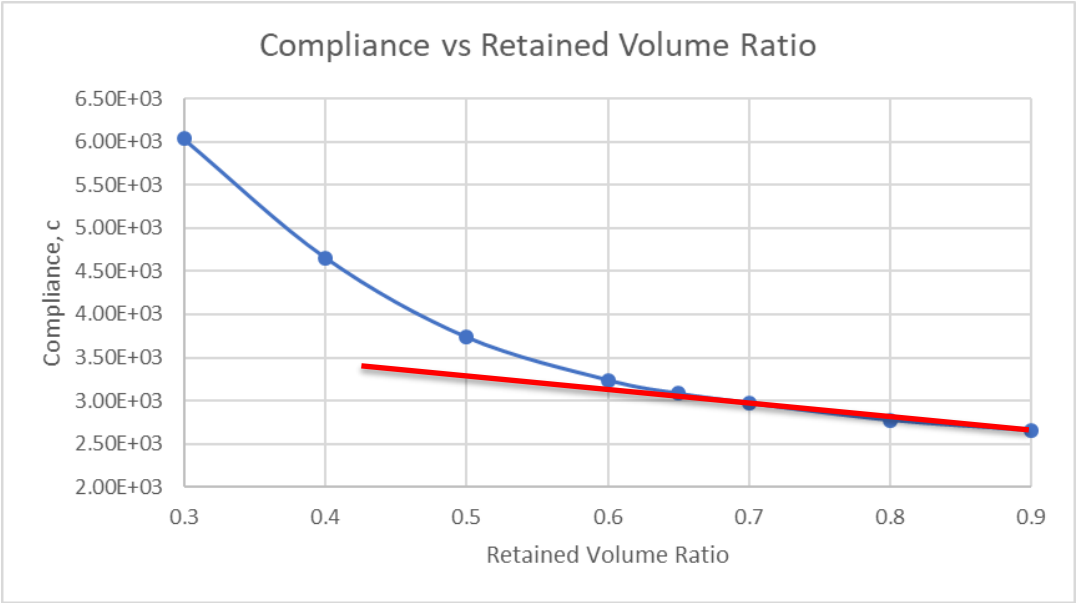


Figure 6-2: Compliance vs Retained Volume Ratio

The graph shown in Figure 6-2 is a compliance versus retained volume ratio plot ranging from 0.3 to 0.9. The objective function defined in this structural mechanics problem described in Chapter 3.2.1 is to minimise the compliance (strain energy) to maximise the stiffness of the beam. As expected, the graph in Figure 6-2 shows the compliance reduces logarithmically as the available material increases. A retained volume ratio of 0.65 was obtained using the best fit method, as shown by a straight red line in Figure 6-2. It shows a linear increment of compliance across the retained

volume ratio. The topology optimisation was performed again at a retained volume ratio of 0.65 to validate the best fit results.

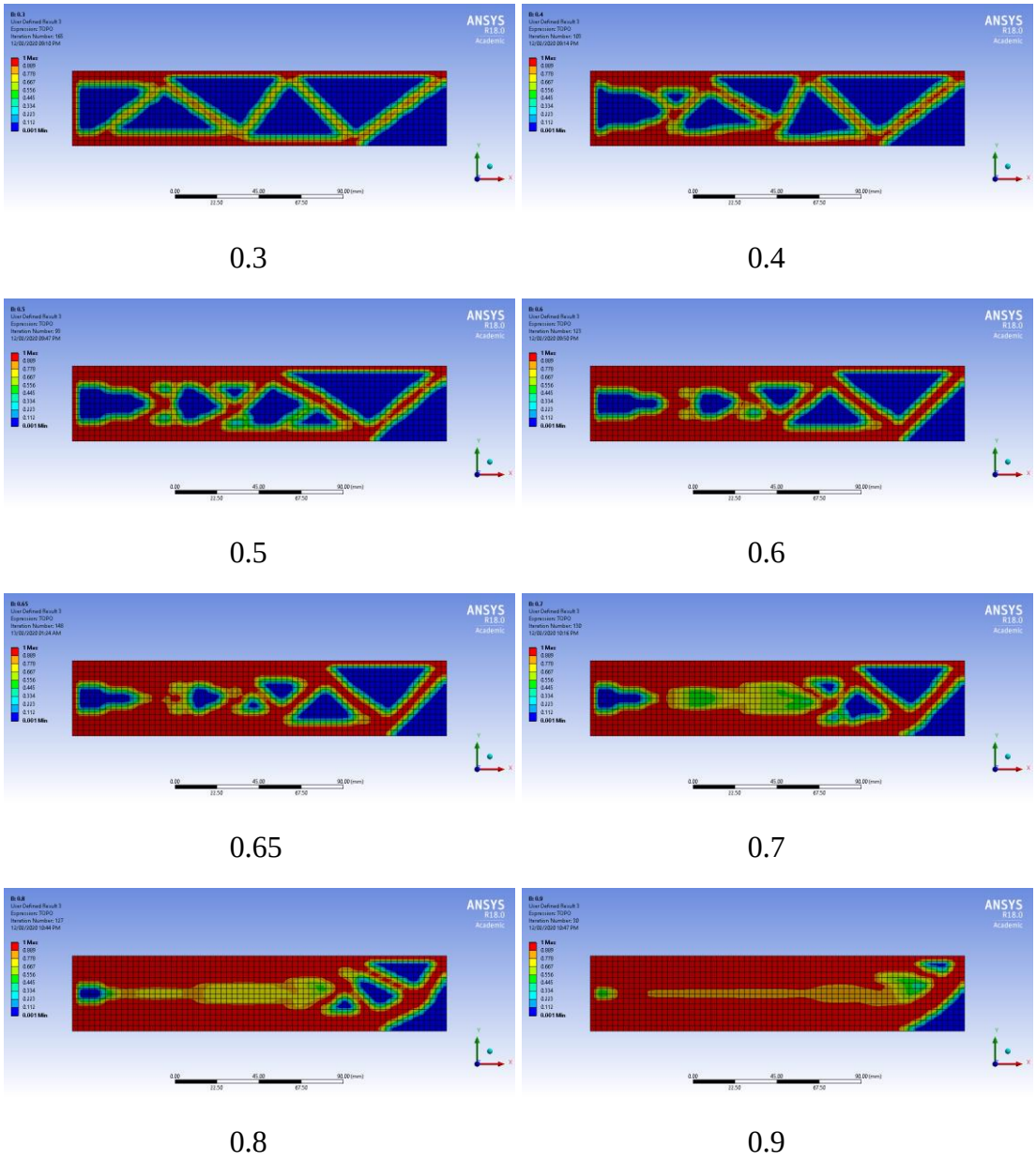


Figure 6-3: Topology plot of a (200mm x 40mm x 1mm) cantilever beam showing the various retained volume ranging from 0.3 to 0.9.

Figure 6-3 shows the set of topology plots ranging from 0.3 to 0.9. The plots for the retained volume ratio of 0.5 and below shows a more distinctive, similar and traditional topology design found in truss designs. Although these plots display a more

unobstructed view of the load path within its structure, the design cannot be introduced in practice as it lacks the stiffness needed to maintain its function. Therefore, for a practical, simple and easily replicable topology design in steel structures, the retained volume ratio of 0.5 is applied in the subsequent analysis.

The results obtained may not be directly feasible for civil engineering application in practice as it only considers a single loading point without considering other loading conditions. Nevertheless, it is often used in the preliminary phase, providing guidance or guidelines for future designs. It should also be noted that these solutions may not be globally optimal, and the resulting design solution it is only an approximation of a tie and strut relating similarly to a truss-like structure. However, its importance in practice may be less significant.

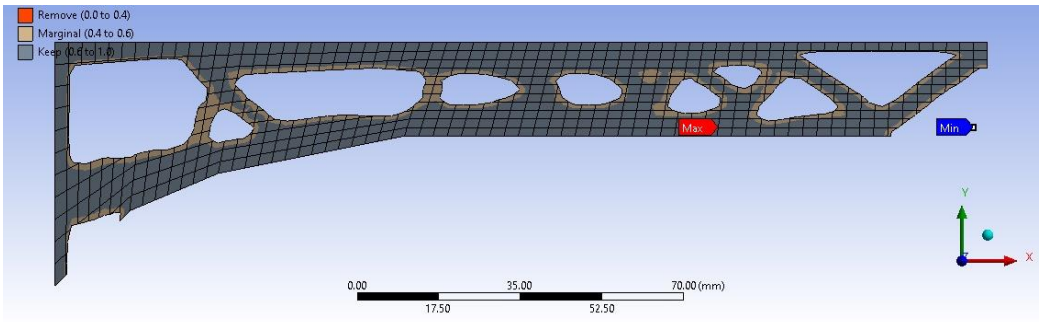
6.2 Load Path of the Various Cantilever Beam Geometries

In continuation of the previous parametric study in Chapter 4 and Chapter 5, a parametric topology study of the various cantilever beam geometries was conducted to investigate the structure's load path or force flow. It also aids in identifying the effective utilisation of the various projections under the cantilever beam. The parameters used in this study are the same as in Chapter 6.1. The evaluated cantilever models are the same as in Chapter 4 and Chapter 5. The dimension is 200mm long, 1mm thick and a depth ranging from 20mm to 40mm, in combination with the various geometrical projection. A total of 720 cantilever models were analysed, including validation of the topology plots. However, only a specific set of topology plots are shown in Appendix B. Each cantilever beam model shown in Appendix B has two topology plots, a retained density plot and a density plot. The retained density plot shows the final topology of the structure while the density plot shows the density value

from 0 to 1, where if the density value is towards 0, it is to be removed, and if it is towards 1, it is to be retained.

The three colour bands in the retained density plots refer to the retained threshold with the software recommendation definition to “remove” as red, “marginal” as yellow, and “keep” as grey. Red indicates a retained threshold value of between 0 to 0.4, yellow indicates a value of between 0.4 to 0.6, and grey indicates a value greater than 0.6. It is understood that a reduced amount of stiffness can lead to higher deformation and internal stresses. As such, a value of 0.4 retained threshold value was utilised to ensure sufficient material is available to maintain a certain degree of stiffness and stability. It should be noted that the retained threshold does not directly equate to the amount of retained volume. Hence, the retained volume of the various cantilever beam geometries across all beam depths varies between a value of 0.58 to 0.64. An example of the two topology plots is shown here in Figure 6-4.

(a)



(b)

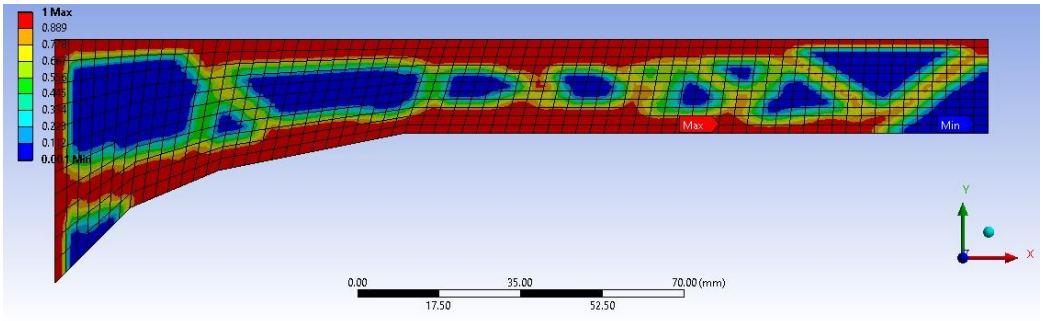


Figure 6-4: Topology plots for 75mm MTT cantilever beam (a) retained density plot (b) density plot

6.2.1 Topology Plots

In this section, the obtained topology plots are discussed solely based on the pattern generated through the optimisation process. Nevertheless, it should provide some insights into why certain geometrical designs are better than others.

6.2.1.1 Method of Tensile Triangles (20mm to 40mm depth)

For all the MTT cantilever beam depths, the topology of the triangular projection becomes more simplified across the projection from 5mm to 200mm. The MTT topologies also show the underutilisation of the triangular projections when the projection length is longer than 30mm, regardless of depth. An example of the utilisation of the triangular projection is shown in Figure 6-5. It may be why the projection becomes ineffective in resisting deflection towards the projection length increments. The MTT cantilever beam shows a similar topology with the ID cantilever at the cantilever end across all depths when the projection is small.

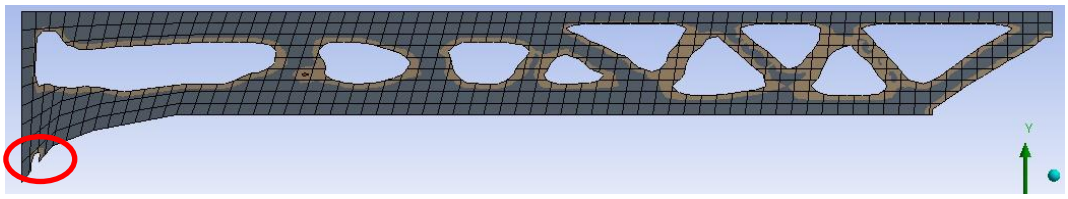


Figure 6-5:Underutilisation of the triangular projection in the MTT beam (200mm x 20mm x 1mm) with a 30mm projection.

As the triangular projection length approaches 100mm, the topology at the end of the beam becomes less distinctive and slowly replaced by a simpler structure. The topology at the end of the beam has significantly less structured members to provide

stability, especially in slender beams, and this example is shown in Figure 6-6. It has created a head heavy cantilever beam that is not very ideal for resisting deformation.

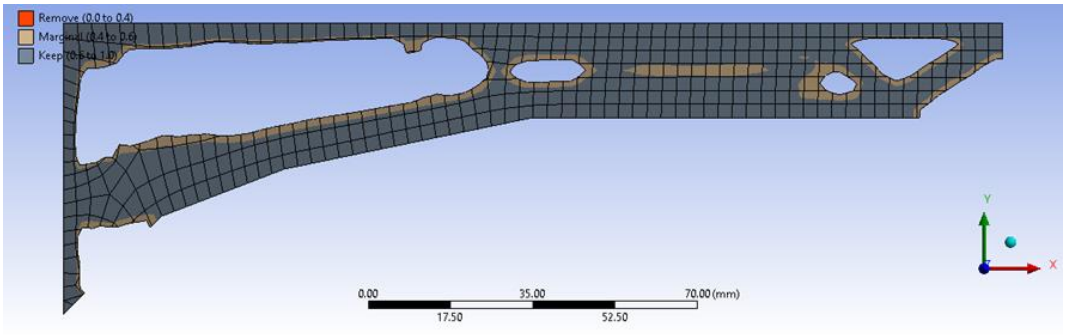


Figure 6-6: Less structured topology at the end of the MTT beam (200mm x 20mm x 1mm) with a 100mm triangular projection

6.2.1.2 Method of Tensile Triangles Rule of Thumb (20mm to 40mm depth)

The MTTR beams also show a similar pattern as in the MTT beams but develop a very clear and distinctive triangle-shaped topology as it approaches the 200mm projection length. An example of this is shown in Figure 6-7.

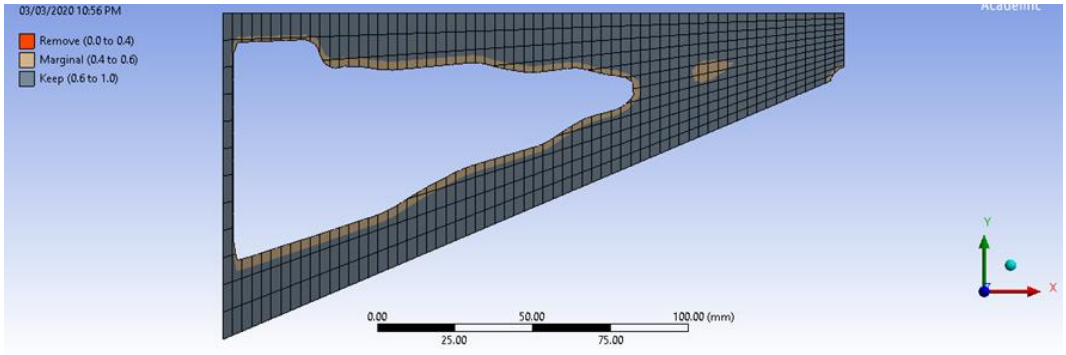


Figure 6-7: Triangle-shaped topology in MTTR beam (200mm x 20mm x 1mm) with a 200mm projection

6.2.1.3 Standard Triangle (20mm to 40mm depth)

The ST beam also shares a similar topology as in MTT and MTTR beams, where multiple sectioned triangles convergences towards fewer but larger triangles across the

incremental size of the triangular projection. The ST beam also forms a clear distinctive triangle-shaped topology as in the MTTR beam as it approaches the higher inclination angle. MTT beam does not form a load path along with its triangular projection like the MTTR and ST due to its less consistent geometry, preventing the load path from moving in a straight form. A straight line along the bottom projections form the shortest path between the loading point and the support.

6.2.1.4 Increased Depth (20mm to 67mm total depth)

From the topology plots in Appendix C.a.d, it can be seen that the depth ranging from 20mm to 67mm, the topology becomes less complicated with more defined features. The total number of members were fewer and thicker. This can be seen in Figure 6-8.

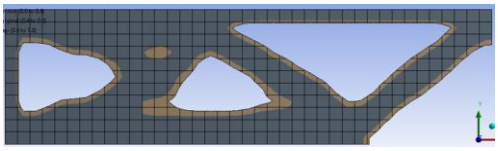
(a)  (b) 

Figure 6-8: Increased Depth Topology (a) 25mm (b) 55mm

6.2.1.5 All Cantilever Beam Geometries

Overall, the topologies generated are different from one to another. This is because the load path from its loading point to its support are differed/bounded by its geometry. All the cantilever beam geometries show that the topology becomes more pronounced and simplified towards higher depth and/or towards the entire length of the triangular projection. The topology shows the shortest pathway between the point of loading and support. Triangular shaped structures appear in all cantilever beam geometries and along the various depths. Their size and location are the only features that differ in the triangular-shaped members. They tend to form towards a single large triangle unit as the triangular projection gets larger or have a higher inclination angle (e.g. ST

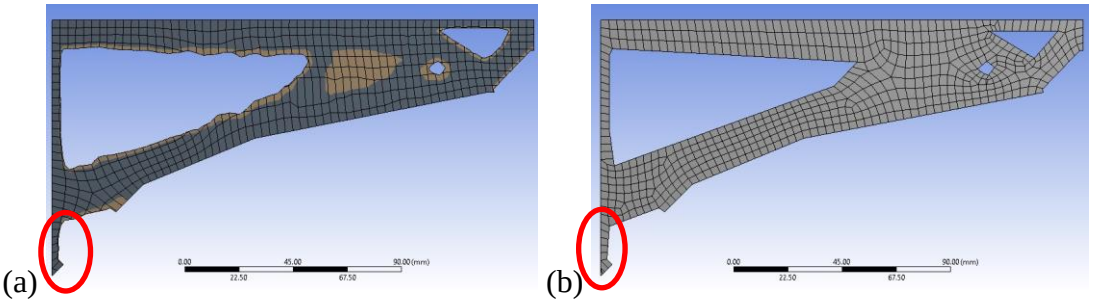
cantilever beam). Triangles or triangular-shaped objects are also shown here to be a very stable design. It is worth noting that the topology of deeper beams tends to be more developed, structured and simplified than slender beams. The obtained topology, as mentioned earlier, is most likely due to the force flow that allows better distribution of internal forces. One would favour topologies with fewer and thicker members than those with many thin members in terms of fire safety. This is because thinner members are more susceptible to heat breakage than thicker members, leading to earlier failure.

6.3 Replicating the Topology Optimised Models

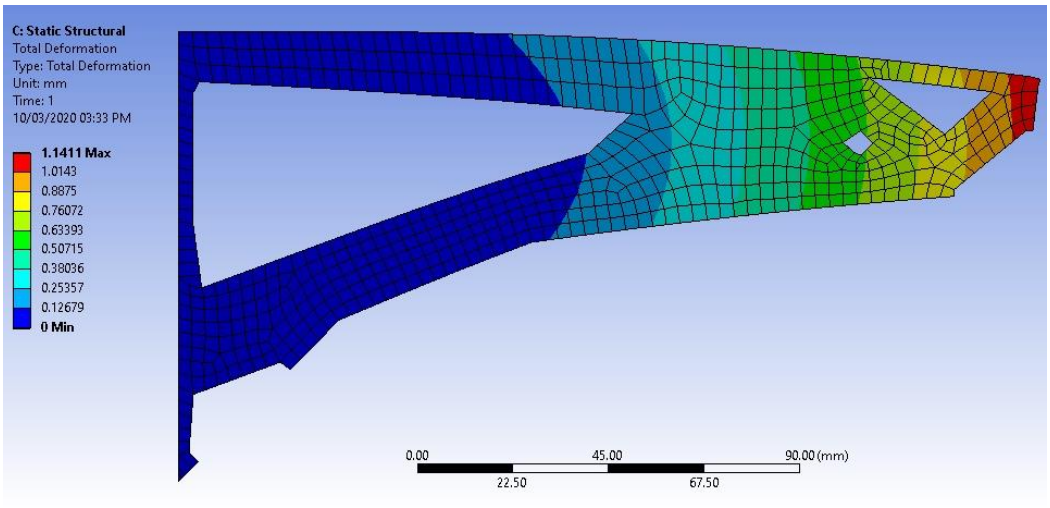
In the previous section 6.2.1, the load path of the various cantilever beam geometries was discussed. The study looks into replicating the topology obtained as a structural component and subsequently to identify the possibility of replicating the said topology generated models in Chapter 6 as trusses. Thus, the study intends to bridge the application gap of topology generated models in actual construction. The optimised models in Chapter 6.2 are further analysed by performing a design validation. The design validation of the generated topologies is performed through finite element analysis (FEA) to determine its structural performance. The parameters used in this analysis are the same as in Chapter 4 and Chapter 5 to enable a comparative study with its original cantilever beam design on the effectiveness of its optimised design.

The example shown in Figure 6-9 is a 200mm x 30mm x 1mm cantilever beam with a 180mm length Method of Tensile Triangles projection. Figure 6-9 shows a simplified process of validating the optimised cantilever beam from (a) to (b). First, the rough edges were smoothened and simplified with straight lines. Next, the marginal density elements (0.4–0.6) were filled as a solid element. Lastly, the protrusion tail (circled red in Figure 6-9) at the support should or can be removed, but it is maintained to

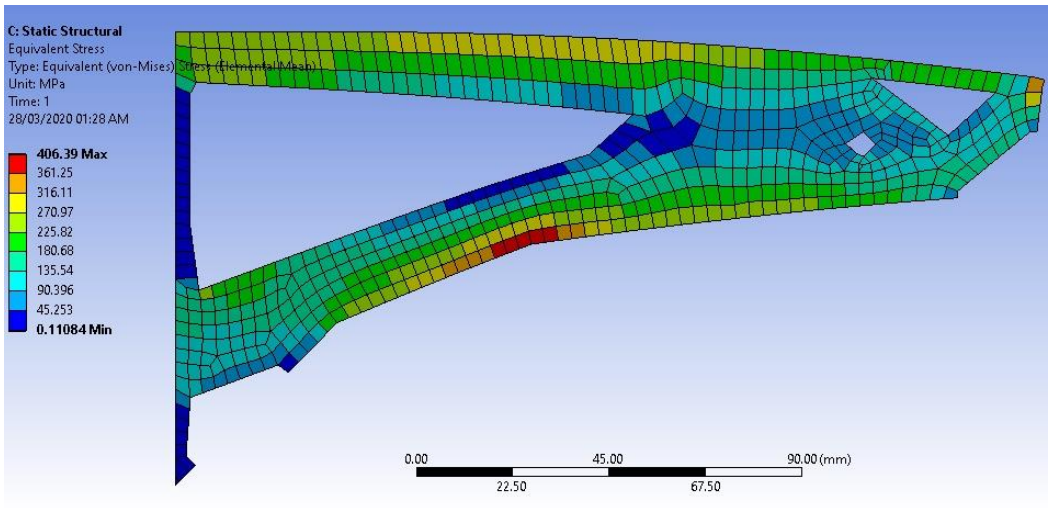
ensure the processed topology remained as similar as possible without introducing other geometrical factors that may affect the results.



(a) (b)



(c)



(d)

Figure 6-9: Method of Tensile Triangles cantilever beam (200mm x30mm x 1mm) with a 180mm triangle projection (a) Topology generated (b) Post-processed topology (c) Deflection plot (mm) (d) Stress plot (MPa)

Figure 6-9(c) and Figure 6-9(d) are the deflection plot and the stress plot, respectively. The stress profile is once again plagued by a stress singularity issue that appears in all cantilever beam analysis. The stress singularity often appears at the support, point of load or the transition corners (as shown in Figure 6-9). Although the maximum stress is not accurate, it is still possible to obtain a general idea of the stresses through a direct comparison of the deflection value. As mentioned earlier, the deflection values are not affected by stress singularities. Hence, the discussion/comparison of the cantilever beam geometries is based on deflection values. Therefore, the comparison of stress profile across the different cantilever beam geometries is compared with similar deflection values.

The average difference in the amount of deflection, stress and volume between the processed topology and the original cantilever are shown in Table 6-1, Figure 6-10 and Figure 6-11. The results shown in Table 6-1 are expected as there is a reduced amount of element/material that provided the stiffness. Nevertheless, the data shows that the generated topology for all the cantilever beam geometries except for the ID cantilever beam is better optimised across the deeper cantilever beam depth. This is because, as mentioned in section 6.2.1, the deeper beam depth provided space for the load path to form the shortest path between its loading point and its support. Generally, the generated topologies can reduce more than 30% of the total volume of the cantilever beam while maintaining a deflection difference of less than 28%. It also shows that the generated topologies for the MTT and the MTTR cantilever beam are better than the others as they can reduce a similar or more amount of material while maintaining a deflection difference of under 20%. The generated topology is better in the MTTR than the MTT as it can reduce its volume further while maintaining a lower deflection difference except for the 30mm MTTR cantilever beams. It could be due to the angle

of approach in the topology of the triangular projection in the MTTR cantilever beam. The ST cantilever beam benefited less through the generated topology as its deflection difference increases across the increment of the cantilever depth.

Table 6-1: Average deflection and stress between the processed topology and the original cantilever beam.

	Deformation (Ave %)	Stress (Ave %)	Volume (Ave %)	Removed volume (Ave %)
20mm				
MTT	13	19.5	68.2	31.8
MTTR	11.8	7.5	66.2	33.8
ST	11.6	26.7	68.6	31.4
30mm				
MTT	15.5	12.3	64.6	35.4
MTTR	19.2	10.2	61.9	38.1
ST	17.3	17.7	64.1	35.9
40mm				
MTT	17.3	10.6	62.7	37.3
MTTR	16.5	13.1	62.1	37.9
ST	26.6	12.4	65.1	34.9
20mm to 40mm				
ID	27.6	28	63.5	36.5

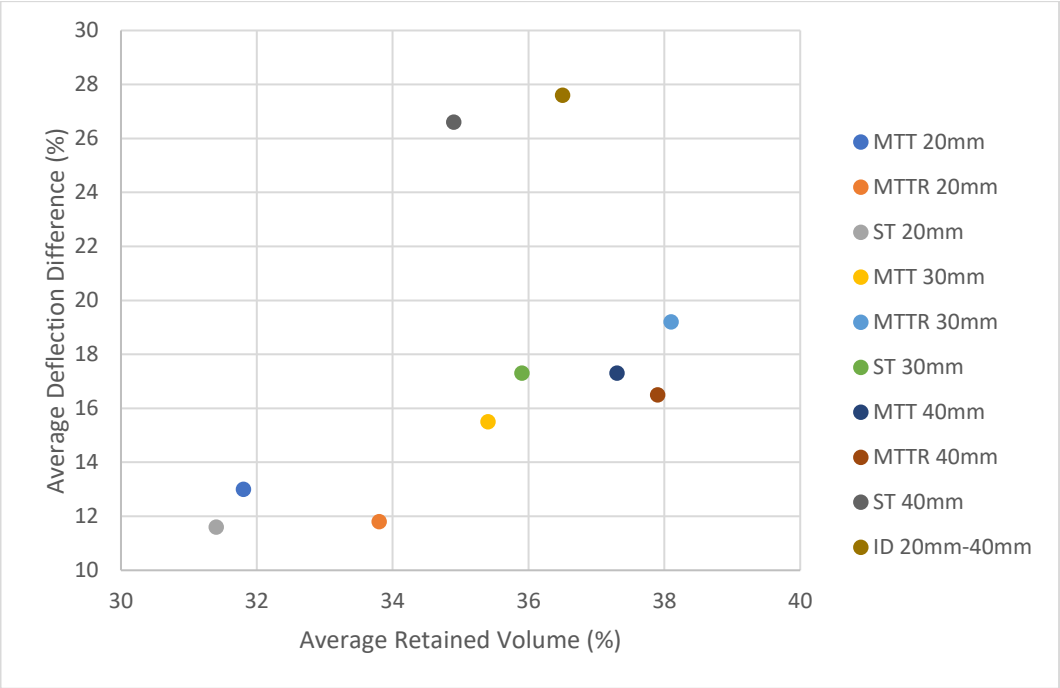


Figure 6-10:Average Deflection Difference Between The Optimised and the Original Cantilever Beam

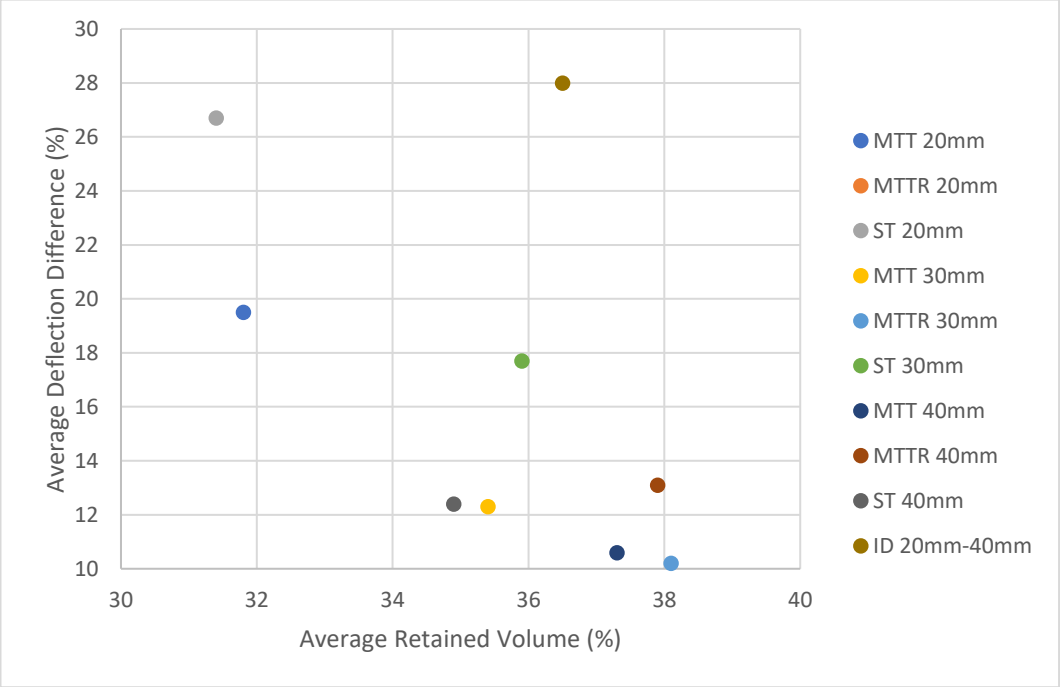


Figure 6-11: Average Stress Difference Between The Optimised and the Original Cantilever Beam

Although the topology optimised cantilever beams are not better than their original counterpart in terms of their structural performance, the topology optimised cantilever beam can perform better than the original cantilever beam design of similar volume. Figure 6-12 shows a set of graphs showing the difference in the deflection between the original and the topology optimised of each cantilever beam models. Figure 6-13 shows a set of graphs showing the difference in the stresses between the original and the topology optimised of each cantilever beam models. The fluctuations in the deflection values and the stresses in all the topology optimised cantilever beam models are due to the difference in volume. As discussed earlier, the volume difference in each cantilever beam is derived from the post-processing of the individual geometry obtained. The equations for the 2 line curves in Figure 6-12 and Figure 6-13 are shown in the plots in Appendix C.b.

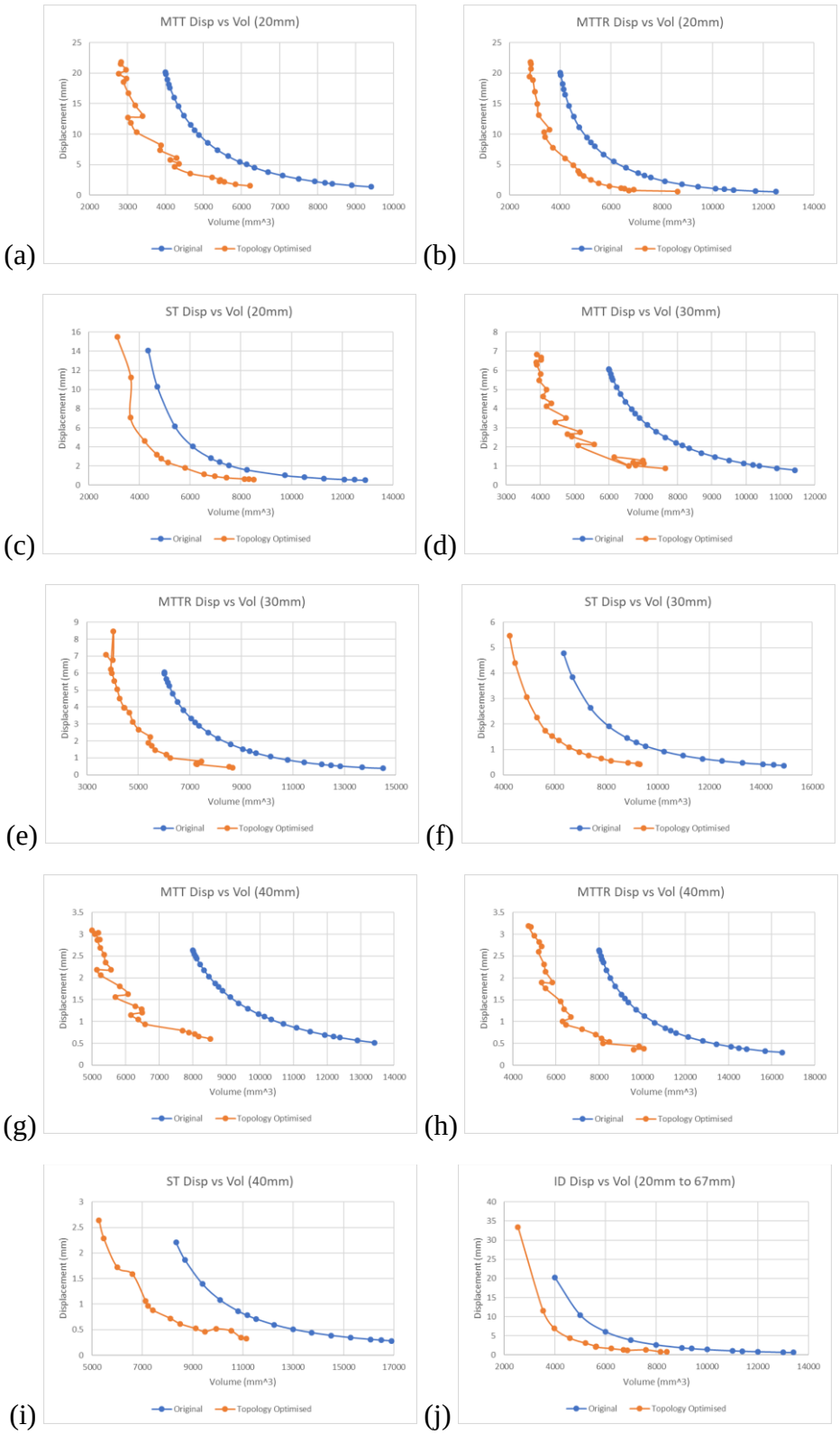


Figure 6-12: Comparison of the deflection vs volume between the original cantilever and the topology optimised model. (a) 20mm MTT (b) 20mm MTTR (c) 20mm ST (d) 30mm MTT (e) 30mm MTTR (f) 30mm ST (g) 40mm MTT (h) 40mm MTTR (i) 40mm ST (j) 20mm–40mm ID

All the line curves across the different cantilever beam models are initially parallel to each other, followed by a convergence of the 2 line curves. The convergence rate between the 2 line curves (blue and orange) suggests the effectiveness of the triangular projection beneath the cantilever beam. The 2 line curves are found to be further apart across the higher cantilever beam depth except for the ID cantilever beam. The closeness of line curves between the topology optimised and the original cantilever across the lower beam depths suggest that the triangular projection provided lesser deflection resistance. The line curves in the deflection versus volume plot for both MTT and MTTR cantilever beams maintain parallel or apart across the volume increment longer than the ST and ID cantilever beams. Both the MTT and the MTTR cantilever beams converged at a higher volume than the ST and ID cantilever beam by 500 – 1000mm^3 and 500 – 3000$mm^{3,}$ respectively, across the different cantilever depths.

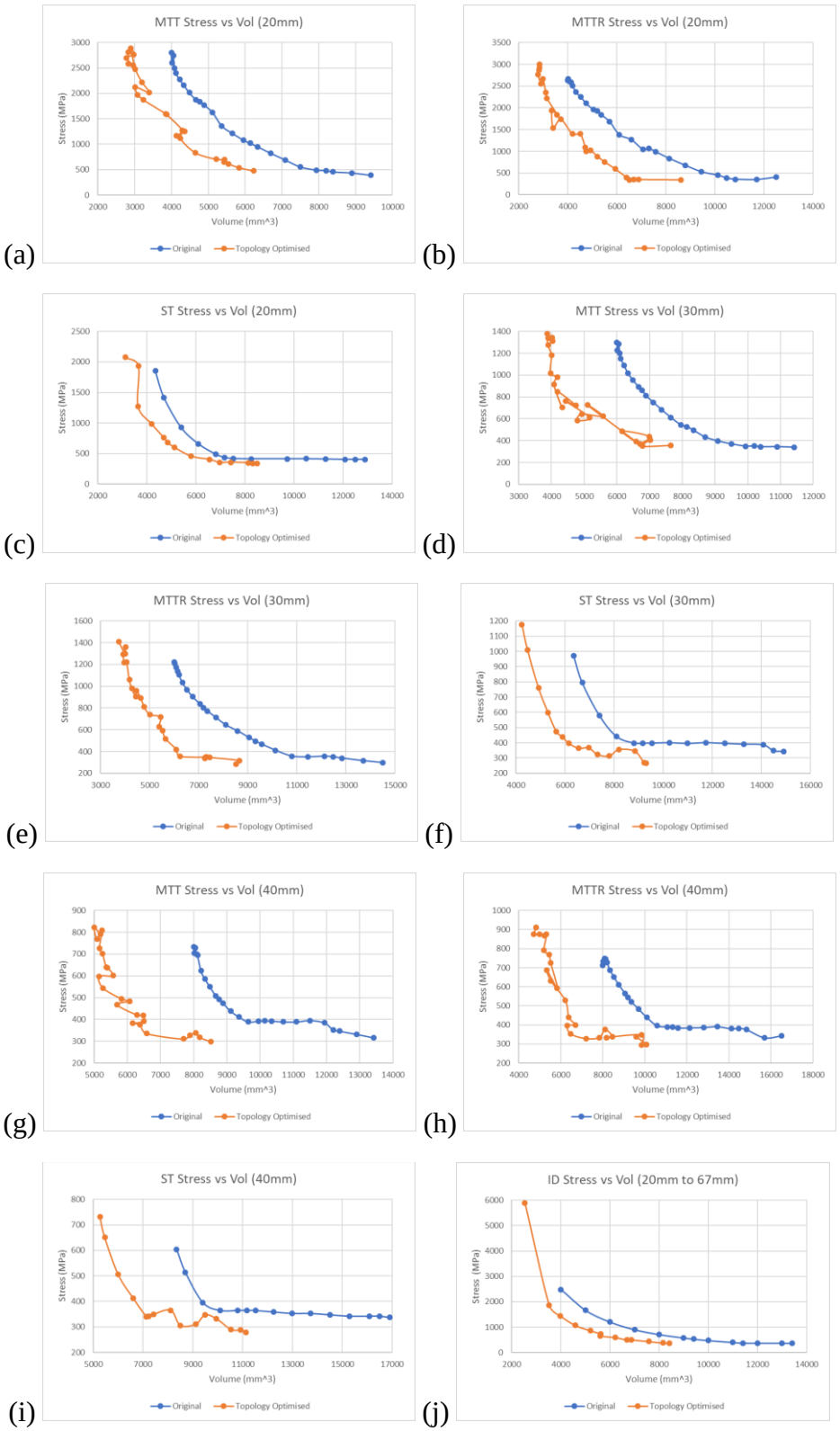


Figure 6-13: Comparison of the stress vs volume between the original cantilever and the topology optimised model. (a) 20mm MTT (b) 20mm MTTR (c) 20mm ST (d) 30mm MTT (e) 30mm MTTR (f) 30mm ST (g) 40mm MTT (h) 40mm MTTR (i) 40mm ST (j) 20mm–40mm ID

The results suggest that the topology optimised cantilever beam designs provided lesser benefit to the ST and ID cantilever beam when compared to the MTT and MTTR. This is due to the simplification of the topology across the longer/larger triangular projection, providing better load transfers compared to the cantilever beam of similar volume. The topology of a larger triangular projection is more triangular than a long truss-like truss, which improves the load transfer between the loading point and its support. Whereas a smaller triangular projection topology will have a topology similar to the ID cantilever beam, the triangular projection has less influence on the load path. Hence, a disadvantage for the topology optimised cantilever beam. The difference in the topology generated can be seen in Figure 6-14.

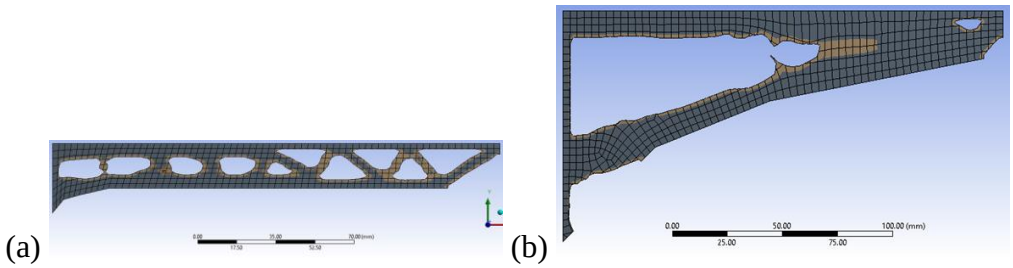


Figure 6-14: Triangular projection of a 20mm MTT cantilever beam (a) 25mm length (b) 200mm length

Although the triangular projection in the ST cantilever beam was not as effective as MTT and the MTTR cantilever beam, it is slightly poorer compared to them, but the topology generated is still more effective than the ID cantilever beam. This is because the changes in the aspect ratio of the ID cantilever beam is not significant enough to change its topology significantly that could provide more effective load transfer. Regardless of the size of the projection, the triangular projection in the ST cantilever beam is still being utilised effectively, as shown in Figure 6-15. The graphs in Figure 6-13 show that a lighter cantilever beam that satisfies the deflection can be created at a larger cantilever beam projection cost. The further apart the 2 line curves, the higher

the material saving. Hence, the topology optimisation can develop a lighter structure but at the cost of its overall size.

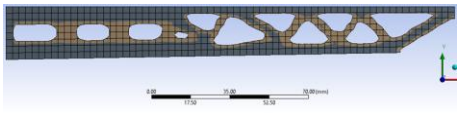
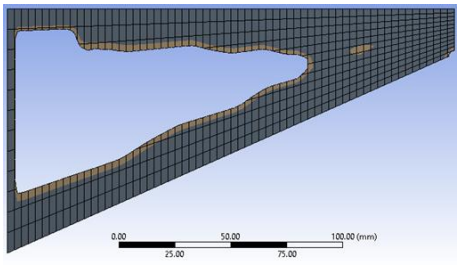
(a)  (b) 

Figure 6-15: Triangular projection in a 20mm St cantilever beam (a) 1mm depth (b) 24mm depth

Figure 6-16 shows the deflection versus volume plot and the stress versus volume plot for the various cantilever beam geometries across the depths between 20mm–40mm. As mentioned earlier, the plots shown in Figure 6-16 are erratic due to the post-processing in the topology of the cantilever beams. However, the plot can still provide a general idea of the structural performance of the various cantilever beam geometries. The plots show that the ID cantilever beam performed the worst across all volumes. Hence, only the three cantilever beam geometries will be further discussed. Across the lower volumes of all cantilever beam depths, the MTT cantilever beam performed the best, followed by the MTTR and the ST cantilever beam.

In comparison, the MTTR cantilever beam performed the best in cantilever beam depths (20mm-30mm) across higher volumes. This is followed by the ST and the MTT cantilever beam. For the 40mm depth, the MTT cantilever beam performed better than the ST cantilever beam. Across the intermediate volumes for the 20mm cantilever beam depth, the ST cantilever beam performed the best; this is followed by the MTTR and the MTT cantilever beam. This may be due to the combination of the cantilever beam's slenderness and the full-length triangular projection that created a more

simplified topology for an effective load transfer. For the 30mm and 40mm cantilever beam depth across the intermediate volume, the MTT and the MTTR cantilever beams have similar structural performance, with a slight indication of the MTTR performing better than the MTT cantilever beam. Hence, the MTT cantilever beam still performs best under the lower volumes, while the MTTR cantilever beam can be a better option across the higher volumes if the cantilever beam has sufficient depth. The ST cantilever beam is best suited across the higher volume of a slender cantilever beam.

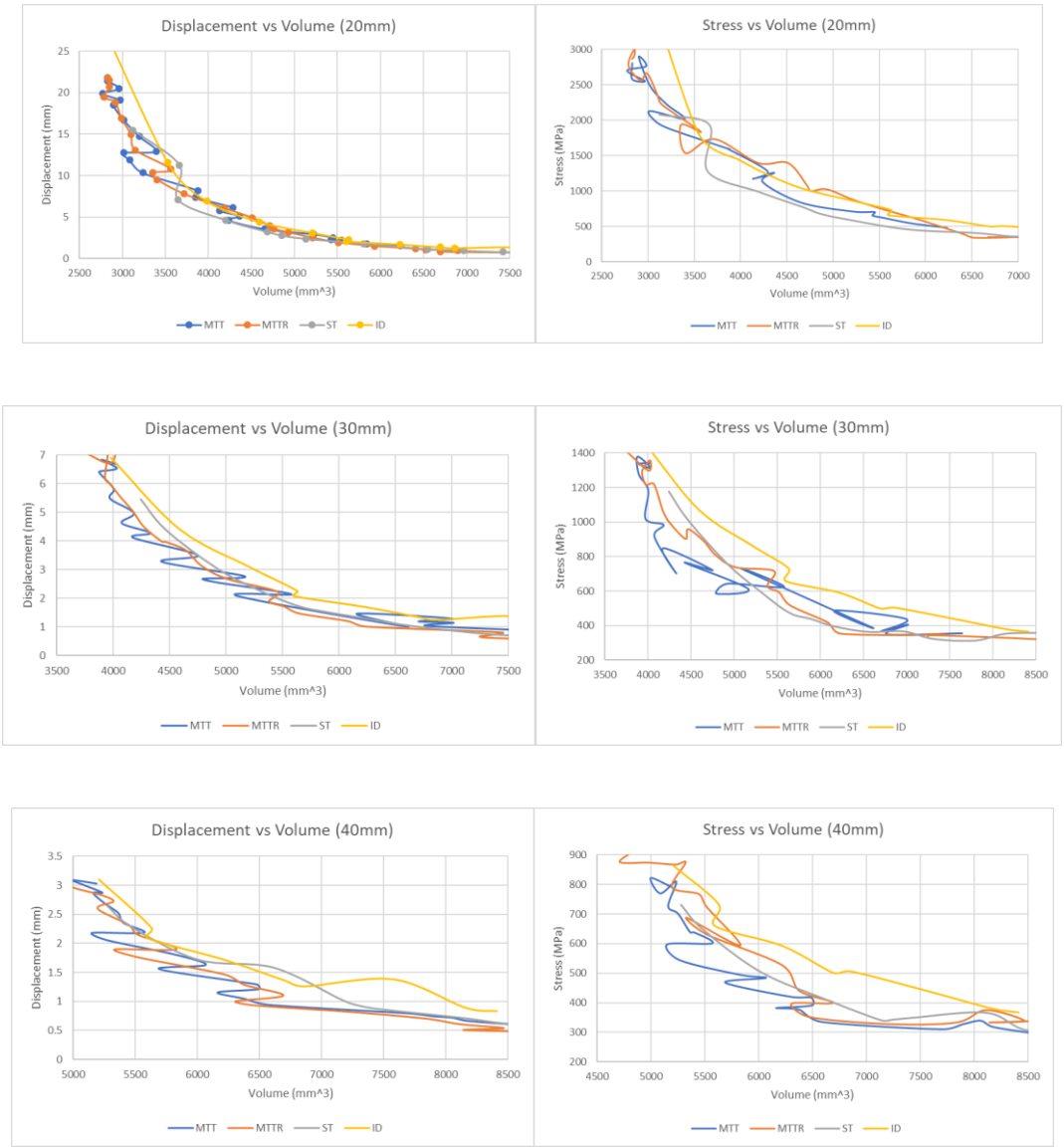


Figure 6-16: Deflection vs volume and Stress vs Volume Plot for the various cantilever beam geometries, (1st row) 20mm, (2nd row) 30mm, (3rd row) 40mm

In summary, the topology optimised plots obtained were not better than their original counterpart, but the plots have provided an alternative to designing a cantilever that needs a lower amount of materials. It should be noted that the optimised plots may perform slightly better than the results obtained if more refinements were placed in the post-processing of the final topology.

6.4 Replicating the Topology Plots as Trusses

In this section, one model is selected from each cantilever beam geometry to identify the practicality of replicating the topology plots as trusses. The models are compared with the topology generated and the original cantilever as analysed in Chapter 4, Chapter 5 and Chapter 6.3. The deflection and stress profile plots for both the topology optimised design and the original are shown in Appendix C.b. The deflection considered is in the y-axis only. The material utilised is of structural steel with Young's modulus of 200GPa and Poisson ratio of 0.3. The replicated truss model has the following applied rules:

- Stable and internally determinate for the pin and roller support.
- Stable and internally indeterminate for the pin and pin support.

Analysing the truss as a pin and roller support only will not provide a fair comparison against the cantilever beam. Hence, two different support systems are analysed.

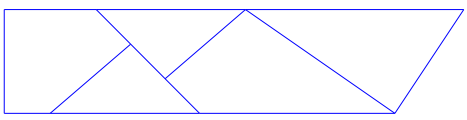
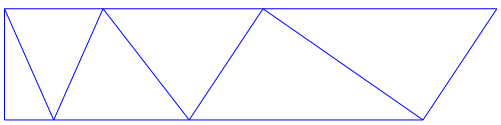
(a)  (b) 

Figure 6-17: Topology of the truss design (a) according to the generated topology (b) modified topology

Figure 6-17(a) shows an example of a truss design that follows closely to the topology generated. The truss shown in this example is the Increased Depth cantilever beam with a total depth of 45mm. However, the truss design is not stable and will ultimately disrupt its ability to distribute loads and stresses well. Hence, reducing its resistance to deflections. Therefore, the truss is modified, as shown in Figure 6-17(b). Hence, the replicated trusses analysed are adjusted accordingly and may not utilise the exact topology as analysed in chapter 6.3.

6.4.1 Pin and Roller Support

The support system defined in this section for all various trusses has pin support at the top and roller support at the bottom. The supports are applied at the nodes on the left-hand side of the truss, and the load applied is a single 1kN point load at the end of the truss model.

6.4.1.1 Method of Tensile Triangles (MTT)

Figure 6-18 shows the replicated truss model for the Method of Tensile Triangles with a projection length of 180mm. A solid rectangular member of 1mm thickness and a width ranging from 3.75mm to 37.5mm was applied in the truss model. The member sizing and the node coordinate are shown in Table C.c.a-0-1 and Table C.c.a -0-2.

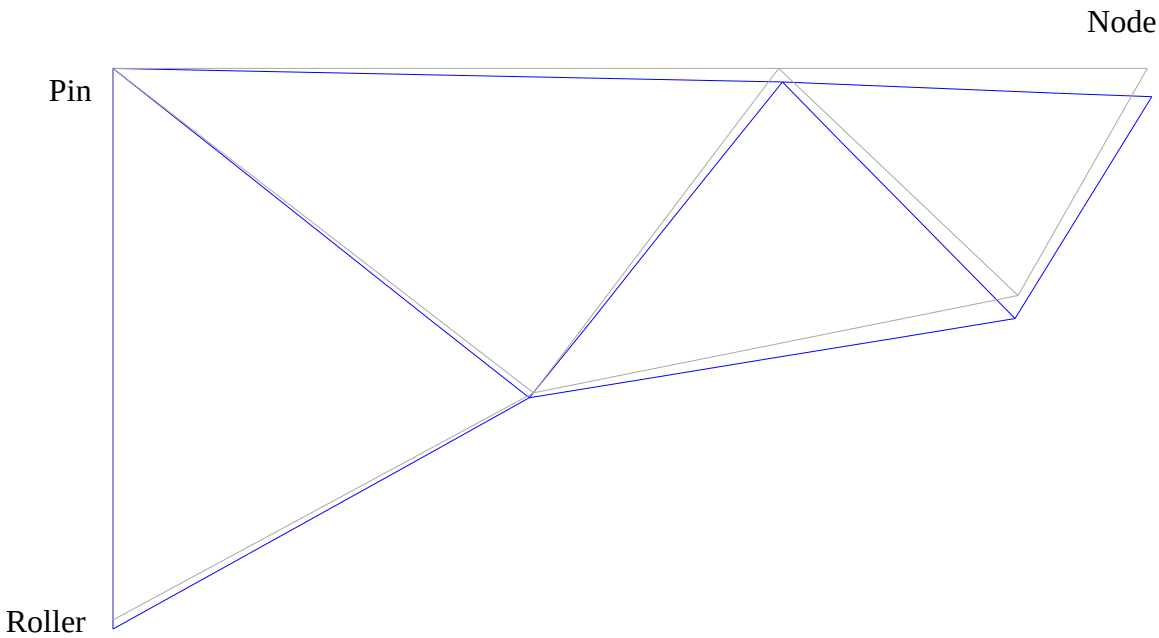


Figure 6-18: Deflection plot for MTT 180mm truss on a pin and roller support

The results obtained are shown in Table 6-2. The replicated truss model shows better performance than the topology optimised cantilever beam as well as its original with its highest deflection at node 3 (0.4389mm). The vertical member on the left experienced the highest stress with a value of 270.3MPa. In comparison between the three models, the deflection value for topology optimised design is 56.55% higher than the truss design, while the original is 37.43% higher. The maximum von mises stress value for topology optimised design is 31.37% higher than the truss design, while the original is 40.7% higher. The deflection and stress profile plots for both the topology optimised design and the original are shown in Appendix C.c.a.

Table 6-2: Results for the MTT truss (pin and roller support)

Model	Deflection (mm)	Difference (%)	Stress (MPa)	Difference (%)
Truss	0.4389	0	270.3	0
Topology	0.68708	56.55	355.01	31.37
Original	0.60319	37.43	380.32	40.7

6.4.1.2 Method of Tensile Triangles Rule of Thumb (MTTR)

Figure 6-19 shows the replicated truss model for the Method of Tensile Triangles Rule of Thumb with a projection length of 200mm. A solid rectangular member with a thickness of 1mm and a width ranging from 4.55mm to 25mm. The member sizing and the node coordinate are shown in Table C.c.b -0-3 and Table C.c.b -0-4.

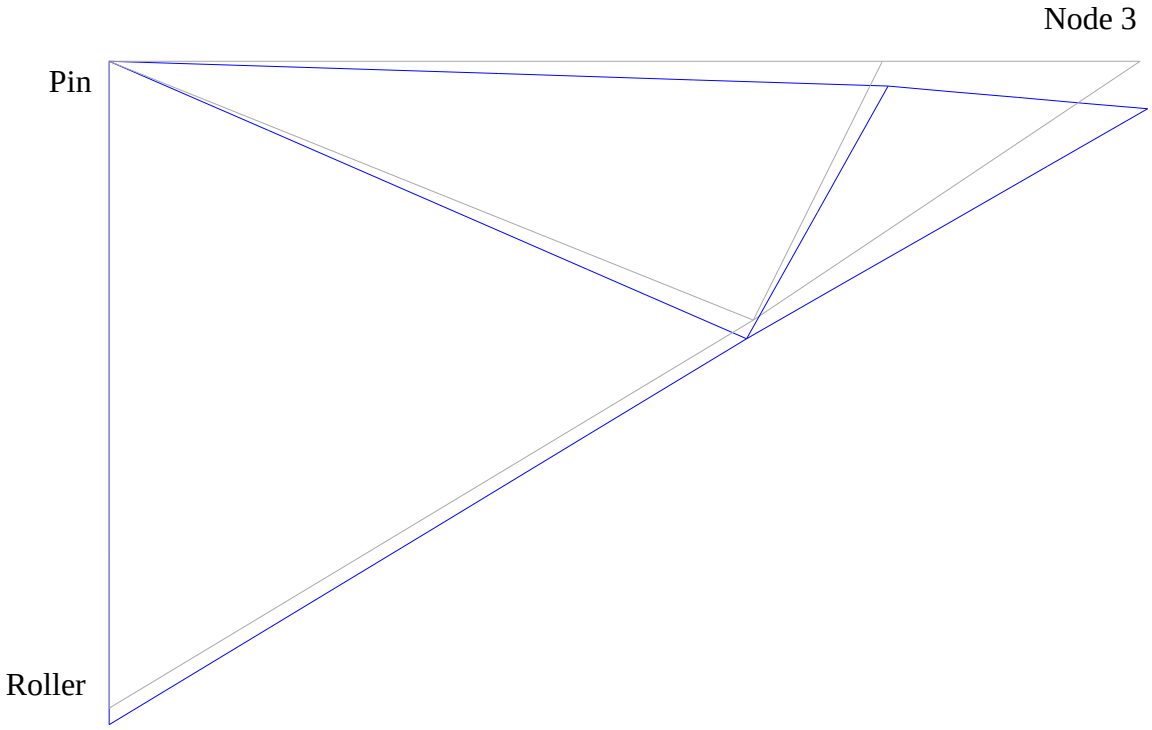


Figure 6-19: Deflection plot for MTTR 200mm truss on a pin and roller support

The results obtained are shown in Table 6-3. The replicated truss model shows poorer performance than the topology optimised cantilever beam as well as its original, with its highest deflection at node 3 (0.3681mm). The vertical member on the left experienced the highest stress with a value of 211MPa. In comparison between the three models, the deflection value for topology optimised design is 7.11% lower than the truss design, while the original is 25.85% lower. The higher deflection value is due to the reduced number of internal members that increases sliding at its roller support. The maximum von mises stress value for topology optimised design is 63.98% higher

than the truss design, while the original is 78.96% higher. The deflection and stress profile plots for both the topology optimised design and the original are shown in Appendix C.c.b.

Table 6-3: Results for the MTTR truss (pin and roller support)

Model	Deflection (mm)	Difference (%)	Stress (MPa)	Difference (%)
Truss	0.3681	0	211	0
Topology	0.34194	7.11	346	63.98
Original	0.27296	25.85	377.61	78.96

6.4.1.3 Standard Triangle (ST)

Figure 6-20 shows the replicated truss model for the standard triangle (24mm). A solid rectangular member of 1mm thickness and a width ranging from 3.75mm to 26.25mm was applied in the truss model. The member sizing and the node coordinates are shown in Table C.c.c -0-5 and Table C.c.c-0-6.

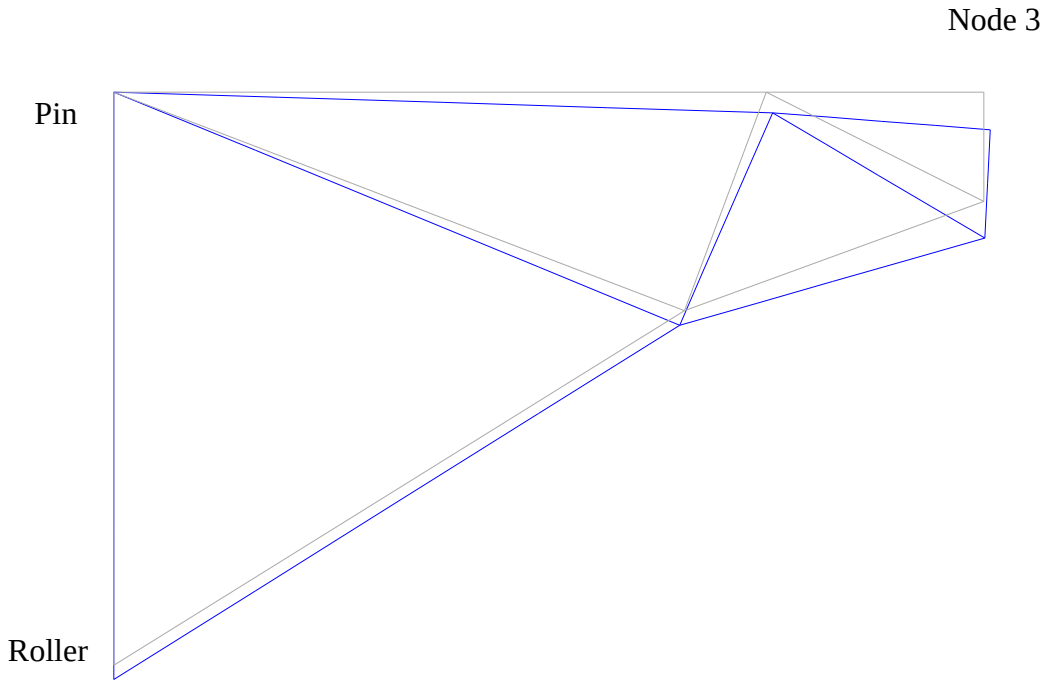


Figure 6-20: Deflection plot for ST 24mm truss on a pin and roller support

The results obtained are shown in Table 6-4. Similar to the MTTR truss earlier, the replicated truss model shows poorer deflection performance with its highest deflection at node 3 (0.4307mm). The vertical member on the left experienced the highest stress with a value of 251.5Mpa. In comparison between the three models, the deflection value for topology optimised design is 28.89% lower than the truss design, while the original is 34.84% lower. The higher deflection is due to sliding at the roller support. There are fewer internal members to provide the stiffness in resisting deformation. The maximum von mises stress value for topology optimised design is 10.89% higher than the truss design, while the original is 48.25% higher. The deflection and stress profile plots for both the topology optimised design and the original are shown in Appendix C.c.c.

Table 6-4: Results for the ST truss (pin and roller support)

Model	Deflection (mm)	Difference (%)	Stress (MPa)	Difference (%)
Truss	0.4307	0	251.5	0
Topology	0.30625	28.89	278.9	10.89
Original	0.25984	34.84	372.86	48.25

6.4.1.4 Increased Depth (ID)

Figure 6-21 shows the replicated truss model for the increased depth with a total depth of 45mm. A solid rectangular member of 1mm thickness and a width ranging from 5 mm to 15mm was applied in the truss model. The vertical member has a width of 5mm, the diagonal members and the top horizontal member has a width of 10mm, and the bottom horizontal member has a width of 15mm. The member sizing and the node coordinates are shown in Table C.c.d -0-7 and Table C.c.a -0-8.

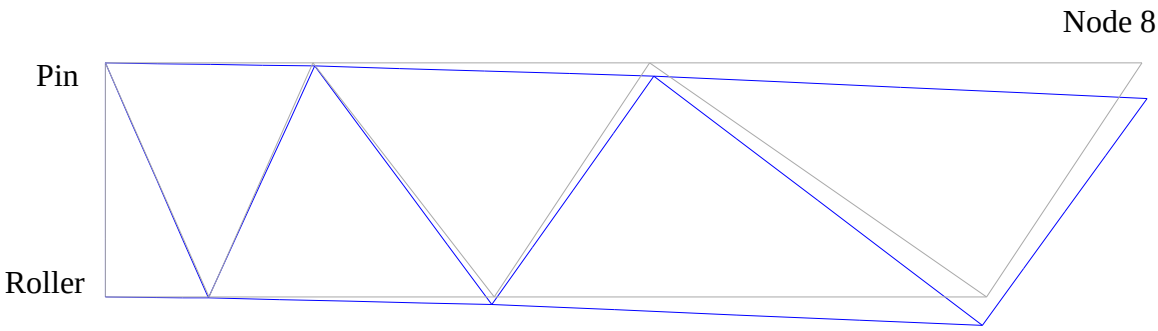


Figure 6-21: Deflection plot for ID 45mm truss on a pin and roller support

The results obtained are shown in Table 6-5. The replicated truss model shows better performance than the topology optimised cantilever beam as well as its original. At node 8 (point of load), the deflection value is 1.367mm and has a maximum stress value of 400MPa at member 11 (top left horizontal member). In comparison between the three models, the deflection value for topology optimised design is 68.71% higher than the truss design, while the original is 36.07% higher. The deflection of the truss in this analysis is lower because there is no sliding of the roller support. The maximum von mises stress value for topology optimised design is 86.6% higher than the truss design, while the original is 44.45% higher. The deflection and stress profile plots for both the topology optimised design and the original are shown in Appendix C.c.d.

Table 6-5: Results for the ID truss (pin and support)

Model	Deflection (mm)	Difference (%)	Stress (MPa)	Difference (%)
Truss	1.367	0	400	0
Topology	2.3062	68.71	746.41	86.6
Original	1.8601	36.07	577.8	44.45

Table 6-6 shows the comparison between the different trusses. The results show that the MTTR truss has the best performance for the amount of deflection per mass. This is followed by the MTT truss, then the ST truss and finally the ID cantilever. Although

the MTTR truss did not perform as well as its original and the topology optimised cantilever beam, it did resist more deflection for the material required. The ID cantilever may have performed better than its topology optimised and the original cantilever, but it did not provide a good deflection resistance for the amount of steel utilised. This is because the load transfer to its support is ineffective.

Table 6-6: Comparison of pin and roller support trusses through their deflection per mass output

	Total Length of Steel (m)	Mass (kg)	Deflection (mm)	Deflection/Mass (mm/kg)
MTT (180mm)	0.7892	0.1077	0.4389	4.075
MTTR (200mm)	0.7514	0.1084	0.3681	3.397
ST (24mm)	0.8335	0.1012	0.4307	4.256
ID (45mm)	0.7577	0.06439	1.367	21.23

6.4.2 Pin and Pin Support

The methodology applied in this section is the same as in the previous Section 6.4.1, except for its support condition. It has a pin and pin support along with the nodes on the left-hand side of the truss.

6.4.2.1 Method of Tensile Triangles (MTT)

Figure 6-22 shows the replicated truss model for the Method of Tensile Triangles with a projection length of 180mm. The details of the truss model defined is the same as in Section 6.4.1.1.

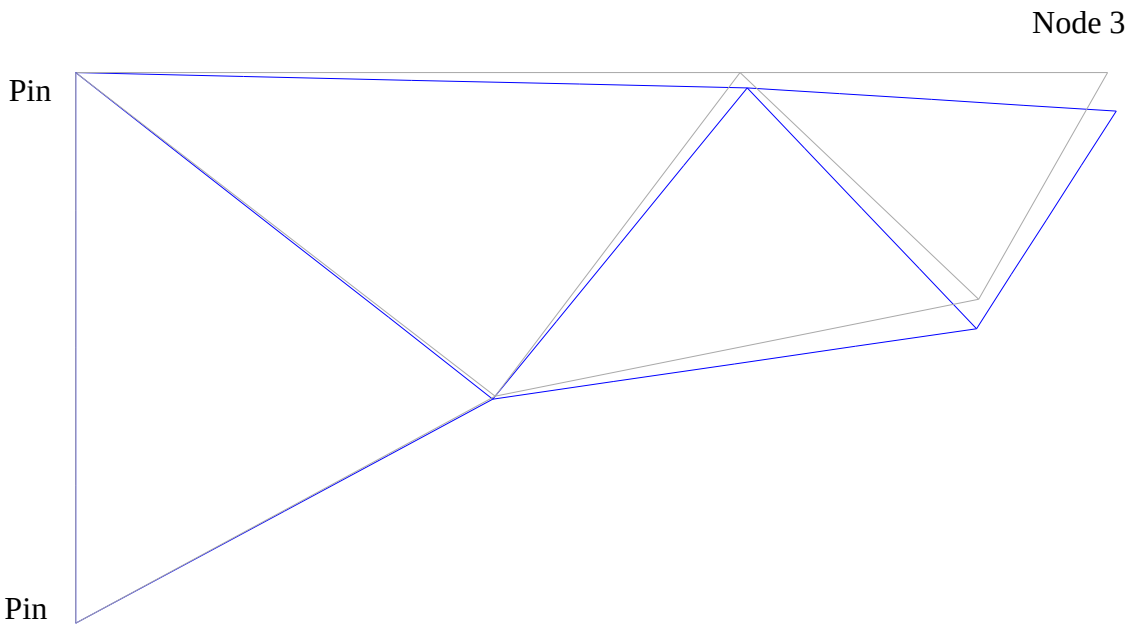


Figure 6-22: Deflection plot for MTT 180mm truss on a pin and pin support

The results obtained are shown in Table 6-7. The replicated truss model shows better performance than the topology optimised cantilever beam as well as its original with its highest deflection at node 3 (0.2969mm). The vertical member on the left experienced the highest stress with a value of 89.41MPa. In comparison between the three models, the deflection value for the topology optimised design is 131.42% higher than the truss design, while the original is 103.16% higher. The maximum von mises stress value for topology optimised design is 297.6% higher than the truss design, while the original is 325.37% higher. However, compared to the truss (roller), the truss (pin) deflection is 47.83% lower and experienced 202.32% lower stress. This is due to restricted movement in the second support. The deflection and stress profile plots for both the topology optimised design and the original are shown in Appendix C.c.a.

Table 6-7: Results for the MTT truss (pin and pin support)

Model	Deflection (mm)	Difference (%)	Stress (MPa)	Difference (%)
Truss (pin)	0.2969	0	89.41	0
Truss (roller)	0.4389	47.83	270.3	202.32
Topology	0.68708	131.42	355.01	297.6
Original	0.60319	103.16	380.32	325.37

6.4.2.2 Method of Tensile Triangles Rule of Thumb (MTTR)

Figure 6-23 shows the replicated truss model for the Method of Tensile Triangles Rule of Thumb with a projection length of 200mm. The details of the truss model defined is the same as in section 6.4.1.2.

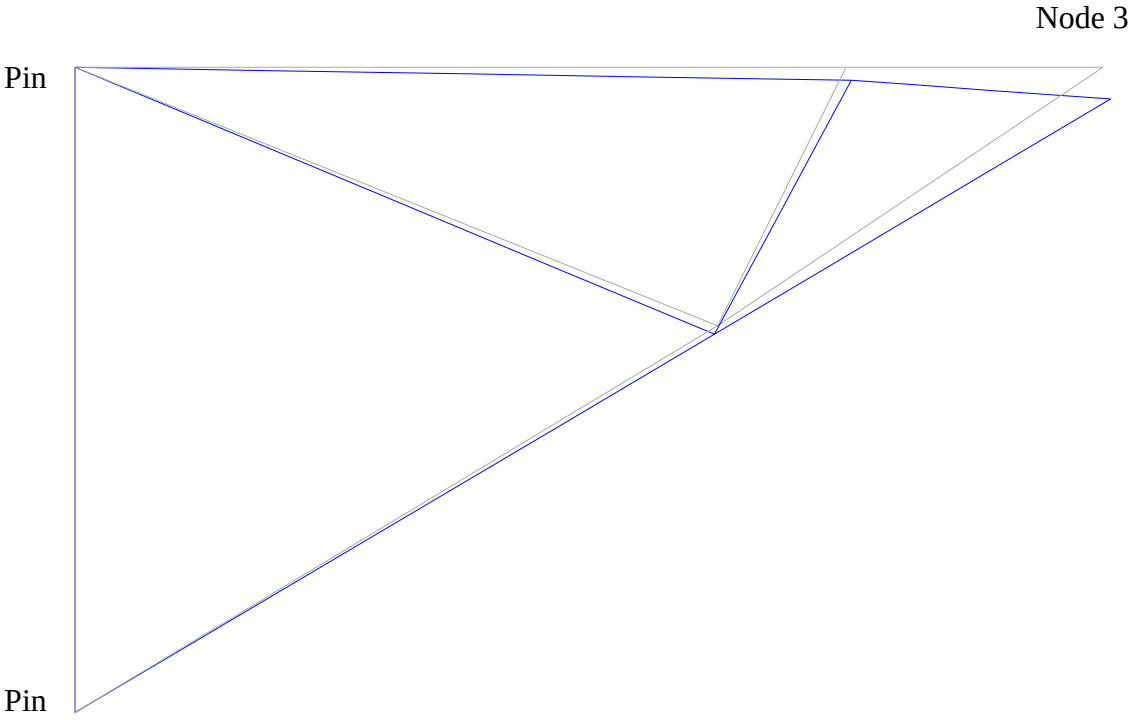


Figure 6-23: Deflection plot for MTTR 200mm truss on a pin and pin support

The results obtained are shown in Table 6-8. The replicated truss model shows better performance than the topology optimised cantilever beam as well as its original, with its highest deflection at node 3 (0.2446mm). The diagonal member on the left

experienced the highest stress with a value of 74.64MPa. In comparison between the three models, the deflection value for topology optimised design is 39.8% higher than the truss design, while the original is 11.59% higher. The maximum von mises stress value for topology optimised design is 363.56% higher than the truss design, while the original is 405.91% higher. However, compared to the truss (roller), the truss (pin) deflection is 50.49% lower and experienced 182.69% lower stress. This is due to restricted movement in the second support. The deflection and stress profile plots for both the topology optimised design and the original are shown in Appendix C.c.b.

Table 6-8: Results for the MTTR truss (pin and pin support)

Model	Deflection (mm)	Difference (%)	Stress (MPa)	Difference (%)
Truss (pin)	0.2446	0	74.64	0
Truss (roller)	0.3681	50.49	211	182.69
Topology	0.34194	39.8	346	363.56
Original	0.27296	11.59	377.61	405.91

6.4.2.3 Standard Triangle (ST)

Figure 6-24 shows the replicated truss model for the standard triangle (24mm). The details of the truss model defined is the same as in section 6.4.1.3.

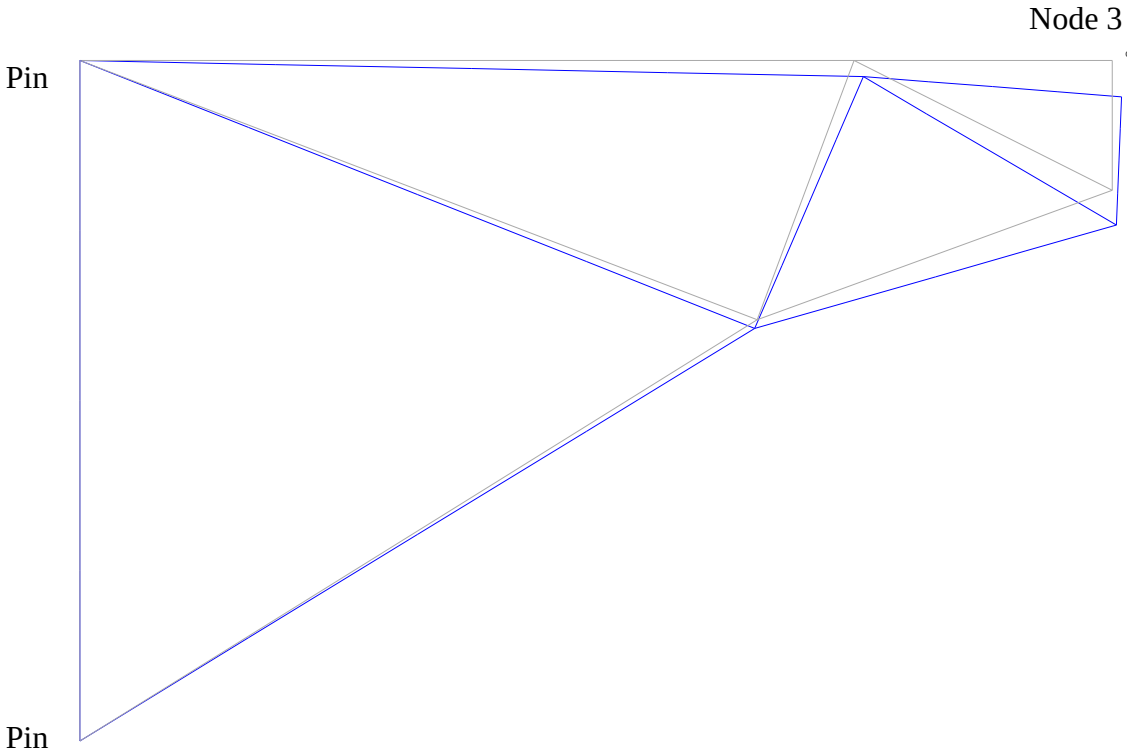


Figure 6-24: Deflection plot for ST 24mm truss on a pin and pin support

The results obtained are shown in Table 6-9. The replicated truss model shows poorer deflection performance with its highest deflection at node 3 (0.2788mm). The diagonal member on the right (element 5) experienced the highest stress with a value of 103.6MPa. In comparison between the three models, the deflection value for topology optimised design is 9.85% higher than the truss design, while the original is 6.8% lower. The maximum von mises stress value for topology optimised design is 169.21% higher than the truss design, while the original is 259.9% higher. However, compared to the truss (roller), the truss (pin) deflection is 54.48% lower and experienced 142.76% lower stress. This is due to restricted movement in the second support. The poorer performance in the ST truss may be due to the splitting of the truss section into two members, namely member “8” and “9”. The ST truss might perform better if the two members were a single continuous member. The deflection and stress profile plots for both the topology optimised design and the original are shown in Appendix C.c.c.

Table 6-9: Results for the ST truss (pin and pin support)

Model	Deflection (mm)	Difference (%)	Stress (MPa)	Difference (%)
Truss (pin)	0.2788	0	103.6	0
Truss (roller)	0.4307	54.48	251.5	142.76
Topology	0.30625	9.85	278.9	169.21
Original	0.25984	-6.8	372.86	259.9

6.4.2.4 Increased Depth (ID)

Figure 6-25 shows the replicated truss model for the increased depth with a total depth of 45mm. The details of the truss model defined is the same as in section 6.4.1.4.

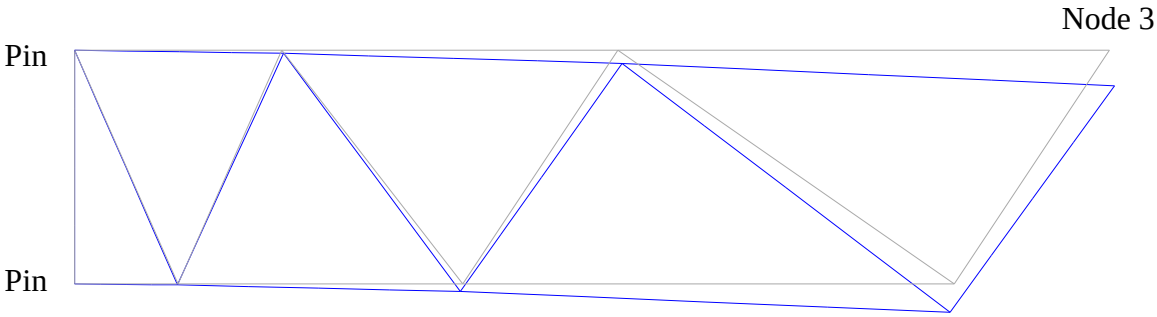


Figure 6-25: Deflection plot for ID 45mm truss on a pin and pin support

The results obtained are shown in Table 6-10. The replicated truss analysed under the two different support conditions shows the same outcome as it shares the same internal force flow. The replicated truss model shows better performance than the topology optimised cantilever beam as well as its original. At node 8 (point of load), the deflection value is 1.367mm and has a maximum stress value of 400MPa at member 11 (top left horizontal member). In comparison between the three models, the deflection value for topology optimised design is 68.71% higher than the truss design, while the original is 36.07% higher. The maximum von mises stress value for topology optimised design is 86.6% higher than the truss design, while the original is 44.45%

higher. The deflection and stress profile plots for both the topology optimised design and the original are shown in Appendix C.c.d.

Table 6-10: Results for the ID truss (pin and pin support)

Model	Deflection (mm)	Difference (%)	Stress (MPa)	Difference (%)
Truss (pin)	1.367	0	400	0
Truss (roller)	1.367	0	400	0
Topology	2.3062	68.71	746.41	86.6
Original	1.8601	36.07	577.8	44.45

Table 6-11 shows the comparison between the different trusses. The results show that the MTTR truss has the best performance for the amount of deflection per mass. This is followed by the ST truss, then the MTT truss and finally the ID cantilever. Although the ST truss did not perform as well as its original and the topology optimised cantilever beam, it did resist more deflection for the material required. The MTT truss under this support condition performs slightly worse than the ST truss regarding its deflection per mass, but the difference is marginal. Some design changes to the MTT truss may help improve its performance. The ID cantilever may have performed better than its topology optimised and the original cantilever, but it did not provide a good deflection resistance for the amount of steel utilised. This is because of its load path, not transferring the load to its support effectively.

Table 6-11: Comparison of pin and pin support trusses through their deflection per mass output

	Total Length of Steel (m)	Mass (kg)	Deflection (mm)	Deflection/Mass (mm/kg)
MTT (180mm)	0.7892	0.1077	0.2969	2.757
MTTR (200mm)	0.7514	0.1084	0.2446	2.256
ST (24mm)	0.8335	0.1012	0.2788	2.755
ID (45mm)	0.7577	0.06439	1.367	21.23

Overall, all trusses performed better than the original cantilever beam. The trusses show better deflection resistance than their original counterpart for their total mass of steel. Although the mass of the MTT truss was higher than its original, the deflection resistance was significantly higher. The increase in the total weight of the MTT truss is most likely because of the overestimation of the section size on member 8, as shown in Appendix C.c.a. The results are slightly different in the ST cantilever beam. Although the original ST cantilever has a lower deflection than the ST truss, the material saving in the truss was much higher than the original. Hence, it is still considered better than its original. As mentioned earlier, the ST truss might perform better if the two members were a single continuous member instead of separate members. The results shown in Table 6-12 and Figure 6-26 show the practicality of replicating the topology obtained as trusses. Hence, it is a feasible alternative.

Table 6-12:Comparison of the mass and deflection between the truss and the original cantilever beam

	Original Mass (kg)	Truss Mass (kg)	Difference (%)	Original Deflection (mm)	Truss (pin) Deflection (mm)	Difference (%)
MTT (180mm)	0.0973	0.1077	+10.79	0.60319	0.2969	-50.78
MTTR (200mm)	0.12952	0.1084	-16.31	0.27296	0.2446	-10.39
ST (24mm)	0.13267	0.1012	-23.72	0.25984	0.2788	-7.3
ID (45mm)	0.0765	0.06439	-15.83	1.8601	1.367	-26.51

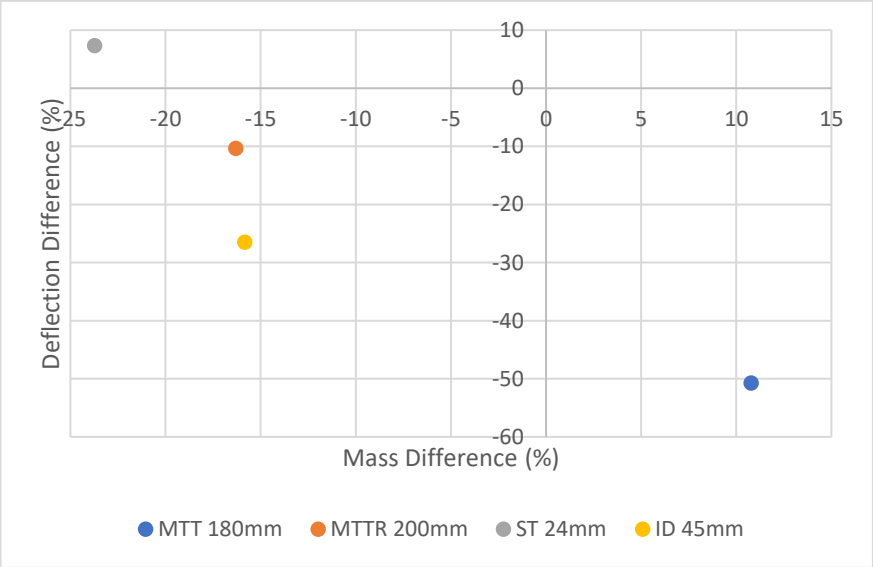


Figure 6-26: Difference in Mass and Deflection Between The Truss and The Original Cantilever Beam

6.5 Discussion

The topology provides a good insight into why certain geometry and size provide greater deformation resistance than others. The topology plots show how the load path is distributed in the various cantilever beam geometries. Although the generated optimised plots did not create a better beam, they created a larger but lighter beam. The larger size of the topology optimised cantilever beam provided a better load

transfer and a lighter design. The optimised MTT cantilever beam is better than the other cantilever beam geometries at various depths across lower volumes.

In contrast, the optimised MTTR cantilever beam is better than the other cantilever beam geometries towards the higher volume in the cantilever beam depths of 30mm and above. On the other hand, the optimised ST cantilever beam performed best across the higher volumes with a cantilever beam depth of 20mm. One of the logical reasons why the MTT cantilever beam could not perform well across the higher volumes is that there is an underutilisation of the triangular projection, whereas the MTTR and the ST cantilever will fully utilise the shape of its triangular projection to provide the support needed. However, the topology optimised plots still provide an alternative to designing a cantilever that would need to meet a requirement of a lower amount of materials.

As iterated earlier, the generated topology plots did not create a better beam, but they can serve as a guide to create a better one. It was shown in section 6.4, where the optimised topology model built the foundation in the design consideration of the truss model and created a better cantilever beam. Needless to say, the optimised topology did indirectly create a way of designing a cantilever beam, even though it did not achieve a lower deflection and stress value when compared to its original. It should also be noted that the volume constraints were a bit tight, and it should be above 0.65 for a reasonable design. However, as mentioned earlier, it provides better visibility of the load path for replicating the topology as a truss design. The other aspect worth noting that contributed to its poorer performance is the post-processing of the topology obtained. A further refinement in the post-processing phase of the topology optimised design can help reduce the performance difference between the finalised cantilever beam design and its original. This example can be seen during the replication of the

truss design, as shown in Figure 6-17, where the topology obtained was clearly not a stable and viable structure.

As shown in section 6.4.1 and 6.4.2, the results show the practicality of replicating the obtained topology as a truss design. As mentioned earlier, some modification was applied to the topology of the truss design to ensure the truss is in a stable condition. The trusses analysed in section 6.4.1 have a higher deflection value than those analysed in section 6.4.2 due to the sliding effect at the roller support. Trusses like the MTTR and the ST suffer significant sliding of the roller that causes a higher deflection than both the topology optimised and the original cantilever beam. They slide more than the MTT due to the reduced amount of internal members that provide the necessary stiffness. It may also be partly due to the larger member sections utilised in the MTT truss. All trusses show better performance in the pin and pin support except for the ID truss, as there was no sliding of the roller support.

Although the topologies in both the topology optimised model and the truss model were slightly different, it does not neglect the fact that the topology optimised model built the foundation in the design consideration of the truss model. It has provided a sense of direction towards the assembly of the truss members. The truss models with the pin and pin support have consistently outperformed the truss models with pin and roller support. This is mainly due to the roller support allowing for sliding movement and placing some additional stress on its member while the other does not as it goes directly to support, and sliding was prevented.

Compared to its original cantilever beam, the topology optimised cantilever has a material saving difference between 31.8% to 38.1%. However, depending on its geometry, it can cause a higher deflection between 11.6% to 27.6%. The trusses

performed better than all of their other counterpart. It can provide material saving between 10% to 24% and an increased deflection resistance of between 7.3% to 51% depending on its geometry.

6.6 Summary

The topology optimised cantilever beams create a new way of designing a cantilever beam. The topology optimised cantilever beam may perform better than its original if the volume constraints were set to 0.65 and above. The value of 0.5 volume constraints may have been too strict and did not provide direct benefit. However, the stricter volume constraints allowed the replication of the topology design in trusses. The load path in the cantilever beams obtained through the topology optimisation study provides the foundation in the design consideration of its truss member in terms of orientation and size.

Although the generated optimised plots did not create a better beam than its counterpart, it created a larger but lighter beam. The larger size of the topology optimised cantilever beam provided a better load transfer and a lighter design. It should be noted that the optimised may perform slightly better than the results obtained if more refinements were placed in the post-processing of the final topology. The replicated truss performed better than its counterpart in terms of material saving and deflection resistance.

Based on the result obtained in the last three chapters, the Method of Tensile Triangles' Shape Profile has proven to be research worthy for other civil engineering applications like building structures. Hence, in the next chapter, the research further investigates the application of replicating nature's design profile in the joints/connections of multistorey buildings.

Chapter 7 Replicating Nature's Design in Multistorey Structures

Through many years of structural designs, the structure's form, shape and material can affect its cost, functionality and performance. The study investigates the effectiveness of the introduction of nature's design in the columns of a multistorey building. Hence, to eliminate other factors that may influence the result in this study, the model was simplified to moment-resisting framed steel structures, regular symmetrical shape for both plan and elevation layout.

7.1 Detail of the Finite Element Model

The study investigates the behaviour and performance of introducing nature's design as a frame structure of a multistorey building. Hence, the models are regular symmetrical shaped, unbraced (pure frame), fixed jointed foundation and constructed of a single material to reduce other factors that may influence the result. The models defined are moment resisting steel frame structures. The material utilised is of S355 grade. Steel I cross-sections are utilised for the frame structure. IPE European I beam sections and HE European wide flange beams were utilised for the beams and columns, respectively. The storey height is fixed at 3m. The internal column configuration is a 5 x 5 model with a column to column spacing of 3m. The plan and elevation layout view of the multistorey structure is shown in Figure 7-1. The five different storey heights considered in each multistorey building design analysis covers low to high rise buildings (e.g. 3, 9, 15, 21 and 27). A total of 50 models analysed. The buildings have a slenderness ratio (or height to base ratio) of less than 4.

The type of earthquake analysis included in this study is the modal analysis, equivalent lateral force (Eqx) and the response spectrum (RS). The horizontal members should

ideally fail before the vertical members in a framed structure in practice and safety concerns. Thus, the columns are usually designed to be stronger than the beams in earthquake-prone areas.

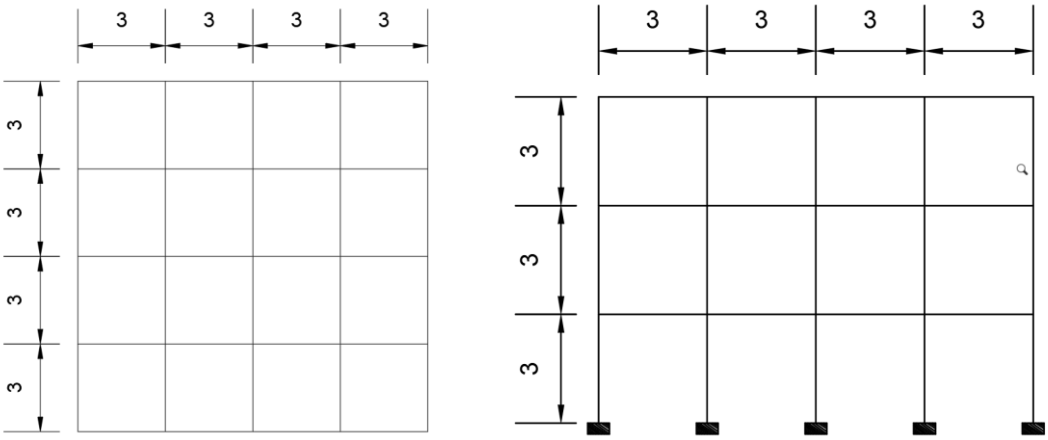


Figure 7-1: Plan and elevation layout of a three-storey building structure

The joints of the beam to column connection are assumed rigid where the beam meets the centre of the column. A diaphragm constraint is assigned on all floors to create a link between joints located within a plane to ensure they move together as a planar diaphragm. The slab defined has no stiffness, mass or weight and only carry load directly to the frames. The load applied for the floor slabs are 4.6kN dead load and 5kN live load. The design response spectrum utilised is a Type 1 spectrum, soil type C, reference peak acceleration of 3m/s^2, importance factor of the building is 1 and a behaviour factor of 4.

The seismic mass utilised in the analysis is associated with a load combination of G + $\Psi_{E,i}$Q where $\Psi_{E,i}$ is taken as 0.3. The load combination considered for the analysis is G + $\Psi_{E,i}$Q+ E. The Equivalent Lateral Force Method and Response Spectrum Analysis are considered in the study to ensure the results obtained corresponds with each other. For the auto lateral load, Eurocode 8 2004 was applied. The seismic evaluation

considered is in the X-direction of the plan. The correction factor, lambda, eccentricity ratio, modal damping and C_t defined are 0.85, 0.05, 0.05 and 0.085 respectively. For the response spectrum analysis, the modal and directional combination/type utilised are CQC and SRSS. A 90% mass participation criteria are used per code to ensure the modal analysis sufficiently captures the response of all modes of vibration contributing to the global response of the structure. The analysis includes the self-weight of the structure.

For the initial sizing, a wide variety of I and HE European beams ranging from 80 to 750mm height and 100 to 1100mm height were added to the list of frame sections for consideration in the analysis. SAP2000 initiates the analysis with a median frame section to determine whether the steel sections applied to meet the design requirements of EC3. Through the iteration of the steel frame design checks, frame sections are suggested for the various beams and columns throughout the structure. A more focused selection of the frame sections is applied through the steel design iteration process to narrow the number of frame sections to 2 types, one for the beam and the other for the column. The steel frame design checks defined are for DCH-MRF instead of DCM-MRF. Thus, the suggested frame sections will be larger. The complete details on the steel frame design checks defined are shown in Appendix D.b.a. Although frame sections applied to vary with height in practice, the sections are maintained throughout the structure for this study.

7.2 Replicating MTT Design Profile in the Columns

The analysis is broken down into three sections. The first is the " MTT Column Design using Industry Sections versus Custom Section", the second is "Reduction in Beam

Section", and lastly is "Minimising the Capacity in both Beam and Column". In the first study, the MTT column designs use two different approaches in creating the non-prismatic frame section. The first analysis utilises a set of commercial steel sections and the second analysis uses a set of the modified version of the selected frame section (utilised in the base model) to create the non-prismatic section. The two different approaches utilised in creating the non-prismatic section are due to the lack of study in a customised non-prismatic section which may lead to a less accurate assumption on its structural performance. The assumption of the SAP2000 leads to studying the two different sizes in the model as it assumes the non-prismatic frame section is at its centre line.

Reducing the beam size or increasing the column size can prevent the beam/column flexural capacity ratio from exceeding its design limit. In continuation of the first study, the reduction of the beam section was studied to identify the lowest possible steel beam section assignment before it becomes unacceptable. The study of maintaining the beam section of the structure with reducing the column sections is not possible as it will lead to yielding in the columns. In the second study, the customised sections obtained from the first study were applied. The same base model frame sections are utilised in the first two studies for the comparison against the Method of Tensile Triangles (MTT) column design. The base model frame sections identified based on user discretion is shown in Table 7-1. The triangular projections sizes (e.g. large and small) are based on the initial column width, the first is based on the size of the column width, and the other is based on half of the column width. For example, IPE270 has a total height of 270mm, and half of that height will be 135mm. The results are summarised in Table 7-2. The self-weight considers only the frame section.

Table 7-1: Base frame section

Floors	Beam	Column
3	IPE180O	HE220M
9	IPE240O	HE240M
15	IPE270O	HE280M
21	IPE270R	HE300M
27	IPE270O	HE320M

Table 7-2: Results for the MTT Column Design using Industry Section vs Custom Section

Storey	**Categories**						
3	Base	240mm	240mm custom	120mm	120mm custom	240mm custom RB	120mm custom RB
Eqx (m)	0.02316	0.01819	0.01821	0.02101	0.02113	0.02365	0.02295
RS (m)	0.02331	0.01787	0.01789	0.02062	0.02074	0.02282	0.02215
Self (kN)	333.148	366.313	342.557	359.02	335.894	329.789	327.012
9	Base	270mm	270mm custom	135mm	135mm custom	270mm custom RB	135mm custom RB
Eqx (m)	0.06996	0.05295	0.0531	0.06298	0.0624	0.06751	0.0791
RS (m)	0.05472	0.04654	0.04653	0.05108	0.05072	0.05286	0.05668
Self (kN)	1402.42	1411.199	1445.557	1374.006	1415.199	1391.907	1362.202
15	Base	310mm	310mm custom	155mm	155mm custom	310mm custom RB	155mm custom RB
Eqx (m)	0.0956	0.0707	0.0716	0.0848	0.0846	0.10655	0.12608
RS (m)	0.0778	0.0655	0.066	0.0718	0.0717	0.08027	0.08697
Self (kN)	2823.681	3174.49	2921.333	2877.639	2852.939	2713.366	2647.134
21	Base	340mm	340mm custom	170mm	170mm custom	340mm custom RB	170mm custom RB
Eqx (m)	0.14419	0.10684	0.10763	0.1283	0.12699	0.16312	0.17837
RS (m)	0.1226	0.09335	0.0939	0.10804	0.10722	0.13296	0.14509
Self (kN)	4759.59	4729.916	4939.273	4700.893	4812.205	4603.598	4569.91
27	Base	359mm	359mm custom	179.5mm	179.5mm custom	359mm custom RB	179.5mm custom RB
Eqx (m)	0.24055	0.17852	0.17783	0.21073	0.2083	0.23355	0.23251
RS (m)	0.2185	0.16075	0.1601	0.19002	0.18781	0.21051	0.20972
Self (kN)	6204.89	6468.57	6459.212	6287.367	6279.172	6197.851	6081.553

Table 7-3: Results for the Minimising Capacity in both Beam and Column

Storey		**Category**				
3		Base	220mm custom	(%)	110mm custom	(%)
	Eqx (m)	0.02601	0.02073	-20.2999	0.02385	-8.3045
	RS (m)	0.0257	0.0205	-20.2335	0.02358	-8.24903
	Self (kN)	301.974	309.636	2.537305	304.187	0.732845
9		Base	240mm custom	(%)	120mm custom	(%)
	Eqx (m)	0.08555	0.06655	-22.2092	0.07715	-9.81882
	RS (m)	0.06037	0.05256	-12.9369	0.05614	-7.00679
	Self (kN)	1099.2	1131.454	2.934316	1109.446	0.932132
15		Base	270mm custom	(%)	135mm custom	(%)
	Eqx (m)	0.14511	0.11139	-23.2375	0.1295	-10.7574
	RS (m)	0.10043	0.08236	-17.9926	0.08923	-11.152
	Self (kN)	2337.366	2409.868	3.101868	2358.961	0.923903
21		Base	270mm custom	(%)	135mm custom	(%)
	Eqx (m)	0.20158	0.15807	-21.5845	0.18208	-9.67358
	RS (m)	0.16883	0.12928	-23.4259	0.14858	-11.9943
	Self (kN)	3314.986	3421.167	3.20306	3347.498	0.980758
27		Base	310mm custom	(%)	155mm custom	(%)
	Eqx (m)	0.26959	0.20857	-22.6344	0.23932	-11.2282
	RS (m)	0.2447	0.18766	-23.3102	0.21588	-11.7777
	Self (kN)	5082.625	5259.356	3.47716	5135.762	1.045464

The terms “Eqx”, “RS”, Self” and “RB” in this chapter refers to the Equilavelent Lateral Force method, Response Spectrum, Selfweight and Reduced Beam. “Base”, “e.g. 240mm”, and “e.g. 220mm custom” refers to the column section type. For example, the number in the column section type “220mm custom” refers to the projection size.

7.2.1 Modal Analysis

The following figures shown in Figure 7-2 are the "1st mode" of the individual base models. All 10 modes on the various floors are shown in Appendix D.b.c.b.a.

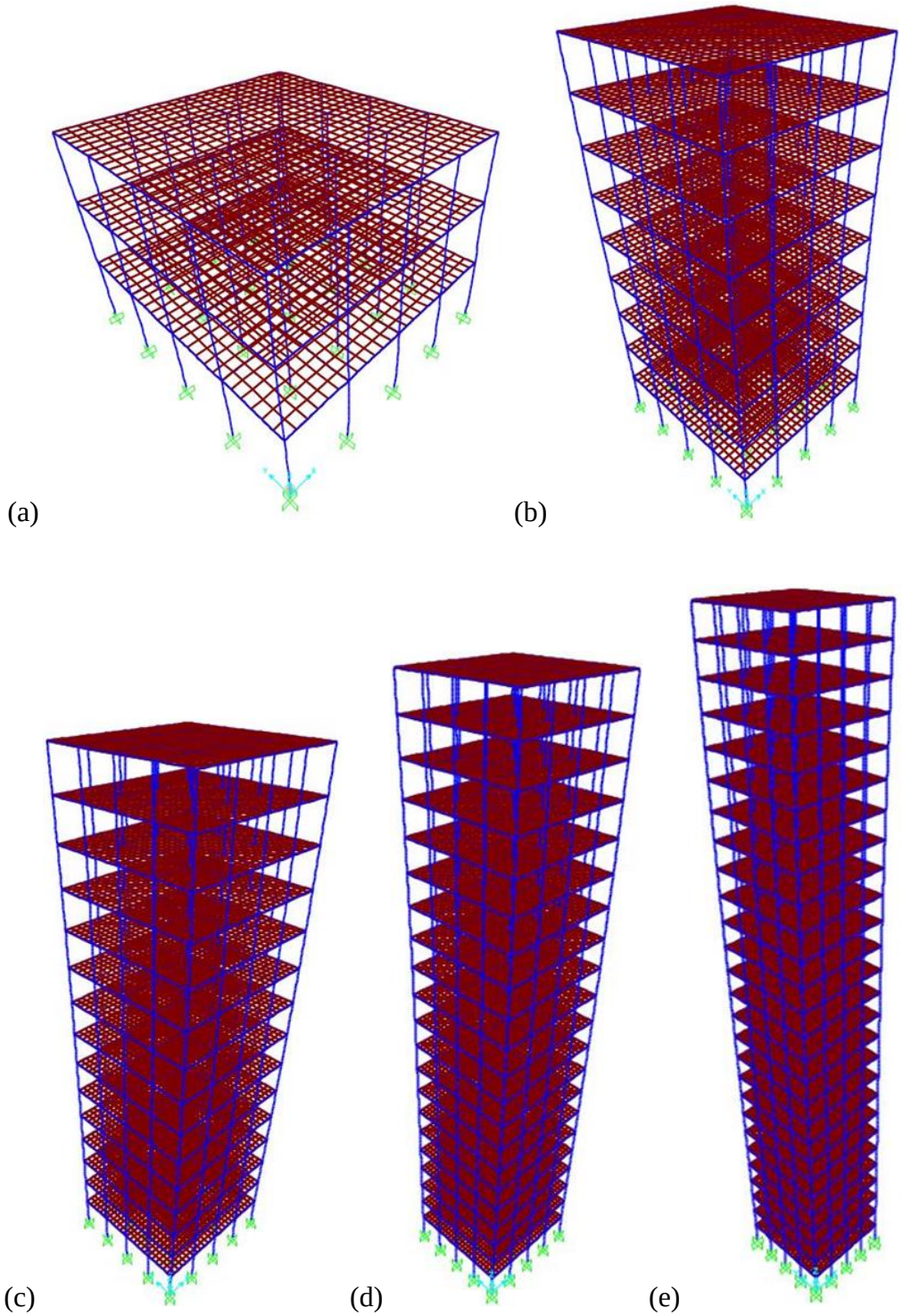


Figure 7-2: 1st Mode of the various floors model (a) 3 floors (b) 9 floors (c) 15 floors (d) 21 floors (e) 27 floors

7.2.2 MTT Column Design using Industry Sections versus Custom Sections

In this section, the study looks into the two non-prismatic design approaches that can affect the structure's performance. Each non-prismatic member consists of 4 different steel section due to the shape of the triangular projection. The industry profile design approach uses a variety of commercially available steel sections to build up the non-prismatic section. The custom section design approach uses the existing steel section and only modifies the steel's overall web height to create the non-prismatic beam. It should be noted that both methods have their limitation. The steel section for the industry profile suffers a non-homogenous section that will create weakness between the connecting sections, as shown in Figure 7-4.

On the other hand, the custom section may suffer particularly from torsional effects as the section size was not increased proportionally. Figure 7-3 shows the extruded view of a three-storey multistorey building with the MTT columns. The architecture of the building is similar to all the other MTT column multistorey buildings. The graphs shown from Figure 7-5 to Figure 7-19 are the percentage difference between the base models and the MTT column models. Thus, the category for the base models is not present in the graphs.

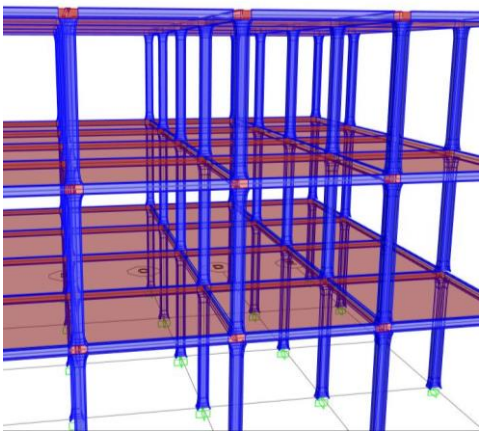
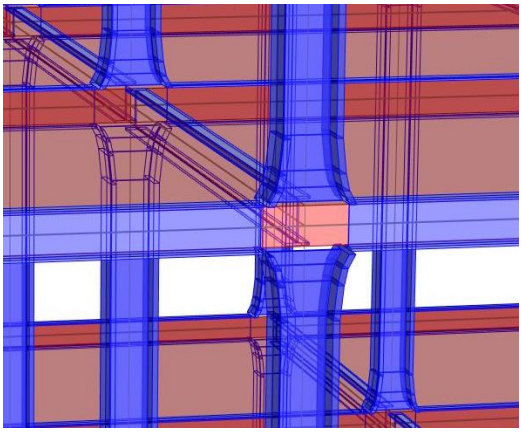
(a)  (b) 

Figure 7-3: 3 storey multistorey building MTT (110mm) custom column design extruded view (a) Overview (b) Magnified view

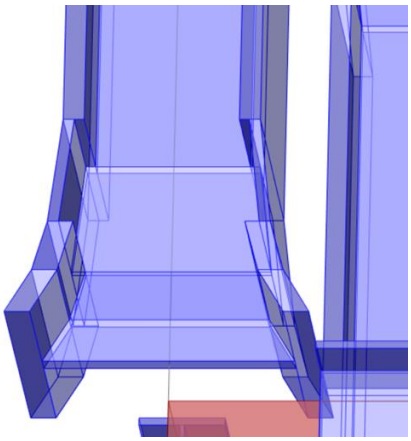
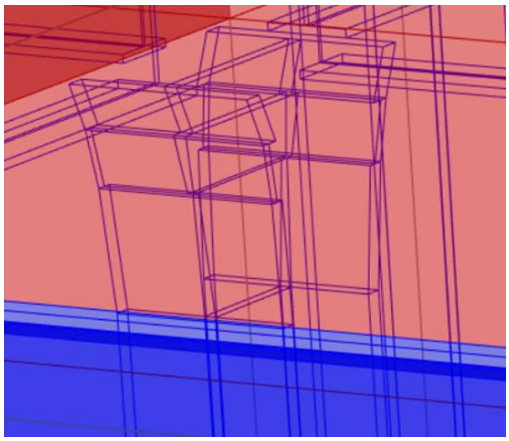
(a)  (b) 

Figure 7-4: Non-continuous section of the MTT column (a) solid view (b) wireframe

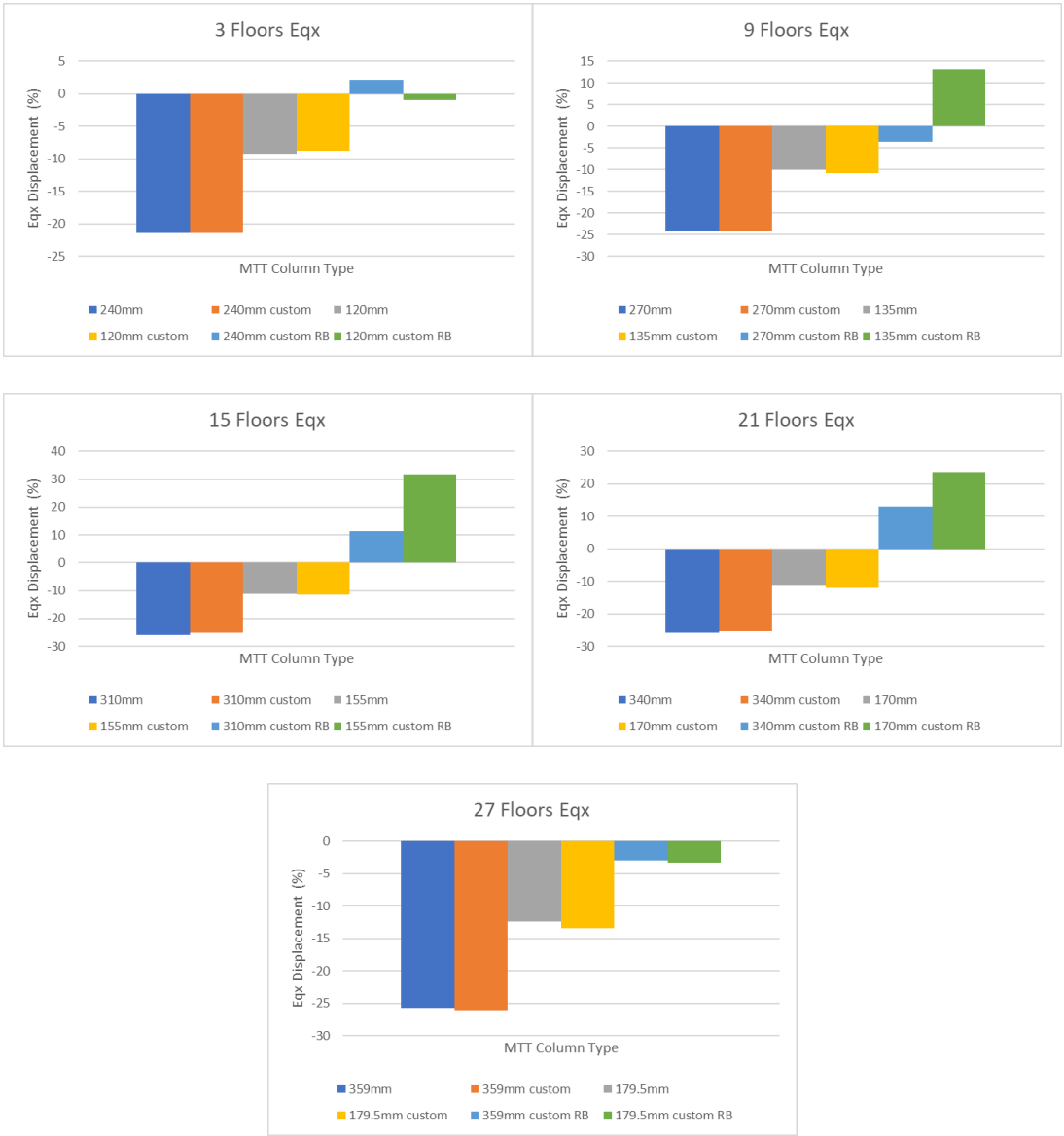


Figure 7-5: Eqx Displacement of MTT Column Design By Floor

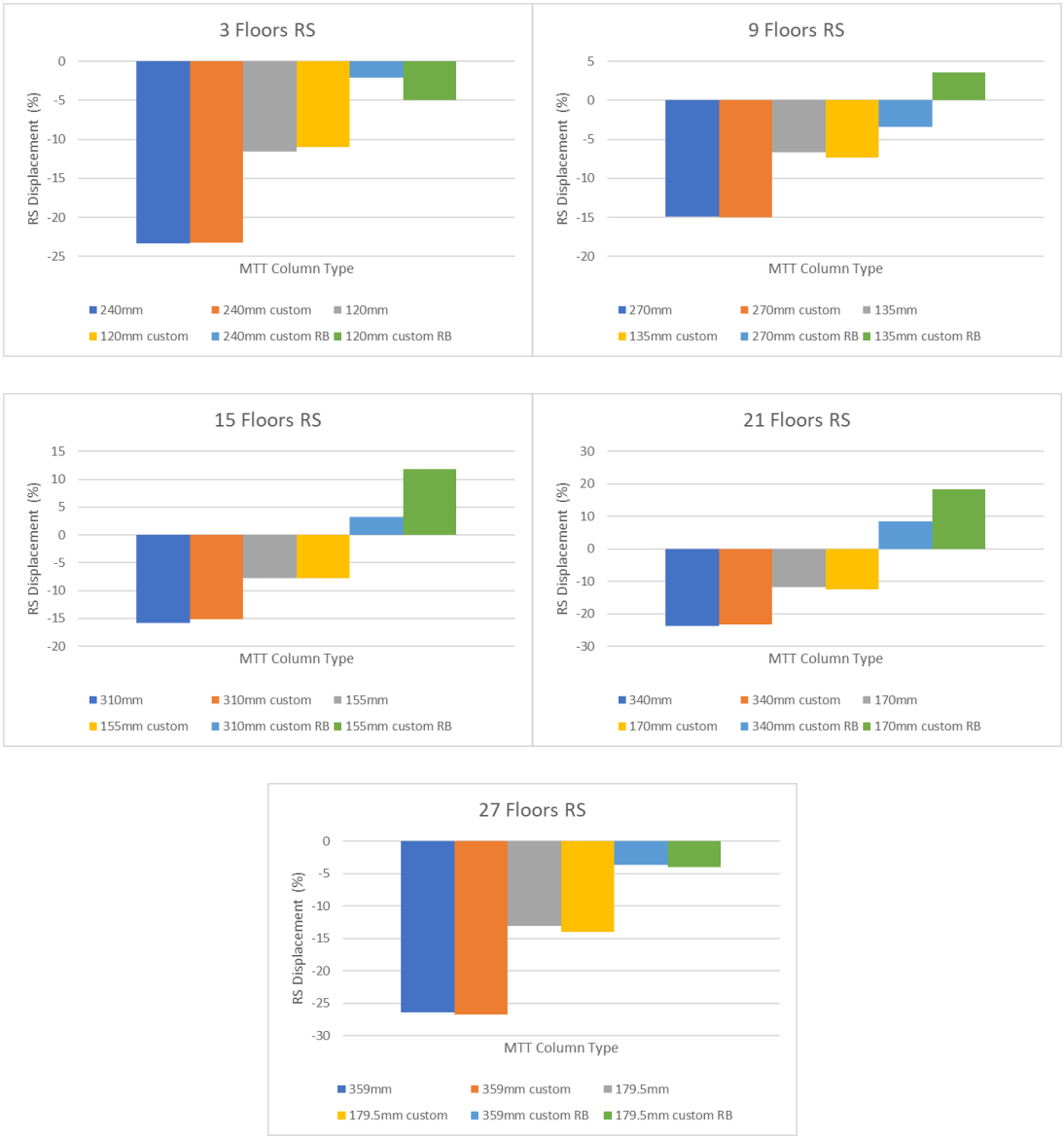


Figure 7-6: RS Displacement of MTT Column Design By Floor

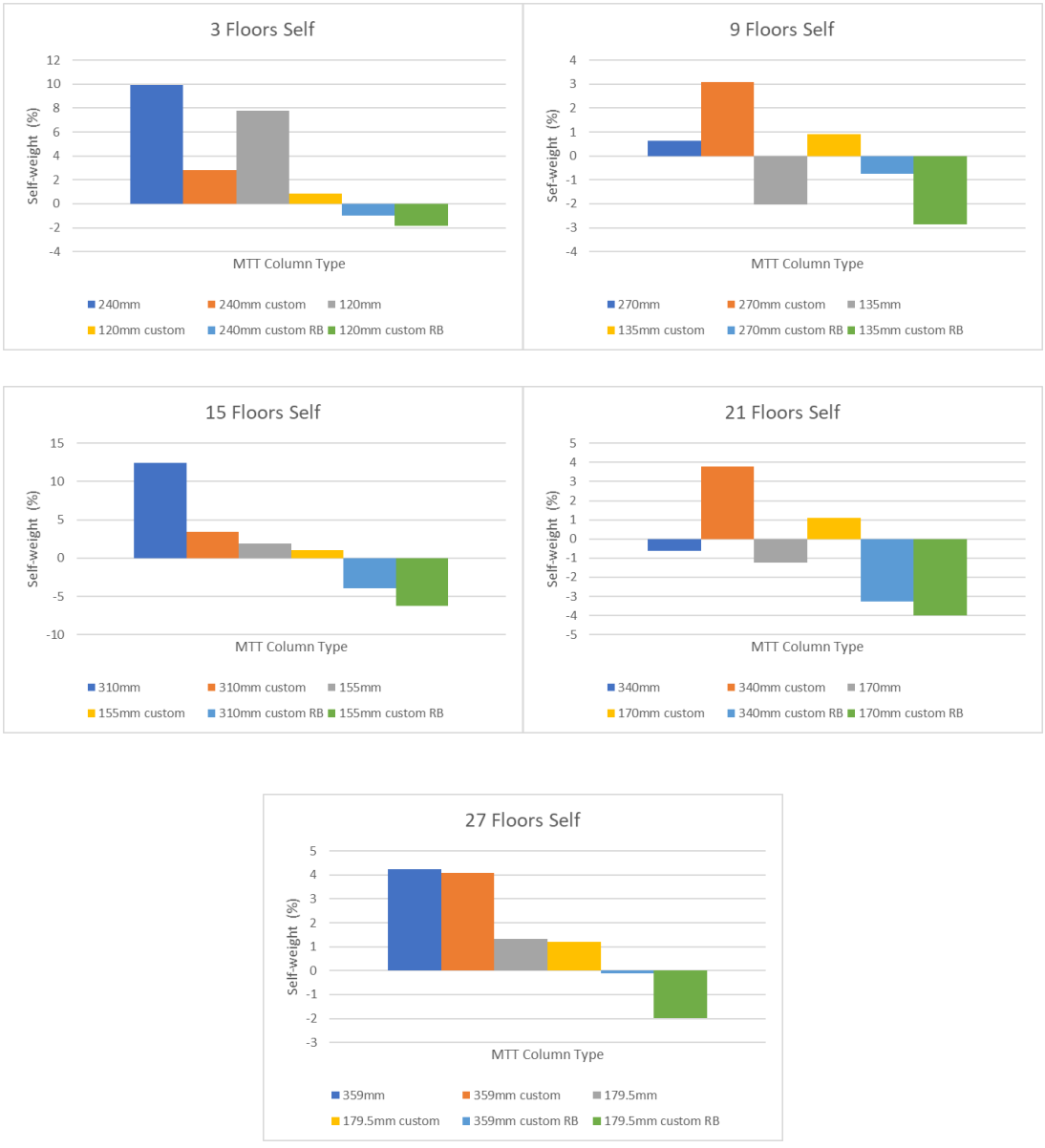


Figure 7-7: Self-Weight of MTT Column Design By Floor

7.2.2.1 Comparison of Displacement and Self-weight by Floor

In most of the building storey heights except for the '27 floors", the large non-customised size experienced lower displacement for both Eqx and RS, as shown in Figure 7-5 and Figure 7-6, whereas for the smaller section, the customised section experienced lower displacement for both Eqx and RS across all building heights except for the "3 floors". The better displacement performance in the non-customised larger

section is likely linked to the strength of the frame section. For the smaller section of the customised version, its displacement performance most likely stems from the benefits of a homogenous frame section. The lack of homogeneity in the non-customised sections leads to a lighter structural weight across some of the different storey heights, as shown in Figure 7-7. No doubt, based on the results, some of these discontinuities are not only lighter but performed just as well as their counterpart.

Across all storey heights and for both Eqx and RS loading, the displacement resistance achieved in the larger section is between 15% and 26%, and the self-weight is between –0.6% to 12.4%. While in the smaller section, the displacement resistance is between 6.6% - 14%, slightly better for being about half of its weight compared to the larger section, and the self-weight is between –2% - 7.7%.

If only considering the two customised sections, the range of self-weight is much lower. For the larger section, the self-weight increment is between (2.8% - 4%) while the smaller section is between (0.83% - 1.2%), for a displacement resistance between (15% - 26%) in the larger section and (7.3% - 14%) in the smaller section for both Eqx and RS load. This would result in a more acceptable structural performance. Nevertheless, the MTT column design still provides better displacement resistance per weight regardless of the method applied.

7.2.2.2 Comparison of Displacement and Self-weight across the Storey Heights

The MTT column exhibits a similar pattern in Eqx and RS loading condition, as shown in Figure 7-8 and Figure 7-9. Generally, they both show a slight improvement across the increasing storey heights except for the RS, where there is a slight drop in the displacement resistance. The Eqx load for the smaller sections shows a more linear improvement across the increasing storey height, suggesting that each floor's

cumulative strengthening is still being added up to the total displacement performance. In the larger sections under Eqx load, the improvement across the increasing height is becoming less effective. However, it still provides an excellent overall displacement resistance. Therefore, it should be expected that the self-weight in the non-customised section has a less consistent pattern across the increasing storey height while the customised section is a more linear increase in self-weight, as shown in Figure 7-10.

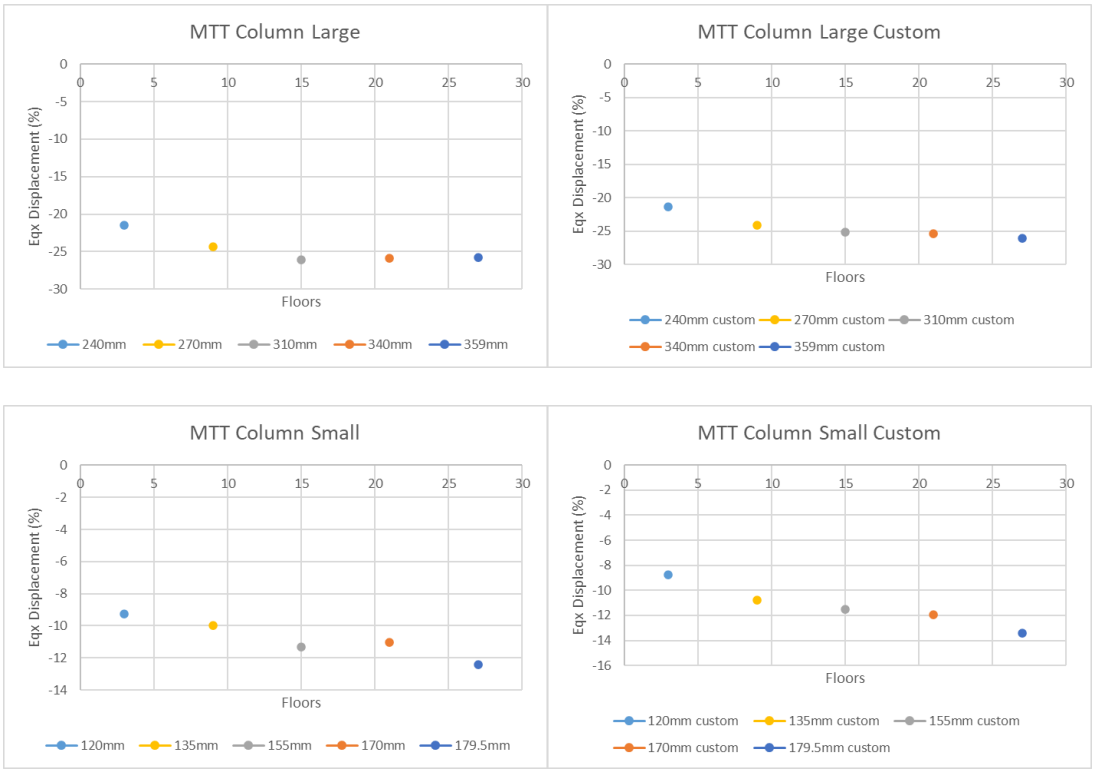


Figure 7-8: Eqx Displacement of MTT Column Industry vs Custom Section across Storey Height

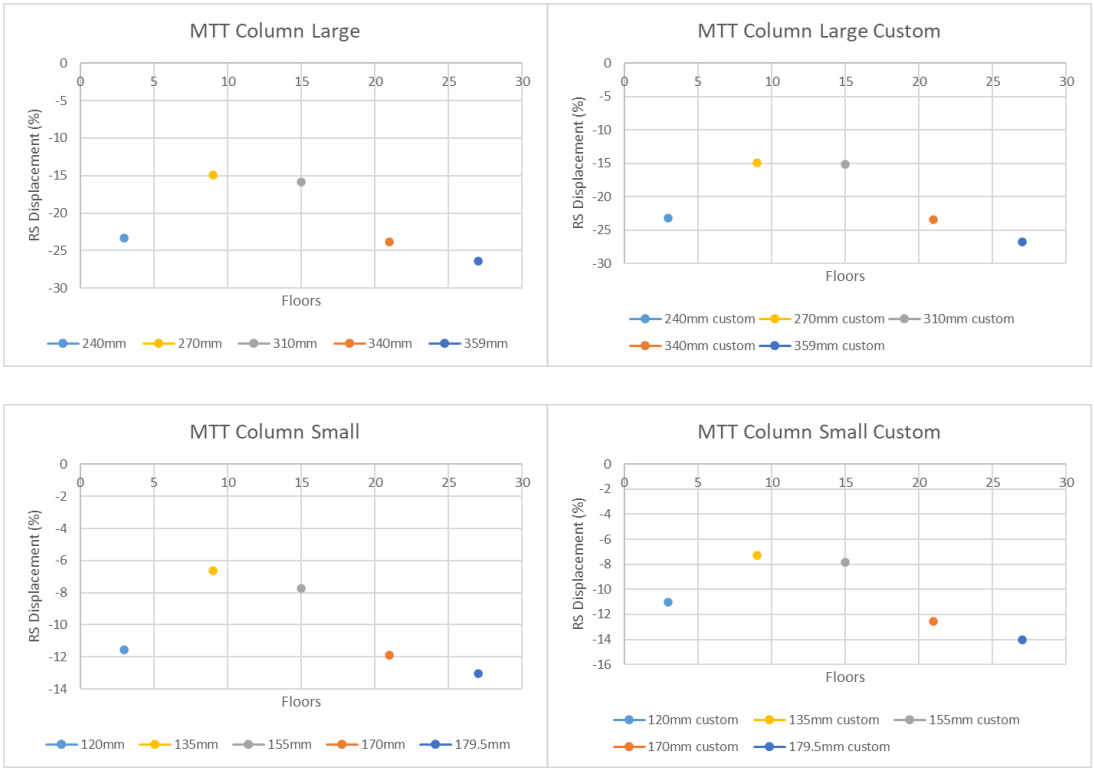


Figure 7-9: RS Displacement of MTT Column Industry vs Custom Section across Storey Height

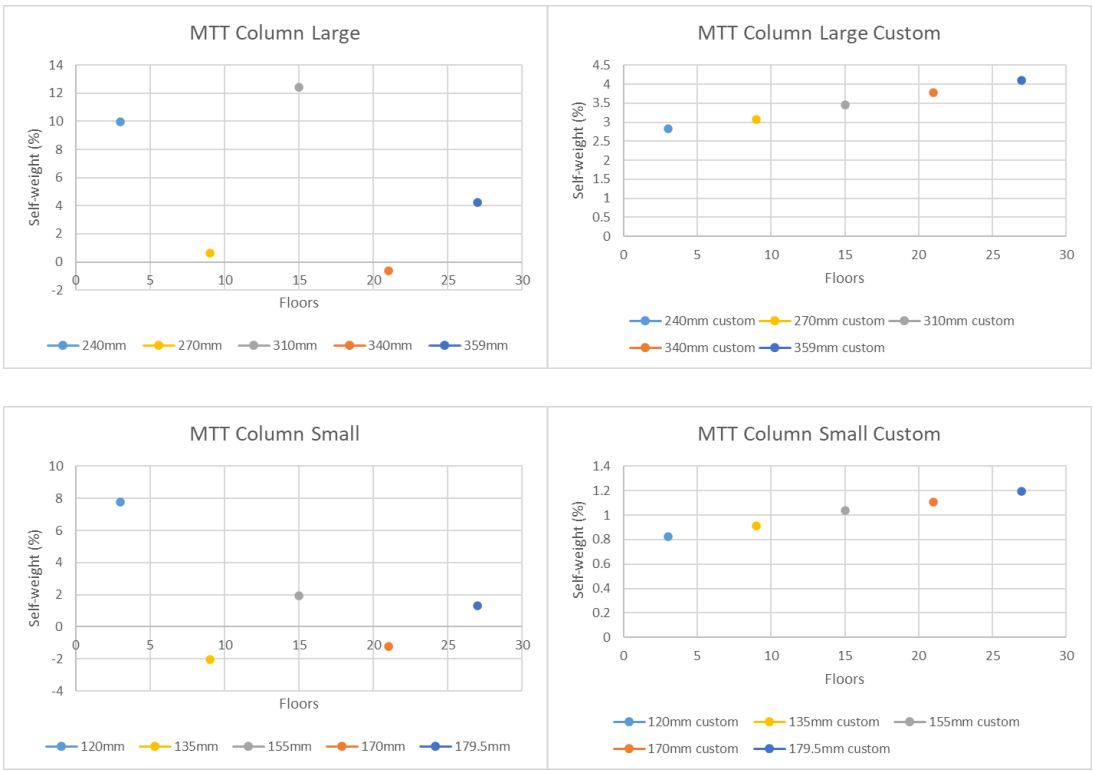


Figure 7-10: Self-Weight of MTT Column Industry vs Custom Section across Storey Height

7.2.3 The Effect of Reduction in Beam Section

7.2.3.1 Comparison of Displacement and Self-weight by Floor

Since the study is about reducing the beam section, there is no doubt that the structure's overall weight is expected to be lighter and inevitably leads to a higher overall displacement. This is seen in between the floors of 9 to 21. They display a displacement increment of between 3.3% - 11.7% for a weight reduction of between 0.7% - 3.98%. This may not be an ideal result for anyone seeking to improve current design structures.

Interestingly, floors 3 and 27 show better displacement resistance by 2% to 5% than their base model while providing a weight reduction of between 1% to 2%. However, it should be noted that the three-storey building has a 2.11% higher displacement in the larger section for the Eqx load for a 1% weight reduction which is unfavourable. Nevertheless, it shows that carefully design consideration and planning can still lead to a better structure.

7.2.3.2 Comparison of Displacement and Self-weight across the Storey Heights

As shown in Figure 7-12, a steady linear displacement increment is seen across the storey heights except for the 27 floors in the RS graph of both section sizes. The Eqx displacement across the increasing storey height is more of a wave pattern in the larger section, while a bell curve like pattern is seen in the smaller section, as shown in Figure 7-11. Interpreting from the self-weight graph, the likely reason for the displacement increment of floors (15-21) stems from the excessive reduction of the beam sections, eventually leading to a poorer design structure. The steep reduction of the beam sections is seen in Figure 7-13.

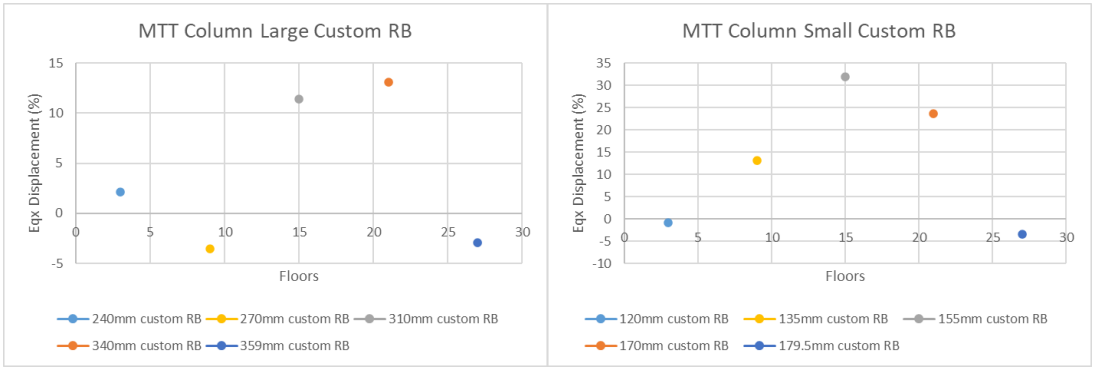


Figure 7-11: Eqx Displacement of MTT Column Reduced Beam Section across Storey Height

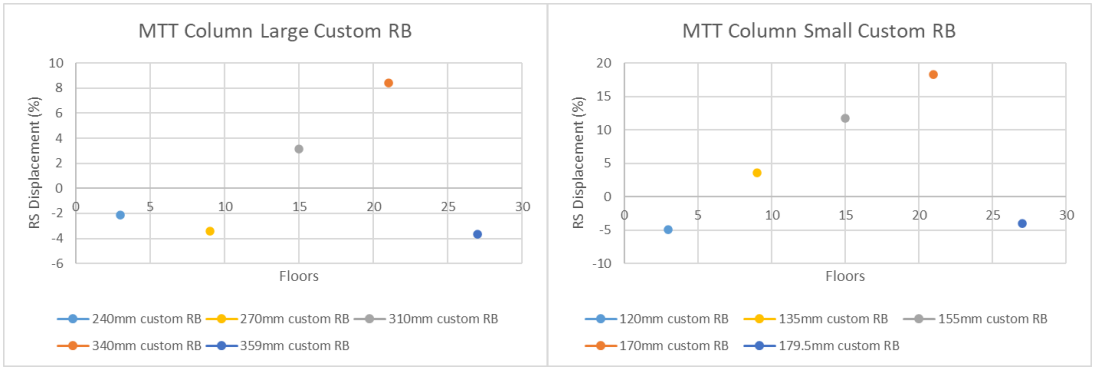


Figure 7-12: RS Displacement of MTT Column Reduced Beam Section across Storey Height

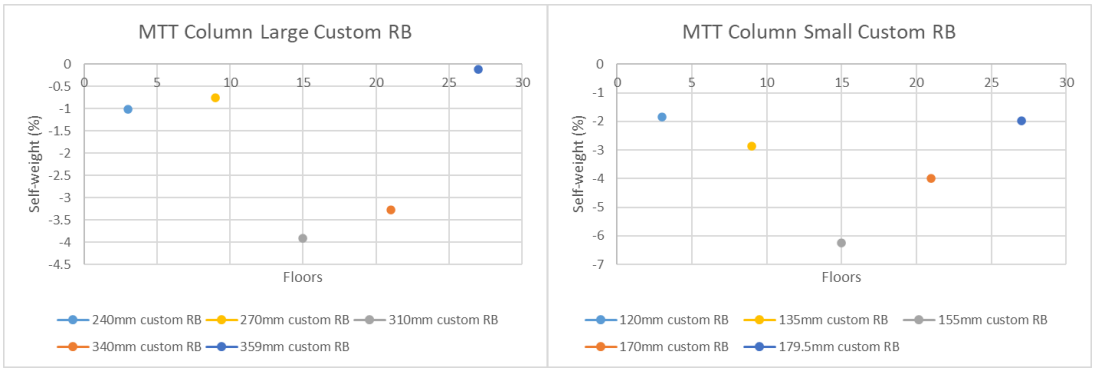


Figure 7-13: Self-Weight of MTT Column Reduced Beam Section across Storey Height

7.2.4 Minimising the Capacity in both Beam and Column Sections

In this study, both the beam and column capacities are minimized to place both beams and columns in critical conditions. This is to study the consistency of its performance using MTT columns. Table 7-4 shows a set of steel sections utilised in the base model study.

Table 7-4: Minimum frame section for both beam and column

Floors	Beam	Column
3	IPE180O	HE200M
9	IPE240	HE220M
15	IPE240O	HE240M
21	IPE270	HE240M
27	IPE270O	HE280M

7.2.4.1 Comparison of Displacement and Self-weight by Floor

By floors basis, it is noticeable that both the Eqx and RS for the larger section have at least twice the displacement performance than the smaller section, as shown in Figure 7-14 and Figure 7-15. Clearly, both sections have significant improvement over the base model as the weight increment is small. Without question, the larger section inevitably has a larger weight than the smaller section, as shown in Figure 7-16. Nevertheless, the smaller section is better than the larger section because the larger requires 2.5x to 3.5x more weight to achieve that level of displacement performance. It should be noted that towards the higher storey level (21 storeys and above), the RS load experience lower displacements than the Eqx load.

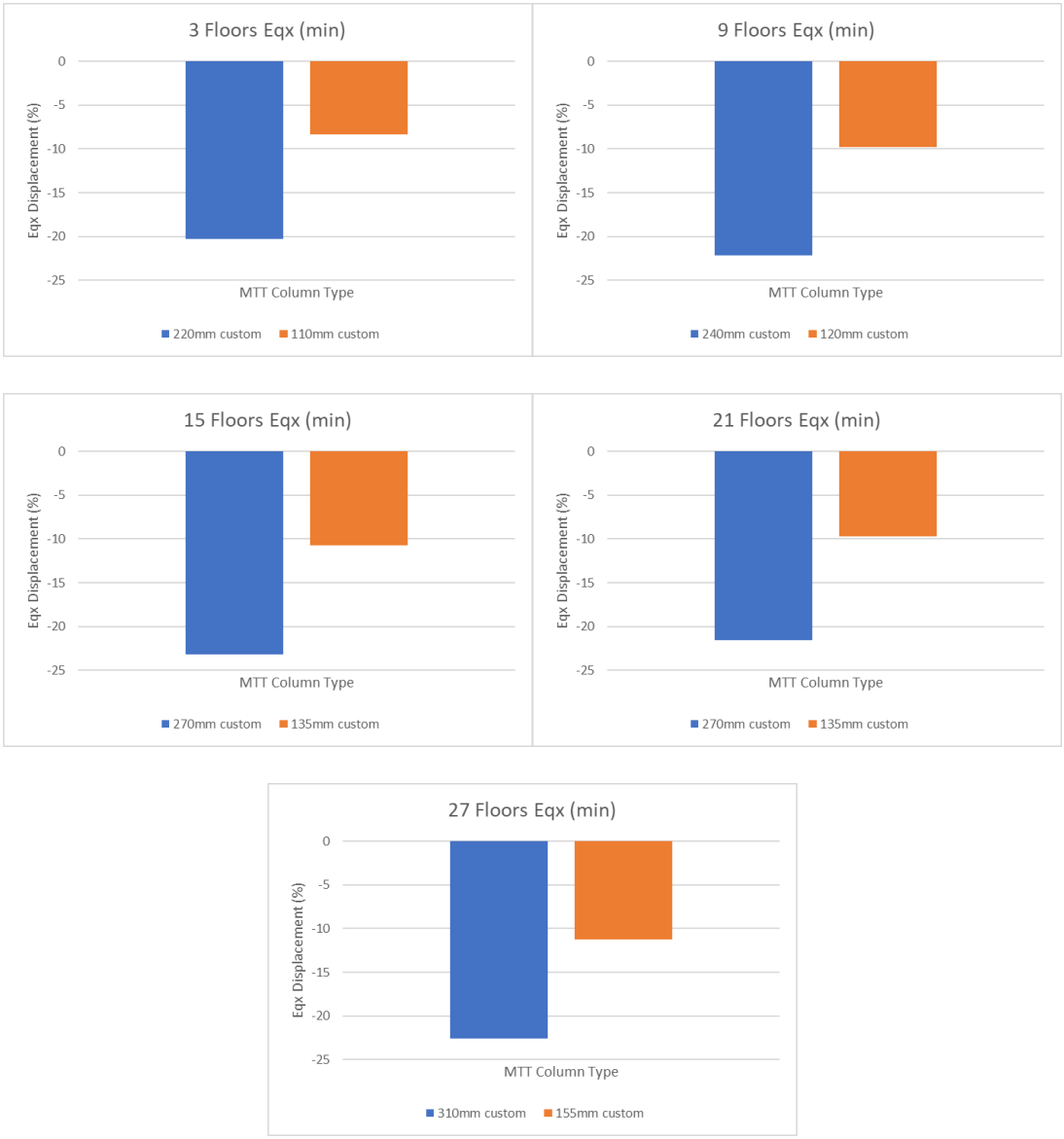


Figure 7-14: Eqx Displacement of MTT Column Min Capacity in Beam and Column By Floor

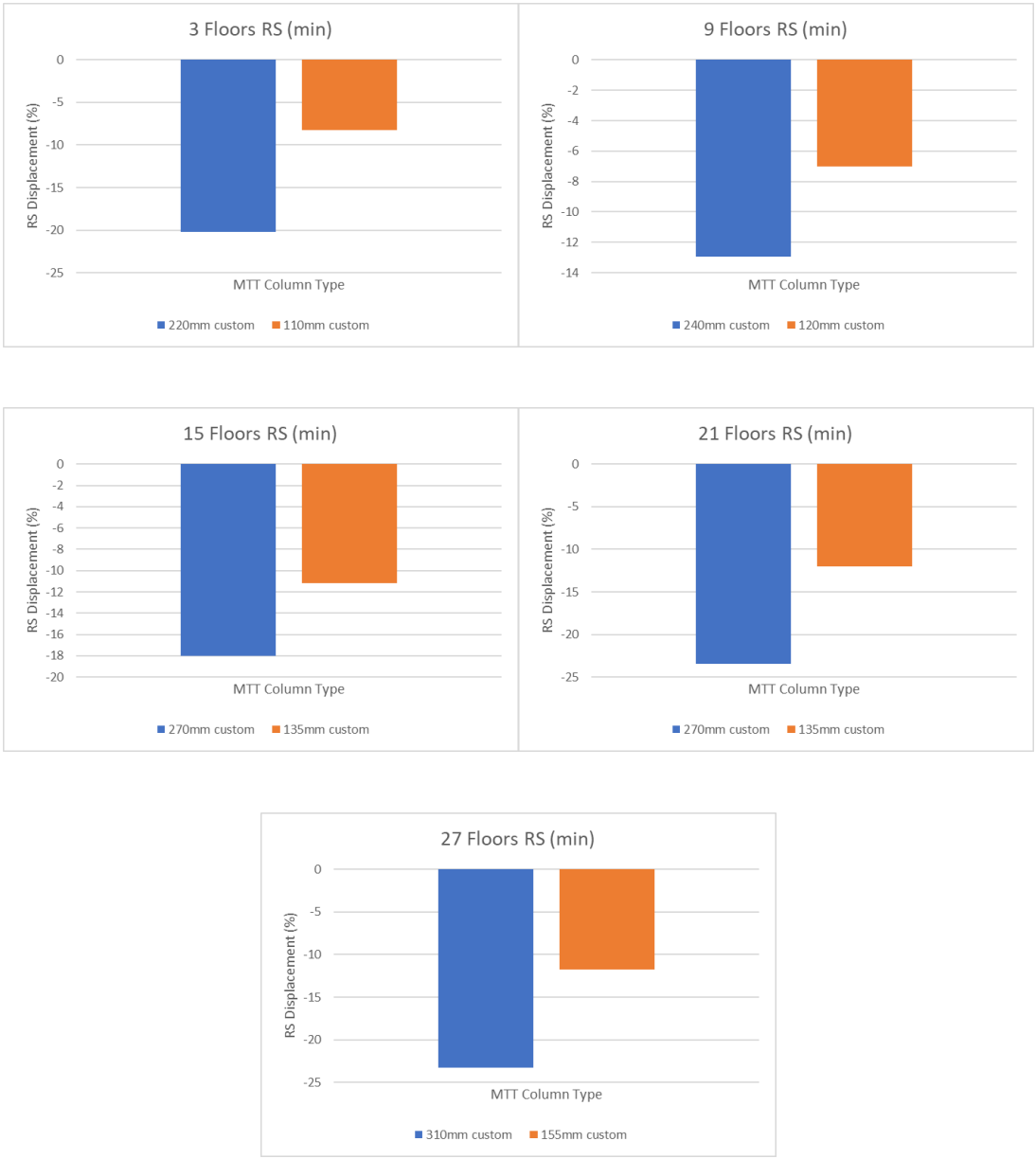


Figure 7-15: RS Displacement of MTT Column Min Capacity in Beam and Column By Floor

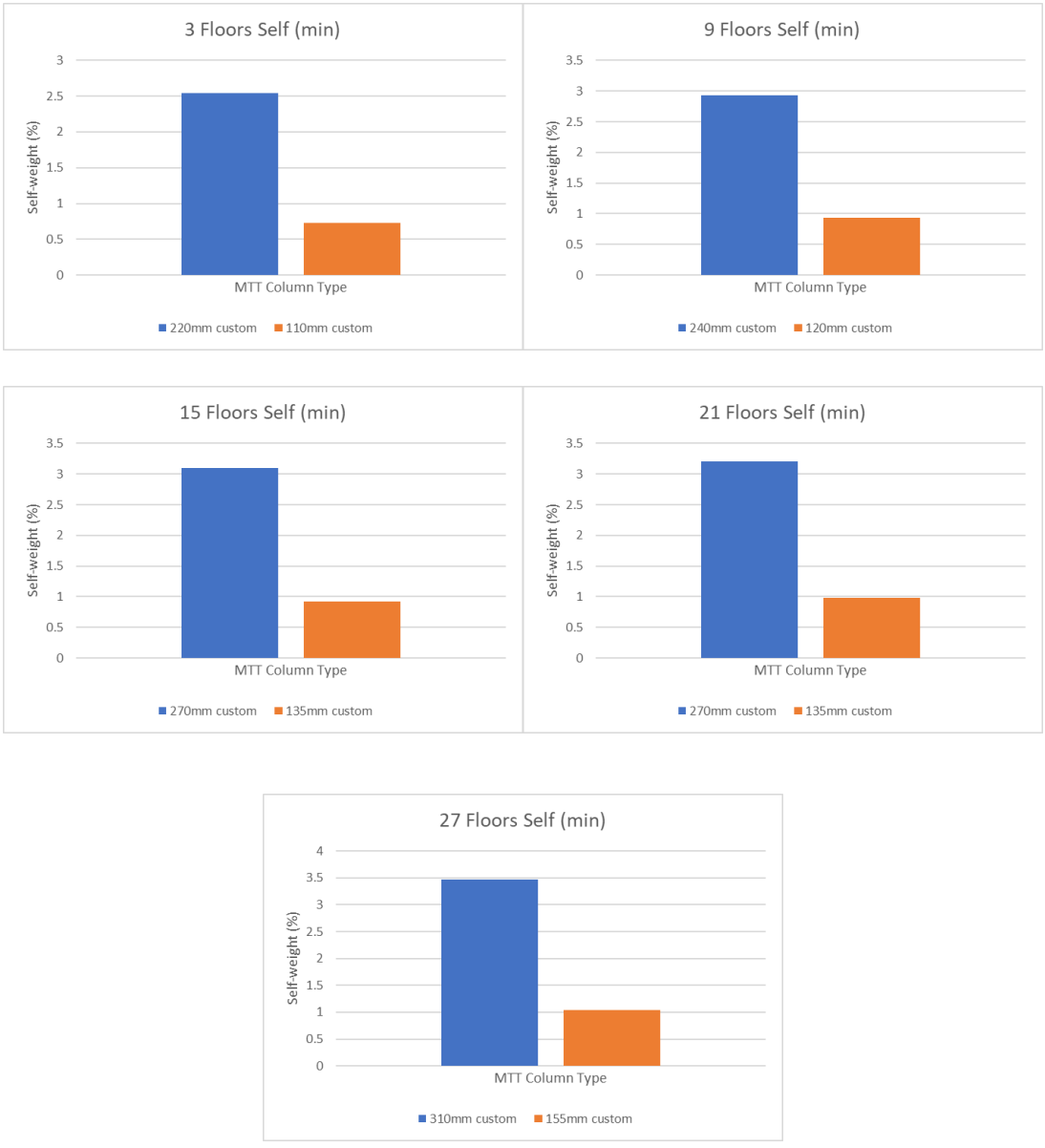


Figure 7-16: Self-Weight of MTT Column Min Capacity in Beam and Column By Floor

7.2.4.2 Comparison of Displacement and Self-weight across the Storey Heights

As shown in Figure 7-19, the results show a linear increase in structural weight as the number of floors increases. This is expected; however, its performance differs between the two section sizes. Across the storey heights, it can be seen in Figure 7-17 and Figure 7-18 that the MTT column performance enhancement is inconsistent. However, if the storey heights considered is between 3 to 15 storeys, it can be seen that the

displacement resistance is increasing linearly across the storey heights in both sizes of the sections for the Eqx load. Nevertheless, the displacement resistance under RS loading paints a slightly different pattern. It can be seen that the displacement towards the higher storey heights of 21 storeys and above have somewhat reached a limit where there are no more further improvements. This suggests that the enhancement in displacement resistance of MTT columns are indeed local and not global. However, it should be noted that the local enhancement cumulatively contributes to the global structure.

Generally, the MTT column for the larger section can expect at least 20% lesser displacement, while for the smaller section, at least 8% lesser displacement under Eqx loading condition. However, it can achieve a maximum displacement resistance of 23% for the larger section and 12% for the smaller section. In addition, the smaller section shows better performance per weight as the weight can be up to 3.5x lesser than the large section.

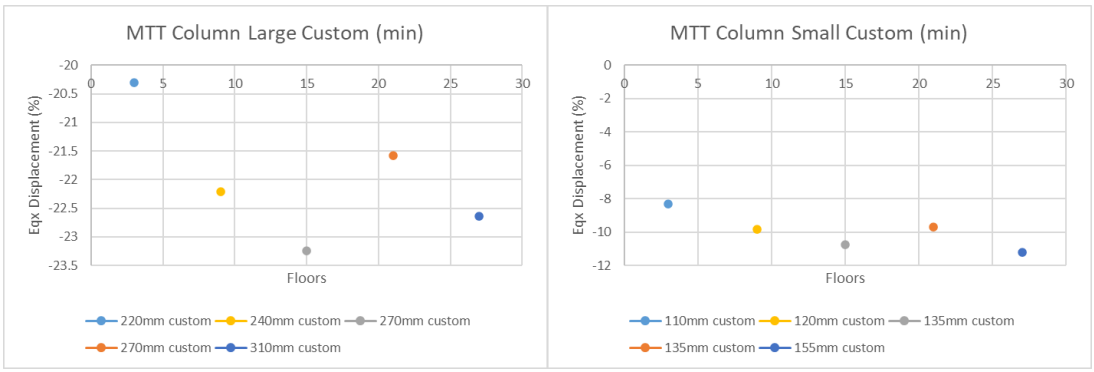


Figure 7-17: Eqx Displacement of MTT Column Min Capacity in Beam and Column across Storey Height

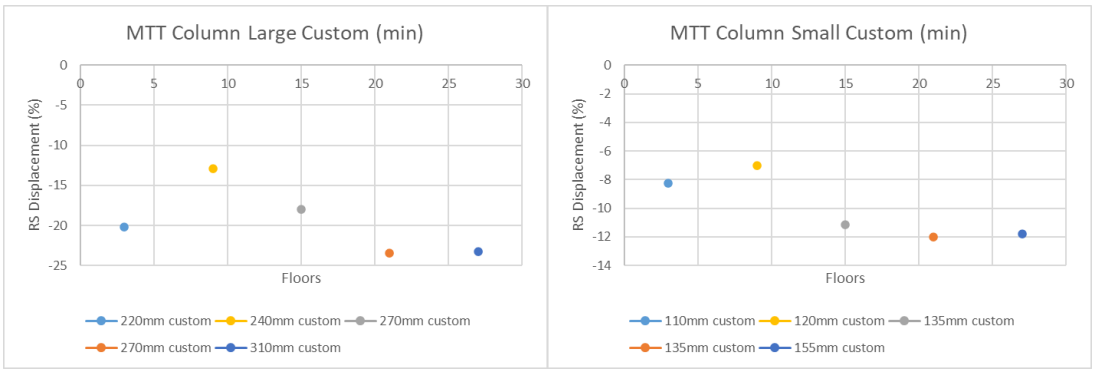


Figure 7-18: RS Displacement of MTT Column Min Capacity in Beam and Column across Storey Height

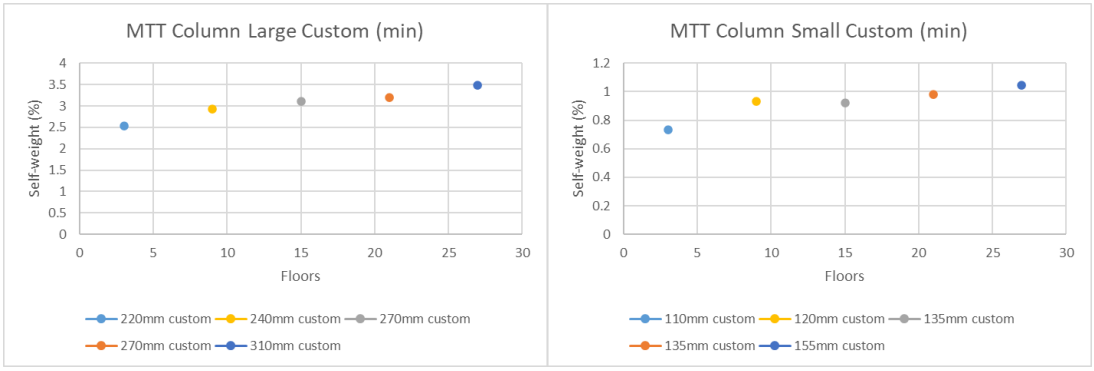


Figure 7-19: Self-Weight of MTT Column Min Capacity in Beam and Column across Storey Height

7.3 Discussion

The analysis of this study covers a wide range of multistorey buildings from low rise (<5 storeys) to high rise buildings (10<generally<40 storeys). The study does not include skyscrapers or super-slender buildings due to the known drift limitation in moment-resisting frames. In general, the IBC code considers the maximum drift of the building to be within 0.01 - 0.02 of the building's total height.

All three studies show the benefit of introducing nature's design in the column design of the multistorey. The MTT columns show improved displacement resistance for a minimal increase in weight. The localised enhancement provided by the MTT

Columns on each floor contributes to improving the overall structure. The smaller section is shown to provide better displacement per weight than the larger section. The larger sections no doubt have better displacement resistance than the smaller sections, but a more prominent trendline is seen in the smaller sections to be able to provide further displacement resistance beyond 27 floors.

The displacement resistance and the total self-weight for the non-customised section are at times better than its customised counterpart and vice versa. Hence, better displacement and further weight reduction may be achieved if specialised design sections are introduced into the structure. However, it should be noted that the weight reduction in the non-customised sections is not a direct or a practical benefit as it will lead to breakages between the connected steel section due to their non-continuous section. Other problems include the practicality of welding different steel sections together as one unit that will never meet practical design considerations. However, it still shows the possibility of creating a better structure through shapes.

Although the study in the reduction is beam section generally did not show a better structure across most of the floors studied, the highest storey height showed better displacement resistance of about 2% – 5% and a weight reduction of about 0.1% to 2%. This again suggests that closer planning into the development of the steel section of the MTT column can contribute towards a better structure.

The study of minimising the capacity of beams and columns shows a more consistent displacement resistance pattern and has a similar reason as the previous two studies. It is no doubt that the shape of the column as its connections or joints does play a vital role in providing better stability towards the overall structure. Hence, the idea of retrofitting the design in existing structures to improve structural performance may be

possible. The amount of increased weight with regards to its displacement resistance in the MTT columns shows that a more optimised structure is achievable. The study also confirms that the MTT projection should be small to provide the highest displacement resistance to weight ratio output.

7.4 Summary

The introduction of nature's design in column design using the Method of Tensile Triangles shape profile can provide better overall displacement resistance while requiring minimal increased weight. In addition, a customised steel section may further enhance the structural performance of the MTT columns.

Chapter 8 Conclusion and Recommendations for Future Works

The research intends to investigate the applicability of nature's design in steel structures to enhance structural performance under transverse loading. A set of finite element model simulation is performed to meet the aim and objectives of this research. The analysis software is validated against research paper, textbook, guidance example, or MATLAB coding.

8.1 Conclusions

The thesis began by looking into how engineers can improve current design structures and to what and why replicating nature's design can improve the current design. The literature review has shown how replicating nature's design can improve mechanical component and their applicability in civil engineering structures. The literature study found that the connections/joints in structures may be a good start for applying nature's design to improve structural performance. It was concluded that the MTT shape profile is a better choice of replication due to its simplicity and possible improvement in structural design.

The findings obtained in the literature review, the study investigates the effectiveness of replicating MTT shape profile in structures through cantilever structure (e.g. cantilever beams). The study compares various geometries and sizes through a parametric study to identify the cantilever beam's behaviour. The study was extended into the different aspect ratio and load faces to identify its behaviour in those aspects. Both studies found that the MTT triangular projection performs best only if the triangular projection is small.

The topology study was then conducted to identify the cantilever's load path analysed earlier to understand why the MTT projections perform better when it is small. The study found that the load path does not run through the larger MTT projections, rendering it less effective towards resisting transverse loading in the single point load test. The research is extended to identifying the practicality of replicating such topologies in truss designs, and it was found that the topologies require some modification to ensure the truss structure is stable. Nevertheless, the results show that it is possible to design a better truss design with the appropriate modification. Hence, the topologies obtained can serve as a guide towards designing a better truss structure. Finally, the study investigates the MTT projections' behaviour through a moment-framed structure as an integrated system. The study looks into replicating its design in the column connections/joints of the multistorey structure. It was found that for both analysis under the equivalent lateral force method and the response spectrum, the multistorey achieves better lateral resistance through the introduction of a better connections/joints system. Through all the studies performed, the MTT shape profile or replicating nature’s shape profile in steel structures can lead to better structural design.

A list of summarised conclusion:

1. The MTT triangular projection provides better structural performance when the projection considered is small. As a result, it can lead to lower displacements as well as higher material savings compared to the other geometries.
2. The MTT triangular projection is best utilised or more effective with cantilever beams of sufficient depth. The topologies obtained shows the reason why the

MTT projection is only effective when the projection considered is small. It can also serve as a guide for future design in trusses.

3. The introduction of the MTT projection in the multistorey structure columns resulted in a better structure, enhancing lateral resistance performance for a minimal increase to the overall weight.

8.2 Recommendations for Future Works

More studies and laboratory experiments are still required to have a deeper understanding, validate the numerical model, and identify possible implications from applying the shape profile in civil engineering structures. Hence, the following aspects may be considered for further research:

- An extension of the cantilever beam study may include other material, e.g. concrete and other composites.
- An extension of the topology optimisation of the cantilever beams study may include dynamic analysis.
- The truss analysis study could be extended into the retrofitting of the truss designs in existing structures.
- The extended study in multistorey can range to a whole multitude of research studies (e.g. different frame system, construction material, joint systems, geometry, retrofitting, interaction with non-structural elements, plastic zones)
- The extension could include different types of structures, (e.g. counterforts, water dam, open channels)
- Experimental validation should be conducted to validate all the numerical models conducted in this thesis.

References

ACI Committee 445 (1998) 'Recent Approaches to Shear design of Structural Concrete', *Journal of Structural Engineering*, 124(12), pp. 1374–1417. Available at: http://www.xiaonianduan.com/media/ACI445R_99.pdf.

de Albuquerque Simões, D., de Castro, J. T. P. and Meggiolaro, M. A. (2011) 'On the improved notch shape', in *21st Brazilian Congress of Mechanical Engineering*. Natal, RN, Brazil. Available at: http://meggi.usuarios.rdc.puc-rio.br/paper/C141_COBEM11_On_the_improved_notch_shape.pdf.

de Albuquerque Simões, D., de Castro, J. T. P. and Meggiolaro, M. A. (2012) 'Improved Fatigue Test Specimens With Minimum', in *67th ABM International Congress*. Rio de 2 Janeiro, RJ, Brazil, pp. 1911–1923. Available at: http://meggi.usuarios.rdc.puc-rio.br/paper/C148_ABM12_Improved_fatigue_test_specimens.pdf.

Alexander, R. M. (1971) *Size and shape*. London: Edward Arnold.

Allahdadian, S. and Boroomand, B. (2016) 'Topology optimization of planar frames under seismic loads induced by actual and artificial earthquake records', *Engineering Structures*. Elsevier, 115, pp. 140–154. doi: 10.1016/J.ENGSTRUCT.2016.02.022.

Allahdadian, S., Boroomand, B. and Barekatein, A. R. (2012) 'Towards optimal design of bracing system of multi-story structures under harmonic base excitation through a topology optimization scheme', *Finite Elements in Analysis and Design*. Elsevier, 61, pp. 60–74. doi: 10.1016/J.FINEL.2012.06.010.

Almeida, V. S., Simonetti, H. L. and Neto, L. O. (2013) 'Comparative analysis of strut-and-tie models using Smooth Evolutionary Structural Optimization', *Engineering Structures*. Elsevier, 56, pp. 1665–1675. doi: 10.1016/J.ENGSTRUCT.2013.07.007.

Amir, O. (2013) 'A topology optimization procedure for reinforced concrete structures', *Computers & Structures*. Pergamon, 114–115, pp. 46–58. doi: 10.1016/J.COMPSTRUC.2012.10.011.

Amir, O. and Sigmund, O. (2013) 'Reinforcement layout design for concrete structures based on continuum damage and truss topology optimization', *Structural and Multidisciplinary Optimization*. Springer-Verlag, 47(2), pp. 157–174. doi: 10.1007/s00158-012-0817-1.

Astaneh-Asl, A. (1997) *Seismic design of steel column-tree moment-resisting frames*. Structural Steel Educational Council. Available at: https://www.academia.edu/31079963/Seismic_Design_of_Steel_Column-Tree_Moment-Resisting_Frames.

Astaneh-Asl, A. (1999) 'Seismic Performance and Design of Bolted Steel Moment-Resisting Frames', *Engineering Journal*, 36, pp. 105–120. Available at: https://www.aisc.org/Seismic-Performance-and-Design-of-Bolted-Steel-Moment-

Resisting-Frames (Accessed: 14 September 2020).

Bar-cohen, Y. (2012) *Biomimetics: Nature-based Innovation*. CRC Press. Available at: https://books.google.com/books?id=hafMBQAAQBAJ&pgis=1 (Accessed: 16 July 2016).

Baud, R. V. (1934) 'Fillet profiles for constant stress', *Product Engineering*, 5(4), pp. 133–134.

Beghini, L. L., Beghini, A., Katz, N., Baker, W. F. and Paulino, G. H. (2014) 'Connecting architecture and engineering through structural topology optimization', *Engineering Structures*. Elsevier, 59, pp. 716–726. doi: 10.1016/J.ENGSTRUCT.2013.10.032.

Bendsøe, M. P. and Sigmund, O. (Ole) (2004) *Topology optimization : theory, methods, and applications*. second. Springer-Verlag Berlin Heidelberg. doi: 10.1007/978-3-662-05086-6.

Bogomolny, M. and Amir, O. (2012) 'Conceptual design of reinforced concrete structures using topology optimization with elastoplastic material modeling', *International Journal for Numerical Methods in Engineering*. John Wiley & Sons, Ltd, 90(13), pp. 1578–1597. doi: 10.1002/nme.4253.

Bone Clones Inc. (2016) *Set of 10 Cat Claws in Riker Box - Bone Clones, Inc. - Osteological Reproductions*. Available at: https://boneclones.com/product/set-of-10-cat-claws-in-riker-box-KO-100-CATS/category/zoology-claws-talons-spines/zoology (Accessed: 12 May 2016).

BRANZ's Seismic Resilience (2020) *Steel structures*. Available at: http://www.seismicresilience.org.nz (Accessed: 14 September 2020).

Bruggi, M. (2009) 'Generating strut-and-tie patterns for reinforced concrete structures using topology optimization', *Computers & Structures*. Pergamon, 87(23–24), pp. 1483–1495. doi: 10.1016/J.COMPSTRUC.2009.06.003.

Bruggi, M. (2016) 'A numerical method to generate optimal load paths in plain and reinforced concrete structures', *Computers & Structures*. Pergamon, 170, pp. 26–36. doi: 10.1016/J.COMPSTRUC.2016.03.012.

Bruggi, M. and Taliercio, A. (2013) 'Topology optimization of the fiber-reinforcement retrofitting existing structures', *International Journal of Solids and Structures*, 50(1), pp. 121–136. doi: https://doi.org/10.1016/j.ijsolstr.2012.09.009.

Buchanan, A. H., Bull, D., Dhakal, R., MacRae, G., Palermo, A. and Pampanin, S. (2011) *Base Isolation and Damage-Resistant Technologies for Improved Seismic Performance of Buildings*.

Carpi, A. and Brebbia, C. A. (2010) *Design & nature V: comparing design in nature with science and engineering*. WIT Press. Available at: http://books.google.com/books?id=9hOaEMFchvMC&pgis=1 (Accessed: 20 July 2016).

Chapman, C. a., Kaufman, L. and Chapman, L. J. (1998) 'Buttress formation and directional stress experienced during critical phases of tree development', *Journal of*

Tropical Ecology, 14(3), pp. 341–349. doi: 10.1017/S0266467498000261.

Chen, C.-C. and Lin, C.-C. (2013) 'Seismic performance of steel beam-to-column moment connections with tapered beam flanges', *Engineering Structures*, 48, pp. 588–601. doi: https://doi.org/10.1016/j.engstruct.2012.10.003.

Chen, C.-C., Lin, C.-C. and Lin, C.-H. (2006) 'Ductile moment connections used in steel column-tree moment-resisting frames', *Journal of Constructional Steel Research*, 62(8), pp. 793–801. doi: https://doi.org/10.1016/j.jcsr.2005.11.012.

Chen, H., Yi, W.-J. and Hwang, H.-J. (2018) 'Cracking strut-and-tie model for shear strength evaluation of reinforced concrete deep beams', *Engineering Structures*. Elsevier, 163, pp. 396–408. doi: 10.1016/J.ENGSTRUCT.2018.02.077.

Chen, W., Tong, L. and Liu, S. (2017) 'Concurrent topology design of structure and material using a two-scale topology optimization', *Computers & Structures*. Pergamon, 178, pp. 119–128. doi: 10.1016/J.COMPSTRUC.2016.10.013.

Christensen, P. W. and Klarbring, A. (2009) *An Introduction to Structural Optimization*, *An Introduction to Structural Optimization*. Dordrecht: Springer Netherlands. doi: 10.1007/978-1-4020-8666-3.

Christiansen, A. N., Bærentzen, J. A., Nobel-Jørgensen, M., Aage, N. and Sigmund, O. (2015) 'Combined shape and topology optimization of 3D structures', *Computers & Graphics*. Pergamon, 46, pp. 25–35. doi: 10.1016/J.CAG.2014.09.021.

Chu, D. N., Xie, Y. M., Hira, A. and Steven, G. P. (1996) 'Evolutionary structural optimization for problems with stiffness constraints', *Finite Elements in Analysis and Design*, 21(4), pp. 239–251. doi: 10.1016/0168-874X(95)00043-S.

Ciomber, I. and Jakel, R. (2014) *Systematic Analysis and Comparison of Stress Minimizing Notch Shapes: Obtaining a stress concentration factor of Kt=1 without FEM-Code*. Available at: http://nbn-resolving.de/urn:nbn:de:bsz:ch1-qucosa-140513 (Accessed: 16 July 2016).

Coutts, M. P. (1983) 'Root architecture and tree stability', *Plant and Soil*, 71(1–3), pp. 171–188. doi: 10.1007/BF02182653.

Coutts, M. P. (1986) 'Components of tree stability in sitka spruce on peaty gley soil', *Forestry*, 59(2), pp. 173–197. doi: 10.1093/forestry/59.2.173.

Crook, M. J., Ennos, a R. and Banks, J. R. (1997) 'The function of buttress roots: a comparative study of the anchorage systems of buttressed (Aglaia and Nephelium ramboutan species) and non-buttressed (Mallotus wrayi) tropical trees', *Journal of Experimental Botany*, 48(314), pp. 1703–1716. doi: 10.1093/jxb/48.9.1703.

Desnerck, P., Lees, J. M. and Morley, C. T. (2018) 'Strut-and-tie models for deteriorated reinforced concrete half-joints', *Engineering Structures*. Elsevier, 161, pp. 41–54. doi: 10.1016/J.ENGSTRUCT.2018.01.013.

DOMBERNOWSKY, P. and SØNDERGAARD, A. (2009) 'Three-dimensional topology optimisation in architectural and structural design of concrete structures', in *Proceedings of the International Association for Shell and Spatial Structures (IASS) Symposium*, p. 11. Available at: http://fluxstructures.net/_artikler/artikel_iass.pdf.

Eichenberger, R., Monti, E., Kiser, A., Burkert, R. and Damm, B. (2011) ‘Connection 41’, *Reichle & De-Massari AG*, September, p. 48. Available at: http://www.fibernet.si/f/docs/Literatura/Customer_Magazine_Connections_41.pdf.

ElDin, N. N., Abdou, A. and ElGawad, I. A. (2016) ‘Biomimetic Potentials for Building Envelope Adaptation in Egypt’, *Procedia Environmental Sciences*. Elsevier, 34, pp. 375–386. doi: 10.1016/J.PROENV.2016.04.033.

Elghazouli, A. (2009) *Seismic Design of Buildings to Eurocode 8*. London: Taylor & Francis Ltd.

Elghazouli, A. Y. (2015) ‘Seismic code developments for steel and composite structures’, *Geotechnical, Geological and Earthquake Engineering*. Kluwer Academic Publishers, 39, pp. 129–151. doi: 10.1007/978-3-319-16964-4_5.

Encyclopedia of Earthquake Engineering (2015) *Encyclopedia of Earthquake Engineering*. Springer Berlin Heidelberg. doi: 10.1007/978-3-642-35344-4.

G. MacRae, C. C. (2013) ‘Low Damage Design of Steel Structures’, in *Steel Innovations 2013 Workshop*. Available at: https://www.scnz.org/site/scnz/images/Documents/Steel Innovations 2013/Low Damage Design of Steel Structures_MacRae_Clifton.pdf.

Gaudi, A. (2014) *The Nature of Gaudi*, *Technical Nature*. Available at: https://technicalnature.org.uk/2014/10/the-nature-of-gaudi/ (Accessed: 30 August 2020).

Gordon, J. E. (1978) *Structures or Why things don’t fall down*. Boston, MA: Springer US. doi: 10.1007/978-1-4615-9074-3.

Graham, R. (2007) ‘Assessment of hazardous trees’, *New Zealand Garden Journal*, 10(1), pp. 2–5. Available at: https://www.researchgate.net/publication/242613085_Assessment_of_hazardous_trees (Accessed: 16 July 2016).

Guillemin, G., Patat, J. L. L., Fournie, J. and Chetail, M. (1987) ‘The use of coral as a bone graft substitute’, *Journal of biomedical materials research*. John Wiley & Sons, Inc., 21(5), pp. 557–567. doi: 10.1007/BF00178755.

Hakim (2015) *Colosseum Rome, Italy | Vacationio.com*. Available at: http://vacationio.com/colosseum-rome-italy/ (Accessed: 7 May 2016).

Hanoon, A. N., Jaafar, M. S., Al Zaidee, S. R., Hejazi, F. and Aziz, F. N. A. A. (2017) ‘Effectiveness factor of the strut-and-tie model for reinforced concrete deep beams strengthened with CFRP sheet’, *Journal of Building Engineering*. Elsevier, 12, pp. 8–16. doi: 10.1016/J.JOBE.2017.05.001.

Hardjasaputra, H. (2015) ‘Evolutionary Structural Optimization as Tool in Finding Strut-and-tie-models for Designing Reinforced Concrete Deep Beam’, *Procedia Engineering*. Elsevier, 125, pp. 995–1000. doi: 10.1016/J.PROENG.2015.11.153.

Hutchinson, J. W. and Suo, Z. (1992) ‘Mixed Mode Cracking in Layered Materials’, *Advances in Applied Mechanics*. Elsevier, 29(C), pp. 63–191. doi: 10.1016/S0065-2156(08)70164-9.

Jones, S. L., Fry, G. T. and Engelhardt, M. D. (2002) ‘Experimental Evaluation of Cyclically Loaded Reduced Beam Section Moment Connections’, *Journal of Structural Engineering*. American Society of Civil Engineers, 128(4), pp. 441–451. doi: 10.1061/(ASCE)0733-9445(2002)128:4(441).

Kazakis, G., Kanellopoulos, I., Sotiropoulos, S. and Lagaros, N. D. (2017) ‘Topology optimization aided structural design: Interpretation, computational aspects and 3D printing’, *Heliyon*. Elsevier, 3(10), p. e00431. doi: 10.1016/J.HELIYON.2017.E00431.

Khennane, A. (2013) *Introduction to Finite Element Analysis Using MATLAB® and Abaqus*. 1st edn, *CRC Press*. 1st edn. CRC Press. doi: 10.1201/b15042.

Kim, D.-J., Lee, J. and Lee, Y. H. (2014) ‘Effectiveness factor of strut-and-tie model for concrete deep beams reinforced with FRP rebars’, *Composites Part B: Engineering*. Elsevier, 56, pp. 117–125. doi: 10.1016/J.COMPOSITESB.2013.08.009.

Kim, T. and Yu, E. (2019) ‘Seismic analysis of steel moment frames with column-tree connections (In Press)’, *Journal of Constructional Steel Research*. Elsevier Ltd. doi: 10.1016/j.jcsr.2019.105871.

Komarla, N. (2011) *Optimization of Shoulder Fillet Specimen Using Catia V5*. Available at: http://mbi-wiki.uni-wuppertal.de/wp-content/uploads/2011/12/Optimization-of-a-shoulder-fillet-specimen-using-CATIA-V5.pdf.

Kong, F. K. and Sharp, G. R. (1977) ‘Structural Idealization for Deep Beams With Web Openings’, *Magazine of Concrete Research*. THOMAS TELFORD HOUSE, 1 HERON QUAY, LONDON, ENGLAND E14 4JD: THOMAS TELFORD SERVICES LTD, 29(99), pp. 81–91.

Lee, C. H. and Park, J. W. (1998) ‘Cyclic Seismic Testing of Full-Scale Column-Tree Type Steel Moment Connections’, *Journal of Korean Society of Steel Construction*, 10(4), pp. 629–639. Available at: https://www.koreascience.or.kr/article/JAKO199810102454051.page.

Lee, D.-K., Yang, C.-J. and Starossek, U. (2012) ‘Topology design of optimizing material arrangements of beam-to-column connection frames with maximal stiffness’, *Scientia Iranica*. No longer published by Elsevier, 19(4), pp. 1025–1032. doi: 10.1016/J.SCIENT.2012.06.004.

Lee, K., Li, R., Chen, L., Oh, K. and Kim, K.-S. (2014) ‘Cyclic testing of steel column-tree moment connections with various beam splice lengths’, *Steel and Composite Structures*, 16. doi: 10.12989/scs.2014.16.2.221.

Lee, S.-W., Mao, C., Flynn, C. E. and Belcher, A. M. (2002) ‘Ordering of Quantum Dots Using Genetically Engineered Viruses’, *Science*, 296(5569), pp. 892–895. doi: 10.1126/science.1068054.

Lee, S. W., Lee, S. K. and Belcher, A. M. (2003) ‘Virus-based alignment of inorganic, organic, and biological nanosized materials’, *Advanced Materials*, 15(9), pp. 689–692. doi: 10.1002/adma.200304818.

Li, H., Luo, Z., Gao, L. and Qin, Q. (2018) ‘Topology optimization for concurrent

design of structures with multi-patch microstructures by level sets', *Computer Methods in Applied Mechanics and Engineering*. North-Holland, 331, pp. 536–561. doi: 10.1016/J.CMA.2017.11.033.

Lian, H., Christiansen, A. N., Tortorelli, D. A., Sigmund, O. and Aage, N. (2017) 'Combined shape and topology optimization for minimization of maximal von Mises stress', *Structural and Multidisciplinary Optimization*. Springer Berlin Heidelberg, 55(5), pp. 1541–1557. doi: 10.1007/s00158-017-1656-x.

Liang, Q. Q. (2007) 'Effects of continuum design domains on optimal bracing systems for multistory steel building frameworks', in *5th Australasian Congress Applied Mechanics*. Australia. Available at: http://espace.uq.edu.au/eserv/UQ:132198/P2.10.pdf.

Liang, Q. Q., Xie, Y. M. and Steven, G. P. (1999) 'OPTIMAL TOPOLOGY SELECTION OF CONTINUUM STRUCTURES WITH STRESS AND DISPLACEMENT CONSTRAINTS', in *The Seventh East Asia-pacific Conference on Structural Engineering & Construction*. Kochi, Japan, pp. 560–565. Available at: https://core.ac.uk/download/files/333/11036976.pdf.

Liang, Q. Q., Xie, Yi Min and Steven, G. P. (2000a) 'Optimal Topology Design of Bracing Systems for Multistory Steel Frames', *Journal of Structural Engineering*, 126(7), pp. 823–829. doi: 10.1061/(ASCE)0733-9445(2000)126:7(823).

Liang, Q. Q., Xie, Y. M. and Steven, G. P. (2000) 'Optimal topology selection of continuum structures with displacement constraints', *Computers and Structures*, 77(6), pp. 635–644. doi: 10.1016/S0045-7949(00)00018-3.

Liang, Q. Q., Xie, Yi Min and Steven, G. P. (2000b) 'Topology optimization of strut-and-tie models in reinforced concrete structures using an evolutionary procedure', *ACI Structural Journal*, 97(2), pp. 322–330. doi: 10.14359/863.

Liberato, R. (2006) *All Giza Pyramids in one shot*. Available at: https://en.wikipedia.org/wiki/Giza_pyramid_complex (Accessed: 7 May 2016).

Lim, E. and Hwang, S.-J. (2016) 'Modeling of the strut-and-tie parameters of deep beams for shear strength prediction', *Engineering Structures*. Elsevier, 108, pp. 104–112. doi: 10.1016/J.ENGSTRUCT.2015.11.024.

Luo, Y., Wang, M. Y., Zhou, M. and Deng, Z. (2015) 'Topology optimization of reinforced concrete structures considering control of shrinkage and strength failure', *Computers & Structures*. Pergamon, 157, pp. 31–41. doi: 10.1016/J.COMPSTRUC.2015.05.009.

Madsen, S., Lange, N. P., Giuliani, L., Jomaas, G., Lazarov, B. S. and Sigmund, O. (2016) 'Topology optimization for simplified structural fire safety', *Engineering Structures*. Elsevier, 124, pp. 333–343. doi: 10.1016/J.ENGSTRUCT.2016.06.018.

Mahin, S. A. (1998) 'Lessons from damage to steel buildings during the Northridge earthquake', *Engineering Structures*. Elsevier Ltd, 20(4), pp. 261–270. doi: 10.1016/S0141-0296(97)00032-1.

Mattheck, C. (1990a) 'Engineering components grow like trees', *Materialwissenschaft und Werkstofftechnik*. WILEY-VCH Verlag GmbH, 21(4), pp. 143–168. doi:

10.1002/mawe.19900210403.

Mattheck, C. (1990b) ‘Why They Grow, How They Grow: the Mechanics of Trees’, *Arboricultural Journal*, 14(1), pp. 1–17. doi: 10.1080/03071375.1990.9746820.

Mattheck, C. (1991) *Trees: The Mechanical Design*. New York. Available at: https://books.google.com/books?id=lvajUuBH6kEC&pgis=1 (Accessed: 18 July 2016).

Mattheck, C. (1998) *Design in Nature, Nature*. doi: 10.1007/978-3-642-58747-4.

Mattheck, C. (2004) *The Face of Failure in Nature and Engineering*. Forschungszentrum Karlsruhe. Available at: https://books.google.com.my/books/about/The_Face_of_Failure_in_Nature_and_Engine.html?id=WFVHAAAACAAJ&pgis=1 (Accessed: 16 July 2016).

Mattheck, C. (2006) ‘Teacher tree: The evolution of notch shape optimization from complex to simple’, *Engineering Fracture Mechanics*, 73(12), pp. 1732–1742. doi: 10.1016/j.engfracmech.2006.02.007.

Mattheck, C. (2007) *Secret Design Rules of Nature (Optimum Shapes without computers)*. Forschungszentrum Karlsruhe. Available at: https://books.google.com.my/books/about/Secret_Design_Rules_of_Nature.html?id=l-lFOgAACAAJ&pgis=1 (Accessed: 16 July 2016).

Mattheck, C., Bethge, K. and Schäfer, J. (1993) ‘Safety factors in trees’, *Journal of Theoretical Biology*, 165(2), pp. 185–189. doi: 10.1006/jtbi.1993.1184.

Mattheck, C., Kappel, R. and Sauer, A. (2007) ‘Shape optimization the easy way: The “method of tensile triangles”’, *International Journal of Design and Nature*. WIT Press, 2(4), pp. 301–309. doi: 10.2495/JDN-V2-N4-301-309.

Mattheck, C. and Reuss, S. (1991) ‘The claw of the tiger: An assessment of its mechanical shape optimization’, *Journal of Theoretical Biology*, 150(3), pp. 323–328. doi: 10.1016/S0022-5193(05)80431-X.

Mattheck, C., Wissner, C., Tesari, I. and Bethge, K. (2010) ‘Easing cracks with the method of tensile triangles’, in *WIT Transactions on Ecology and the Environment*, pp. 461–467. doi: 10.2495/DN100411.

Mazurek, A., Baker, W. F. and Tort, C. (2011) ‘Geometrical aspects of optimum truss like structures’, *Structural and Multidisciplinary Optimization*. Springer-Verlag, 43(2), pp. 231–242. doi: 10.1007/s00158-010-0559-x.

McMullin, K. M. and Astaneh-Asl, A. (2003) ‘Steel semirigid column-tree moment resisting frame seismic behavior’, *Journal of Structural Engineering*, 129(9), pp. 1243–1249. doi: 10.1061/(ASCE)0733-9445(2003)129:9(1243).

Mehedi, M. A. H. M., Kundu, C. and Chowdhury, Q. (2012) ‘Patterns of tree buttressing at Lawachara National Park, Bangladesh’, *Journal of Forestry Research*, 23(3), pp. 461–466. doi: 10.1007/s11676-012-0285-x.

Miller, D. K. (1998) ‘Lessons learned from the Northridge earthquake’, *Engineering structures*. Elsevier BV, 20(4–6), pp. 249–260. doi: 10.1016/s0141-0296(97)00031-x.

Moradi, M. and Esfahani, M. R. (2017) ‘Application of the strut-and-tie method for steel fiber reinforced concrete deep beams’, *Construction and Building Materials*. Elsevier, 131, pp. 423–437. doi: 10.1016/J.CONBUILDMAT.2016.11.042.

Nakashima, M., Inoue, K. and Tada, M. (1998) ‘Classification of damage to steel buildings observed in the 1995 Hyogoken-Nanbu earthquake’, *Engineering structures*. Elsevier BV, 20(4–6), pp. 271–281. doi: 10.1016/s0141-0296(97)00019-9.

Nakshatrala, P. B. and Tortorelli, D. A. (2016) ‘Nonlinear structural design using multiscale topology optimization. Part II: Transient formulation’, *Computer Methods in Applied Mechanics and Engineering*. North-Holland, 304, pp. 605–618. doi: 10.1016/J.CMA.2016.01.003.

Nakshatrala, P. B., Tortorelli, D. A. and Nakshatrala, K. B. (2013) ‘Nonlinear structural design using multiscale topology optimization. Part I: Static formulation’, *Computer Methods in Applied Mechanics and Engineering*. North-Holland, 261–262, pp. 167–176. doi: 10.1016/J.CMA.2012.12.018.

Navez, A. E. (1930) ‘on the Distribution of Tabular Roots in Ceiba (Bombacaceae)’, *Proceedings of the National Academy of Sciences of the United States of America*, 16(5), pp. 339–344. Available at: http://www.ncbi.nlm.nih.gov/pmc/articles/PMC526643/.

Needleman, A. and Rosakis, A. J. (1999) ‘The Effect of Bond Strength and Loading Rate on the Conditions Governing the Attainment of Intersonic Crack Growth along Interfaces’, *Journal of the Mechanics and Physics of Solids*. Pergamon, 47(12), pp. 2411–2449. doi: 10.1016/S0022-5096(99)00012-5.

Newbery, D. M., Schwan, S., Chuyong, G. B. and Van Der Burgt, X. M. (2009) ‘Buttress form of the central African rain forest tree Microberlinia bisulcata, and its possible role in nutrient acquisition’, *Trees - Structure and Function*, 23(2), pp. 219–234. doi: 10.1007/s00468-008-0270-3.

Oh, K., Lee, K., Chen, L., Hong, S.-B. and Yang, Y. (2015) ‘Seismic performance evaluation of weak axis column-tree moment connections with reduced beam section’, *Journal of Constructional Steel Research*, 105, pp. 28–38. doi: https://doi.org/10.1016/j.jcsr.2014.10.005.

Oh, K., Li, R., Chen, L., Hong, S.-B. and Lee, K. (2014) ‘Cyclic testing of steel column-tree moment connections with weakened beam splices’, *International Journal of Steel Structures*, 14(3), pp. 471–478. doi: 10.1007/s13296-014-3004-y.

Oh, K., So, J., Ha, H. and Lee, K. (2016) ‘Seismic performance evaluation of Korean column-tree steel moment connections’, *International Journal of Steel Structures*. Seoul: Korean Society of Steel Construction, 16(4), pp. 1287–1298. doi: 10.1007/s13296-016-0089-5.

Ohsaki, M., Tagawa, H. and Pan, P. (2009) ‘Shape optimization of reduced beam section under cyclic loads’, *Journal of Constructional Steel Research*, 65(7), pp. 1511–1519. doi: https://doi.org/10.1016/j.jcsr.2009.03.001.

Pachoumis, D. T., Galoussis, E. G., Kalfas, C. N. and Christitsas, A. D. (2009) ‘Reduced beam section moment connections subjected to cyclic loading: Experimental

analysis and FEM simulation', *Engineering Structures*, 31(1), pp. 216–223. doi: https://doi.org/10.1016/j.engstruct.2008.08.007.

Perera, R. and Vique, J. (2009) 'Strut-and-tie modelling of reinforced concrete beams using genetic algorithms optimization', *Construction and Building Materials*. Elsevier, 23(8), pp. 2914–2925. doi: 10.1016/J.CONBUILDMAT.2009.02.016.

Petch, T. (1930) 'Buttress Roots', *Annals of the Royal Botanic Gardens Peradeniya 11*, pp. 277–285.

Petite, H., Viateau, V., Bensaid, W., Meunier, A., de Pollak, C., Bourguignon, M., Oudina, K., Sedel, L., Guillemin, G., Bensaïd, W., Meunier, A., de Pollak, C., Bourguignon, M., Oudina, K., Sedel, L. and Guillemin, G. (2000) 'Tissue-engineered bone regeneration.', *Nature biotechnology*, 18(9), pp. 959–963. doi: Doi 10.1038/79449.

Philippe, B., Eduardo, C., Herve, D., Peter, F., Michael, F., Paolo, F., Maja, K., Alain, P., Paolo, P., Andre, P., Hughes, S., Georgios, T., Eduardo, C., Michael, F., Bora, A., Adamantia, A. and Artur, P. V. (2012) *Eurocode 8: Seismic Design of Buildings - Worked examples*. Lisbon: Publications Office of the European Union. doi: 10.2788/91658.

Pilkey, W. D., Deborah F. Pilkey, Pilkey, D. F. and Deborah F. Pilkey (2007) *Peterson's Stress Concentration Factors*. John Wiley & Sons. doi: 10.1002/9780470211106.

Prager, W. (1977) 'Optimal layout of cantilever trusses', *Journal of Optimization Theory and Applications*. Kluwer Academic Publishers-Plenum Publishers, 23(1), pp. 111–117. doi: 10.1007/BF00932301.

Prager, William (1978) 'Nearly optimal design of trusses', *Computers & Structures*. Pergamon, 8(3–4), pp. 451–454. doi: 10.1016/0045-7949(78)90190-6.

Prager, W. (1978) 'Optimal layout of trusses with finite numbers of joints†', *Journal of the Mechanics and Physics of Solids*. Pergamon, 26(4), pp. 241–250. doi: 10.1016/0022-5096(78)90019-4.

Radwan, G. A. N. and Osama, N. (2016) 'Biomimicry, an Approach, for Energy Effecient Building Skin Design', *Procedia Environmental Sciences*. Elsevier, 34, pp. 178–189. doi: 10.1016/J.PROENV.2016.04.017.

Refractories World Forum (ed.) (2011) 'Thinking Tools Modelled on Nature'. Available at: https://www.refractories-worldforum.com/images/newsletter/hot_topics_1-2011.pdf.

Richards, P. W. (1952) *The tropical rain forest. An ecological study, Cambridge Univ. Press, Cambridge, 450 pp*. Cambridge University Press. Available at: https://books.google.com.my/books/about/The_Tropical_Rain_Forest.html?id=43S-QgAACAAJ&pgis=1 (Accessed: 16 July 2016).

Richards, P. W., Walsh, R. P. D., Baillie, I. C. and Grieg-Smith, P. (1996) *The tropical rain forest: an ecological study, The tropical rain forest: an ecological study*. Available at: http://www.cambridge.org/gb/knowledge/isbn/item1141918/?site_locale=en_GB.

Richter, W. (1984) ‘A Structural Approach to the Function of Buttresses of Quararibea Asterolepis’, *Ecological Society of America*, 65(5), pp. 1429–1435. doi: 10.2307/1939123.

Ritter, K. W. (1899) ‘Die Bauweise Hennebique (The Hennebique System)’, *Schweizerische Bauzeitung*. Zurich, Switzerland: Drck Zurchet & Furrer, 33(7), pp. 59–61. Available at: https://www.e-rara.ch/doi/10.3931/e-rara-20036.

Rong, J. H., Tang, Z. L., Xie, Y. M. and Li, F. Y. (2013) ‘Topological optimization design of structures under random excitations using SQP method’, *Engineering Structures*. Elsevier, 56, pp. 2098–2106. doi: 10.1016/J.ENGSTRUCT.2013.08.012.

Schlaich, J., Schafer, K. and Jennewein, M. (1987a) ‘Toward a Consistent Design of Structural Concrete’, *PCI Journal*, 32(3), pp. 74–150. doi: 10.15554/pcij.05011987.74.150.

Schlaich, J., Schafer, K. and Jennewein, M. (1987b) ‘Toward a Consistent Design of Structural Concrete’, *PCI Journal*, 32(3), pp. 74–150. doi: 10.15554/pcij.05011987.74.150.

Schneider, S. P. and Teeraparbwong, I. (2002) ‘Inelastic Behavior of Bolted Flange Plate Connections’, *Journal of Structural Engineering*. American Society of Civil Engineers, 128(4), pp. 492–500. doi: 10.1061/(ASCE)0733-9445(2002)128:4(492).

Sidwell G. (2010) ‘“Low Damage Buildings - the Realisation’, in *Proceedings of the Steel Structures Workshop 2010*.

Sigmund, O. (2001) ‘A 99 line topology optimization code written in Matlab’, *Structural and Multidisciplinary Optimization*, 21(2), pp. 120–127. doi: 10.1007/s001580050176.

Sigmund, O. and Bendsøe, M. P. (2004) ‘Topology optimization -- from airplanes to nanooptics’, in. Kgs. Lyngby: Technical University of Denmark (DTU), pp. 40-51 BT-BRIDGING from technology to society.

SimuTechGroup (2020) *ANSYS Workbench Mechanical: Averaged vs. Unaveraged Contour Results*. Available at: https://www.simutechgroup.com/tips-and-tricks/fea-articles/93-fea-tips-tricks-pinball-contour-results (Accessed: 7 July 2020).

Stromberg, L. L., Beghini, A., Baker, W. F. and Paulino, G. H. (2011) ‘Application of layout and topology optimization using pattern gradation for the conceptual design of buildings’, *Structural and Multidisciplinary Optimization*. Springer-Verlag, 43(2), pp. 165–180. doi: 10.1007/s00158-010-0563-1.

Stromberg, L. L., Beghini, A., Baker, W. F. and Paulino, G. H. (2012) ‘Topology optimization for braced frames: Combining continuum and beam/column elements’, *Engineering Structures*. Elsevier, 37, pp. 106–124. doi: 10.1016/J.ENGSTRUCT.2011.12.034.

Suksuwan, A. and Spence, S. M. J. (2018) ‘Performance-based multi-hazard topology optimization of wind and seismically excited structural systems’, *Engineering Structures*. Elsevier, 172, pp. 573–588. doi: 10.1016/J.ENGSTRUCT.2018.06.039.

Suzuki, K. and Kikuchi, N. (1991) ‘A homogenization method for shape and topology

optimization', *Computer Methods in Applied Mechanics and Engineering*, 93(3), pp. 291–318. doi: 10.1016/0045-7825(91)90245-2.

Svanberg, K. (1987) 'The method of moving asymptotes—a new method for structural optimization', *International Journal for Numerical Methods in Engineering*. John Wiley & Sons, Ltd, 24(2), pp. 359–373. doi: 10.1002/nme.1620240207.

Swayne, S. (1978) *The Parthenon*. Available at: https://en.wikipedia.org/wiki/Acropolis_of_Athens (Accessed: 7 May 2016).

Tavsan, C., Tavsan, F. and Sonmez, E. (2015) 'Biomimicry in Architectural Design Education', *Procedia - Social and Behavioral Sciences*. Elsevier, 182, pp. 489–496. doi: 10.1016/J.SBSPRO.2015.04.832.

Thompson, D. W. (1942) *On Growth and Form*. Edited by J. T. Bonner. Cambridge: Cambridge University Press. doi: 10.1017/CBO9781107325852.

Tsavdaridis, K. D., Kingman, J. J. and Toropov, V. V. (2015) 'Application of structural topology optimisation to perforated steel beams', *Computers & Structures*. Pergamon, 158, pp. 108–123. doi: 10.1016/J.COMPSTRUC.2015.05.004.

Van der Waals and the Gecko (2014). Available at: http://www.naturphilosophie.co.uk/van-der-waals-gecko/ (Accessed: 9 May 2016).

Wahala, S., Huang, S. and Dibor, L. anak (2005) 'Buttress variation between trees growing on flat and inclined terrain', *Proceedings of the CTFS-AA International Field Biology Course 2005*, (July), pp. 49–52.

Wilson, B. F. and Archer, R. R. (1979) 'Tree Design: Some Biological Solutions to Mechanical Problems', *BioScience*, 29(5), pp. 293–298. doi: 10.2307/1307825.

Woodcock, D., Santos, G. Dos and Taylor, D. (2000) 'The Buttressed Blue Marble Tree: Wood and Growth Characteristics of Elaeocarpus angustifolius (Elaeocarpaceae)', *Annals of Botany*, 85(1), pp. 1–6. doi: 10.1006/anbo.1999.0985.

Wu, J., Gao, J., Luo, Z. and Brown, T. (2016) 'Robust topology optimization for structures under interval uncertainty', *Advances in Engineering Software*. Elsevier, 99, pp. 36–48. doi: 10.1016/J.ADVENGSOFT.2016.05.002.

Xie, Y. M. and Steven, G. P. (1993) 'A simple evolutionary procedure for structural optimization', *Computers and Structures*, 49(5), pp. 885–896. doi: 10.1016/0045-7949(93)90035-C.

Xu, L. R. (2004) 'Dissimilar Material Joints With and Without Free-edge Stress Singularities: Part I. A Biologically Inspired Design', *Experimental Mechanics*, 44(6), pp. 608–615. doi: 10.1177/0014485104049399.

Xu, L. R., Huang, Y. Y. and Rosakis, A. J. (2003) 'Dynamic Crack Deflection and Penetration at Interfaces in Homogeneous Materials: Experimental Studies and Model Predictions', *Journal of the Mechanics and Physics of Solids*. Pergamon, 51(3), pp. 461–486. doi: 10.1016/S0022-5096(02)00080-7.

Xu, L. R. and Sengupta, S. (2004) 'Dissimilar material joints with and without free-edge stress singularities: Part II. An integrated numerical analysis', *Experimental*

Mechanics. Kluwer Academic Publishers, 44(6), pp. 616–621. doi: 10.1007/BF02428251.

Yang, Y., Zhu, M., Shields, M. D. and Guest, J. K. (2017) 'Topology optimization of continuum structures subjected to filtered white noise stochastic excitations', *Computer Methods in Applied Mechanics and Engineering*. North-Holland, 324, pp. 438–456. doi: 10.1016/J.CMA.2017.06.015.

Yap, K. L., Mohammed Parvez, A., Jaganathan, J., Elleithy, W. and Lau, T. L. (2019) 'Feasibility of Replication and Optimization of Nature's Design Shapes in Civil Engineering Structures to Enhance Performance and Efficiency: A review', *International Journal of Innovative Technology and Exploring Engineering (IJITEE)*, 8(6S3), pp. 2278–3075. Available at: https://www.ijitee.org/wp-content/uploads/papers/v8i6s3/F10140486S319.pdf.

Young, T. P. and Perkocha, V. (1994) 'Treefalls, crown asymmetry, and buttresses', *Journal of Ecology*, pp. 319–324. doi: S.

Zhang, W., Liu, H. and Gao, T. (2015) 'Topology optimization of large-scale structures subjected to stationary random excitation: An efficient optimization procedure integrating pseudo excitation method and mode acceleration method', *Computers & Structures*. Pergamon, 158, pp. 61–70. doi: 10.1016/J.COMPSTRUC.2015.05.027.

Zhao, J., Yoon, H. and Youn, B. D. (2019) 'An efficient concurrent topology optimization approach for frequency response problems', *Computer Methods in Applied Mechanics and Engineering*. North-Holland, 347, pp. 700–734. doi: 10.1016/J.CMA.2019.01.004.

Zhong, J. T., Wang, L., Deng, P. and Zhou, M. (2017) 'A new evaluation procedure for the strut-and-tie models of the disturbed regions of reinforced concrete structures', *Engineering Structures*. Elsevier, 148, pp. 660–672. doi: 10.1016/J.ENGSTRUCT.2017.07.012.

Zhu, M., Yang, Y., Guest, J. K. and Shields, M. D. (2017) 'Topology optimization for linear stationary stochastic dynamics: Applications to frame structures', *Structural Safety*. Elsevier, 67, pp. 116–131. doi: 10.1016/J.STRUSAFE.2017.04.004.

Appendix A. MATLAB Script

Figures in the Appendix are removed from the thesis due to the substantial quantities and size. Hence, kindly find the full Appendix here.

A.a. Finite Element Modelling and Topology Optimisation

A.a.a The Main Script

A.a.b Finite Element Subscript

A.b. Trusses

A.b.a The Main Script

A.b.b Parameters and Details of the Model

A.b.c Results Output

MATLAB

Node	x	y	Disp_x (m)	Disp_y (m)	Element	Node 1	Node 2	Force(N)	Stress (Pa)
1	0	0	0	0	1	1	2	-2500000	-7.9577e+09
2	0	2	1.00720	-0.07958	2	1	3	10000000	3.1831e+10
3	2	0	0.31831	-0.99355	3	2	3	3535533.91	1.1254e+10
4	2	2	0.92762	-0.99355	4	2	4	-2500000	-7.9577e+09
5	4	0	0.31831	0	5	3	4	0	6.7676e-06
6	4	2	0.84805	-0.39789	6	3	6	17677669.53	5.6270e+10
					7	3	5	0	-1.0355e-07
					8	4	6	-2500000	-7.9577e+09
					9	6	5	-12500000	-3.9789e+10

GSA

Node	x	y	Disp_x (mm)	Disp_y (mm)	Element	Force(kN)	Stress (MPa)
1	0	0	0	0	1	-2500	-7958
2	0	2	982.6	-77.64	2	10000	31830
3	2	0	310.5	-967.3	3	3536	11250
4	2	2	905	-967.3	4	-2500	-7958
5	4	0	310.5	0	5	0	0
6	4	2	827.4	-388.2	6	17680	56270
					7	0	0
					8	-2500	-7958
					9	-12500	-39790

Appendix B. Effects of Load Face on the Various Cantilever Beam Geometries

B.a. Displacement

B.a.a Plots

B.a.a.a Depth of 40mm

B.a.a.a.a Method of Tensile Triangles (MTT)

25mm, 50mm, 75mm, 100mm, 125mm, 150mm, 175mm, 200mm

STD, SBD, STU, SBU, TTD

B.a.a.a.b Method of Tensile Triangles Rule of Thumb (MTTR)

25mm, 50mm, 75mm, 100mm, 125mm, 150mm, 175mm, 200mm

STD, SBD, STU, SBU, TTD

B.a.a.a.c Standard Triangle (ST)

1mm, 2mm, 4mm, 6mm, 9mm, 12mm, 24mm

STD, SBD, STU, SBU, TTD

B.a.a.b Depth of 30mm

B.a.a.b.a Method of Tensile Triangles (MTT)

25mm, 50mm, 75mm, 100mm, 125mm, 150mm, 175mm, 200mm

STD, SBD, STU, SBU, TTD

B.a.a.b.b Method of Tensile Triangles (MTTR)

25mm, 50mm, 75mm, 100mm, 125mm, 150mm, 175mm, 200mm

STD, SBD, STU, SBU, TTD

B.a.a.b.c Standard Triangle (ST)

1mm, 2mm, 4mm, 6mm, 9mm, 12mm, 24mm

STD, SBD, STU, SBU, TTD

B.a.a.c Depth of 20mm

B.a.a.c.a Method of Tensile Triangles (MTT)

25mm, 50mm, 75mm, 100mm, 125mm, 150mm, 175mm, 200mm

STD, SBD, STU, SBU, TTD

B.a.a.c.b Method of Tensile Triangles Rule of Thumb (MTTR)

25mm, 50mm, 75mm, 100mm, 125mm, 150mm, 175mm, 200mm

STD, SBD, STU, SBU, TTD

B.a.a.c.c Standard Triangle (ST)

1mm, 2mm, 4mm, 6mm, 9mm, 12mm, 24mm

STD, SBD, STU, SBU, TTD

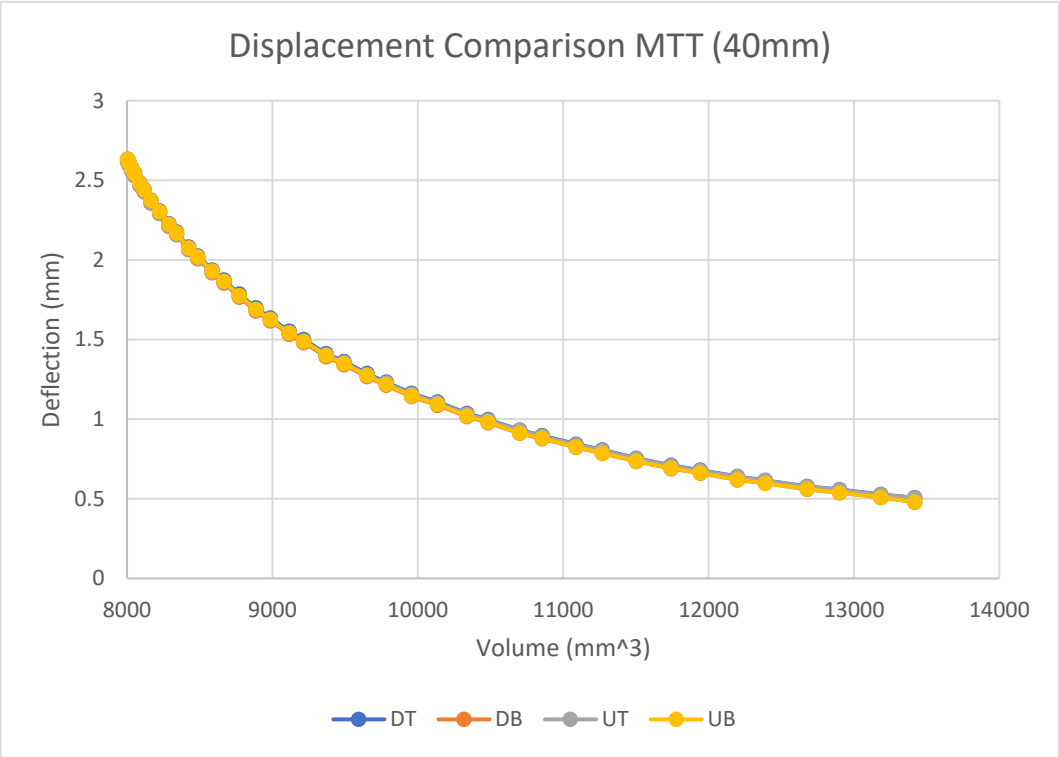
B.a.a.d Increased Depth (20mm to 67mm)

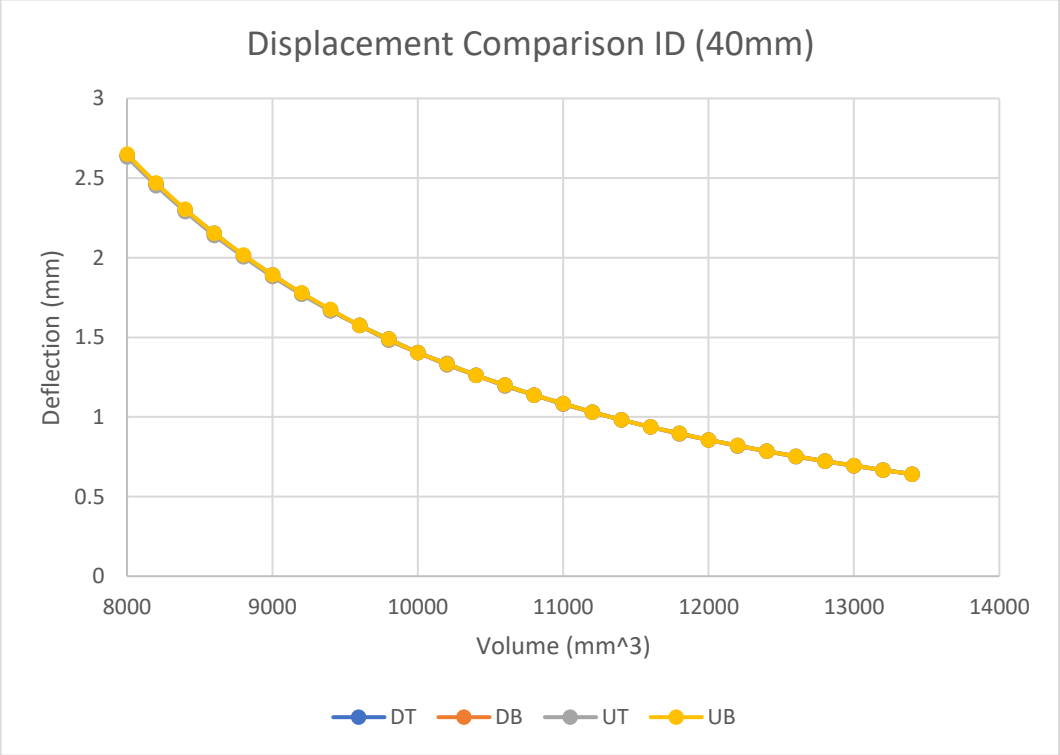
20mm, 25mm, 30mm, 35mm, 40mm, 45mm, 50mm, 55mm, 60mm, 65mm

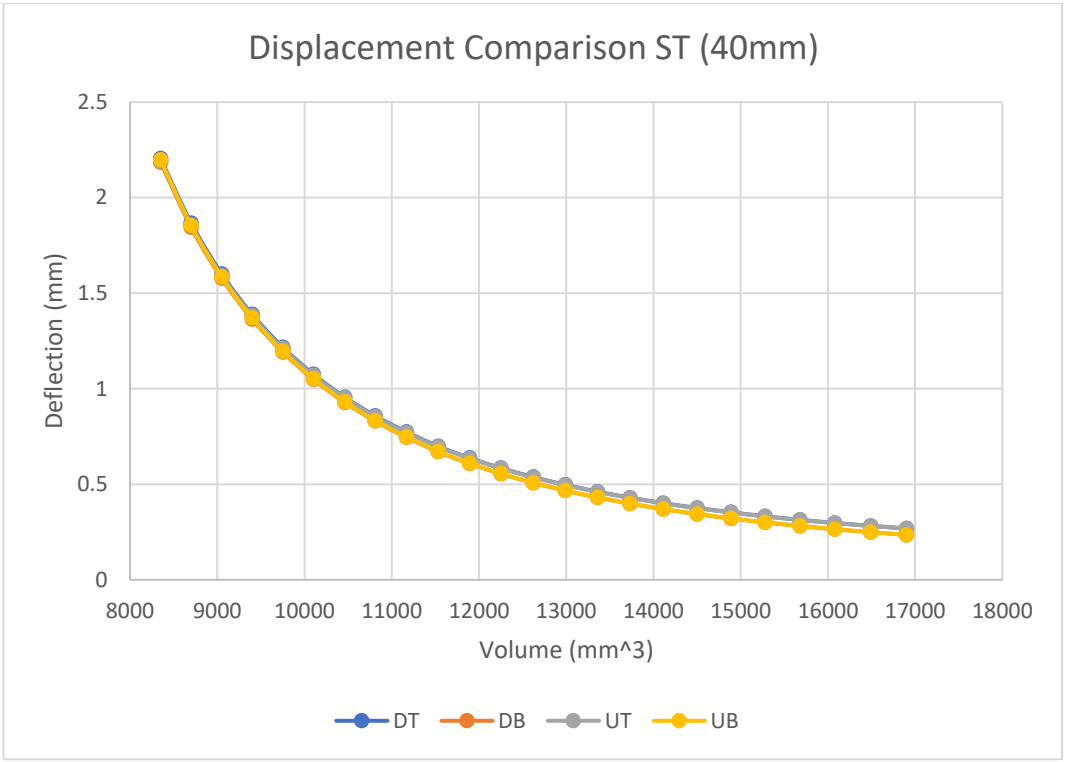
STD, SBD, STU, SBU, TTD

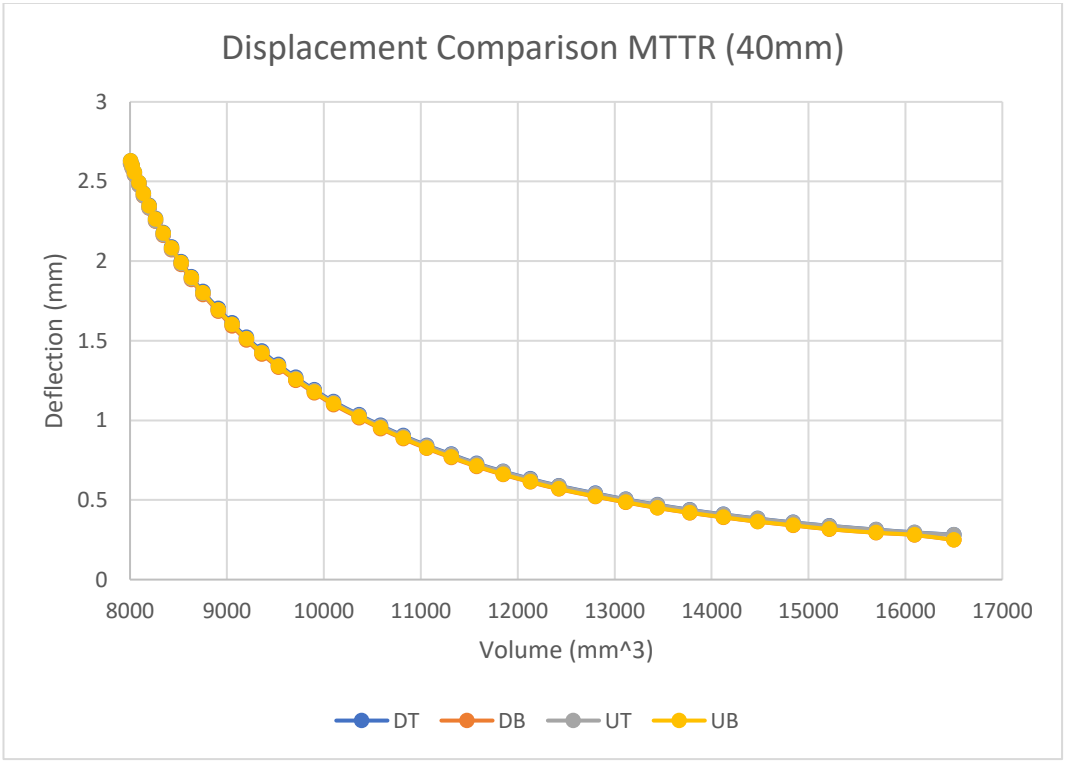
B.a.b Charts

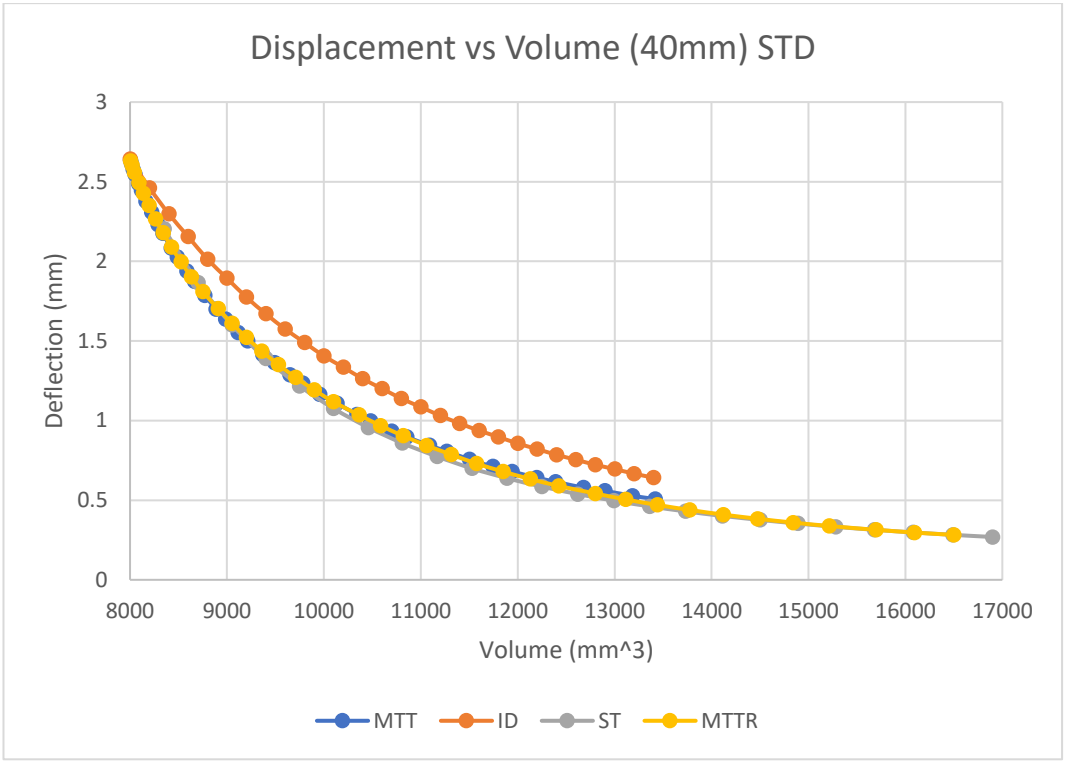
B.a.b.a Depth of 40mm

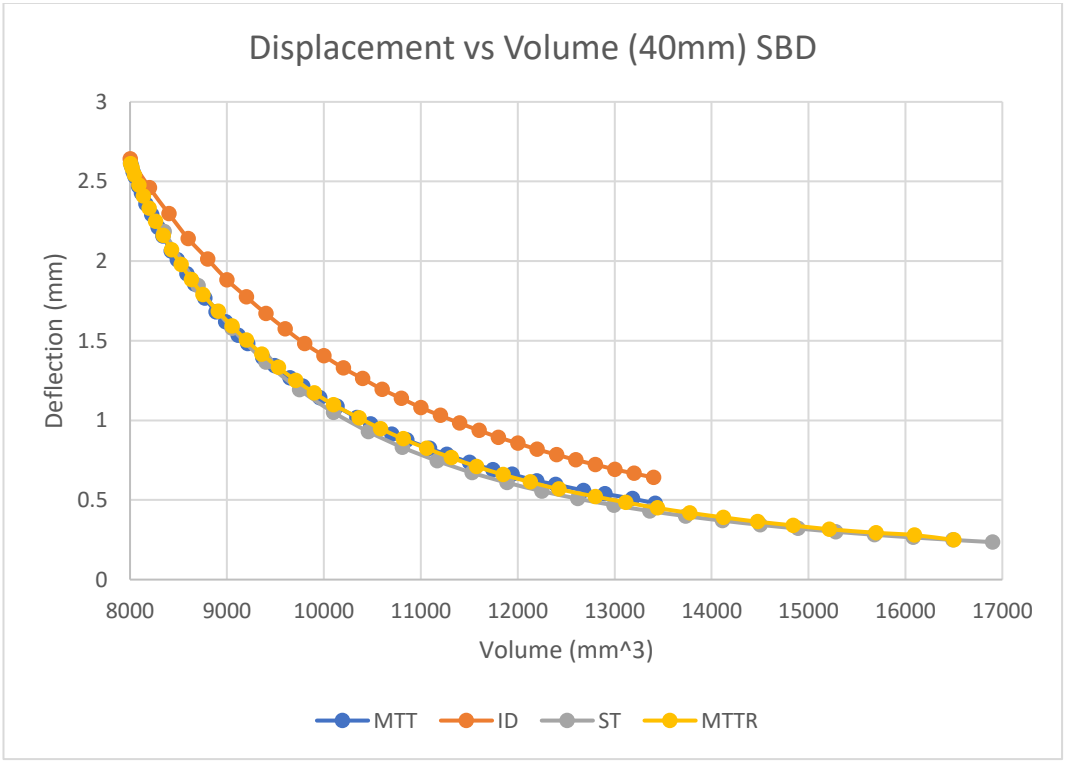


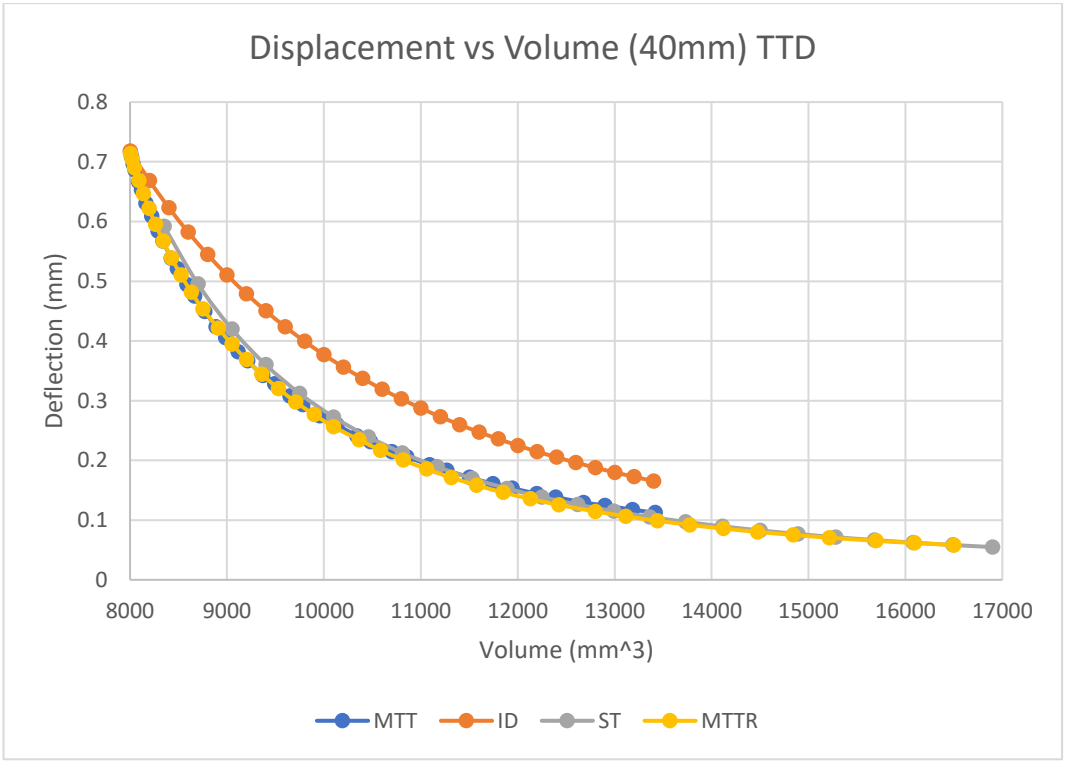


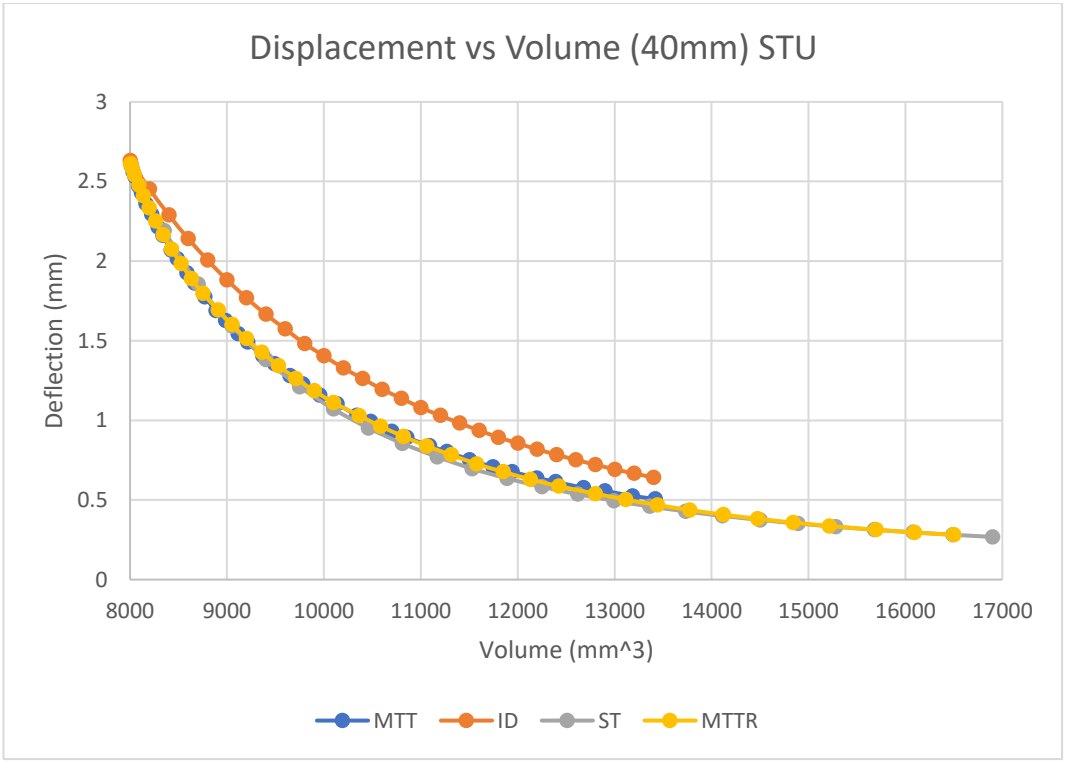

Displacement Comparison ST (40mm)
Deflection (mm)
2.5
2
1.5
1
0.5
0
8000
9000
10000
11000
12000
13000
14000
15000
16000
17000
18000
Volume (mm^3)
DT
DB
UT
UB

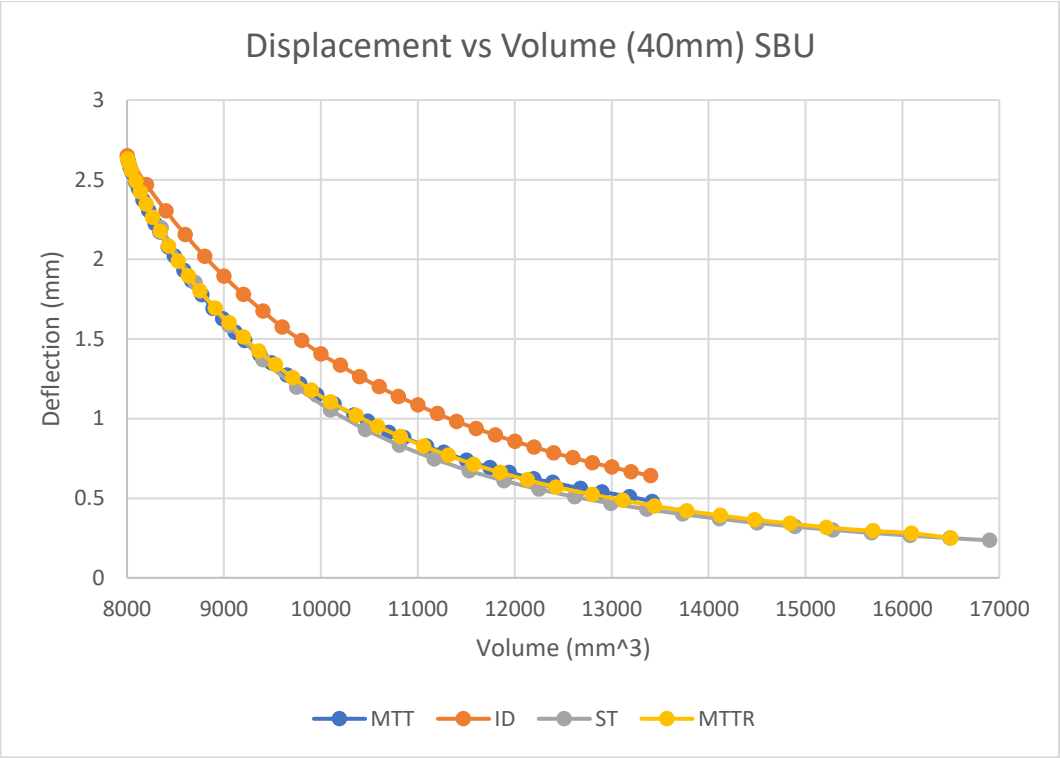

Displacement Comparison MTTR (40mm)
Deflection (mm)
3
2.5
2
1.5
1
0.5
0
8000
9000
10000
11000
12000
13000
14000
15000
16000
17000
Volume (mm^3)
DT
DB
UT
UB


Displacement vs Volume (40mm) STD
Deflection (mm)
3
2.5
2
1.5
1
0.5
0
8000
9000
10000
11000
12000
13000
14000
15000
16000
17000
Volume (mm^3)
MTT
ID
ST
MTTR

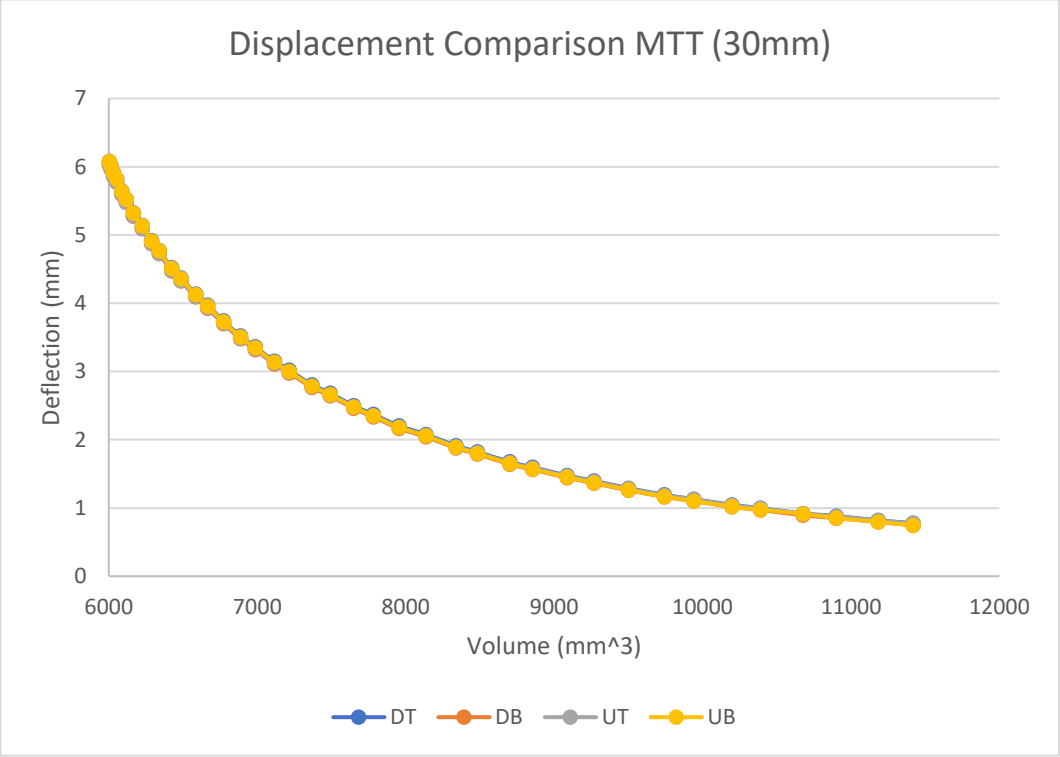

Displacement vs Volume (40mm) SBD
Deflection (mm)
3
2.5
2
1.5
1
0.5
0
8000
9000
10000
11000
12000
13000
14000
15000
16000
17000
Volume (mm^3)
MTT
ID
ST
MTTR

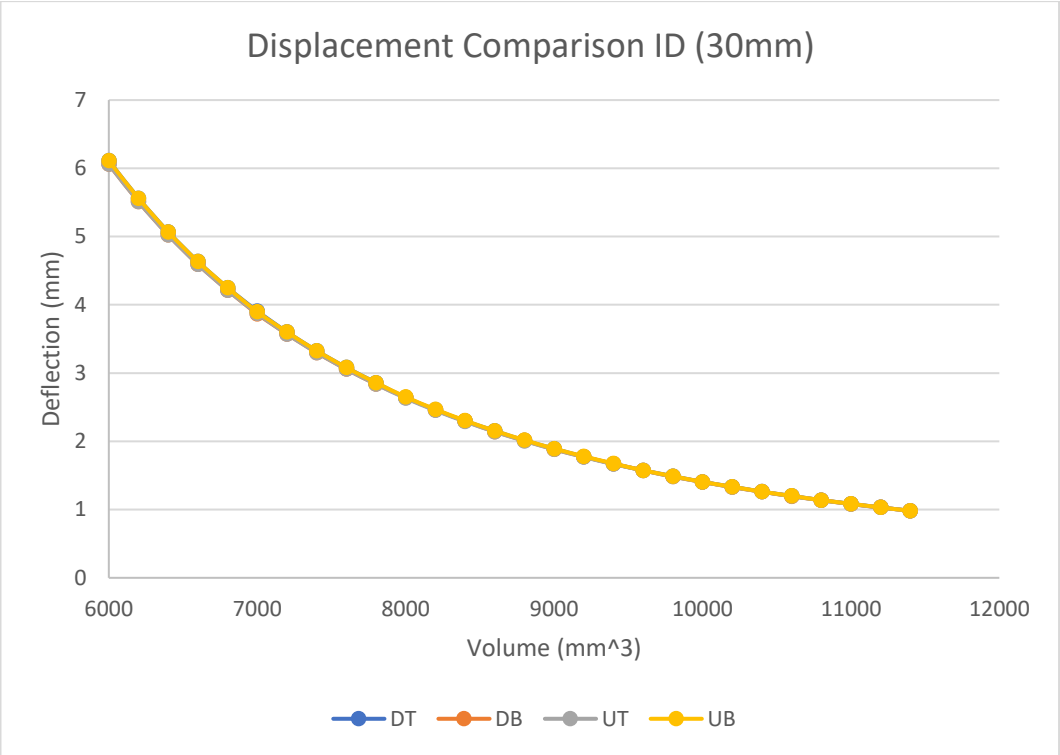

Displacement vs Volume (40mm) TTD
Deflection (mm)
0.8
0.7
0.6
0.5
0.4
0.3
0.2
0.1
0
8000
9000
10000
11000
12000
13000
14000
15000
16000
17000
Volume (mm^3)
MTT
ID
ST
MTTR

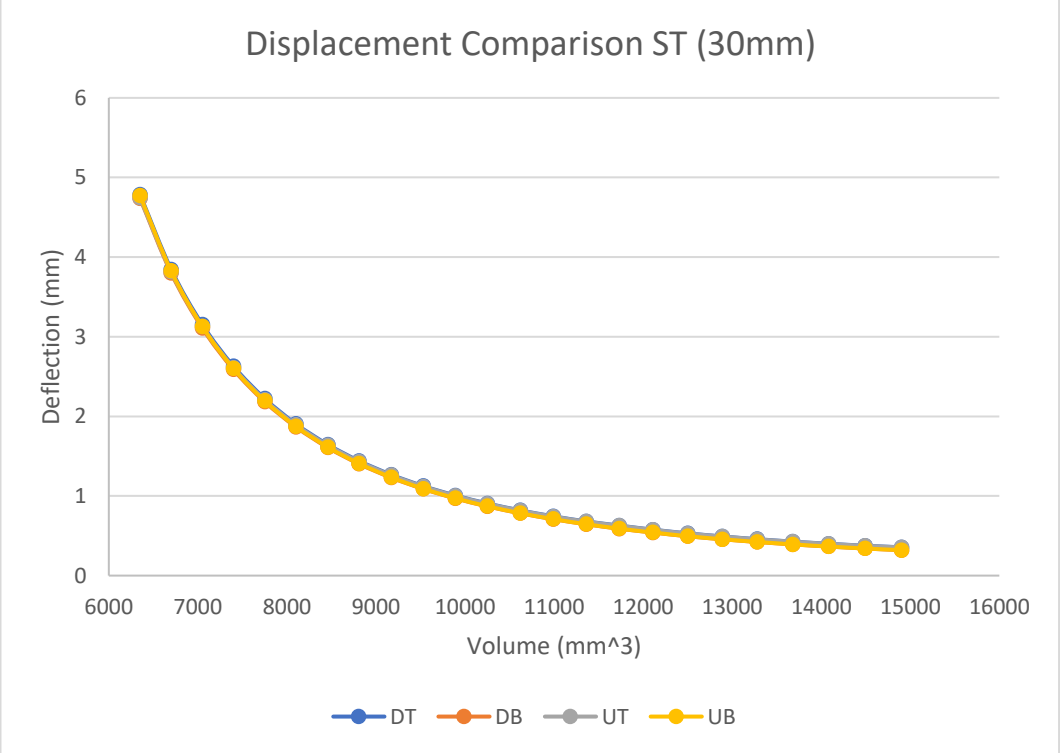

Displacement vs Volume (40mm) STU
Deflection (mm)
3
2.5
2
1.5
1
0.5
0
8000
9000
10000
11000
12000
13000
14000
15000
16000
17000
Volume (mm^3)
MTT
ID
ST
MTTR

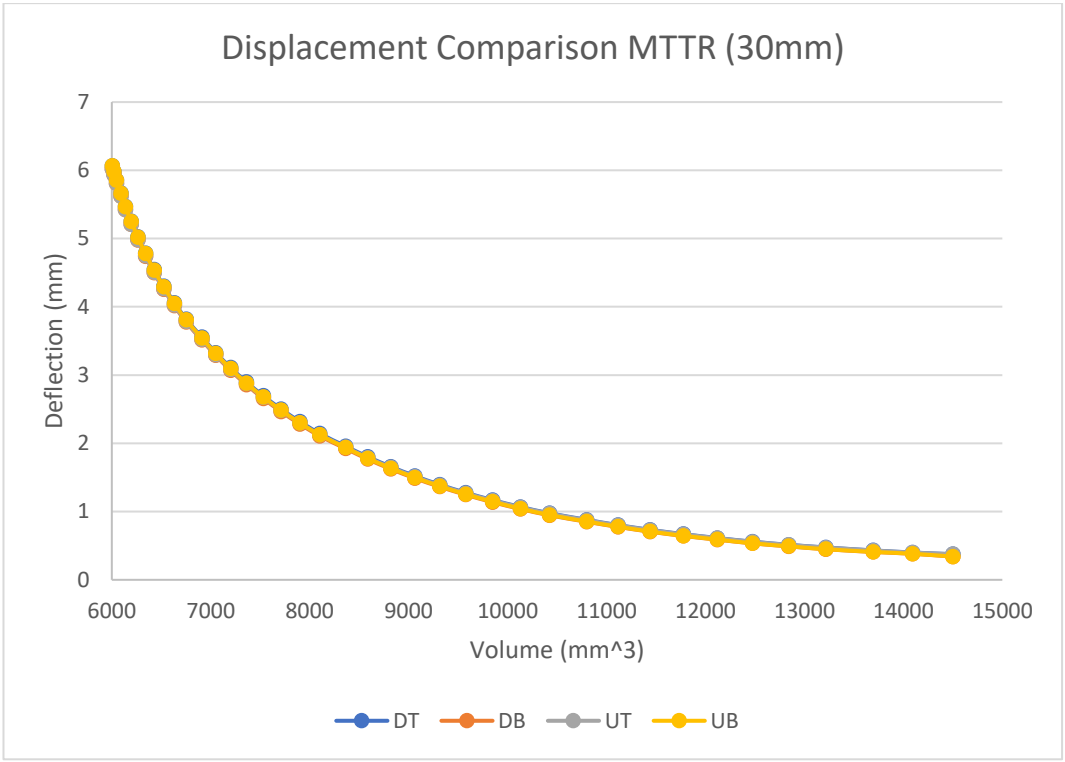


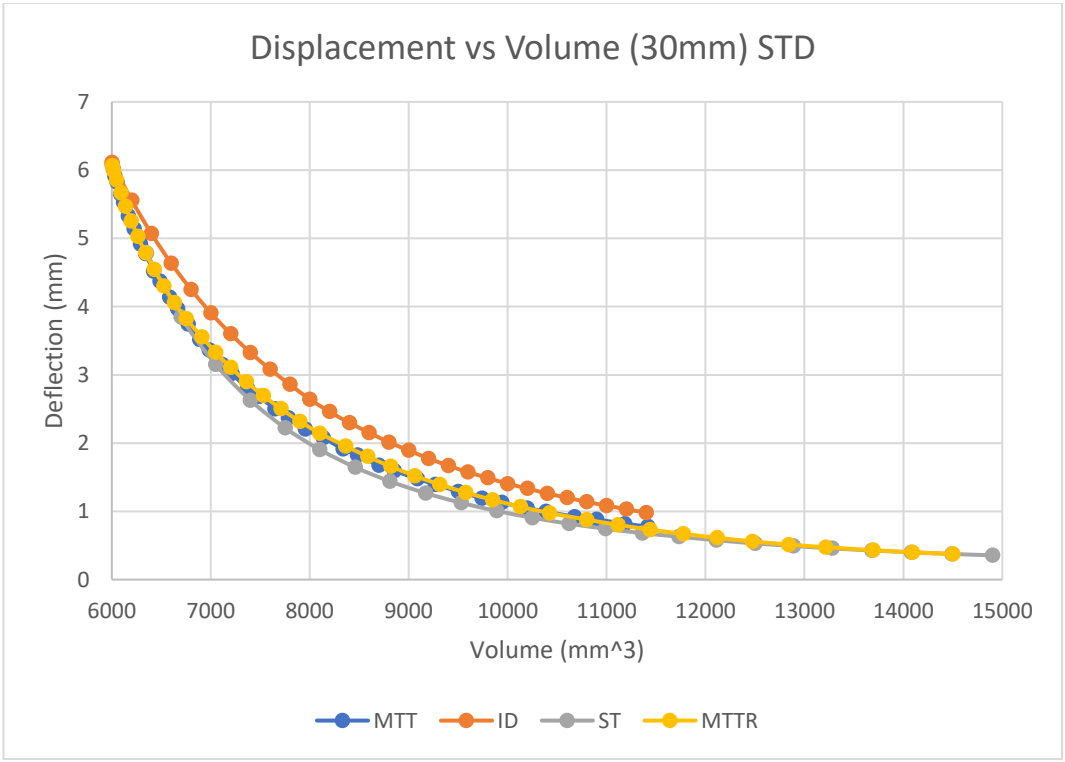
B.a.b.b Depth of 30mm

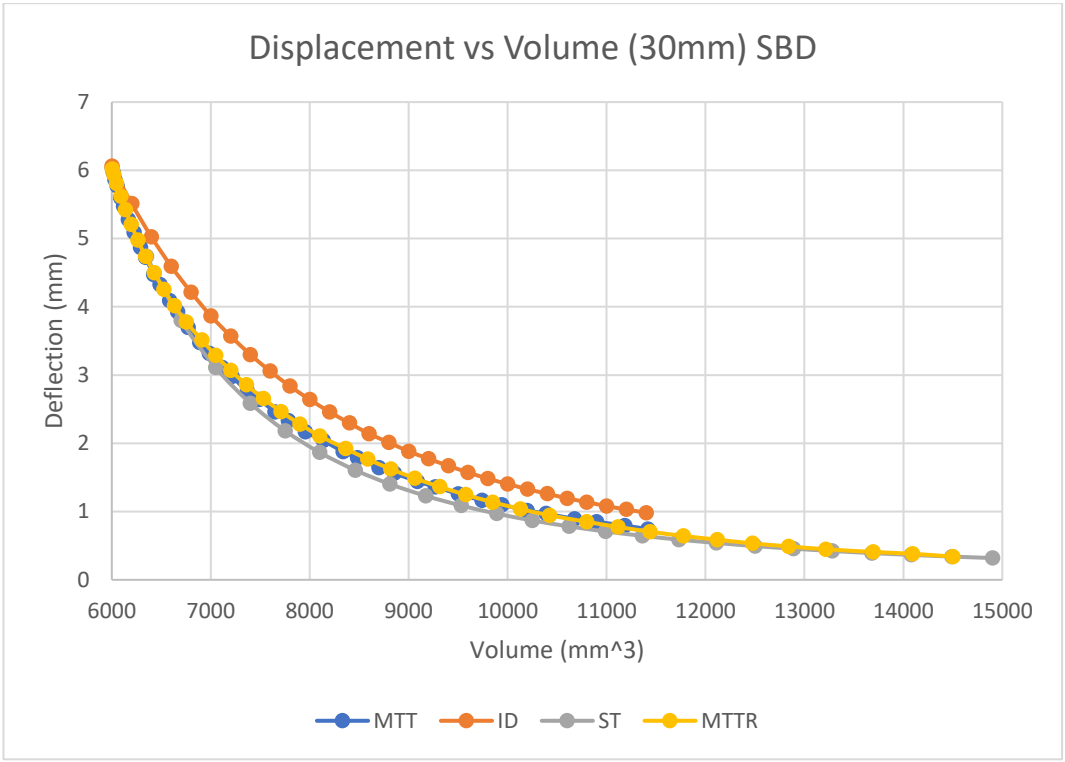


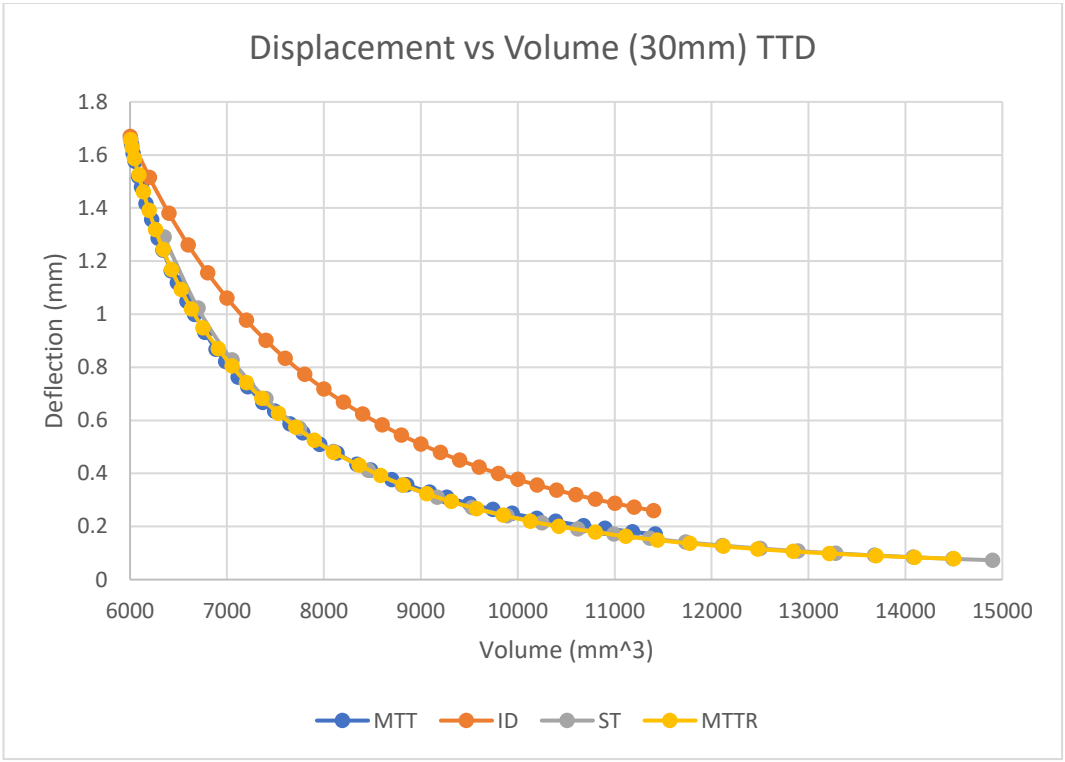

Displacement Comparison ID (30mm)
Deflection (mm)
0
1
2
3
4
5
6
7
6000
7000
8000
9000
10000
11000
12000
Volume (mm^3)
DT
DB
UT
UB

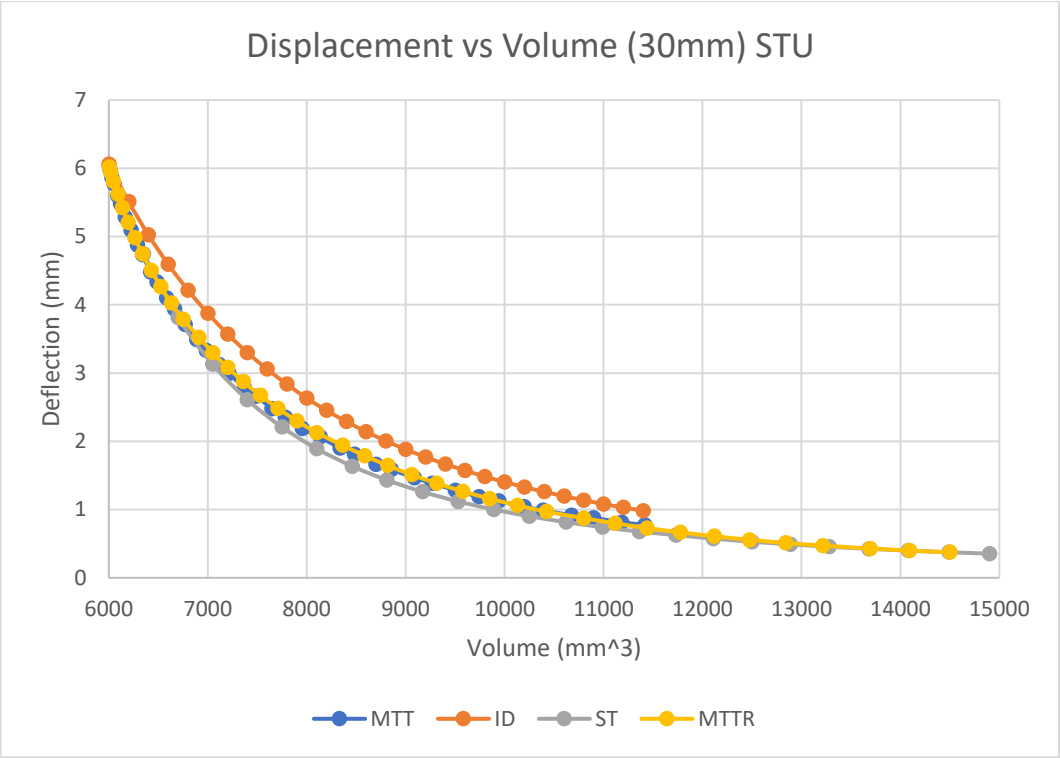

Displacement Comparison ST (30mm)
Deflection (mm)
0
1
2
3
4
5
6
6000
7000
8000
9000
10000
11000
12000
13000
14000
15000
16000
Volume (mm^3)
DT
DB
UT
UB

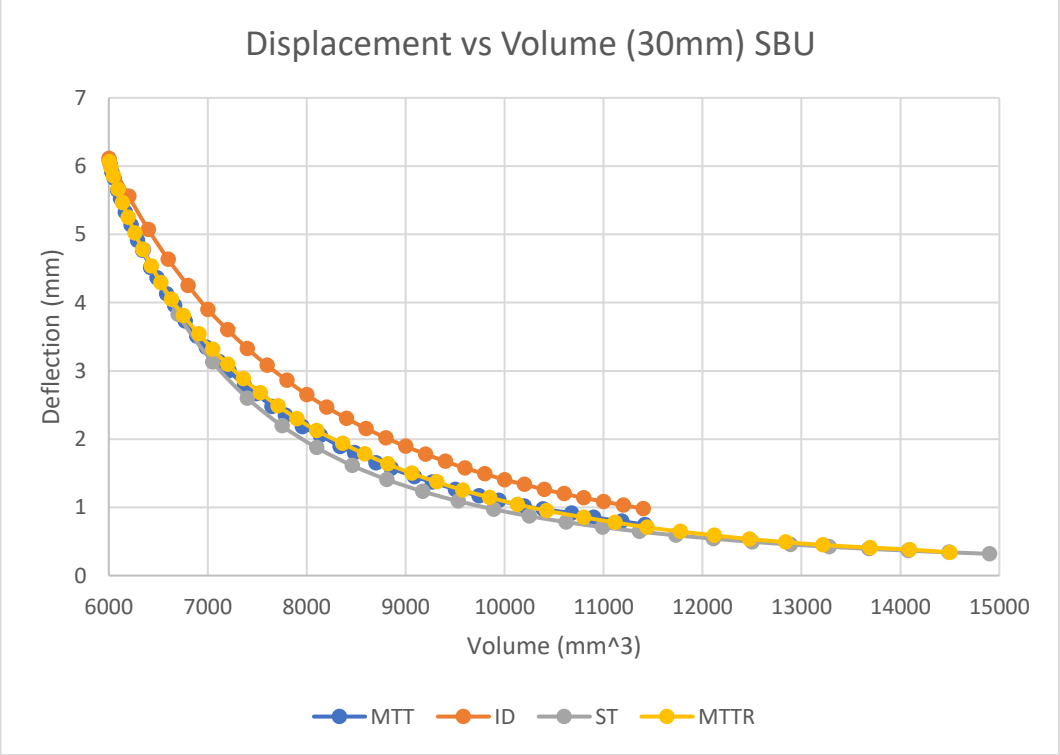

Displacement Comparison MTTR (30mm)
Deflection (mm)
0
1
2
3
4
5
6
7
6000
7000
8000
9000
10000
11000
12000
13000
14000
15000
Volume (mm^3)
DT
DB
UT
UB


Displacement vs Volume (30mm) STD
Deflection (mm)
0
1
2
3
4
5
6
7
6000
7000
8000
9000
10000
11000
12000
13000
14000
15000
Volume (mm^3)
MTT
ID
ST
MTTR

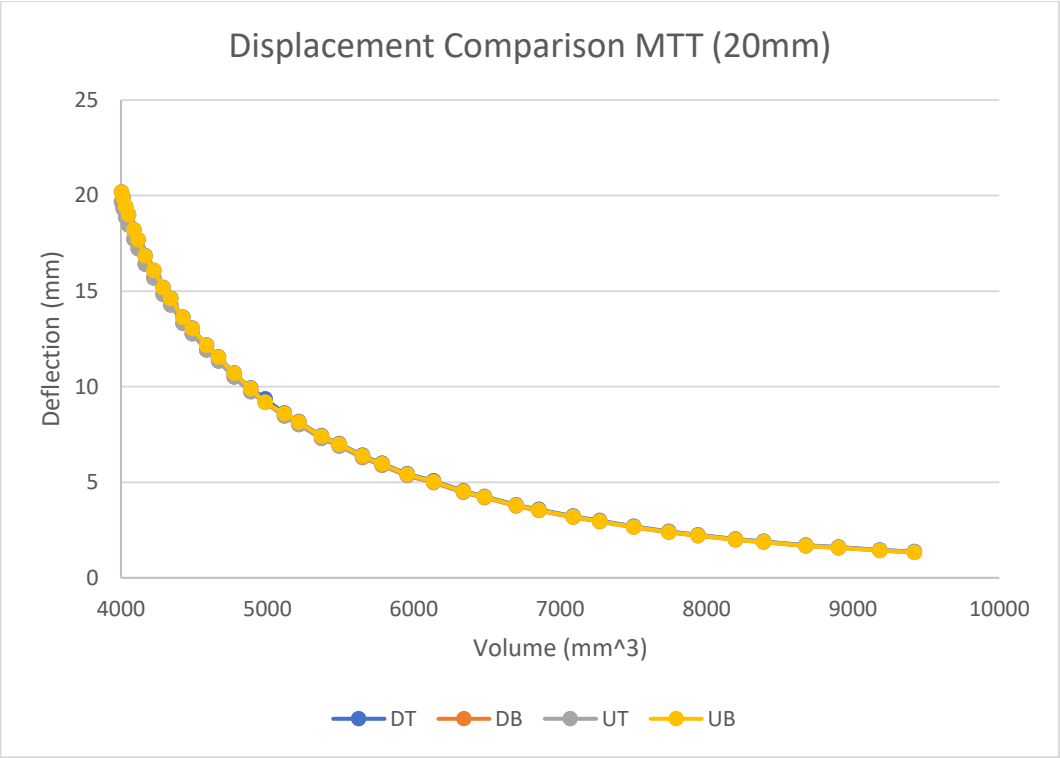

Displacement vs Volume (30mm) SBD
Deflection (mm)
0
1
2
3
4
5
6
7
6000
7000
8000
9000
10000
11000
12000
13000
14000
15000
Volume (mm^3)
MTT
ID
ST
MTTR

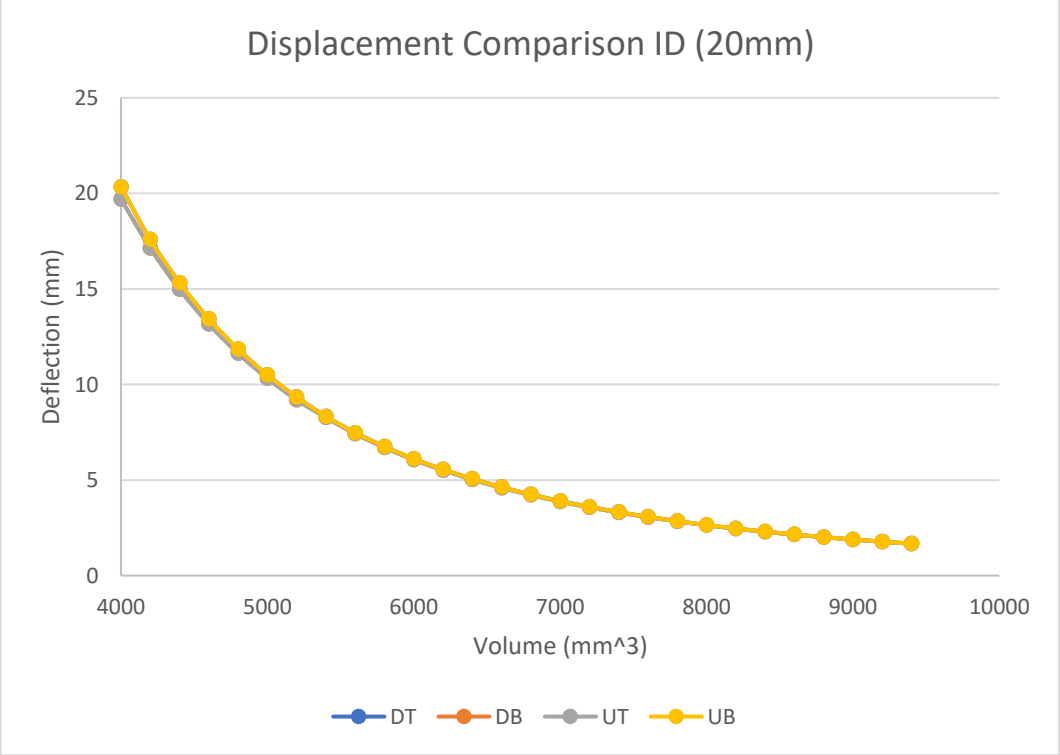

Displacement vs Volume (30mm) TTD
Deflection (mm)
0
0.2
0.4
0.6
0.8
1
1.2
1.4
1.6
1.8
6000
7000
8000
9000
10000
11000
12000
13000
14000
15000
Volume (mm^3)
MTT
ID
ST
MTTR

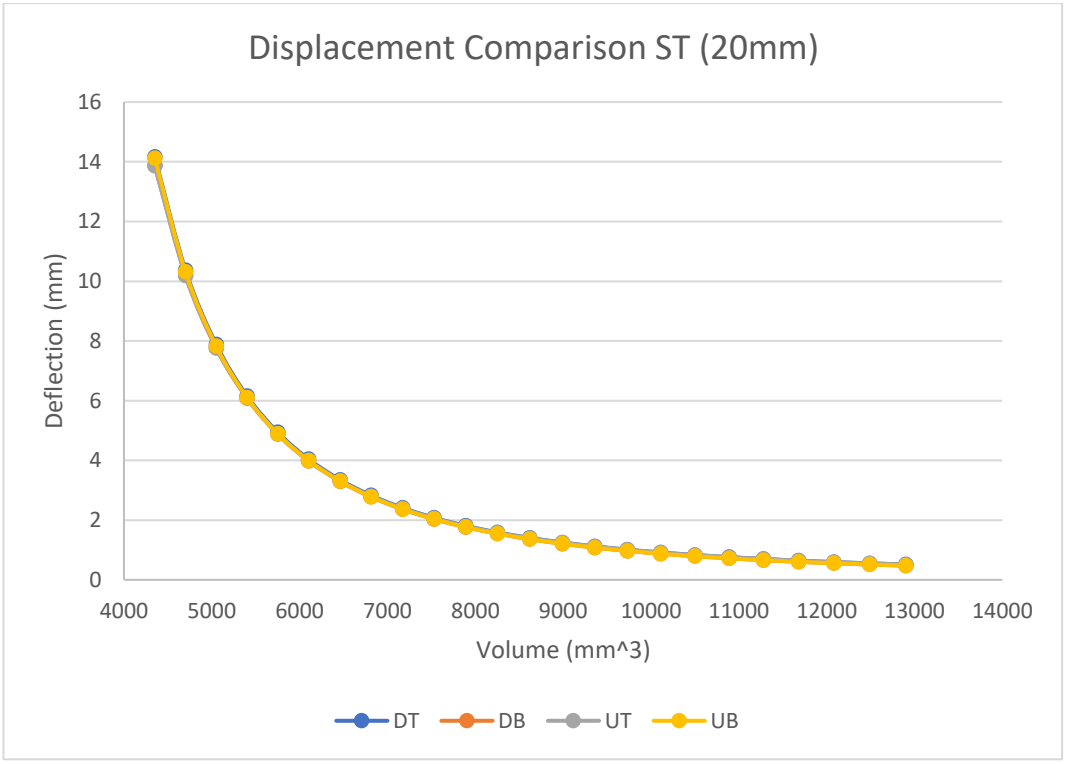


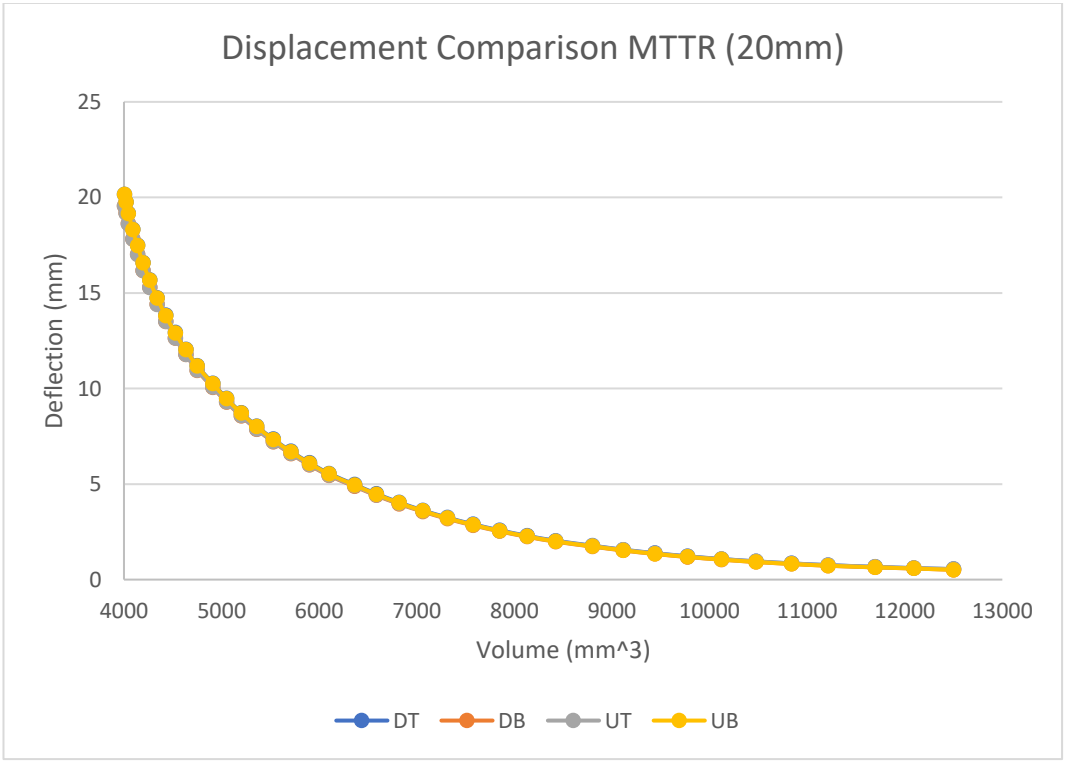


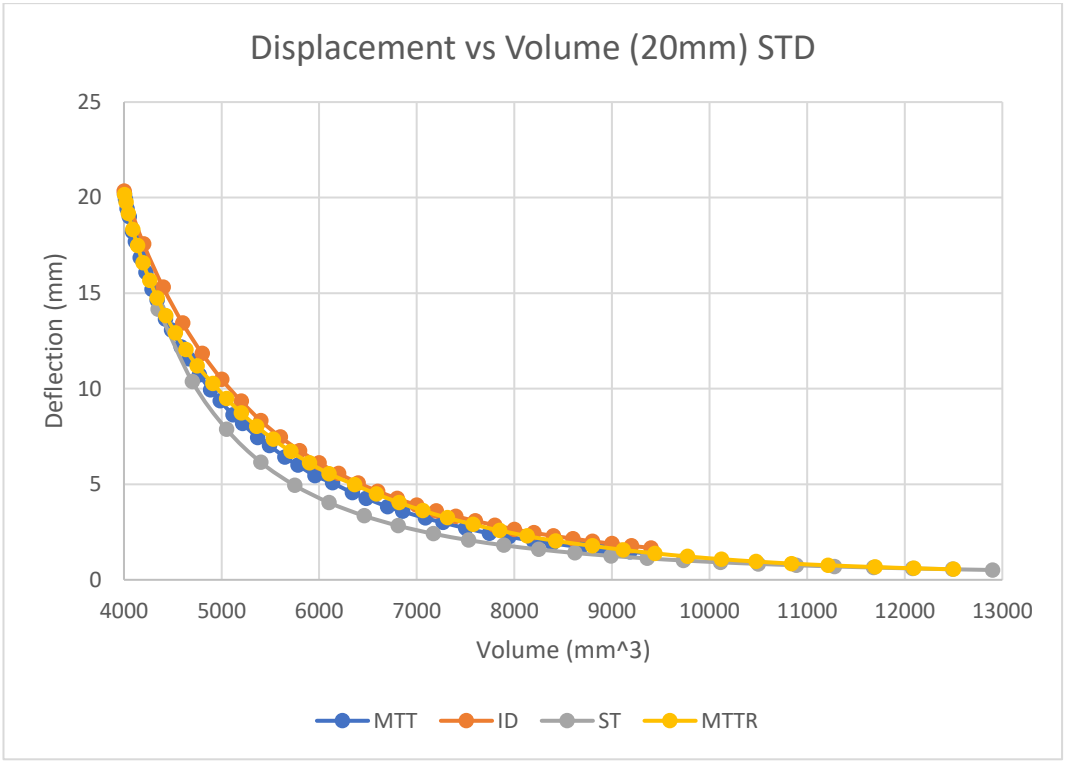
B.a.b.cDepth of 20mm

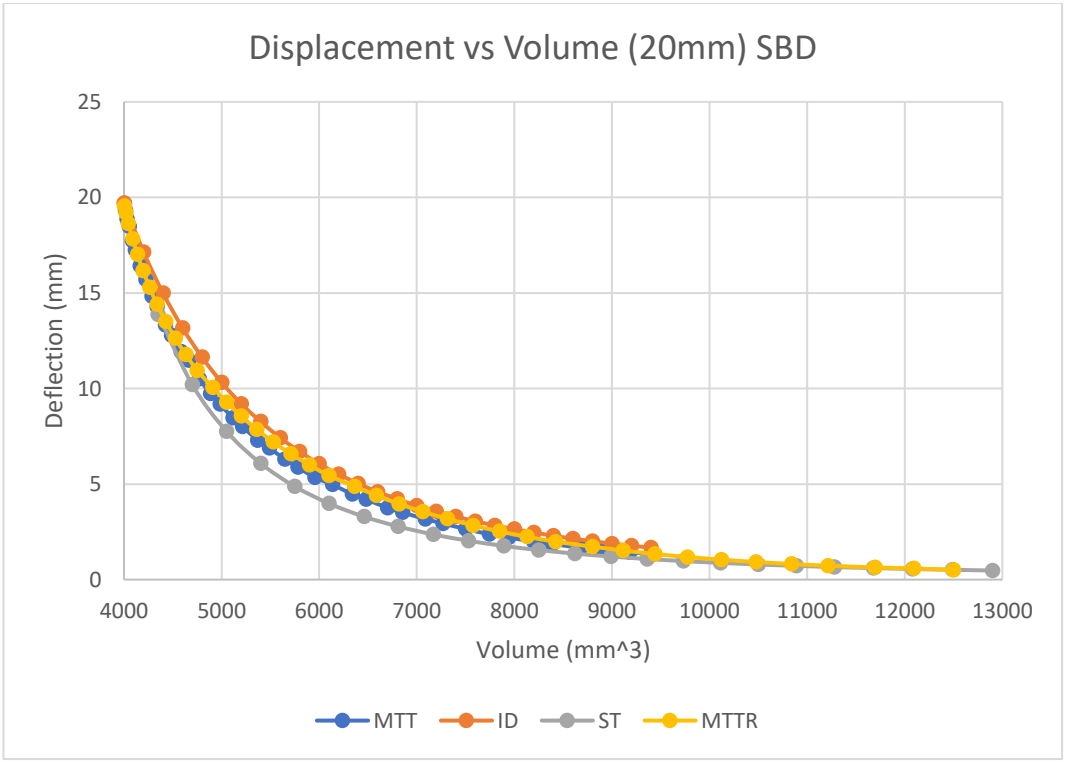

Displacement Comparison MTT (20mm)
25
20
15
10
5
0
Deflection (mm)
4000
5000
6000
7000
8000
9000
10000
Volume (mm^3)
DT
DB
UT
UB

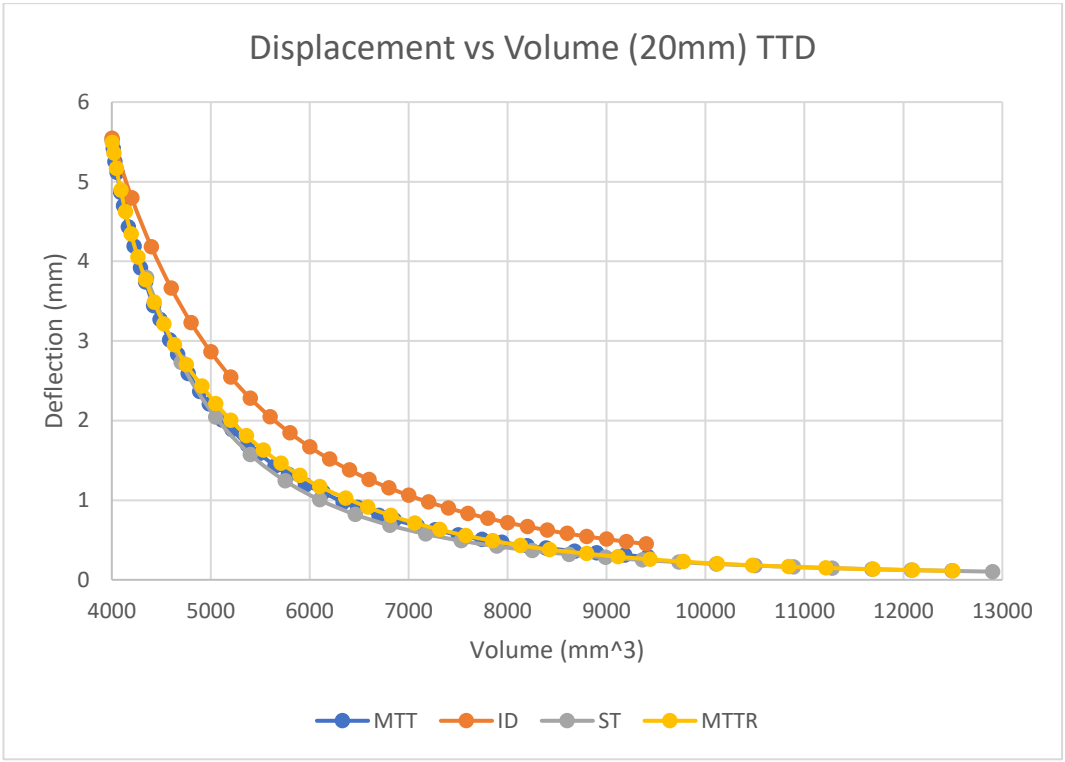

Displacement Comparison ID (20mm)
25
20
15
10
5
0
Deflection (mm)
4000
5000
6000
7000
8000
9000
10000
Volume (mm^3)
DT
DB
UT
UB

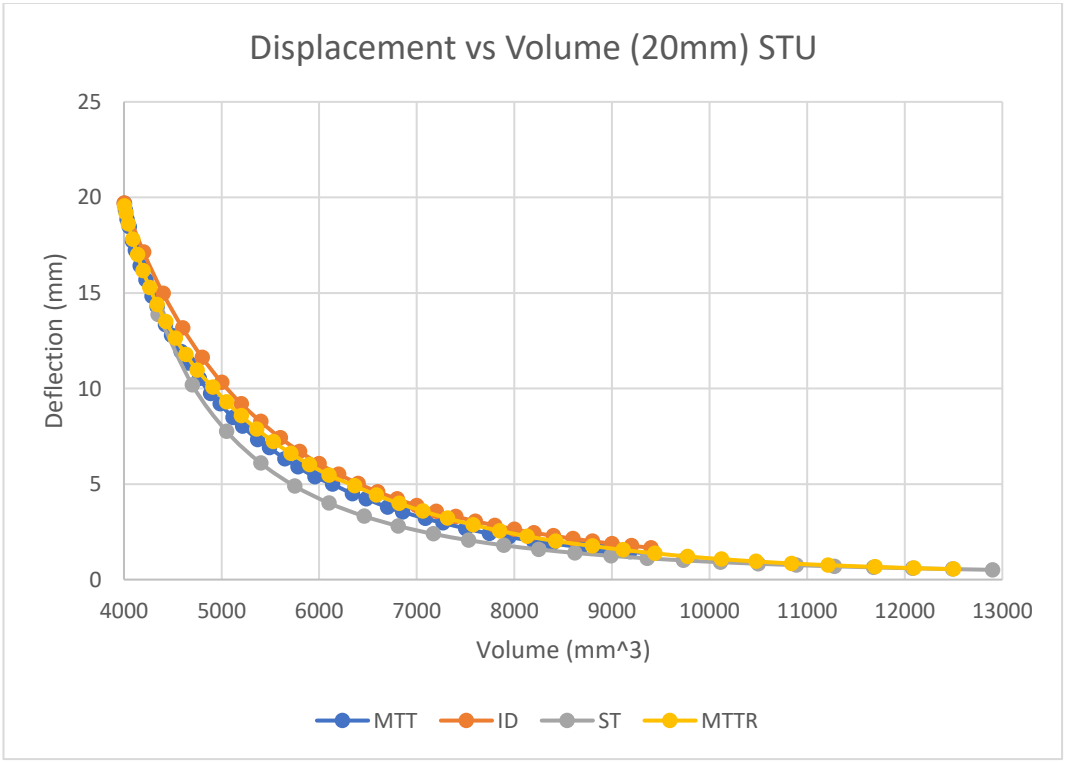

Displacement Comparison ST (20mm)
Deflection (mm)
16
14
12
10
8
6
4
2
0
4000
5000
6000
7000
8000
9000
10000
11000
12000
13000
14000
Volume (mm^3)
DT
DB
UT
UB

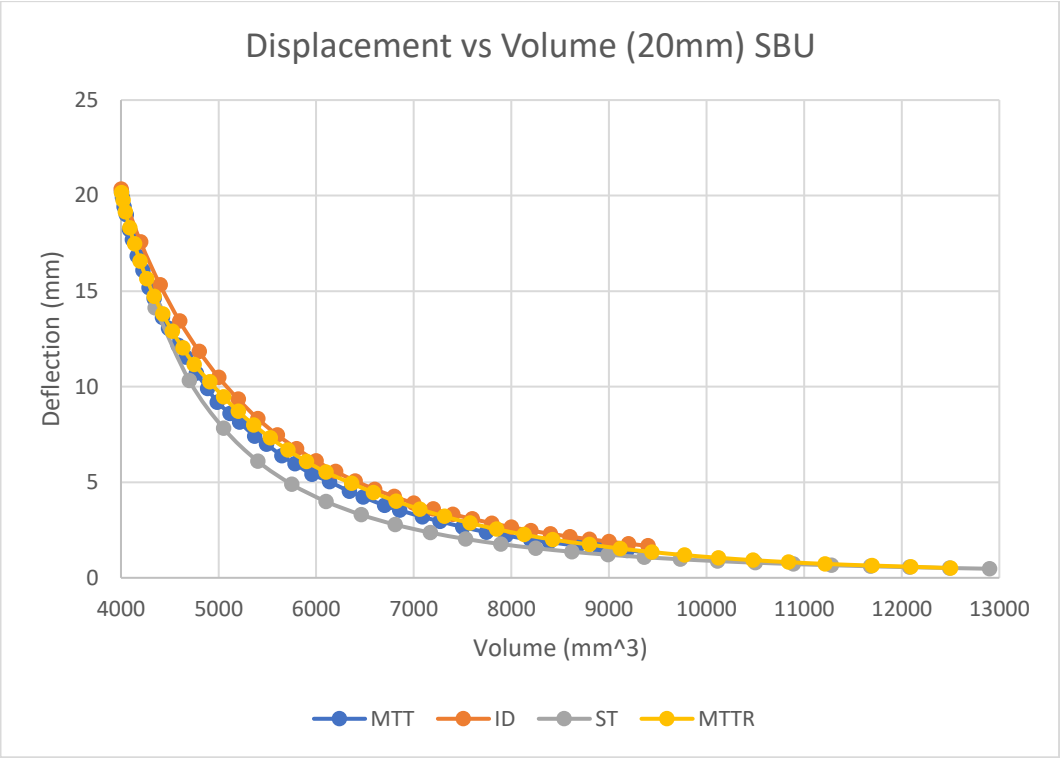

Displacement Comparison MTTR (20mm)
Deflection (mm)
25
20
15
10
5
0
4000
5000
6000
7000
8000
9000
10000
11000
12000
13000
Volume (mm^3)
DT
DB
UT
UB


Displacement vs Volume (20mm) STD
Deflection (mm)
25
20
15
10
5
0
4000
5000
6000
7000
8000
9000
10000
11000
12000
13000
Volume (mm^3)
MTT
ID
ST
MTTR


Displacement vs Volume (20mm) SBD
Deflection (mm)
25
20
15
10
5
0
4000
5000
6000
7000
8000
9000
10000
11000
12000
13000
Volume (mm^3)
MTT
ID
ST
MTTR


Displacement vs Volume (20mm) TTD
Deflection (mm)
0
1
2
3
4
5
6
4000
5000
6000
7000
8000
9000
10000
11000
12000
13000
Volume (mm^3)
MTT
ID
ST
MTTR


Displacement vs Volume (20mm) STU
Deflection (mm)
0
5
10
15
20
25
4000
5000
6000
7000
8000
9000
10000
11000
12000
13000
Volume (mm^3)
MTT
ID
ST
MTTR



B.b. Stress Profile

B.b.a Plots

B.b.a.aDepth of 40mm

B.b.a.a.a Method of Tensile Triangles (MTT)

25mm, 50mm, 75mm, 100mm, 125mm, 150mm, 175mm, 200mm

STD, SBD, STU, SBU, TTD

B.b.a.a.b Method of Tensile Triangles Rule of Thumb (MTTR)

25mm, 50mm, **75mm**, **100mm, 125mm, 150mm, 175mm, 200mm**

STD, SBD, STU, SBU, TTD

B.b.a.a.c Standard Triangle (ST)

1mm, 2mm, 4mm, 6mm, 9mm, 12mm, 24mm

STD, SBD, STU, SBU, TTD

B.b.a.b Depth of 30mm

B.b.a.b.a Method of Tensile Triangles (MTT)

25mm, 50mm, 75mm, 100mm, 125mm, 150mm, 175mm, 200mm

STD, SBD, STU, SBU, TTD

B.b.a.b.b Method of Tensile Triangles Rule of Thumb (MTTR)

25mm, 50mm, 75mm, 100mm, 125mm, 150mm, 175mm, 200mm

STD, SBD, STU, SBU, TTD

B.b.a.b.c Standard Triangle (ST)

1mm, 2mm, 4mm, 6mm, 9mm, 12mm, 24mm

STD, SBD, STU, SBU, TTD

B.b.a.c Depth of 20mm

B.b.a.c.a Method of Tensile Triangles (MTT)

25mm, 50mm, 75mm, 100mm, 125mm, 150mm, 175mm, 200mm

STD, SBD, STU, SBU, TTD

B.b.a.c.b Method of Tensile Triangles (MTTR)

25mm, 50mm, 75mm, 100mm, 125mm, 150mm, 175mm, 200mm

STD, SBD, STU, SBU, TTD

B.b.a.c.c Standard Triangle (ST)

<u>1mm, 2mm, 4mm, 6mm, 9mm, 12mm, 24mm</u>

STD, SBD, STU, SBU, TTD

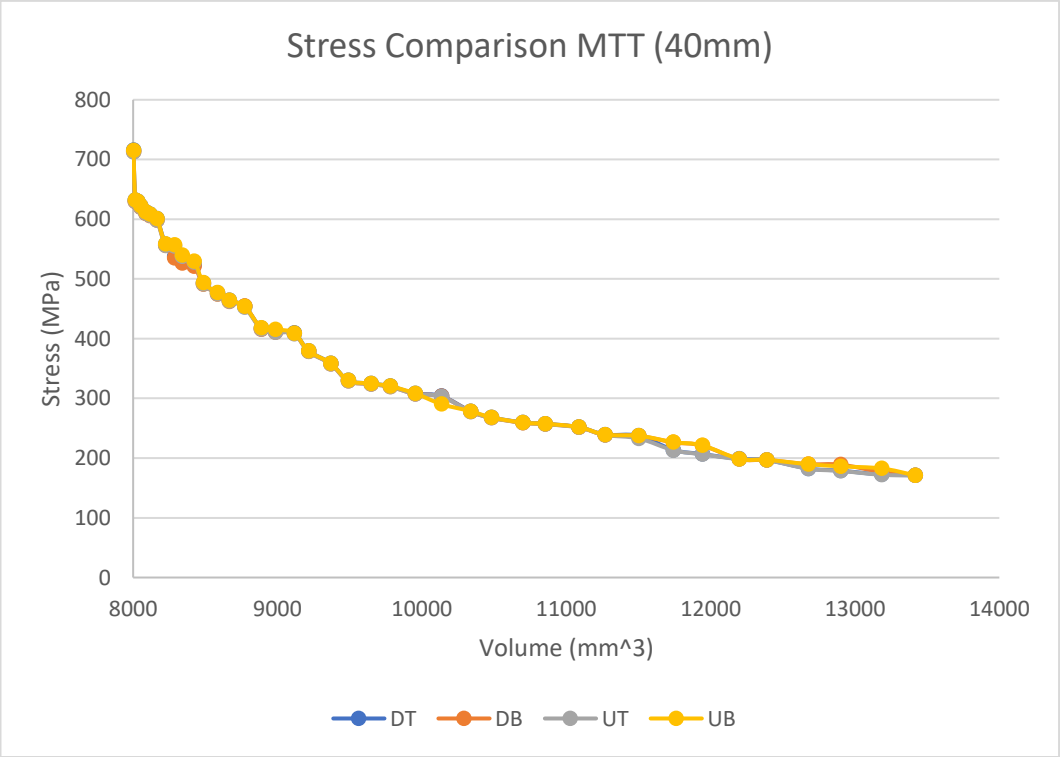
B.b.a.d Increased Depth (20mm to 67mm)

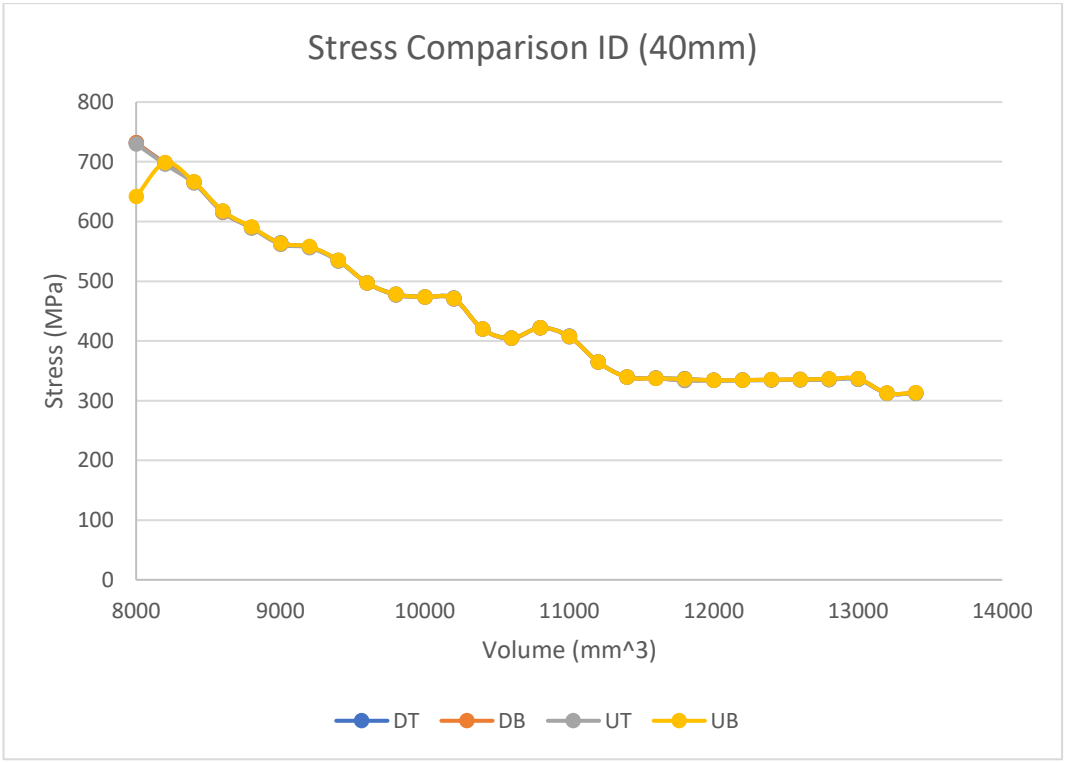
<u>20mm, 25mm, 30mm, 35mm, 40mm, 45mm, 50mm, 55mm, 60mm, 65mm</u>

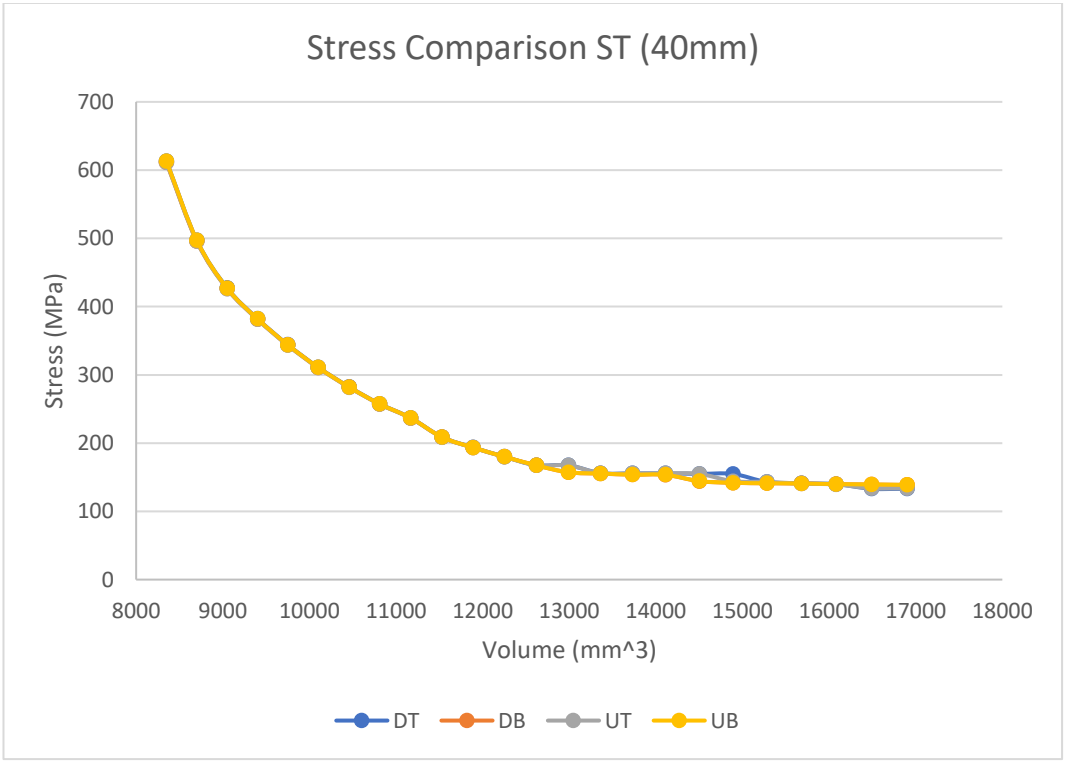
STD, SBD, STU, SBU, TTD

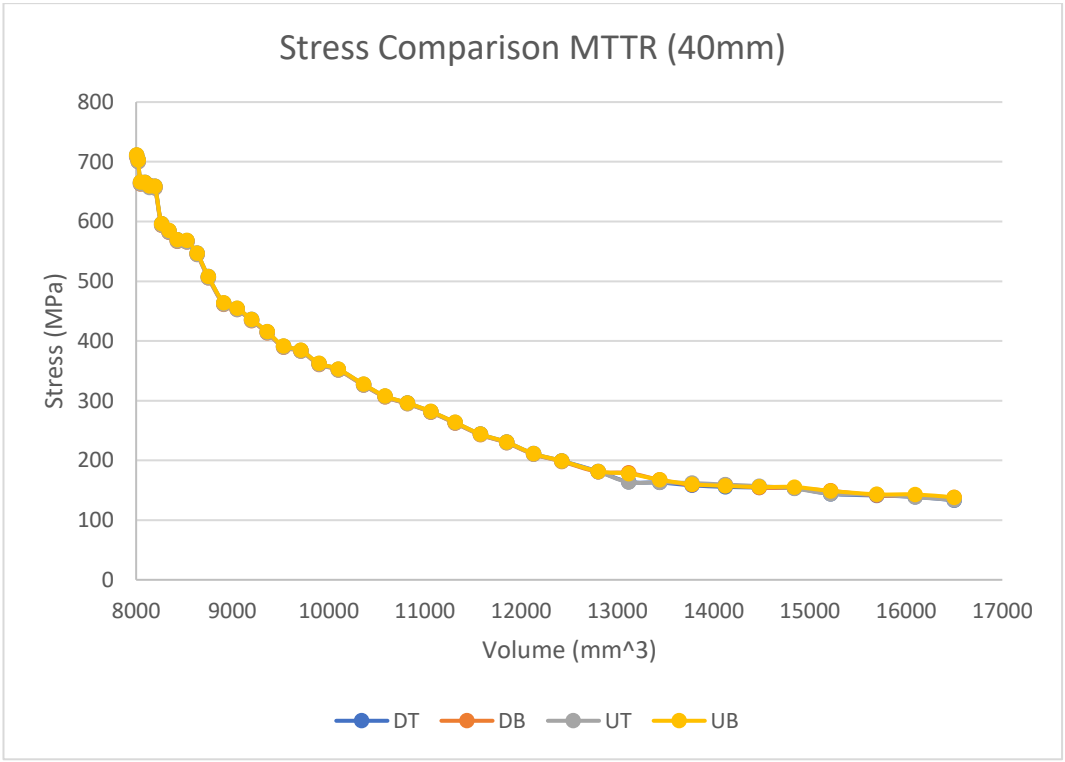
B.b.b Charts

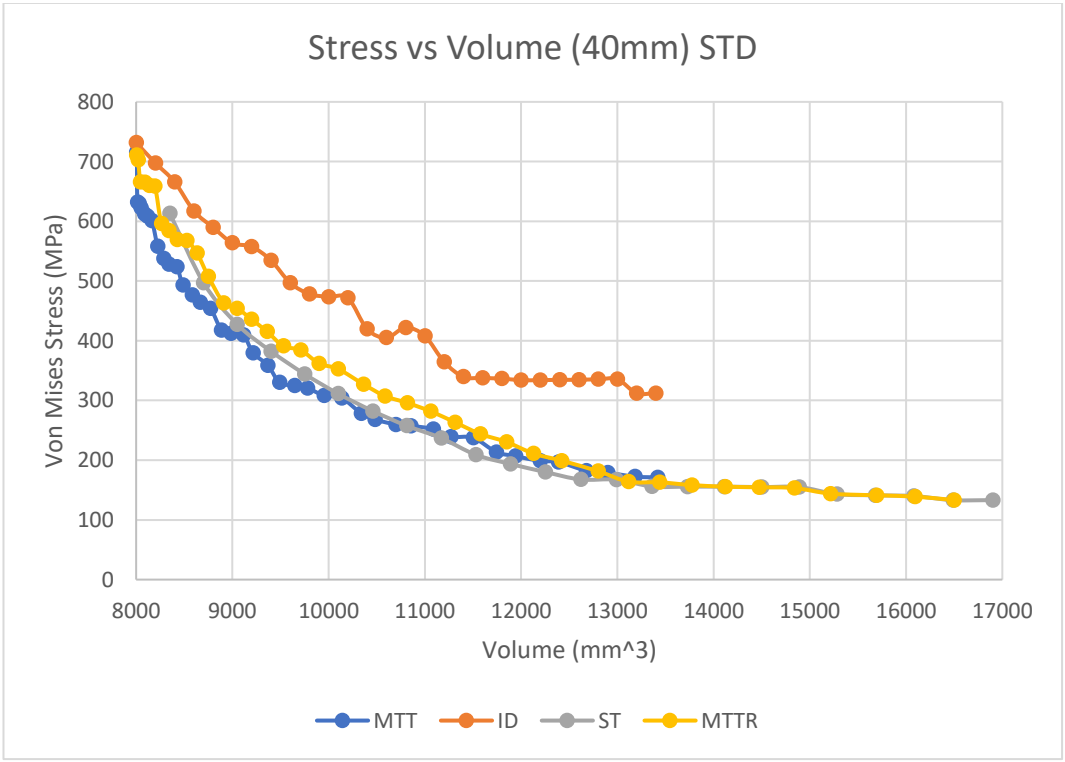
B.b.b.a Depth of 40mm

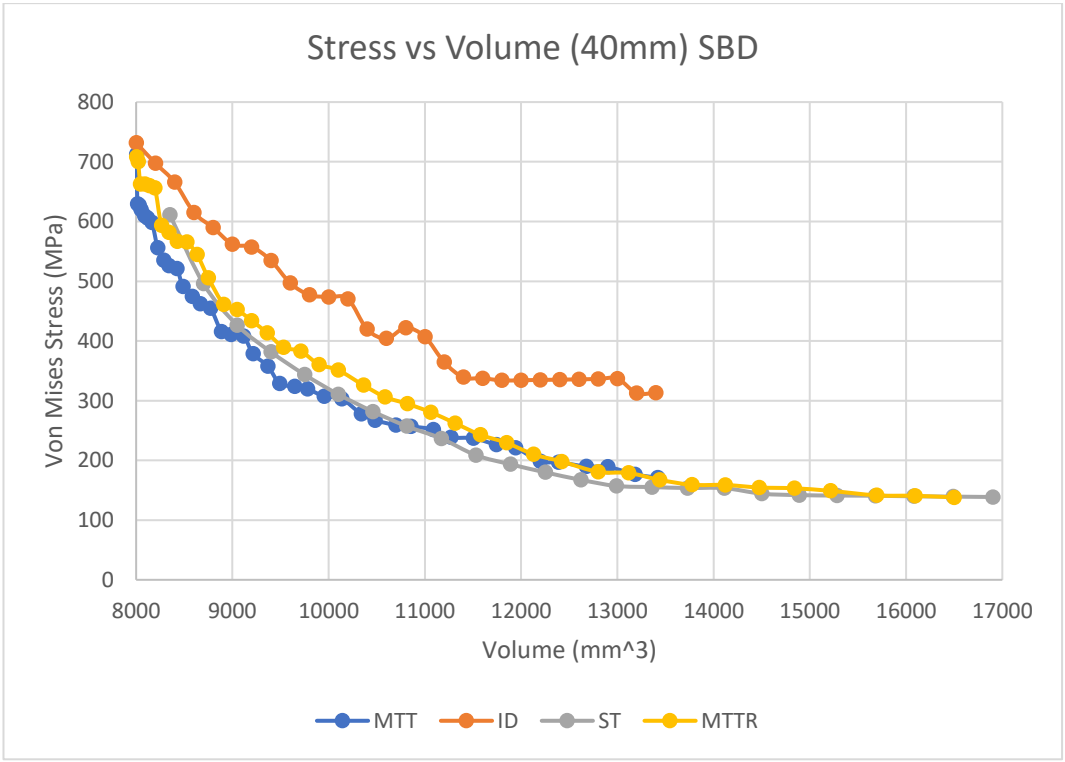


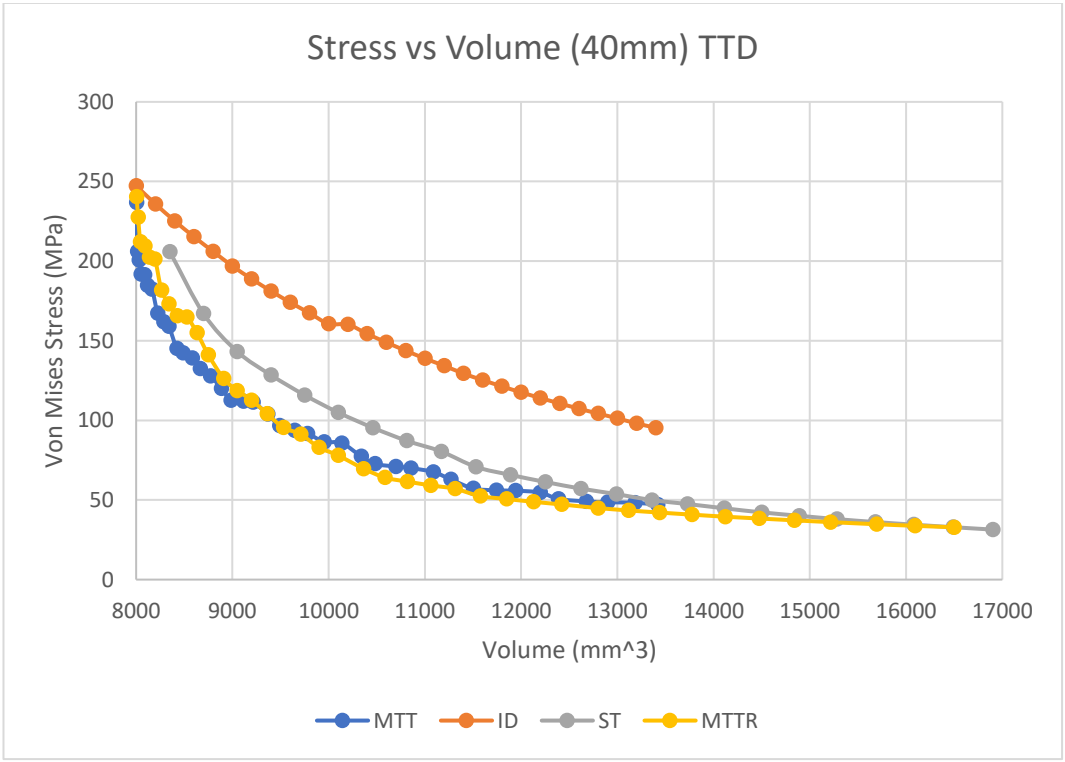

Stress Comparison ID (40mm)
800
700
600
500
400
300
200
100
0
Stress (MPa)
8000
9000
10000
11000
12000
13000
14000
Volume (mm^3)
DT
DB
UT
UB

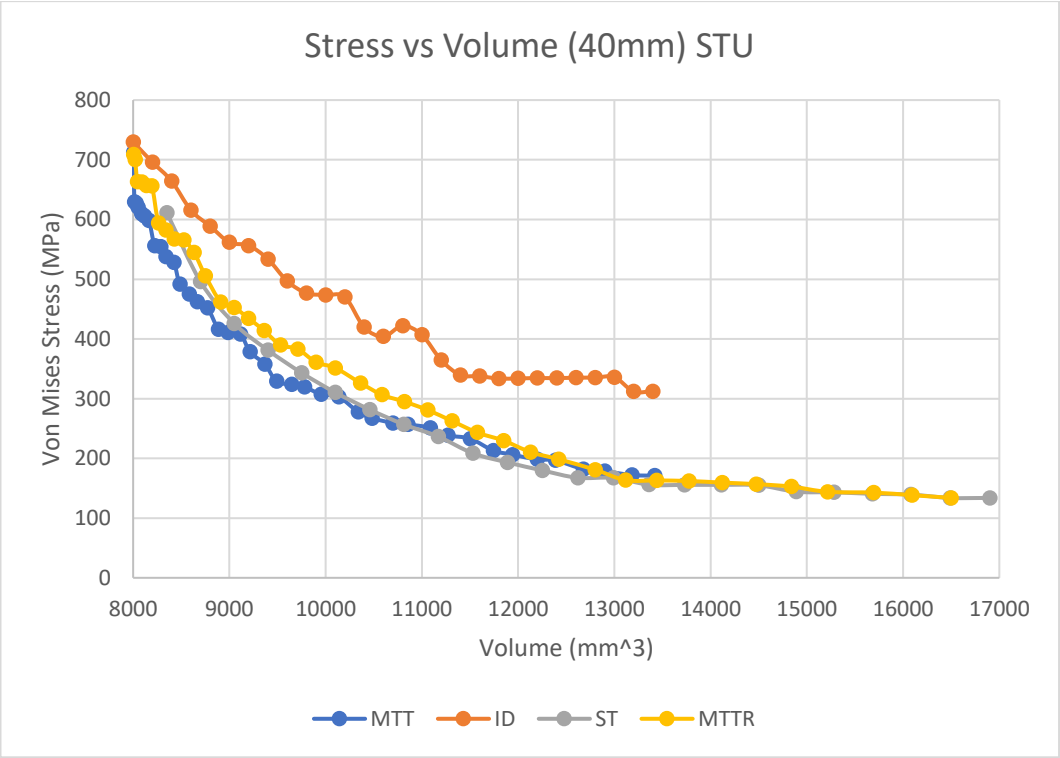

Stress Comparison ST (40mm)
700
600
500
400
300
200
100
0
Stress (MPa)
8000
9000
10000
11000
12000
13000
14000
15000
16000
17000
18000
Volume (mm^3)
DT
DB
UT
UB

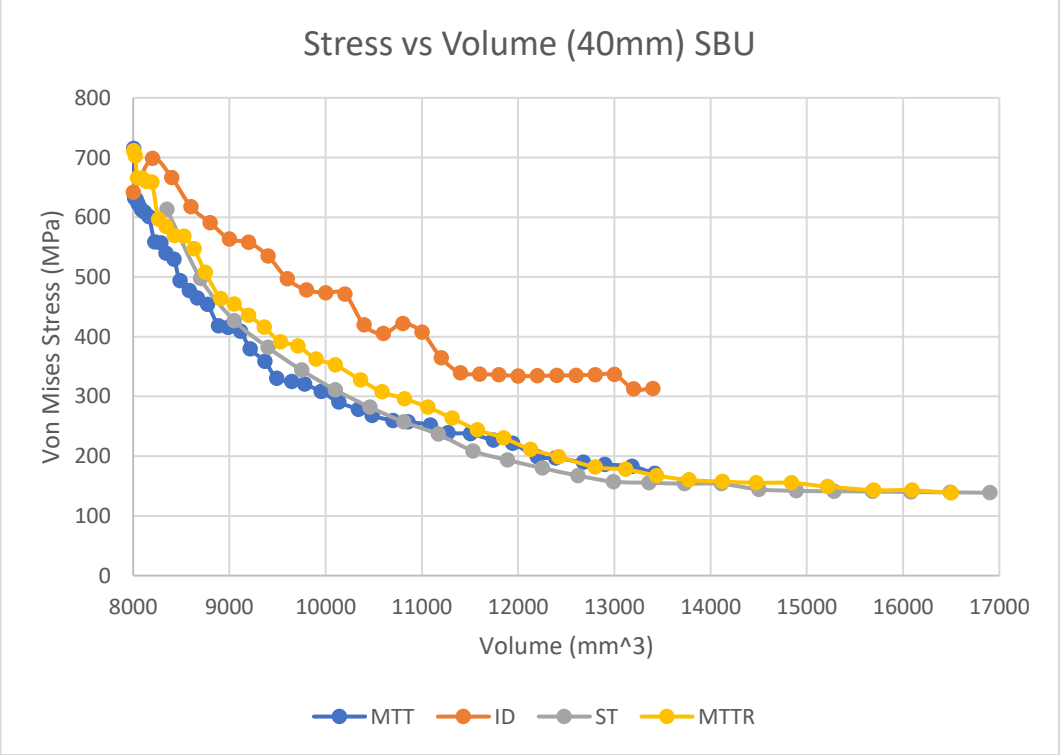

Stress Comparison MTTR (40mm)
800
700
600
500
400
300
200
100
0
Stress (MPa)
8000
9000
10000
11000
12000
13000
14000
15000
16000
17000
Volume (mm^3)
DT
DB
UT
UB


Stress vs Volume (40mm) STD
800
700
600
500
400
300
200
100
0
Von Mises Stress (MPa)
8000
9000
10000
11000
12000
13000
14000
15000
16000
17000
Volume (mm^3)
MTT
ID
ST
MTTR

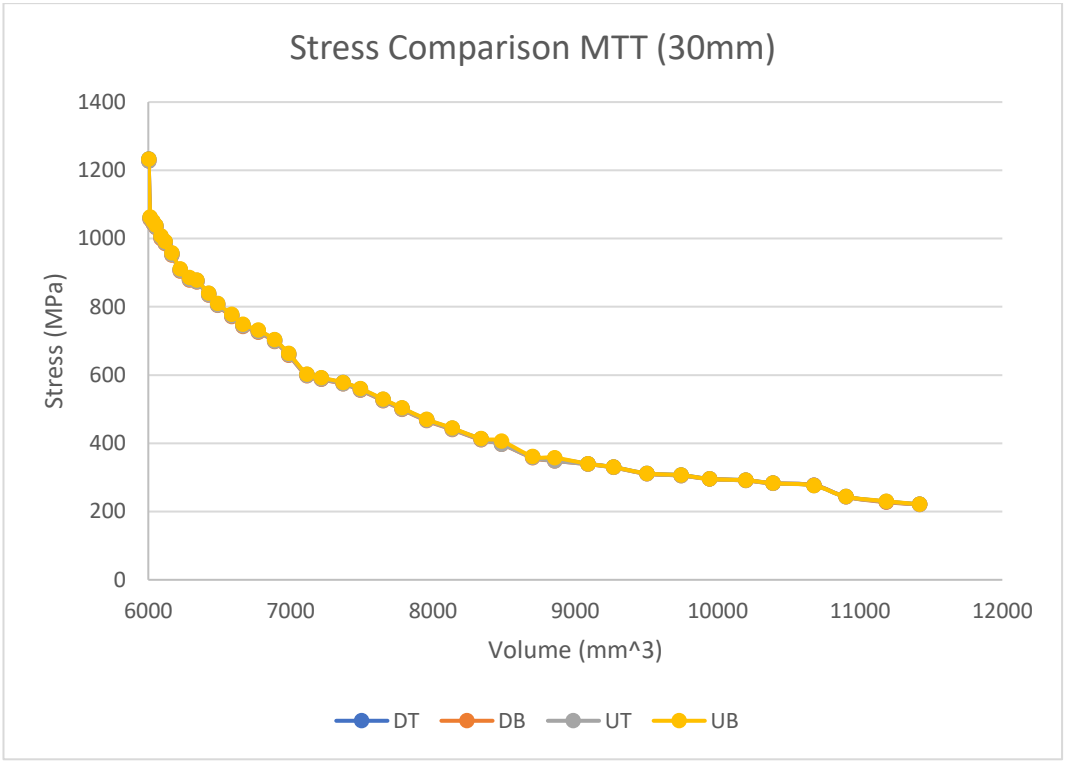

Stress vs Volume (40mm) SBD
Von Mises Stress (MPa)
800
700
600
500
400
300
200
100
0
8000
9000
10000
11000
12000
13000
14000
15000
16000
17000
Volume (mm^3)
MTT
ID
ST
MTTR

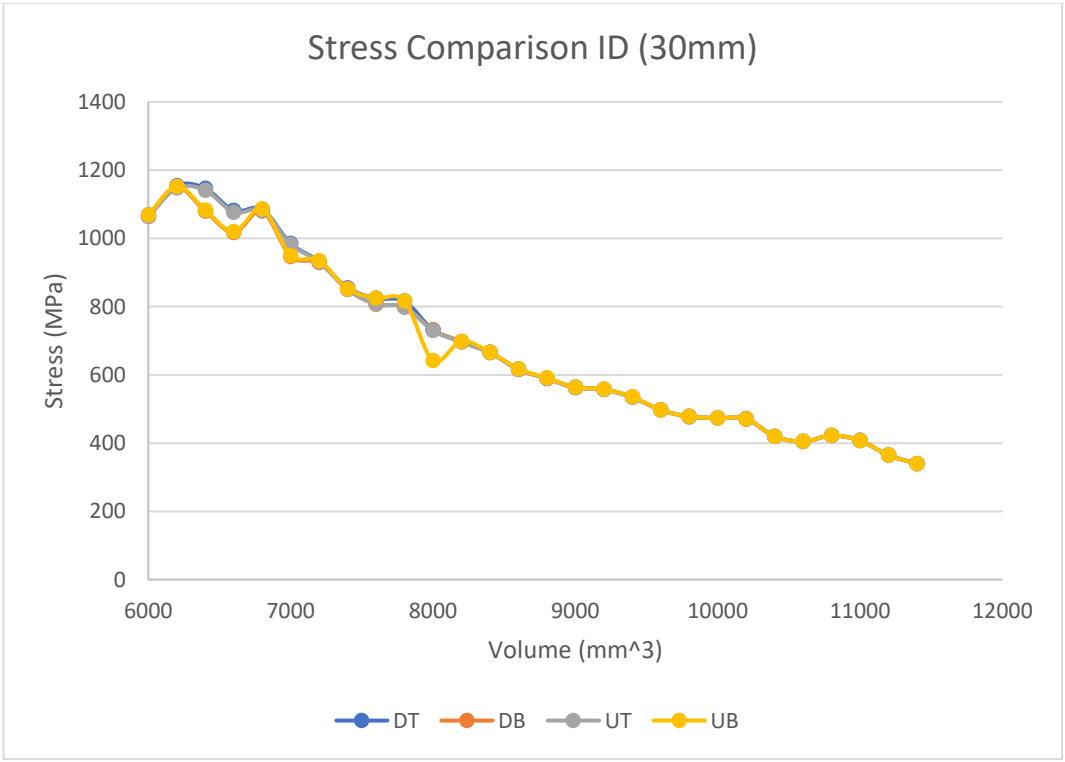

Stress vs Volume (40mm) TTD
Von Mises Stress (MPa)
300
250
200
150
100
50
0
8000
9000
10000
11000
12000
13000
14000
15000
16000
17000
Volume (mm^3)
MTT
ID
ST
MTTR

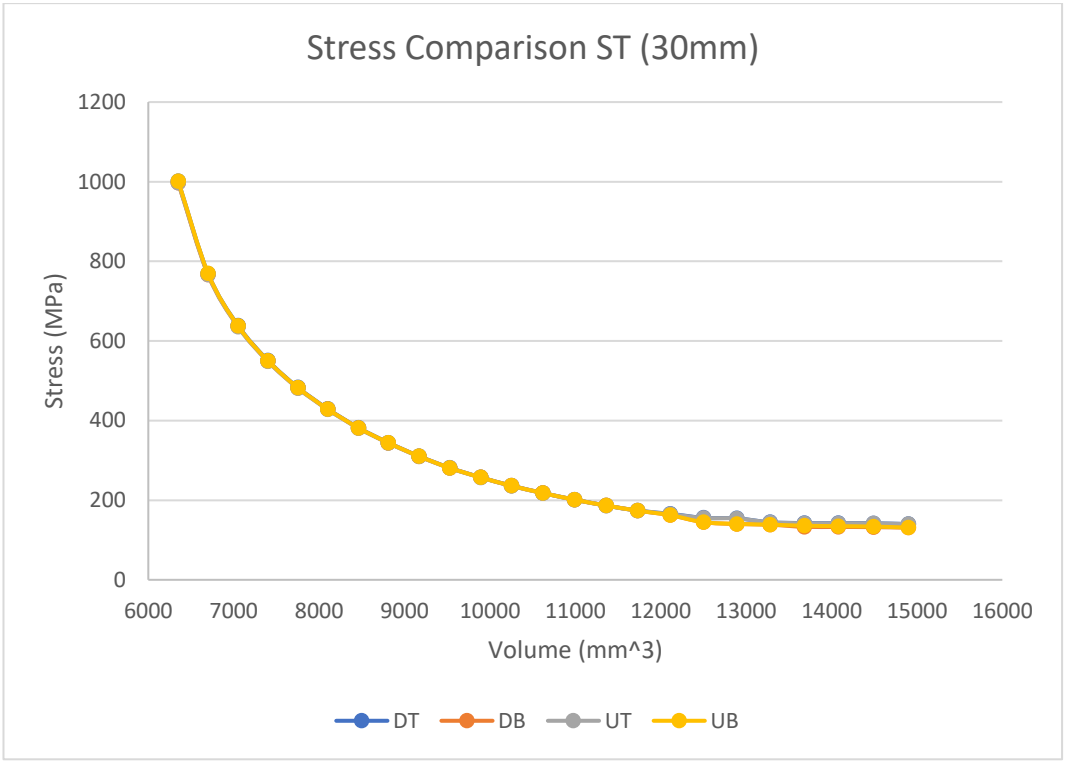


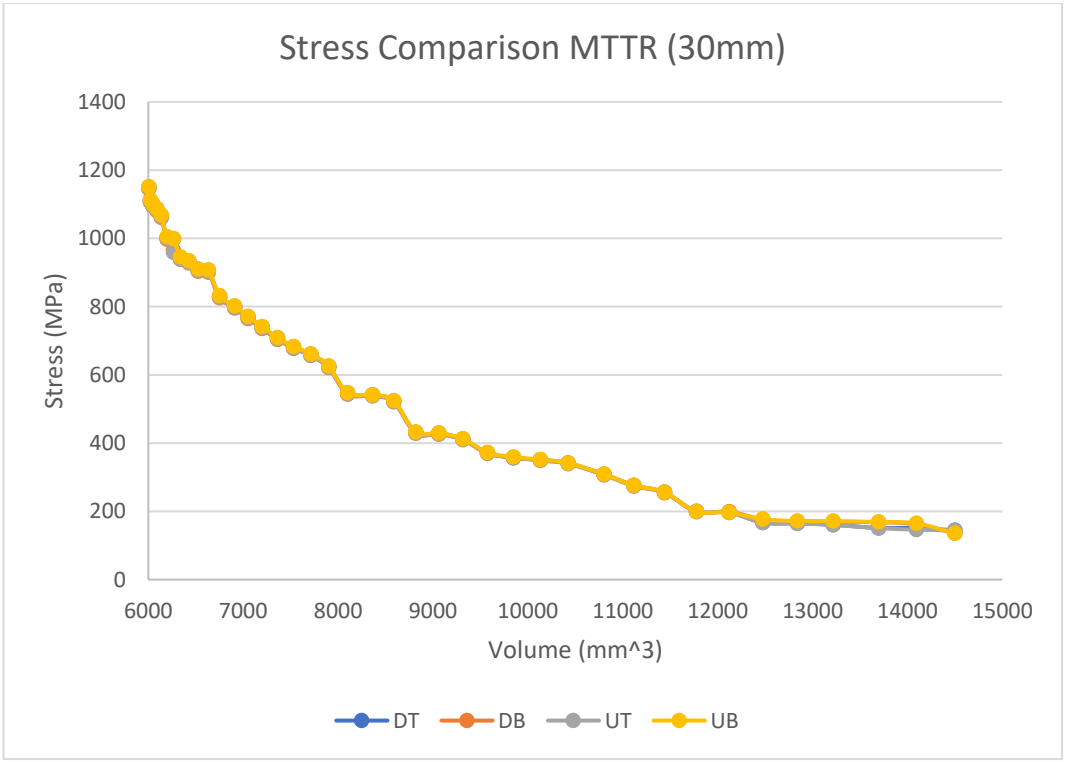


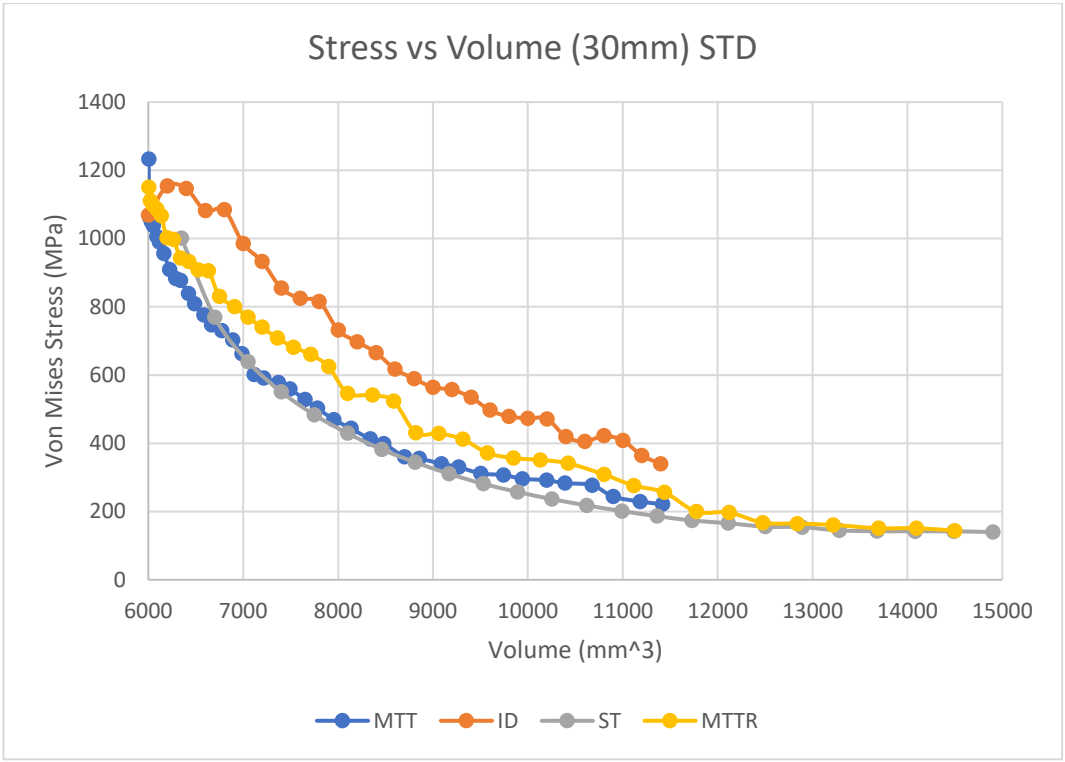
B.b.b.b Depth of 30mm

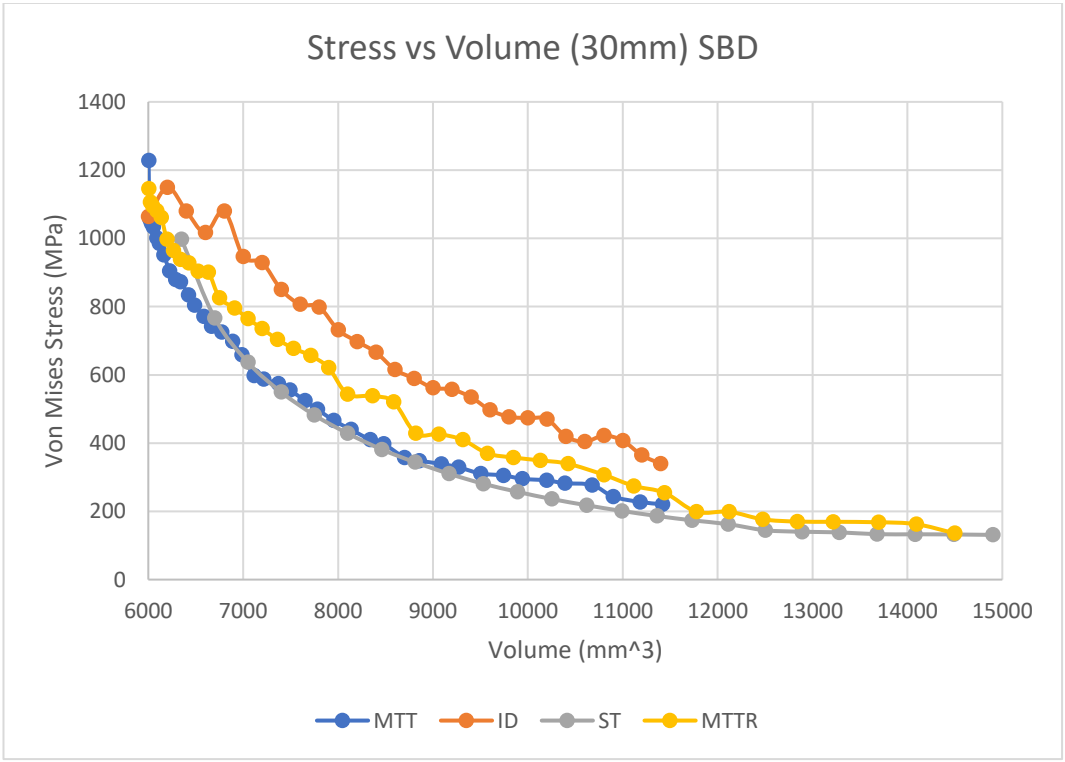

Stress Comparison MTT (30mm)
1400
1200
1000
800
600
400
200
0
Stress (MPa)
6000
7000
8000
9000
10000
11000
12000
Volume (mm^3)
DT
DB
UT
UB

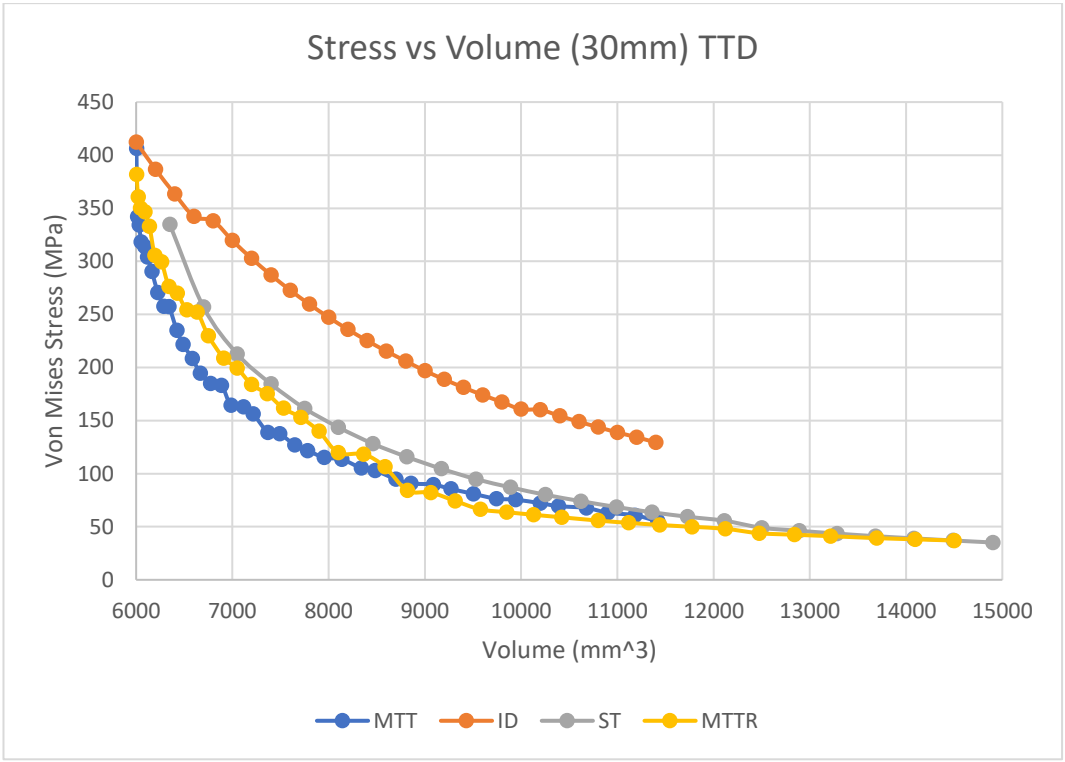

Stress Comparison ID (30mm)
1400
1200
1000
800
600
400
200
0
Stress (MPa)
6000
7000
8000
9000
10000
11000
12000
Volume (mm^3)
DT
DB
UT
UB

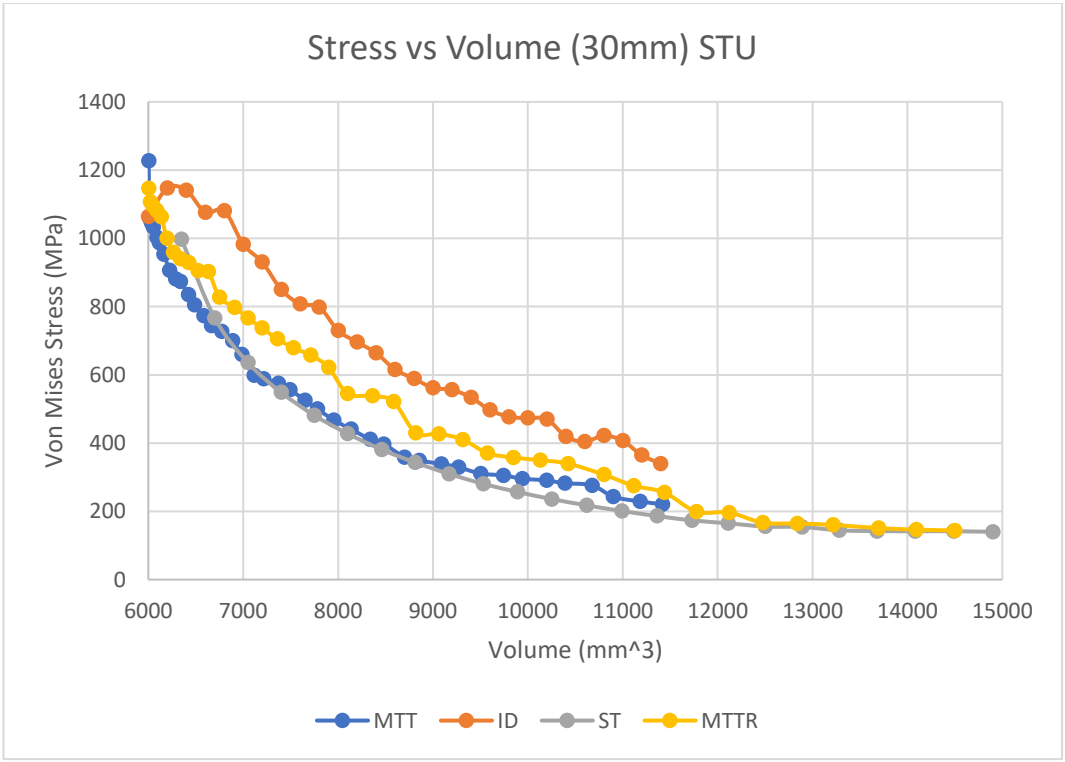

Stress Comparison ST (30mm)
1200
1000
800
600
400
200
0
Stress (MPa)
6000
7000
8000
9000
10000
11000
12000
13000
14000
15000
16000
Volume (mm^3)
DT
DB
UT
UB

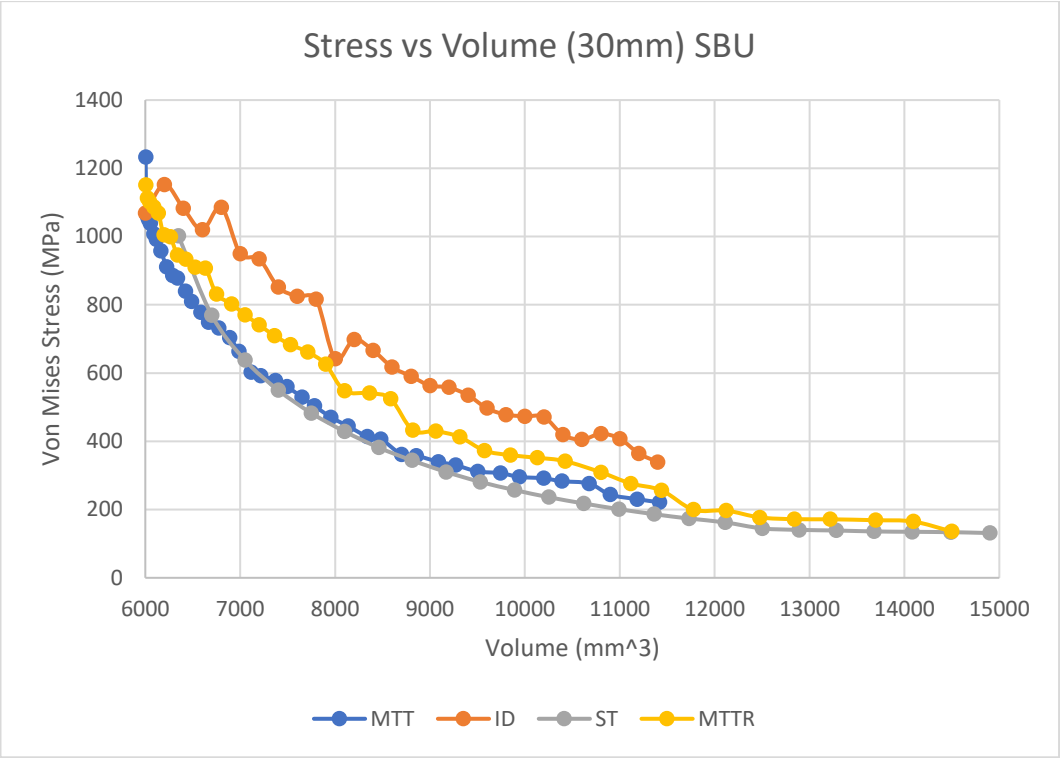

Stress Comparison MTTR (30mm)
1400
1200
1000
800
600
400
200
0
Stress (MPa)
6000
7000
8000
9000
10000
11000
12000
13000
14000
15000
Volume (mm^3)
DT
DB
UT
UB


Stress vs Volume (30mm) STD
Von Mises Stress (MPa)
1400
1200
1000
800
600
400
200
0
6000
7000
8000
9000
10000
11000
12000
13000
14000
15000
Volume (mm^3)
MTT
ID
ST
MTTR

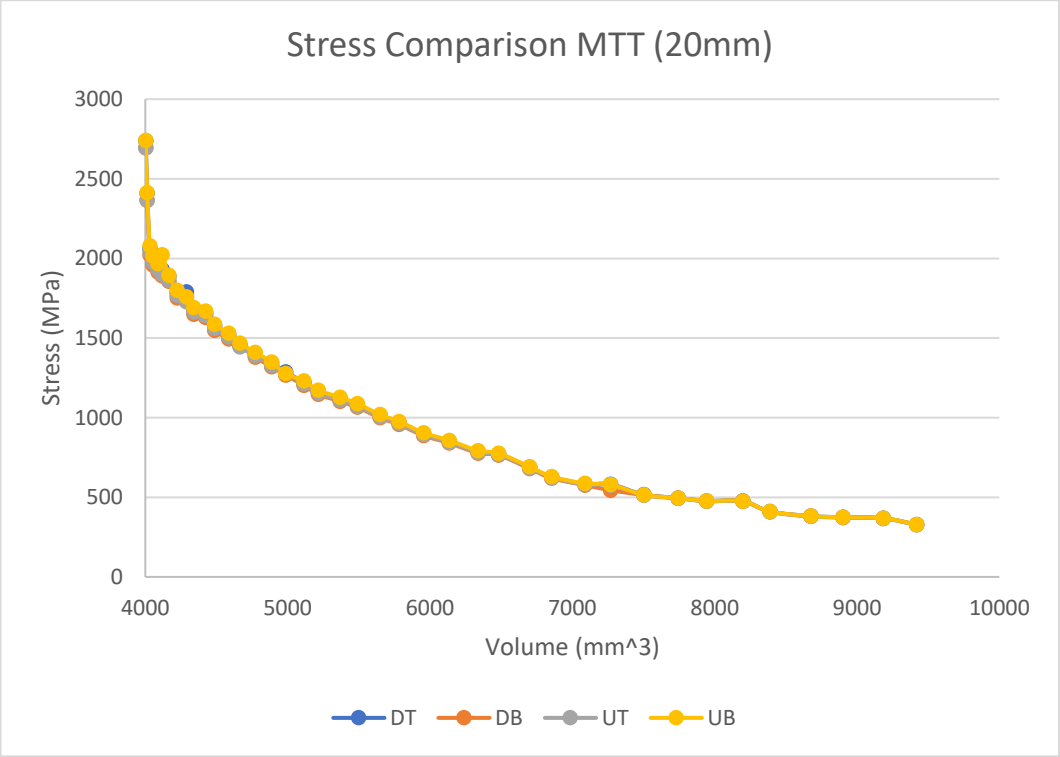

Stress vs Volume (30mm) SBD
Von Mises Stress (MPa)
1400
1200
1000
800
600
400
200
0
6000
7000
8000
9000
10000
11000
12000
13000
14000
15000
Volume (mm^3)
MTT
ID
ST
MTTR

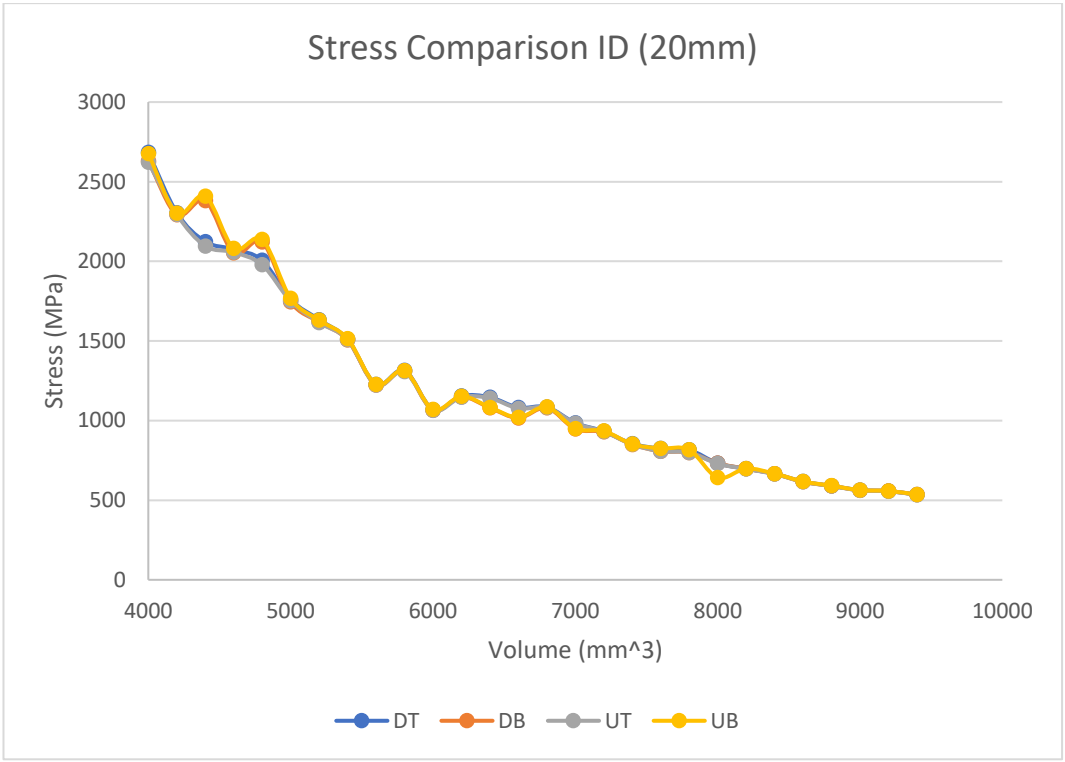

Stress vs Volume (30mm) TTD
Von Mises Stress (MPa)
450
400
350
300
250
200
150
100
50
0
6000
7000
8000
9000
10000
11000
12000
13000
14000
15000
Volume (mm^3)
MTT
ID
ST
MTTR

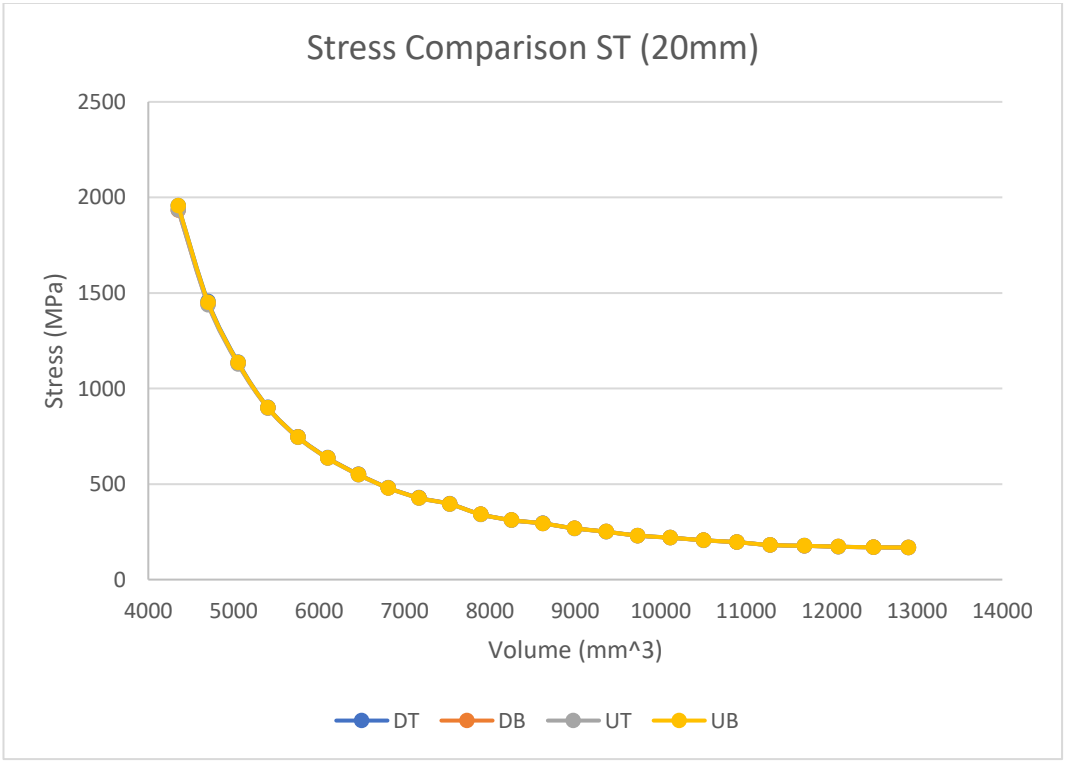

Stress vs Volume (30mm) STU
Von Mises Stress (MPa)
1400
1200
1000
800
600
400
200
0
6000
7000
8000
9000
10000
11000
12000
13000
14000
15000
Volume (mm^3)
MTT
ID
ST
MTTR

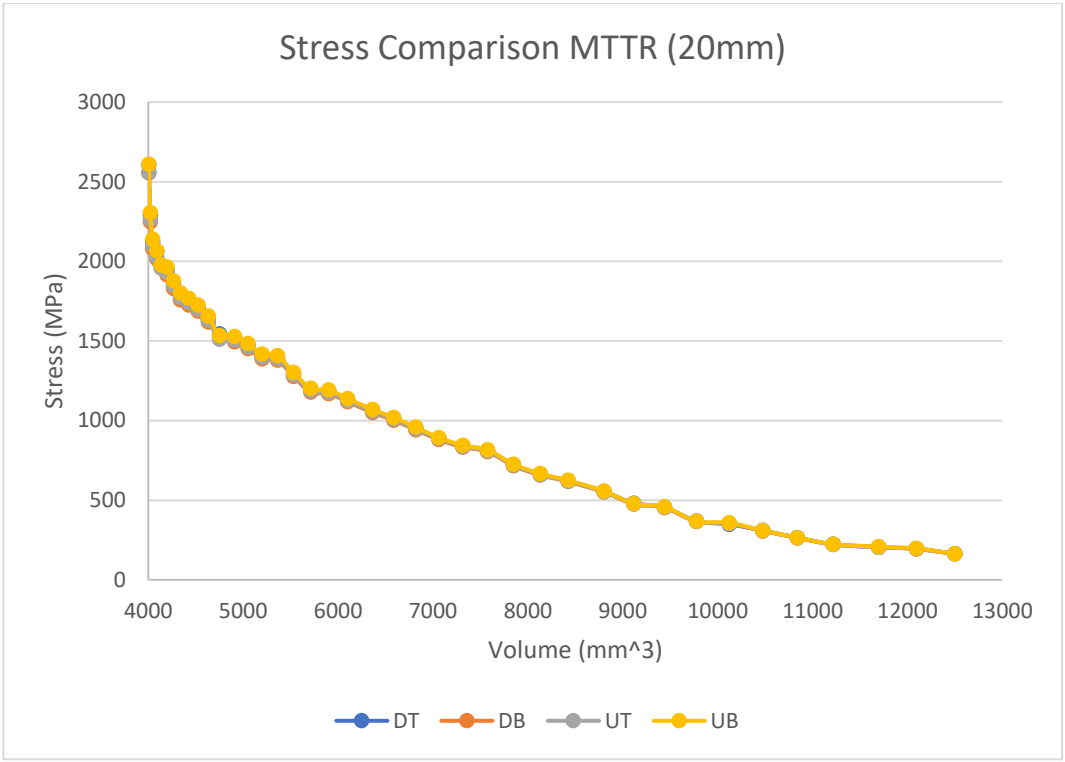


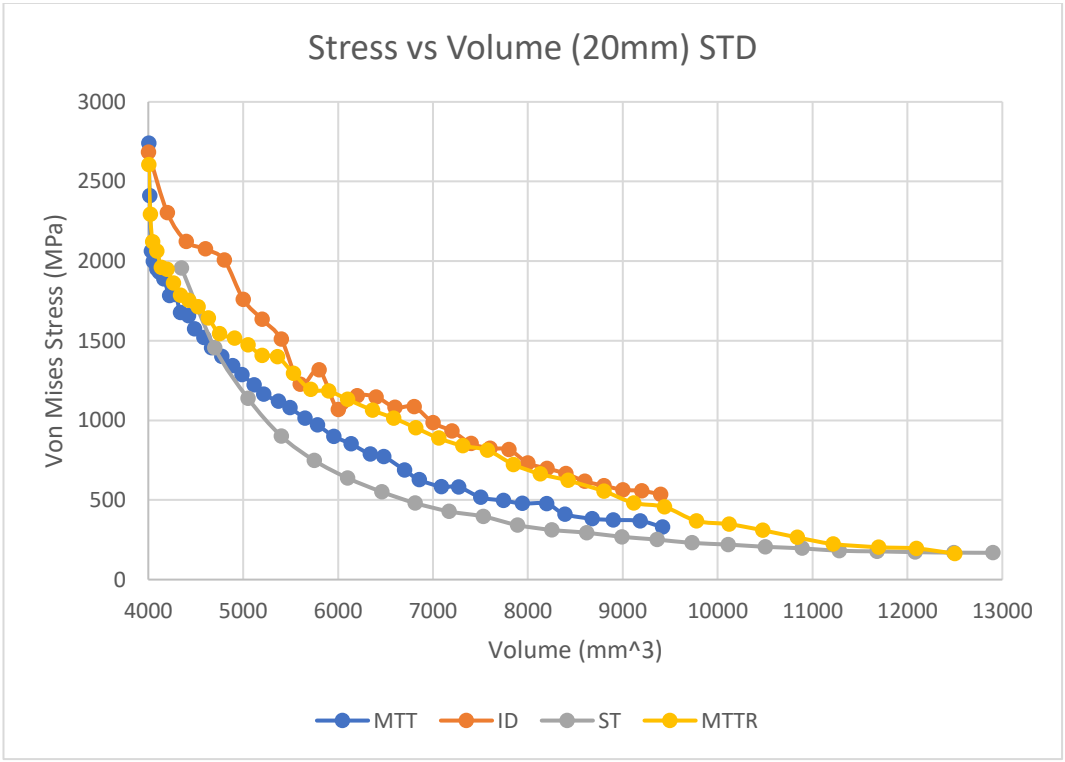
B.b.b.c Depth of 20mm

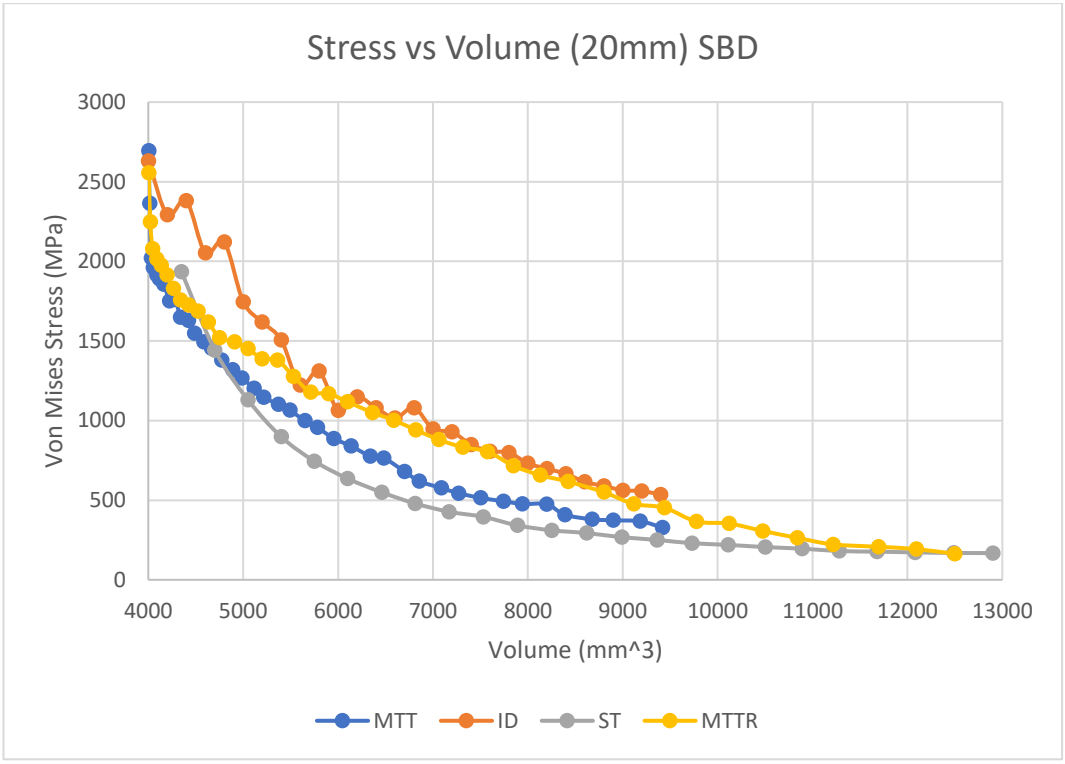


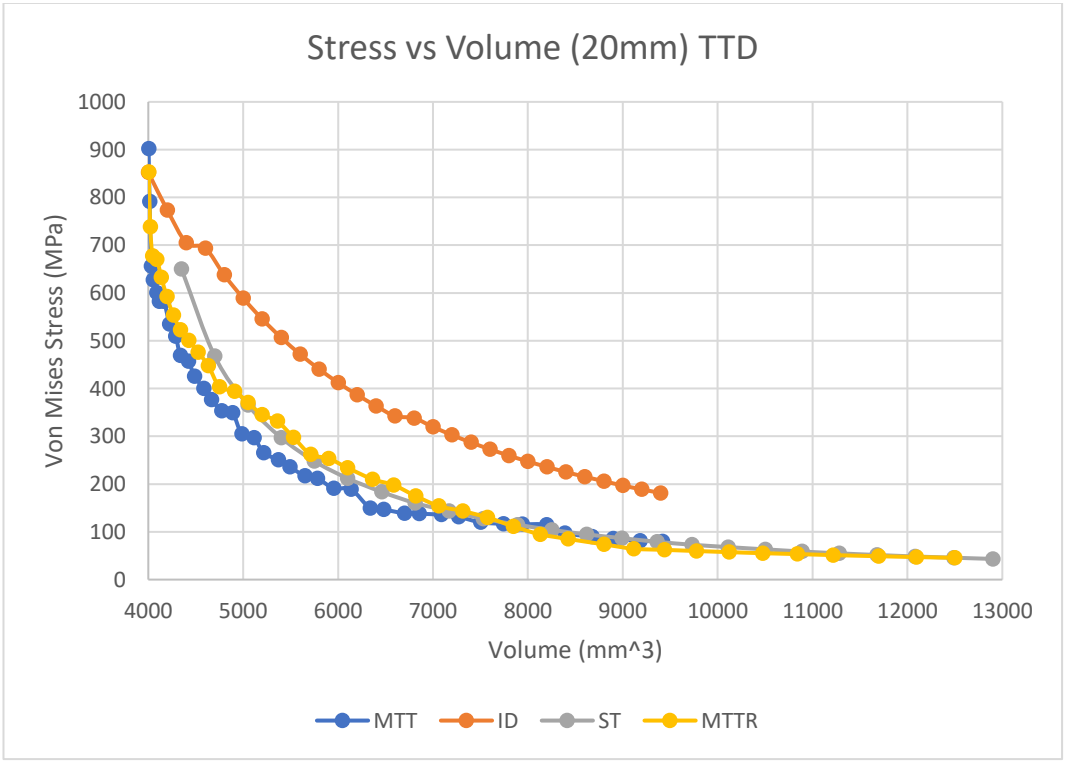

Stress Comparison ID (20mm)
3000
2500
2000
1500
1000
500
0
Stress (MPa)
4000
5000
6000
7000
8000
9000
10000
Volume (mm^3)
DT
DB
UT
UB

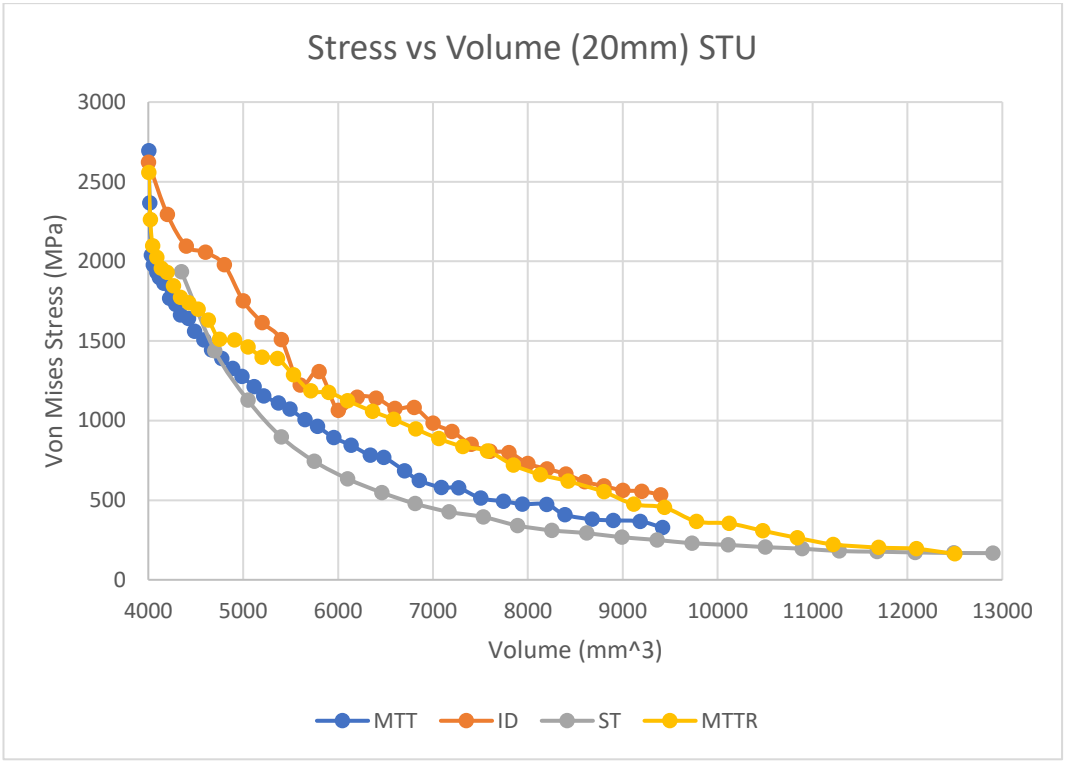

Stress Comparison ST (20mm)
2500
2000
1500
1000
500
0
Stress (MPa)
4000
5000
6000
7000
8000
9000
10000
11000
12000
13000
14000
Volume (mm^3)
DT
DB
UT
UB

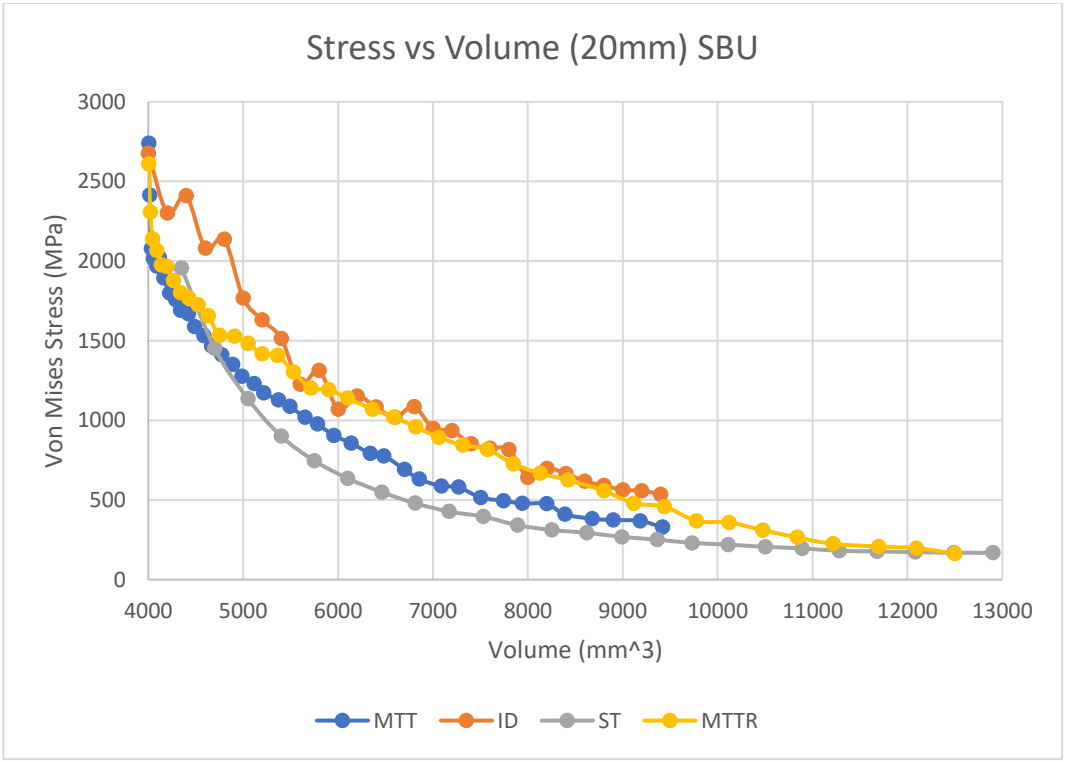

Stress Comparison MTTR (20mm)
Stress (MPa)
3000
2500
2000
1500
1000
500
0
4000
5000
6000
7000
8000
9000
10000
11000
12000
13000
Volume (mm^3)
DT
DB
UT
UB


Stress vs Volume (20mm) STD
Von Mises Stress (MPa)
3000
2500
2000
1500
1000
500
0
4000
5000
6000
7000
8000
9000
10000
11000
12000
13000
Volume (mm^3)
MTT
ID
ST
MTTR


Stress vs Volume (20mm) SBD
Von Mises Stress (MPa)
3000
2500
2000
1500
1000
500
0
4000
5000
6000
7000
8000
9000
10000
11000
12000
13000
Volume (mm^3)
MTT
ID
ST
MTTR


Stress vs Volume (20mm) TTD
Von Mises Stress (MPa)
1000
900
800
700
600
500
400
300
200
100
0
4000
5000
6000
7000
8000
9000
10000
11000
12000
13000
Volume (mm^3)
MTT
ID
ST
MTTR


Stress vs Volume (20mm) STU
Von Mises Stress (MPa)
3000
2500
2000
1500
1000
500
0
4000
5000
6000
7000
8000
9000
10000
11000
12000
13000
Volume (mm^3)
MTT
ID
ST
MTTR


Stress vs Volume (20mm) SBU
Von Mises Stress (MPa)
3000
2500
2000
1500
1000
500
0
4000
5000
6000
7000
8000
9000
10000
11000
12000
13000
Volume (mm^3)
MTT
ID
ST
MTTR

Appendix C. Topology Optimisation of a Cantilever Beam

C.a. Topology Plots

Every cantilever beam geometry shown in this section consists of two figures. The first is the retained topology plot, and the second is the topology plot.

C.a.a Depth of 20mm

C.a.a.a Method of Tensile Triangles (MTT)

25mm, 50mm, 75mm, 100mm, 125mm, 150mm, 175mm, 200mm

C.a.a.b Method of Tensile Triangles Rule of Thumb (MTTR)

20mm, 40mm, 60mm, 80mm, 100mm, 120mm, 140mm, 160mm, 200mm

C.a.a.c Standard Triangle (ST)

1mm, 2mm, 4mm, 6mm, 9mm, 12mm, 23mm, 24mm

C.a.b Depth of 30mm

C.a.b.a Method of Tensile Triangles (MTT)

25mm, 50mm, 75mm, 100mm, 125mm, 150mm, 175mm, 200mm

C.a.b.b Method of Tensile Triangles Rule of Thumb (MTTR)

20mm, 40mm, 60mm, 80mm, 100mm, 120mm, 140mm, 160mm, 200mm

C.a.b.c Standard Triangle (ST)

1mm, 2mm, 4mm, 6mm, 9mm, 12mm, 23mm, 24mm

C.a.c Depth of 40mm

C.a.c.a Method of Tensile Triangles (MTT)

25mm, 50mm, 75mm, 100mm, 125mm, 150mm, 175mm, 200mm

C.a.c.b Method of Tensile Triangles Rule of Thumb (MTTR)

20mm, 40mm, 60mm, 80mm, 100mm, 120mm, 140mm, 160mm, 200mm

C.a.c.c Standard Triangle (ST)

1mm, 2mm, 4mm, 6mm, 9mm, 12mm, 23mm, 24mm

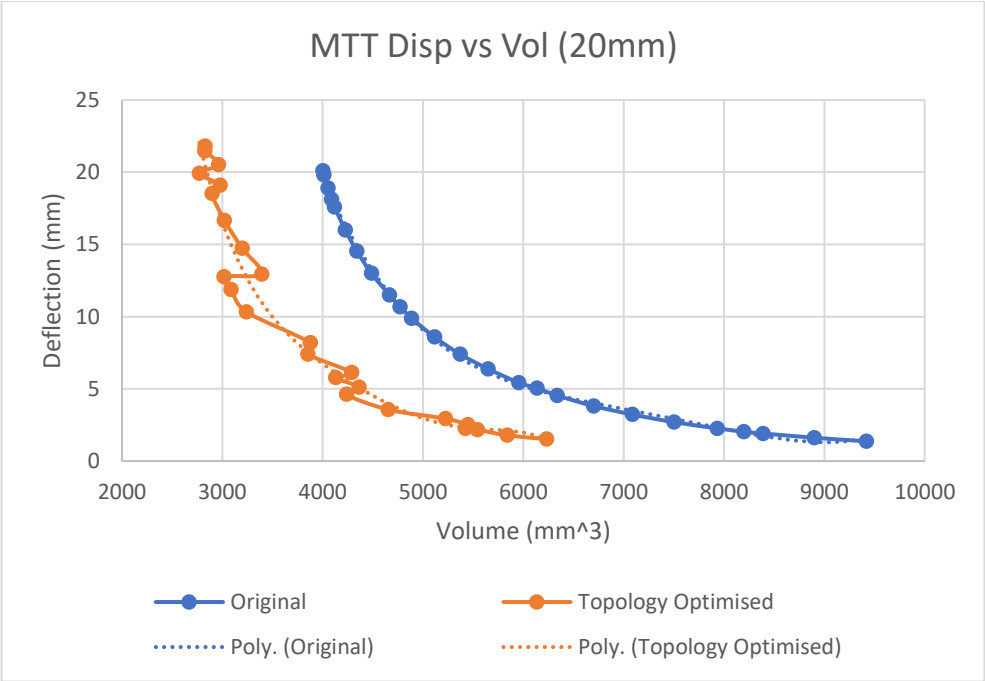
C.a.d Increased Depth (20mm to 67mm)

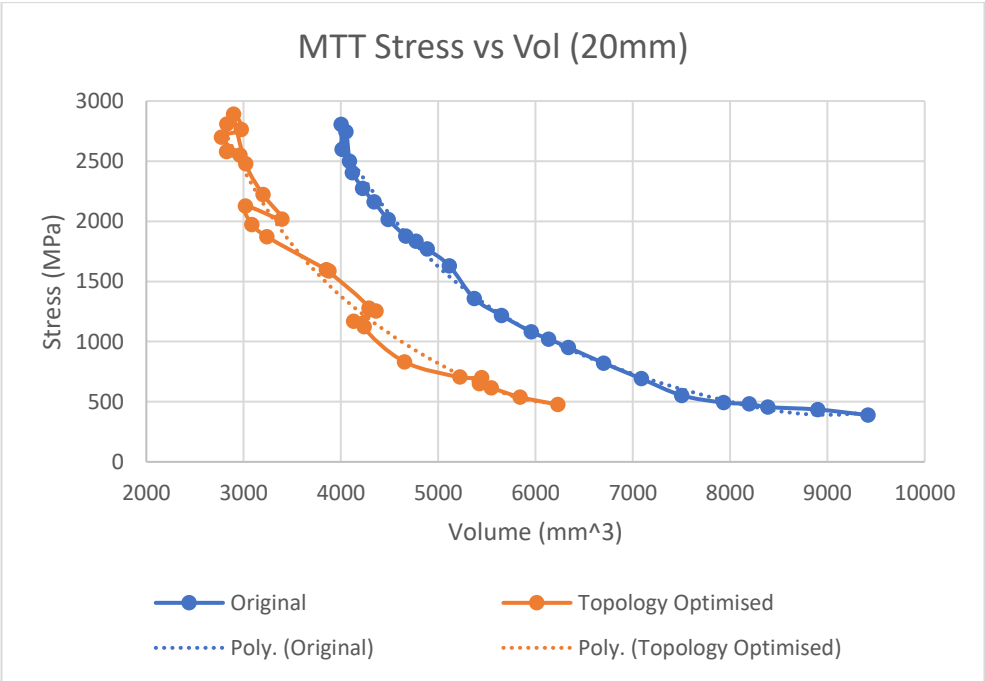
20mm, 25mm, 30mm, 35mm, 40mm, 45mm, 47mm, 50mm, 55mm, 57mm, 60mm, 65mm, 67mm

C.b. Topology Optimised Models

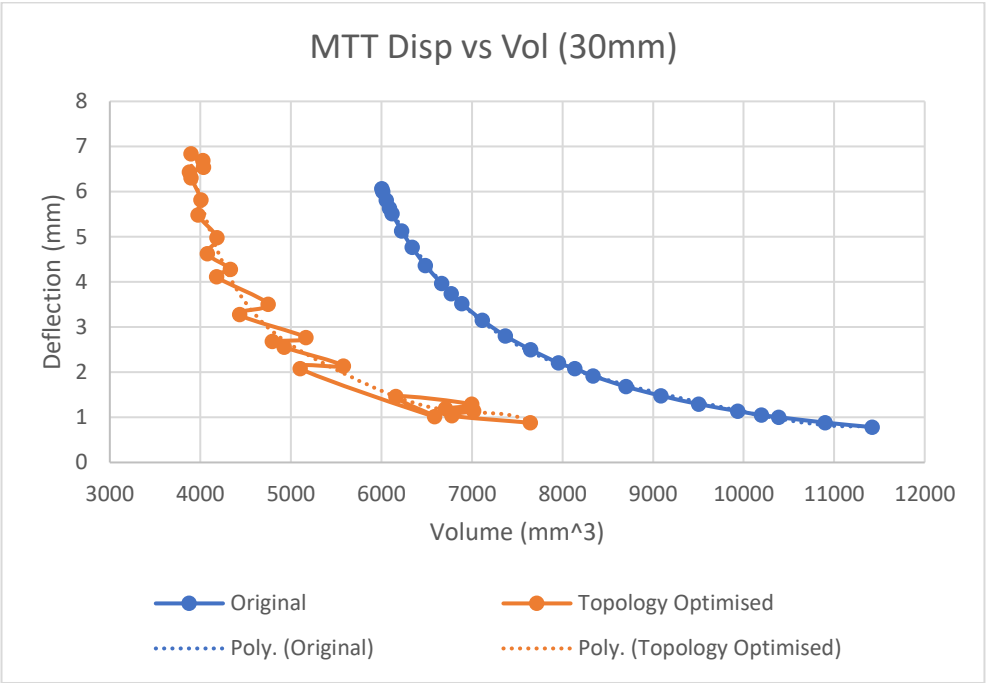
C.b.a Method of Tensile Triangles (MTT)

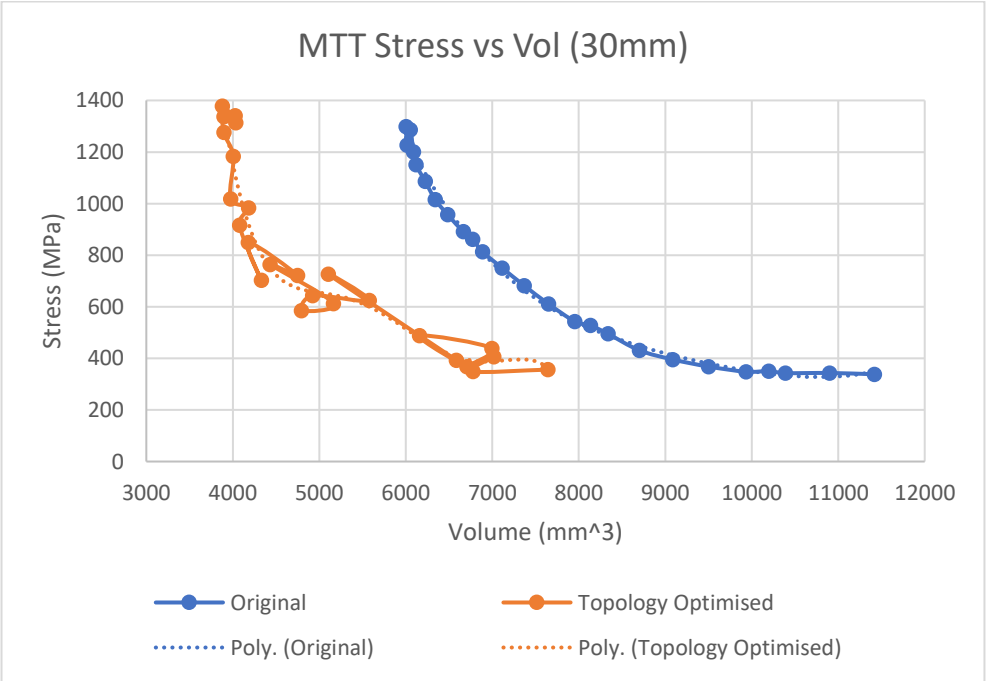
20mm



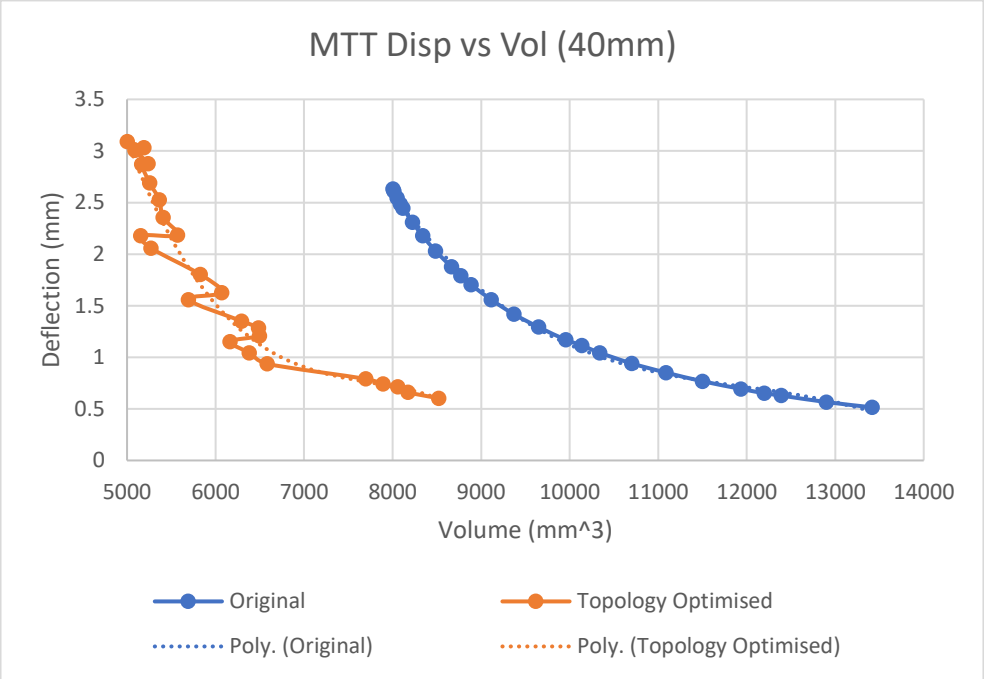


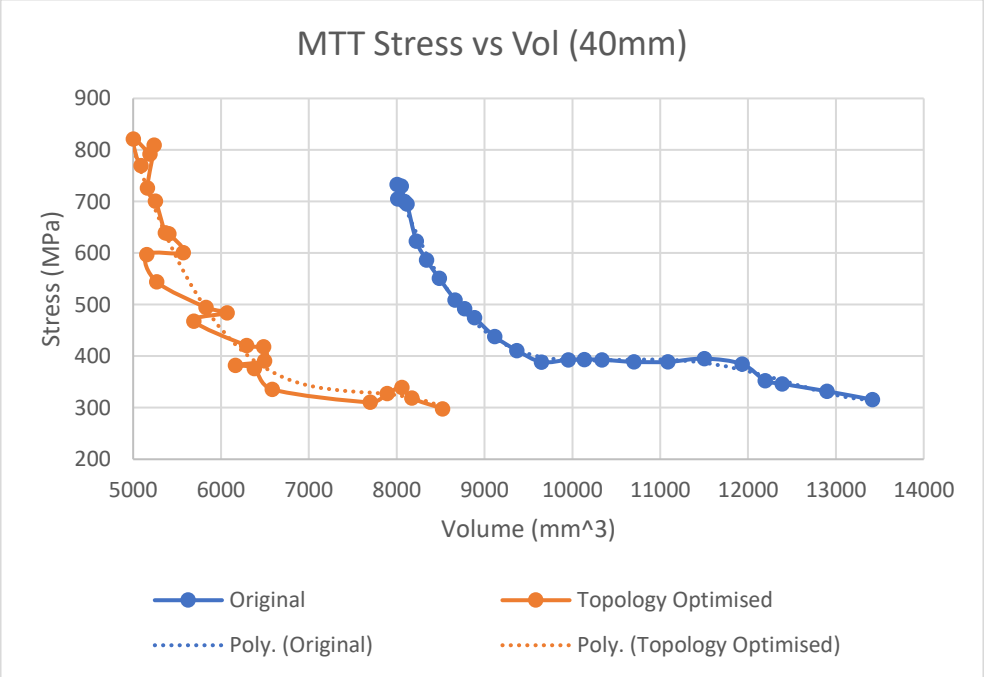
30mm


MTT Disp vs Vol (30mm)
Deflection (mm)
0
1
2
3
4
5
6
7
8
3000
4000
5000
6000
7000
8000
9000
10000
11000
12000
Volume (mm^3)
Original
Topology Optimised
Poly. (Original)
Poly. (Topology Optimised)


MTT Stress vs Vol (30mm)
Stress (MPa)
0
200
400
600
800
1000
1200
1400
3000
4000
5000
6000
7000
8000
9000
10000
11000
12000
Volume (mm^3)
Original
Topology Optimised
Poly. (Original)
Poly. (Topology Optimised)

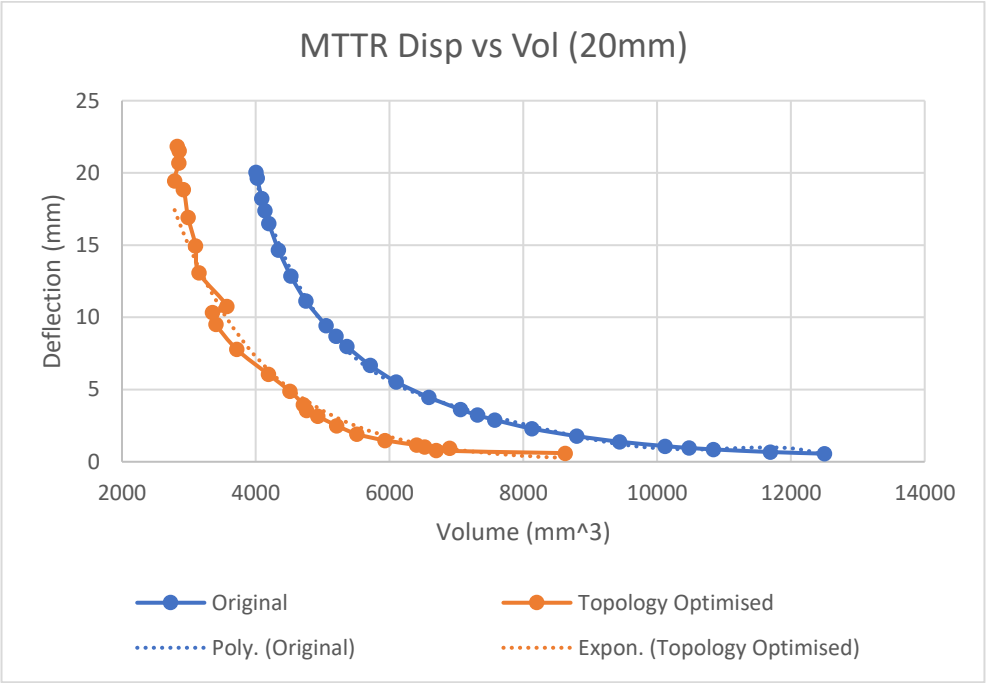
40mm

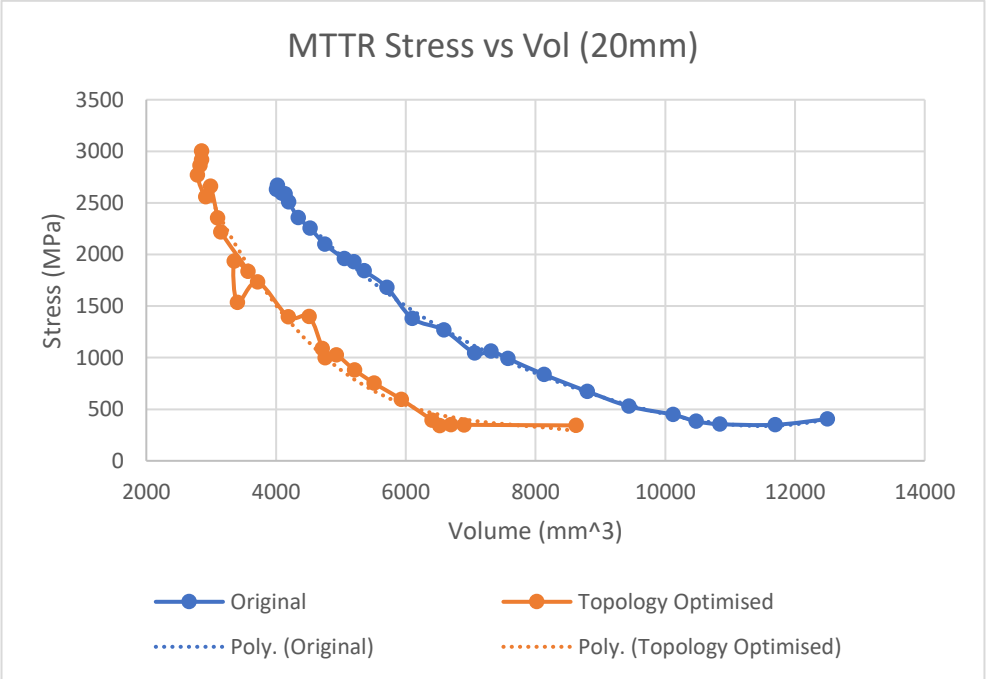

MTT Disp vs Vol (40mm)
Deflection (mm)
3.5
3
2.5
2
1.5
1
0.5
0
5000
6000
7000
8000
9000
10000
11000
12000
13000
14000
Volume (mm^3)
Original
Topology Optimised
Poly. (Original)
Poly. (Topology Optimised)


MTT Stress vs Vol (40mm)
Stress (MPa)
900
800
700
600
500
400
300
200
5000
6000
7000
8000
9000
10000
11000
12000
13000
14000
Volume (mm^3)
Original
Topology Optimised
Poly. (Original)
Poly. (Topology Optimised)

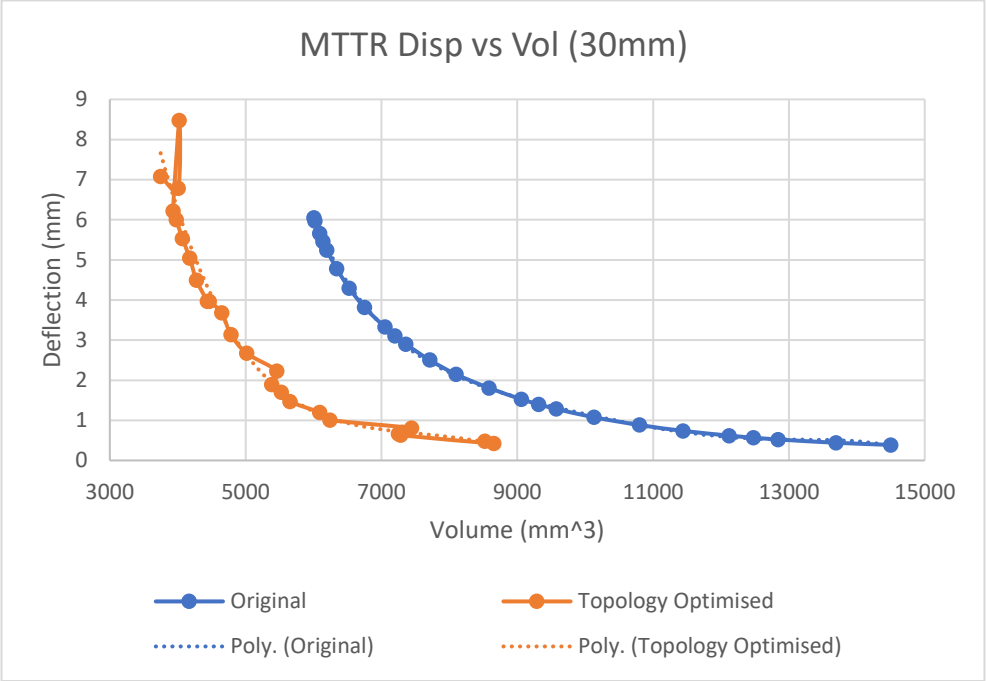
C.b.b Method of Tensile Triangles Rule of Thumb (MTTR)

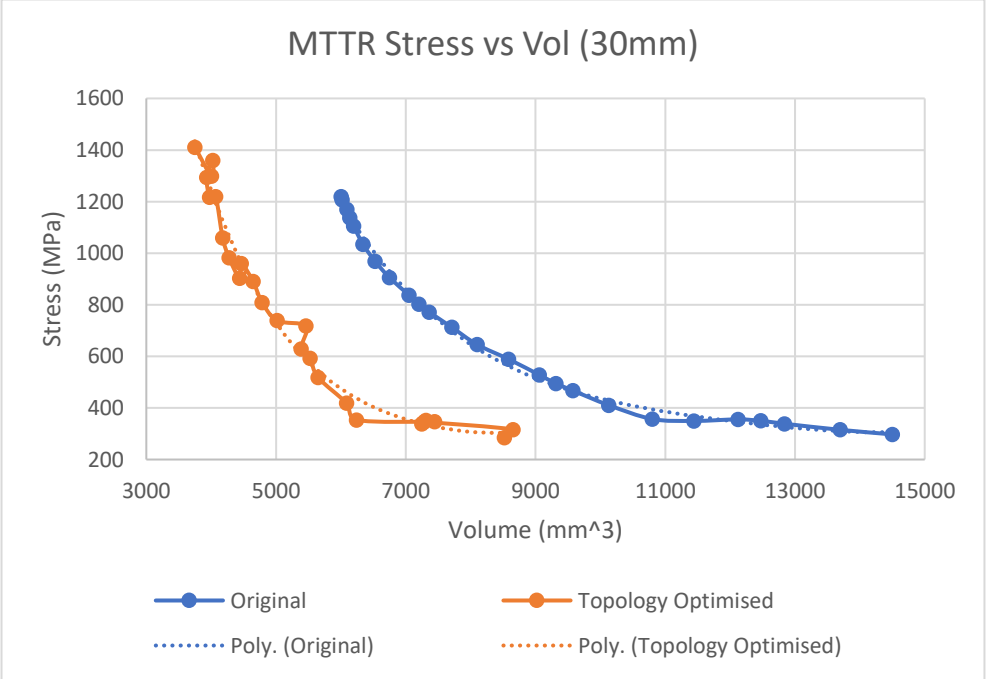
20mm



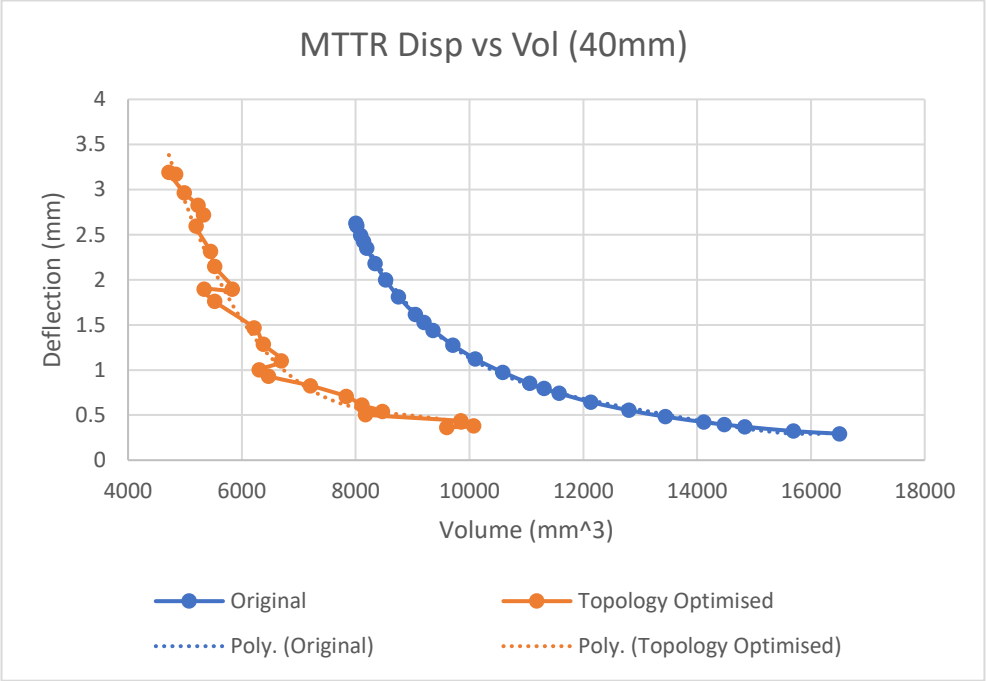


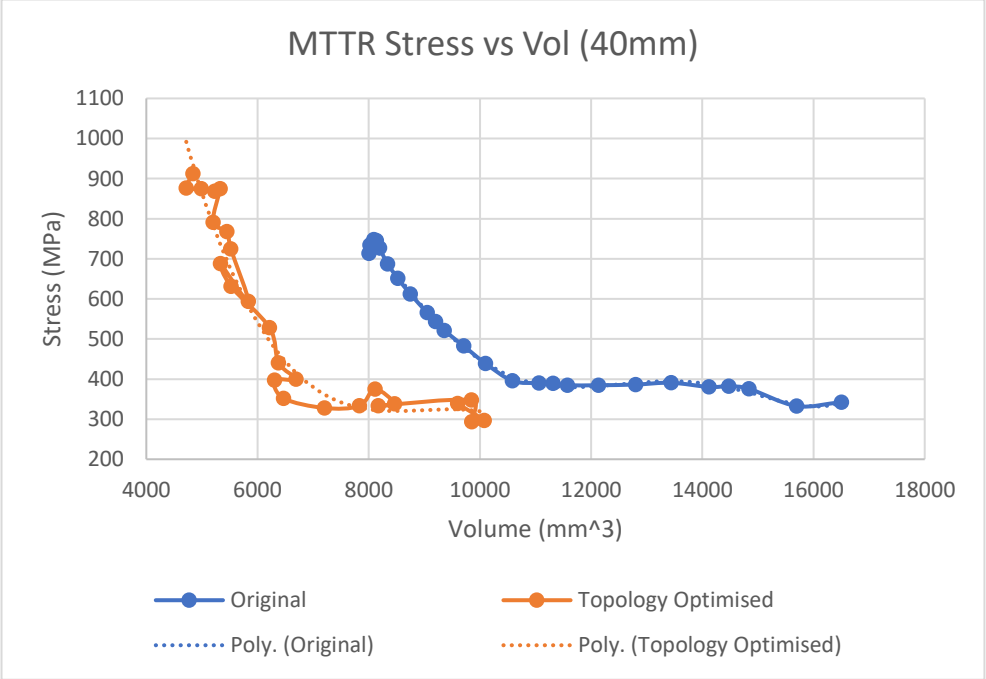
30mm


MTTR Disp vs Vol (30mm)
Deflection (mm)
0
1
2
3
4
5
6
7
8
9
3000
5000
7000
9000
11000
13000
15000
Volume (mm^3)
Original
Topology Optimised
Poly. (Original)
Poly. (Topology Optimised)


MTTR Stress vs Vol (30mm)
Stress (MPa)
200
400
600
800
1000
1200
1400
1600
3000
5000
7000
9000
11000
13000
15000
Volume (mm^3)
Original
Topology Optimised
Poly. (Original)
Poly. (Topology Optimised)

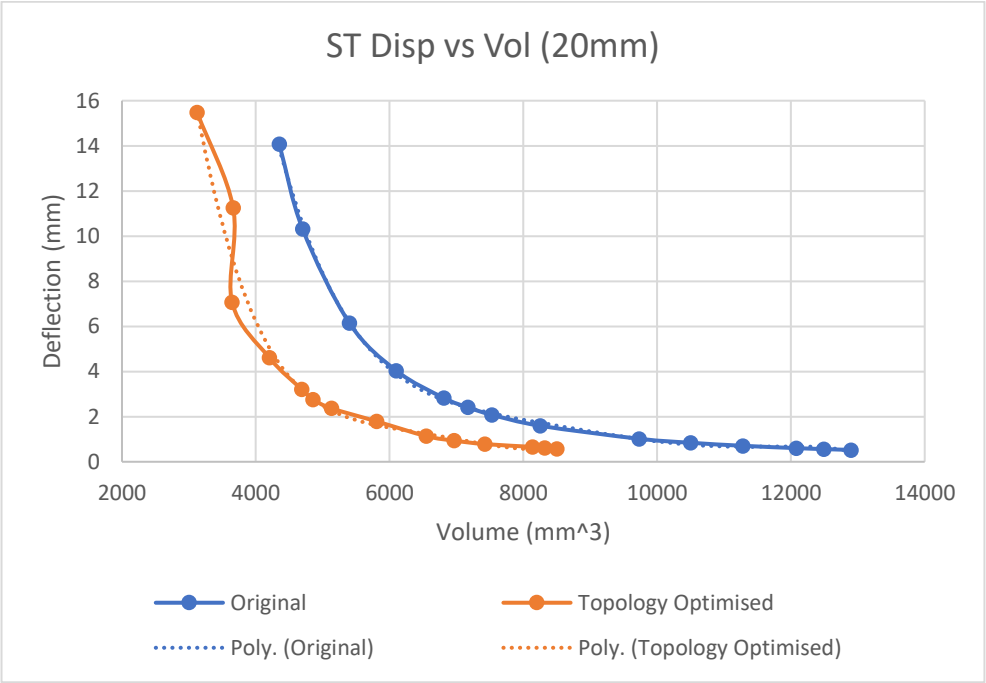
40mm

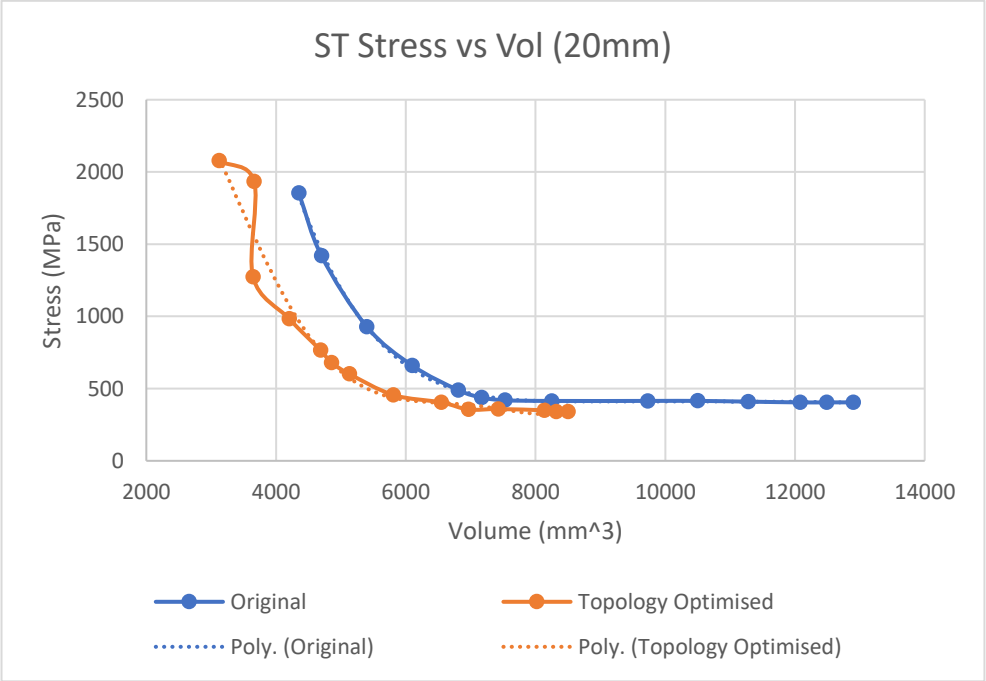

MTTR Disp vs Vol (40mm)
Deflection (mm)
4
3.5
3
2.5
2
1.5
1
0.5
0
4000
6000
8000
10000
12000
14000
16000
18000
Volume (mm^3)
Original
Topology Optimised
Poly. (Original)
Poly. (Topology Optimised)


MTTR Stress vs Vol (40mm)
Stress (MPa)
1100
1000
900
800
700
600
500
400
300
200
4000
6000
8000
10000
12000
14000
16000
18000
Volume (mm^3)
Original
Topology Optimised
Poly. (Original)
Poly. (Topology Optimised)

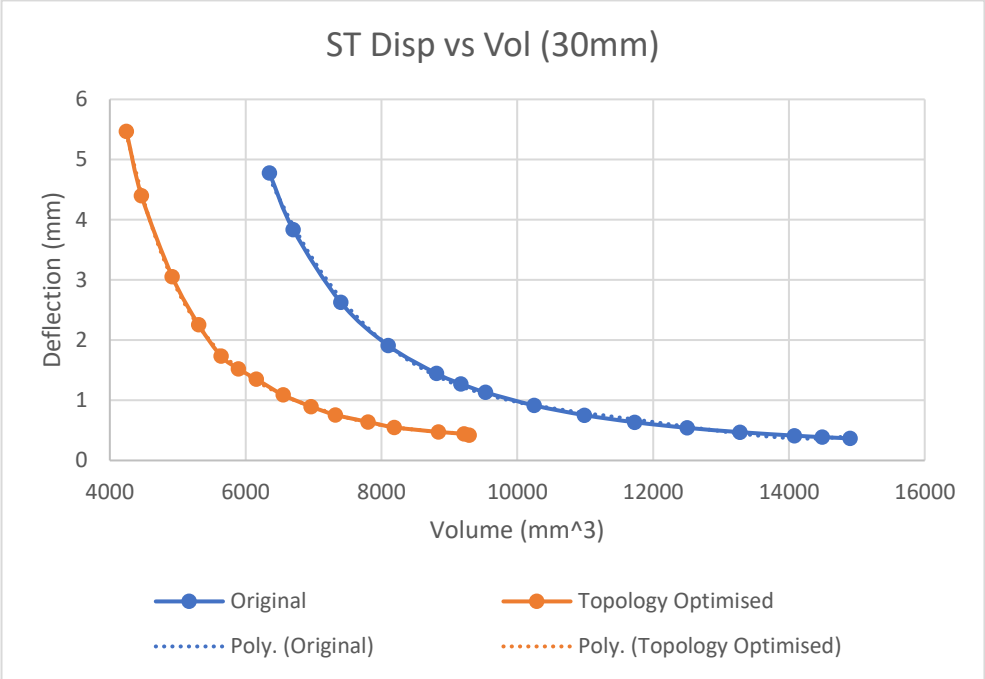
C.b.c Standard Triangle (ST)

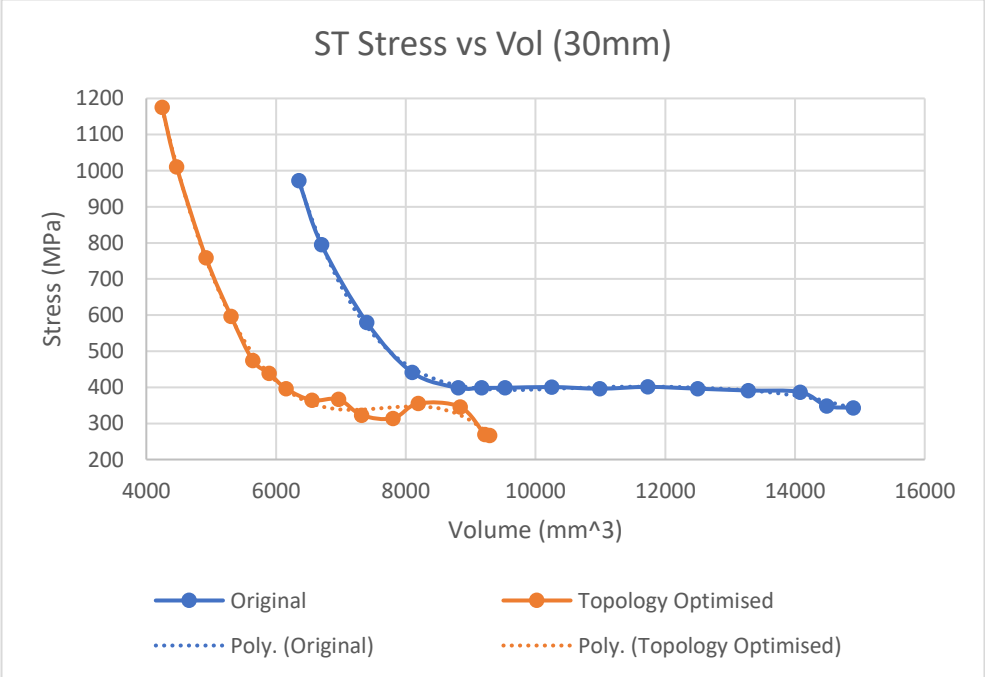
20mm



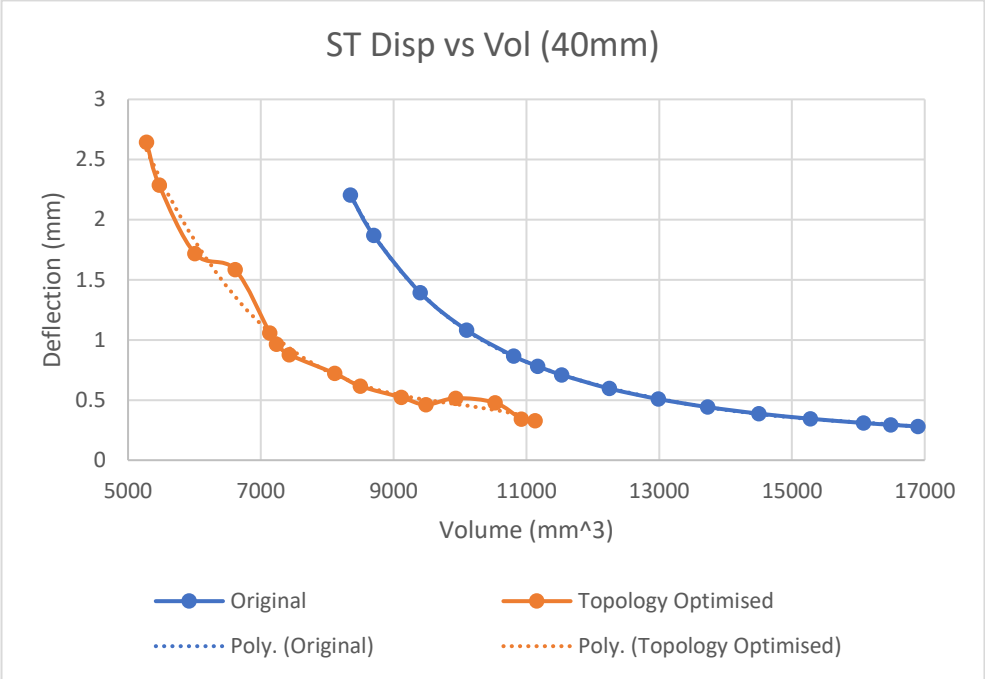


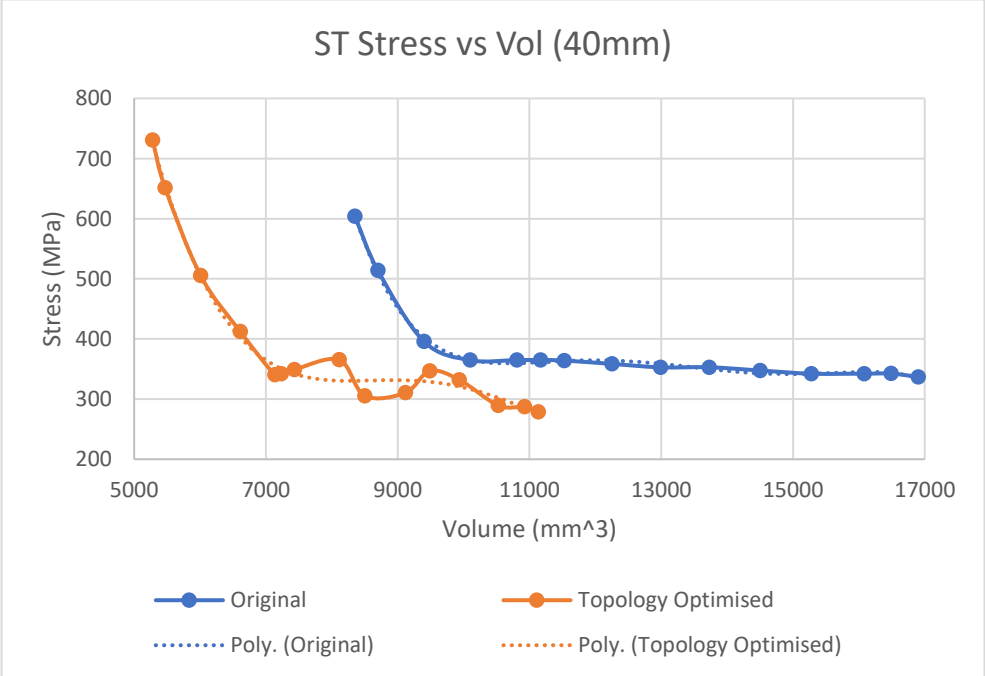
30mm


ST Disp vs Vol (30mm)
Deflection (mm)
0
1
2
3
4
5
6
4000
6000
8000
10000
12000
14000
16000
Volume (mm^3)
Original
Topology Optimised
Poly. (Original)
Poly. (Topology Optimised)

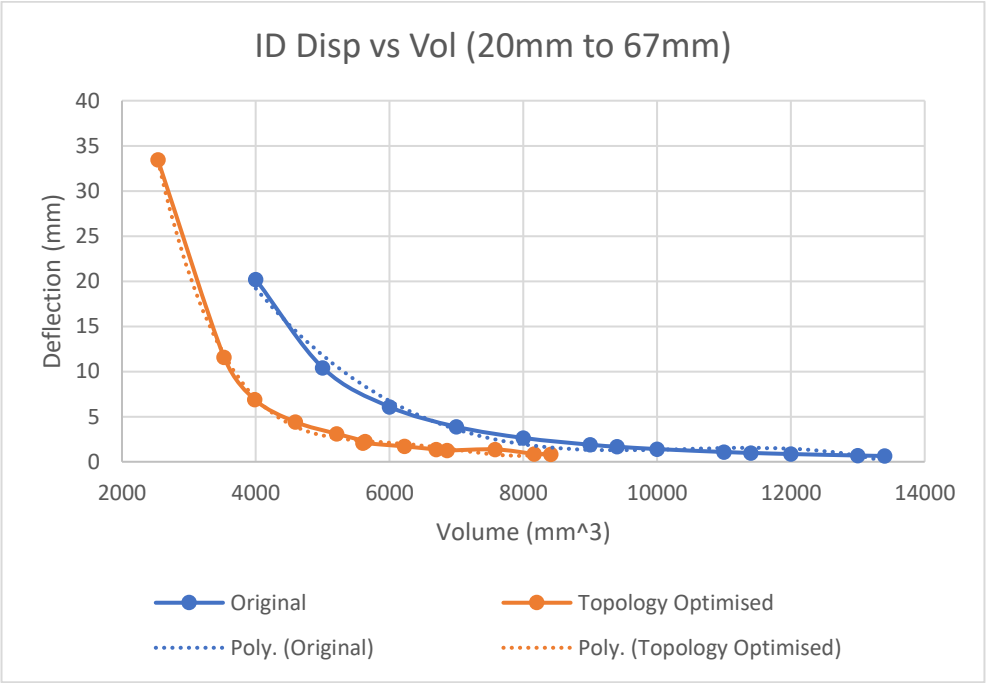

ST Stress vs Vol (30mm)
Stress (MPa)
200
300
400
500
600
700
800
900
1000
1100
1200
4000
6000
8000
10000
12000
14000
16000
Volume (mm^3)
Original
Topology Optimised
Poly. (Original)
Poly. (Topology Optimised)

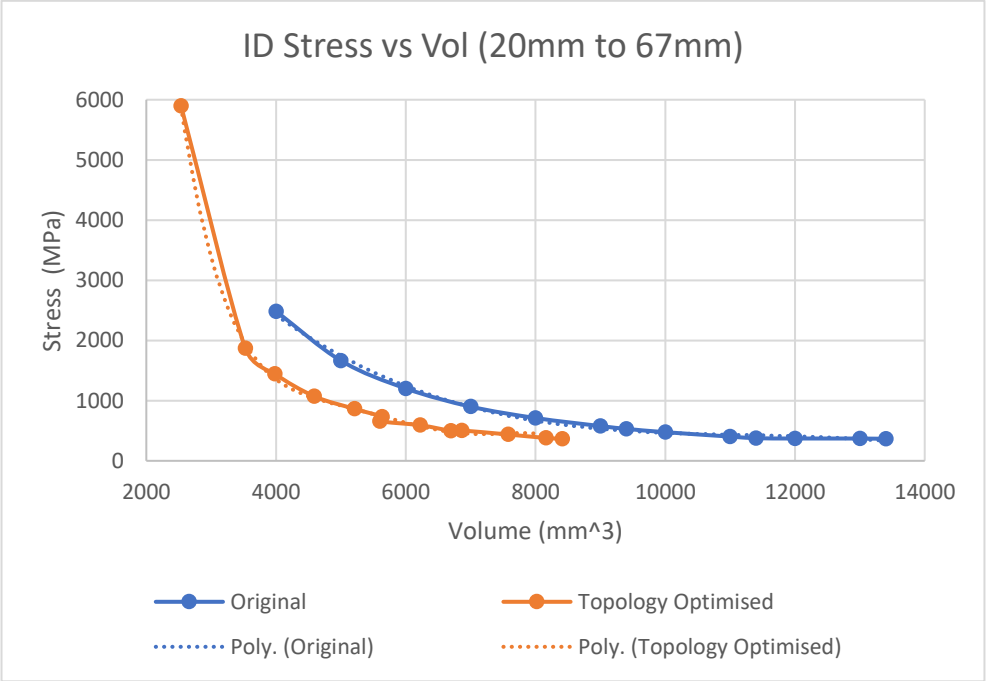
40mm

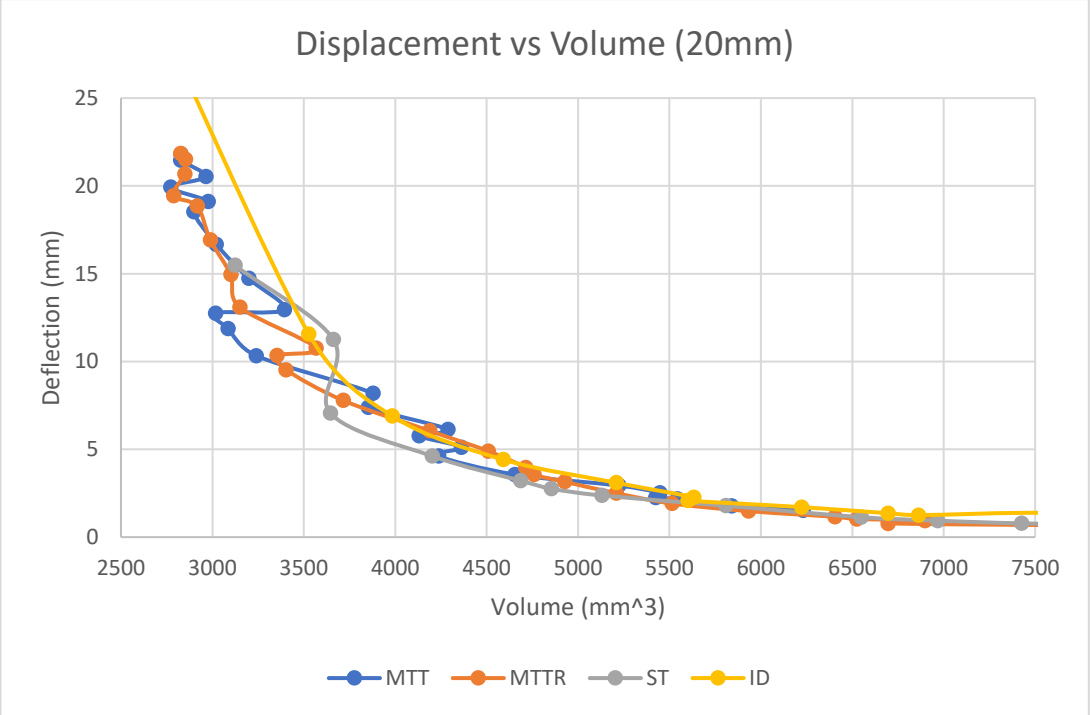

ST Disp vs Vol (40mm)
Deflection (mm)
3
2.5
2
1.5
1
0.5
0
5000
7000
9000
11000
13000
15000
17000
Volume (mm^3)
Original
Topology Optimised
Poly. (Original)
Poly. (Topology Optimised)

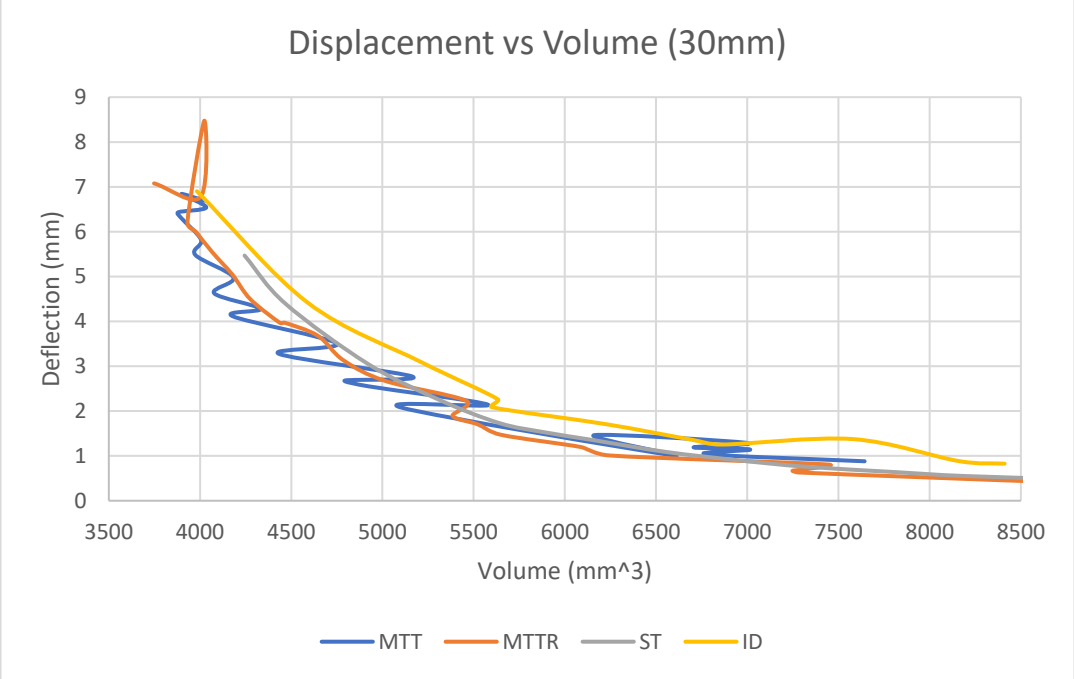

ST Stress vs Vol (40mm)
Stress (MPa)
800
700
600
500
400
300
200
5000
7000
9000
11000
13000
15000
17000
Volume (mm^3)
Original
Topology Optimised
Poly. (Original)
Poly. (Topology Optimised)

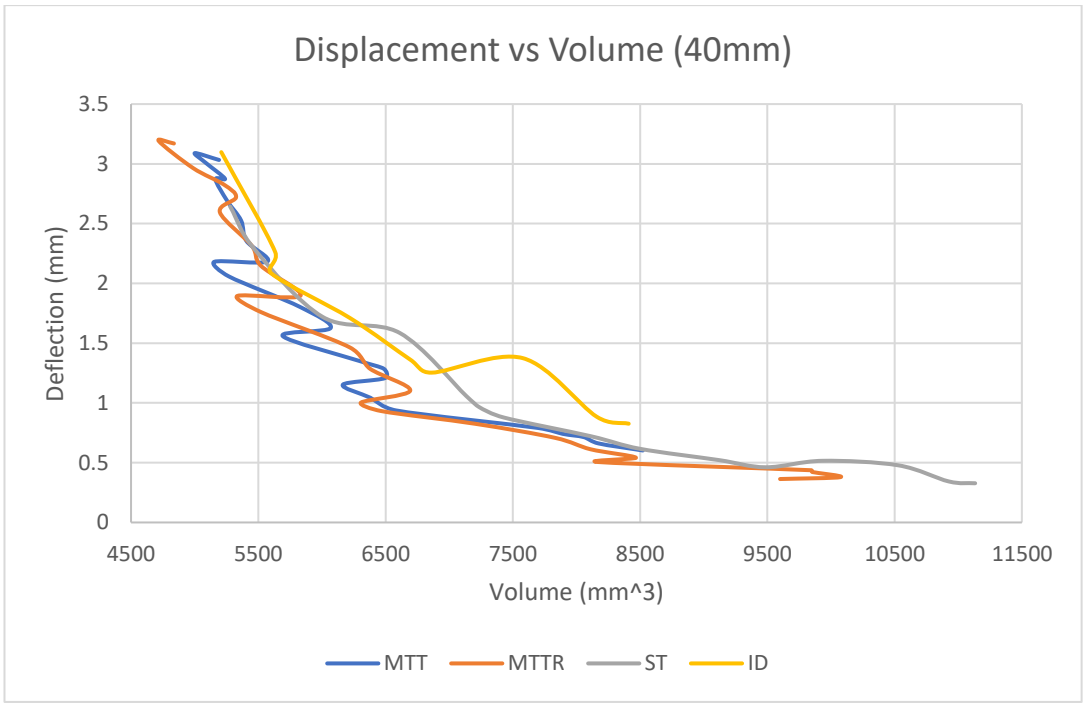
C.b.d Increased Depth (ID)

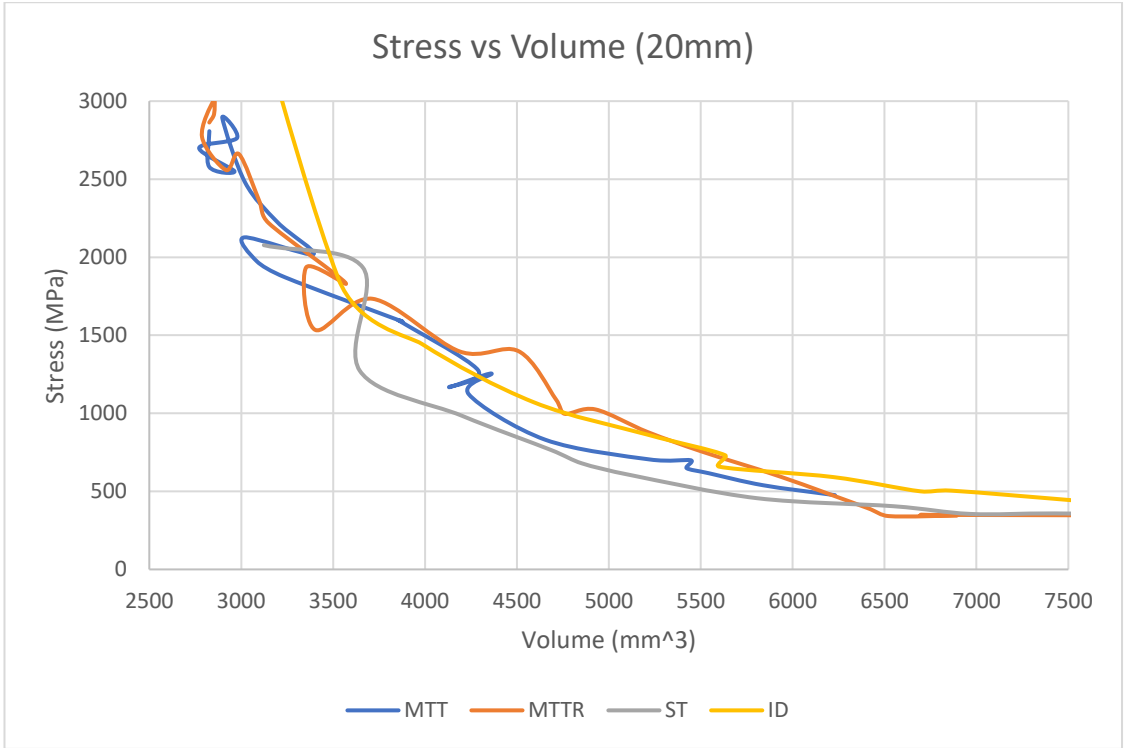


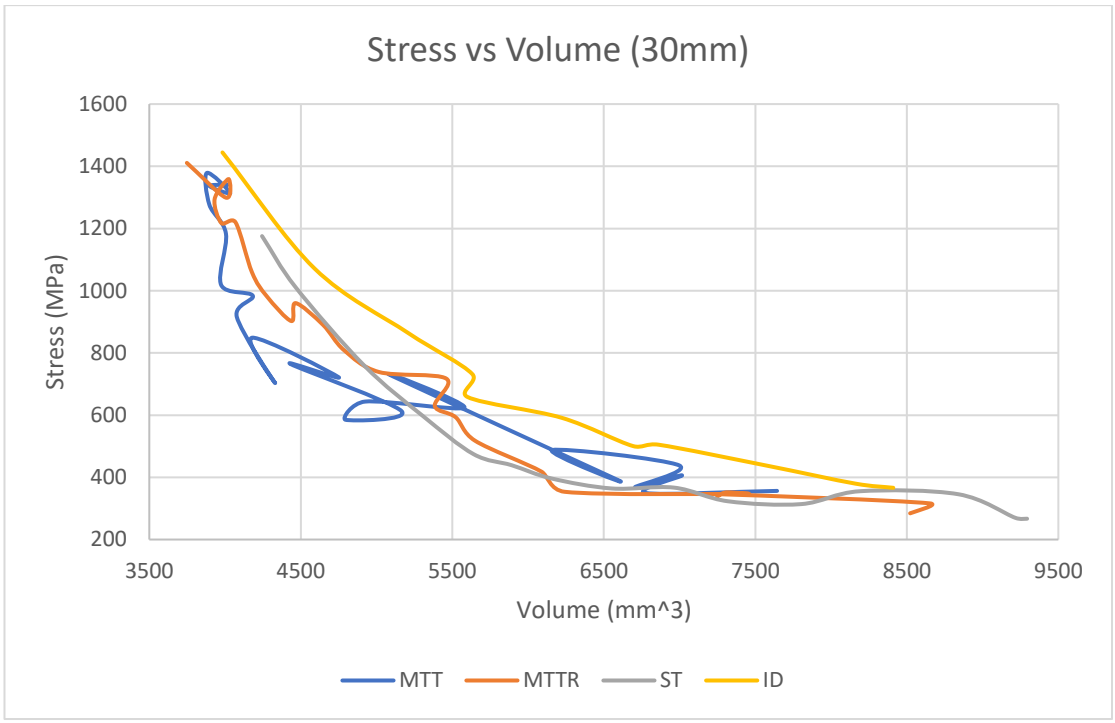


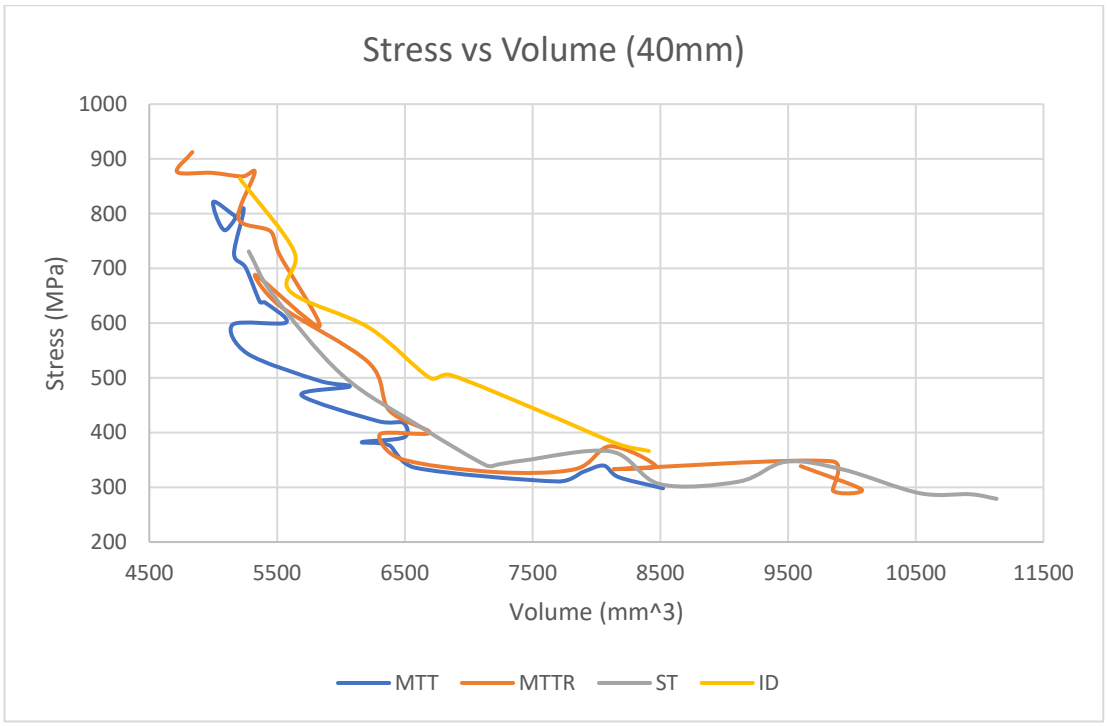

Displacement vs Volume (20mm)
Deflection (mm)
25
20
15
10
5
0
2500
3000
3500
4000
4500
5000
5500
6000
6500
7000
7500
Volume (mm^3)
MTT
MTTR
ST
ID


Displacement vs Volume (30mm)
Deflection (mm)
9
8
7
6
5
4
3
2
1
0
3500
4000
4500
5000
5500
6000
6500
7000
7500
8000
8500
Volume (mm^3)
MTT
MTTR
ST
ID


Displacement vs Volume (40mm)
Deflection (mm)
3.5
3
2.5
2
1.5
1
0.5
0
4500
5500
6500
7500
8500
9500
10500
11500
Volume (mm^3)
MTT
MTTR
ST
ID


Stress vs Volume (20mm)
Stress (MPa)
3000
2500
2000
1500
1000
500
0
2500
3000
3500
4000
4500
5000
5500
6000
6500
7000
7500
Volume (mm^3)
MTT
MTTR
ST
ID


Stress vs Volume (30mm)
1600
1400
1200
1000
800
600
400
200
Stress (MPa)
3500
4500
5500
6500
7500
8500
9500
Volume (mm^3)
MTT
MTTR
ST
ID


Stress vs Volume (40mm)
1000
900
800
700
600
500
400
300
200
Stress (MPa)
4500
5500
6500
7500
8500
9500
10500
11500
Volume (mm^3)
MTT
MTTR
ST
ID

C.c. Comparison plot between the Replicated Truss versus Topology Optimised versus Original

The details provided in this section are according to this sequence:

1. Node coordinate
2. Element details
3. Original cantilever beam displacement plot
4. Original cantilever beam elemental mean von-mises stress plot
5. Topology optimised cantilever beam displacement plot
6. Topology optimised cantilever beam elemental mean von-mises stress plot

C.c.a Method of Tensile Triangles (MTT)

Table C.c.a-0-1: Node coordinate for the MTT truss

Node	x (m)	z (m)
1	0	0
2	0.12875	0
3	0.2	0
4	0	-0.10625
5	0.08125	-0.0625
6	0.175	-0.04375

Table C.c.a -0-2: Element details for the MTT truss

Element	Type	Depth (mm)	Width (mm)
1	Bar	3.75	1
2	Bar	21.25	1
3	Bar	21.25	1
4	Bar	15	1
5	Bar	13.75	1
6	Bar	16.25	1
7	Bar	11.25	1
8	Bar	37.5	1
9	Bar	15	1

C.c.b Method of Tensile Triangles Rule of Thumb (MTTR)

Table C.c.b -0-3: Node coordinate for the MTTR truss

Node	x (m)	z (m)
1	0	0
2	0.15	0
3	0.2	0
4	0	-0.125
5	0.125	0.05

Table C.c.b -0-4:Element details for the MTTR truss

Element	Type	Depth (mm)	Width (mm)
1	Bar	4.55	1
2	Bar	25	1
3	Bar	25	1
4	Bar	25	1
5	Bar	9.09	1
6	Bar	13.64	1
7	Bar	25	1

C.c.c Standard Triangle (ST)

Table C.c.c -0-5: Node coordinate for the ST truss

Node	x (m)	z (m)
1	0	0
2	0.15	0
3	0.2	0
4	0	-0.13125
5	0.13125	0.05
6	0.2	-0.025

Table C.c.c-0-6: Element details for the ST truss

Element	Type	Depth (mm)	Width (mm)
1	Bar	3.75	1
2	Bar	13.75	1
3	Bar	13.75	1
4	Bar	12.5	1
5	Bar	12.5	1
6	Bar	7.5	1
7	Bar	18.75	1
8	Bar	26.25	1
9	Bar	21.25	1

C.c.d Increased Depth (ID)

Node coordinate for ID truss

Table C.c.d -0-7: Node coordinate for ID truss

Node	x (m)	z (m)
1	0	0
2	0.02	0
3	0.075	0
4	0.17	0
5	0	0.045
6	0.04	0.045
7	0.105	0.045
8	0.2	0.045

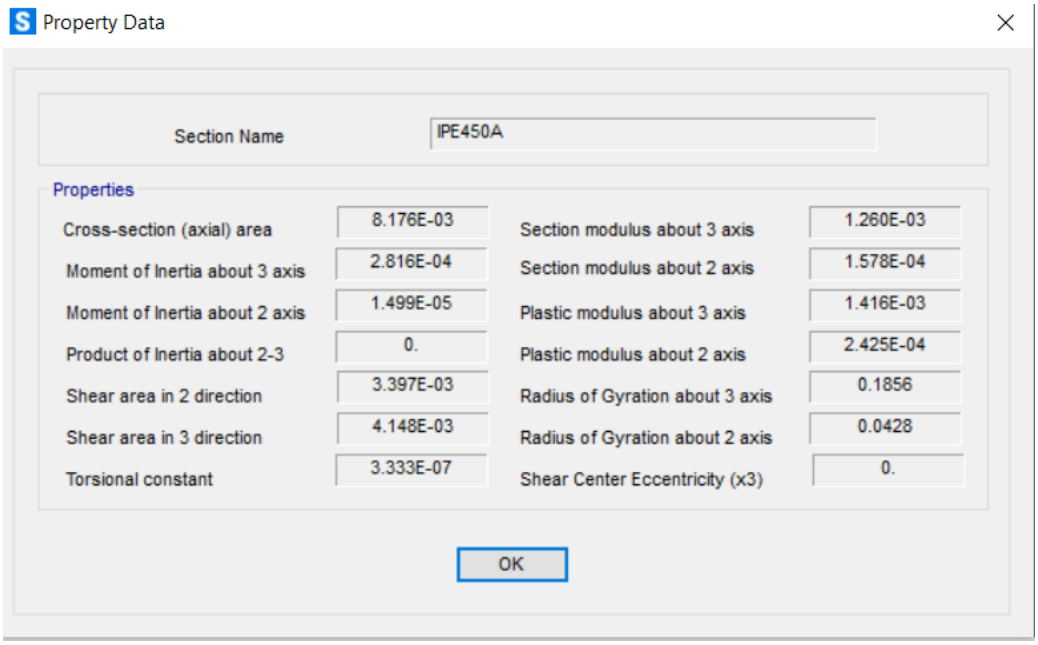
Table C.c.a -0-8: Element details for the ID truss

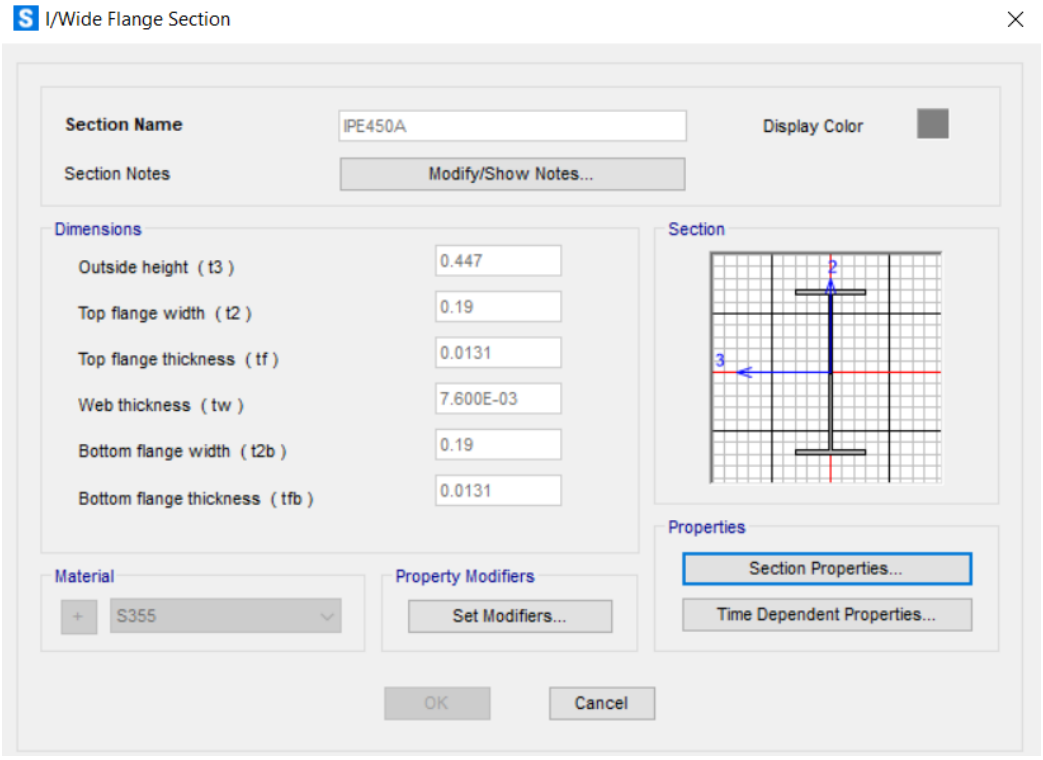
Element	Type	Depth (mm)	Width (mm)
1	Bar	15	1
2	Bar	10	1
3	Bar	10	1
4	Bar	10	1
5	Bar	10	1
6	Bar	10	1
7	Bar	10	1
8	Bar	5	1
9	Bar	5	1
10	Bar	5	1
11	Bar	10	1
12	Bar	10	1
13	Bar	10	1

Appendix D. Multistorey

D.a. SAP2000 Verification

D.a.a Eurocode 8 Worked Example





D.b. Multistorey Structure

D.b.a Assumptions

SAP2000 Steel Frame Design Preferences for Eurocode 3-2005

No.	Item	Value
1	Design Code	Eurocode 3-2005
2	Country	CEN default
3	Combinations Equations	Max of Eq. 610a/6.10b
4	Reliability Class	Class 2
5	Interaction Factors Method	Method 2 (Annex B)
6	Multi Response Case Design	Envelopes
7	Framing Type	DCH-MRF
8	Behaviour Factor, q	4
9	System Overstrength Factor, Omega	1
10	Consider P-Delta Done?	Yes
11	Consider Torsion?	Yes
12	GammaM0	1
13	GammaM1	1
14	GammaM2	1.25
15	Ignore Seismic Code?	No
16	Ignore Special Seismic Load?	No
17	Is double Plate Plug-Welded?	Yes
18	Consider Deflection?	Yes
19	DL Limit, L/	120
20	Super DL+LL Limit, L/	120
21	Live Load Limit, L/	360
22	Total Limit, L/	240
23	Total-Camber Limit, L/	240
24	Pattern Live Load Factor	0.75
25	Demand/Capacity Ratio Limit	0.95

D.b.b Base Model

D.b.c MTT Model

D.b.c.aSections

3 Floors

Beam section: IPE180O Column section: HE220M

Non-prismatic column (120mm)

Column	Section 1	Section 2	Section 3	Section 4
	HE320M	HE300B	HE240M	HE220M
Original				0.27
Required	0.360	0.300	0.270	nil
Height	0.359	0.300	0.270	nil

Non-prismatic column (240mm)

Column	Section 1	Section 2	Section 3	Section 4
	HE450M	HE360B	HE300B	HE220M
Original				0.27
Required	0.480	0.360	0.300	nil
Height	0.478	0.360	0.300	nil

Non-prismatic column (120mm) custom with reduced beam

Beam section: IPE180 Column section: HE220M custom

Non-prismatic column (240mm) custom with reduced beam (min)

Beam section: IPE160R Column section: HE220M custom

For

1. Non-prismatic column (110mm) custom with reduced beam (min)

2. Non-prismatic column (220mm) custom with reduced beam (min)

Beam: IPE180O (unchanged) Column section: HE200M custom

D.b.c.a.a 9 Floors

Beam section: IPE240O Column section: HE240M

Non-prismatic column (135mm)

Column	Section 1	Section 2	Section 3	Section 4
	HE400B	HE340B	HE300B	HE240M
Original				0.27
Required	0.405	0.3375	0.30375	nil
Height	0.4	0.34	0.3	nil

Non-prismatic column (270mm)

Column	Section 1	Section 2	Section 3	Section 4
	HE550B	HE400B	HE340B	HE240M
Original				0.27
Required	0.54	0.405	0.3375	nil
Height	0.55	0.4	0.34	nil

Non-prismatic column (135mm) custom with reduced beam

Beam section: IPE220O Column section: HE240M custom

Non-prismatic column (270mm) custom with reduced beam

Beam section: IPE220O Column section: HE240M custom

For

1. Non-prismatic column (120mm) custom with reduced beam (min)

2. Non-prismatic column (240mm) custom with reduced beam (min)

Beam section: IPE240 Column section: HE220M custom

D.b.c.a.b 15 Floors

Beam section: IPE270O Column section: HE280M

Non-prismatic column (155mm)

Column	Section 1	Section 2	Section 3	Section 4
	HE450M	HE360M	HE360A	HE280M
Original				0.31
Required	0.465	0.3875	0.34875	nil
Height	0.478	0.395	0.35	nil

Non-prismatic column (310mm)

Column	Section 1	Section 2	Section 3	Section 4
	HE600M	HE450M	HE360M	HE280M
Original				0.31
Required	0.62	0.465	0.3875	nil
Height	0.62	0.478	0.395	nil

Non-prismatic column (155mm) custom with reduced beam

Beam section: IPE240 Column section: HE280M custom

Non-prismatic column (310mm) custom with reduced beam

Beam section: IPE240 Column section: HE280M custom

For

1. Non-prismatic column (135mm) custom with reduced beam (min)

2. Non-prismatic column (270mm) custom with reduced beam (min)

Beam section: IPE240 Column section: HE240M custom

D.b.c.a.c 21 Floors

Beam section: IPE270R Column section: HE300M

Non-prismatic column (170mm)

Column	**Section 1**	**Section 2**	**Section 3**	**Section 4**
	HE500B	HE400M	HE340M	HE300M
Original				0.34
Required	0.51	0.425	0.3825	nil
Height	0.5	0.432	0.377	nil

Non-prismatic column (340mm)

Column	**Section 1**	**Section 2**	**Section 3**	**Section 4**
	HE700B	HE500B	HE400M	HE300M
Original				0.34
Required	0.68	0.51	0.425	nil
Height	0.7	0.5	0.432	nil

Non-prismatic column (170mm) custom with reduced beam

Beam section: IPE240O Column section: HE300M custom

Non-prismatic column (340mm) custom with reduced beam

Beam section: IPE240 Column section: HE300M custom

For

1. Non-prismatic column (135mm) custom with reduced beam (min)

2. Non-prismatic column (270mm) custom with reduced beam (min)

Beam section: IPE270 Column section: HE240M custom

D.b.c.a.d 27 Floors

Beam section: IPE270O Column section: HE320M

Non-prismatic column (179.5mm)

Column	**Section 1**	**Section 2**	**Section 3**	**Section 4**
	HE500M	HE400M	HE360M	HE320M
Original				0.359
Required	0.5385	0.44875	0.403875	nil
Height	0.524	0.432	0.395	nil

Non-prismatic column (359mm)

Column	**Section 1**	**Section 2**	**Section 3**	**Section 4**
	HE700M	HE500M	HE400M	HE320M
Original				0.359
Required	0.718	0.5385	0.44875	nil
Height	0.716	0.524	0.432	nil

Non-prismatic column (179.5mm) custom with reduced beam

Beam section: IPE270 Column section: HE320M custom

Non-prismatic column (359mm) custom with reduced beam

Beam section: IPE240O Column section: HE320M custom

For

1. Non-prismatic column (155mm) custom with reduced beam (min)

2. Non-prismatic column (310mm) custom with reduced beam (min)

Beam section: IPE270O (unchanged) Column section: HE280M custom

D.b.c.b Results

D.b.c.b.a Modal

3 Floors

Mode 1 – Mode 9

9 Floors, 15 Floors, 21 Floors, 27 Floors

Mode 1 – Mode 10

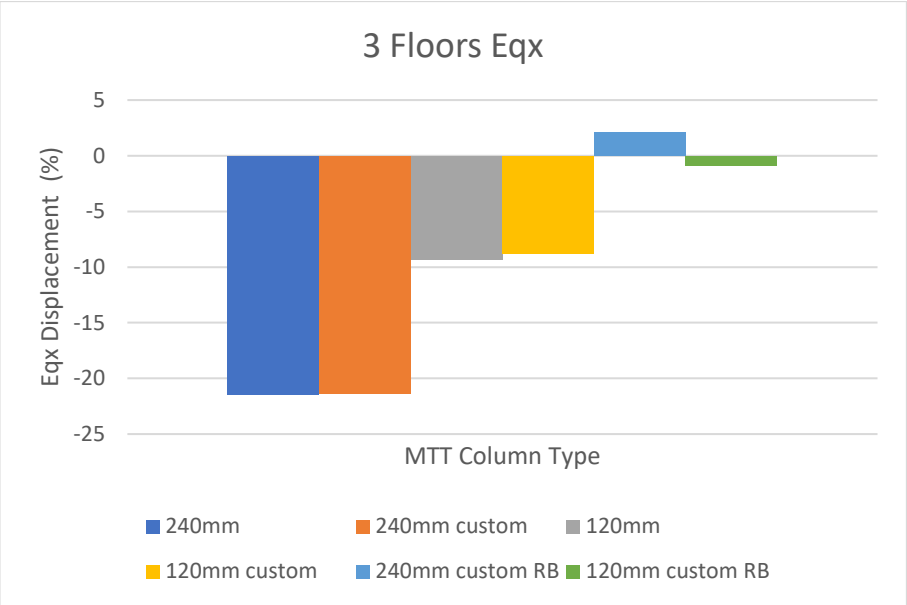
D.b.c.b.b MTT Column Design (Industry section versus Custom section)

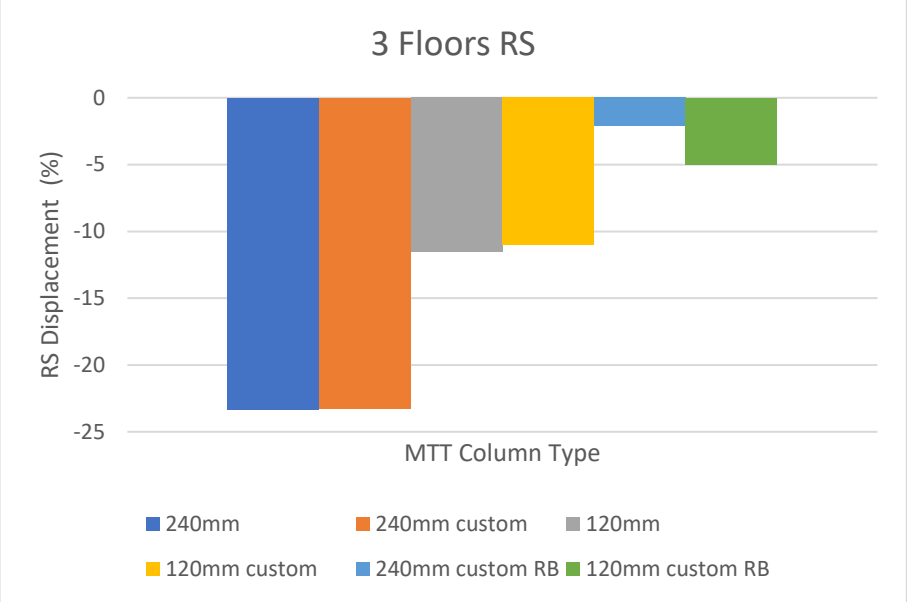
Storey		Categories						
3		Base	240mm	240mm custom	120mm	120mm custom	240mm custom RB	120mm custom RB
	Eqx (m)	0.02316	0.01819	0.01821	0.02101	0.02113	0.02365	0.02295
	RS (m)	0.02331	0.01787	0.01789	0.02062	0.02074	0.02282	0.02215

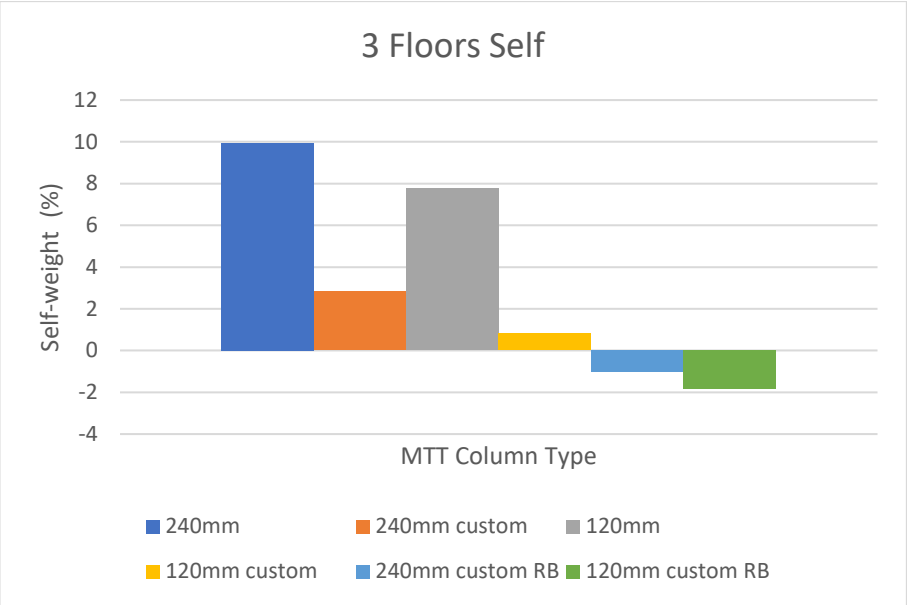
	Self (kN)	333.148	366.313	342.557	359.02	335.894	329.789	327.012
		Base	270mm	270mm custom	135mm	135mm custom	270mm custom RB	135mm custom RB
9	Eqx (m)	0.06996	0.05295	0.0531	0.06298	0.0624	0.06751	0.0791
	RS (m)	0.05472	0.04654	0.04653	0.05108	0.05072	0.05286	0.05668
	Self (kN)	1402.42	1411.199	1445.557	1374.006	1415.199	1391.907	1362.202
		Base	310mm	310mm custom	155mm	155mm custom	310mm custom RB	155mm custom RB
15	Eqx (m)	0.0956	0.0707	0.0716	0.0848	0.0846	0.10655	0.12608
	RS (m)	0.0778	0.0655	0.066	0.0718	0.0717	0.08027	0.08697
	Self (kN)	2823.681	3174.49	2921.333	2877.639	2852.939	2713.366	2647.134
		Base	340mm	340mm custom	170mm	170mm custom	340mm custom RB	170mm custom RB
21	Eqx (m)	0.14419	0.10684	0.10763	0.1283	0.12699	0.16312	0.17837
	RS (m)	0.1226	0.09335	0.0939	0.10804	0.10722	0.13296	0.14509
	Self (kN)	4759.59	4729.916	4939.273	4700.893	4812.205	4603.598	4569.91
		Base	359mm	359mm custom	179.5mm	179.5mm custom	359mm custom RB	179.5mm custom RB
27	Eqx (m)	0.24055	0.17852	0.17783	0.21073	0.2083	0.23355	0.23251
	RS (m)	0.2185	0.16075	0.1601	0.19002	0.18781	0.21051	0.20972
	Self (kN)	6204.89	6468.57	6459.212	6287.367	6279.172	6197.851	6081.553

By Floor (Industry Section versus Custom Section)

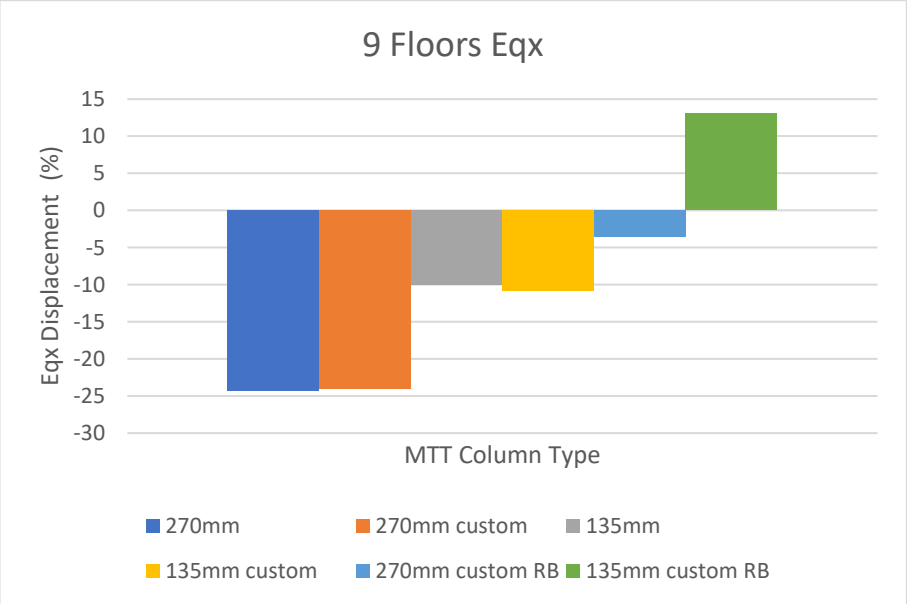
3 Floors

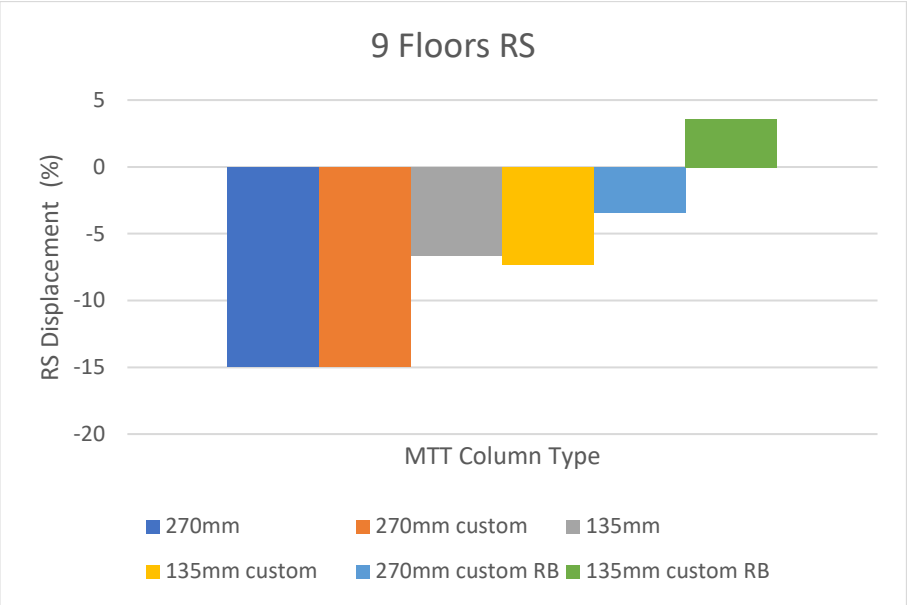

3 Floors Eqx
5
0
-5
-10
-15
-20
-25
Eqx Displacement (%)
MTT Column Type
240mm
240mm custom
120mm
120mm custom
240mm custom RB
120mm custom RB

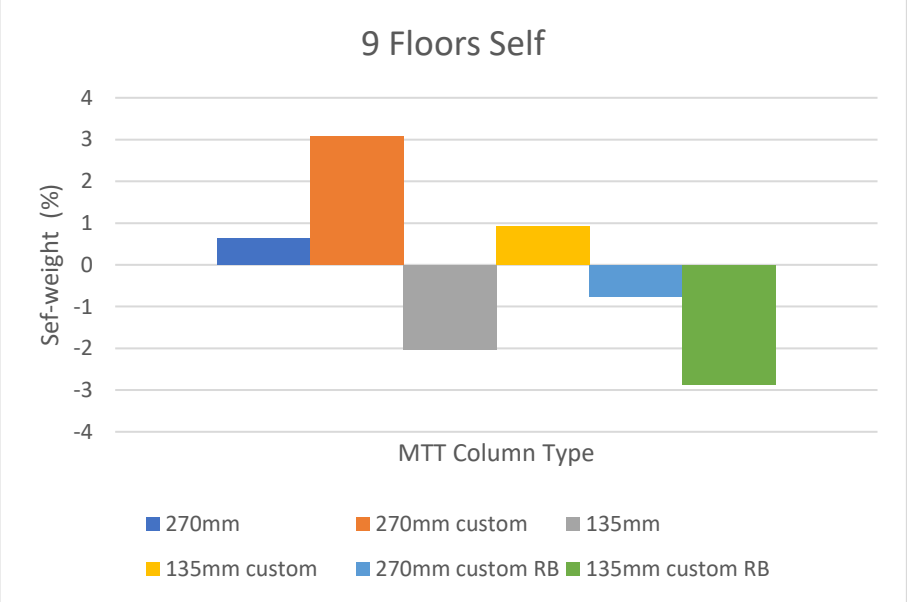

3 Floors RS
0
-5
-10
-15
-20
-25
RS Displacement (%)
MTT Column Type
240mm
240mm custom
120mm
120mm custom
240mm custom RB
120mm custom RB


3 Floors Self
12
10
8
6
4
2
0
-2
-4
Self-weight (%)
MTT Column Type
240mm
240mm custom
120mm
120mm custom
240mm custom RB
120mm custom RB

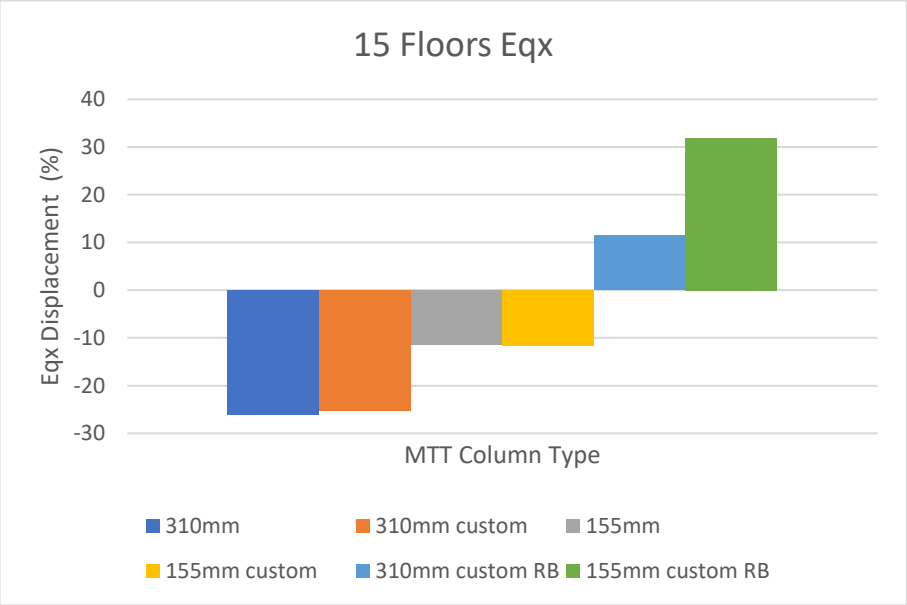
9 Floors

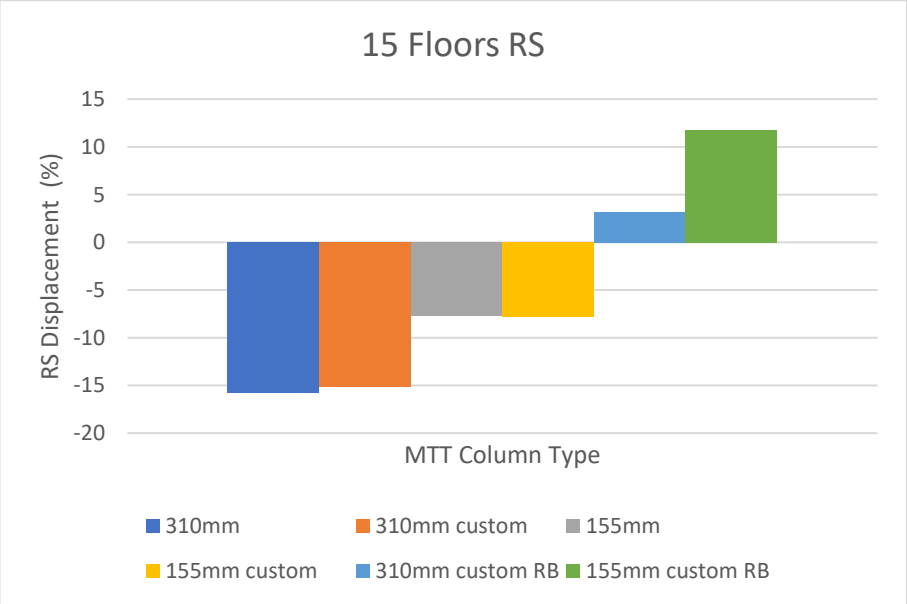

9 Floors Eqx
15
10
5
0
-5
-10
-15
-20
-25
-30
Eqx Displacement (%)
MTT Column Type
270mm
270mm custom
135mm
135mm custom
270mm custom RB
135mm custom RB

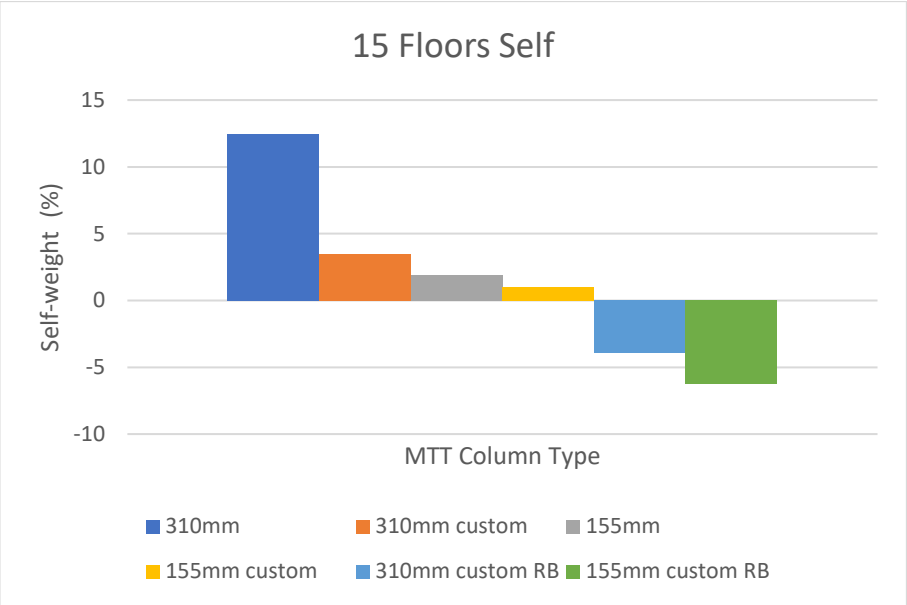

9 Floors RS
5
0
-5
-10
-15
-20
RS Displacement (%)
MTT Column Type
270mm
270mm custom
135mm
135mm custom
270mm custom RB
135mm custom RB


9 Floors Self
4
3
2
1
0
-1
-2
-3
-4
Sef-weight (%)
MTT Column Type
270mm
270mm custom
135mm
135mm custom
270mm custom RB
135mm custom RB

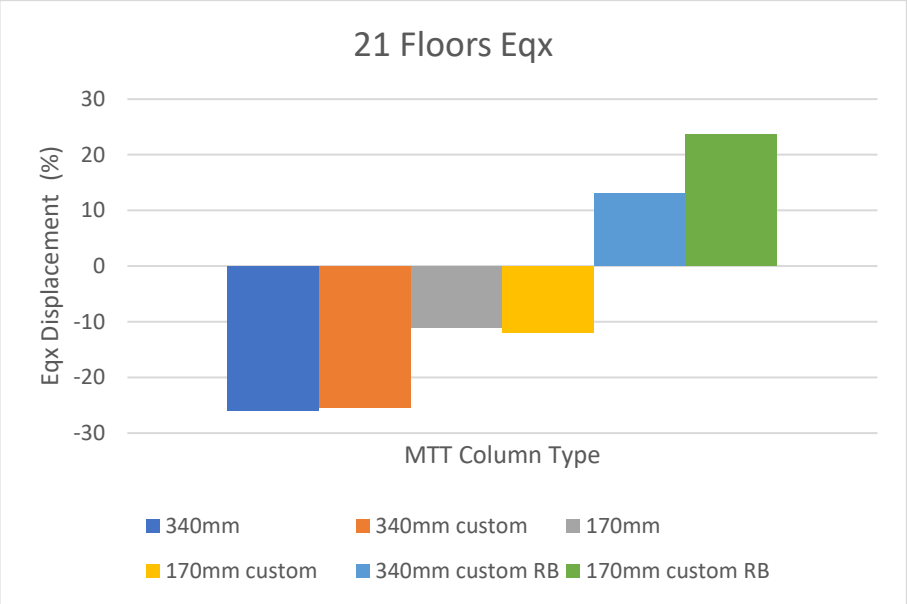
15 Floors

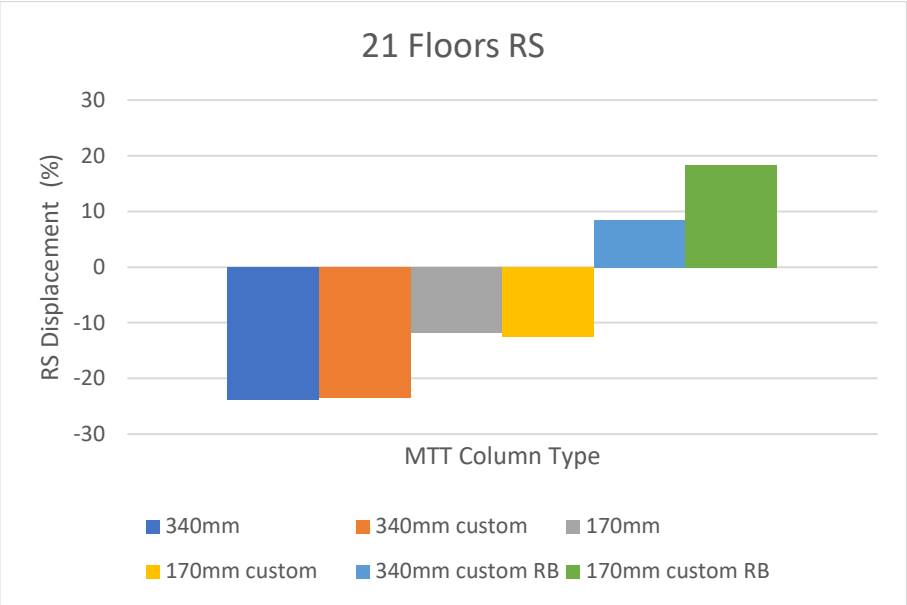

15 Floors Eqx
Eqx Displacement (%)
40
30
20
10
0
-10
-20
-30
MTT Column Type
310mm
310mm custom
155mm
155mm custom
310mm custom RB
155mm custom RB

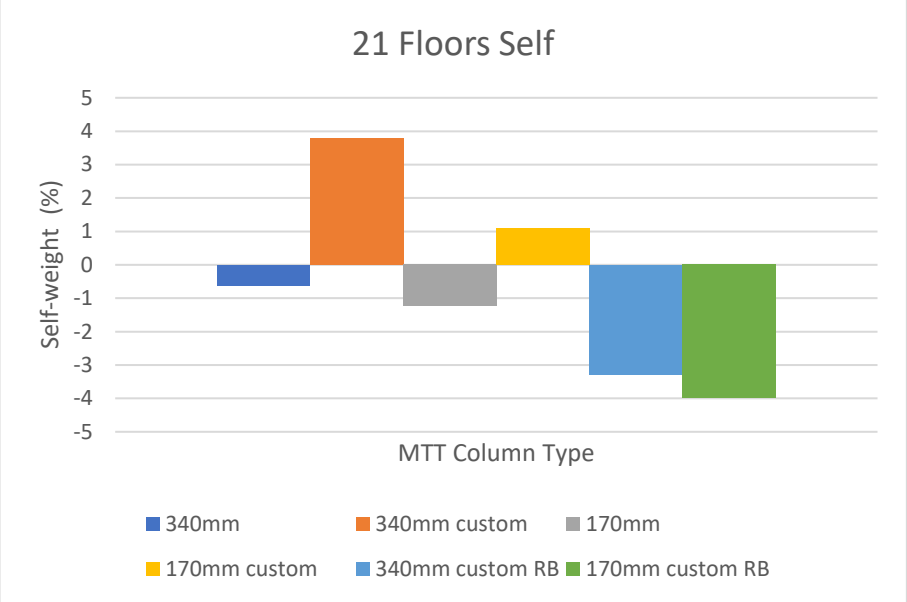

15 Floors RS
RS Displacement (%)
15
10
5
0
-5
-10
-15
-20
MTT Column Type
310mm
310mm custom
155mm
155mm custom
310mm custom RB
155mm custom RB


15 Floors Self
15
10
5
0
-5
-10
Self-weight (%)
MTT Column Type
310mm
310mm custom
155mm
155mm custom
310mm custom RB
155mm custom RB

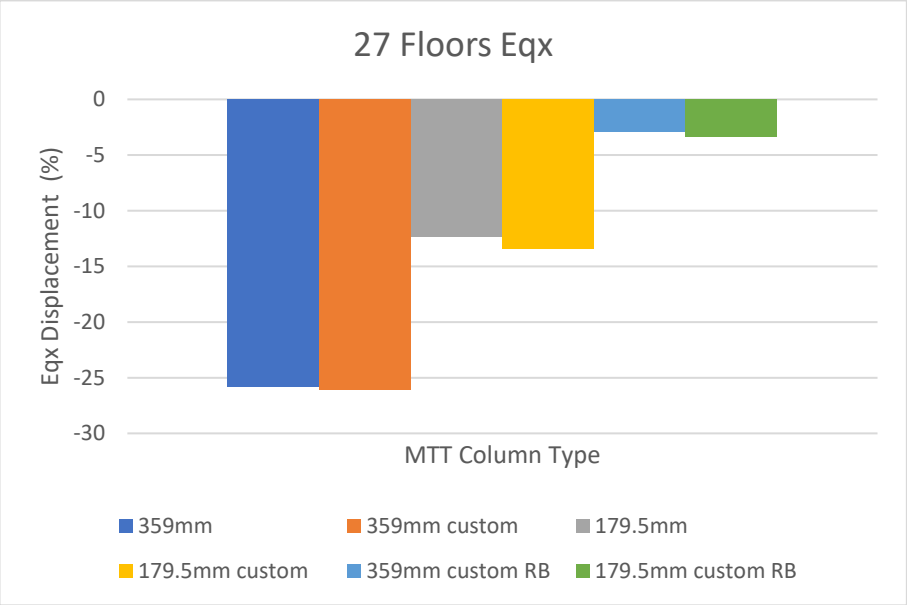
21 Floors

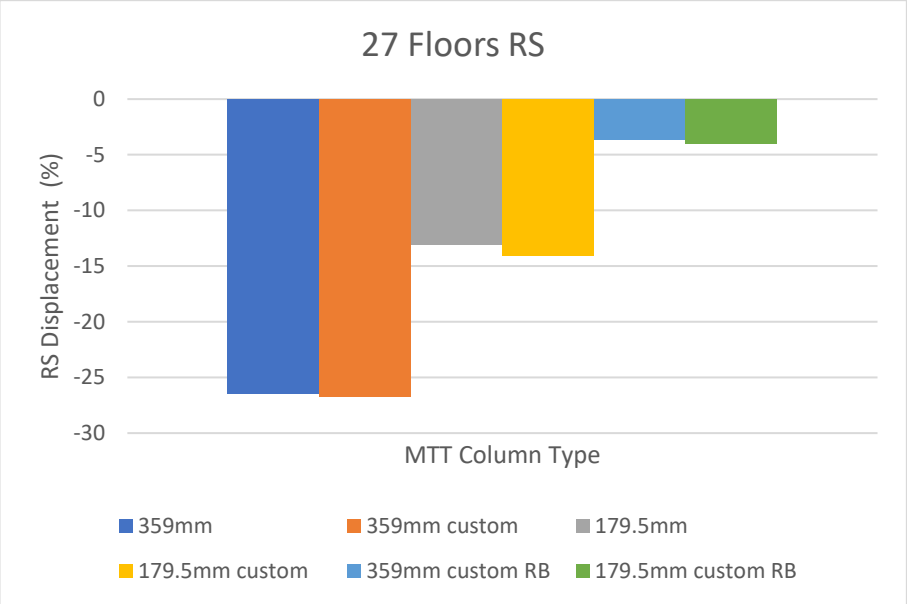

21 Floors Eqx
30
20
10
0
-10
-20
-30
Eqx Displacement (%)
MTT Column Type
340mm
340mm custom
170mm
170mm custom
340mm custom RB
170mm custom RB

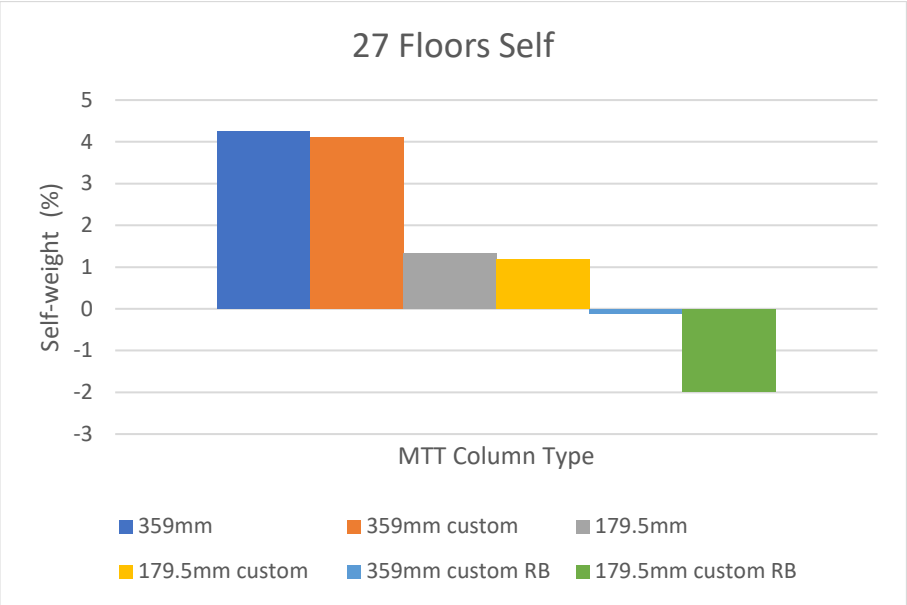

21 Floors RS
30
20
10
0
-10
-20
-30
RS Displacement (%)
MTT Column Type
340mm
340mm custom
170mm
170mm custom
340mm custom RB
170mm custom RB


21 Floors Self
5
4
3
2
1
0
-1
-2
-3
-4
-5
Self-weight (%)
MTT Column Type
340mm
340mm custom
170mm
170mm custom
340mm custom RB
170mm custom RB

27 Floors

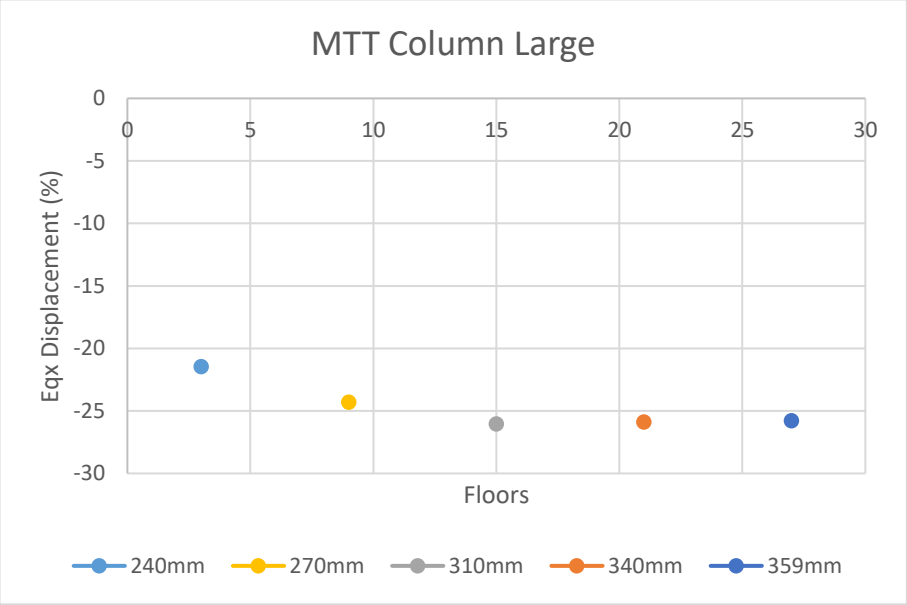

27 Floors Eqx
0
-5
-10
-15
-20
-25
-30
Eqx Displacement (%)
MTT Column Type
359mm
359mm custom
179.5mm
179.5mm custom
359mm custom RB
179.5mm custom RB

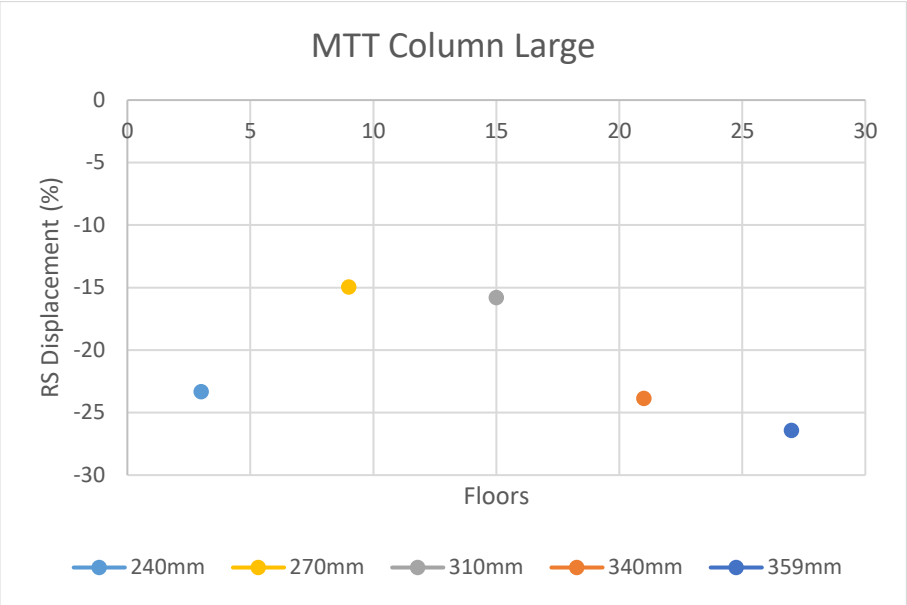

27 Floors RS
0
-5
-10
-15
-20
-25
-30
RS Displacement (%)
MTT Column Type
359mm
359mm custom
179.5mm
179.5mm custom
359mm custom RB
179.5mm custom RB

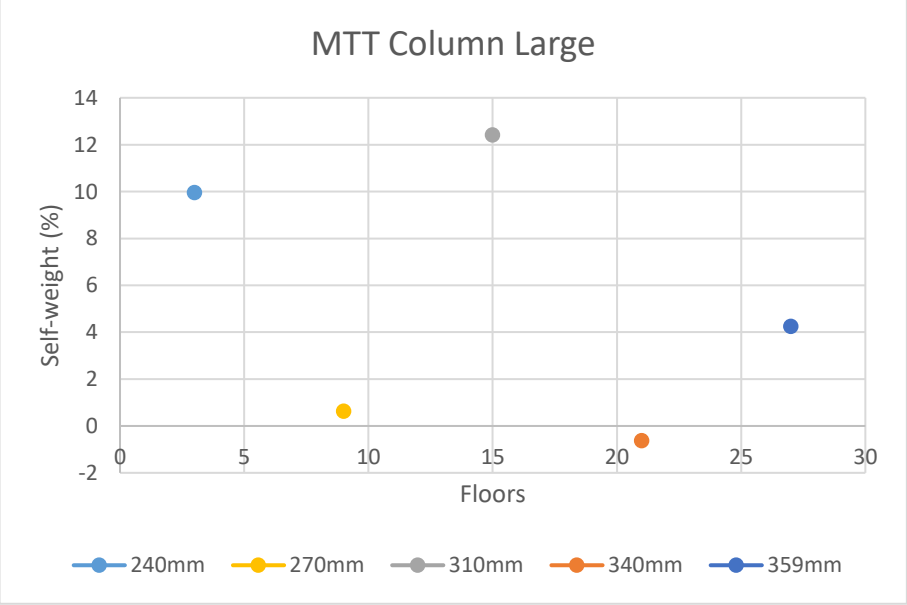


Across Storey Heights (Industry Section versus Custom Section)

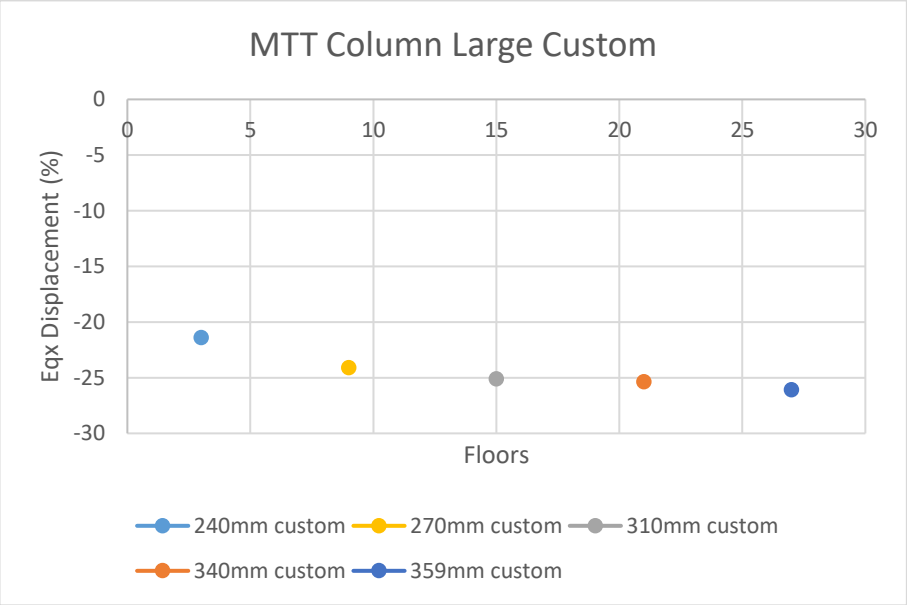
MTT Column Large

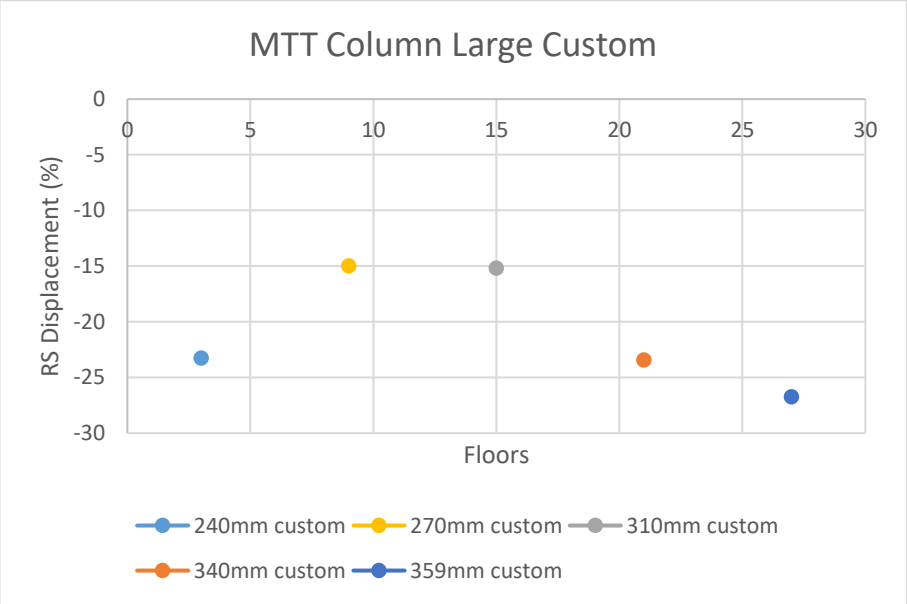


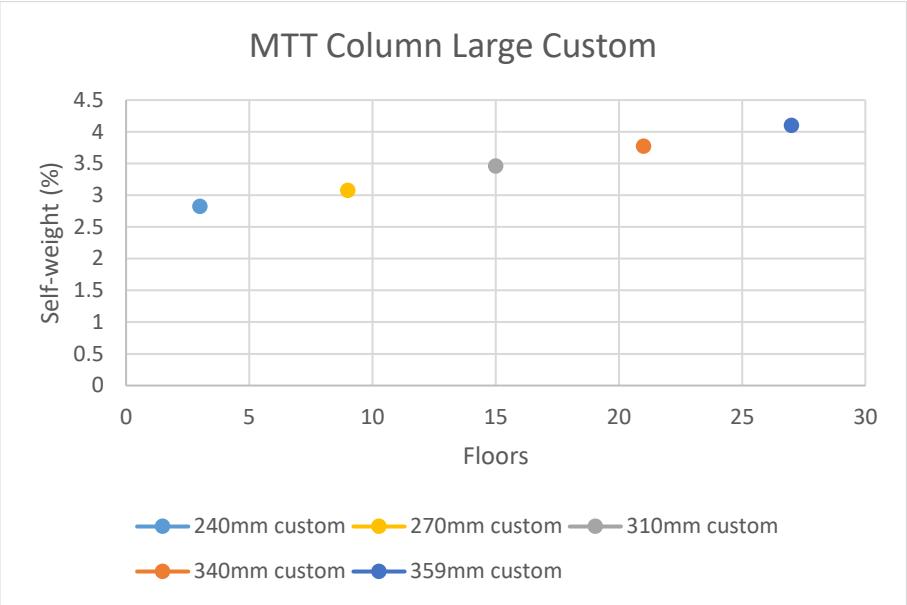

MTT Column Large
RS Displacement (%)
0
-5
-10
-15
-20
-25
-30
0
5
10
15
20
25
30
Floors
240mm
270mm
310mm
340mm
359mm


MTT Column Large
Self-weight (%)
14
12
10
8
6
4
2
0
-2
0
5
10
15
20
25
30
Floors
240mm
270mm
310mm
340mm
359mm

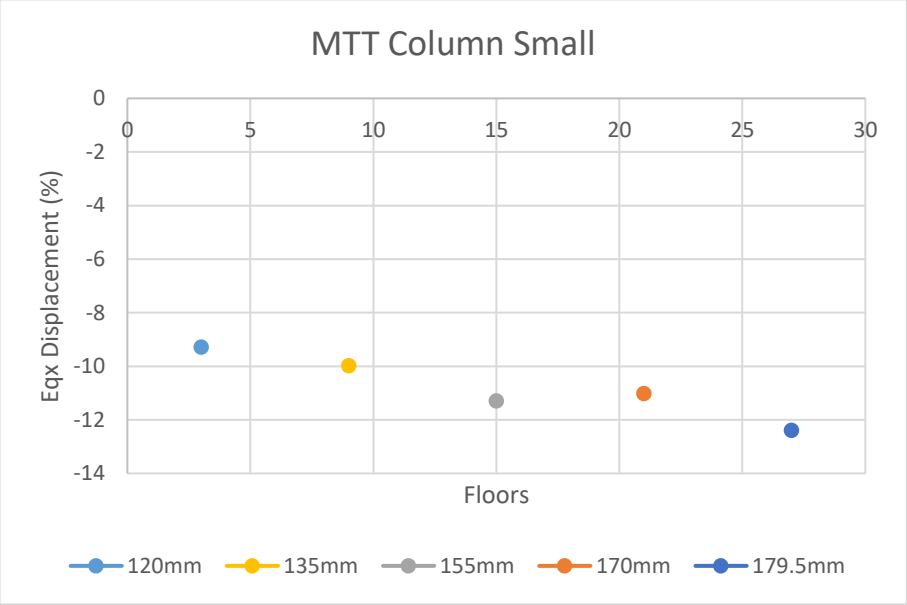
MTT Column Large Custom

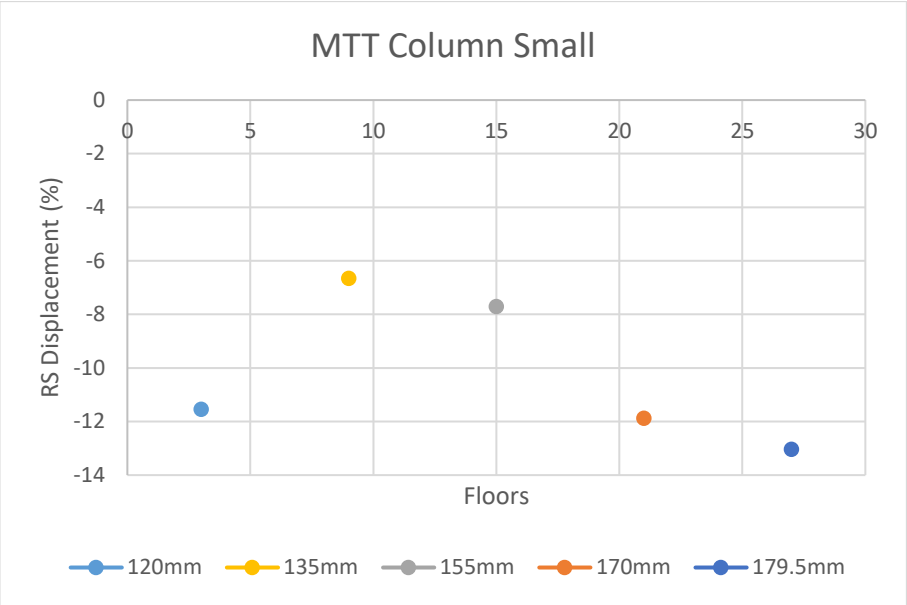


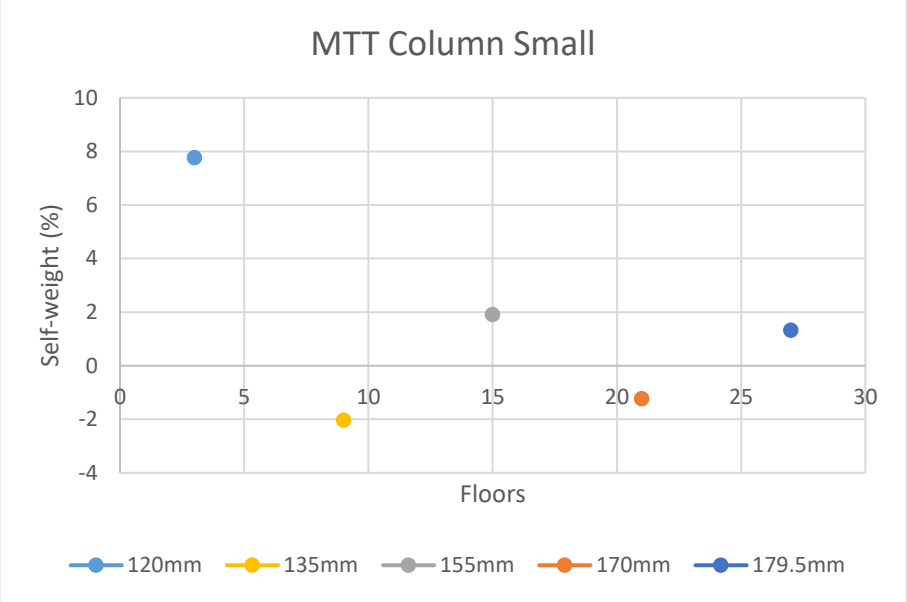




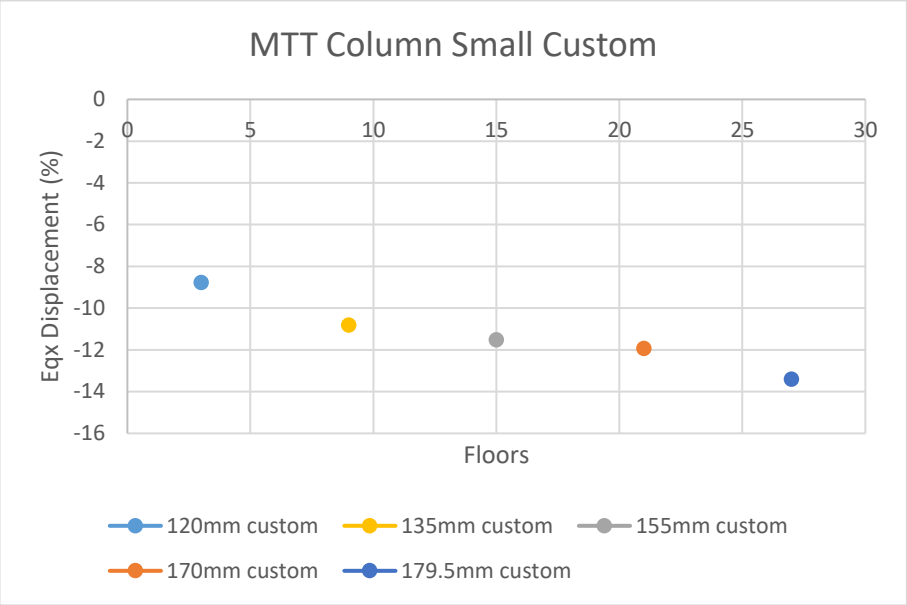
MTT Column Small

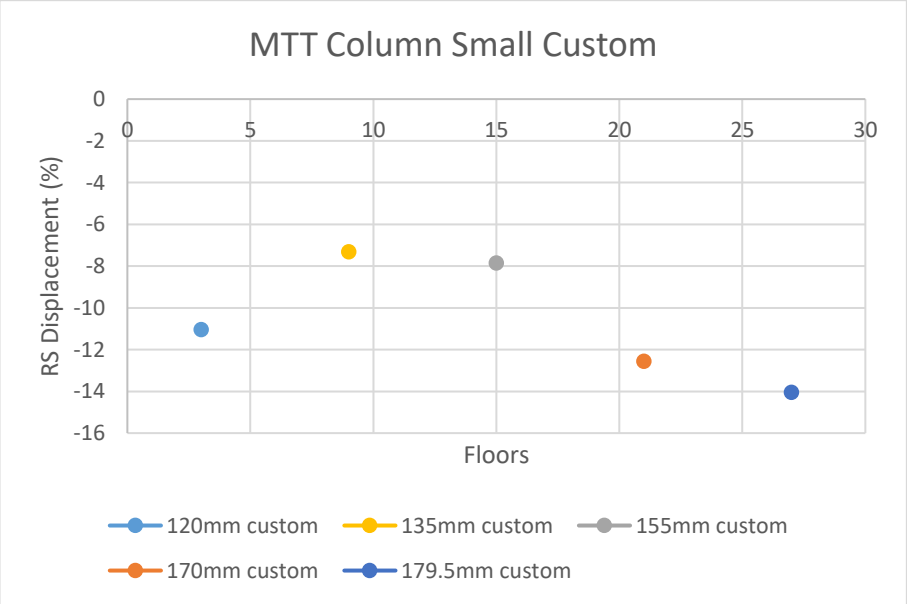


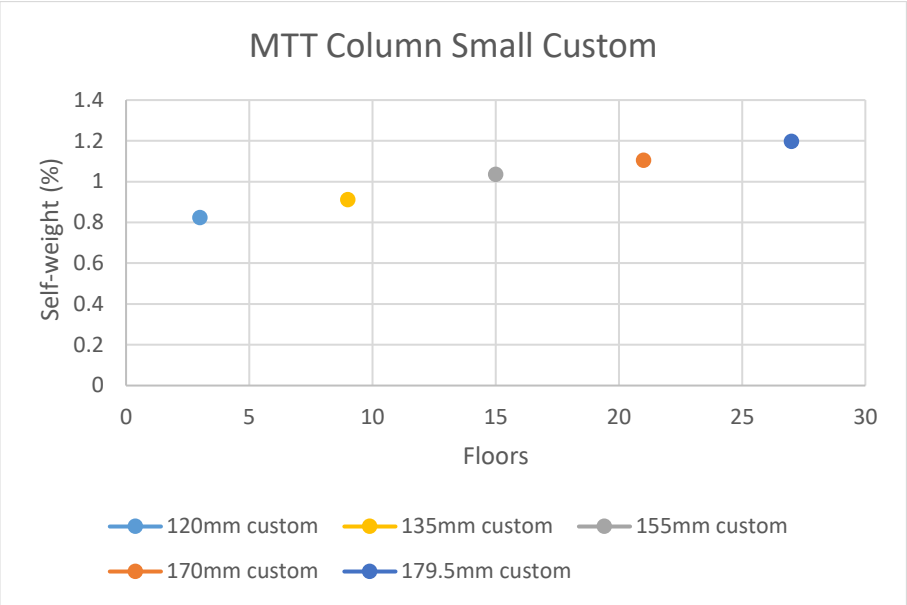

MTT Column Small
RS Displacement (%)
0
-2
-4
-6
-8
-10
-12
-14
0
5
10
15
20
25
30
Floors
120mm
135mm
155mm
170mm
179.5mm


MTT Column Small
Self-weight (%)
10
8
6
4
2
0
-2
-4
0
5
10
15
20
25
30
Floors
120mm
135mm
155mm
170mm
179.5mm

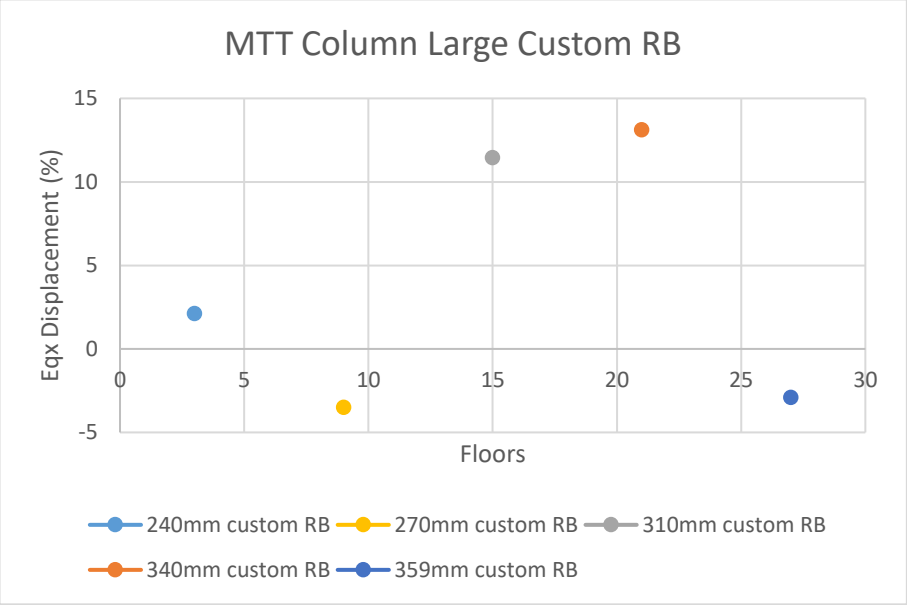
MTT Column Small Custom

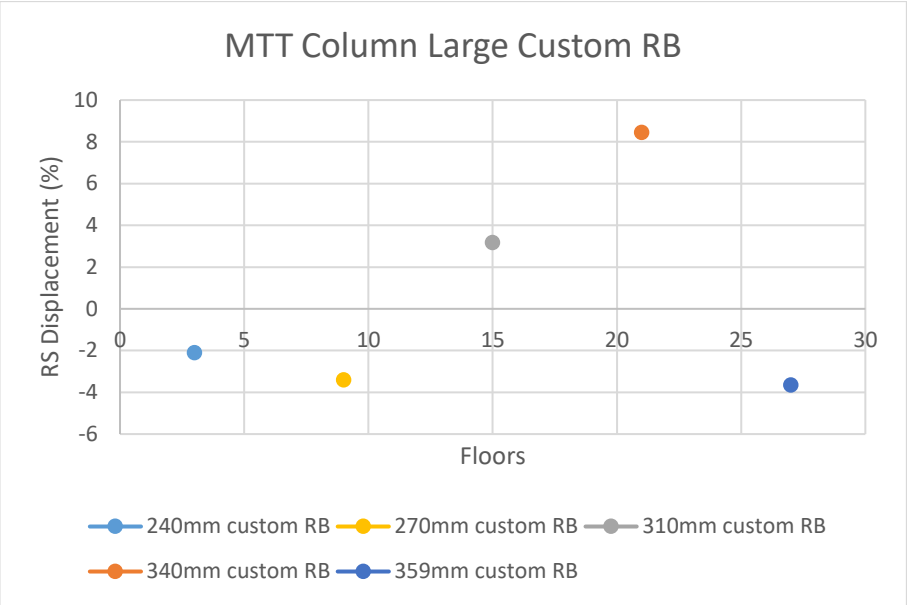


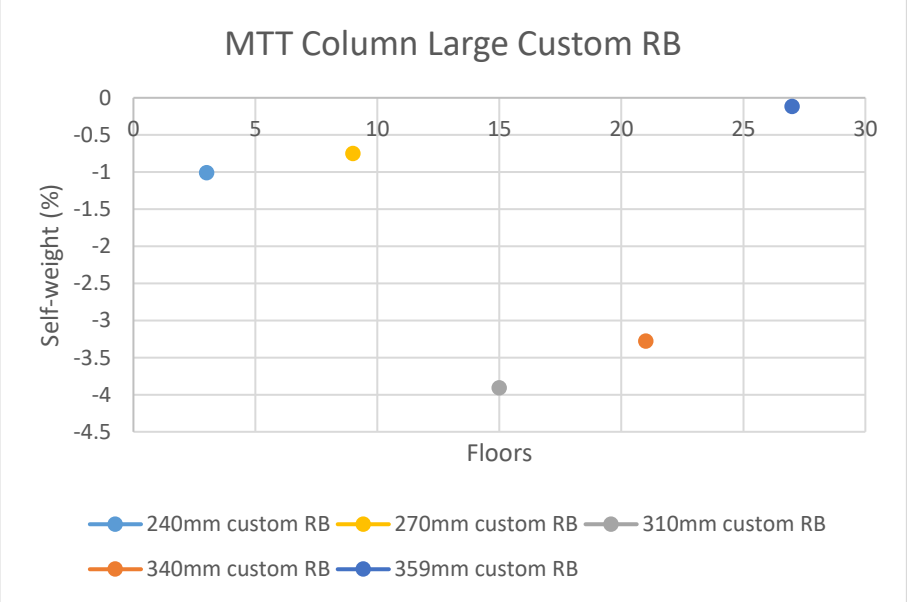




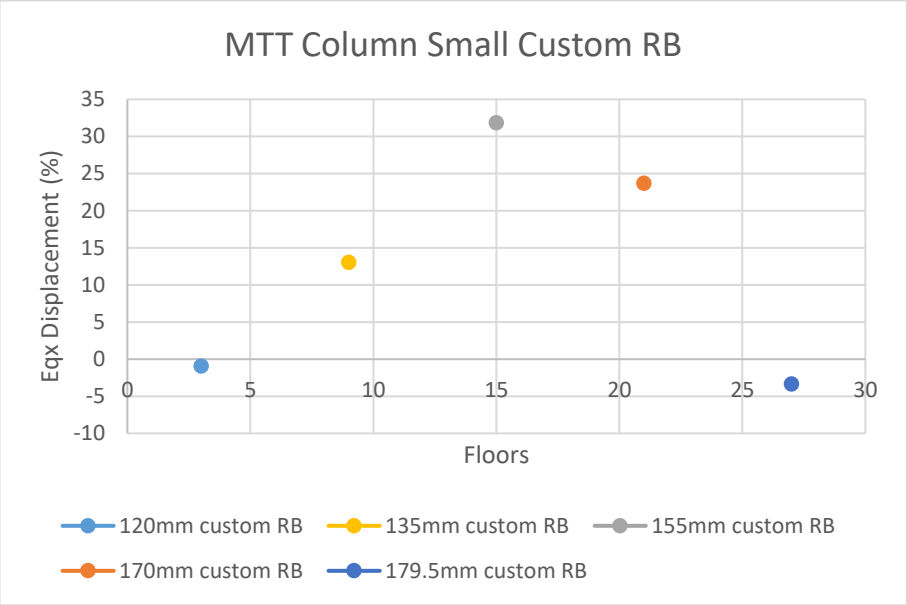
MTT Column Large Custom RB

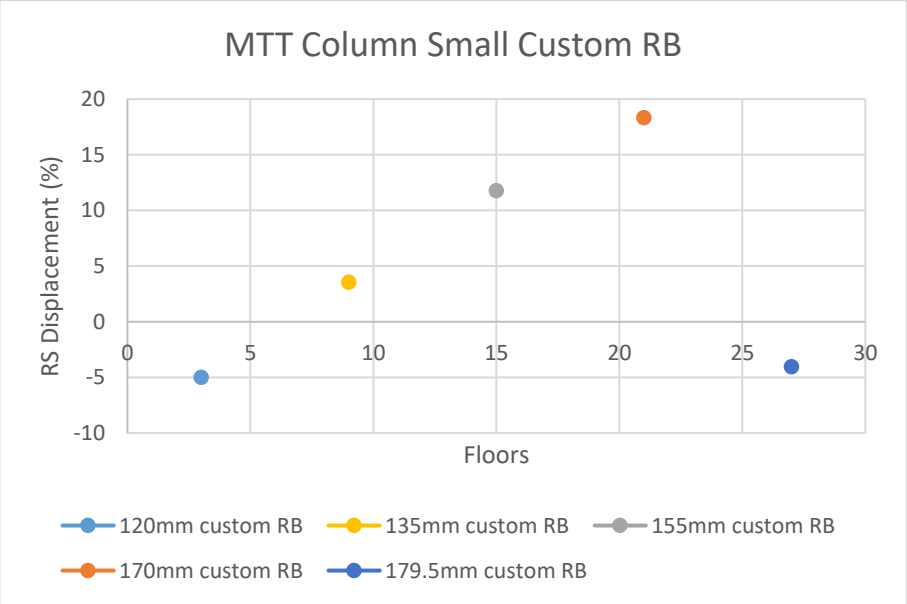


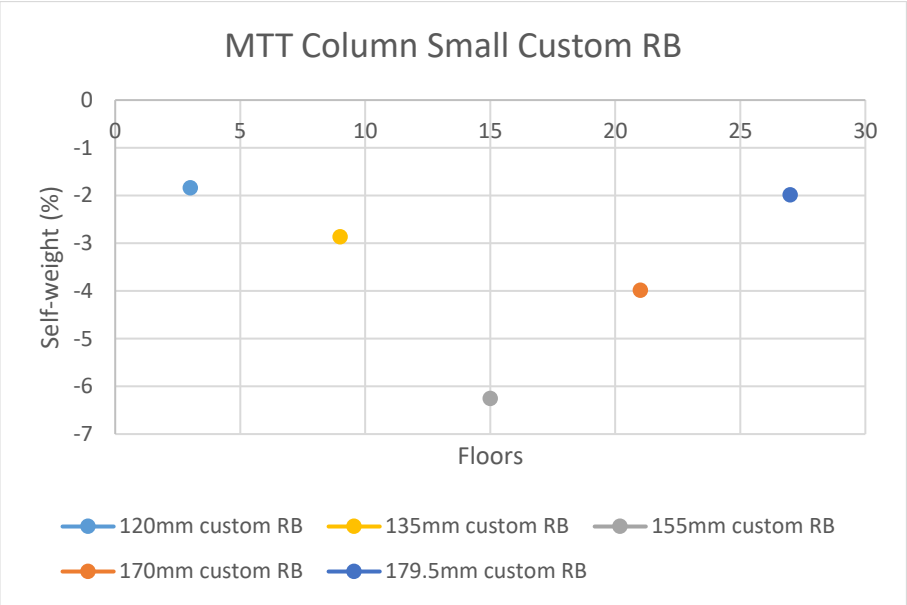

MTT Column Large Custom RB
RS Displacement (%)
10
8
6
4
2
0
-2
-4
-6
0
5
10
15
20
25
30
Floors
240mm custom RB
270mm custom RB
310mm custom RB
340mm custom RB
359mm custom RB


MTT Column Large Custom RB
Self-weight (%)
0
-0.5
-1
-1.5
-2
-2.5
-3
-3.5
-4
-4.5
0
5
10
15
20
25
30
Floors
240mm custom RB
270mm custom RB
310mm custom RB
340mm custom RB
359mm custom RB

MTT Column Small Custom RB

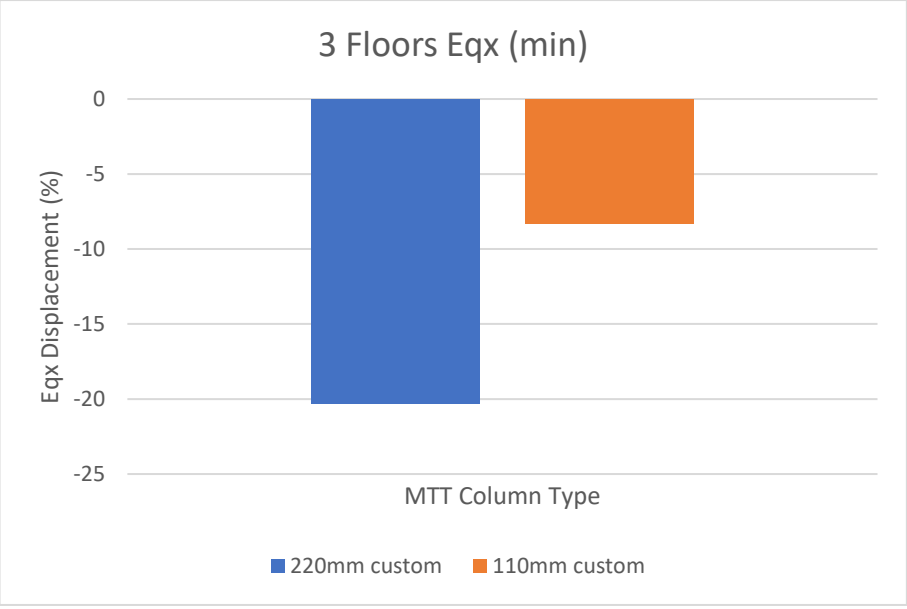


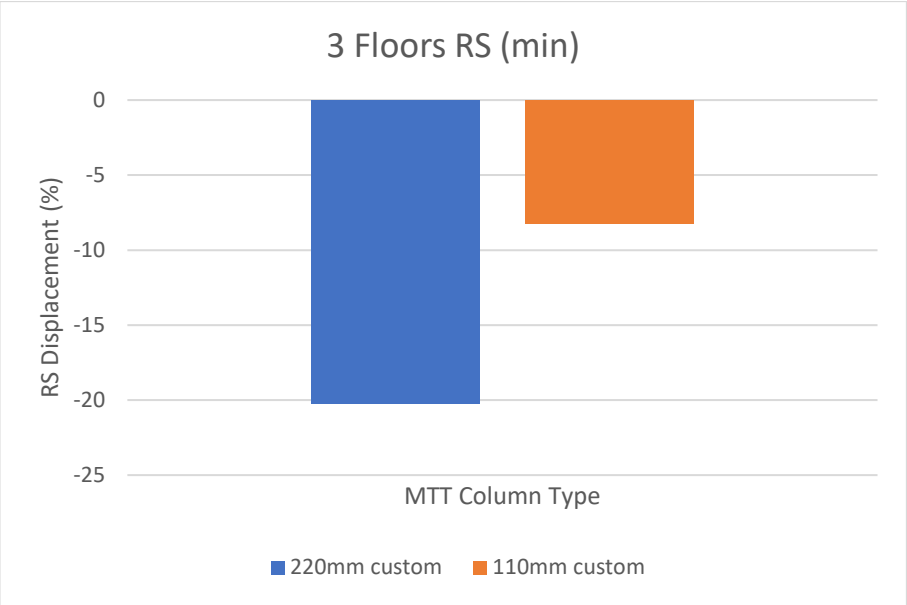


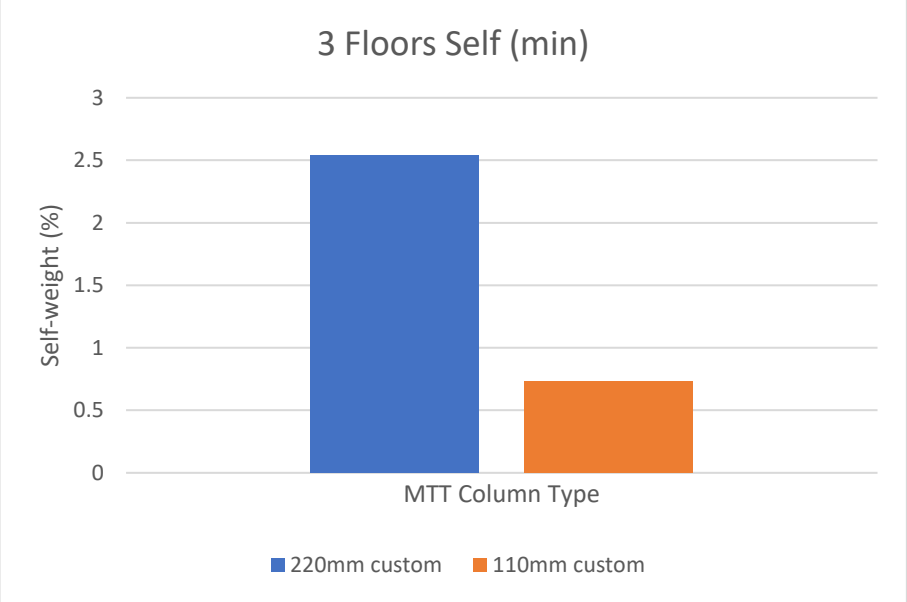


D.b.c.b.c Minimising the Capacity in both Beam and Column By Floors (Min Beam and Min Column)

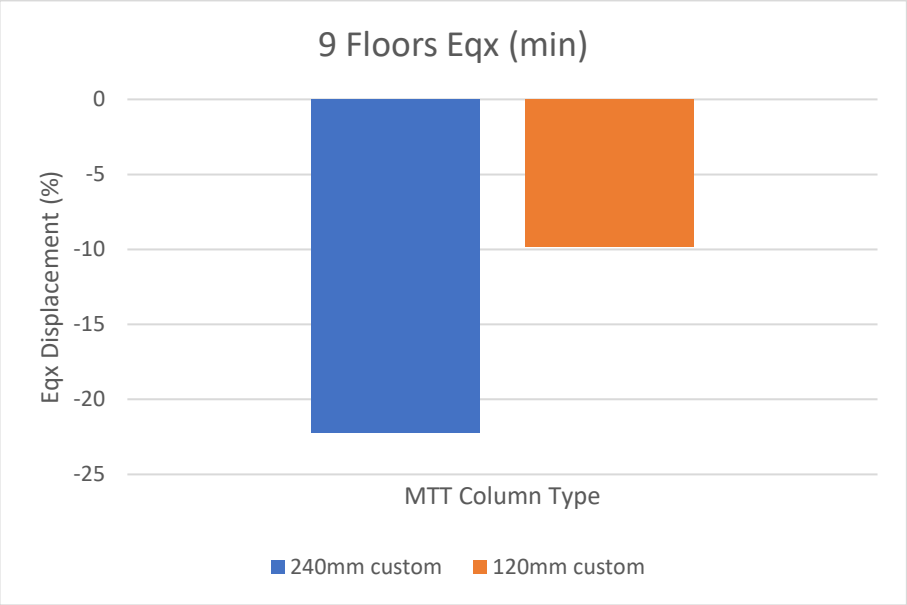
3 Floors

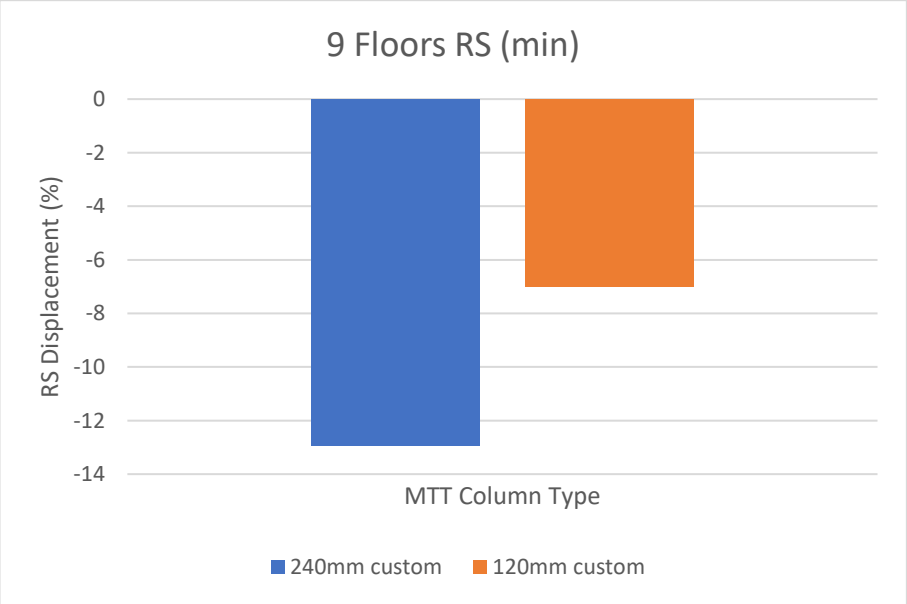



3 Floors RS (min)
0
-5
-10
-15
-20
-25
RS Displacement (%)
MTT Column Type
220mm custom
110mm custom


3 Floors Self (min)
3
2.5
2
1.5
1
0.5
0
Self-weight (%)
MTT Column Type
220mm custom
110mm custom

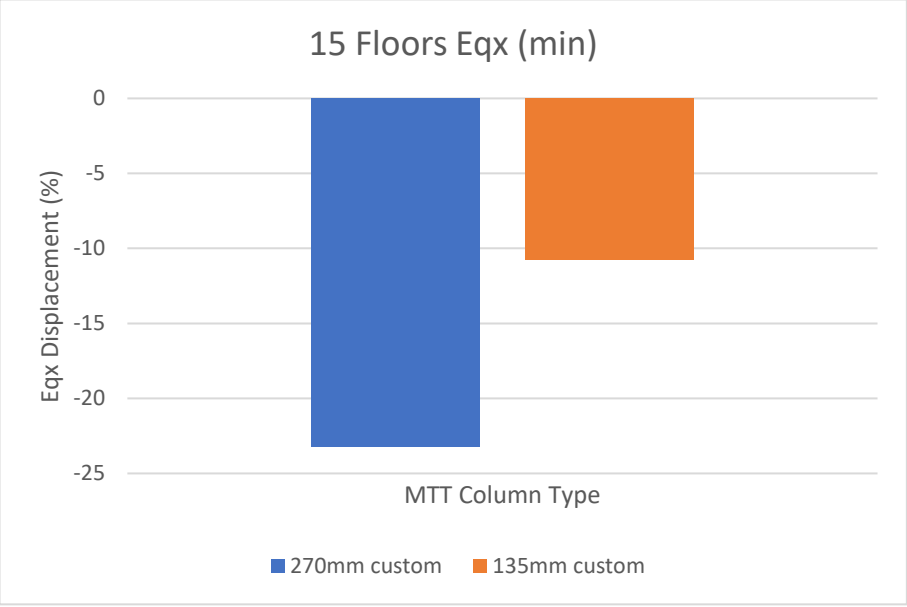
9 Floors

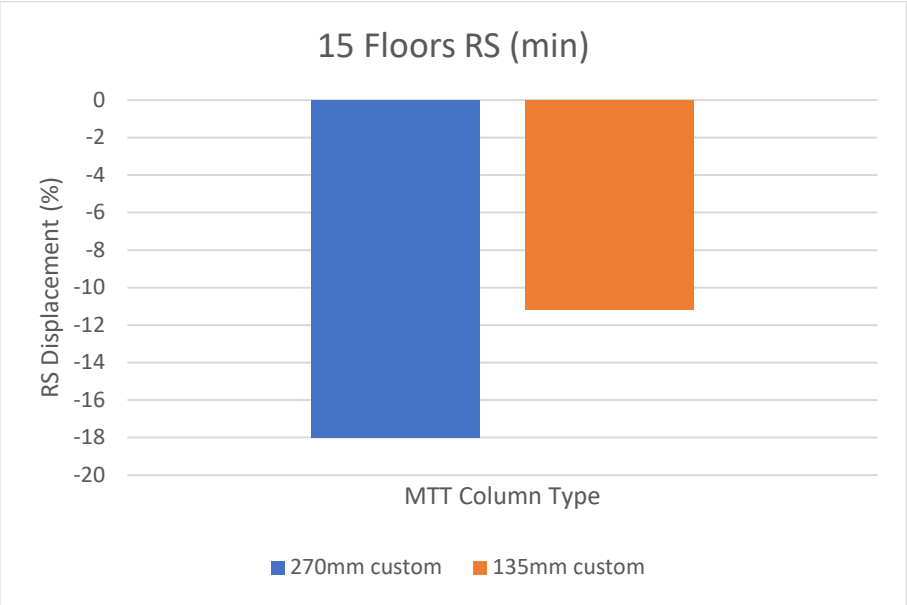

9 Floors Eqx (min)
0
-5
-10
-15
-20
-25
Eqx Displacement (%)
MTT Column Type
240mm custom
120mm custom

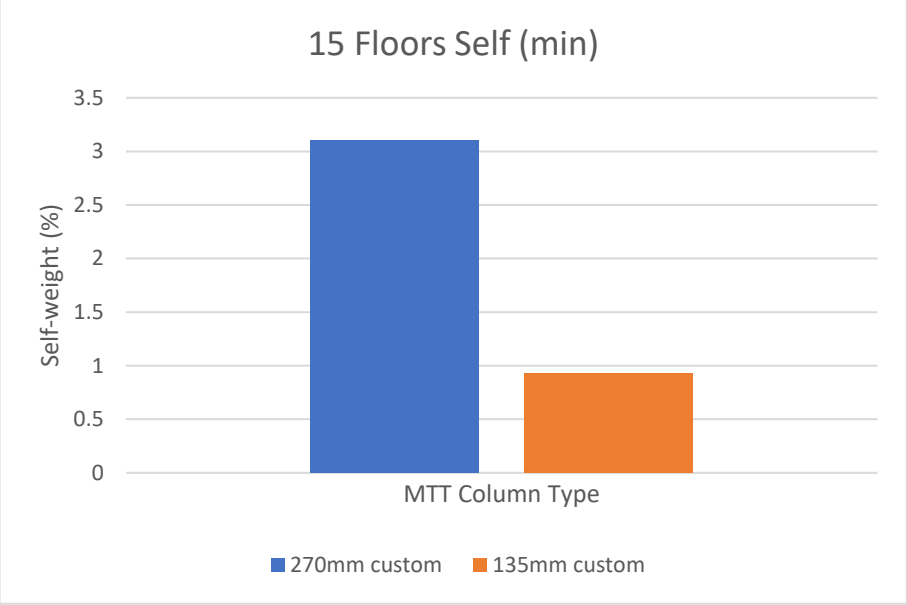

9 Floors RS (min)
0
-2
-4
-6
-8
-10
-12
-14
RS Displacement (%)
MTT Column Type
240mm custom
120mm custom


9 Floors Self (min)
3.5
3
2.5
2
1.5
1
0.5
0
Self-weight (%)
MTT Column Type
240mm custom
120mm custom

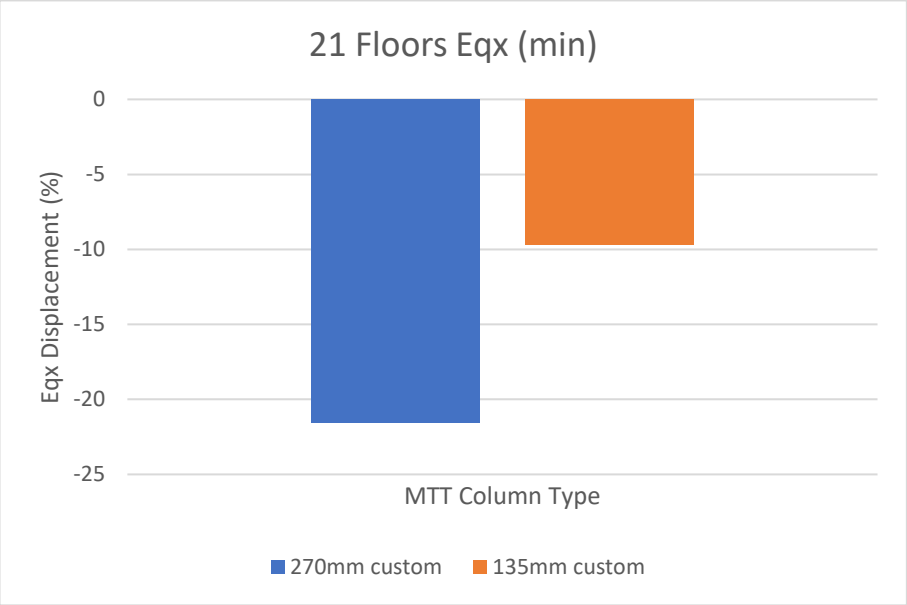
15 Floors

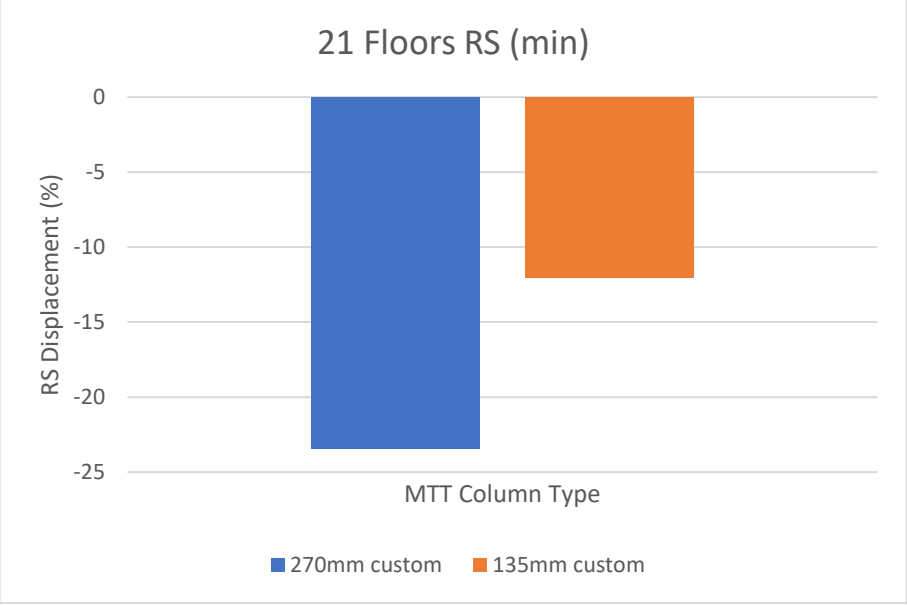

15 Floors Eqx (min)
0
-5
-10
-15
-20
-25
Eqx Displacement (%)
MTT Column Type
270mm custom
135mm custom


15 Floors RS (min)
RS Displacement (%)
0
-2
-4
-6
-8
-10
-12
-14
-16
-18
-20
MTT Column Type
270mm custom
135mm custom


15 Floors Self (min)
Self-weight (%)
3.5
3
2.5
2
1.5
1
0.5
0
MTT Column Type
270mm custom
135mm custom

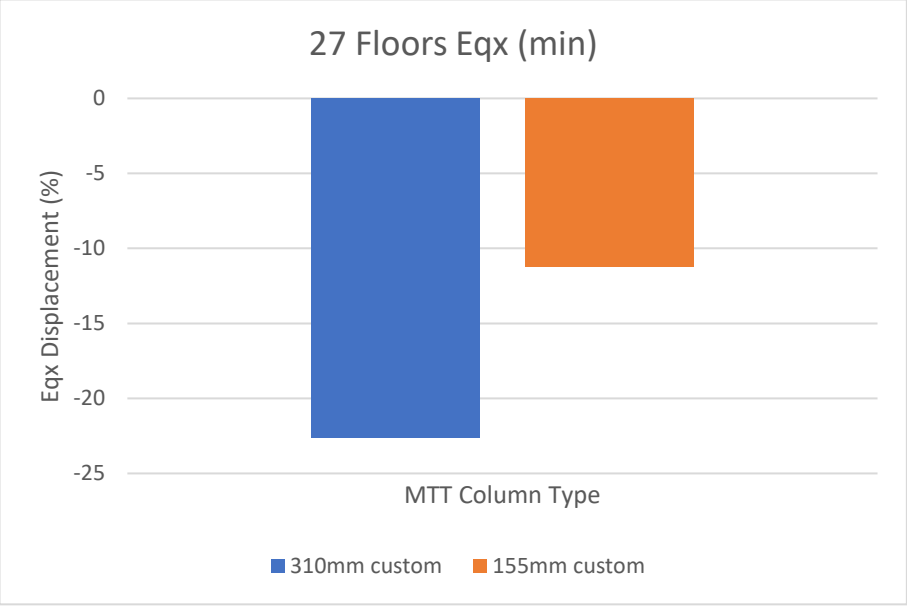
21 Floors

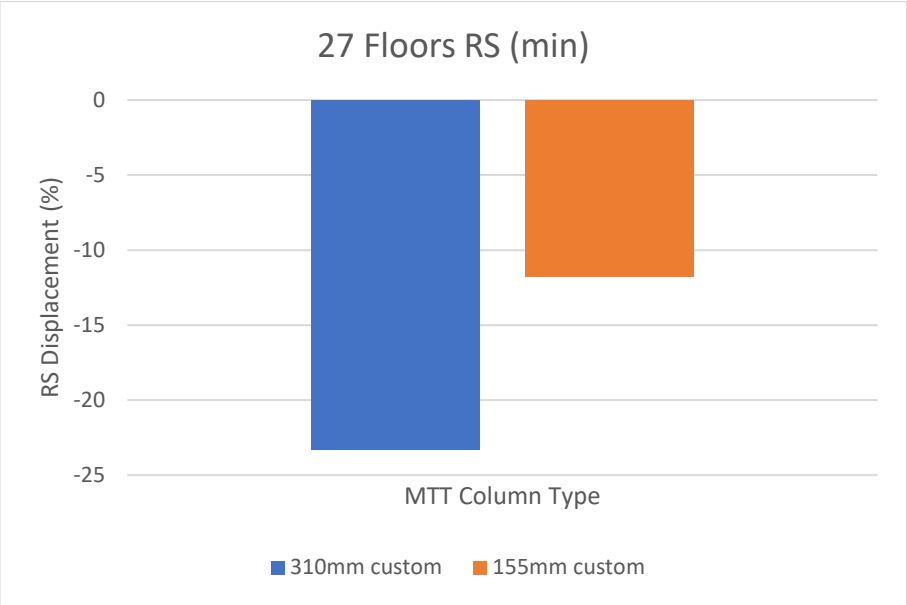

21 Floors Eqx (min)
0
-5
-10
-15
-20
-25
Eqx Displacement (%)
MTT Column Type
270mm custom
135mm custom

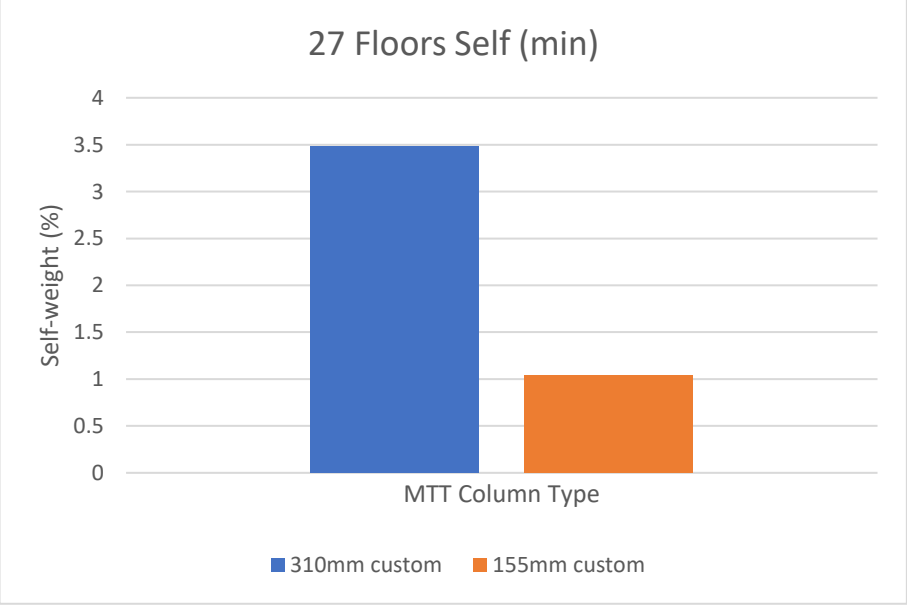

21 Floors RS (min)
0
-5
-10
-15
-20
-25
RS Displacement (%)
MTT Column Type
270mm custom
135mm custom


21 Floors Self (min)
3.5
3
2.5
2
1.5
1
0.5
0
Self-weight (%)
MTT Column Type
270mm custom
135mm custom

27 Floors

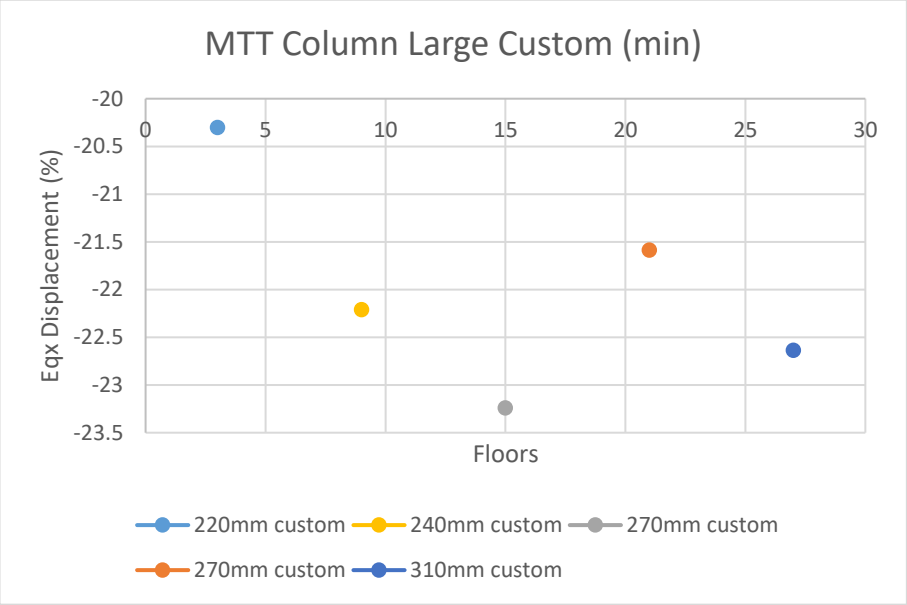

27 Floors Eqx (min)
0
-5
-10
-15
-20
-25
Eqx Displacement (%)
MTT Column Type
310mm custom
155mm custom

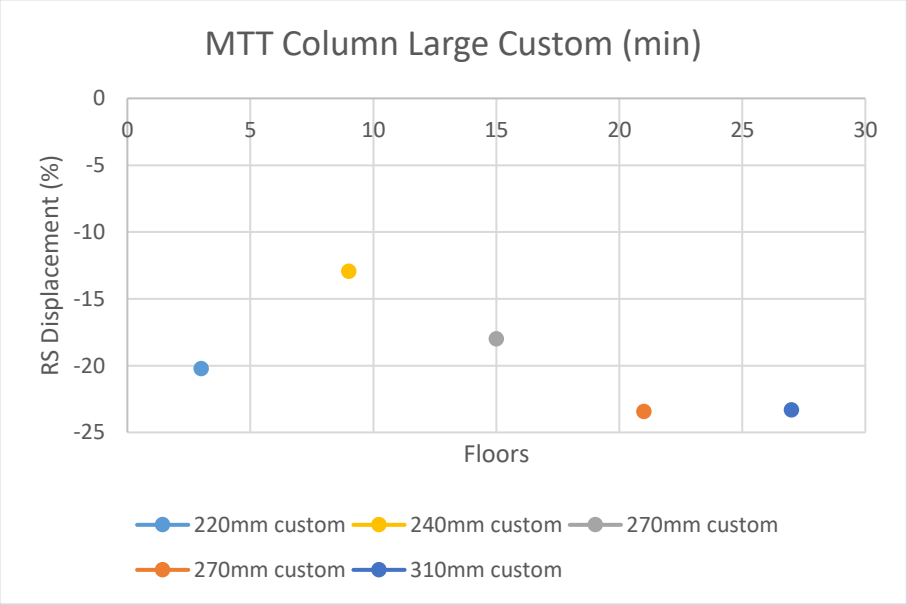

27 Floors RS (min)
RS Displacement (%)
0
-5
-10
-15
-20
-25
MTT Column Type
310mm custom
155mm custom

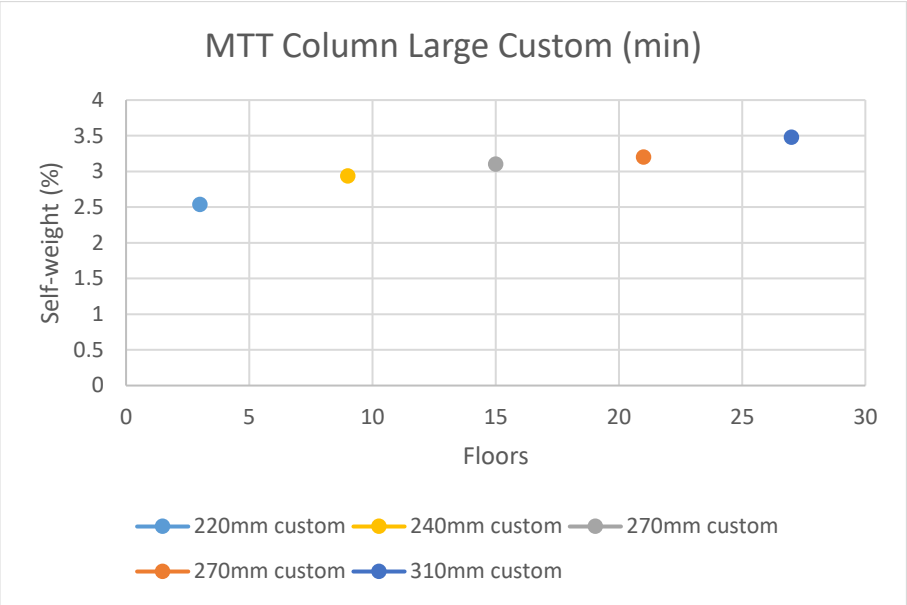

27 Floors Self (min)
Self-weight (%)
4
3.5
3
2.5
2
1.5
1
0.5
0
MTT Column Type
310mm custom
155mm custom

Across Storey Heights (Min Beam and Min Column)

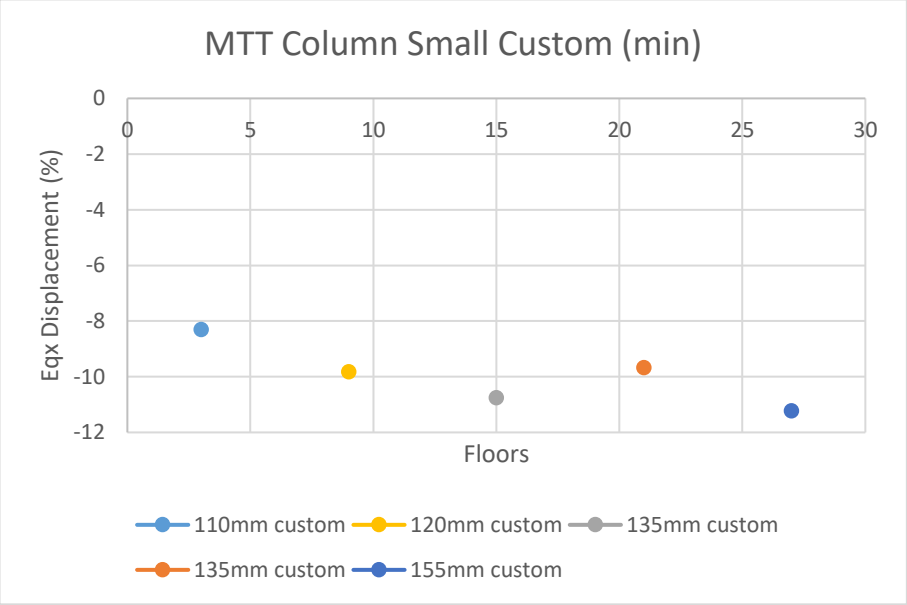
Large Section (310mm custom)

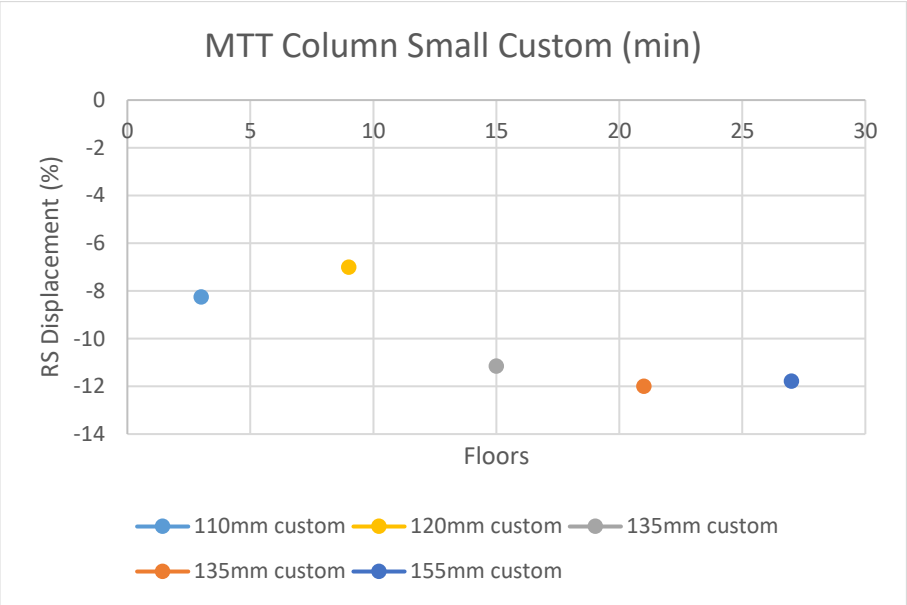


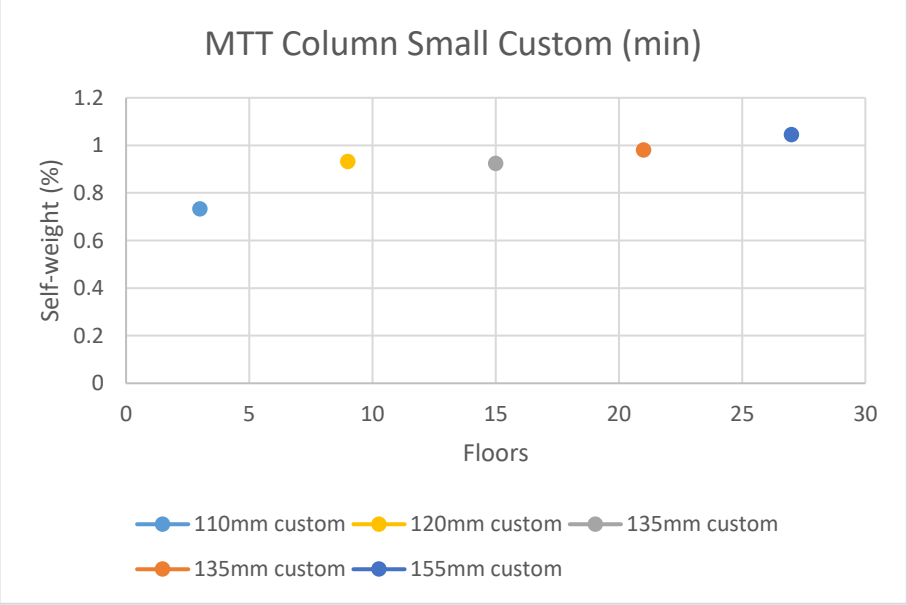




Small Section (155mm custom)




MTT Column Small Custom (min)
RS Displacement (%)
0
-2
-4
-6
-8
-10
-12
-14
0
5
10
15
20
25
30
Floors
110mm custom
120mm custom
135mm custom
135mm custom
155mm custom


MTT Column Small Custom (min)
Self-weight (%)
1.2
1
0.8
0.6
0.4
0.2
0
0
5
10
15
20
25
30
Floors
110mm custom
120mm custom
135mm custom
135mm custom
155mm custom